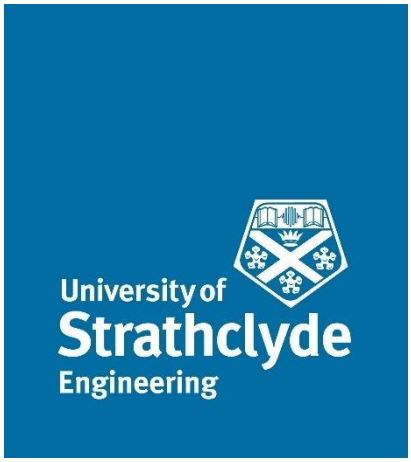

Understanding RF Gel Formation: Modelling Fundamental Nanoscale Processes for Enhanced Material Development

Elisha Martin

Department of Chemical and Process Engineering

University of Strathclyde

This dissertation is submitted for the degree of

Doctor of Philosophy

September 2021

Declaration of Authorship

This thesis is the result of the author's original research. It has been composed by the author and has not been previously submitted for examination which has led to the award of a degree.

Elisha Martin
September 2021

Acknowledgements

The completion of this PhD project would not have been possible without the help and support I've received from numerous people over the past four years and beyond. Firstly, I'd like to thank my primary supervisor, Prof Ashleigh Fletcher, although I won't be able to fully convey just how grateful I am to have had her endless encouragement and mentorship throughout my PhD. I feel genuinely privileged not only to have had Ashleigh as a supervisor, but also just to know her as a person. Her impact and influence have extended far beyond academia, and I don't believe my PhD experience could have been anywhere near as enjoyable within any other research group. I'd also like to thank my second supervisor, Dr Paul Mulheran, whose amazing expertise and guidance were invaluable, and who always set aside the time to patiently work through any issues that arose along the way. I really couldn't imagine two better supervisors.

I want to give a special thanks to Dr Martin Prostredný, whose work my PhD project built upon, and who helped me continuously throughout the four years. Martin taught me so much, both experimentally and computationally, and was always available to answer my many questions. Our weekly joint supervisor meetings with Ashleigh and Paul will always stand out as a highlight. I'd also like to thank the laboratory technicians for their help over the years, and for always being there to guide, teach, and support in so many ways.

The personal support I've received from a number of people over the years has made the completion of this PhD project possible, for which I'll always be grateful. In particular, I'd like to thank my parents, who have always encouraged me academically and supported me in so many ways. My siblings, who have become some of my closest friends; my nieces, who have always been a constant source of happiness; and my soul mates: Emma, Megan, and Charlotte, who have always been there when I've needed them most.

Finally, I want to give a very special acknowledgement to Danny, who has changed my life for the better in so many ways, and has always kept me upbeat and laughing even when things have been difficult.

Abstract

The wide-ranging application potential for porous materials has been of significant interest over the years, with a particular focus on those which possess attractive properties, such as low densities and high surface areas. Materials such as these have proven to be effective in a wide range of applications, many of which are imperative in reducing or eradicating detrimental environmental impacts of industry, heightening their pertinence to recent research. This work focuses on one such class of organic porous materials—resorcinol–formaldehyde (RF) gels—which are formed via a sol–gel process and subsequently dried, producing the lightweight, nanoporous structure of the final gel. Despite extensive research into these materials in recent years, a number of questions still remain around their formation mechanism and the impact of various parameters associated with their synthesis. As a result of this, their application potential is yet to be fully realised, especially given the wide range of properties that can be achieved through fine tuning and optimisation of the RF gel synthesis process.

In this work, the formation mechanism of RF gels is explored through both experimental and computational means. Through experimental analysis of the final textural properties of synthesised gels, the impact of variations in catalyst concentration and catalyst species are investigated, aiming to elucidate the specific role the catalyst compound plays within the RF reaction – something that, to date, has been widely debated. The importance of the metal cation within the catalyst is highlighted through the results presented here, its concentration decoupled with the initial solution pH, and the significance of both discussed in detail. The comparative efficacy of different solvents used within the solvent exchange step of gel synthesis is also investigated, measured in their ability to preserve the structure during drying, minimising the pore shrinkage and collapse that takes place. The implications of the results obtained are discussed in relation to process optimisation to achieve desirable properties applicable to specific uses.

The synthesis and analysis of RF gels is time consuming, therefore, simulating these processes computationally in an efficient manner could be pivotal to facilitating their widespread use. In this work, a three-dimensional model is developed which captures the formation and growth of RF gels using lattice-based kinetic Monte Carlo theory, accounting for varying catalyst concentration and solids content – two parameters proven to control gel properties in experimental work. The textural properties of the resulting simulated materials are analysed, including the accessible surface area and accessible porosity, the values of which reflect the increased structural density and inter-connected complexity associated with increasing solids content and catalyst concentration. Furthermore, the fractal properties of these materials are analysed through correlation dimension and Hurst exponent calculations, the results demonstrating that while fractal properties are not typically observed in scattering experiments for RF gels, they are possible to achieve with sufficiently low solids content and catalyst concentration.

As the most commonly employed method of assessing properties of porous materials experimentally, adsorption analysis was carried out computationally for the simulated RF gel structures. The results indicated that both low catalyst concentrations and low solids contents

resulted in structures with open transport pores that were larger in width, while high catalyst concentrations and solids contents resulted in structures with bottleneck pores that were narrower. Importantly, the computational isotherm data and pore size distributions were also compared to those obtained experimentally, showing a promising agreement in trends between the two for varying catalyst concentrations, providing validation for the kinetic Monte Carlo model developed.

Finally, the performance of RF gels in a specific application is tested, assessed in their ability to remove an endocrine disrupting pollutant from water through UV-Vis concentration measurements. Using the results obtained from both the experimental and computational analysis of the materials, the comparative efficacy of two RF gels synthesised under different catalyst concentrations is predicted and subsequently explored, and the properties required for optimal performance determined. This work not only highlights the potential for RF gels to be used for vital environmental applications, but also introduces the potential way in which a computational model could be used to predict and tailor the properties of these materials for maximum effectiveness in a given application.

Table of Contents

List of Abbreviations

BET - Brunauer-Emmett-Teller

BJH - Barrett-Joyner-Halenda

C_c - percentage of activated monomers

d_{avg} - average pore width

D_C - correlation dimension

H - Hurst exponent

IUPAC - International Union of Pure and Applied Chemistry

kMC - kinetic Monte Carlo

λ/λ_0 - relative activity

p/p_0 - relative pressure

PSD - pore size distribution

R/C - resorcinol/catalyst molar ratio

RF - resorcinol-formaldehyde

S_{BET} - BET surface area

S_c - solids content

γ - surface tension

V_T - total pore volume

Chapter 1: Introduction

1.1 Aerogel Discovery

The attractive properties of porous materials have proven their relevance to a wide variety of applications, with natural materials such as wood, plant fibres, volcanic rock, and cork achieving widespread use since their properties were first discovered. Although these materials are beneficial in their natural availability, as well as their sustainability as renewable resources, the inability to alter their structure for optimal efficacy in each application sets limitations on their use. Various methods were, therefore, established in an effort to produce synthetic porous materials that could be tailored according to their desired use, with the sol-gel method first applied in the synthesis of porous silica gels by Ebelman in 1846.[1,2]

The term 'sol-gel' describes the process during which a colloidal suspension of molecules within a solution (a sol) is transformed into a three-dimensional network structure, comprising of a "continuous solid skeleton enclosing a continuous liquid phase" (a gel).[3] Further processing of these gels, such as employing various drying methods, can result in the formation of lightweight, porous materials possessing various properties suitable for a wide range of applications, the details of which will be discussed in subsequent sections. In his synthesis of the first silica gel, Ebelman combined tetrachlorosilane with ethanol, the reaction between which formed an interconnected structure of molecules linked by silica bridges. These materials have been subject to extensive research since this time, including investigations of alternative silica-based reagents, explorations of gel-doping with metal alkoxides, and the direct testing of these within applications.[4,5]

In the 1930s, building upon the work carried out by Ebelman, Kistler investigated the displacement of the liquid phase within the silica gel structure, leaving a low-density, solid material with pores filled only with gas.[6] The synthesis of these gels began with the reaction between sodium silicate and hydrochloric acid (Equation 1.1), forming a silica gel with pores filled with water and sodium chloride (a hydrogel). In Kistler's early attempts at removing the liquid phase, he employed a simple ambient pressure thermal drying method, using an increase in temperature to evaporate the water within the pores, forming a class of materials now known as xerogels. As a result of the high surface tension value of water, however, the gels were subject to substantial shrinkage and structural collapse upon drying. In an attempt to preserve the gel structure throughout this step, Kistler utilised the supercritical drying method, initially enforcing the extreme conditions required for water to reach its supercritical point. Under these conditions, however, the supercritical water began to break down the silica network, leading Kistler to introduce a solvent exchange step replacing the water with ethanol before drying commenced. These silica gels, which were dried under supercritical conditions, established a new class of materials – this time known as aerogels.

$$Na_2SiO_3 + 2HCl + (a-1)H_2O \rightarrow SiO_2\ aH_2O + 2NaCl$$

Equation 1.1

1.1.1 Silica Aerogels

The synthesis process for silica aerogels continued to be refined in the studies that followed the work of Kistler, with an initial focus on time efficiency given that the supercritical drying method required a solvent exchange step to replace the water within the pores. In order to mitigate this step, Nicholaon and Teichner produced silica aerogels from tetramethoxysilane in a methanol solution, resulting in a silica gel structure with pores filled with methanol, which required less extreme supercritical conditions than water, and did not interfere with the silica structure.[7] Further work carried out at the Lawrence Berkeley Laboratory focused on the safety of the silica aerogel synthesis process, establishing alternative reagents in place of the potentially toxic tetramethoxysilane, in addition to applying CO_2-based supercritical drying, requiring significantly lower temperature and pressure conditions.[8]

1.1.2 Aerogel Development

Given the number of exceptional properties the silica aerogels produced were found to possess, they were, therefore, the focus of extensive research in the years that followed. Their attributes, although adjustable, include high porosities, large surface areas, low densities, and low thermal conductivities. They were also found to be very hydrophobic, as well as possessing a high level of optical transparency. This unique combination of properties has made them attractive for a variety of applications, as displayed within Figure 1.1.[9]

Perhaps most notably, these materials were used at NASA, who discovered that although space dust particles could be difficult to collect, it was possible to trap them within the lightweight, porous structures of aerogels.[10] Their high porosities and surface areas also lend to effective use as a storage media for dangerous substances, as drug delivery systems requiring biocompatibility, and in a variety of catalysis applications.[11] Research into their application potential also extended to the adsorption of oils and organic solvents, where their high porosity and hydrophobic nature proved effective in the removal of substances such as petrol, diesel, toluene, and benzene from water, showing promise for their use in similar environmental scenarios.[12] Not only were the silica aerogels in this study proficient as adsorbents in their first use, but it was discovered that they could also desorb the adsorbed substances, allowing them to be used at least three more times without structural change. Their low thermal conductivity also proved beneficial, which, combined with their complex porous structure, makes them very effective as thermal insulators[11,13], which could help to reduce the energy consumption of buildings and houses, or improve the thermal efficiency of refrigeration systems.

Although the first aerogels produced were based around silica, a broad spectrum of aerogels with varying elemental compositions have since been produced, now encompassing a diverse range of solid materials that possess large surface areas, low densities, and high porosities. One of the most prominent developments within this field was the discovery of resorcinol-formaldehyde (RF) aerogels by Pekala in 1989 [14] – the first organic aerogel to be synthesised, and the material that the work presented here focuses on.

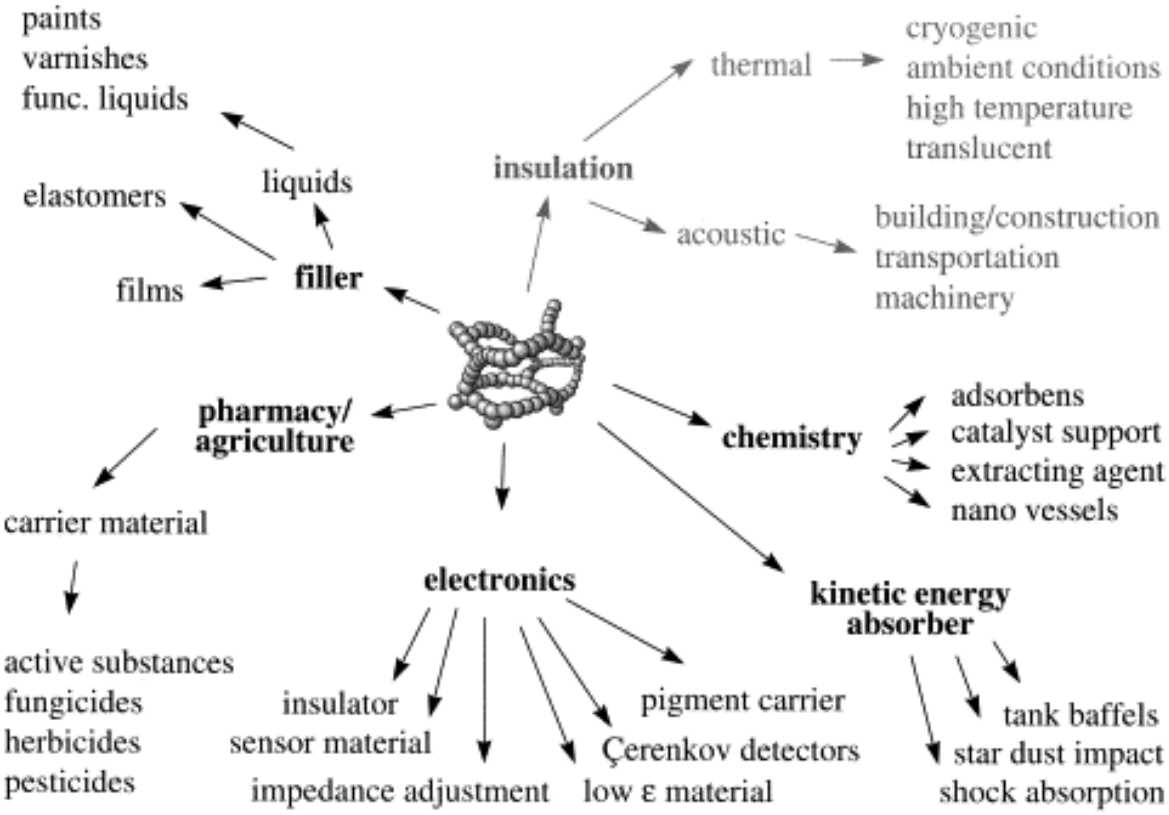

Figure 1.1: Various potential uses for aerogel materials.[9]

1.2 Resorcinol-Formaldehyde (RF) Gels

1.2.1 RF Gel Discovery

Taking inspiration from the sol-gel synthesis of silica aerogels, in addition to the CO_2 supercritical drying method established for aerogels at the same institution, Pekala investigated the base-catalysed reaction between resorcinol and formaldehyde, observing the eventual formation of a hydrogel. After a solvent exchange step replacing the water within the pores for a solvent miscible with CO_2, the RF gels were dried under supercritical conditions, leaving only the lightweight solid structure of the gel. This was the formation of the first organic aerogel, opening up new avenues for potential applications such as those requiring specific organic surface chemistry, as well as the possibility of electrical conductivity applications in the carbonised form of these materials. The application potential of these materials is discussed in detail in Section 1.4, while the preceding sections first explore the RF gel reaction and synthesis process.

1.2.2 RF Gel Reactants

Resorcinol is the common name for the chemical compound 1,3-dihydroxybenzene – an aromatic benzene ring with two hydroxyl groups; one each on the 1 and 3 carbon atoms, whose resonance forms are depicted in Figure 1.2. The presence of these hydroxyl groups results in an increased reactivity of the 2, 4 and 6 carbon atoms, due to their partial negative charge and subsequent electron donating ability.

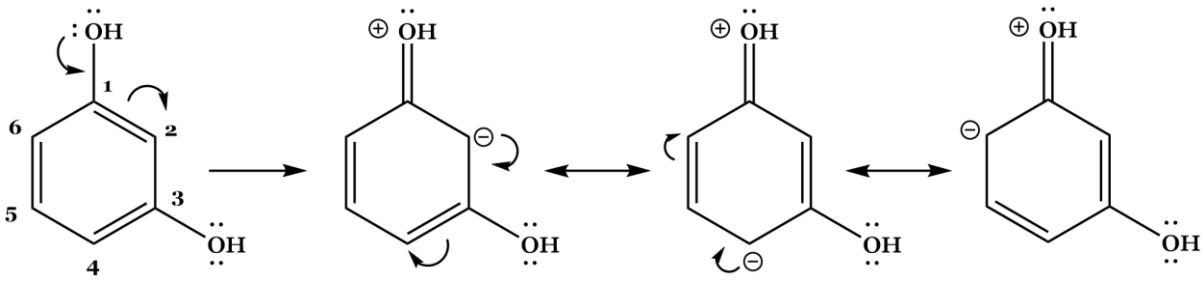

Figure 1.2: Resorcinol molecular structure with its resonance forms.

Formaldehyde, on the other hand, is the simplest of the carbonyl group-containing aldehyde family, consisting of just a single carbon atom bonded with two hydrogens and a double bond to an oxygen atom. As shown in Figure 1.3, formaldehyde can also exist in its resonance form with a single C-O bond, resulting in a partial positive charge at the carbon atom, contributing to the overall reactivity of the molecule.

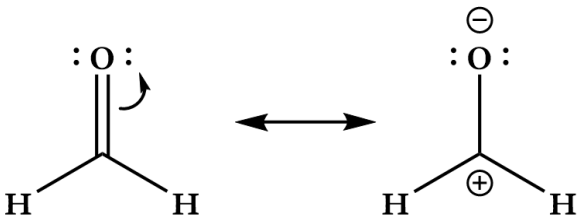

Figure 1.3: Formaldehyde molecular structure with its resonance form.

Uncatalysed Reaction

As a result of the opposing partial charges which are present within the resorcinol and formaldehyde molecules, a reaction can take place between the two when they come into contact, even with no catalyst present. However, this has been shown to take place only under specific synthesis conditions, such as high concentrations of reactants within the initial solution, as explored by Raff and Silverman.[15] Their work showed that, although the uncatalysed reaction kinetics observed are comparatively slow in contrast to those of the catalysed R-F reactions, the reactivity of resorcinol is still significantly greater in comparison

to other alternative precursors. When compared even to catalysed reactions between phenol and formaldehyde – producing a PF gel – the rate constant of the uncatalysed RF reaction was found to be substantially higher under the synthesis conditions studied. Despite this, the successful gelation of an inter-connected porous structure at lower reactant concentrations requires the addition of an acidic or basic catalyst[16] – a fundamental addition whose role is a primary focus of this work. The use of the term 'catalyst' in this application isn't entirely accurate given that the acid or base is consumed throughout the reaction, conflicting with the technical definition of a catalyst. This term is, however, widely accepted within the RF gel research field, and is therefore the term used throughout the work presented here. The reaction between resorcinol and formaldehyde molecules takes place in two stages: firstly, an addition reaction, then followed by a condensation reaction, the proposed mechanisms of which are described below.[17]

Base Catalysed Reaction

In the case where the RF reaction takes place in the presence of a basic catalyst, the addition reaction begins with the abstraction of a proton from the resorcinol molecule, forming an anion, as shown in Figure 1.4.

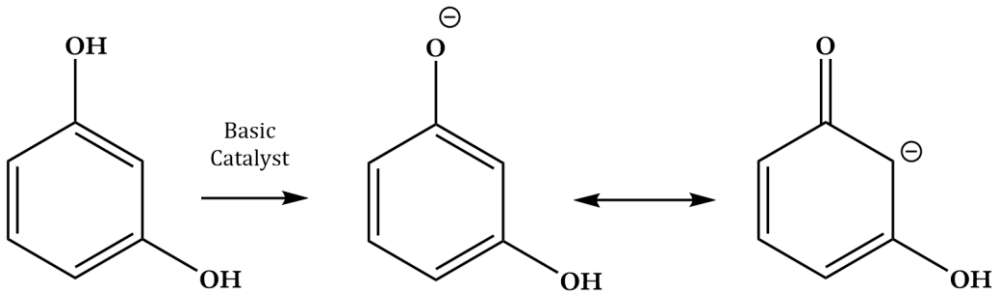

Figure 1.4: Proton abstraction from R under basic catalysis.

This abstraction subsequently leads to increased reactivity of the resorcinol molecules, and the addition reaction proceeds, typically with molecules of formaldehyde positioning themselves at two available carbon atoms on the benzene ring – the 2, 4 or 6 positions – in accordance with steric restrictions (Figure 1.5), forming a hydroxymethyl derivative molecule.

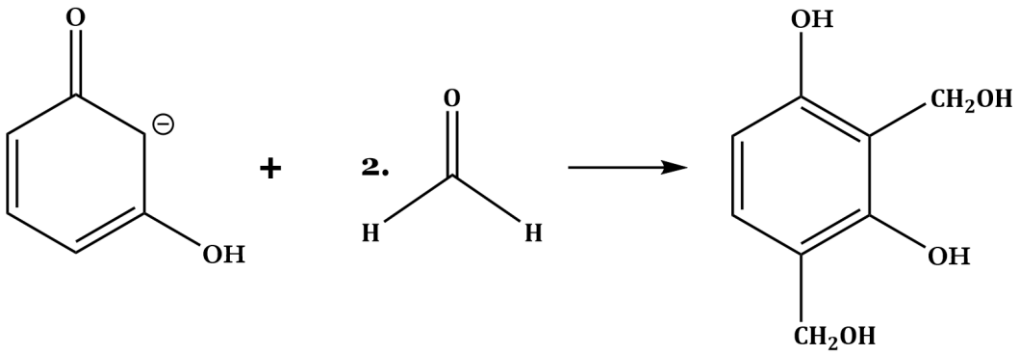

Figure 1.5: Addition reaction between R and F.

Recent work has also suggested that the reaction may take place through the addition of the hydrated form of formaldehyde (methanediol – $CH_2(OH)_2$) to the resorcinol anion.[18] In this case, as a result of the higher electronegativities of the additional oxygen within the molecule, the carbon atom possesses a partial positive charge, once again contributing to its overall reactivity. NMR studies have also pointed towards the formation of a variety of similar monomeric hydroxymethyl derivates during the reaction[19], as shown in Figure 1.6, furthering the complexity and variability of final the structure formed.

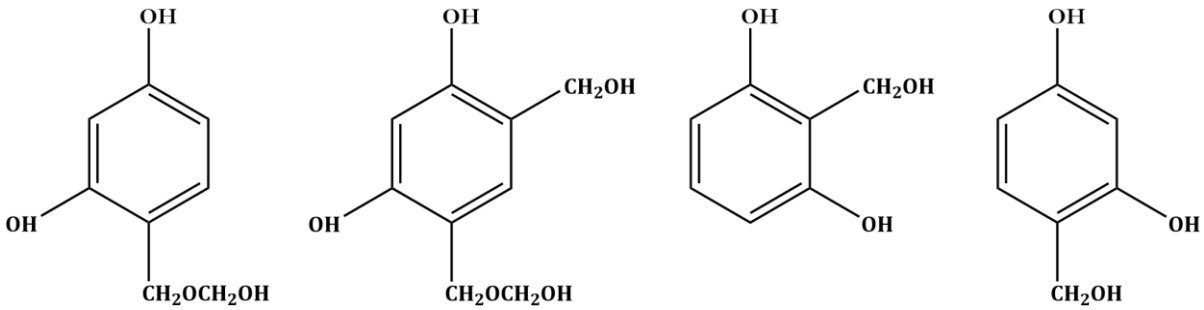

Figure 1.6: Different variations of hydroxymethyl derivates formed during the RF reaction.

The formation of these hydroxymethyl derivatives takes place quickly under basic catalysis[20], and the condensation reaction then proceeds, with the hydroxymethyl derivatives releasing H_2O as they form bridged structures, linking with other hydroxymethyl groups or with unreacted resorcinol molecules. Figure 1.7 shows the condensation reaction that takes places between multiple hydroxymethyl derivatives, resulting in the linking of molecules through methylene ether or methylene bridges. This linking process continues, with the monomers attaching to form individual clusters, and these clusters subsequently linking as the condensation reaction proceeds. The eventual aggregation of these clusters leads to the highly cross-linked network structure of the final gel.[21]

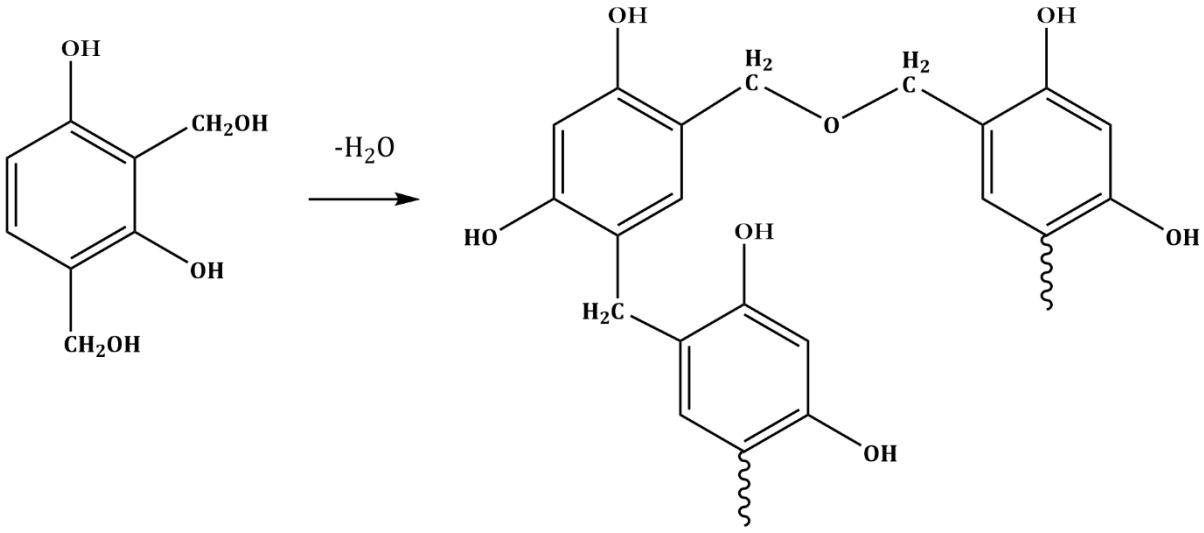

Figure 1.7: Condensation of hydroxymethyl derivatives forming bridged network structures.

Acid Catalysed Reaction

When an acid is used to catalyse the RF reaction, the addition stage begins with the protonation of both the formaldehyde and the resorcinol molecules (Figures 1.8 and 1.9). This protonation enhances the reactivity of the formaldehyde molecule, allowing it to perform effectively as an electrophile, whilst the reactivity of the resorcinol molecule is hindered.[20,22]

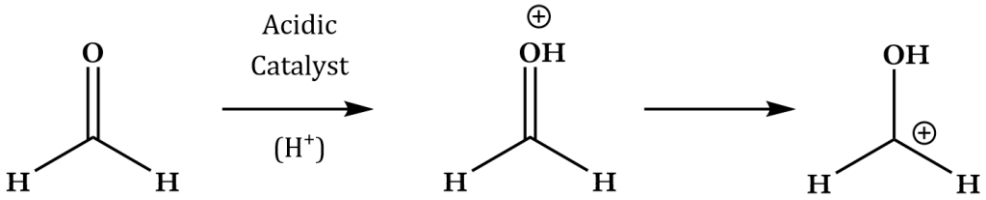

Figure 1.8: Protonation of F during acidic catalysis.

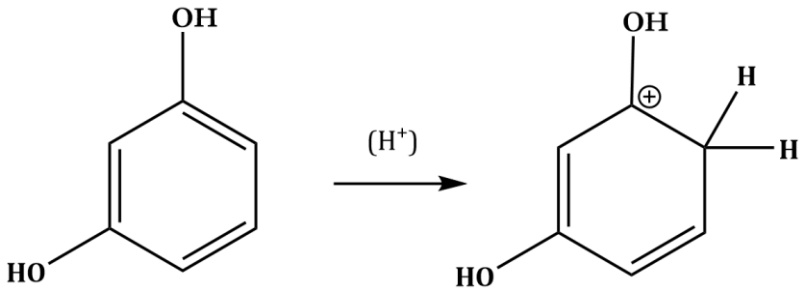

Figure 1.9: Protonation of R during acidic catalysis.

Once again, the addition reaction proceeds to form hydroxymethyl derivatives - a process which takes place relatively slowly for acidic catalysis, in contrast with that which occurs when a basic catalyst is used. The condensation step then follows as before, this time the acid catalyst increasing the rate of reaction through protonation of hydroxymethyl derivatives, shown in Figure 1.10. The hydroxymethyl derivatives subsequently form structures connected via methylene or methyl ether bridges, eventually leading to the final branched network of the gel as before.

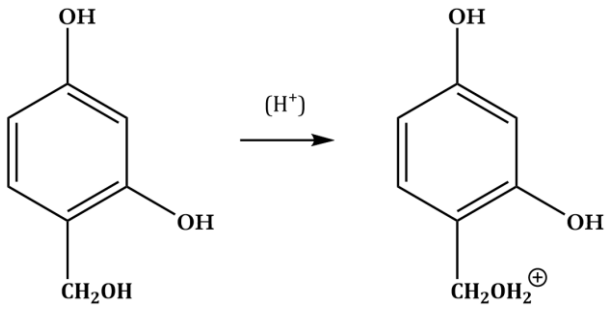

Figure 1.10: Protonation of an example hydroxymethyl derivative.

Gels produced via acidic catalysis are structurally different in comparison to those produced using a basic catalyst, both in appearance and in internal characteristics, the acid-catalysed gels producing gels comprised of branched chains of spherical clusters with lower accessible surface areas.[17,23,24] The difference in structural properties can be attributed to the

previously discussed comparative reaction speeds which take place during acidic and basic catalysis. The addition reaction under basic catalysis is fast, producing numerous hydroxymethyl derivatives which react to form many small clusters, followed by a slower condensation reaction. This is in contrast to that of acidic catalysis, where the addition reaction is slow and produces fewer clusters, followed by an accelerated condensation reaction, therefore impacting the final structure of the gel formed.[25] Furthermore, the impact of initial solution pH, both with acidic and basic catalysis, on the overall gelation time for the materials has also been studied, with peak gelation times observed for a pH of approximately 3. Although the pH used must fall within a range of pH values viable for gel formation, in general, faster gelation times are observed at lower pH values for acidic catalysis and at higher pH values for basic catalysis.[26]

1.3 Tailoring RF Gel Properties

Taking into consideration the RF gel reaction pathway, in addition to the subsequent synthesis steps established, a variety of opportunities emerge to alter the final materials and their structural and chemical properties. This can be achieved during the sol-gel reaction itself through variations in the catalyst used, as well as through the addition of doping agents. The ease with which these materials can be altered during the sol-gel process is beneficial to their widespread use, provided any additional reagents can be dissolved into the precursor solution and then remain intact as gelation takes place, their presence can help achieve a diverse range of material properties. Furthermore, vital steps within the synthesis process such as post-gelation solvent exchange and subsequent drying methods can also be significant factors in determining the final material properties, as well as additional steps such as material pyrolysis. The tailoring of RF gels for various applications is an important focus of this work, therefore, understanding the way in which each of these parameters and synthesis steps affect the final material is pivotal. This section discusses the research that has been conducted to date on various synthesis parameters, investigating the effect of each on gel properties such as pore volume, pore width, and accessible surface area, in addition to exploring how materials with electrical or fractal properties can be produced.

1.3.1 Altering The Resorcinol/Catalyst Molar Ratio

The molar ratio of resorcinol to catalyst (R/C ratio) is crucial in determining the final textural properties of the gel formed. A higher R/C ratio corresponds to a lower concentration of catalyst present, whilst a lower R/C ratio corresponds to a higher concentration of catalyst present. The impact of varying R/C ratios has been studied widely, with methods such as adsorption analysis and dynamic light scattering (DLS) being utilised to gain a deeper understanding of how catalyst concentration effects the structural growth of the gels.[27] In cases where a higher R/C ratio is used, and therefore a lower concentration of catalyst, the resulting gels are softer and pale orange in appearance, in addition to possessing larger average pore widths. This is in contrast with that of RF gels formed using a lower R/C ratio, and therefore a higher concentration of catalyst, where the resulting gels are firmer and dark red in appearance, in addition to possessing smaller average pore widths.

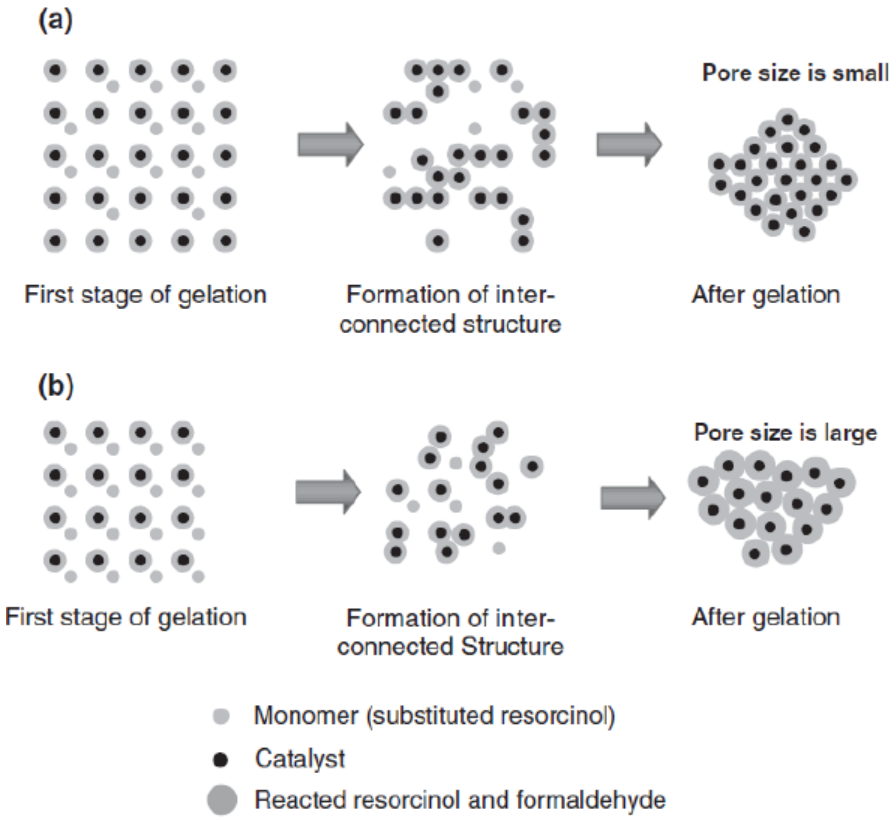

Figure 1.11: Schematic of gelation mechanism for low R/C ratios (a), and high R/C ratios (b).[17]

The increase in pore size associated with high R/C ratios is thought to be as a result of the reduced number of initial clusters formed, the growth of which produces larger final clusters, a process which takes place at a slower rate. These larger clusters subsequently have larger pores between them, impacting the textural properties and overall appearance of the resulting gels. The higher concentration of catalyst present in gels synthesised using lower R/C ratios results in a higher number of initial clusters formed, the growth of which will produce smaller final cluster sizes, a process which takes place more rapidly. Given that the clusters formed are of smaller average size, they subsequently have smaller pores between them, once again impacting the textural properties and overall appearance of the gels formed. This is shown pictorially in Figure 1.11.[17]

1.3.2 Altering Catalyst Species

The Effect of pH

When Pekala first established the process of synthesising RF gels, he made use of a basic catalyst – sodium carbonate (Na_2CO_3) – which has remained as the most common catalyst for subsequent studies.[17] As previously mentioned, acid catalysts can also be utilised, in addition to other basic compounds such as potassium hydroxide[28], lithium carbonate[27], and sodium hydrogen carbonate[29], amongst others. The nature of the catalyst, being acidic or basic, in addition to its concentration, will impact the initial pH value of the RF solution, consequently impacting the rate at which the RF gel addition and condensation reactions take

place and, therefore, impacting the final structural properties. The role of the catalyst beyond this has been subject to some debate, where many works have concluded that the pH-determining impact of the anion (CO_3^{2-} in the case of sodium carbonate) is the predominant role, if not the sole role. Other works, meanwhile, have explored the impact of the cation (Na^+ in the case of sodium carbonate), concluding that it is also significant in determining final gel properties, and that its role cannot be discounted. Both conclusions are discussed in detail below, where each of the individual studies and their findings are analysed. Direct comparisons between research presented in the literature is, however, very complex, given that the wide variety of synthesis conditions used within each study leads to the formation of materials with markedly different textural properties, some of which result in the observation of differing trends.

In an attempt to understand the role of pH alone, research was carried out by Lin and Ritter[30] which made use of dilute nitric acid (HNO_3) to adjust the initial solution pH of sodium carbonate-catalyzed RF gels. This work involved the synthesis of R/C 50 gels with initial solutions containing 5% w/v solids, which then underwent acetone solvent exchange before ambient drying, followed by gel pyrolysis. Nitrogen adsorption analysis of the final gels revealed a clear trend – as the initial solution pH incrementally decreased from pH 7 to pH 6, the resulting gel surface area increased significantly. Gels produced from initial solution pH values above 7 were found to yield almost no surface area, whilst those produced from pH values between 5.5 and 6 achieved equally high surface areas. This work highlights the crucial role of pH in the RF gel reaction, where the condensation reaction rate is increased by the presence of additional H^+ ions, resulting in the formation of increasingly cross-linked structures. Despite this, the specific roles of the catalyst components were not explored in this work, and new components were included in the system through the addition of HNO_3. This could have implications on the final gel structure, including through the potential acid-base reaction that may have taken place, with the addition of HNO_3 resulting in decreased concentration of carbonate, given that HNO_3 is a stronger acid and carbonic acid is unstable. In the cases where an acidic catalyst alone is used, studies have found that the initial mixture must possess a pH within the range of 1 - 4 in order to produce a gel with a viable structure, albeit with visual and textural properties that are distinct from those of base-catalyzed reactions.[31] Finally, initial solution pH values below 1 have been shown to result in precipitation, while pH values within the range of 4 - 5.5 have been found to be insufficient for the successful catalysis of either the addition or the condensation reactions taking place, the resulting product being a non-porous powder rather than an interlinked porous structure.[27] From experiments carried out within our research group, the pH of an initial RF gel solution with no catalyst added whatsoever is 4.1, which, as expected, fails to produce an inter-connected porous material.[16]

The role of pH was explored further by Job *et al*.[32], who synthesized RF gels using sodium hydroxide solution to achieve set initial solution pH values ranging from 5.45 to 7.35. For gels analysed after vacuum drying, as solution pH increased from 5.45 to 6.5, the material's surface area also increased from 330 to 510 m^2/g, with a decrease observed after this point at pH 7.35. Given that the increasing solution pH corresponds to increasing Na^+ concentration from the

addition of sodium hydroxide solution, the role of Na^+ could be considered in this work, however, Job et al conclude that the cation present in the standard Na_2CO_3 catalyst plays no direct role whatsoever and that pH alone is the determining factor in final gel properties. Subsequent studies have affirmed "pH-adjusting" as the catalyst's sole purpose, this becoming the general consensus within the field, with suggestions that the same effects from pH alterations could be achieved using any base that does not react with resorcinol or formaldehyde.[33,34]

The Role of Individual Catalyst Components

A small number of studies have attempted to look beyond the pH-adjusting role of the catalyst, and instead focus on the role of its components in greater detail. One such study by Horikawa *et al*.[29] investigated the impacts of changing both the anion and cation present, comparing the textural properties of pyrolyzed RF aerogels catalysed by Na_2CO_3, K_2CO_3, $NaHCO_3$, and $KHCO_3$ at R/C 50. Nitrogen adsorption analysis of the resulting gels produced isotherm profiles for each – the visual inspection of which can provide insight into both the size and type of pores present. The results revealed clear similarities, with Na_2CO_3 and K_2CO_3 gels producing visually comparable isotherms, suggesting that their structural properties were also comparable. The isotherm profiles of $NaHCO_3$ and $KHCO_3$ were also visually similar, indicating that the impact of changing cation from Na^+ to K^+ is negligible. The change in structural properties when the anion was changed from CO_3^{2-} to HCO_3^- were evident, including in the isotherm profile, the total pore volume, and the average pore width observed across the four gel samples, with HCO_3^- gels possessing larger pores with a greater total pore volume in comparison to those of the CO_3^{2-} gels. In this case, an additional complexity is involved, given that changing the anion from CO_3^{2-} to HCO_3^- also halves the concentration of metal cations present, making the specific role of each difficult to ascertain.

A study carried out by Calvo *et al*.[35] took a different approach to investigating the role of the catalyst in the RF reaction, this time producing microwave-synthesized xerogels catalysed by five different compounds - Na_2CO_3, Li_2CO_3, $NaHCO_3$, $Ca(OH)_2$, and NaOH. In this work, as opposed to synthesizing gels at a set R/C ratio, the catalyst was added until the desired pH was reached, therefore the mass of catalyst added depended on its alkalinity. No definitive trends were observed for variations in the cation used, however, clear porosity differences were evident for anion variations. Gels synthesized using hydroxide catalysts ($Ca(OH)_2$, and NaOH) possessed smaller pores, also with narrower pore size distributions, in comparison to those synthesized by carbonate catalysts. The total mesopore volumes of the gels were also significantly reduced, with hydroxide catalysed gels possessing mesopore volumes approximately one-third of those observed for gels produced from carbonate catalysts. Calvo *et al*. suggest that this could be attributable to the size of the anions used, with the larger CO_3^{2-} ions causing steric hindrances and leading to the formation of wider pores. The conclusion drawn was that the role of the anion within the catalyst is far more significant than that of the cation, however, the same complexity discussed previously still applies. Although the pH

values of the initial solutions are equal for each gel synthesized in this study, the concentration of both cations and anions vary depending on the catalyst alkalinity, therefore elucidating their individual roles is more complex.

Further research by Job *et al*.[36] included the preparation of RF xerogels using six different catalysts – LiOH, NaOH, KOH, $Ca(OH)_2$, $Ba(OH)_2$, and $Sr(OH)_2$ – once again with different masses added until the desired pH was reached. Their findings revealed distinct differences in the properties of gels formed by alkali metal hydroxides (LiOH, NaOH, and KOH, each possessing cations of M+ charge) in comparison to those of alkaline earth metal hydroxides ($Ca(OH)_2$, $Ba(OH)_2$, and $Sr(OH)_2$, each possessing cations of M^{2+} charge), with the two groups producing structures with average pore widths in the ranges of 50-80 nm and 70-100 nm, respectively. Taylor *et al*.[27,37] investigated the specific role of the cation further, this time using RF xerogels synthesized using four alkali metal carbonates - Li_2CO_3, Na_2CO_3, K_2CO_3, and Cs_2CO_3 - all prepared at equal R/C ratios, alongside their subsequent work which included alkaline earth metal carbonates, $CaCO_3$ and $BaCO_3$. Once again, gels synthesized using alkaline earth metal carbonates, possessing M^{2+} cations as opposed to M^{+} within alkali metal carbonates, comprised of pores larger in diameter alongside an observed increase in total pore volume, indicating that the role of the cation present could be significant.

Earlier research carried out by Grenier-Loustalot *et al*.[38] investigated the impact of the valency and ionic radius of the metal cation used within the catalyst for the formation of phenol-formaldehyde (PF) gels. This study found that the use of divalent cations resulted in an increased rate of formaldehyde consumption during the PF reaction in comparison to monovalent, as did the use of cations with larger ionic radii, concluding that the nature of the cation played an important role in the reaction kinetics. The study proposes a mechanism by which this could take place, where the metal cation participates in establishing an intermediate chelated molecule during the phenol-formaldehyde addition reaction, which has been reimagined in Figure 1.12 for the RF reaction.

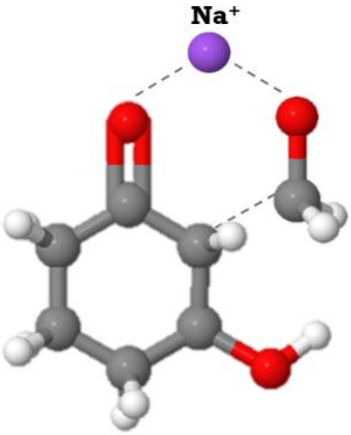

Figure 1.12: Proposed mechanism by which the Na^+ ion participates in the RF gel reaction, based on the work of Grenier-Loustalot.

The studies discussed here, which often produce variable or conflicting results, demonstrate the complexity of the RF gel formation mechanism, and the difficultly associated with accurately ascertaining the role of the catalyst within the RF reaction. The work carried out to date has provided valuable insight into the different parameters influencing the RF reaction, however, the roles of the individual catalyst components are still yet to be fully understood, particularly given the difficultly in decoupling their relationship with one another and with the resulting pH.

Ionic Solution Effects – The Hofmeister Series

Through the work carried out by Taylor *et al.*[27,37], another theory emerged suggesting that the ions present within the catalyst could contribute to RF gel formation based on their ability to 'salt-in' or 'salt-out' macromolecules from solution. This is comparable to The Hofmeister series which was established in 1888 by Franz Hofmeister[39], and which arranges ions based on the stability or instability they create for proteins in solution.

Given that RF gel catalysts studied comprise of ionic compounds, in addition to the pivotal role solubility plays in the sol-gel process, these potential effects could be an important consideration. As the mass of macromolecules increases with cluster growth, in addition to their increased cross-linking, the resulting solubility decreases, eventually reaching the point of gelation where a solid interlinked structure is formed. Investigating how different parameters impact the solubility of macromolecules, such as those observed in the RF reaction, has been the focus of various studies over the years.[40-42] Amongst the theories postulated, the kosmotropic and chaotropic effects of ions is of particular interest. Kosmotropes are compounds that promote the stability and rigidity of macromolecules, stabilising their intramolecular interactions, and facilitating the formation of ordered structures.[43] Chaotropes, on the other hand, contribute to the destabilising and disordering of macromolecules, disrupting non-covalent interactions, and hindering the formation of stable structures.[44]

(a) **Chaotropic** $SCN^- < I^- < ClO_3^- < NO_3^- < Cl^- < F^- < H_2PO_4^- < SO_4^{2-} < CO_3^{2-}$ **Kosmotropic**

(b) **Chaotropic** $N(CH_3)_4^+ < NH_4^+ < Cs^+ < Rb^+ < K^+ < Na^+ < Li^+ < Mg^{2+} < Ca^{2+}$ **Kosmotropic**

Figure 1.13: (a) Reversed Hofmeister series for anions, and (b) Hofmeister series for cations.[45,46]

As previously mentioned, the Hofmeister series was created with respect to the impact of ions on proteins in solution. For hydrophilic surfaces, the effects of anions have shown to be reversed as a result of the ion-surface interactions taking place, and the anion Hofmeister series is reversed to reflect this[46], as shown in Figure 1.13(a), while the Hofmeister series for cations is shown in Figure 1.13(b). Applying this to the hydrophilic RF gels, the traditional catalyst of sodium carbonate ($NaCO_3$), therefore, comprises of a cation with a medium kosmotropic effect and an anion with a significant kosmotropic effect. Interestingly, studies exploring the Hofmeister effects for various systems have found either partial or full reversal of the series,[47,48] with work by Schwierz *et al.*[46] concluding that the original Hofmeister

series is, in fact, the exception and not the rule. In each case, the altered series, and the mechanism behind it, will be specific to the individual system and its array of complexities - from surface functionalities, hydrophilic/phobic character, and the number of different ions present. Experimentally investigating the impact of various cations and anions within the RF reaction catalysis, particularly with respect to their positioning within the Hofmeister series, could provide a deeper understanding of their role. Still, a detailed computational study would be required to fully understand the complex mechanism by which the ions within the series stabilise or destabilise the macromolecules within the system.

1.3.3 Altering The Resorcinol/Formaldehyde Molar Ratio

In addition to the impacts of the R/C molar ratio already discussed, the impact of the resorcinol/formaldehyde (R/F) molar ratio has also been investigated. This has been carried out both under acidic and basic conditions, depending on the catalyst used, and a similar trend observed for the resulting impact on final gel properties.[49]

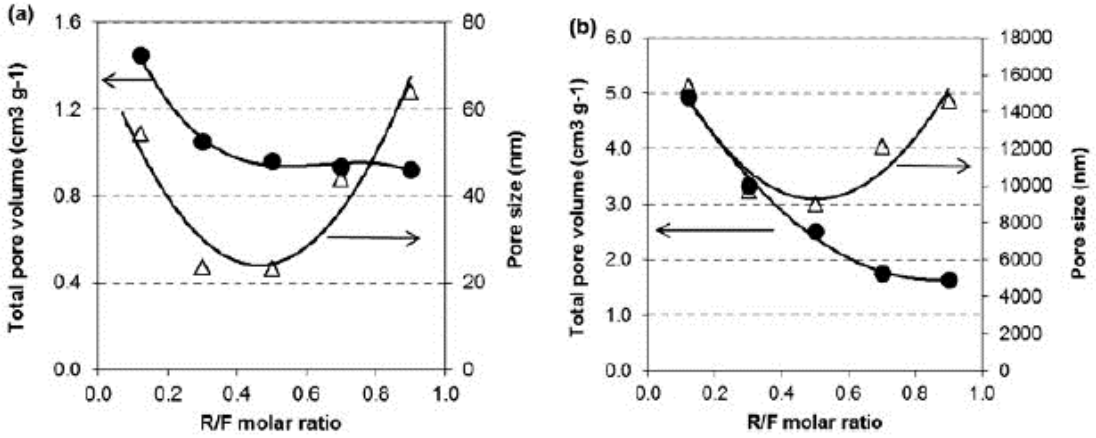

Figure 1.14: Effect of varying R/F ratio on pore size (Δ) and total pore volume (•) for basic catalysis (a, left) and acidic catalysis (b, right).[49]

The stoichiometric coefficients of the resorcinol-formaldehyde addition reaction are at a ratio of 1:2, corresponding to an R/F molar ratio of 0.5. An increase or decrease in this value, therefore creating a limiting reactant, results in an increase in average pore size, as can be seen from the graphs in Figure 1.14(a) and (b) for basic and acidic catalysis, respectively.[49] This is attributed to the increased difficulty resorcinol and formaldehyde molecules have in locating one another efficiently, leading to a decrease in the reaction rate, allowing time for larger clusters to form with larger pores between them. At low R/F ratios, where there is an excess of formaldehyde, the structure formed is highly branched with a comparatively higher mechanical strength, therefore resulting in reduced pore shrinkage during the drying stage of gel synthesis.[50] As a result of this reduced shrinkage, gels with R/F ratios less than 0.5 (excess formaldehyde) consequently possess higher values of total pore volume, whilst those with R/F ratios greater than 0.5 (limited formaldehyde) possess lower total pore volumes, despite their average pore widths following similar trends. Although most works – including that which is presented within this thesis – maintain the stoichiometric coefficient ratios for R and

F (an R/F ratio of 0.5), the results presented in Figure 1.14 show yet another way in which the properties of RF gels can be adjusted.

1.3.4 Varying Methods of Drying

In order for these materials to be classed as aerogels, supercritical drying must take place after gelation, where the system is heated past the critical temperature and pressure of the pore fluid to take it to its supercritical state. With this approach, the fluid is removed from the pores without forming a vapour-liquid interface, therefore no meniscus is formed, and the structural collapse associated with capillary pressure is minimised, as will be discussed further in the following paragraphs. This is commonly carried out using CO_2, and in such cases it is essential that the water present within the gel structure is exchanged for an organic solvent before drying, ensuring that the liquid within the pores is miscible with the liquid CO_2.[50] Following this, the first step within the supercritical drying process can be carried out, where the pore solvent is replaced with liquid CO_2, often through multiple washes. After being taken to its supercritical state, the pressure within the system is slowly reduced and the CO_2 within the pores is consequently removed in a gaseous state, resulting in a solid material with pores filled only with gas.[51]

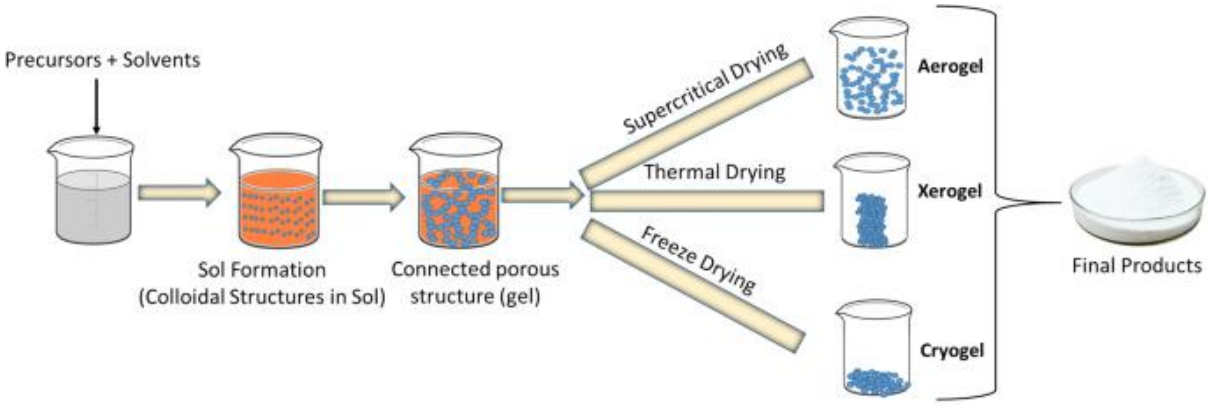

Figure 1.15: Sol-gel process to form aerogels, xerogels, and cryogels. [52]

The efficacy of supercritical drying, the process of which exerts little stress on the pore walls, is evident in the minimal pore shrinkage (<5%) observed in the final aerogel structure.[51] Despite this, the use of supercritical drying does present some disadvantages: it is a costly process which requires specialist equipment, making it much less appealing for industrial applications. Research into alternative drying methods led to the formation of two new classes of nanoporous materials: xerogels and cryogels. The latter makes use of a freeze drying process, whereby the liquid contained within the gel pores is frozen, then subsequently removed via sublimation, resulting in the final cryogel material.[53] Xerogels, on the other hand, make use of subcritical drying conditions, where the liquid within the pores is removed simply through evaporation from heating.[25] Although the subcritical drying method is advantageous in that it is a more cost-effective approach to drying than supercritical or freeze-drying, it can result in substantial shrinkage of the porous structure.

The mechanism by which shrinkage takes place within porous materials is generally attributed to the presence of capillary forces, which arise during drying as a liquid-vapour interface forms within the pore at the meniscus. The resulting stress is determined by a number of parameters, described by Equation 1.2, where P_r is the pressure due to capillary forces (also known as the capillary stress), γ is the surface tension of the liquid-vapour interface, θ is the contact angle of the meniscus to the pore wall, and r is the pore radius.[50,54,55]

$$P_r = \frac{2\gamma cos\theta}{r}$$

Equation 1.2

If the solid structure is not sufficiently strong to withstand these capillary forces, the pore walls become drawn inwards, consequently leading to shrinkage and collapse. The surface tension of the liquid within the pores is particularly important in determining the strength of these forces, the value of which is especially high for water due to the attractive forces between the water molecules themselves, therefore leading to significant structural collapse upon drying.

Another proposed mechanism that is often used to describe shrinkage within very fine pores, studied predominantly in relation to concrete mixtures – a comparable area of research focusing on the drying of porous structures – involves disjoining force theory. This theory postulates that attractive forces exist between the surfaces of the pore walls, separated by just a short distance in structures with narrow porosity, and that these attractive forces are resisted by repulsive forces when the pores are filled with water. As evaporation of the water takes place during drying and these repulsive forces are no longer present, the attractive forces between the surfaces causes the pores walls to contract, therefore shrinking the structure.[56,57] Although this has been theorised mostly in relation to concrete mixtures, it could also be a consideration for the evaporative drying of RF gels, particularly for low R/C ratio gels which possess very fine porosity, where this theory could be applicable.

1.3.5 Varying Solvent Exchange Species

Discovering ways in which structural collapse during subcritical drying can be reduced is an important focus of this research, allowing for a cost-effective process which reflects the original structure of the gel's porous network as accurately as possible. Various steps can be taken to achieve this, such as evaporating the liquid under vacuum pressure conditions, in addition to treatment of the gels prior to drying. For example, exchanging the water within the pores for a lower surface tension solvent is a common practice within RF gel synthesis, as previously mentioned. This reduced surface tension at the interface between the solvent and the pore wall means that, when the solvent is evaporated during drying, the capillary stress is reduced in accordance with Equation 1.2, and the resulting pore shrinkage is therefore reduced. Acetone is commonly used during this solvent exchange step, which possesses a substantially lower surface tension than that of water (see Table 1.1), although some other solvents have been utilised in previous research such as ethanol for the production of xerogels[58], in addition to methanol, isopropanol and amyl acetate for the production of aerogels.[59] Recent research has also discussed the use of two non-polar solvents: heptane

and hexane for solvent exchange with gels whose surface chemistry had been modified to possess water-repelling chemical groups to enhance the solvent exchange process.[55] Despite this, research into the comparative efficacy of different solvents for this step in RF gel synthesis is lacking, therefore, the various factors impacting their performance is not fully understood. One study exploring the optimisation of the solvent exchange step used azeotropic distillation with n-butanol and amyl acetate for the removal of water from the gels, after which point they were washed with acetone and air dried in an oven.[60] In comparison to gels exchanged with acetone under a standard solvent exchange procedure, the total pore volume increased significantly, the resulting value more than doubling for gels that used azeotropic distillation with amyl acetate. In this study, the solvent present within the pores when drying remained as acetone for each, therefore, not providing a direct comparison of solvent species used for the drying stage. It does, however, demonstrate the limits of the standard solvent exchange procedure, indicating that complete exchange of the water within the pores for acetone is not achieved. Only one study was found to directly compare solvents in their performance during drying, with research by Kraiwattanawong *et al.*[61] comparing the use of t-butanol, toluene, acetone, ethanol, and water, for evaporative drying under both ambient pressure conditions and vacuum. The properties cited within this publication for each of these solvents are given in Table 1.1, below, where the surface tension values are taken at 25°C.

Table 1.1: Surface tensions and polarity index values for solvents discussed. Values taken from Kraiwattanawong *et al.*[61]

Solvent	Surface Tension (mN/m)	Polarity Index
Water	71.99	9.0
Ethanol	21.79	5.2
Acetone	23.46	5.1
Toluene	27.93	2.4
t-Butanol	19.96	4.1

The results showed t-butanol as the most effective solvent for reducing pore shrinkage, which was attributed to its low surface tension. Following this logic, based on surface tension, ethanol would be assumed as the next most effective solvent. Despite this, ethanol performed the worst, with the R/C 200 gels which had been exchanged with ethanol performing especially poorly. The research concluded that the polarity index of the solvent played a significant role, given that the polarity of ethanol is marginally higher than that of acetone, and overall the highest of the solvents used in the experiments, excluding water. The reported surface areas of the gels prepared within this study showed some significant differences between those which used ethanol during the solvent exchange step and those which used acetone, despite acetone being less polar by just 0.1 on the polarity index, and also possessing a higher surface tension than ethanol. This difference was particularly prominent at R/C 200, where the vacuum dried gels for acetone and ethanol possessed surface areas of 590 m^2/g and 130 m^2/g, respectively. Furthermore, the R/C 200 ethanol gels which were dried under vacuum pressure performed worse than those under ambient pressure drying; the ambient dried gels possessing a surface area almost double of that of the vacuum dried gels. This is in contrast to the performance of the rest of the samples within the study, all of which showed an increased

surface area for gels dried under vacuum in comparison to ambient, as would be expected due to the reduced pore shrinkage as a result of vacuum drying. Anomalies such as these invite further research into the effectiveness of different solvents used during the exchange step within the RF xerogel synthesis, allowing the process to be optimised for gels with minimal pore shrinkage, and an understanding of the various factors affecting the pore shrinkage to be obtained.

As mentioned previously, a comparable area of research and optimisation is within the synthesis and drying of concrete mixtures, where finding the most effective methods to preserve the structure is paramount, with numerous studies focusing their efforts on minimising structural collapse during drying. This research has led to the development of commercially available shrinkage-reducing admixtures (SRAs), which are surfactants that are added to the concrete mixture during synthesis, achieving a considerable reduction in shrinkage and cracking upon drying by decreasing the surface tension value of the liquid entrained within the structure. [57,62-65] Although this takes a different approach from the solvent exchange method employed within RF gel synthesis, the development of SRAs demonstrate the value of research within this area, with the ongoing optimisation of each aspect within the RF gel synthesis process proving worthwhile for achieving optimal material properties.

1.3.6 Altering Solids Content

Another synthesis parameter that plays an important role in determining the final structure and density of the RF gel is the concentration of solids in the precursor solution. Different studies express the solids content of their system in various manners, such as weight per volume percentages (w/v %), resorcinol to water molar ratio (R/W ratio), and dilution ratio (D), which is calculated as the molar ratio of total solvents to reactants.

Work by Job *et al.*[66] explored the comparative structural properties of aerogels, xerogels, and cryogels synthesised with varying solids contents. In both aerogels and cryogels, lower solids percentages produced materials with larger total pore volumes in addition to larger pore widths, although their structures were found to be brittle and delicate, unable to withstand handling without damage. Variations in solids content during xerogel synthesis, on the other hand, had minimal impacts on the final structural properties within the range of conditions studied, which may have been as a result of the shrinkage that would have taken place upon ambient drying, concealing potential differences in the original hydrogels. This may be especially true for materials with lower solids contents, whose structures were found to be less robust and may, therefore, be more susceptible to shrinkage, reducing the pore volume and pore width that may have been larger in the original low-solids hydrogel. Importantly, studies have also found that the percentage of solids used within the initial gel solution has a substantial impact on the final accessible surface area of the material, with increases in solids content resulting in increases in surface area as the structure becomes more densely packed.[66-69] Despite this, while higher solids percentages increase the potential for surface area available within the material, if the structures become too densely packed then this may reduce the accessibility of surface sites, and therefore an optimal balance between the two must be achieved.

Interestingly, previous studies have also indicated that the concentration of solids within the system may impact the fractal properties of RF gels[24] – something that is largely considered unattainable for these materials, in contrast to their silica counterparts. The possibility of fractal properties within RF gels is discussed in more detail in Section 1.3.7 and is explored further through the work presented here.

1.3.7 Fractal RF Gels

Another route for RF gel tailoring has included exploring the potential for RF gels to exhibit fractal properties, the results of which have been a point of contention across various studies. Over the years, research has been conducted into the fractal properties of RF gels using Small-Angle X-Ray Scattering (SAXS) measurements, with different studies reaching conflicting conclusions. Some studies have categorically concluded that RF gels – unlike their silica gel counterparts – do not possess any fractal properties whatsoever. This includes a study by Pekala and Schaefer[70] which carries out SAXS analysis on base-catalysed RF aerogels. The results obtained show no fractal properties for any of the materials studied, although the authors suggest that fractal behaviour may be possible for samples synthesised with particularly low densities. The results of subsequent studies have pointed towards the possibility of some fractal properties of the gels under certain conditions, with a general consensus yet to be reached. If fractal properties can be observed under specific synthesis conditions, this could be a valuable development, opening additional lucrative avenues for their application potential.

Research published by Tamon and Ishizaka[71] used SAXS analysis to assess the fractal properties of RF gels at different time intervals throughout their gelation process, as well as after a period of aging. The early measurements taken during cluster formation pointed towards mass fractal properties, with subsequent measurements indicating surface fractal properties as particle and structural formation proceeded over time. Analysis was carried out once again after a period of aging following gelation, at which point no fractal properties were observed within the final gel, despite the fractal properties observed throughout the gelation process. Berthon *et al.*[24] also carried out SAXS analysis of RF gels which had been synthesised at two different solids percentages using both acidic and basic reaction conditions, as well as using both acetone and water as solvents for the sol-gel process. The results of this work indicated that fractal properties could be observed for RF gels synthesised at low solids percentages (5%) under acidic reaction conditions using acetone as a solvent, with calculated surface fractal dimension values of 2.5. RF gels synthesised at higher solids percentages (20%), however, did not exhibit any fractal properties, nor did those synthesised under basic conditions at any solids percentages studied.

Further research was carried out by Sharma *et al.*[34] which made use of the box counting method to analyse the fractal properties of RF gels through scanning electron microscopy (SEM) imaging, this time exploring the impact of an additional step within the traditional synthesis process established by Pekala. In this study, spherical droplets of the RF solution were added slowly to cyclohexane alongside a surfactant (non-ionic sorbitan monooleate,

known as Span-80) and the mixture was agitated for various time periods. SEM analysis revealed images of layered fractal-like structures in addition to highly folded, fractal-like carbon "flowers" for materials synthesised at various catalyst concentrations, surfactant concentrations, and stirring times. As the publication identifies, these materials are visually markedly different from those obtained within previous studies over the years, and their textural properties also vary significantly, possessing far lower pore volumes and total surface areas. This suggests that the additional synthesis step introduced by this work – although intriguing in its ability to produce fractal structures – does not produce materials structurally comparable to traditional RF gels.

More recently, research published by Alshrah *et al.*[72] analysed the relationship between fractal and thermal properties within these materials. Following SAXS analysis, the surface fractal dimension (D_s) values were reported for gels synthesised at different catalyst concentrations, as well as dilution ratios of 10, 18, and 22. The D_s values obtained ranged between 2.05 - 2.25, with values below 3 suggesting that the materials do in fact possess fractal properties under the synthesis conditions studied. The dichotomous conclusions reached as a result of the different studies carried out over the years reinforces the unanswered questions around the fractal properties of RF gels, the exploration of which is a focus of the work presented here.

1.3.8 Electrically Conductive RF Gels

Another way in which organic materials, such as RF gels, can be tailored to produce useful properties is through carbonisation, which is an imperative step for any application requiring electrical conductivity. The process of carbonisation, also known as pyrolysis, involves exposure to high temperatures within an inert atmosphere, subsequently removing hydrogen and oxygen from the RF gel structure. This leaves only a network of carbon atoms forming the structure, which reportedly possesses exceptional electrical conductivities ranging between 25 and 100 S/cm.[73] In addition to producing electrically conductive materials, the carbonisation process both shrinks the gel structure as well as opening new available pores as a result of carbon burn-off, leading to the formation of highly microporous materials.[74,75] This increased microporosity (pores < 2 nm in width) could enhance the performance of RF gels within a wide range of adsorption applications, with the materials typically comprised largely of just mesopores (2 – 50 nm) and macropores (> 50 nm) prior to carbonisation, although this does vary with other synthesis parameters.

1.4 RF Gel Applications

As discussed in Section 1.1, silica aerogels have proven their efficacy in a wide range of applications as lightweight, porous materials. Similarly, the exceptional properties of natural carbon materials such as graphene have been utilised in various applications and technologies. Despite the many attractive attributes of natural carbon materials, their application potential is somewhat limited by the fixed nature of their structure, and synthetic carbon materials with tuneable characteristics subsequently emerged as a new alternative. Organic gels, such as RF gels, are amongst these alternative materials, combining the extraordinary properties of carbon-based materials with the tailorability of aerogels,

producing materials whose structural and chemical properties can be optimised according to the desired use. Although significant research into organic gels has been carried out over the years, and their application potential made evident, the number of related patents remains relatively low. The full application potential for these materials, therefore, is still yet to be entirely realised and actioned.

1.4.1 Electrochemical Applications

Supercapacitors

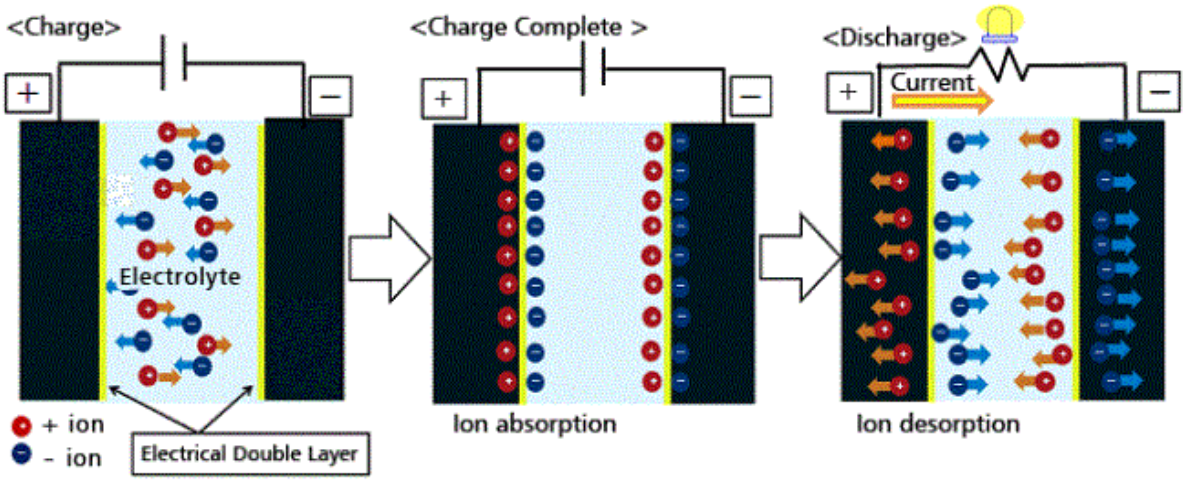

Figure 1.16: Schematic of electrochemical double layer capacitor (EDLC).[76]

Electronic and energy storage devices are now, of course, a central part of modern life, and research into their optimisation has therefore been crucial to their ongoing development. Supercapacitors, or electrochemical double layer capacitors (EDLCs), are often used within these devices, and are comprised of two conductive electrodes possessing opposing charges, separated by an electrolyte solution and a conductive membrane, as shown in Figure 1.16. Depending on the device, the required properties of the electrodes may vary, including the pore size, pore volume, accessible surface area, and the degree of surface affinity for the chosen electrolyte. For maximum power and ion transportation, the pore size must be wide enough to facilitate the diffusion of electrolyte ions, whilst also being narrow enough to produce large overall surface areas throughout the material. As discussed, the tuneable properties of organic gels, in addition to their ability to perform as conductors following pyrolysis, make them strong candidates for use as electrodes in these applications. The performance of RF gels as supercapacitors has been studied[77-82], with investigations carried out into the impacts of synthesis conditions such as catalyst concentration, drying methods, gelation temperature, and pyrolysis temperature for optimisation within specific systems. All studies report positive findings, showing the promise for RF gel use as supercapacitors commercially, particularly those cost-effectively produced from ambient drying.

Capacitive Deionisation

In addition to the potential use of organic gels as adsorbents for water purification, discussed further in subsequent sections, they have also proven effective as electrodes for capacitive deionisation applications removing ionic substances from water systems. The capacitive deionisation process is similar to that of EDLCs, with a voltage being applied to carbonised gel electrodes as an ionic solution is passed through, causing ions to be drawn to the electrode of opposing charge, thereby purifying the water. Studies have focused on the removal of sodium chloride from aqueous systems, finding that these electrodes can be regenerated for repeated use, and suggesting their use for the treatment of brackish water for environmental purposes.[83-85]

1.4.2 Catalysis Applications

In order to enhance the performance of catalysts within chemical reactions, materials known as catalyst supports are often used as a means to maximise the surface area across which the catalyst is distributed. A number of studies have been conducted into organic gels in catalyst support applications, including in the gold-catalysed oxidation of glycerol[86], platinum-catalysed fuel cell applications[87], as well as platinum-on-carbon catalysts commonly used in industry.[88] For many applications, the fine-tuning of the material properties is imperative, with work carried out by Rodrigues *et al.*[86] demonstrating the significant impact pore size can have on catalyst performance, to the extent that reaction products can be altered. Not only this, but although higher surface areas are conducive to maximised performance of the catalyst, this must be balanced with the likely increase in microporosity associated with increased surface area, meaning the accessibility of the pores may be reduced for larger reactants, therefore inhibiting the catalysis process.

1.4.3 Insulation Applications

Developing materials capable of preserving thermal energy and reducing heat losses to the environment is an important aspect of our progression towards a more sustainable future. A material's ability in preserving this thermal energy is dependent on its thermal conductivity – a property that was analysed early on in the RF aerogel development.[89] Since this time, multiple studies have explored this further, some even incorporating additional materials to enhance their thermal and mechanical properties.[90,91] Low thermal conductivity values have been consistently obtained for the materials studied within different works, with research carried out by Rey-Raap *et al.*[92] producing xerogel materials which possessed thermal conductivity values similar to that of industrial insulators, demonstrating their potential for high performance and efficacy in insulation applications.

1.4.4 Gas Adsorption

Once again proving their effectiveness in a range of environmental applications, organic gels have been used for the adsorption and storage of gases, acting as a filter for harmful pollutants such as carbon dioxide (CO_2), or alternatively facilitating the safe adsorption and storage of promising green energy sources such as hydrogen (H_2), shown in Figure 1.17.

A number of investigations into the H_2 storage capacities of organic gels have been carried out, each study adopting a different approach to tailoring the materials for optimal performance. Czakkel *et al.*[93] compared the adsorption behaviours of RF aerogels and xerogels, with all materials studied reportedly exhibiting higher H_2 uptakes than those commonly observed for carbon materials, and the aerogel materials significantly outperforming the xerogels as a result of their higher pore volumes. Xerogels synthesised using an acetic acid catalyst were studied by Tian *et al.*[94] with varying precursor solution pH values between 4.1 – 5.2. The H_2 storage capacity of the materials initially increased with increasing pH, reaching its at pH 4.8, before decreasing once again at pH 5.2. This trend corresponded to the trends observed for accessible surface area and total pore volume of the materials, with peak values of both properties obtained for materials synthesised at pH 4.8. Other approaches to material optimisation for H_2 storage has included the treatment of gels using potassium hydroxide[95], and the doping of materials using nitrogen[96] or nickel[97], with the latter exhibiting H_2 storage capacities of up to 6 wt.%.

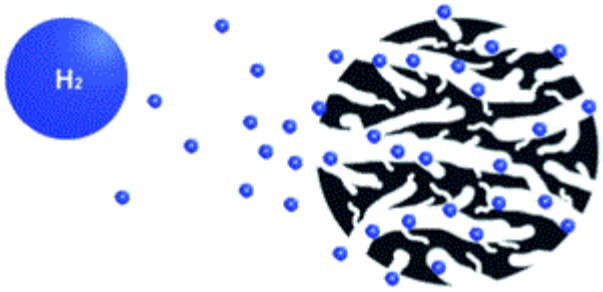

Figure 1.17: Depiction of hydrogen storage by physisorption in porous materials.[98]

Similarly, a number of studies have been carried out into the performance of organic gels in the adsorption of greenhouse gases such as CO_2, once again exploring nitrogen-doping[99] and potassium hydroxide treatment[100], as well as the presence of different surfactants during the carbonisation process.[101] The work carried out by Yapo *et al.*[99] reported especially promising results, with the nitrogen-doped materials exhibiting CO_2 adsorption capacities of up to 3.6 mmol/g at 298K and 4.5 mmol/g at 273K, both at 1 bar pressure.

1.5 Water Pollution Applications

Expanding upon the environmental applications of organic gels, their potential use in the removal of harmful pollutants from water systems could be an important route to further explore. Water pollution is a growing concern amongst the increasingly environmentally conscious population, with an estimated 80% of wastewater produced globally being deposited back into natural waters, predominantly untreated.[102] The demand for water has increased dramatically over the years, particularly as the world population continues to soar, such that by 2050, the world-wide requirements for freshwater is expected to increase by one-third of what it was in 2018.[103] Still, the contamination of global water systems continues, with these harmful substances having detrimental effects on the environment, marine life, and even human life.

The vast array of pollutants commonly found in water systems is extensive, however, they can be grouped into four main categories – pathogens, inorganic compounds, organic material, and macroscopic pollutants. Viruses and bacteria, such as E.coli, are classified as pathogens, and are often found in water as a result of human or animal waste contamination.[104] Heavy metals, such as mercury and lead, which can leach into water from industrial waste[105], are classified as inorganic pollutants, whilst any carbon-based pollutants are classified as organic materials. Both organic and inorganic compounds can accumulate in water systems over the course of decades, and their removal can be complex and time consuming, so their effects may be felt for many years after contamination has taken place. Lastly, macroscopic pollutants are physical items such as plastics, metals, and other large objects, which have usually been disposed of as trash from human use.[106] This work focuses one organic pollutant, 3,4-dichloroaniline, which is part of an emerging class of pollutants known as endocrine-disrupting chemicals (EDCs). These can pose a threat to both marine and human life, and are described by The Endocrine Society as "substances in our environment, food, and consumer products that interfere with hormone biosynthesis, metabolism, or action resulting in a deviation from normal homeostatic control or reproduction".[107]

1.5.1 Endocrine Disrupting Chemicals (EDCs)

The complex and long-term effects of EDCs mean that the exact mechanism by which they effect endocrinology is difficult to ascertain, as is the effects of individual EDCs, given that they are known to work synergistically with other EDCs to affect widespread biological issues, even when present in low concentrations.[108] Across both humans and animals, reproduction and healthy biological function is reliant on an essential balance of a number of hormones, including estrogen, progesterone, and testosterone. EDCs are known to interfere with the natural balance of such hormones in various ways, including binding and blocking hormone receptors within the body, removing hormones from their carrier proteins, and preventing or limiting hormone synthesis.[109]

Extensive research has been carried out into the impact of EDCs on aquatic life, in particular different species of fish, the results of which raise significant concerns. Amongst these impacts, the feminisation or masculisation of species have been identified through hormonal abnormalities, resulting in the formation of intersex fish in increasing numbers. A study which sampled roach fish from eight rivers within the UK found that the percentage of intersex male fish ranged between 40 to 100% in five of these rivers[110], with subsequent works reporting increasingly concerning statistics.[111] Furthermore, an experimental lake in Canada named Lake 260 was dosed with the ethinylestradiol (EE2) – an estrogenic substance commonly found in waters around treated sewage discharge points. The dosing was carried out across a three-year period, and the population of fathead minnow fish was monitored throughout this time and for the following four years, with two EE2-free lakes used as reference sites for comparison. The feminisation of male fish was made apparent through increasing numbers of delayed spermatogenesis, malformed gonaducts, and ovotestis, to the extent that by the

fourth year of the study, all fathead minnow reproduction had come to a halt and the population approached extinction.[112]

In addition to the reproductive impacts of EDCs, the stress response of a species can also be hindered as a result of hormonal interference, given that the production of the hormone cortisol is associated with the ability to respond and adapt appropriately to stressors, as well as being an important factor in proper immune function.[113] The presence of EDCs in water can also threaten thyroid function amongst species, where a complex balance of hormone production is imperative to species growth, metabolism, and reproductive health.[114]

While most of the conclusive research carried out to date has focused on the impact of EDCs on aquatic life, there are increasing concerns around their impact on human health, particularly given that the function and significance of endocrine systems in humans is comparable to that of other vertebrates.[115,116] The implications of this are significant, with the potential for EDCs to affect both male and female reproductive health, increasing hormone-related cancer risks, interfering with thyroid function and metabolic rate, and subsequently increasing the likelihood of obesity.[117] Neurological and cardiovascular impacts have also been reported as a result of endocrine disruption, but the complex nature of human endocrinology means that the full extent of these risks, and the concentrations at which EDCs become problematic, is still not fully understood.[118] Although the direct impacts of EDCs on humans have been difficult to ascertain, particularly given that significant effects may not become evident until years after exposure, the endocrine disrupting effects of certain medications in humans have already been documented, pointing towards the detrimental effects possible for EDCs within the environment.[116]

1.5.2 3,4-dichloroaniline (3,4-DCA)

As mentioned previously, the EDC studied in this work is 3,4-dichloroaniline (3,4-DCA) – a compound comprised of a benzene ring with an amino group at position 1, and two chlorine atoms at positions 3 and 4, as shown in Figure 1.18. This chemical acts as an intermediate in the synthesis of fabric pigmentation, precursors for paints, and pharmaceuticals, as well as extending to use in the production of herbicides which are applied in the farming of numerous crops for human consumption.[119] Environmental contamination with 3,4-DCA arises from the degradation of pesticides into soil and field waters, as well as from industrial wastewater deposits, while human exposure to this chemical is also expected to arise as result of the consumption of food from treated crops.[120]

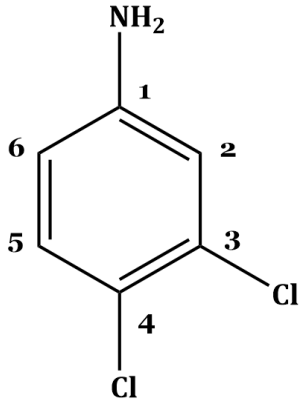

Figure 1.18: 3,4-dichloroaniline

The European Chemicals Bureau within the Institute for Health and Consumer Protection carried out a risk assessment on 3,4-DCA, which concluded that it was "very toxic to aquatic organisms" and "may cause long-term adverse effects in the aquatic environment".[121] The chronic effects of 3,4-DCA are considered to be the most significant, with impacts on the reproductive health observed in Daphina magna as a result of exposure[122,123], in addition to toxicity in species of minnows[124,125], and blockages of androgen receptors in rats.[126] The Predicted No-Effect Concentration (PNEC) for 3,4-DCA – that is, the concentration at which no chronic effects are expected – has been estimated as 0.2 μg/L in freshwater and seawater.[121] Determining efficient methods of removal for pollutants such as 3,4-DCA is of utmost importance, both for the safety of aquatic life and human life, with porous materials such as organic gels emerging as a potential adsorbent for these applications.

1.5.3 Water Purification Using Organic Gels

A common approach to water purification involves the adsorption of pollutants, typically using a porous material possessing a high surface area and an internal structure with channels large enough to facilitate the diffusion of specific pollutant molecules. In addition to the tuneable properties achieved through the synthesis process originally established for organic gels, other methods have been explored to further enhance their adsorption capabilities for water purification applications. A study by Yang *et al.*[127] used nitrogen-doped carbonised xerogels to remove heavy metal ions from water, specifically lead (Pb), zinc (Zn), and copper (Cu) ions, reporting removal efficiencies 1.64 – 1.97 times greater for doped materials in comparison to standard organic gels. Similar work carried out by Vesela and Slovak[128] also investigated the performance of nitrogen-doped carbonised xerogels for the adsorption of Cu(II) and Pb(II) ions, with their doped materials exhibiting adsorption capacities 2-6 times greater than that of standard gels. The use of organic gels in water purification has extended to various other emerging pollutants, including in the work of Alvarez *et al.*[129] who investigated the adsorption of caffeine and diclofenac – two pollutants from the pharmaceutical industry. The maximum caffeine adsorption capacity was observed for xerogels treated with urea, whilst the maximum diclofenac adsorption capacity was observed for xerogels treated with sulfuric acid, highlighting the importance of surface chemistry on

the material's adsorption performance. Other works have focused on the use of organic gels for the adsorption of dyes and pigments from textile production wastewater, including methylene blue[130], reactive orange 16[131], and reactive red 2.[132] The research conducted into the use of organic gels as pollutant adsorbents for water systems is promising, and has the potential to extend to the removal of many more harmful substances, such as the endocrine disrupter 3,4-DCA previously discussed – something that will be explored further through this work.

1.6 Computational Tailoring of Porous Materials

The ability to tailor the properties of RF gels is a considerable advantage to their widespread use within the many applications discussed in the preceding sections, and it is therefore important to focus efforts on creating efficient and effective methods to carry out this optimisation process. Achieving this computationally could significantly expediate the process, starting with the development of a simulation that can model the formation and growth of these materials under varying synthesis conditions, and allow their final properties to be analysed. Modelling of porous materials can be carried out using a variety of techniques, with two main categories established for computational approaches – Interatomic Potential Methods and Electronic Structure Techniques – both of which will be discussed in more detail in subsequent sections.[133]

1.6.1 Interatomic Potential Methods

Interatomic potential methods are typically used for systems that are larger and more complex, operating based upon energy calculations for interacting species, and presenting a more computationally efficient approach than electronic structure techniques. Unlike electronic structure techniques, however, they cannot be used to model reactivity or properties associated with spectroscopy, given that an atom or molecule's electronic structure is central to both. The most simple of the interatomic potential (IP) methods is the energy minimisation (EM) technique, which can be used both by itself or in conjunction with other IP methods.[134-136] The EM technique takes an initial system configuration – one which may be an initial structure estimate or simply a random distribution of atoms – and determines the structural arrangement corresponding to the system energy minimum. Although this approach is beneficial in its computational efficiency and speed, its accuracy is limited by its propensity to determine a local system energy minimum, not a global energy minimum, and therefore produce a final structure that does not reflect the material structure it seeks to model. Other IP methods include molecular dynamics (MD) simulations [137-139] and Monte Carlo simulations [140-142] which, as discussed, may be used in tandem with the EM method. The MD method models the evolution of a system over time using classical dynamics, starting with an initial system configuration and calculating atomic forces and accelerations at each time step. As the simulation proceeds, atom co-ordinates and velocities at each step are recorded, and their trajectory towards the final structural arrangement is documented. The limitations of the MD approach, in contrast to the EM technique, lie within the computational expense and the resulting restrictions imposed on both the simulated time and the system

size. Despite this, systems comprising thousands of atoms are possible, and the associated computational expense is still typically lower than that of electronic structure techniques. Monte Carlo (MC) simulations, on the other hand, are based upon statistical mechanics, and allow larger, more complex systems to be simulated in comparison to MD simulations. Using the MC approach, the movement of particles within a system is based upon defined probabilities, which can also be subject to criteria that determines if a move will be accepted or rejected. The Monte Carlo method is the approach selected in this work to model the cluster-cluster aggregation process during RF gel formation, with its principles and execution discussed in more detail in Chapter 4, while previous work carried out on cluster-cluster aggregation systems more generally is discussed in Section 1.6.3.

1.6.2 Electronic Structure Techniques

Electronic structure methods, unlike interatomic potential approaches, approximate solutions to the Schrodinger equation in their modelling of porous materials. Such methods include the Hartree-Fock (HF) method[143,144], which uses molecular quantum chemistry to model systems, proving beneficial for very small-scale systems, but encountering various inaccuracies when applied to larger structures.[145] Other methods often employed include the application of Density Functional Theory (DFT)[146,147], which can typically be used to model systems on a slightly larger scale than the HF method, as well as Hybrid Quantum Mechanics/Molecular Mechanics (QM/MM)[148], whereby specific system components are approached using electronic structure techniques, while the bulk system beyond these components are approached using interatomic potential techniques. The main hurdle associated with QM/MM techniques is in combining the results of the two approaches for the one system, aiming to create a system that is coherent and reflective of the material being modelled. Once again, simulating materials using electronic structure techniques can be highly valuable, particularly for understanding the finer details of material formation, however, their applicability to larger systems and the associated global properties is limited.[133]

1.6.3 Cluster-Cluster Aggregation Models

In this work, the simulated formation of porous RF gels is carried out using a cluster-cluster aggregation model – an approach that has been used extensively over the years, simulating the formation of complex structures from both diffusion-limited and reaction-limited cluster aggregation.[149-151] Recent studies have furthered this work, with a focus on systems modelled with repulsive and attractive forces in place, and the rotational diffusion of aggregating clusters implemented.[152,153] Studies such as these, while valuable in their ability to model porous materials similar to RF gels, predominantly begin the simulation at a point where primary cluster formation had already taken place[154,155], or alternatively assume primary clusters that have formed are of equal size before aggregation occurs.[156,157] These models, therefore, may not capture important aspects of a real system, where such properties are likely to exhibit some degree of variation.

Computational adsorption analysis as a means to understanding porous structures in greater detail has been studied to provide insight into the adsorption and desorption mechanisms and allow material properties to be determined. Multiple techniques have been employed to model the adsorption process, including classical density functional theory (DFT) calculations [158,159], in addition to Monte Carlo and molecular dynamics simulations, which have explored adsorption within materials such as graphite[160], nanoporous silica[161], and metal organic frameworks[162], producing adsorption isotherms for the simulated materials studied. Recent progress in models such as these has even led to the development of widely-accessible adsorption software.[163] Although adsorption models such as these provide valuable insights into the detailed interactions between adsorbates and adsorbents, their relevance to industrial applications is limited by their significant computational expense.[164] Furthermore, many of the studies that utilise these methods are able to simulate adsorption within just a few structures, or within specific individual pores, as opposed to performing the analysis over a wide range of varying structures that would be valuable for tailoring materials. In an effort to advance towards more computationally efficient adsorption analysis, more recent studies have taken a coarse-grain approach using lattice-based mean field theory (MFT), with studies focusing on understanding the adsorption mechanism within individual pores of varying size and geometries[165-167], and further work extending to adsorption analysis within complex porous structures.[168]

A model capable of simulating both the formation and analysis of materials such as RF gels, under varying synthesis parameters, in a computationally efficient manner is therefore still yet to be developed, and is an important aspect of the work presented here.

1.7 Summary

Bridging the gap between the exceptional properties of natural carbon materials and the tailorable properties of silica gels, the discovery of organic gels by Pekala established a new class of material with an extensive and wide-ranging application potential, as demonstrated within the discussions above. Importantly, the use of organic gels is particularly pertinent to environmental protection – an ever-growing and increasingly alarming global issue. The various ways in which these materials can be tailored, through simple alterations of synthesis parameters, as well as gel doping and post-synthesis treatments, allow effective optimisation for each application. This ranges from adjusting accessible surface areas to optimising electrical and thermal conduction, and even includes the potential of fractal properties. This flexibility is one of the most fundamental advantages of organic gels, and the ability to expediate the tailoring process through computational models could significantly advance their widespread use.

Chapter 2: Aims and Objectives

As discussed in detail in the preceding sections, and demonstrated extensively in the literature, the various ways in which the properties of RF gels can be altered shows promise for their widespread use, with their full application potential yet to be fully elucidated. As the demand for materials suitable for environmental applications grows, tailoring the structure of these materials to specific uses in an efficient manner is of utmost importance. In order to achieve this, the formation mechanism of RF gels and the various synthesis parameters affecting their final properties must first be understood, forming the basis upon which a computational model capable of material optimisation can be developed.

The aims of this project are, therefore:

1. To investigate the formation mechanism of RF gels experimentally, altering various synthesis parameters and assessing the impact on the final gel structure. In this work, these synthesis parameters include:
    - the sodium carbonate catalyst concentration
    - the catalyst species, specifically focusing on the widely debated role of the cation
    - the solvent selected for use during the solvent exchange step following gelation
2. To transform a 2D cluster aggregation code which models the formation of RF gels into a 3D simulation with varying solids percentages and activated monomer percentages, the latter representative of catalyst concentration. Subsequently analysis of the simulated materials will assess the following, with comparisons to experimental results where relevant:
    - cluster size distribution for the structure
    - percentage of accessible pore sites for diffusing particles of different sizes
    - accessible surface area for diffusing particles of different sizes
    - structural correlation dimension
    - Hurst exponent values for diffusing particles of different sizes
3. To perform computational adsorption analysis on:
    - model pores of varying width, length, and geometry
    - simulated structures with varying synthesis parameters, assessing the geometry and width distributions of the pores present, and comparing the results obtained to experimental analysis of RF gels
4. To experimentally test the efficacy of two RF gels synthesised at different R/C ratios in the removal of the pollutant 3,4-DCA from water, assessing the following:
    - the ability to predict performance of materials using both the previous experimental and computational results obtained
    - the adsorption kinetics for the removal of 3,4-DCA by both materials
    - the adsorption isotherm from the removal of 3,4-DCA, and its performance compared to that of other adsorbent materials.

Chapter 3: Experimental Techniques and Theory

This chapter introduces the experimental techniques used within this work, discussing the foundations and theories behind them, as well as the range of valuable insights they can provide into the properties of RF gels and the synthesis parameters affecting them. Adsorption analysis is the technique most commonly used for the characterisation of porous materials and is described in detail in this chapter, including discussions around the theories behind adsorption models such as Langmuir and Brunauer-Emmett-Teller. This is followed by an introduction to two solution analysis techniques: Infra-Red Spectroscopy, which is used for the analysis of solvent mixtures during the solvent exchange step of gel synthesis, as well as UV-Vis Spectroscopy, which is used to determine 3,4-DCA solution concentrations, enabling the performance of RF gels in pollutant removal to be assessed.

3.1 Adsorption Analysis

In order to determine the textural properties of porous materials, such as organic gels, and enable characterisation of the porosity present, adsorption analysis is commonly employed. This is often carried out using nitrogen or helium gas, both of which are beneficial due to their inert qualities and small molecular diameters, allowing them to access narrow pores and passageways, and adsorb and desorb without altering the material itself. This section focuses on the theories behind adsorption analysis, first introducing the concept of adsorption on surfaces and within porous materials, and subsequently discussing the models used to interpret adsorption data in detail. These include Langmuir[169], Brunauer-Emmet-Teller[170], and Barrett-Joyner-Halenda[171] theories which are used to assess properties such as the material's accessible surface area, total pore volume, and average pore size. Each of the properties determined provide valuable insight into the material's structure, and understanding how different synthesis parameters affect these properties, and how these properties in turn contribute to the performance of the materials in different applications, is key to their optimisation and widespread use.

3.1.1 Adsorption Processes

Adsorption of gaseous molecules onto a solid surface can take place through two primary processes – physisorption or chemisorption. Physisorption, or physical adsorption, is the phenomena whereby molecules adhere to a surface through van der Waals intermolecular forces, with no electron pairing taking place between the adsorbate (the gas) and adsorbent (the surface). Chemisorption, or chemical adsorption, on the other hand, takes place when molecules adhere to a surface through chemical bonds formed as a result of electron pairing. Physisorption, involving the formation of relatively weak bonds, is typically an easily reversible process requiring little energy, whilst chemisorption, on the other hand, can be very difficult to reverse, requiring large amounts of energy to break strong chemical bonds, both of which are depicted in Figure 3.1.[172] The behaviour and properties of adsorbed gas

molecules are different from those remaining in the bulk, particularly in their entropy, given that the degree of disorder decreases as adsorbed molecules align themselves at available sites on the adsorbent surface.

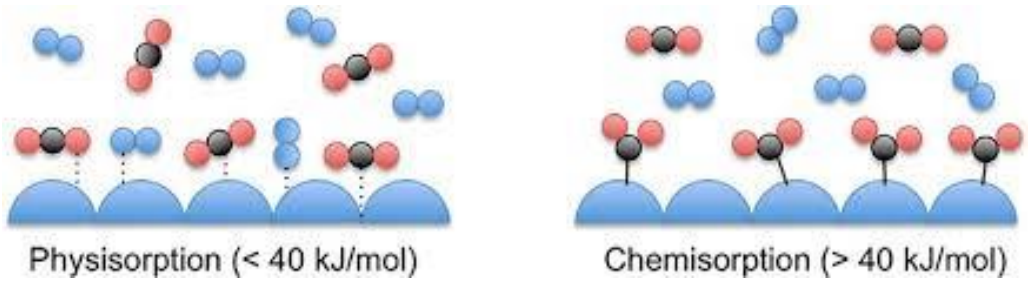

Figure 3.1: Illustration showing physisorption and chemisorption processes.[173]

When surfaces within porous materials are subject to gas adsorption, their internal structure, shape, and degree of porosity will affect the adsorption behaviours observed. The types of pores present within a material can be classified based on their size and shape, in accordance with definitions established by the International Union of Pure and Applied Chemistry (IUPAC).[174] In terms of pore size, three main classifications have been established:

1) Micropores – pores with widths less than 2 nm
2) Mesopores – pores with widths between 2 – 50 nm
3) Macropores – pores with widths greater than 50 nm

The way in which pores fill differs based on their size, with narrow pores requiring significantly fewer molecules to fill the associated cavity, especially where just one layer of adsorbed molecules on each of the pore walls is sufficient, and require much lower relative pressure conditions (relative pressure is typically denoted as $^{p}/_{p_0}$, where p is the equilibrium pressure and p_0 is the saturated vapour pressure). With pores of larger widths, as the gas molecules continue to adsorb with increasing relative pressure, multilayer formation begins to take place. Once these adsorbed layers of gas reach a critical thickness, the pores fill with liquid despite being below the saturated vapour pressure – a phenomenon known as capillary condensation. This process takes place only during the adsorption step, meaning that the mechanism by which adsorption and desorption takes place within such pores will differ.[175] The gradual adsorption of molecules onto a substrate is illustrated in Figure 3.2, depicting initial adsorption onto isolated sites, then progressing to monolayer and multilayer formations as the system pressure increases, eventually leading to condensation of the gas and subsequent pore filling.[176]

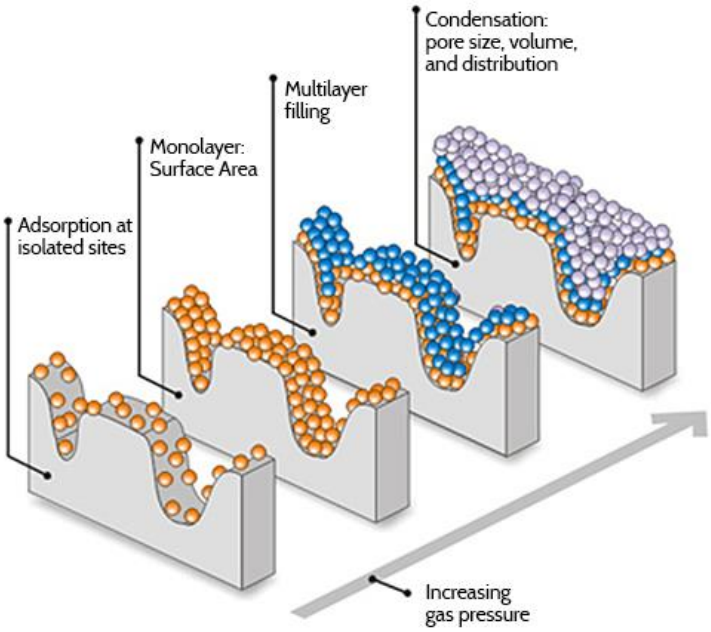

Figure 3.2: Illustration of adsorption process with increasing pressure.[176]

Different geometries of pores may be observed within a porous structure, as depicted in Figure 3.3, including pores that are open at both ends (open pores/open transport pores), pores that are open at just one end (dead end pores/closed base pores), and pores which possess a bottleneck at the entrance (ink-bottle pores/bottle neck pores). Other pore types include closed pores and through pores, also shown in Figure 3.3.[177,178] These pores may be roughly cylindrical in shape, rectilinear, or have a more slit-like structure. For clarification, indentations on a solid surface are typically considered to be pores if their depth exceeds their width, marking their difference to general surface roughness. These porous properties produce various adsorption behaviours, meaning that adsorption analysis data can be used to determine textural characteristics of the adsorbent material, which is discussed in subsequent sections.

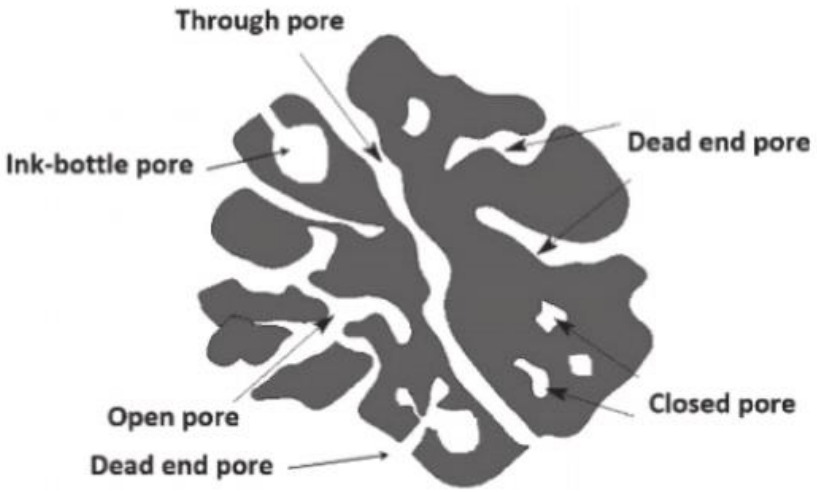

Figure 3.3: Different pore types found within porous structures.[178]

3.1.2 Adsorption Isotherms

Adsorption analysis is typically carried out at constant temperature, where samples of material are immersed in an inert gas and the relative pressure (p/p_0) of the system is increased, leading to the gradual adsorption of gas onto the available surface area within the material, before condensing and filling the pores completely. After this point has been reached, the relative pressure is then decreased, and the adsorbed gas gradually desorbs from the structure. The data collected from adsorption analysis is in the form of an isotherm – a graphical depiction of how the quantity of gas adsorbed onto the sample changes with relative pressure, under isothermal conditions.

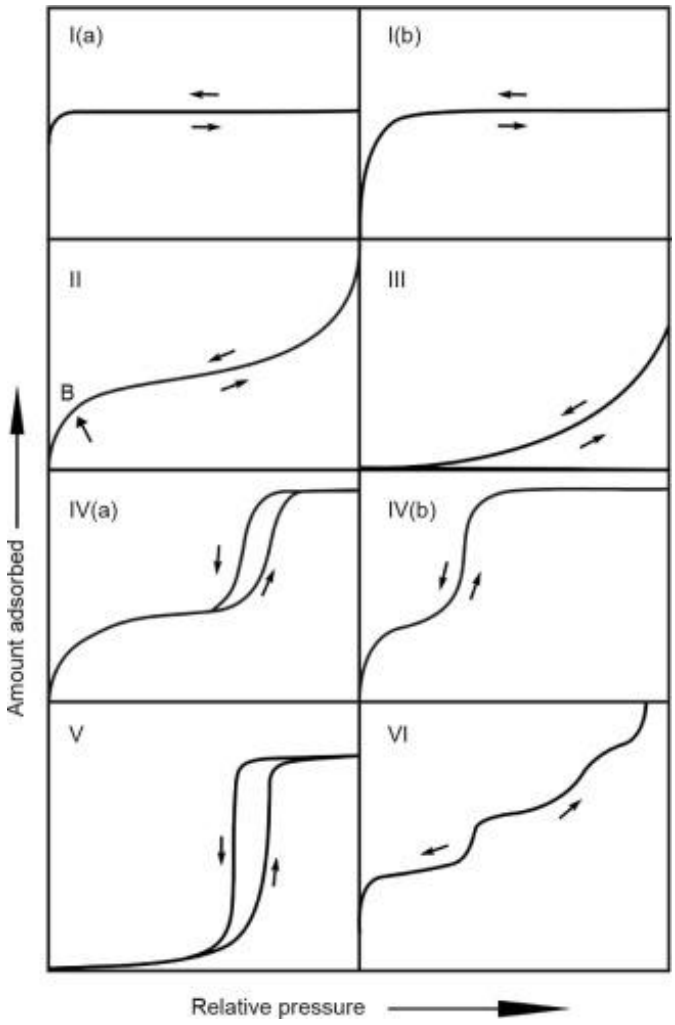

Figure 3.4: Isotherm Types I-VI, as categorised by IUPAC. [174]

Isotherms are commonly categorised into six types according to their shape, with Types I and IV being divided once again into two sub-categories, thereby totalling eight overall (see Figure 3.4).[174] Type I (a) and (b) isotherms show a significant uptake of adsorbate at low pressures before reaching a plateau, with the low relative pressure values at which this takes place pointing towards the presence of micropores. After these micropores have been filled completely, no more adsorption takes place, resulting in the adsorption plateau – the more

gradual plateau of isotherm Type I (b) indicating that a slightly wider range of pore sizes are present. Type II isotherms are typically observed within non-porous materials, where Point B is indicative of the stage at which monolayer formation takes place on a surface, after which point the adsorption uptake with changing pressure begins to plateau. Multilayer formation then proceeds at higher relative pressures, where the adsorption uptake begins to increase once again. Type III isotherms, on the other hand, show no signs of identifiable monolayer formation, with the gradual uptake only at higher pressures suggesting weak interactions between the gas and the surface, where adsorption takes place only at a small number of the most favourable sites.[179] Type IV (a) and (b) isotherms are similar in that they are observed within mesoporous materials, with adsorption taking place as a result of interactions between adsorbent and adsorbate at the pore walls, as well as between adsorbate molecules as they condense within the structure. This is reflected in the initial plateau within the isotherm, once again indicating monolayer formation, followed by an uptake at higher relative pressures as multilayer formation and condensation of the gas takes place, subsequently filling the porous structure. The most significant difference between Types IV (a) and (b) is the presence of the hysteresis loop in (a), which arises as a result of the differing mechanism by which larger pores fill and empty, attributed to the phenomena of capillary condensation.[174] This is discussed in more detail below, where the different types of hysteresis loops are explained. Type V isotherms are comparable to Type III, where weak interactions lead to a slow, gradual uptake of adsorbate, this time taking place within porous structures which exhibit hysteresis in their adsorption behaviour. Finally, Type VI isotherms demonstrate "step-wise" or "layer-by-layer" adsorption, which may take place on certain surfaces. This adsorption takes place through the step-wise addition of layers, with the extent of plateau observed at each step dependent on the degree of overlap between individual layer coverage and further multilayer formation, which will vary from system to system.[180]

3.1.3 Isotherm Hystereses

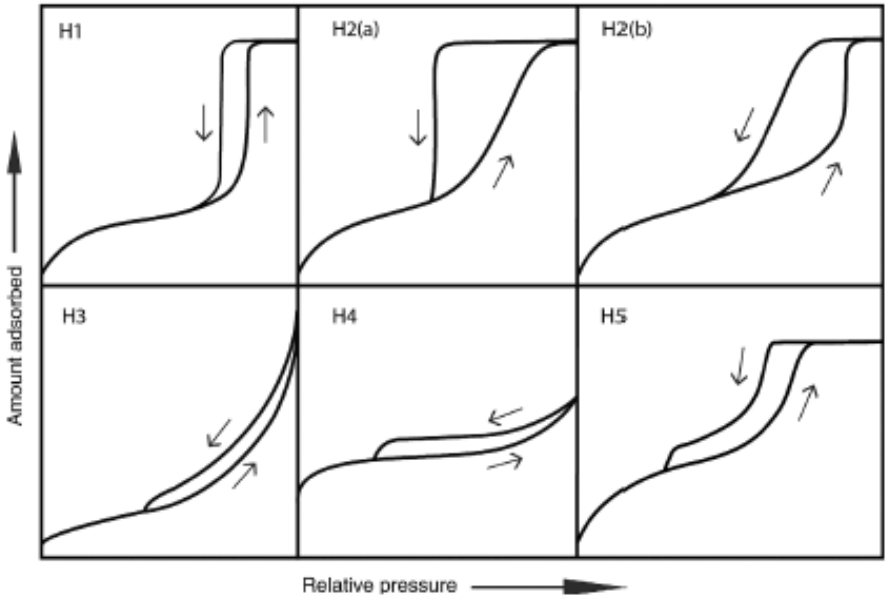

Figure 3.5: Hysteresis types, and the corresponding theoretical pore shape. [174]

The isotherms discussed in Section 3.1.2 provide insight not only into how gases adsorb onto surfaces as the relative pressure is increased, but also the mechanism by which gases desorb as the pressure is reduced once again. If the adsorption and desorption mechanisms differ, a 'hysteresis loop' is observed, as depicted in the Type IV (a) and V isotherms in Figure 3.4. In addition to the IUPAC isotherm classifications, they have also published comprehensive recommendations on reporting physisorption data, which include classifications on the different types of hysteresis loops observed within the isotherms discussed, and the implications of these in terms of a material's structure.[174,181] Six hysteresis classifications have been identified (H1 to H5, shown in Figure 3.5), across which three primary pore geometries were ascertained.

Adsorption isotherms with H1 hysteresis loops – where the two branches are roughly parallel vertically – are typically observed for materials that possess pores open at both ends, referred to as open pores or open transport pores, with these pore channels often being approximately cylindrical in shape.[182] Figure 3.6 shows the proposed process of adsorption and desorption for cylindrical pores, where adsorption takes place through the addition of layers to the pore walls, whilst desorption takes place through the removal of layers from the meniscus.[183] In this illustration, the pore radius is denoted as r_c, the changing internal radius as adsorption takes place is denoted as a, the critical radius at which the pore fills during adsorption is denoted as a_c, and the radius at which the pore empties during desorption is denoted as a_m.

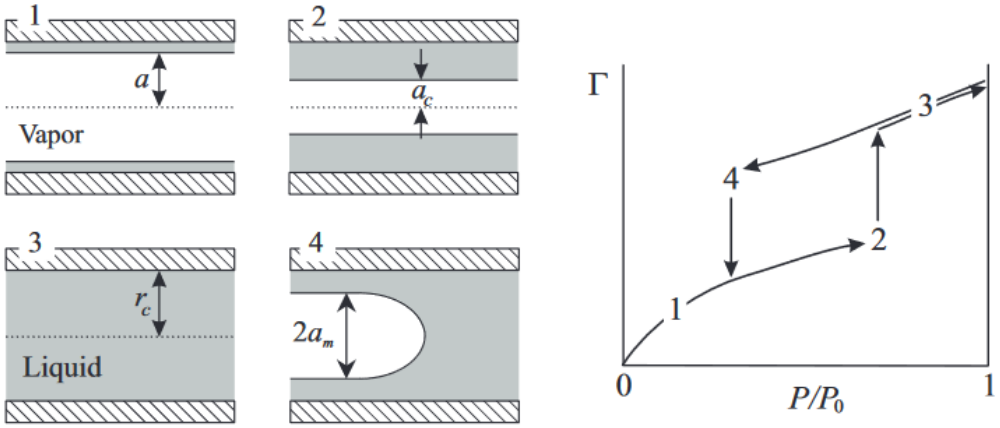

Figure 3.6: Adsorption and desorption process for cylindrical open pores.[183]

In contrast to these H1 hysteresis types, H2 hystereses are observed within complex structures that are typically comprised of bottle neck pores, with H2(a) hystereses corresponding to pores with approximately uniform bottle neck widths, and H2(b) hystereses corresponding to pores with varying bottle neck widths.[180] Figure 3.7 visualises the adsorption and desorption processes in bottle neck pores, where monolayer formation is observed during the initial adsorption steps, followed by the filling of the bottle neck before the complete filling of the pore.[183] As with cylindrical pores, desorption is seen to take place through the removal of layers from the meniscus. Types H3 and H4 hysteresis loops are associated with structures composed of slit-shaped pores and plate-like particles, often observed in materials such as clay or aggregated crystals of zeolites. Type H5 hysteresis loops are observed infrequently,

but are associated with structures that possess both open and partly-blocked mesopores.[174] These conclusions were drawn from adsorption measurements performed for materials whose internal structures were known, and these details have subsequently proven effective for analysing properties of materials whose internal structures are not fully understood.[184]

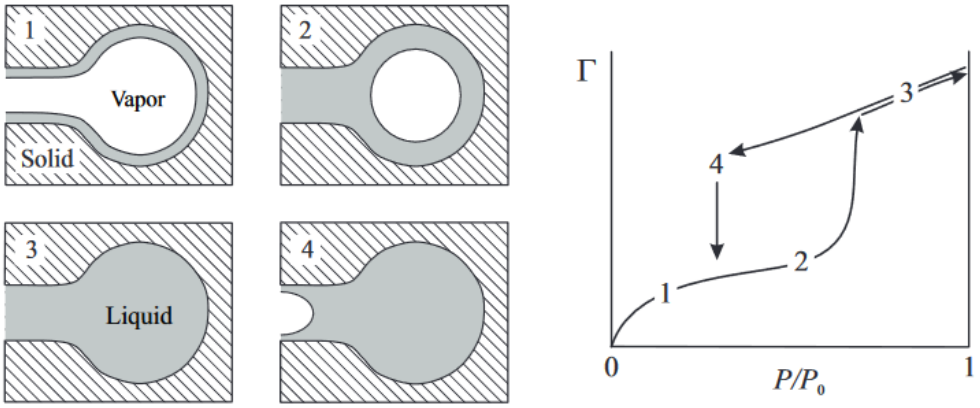

Figure 3.7: Adsorption and desorption process for ink bottle pores.[183]

Not only is the shape of the hysteresis loop an important indication of the geometry of the pores present, but its position relative to the x-axis – i.e. the corresponding relative pressures at which the loop opens and closes – is also representative of the size of pores contained within a structure. Micropores, the narrowest class of pores, typically fill before a relative pressure value of ~0.4, and these pores do not contribute towards the hysteresis loop as their adsorption and desorption mechanisms are unlikely to differ, unlike that of larger pores.[181] As a result of the way in which pores fill and empty – with monolayer and multilayer formation on pore walls – pores that are narrower in width will fill at comparatively low pressures in contrast to wider pores, where multilayer formation will be insufficient to fill the pore cavity, and a higher pressure is required to reach the point of saturation within the pore. For this reason, adsorption isotherms obtained for structures with wider pores exhibit hysteresis loops at higher relative pressure values, whilst structures with narrower pores exhibit hysteresis loops at lower relative pressure values during adsorption analysis.[185]

3.2 Surface Area Analysis

3.2.1 Langmuir Theory

Attempts to establish a mathematical formula that could be used to describe the adsorption behaviour observed within isotherms have led to the development of various adsorption models, such as Langmuir, Freundlich, Harkins-Jura, Temkin, and Brunauer-Emmett-Teller (BET), each based upon their own set of assumptions and limitations.[186] Of these adsorption models, the Langmuir model[169] is one of the most well-known and widely applied, the theory behind which relies on three fundamental assumptions:

1. Only monolayer formation takes place, with no interactions between adsorbed molecules and therefore no multilayers forming at the surface.
2. The adsorption sites on the material surface are capable of adsorbing just one molecule at a given time.
3. All of the adsorption sites on the material surface are identical.

The Langmuir Model uses adsorption and desorption rate equations to produce an expression for the fraction of surface sites occupied by adsorbed molecules (θ) at a given pressure, which is defined as:

$$\theta = \frac{occupied\ sites}{adsorption\ sites} = \frac{V}{V_m}$$

Equation 3.1

Where V is the volume of gas adsorbed at a given pressure, and V_m is the volume of gas required to achieve monolayer coverage on the surface. This can be inserted into the rate equations for adsorption and desorption, which are equal when equilibrium is reached:

$$k_{ads}P(1-\theta) = k_{des}\theta$$

Equation 3.2

Where the left hand side is the adsorption rate equation, the right hand side is the desorption rate equation, with k_{ads} and k_{des} being the individual rate constants for adsorption and desorption, respectively, and P being the relative pressure of the system (also referred to as p/p_0). This can be rearranged to give an expression for the overall rate constant (K):

$$K = \frac{k_{ads}}{k_{des}} = \frac{\theta}{P(1-\theta)}$$

Equation 3.3

Which can then be rearranged once more to provide a new expression for θ:

$$\theta = \frac{KP}{1+KP}$$

Equation 3.4

Combining Equation 3.1 and Equation 3.4 leads to the final Langmuir equation, given by:

$$\frac{P}{V} = \frac{1}{KV_m} + \frac{P}{V_m}$$

Equation 3.5

This equation allows a straight-line graph of $\frac{P}{V}$ against P to be plotted, enabling both V_m and K to be determined from the gradient and y-intercept of the line. The Langmuir equation (Equation 3.5) can also be applied using molar uptake (n) as opposed to volume, allowing the number of moles present within the monolayer (n_m) to be calculated from the straight-line plot. The accessible surface area (S) can then be determined using Equation 3.6:

$$S = \frac{n_m A_m L}{m}$$

Equation 3.6

Where A_m is the area occupied by a single molecule, L is Avogadro's constant, and m is the mass of the adsorbent sample.

3.2.2 Brunauer-Emmett-Teller (BET) Theory

Over 20 years after Langmuir published his adsorption theory, the Brunauer-Emmett-Teller (BET) theory emerged.[170] This was essentially an expansion of the Langmuir theory, this time accounting for the possibility of multilayer formation, and has become the most widely used model for nitrogen adsorption analysis. The additional assumptions included in the BET adsorption model are:

1. The first layer adsorbed onto the material surface exhibits a heat of adsorption, whilst subsequent layers exhibit a heat of condensation.
2. When conditions reach saturation pressure, the multilayer formation is infinite.
3. The final layer adsorbed is in equilibrium with the bulk gas.

The BET equation emerged from this research, Equation 3.7, which is similar to that of the Langmuir equation, where p is the equilibrium pressure, p_0 is the saturation vapour pressure, and C is a dimensionless constant related to the adsorption energy:

$$\frac{p}{V(p_0 - p)} = \frac{1}{V_m C} + \frac{(C-1)p}{V_m C p_0}$$

Equation 3.7

This time, a linear graph of $\frac{p}{V(p_o - p)}$ against $\frac{p}{p_o}$ can be plotted, and therefore values of V_m and C can be calculated from the gradient and y-intercept values.

In order to ensure the BET model can be appropriately applied to the system being analysed, Rouquerol *et al.*[187] published a review of the technique alongside a set of recommendations. These recommendations set out criteria that must be satisfied when using the BET method, aiming to work within the model limitations as well as avoiding subjectivity when selecting pressure ranges, with the three main points being:

1) The calculated value of C must be positive for the model to be applicable within the pressure range.
2) A plot of $V(p_o - p)$ against $\frac{p}{p_o}$ should display a continuous increase in $V(p_o - p)$ with increasing $\frac{p}{p_o}$ within the pressure range selected.
3) The calculated value of V_m must correspond to a relative pressure value located within the range selected.

3.3 Pore Size Analysis

3.3.1 Barrett-Joyner-Halenda (BJH) Method

The Barrett-Joyner-Halenda (BJH) theory[171] is a method which is used to determine the pore size distribution and pore volumes within the meso- and macroporous range, assuming pores of cylindrical shape are present. The principle of the BJH method relies on the calculation of the Kelvin core radius at pressure intervals from the desorption isotherm data, discussed in detail below. In order to calculate the radius of the pores emptied at a given pressure, the BJH theory treats each pore as comprising of three sections, as shown in Figure 3.8. Firstly, the core of the pore – this is the main volume of liquid filling the pore, which evaporates at once when the critical pressure for that pore radius is reached. Secondly, the adsorbed layer – this is a layer of adsorbate which remains adsorbed onto the walls of the pore when the core is initially evaporated, but is gradually removed as the pressure is reduced. Finally, the walls of the pores themselves – leading us to the calculation of the empty pore width.

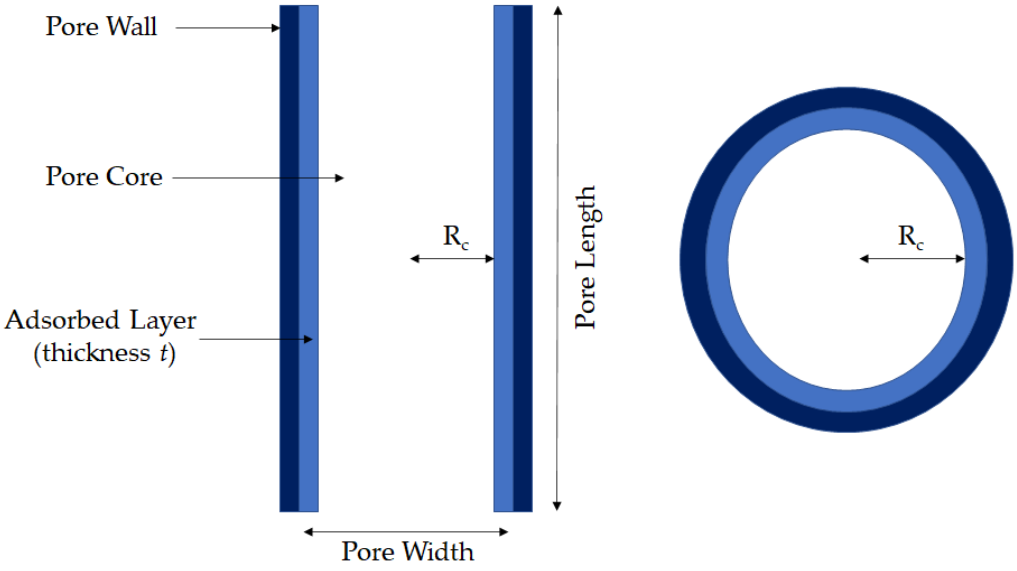

Figure 3.8: Labelled diagram of pore sections (left) and cross-section of pore (right).

The pore size calculations are based around two fundamental equations. The Kelvin equation (Equation 3.8) defines the relationship between relative pressure and pore meniscus radius (r_c), where γ is the surface tension of the liquid-vapour interface and V_m is the liquid molar volume – two parameters which are specific to the adsorbate gas used, R is the universal gas constant and T is temperature.

$$\ln\left(\frac{p}{p_o}\right) = \frac{2\gamma V_m}{r_c RT}$$

Equation 3.8

This equation can then be re-arranged to allow r_c to be determined at each relative pressure value measured.[188] Note that for concave surfaces, r_c is considered negative. The total pore radius is composed of the meniscus radius in addition to the thickness of the remaining layer adsorbed onto the pore walls – a value that is dependent on the interactions between the adsorbent and adsorbate. It is therefore necessary to calculate this thickness in order to calculate the total pore width, and for calculations applicable to nitrogen adsorption onto RF gels, an empirical formula known as the carbon black equation[189] is used:

$$t = 2.98 + 6.45\left(\frac{p}{p_o}\right) + 0.88\left(\frac{p}{p_o}\right)^2$$

Equation 3.9

Where t is the adsorbed layer thickness and $^{p}/_{p_o}$ is the relative pressure. As the relative pressure is decreased, pores of new core diameters will empty, and the thickness of the layer adsorbed onto the pore walls will also decrease as further desorption takes place. The remainder of the calculations are essentially geometric, assuming a cylindrical shaped pore, and using the volume of adsorbate which is being desorbed at each pressure interval within the isotherm to determine whether pores of new core diameters are emptying, or if the volume desorbed is simply from the thinning adsorbed layer on the pore walls. This analysis provides us with the data required to plot the volume adsorbed as a function of pore width, providing a graphical representation of the pore size distribution of the sample.

3.3.2 t-plot Method

In order to specifically analyse the microporosity within a material, that is, the pores less than 2 nm in width, the t-plot method was established by Lippens and Boer.[190] Through this method, isotherm data is transformed, plotting the adsorption uptake as a function of the adsorbed layer thickness using Equation 3.9, as opposed to plotting it as a function of relative pressure, producing what's known as a t-curve.

If microporosity is present within the adsorbent material, distinct sections of the t-curve will be observed. The beginning and ending of the linear section of the plot indicates the point at which multilayer formation and capillary condensation takes place, respectively, neither of which involve the filling of micropores.[191] Determining the straight-line equation of this linear section enables microporous properties to be analysed, with the y-intercept value of adsorbed gas, where the layer thickness is zero, relating directly to micropore volume through Equation 3.10:

$$V_\mu = intercept \times C_\rho$$

Equation 3.10

Where C_ρ is the density conversion factor, which is specific to the gas used for adsorption analysis, calculated as the ratio of density in the gas state to the density in the liquid state. Figure 3.9 shows example t-plots that demonstrate the difference observed for materials comprised solely of micropores and those possessing a mixture of both micro- and mesoporosity.

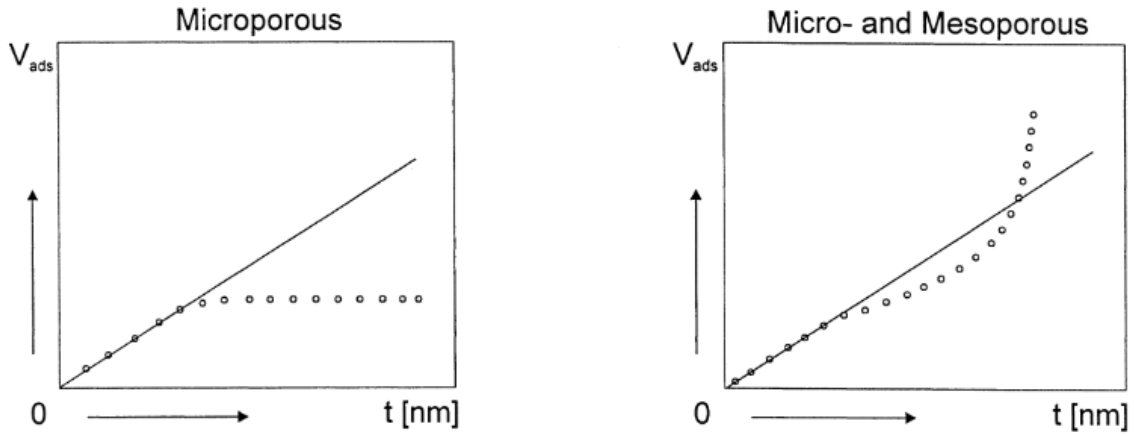

Figure 3.9: Example t-plots for microporous materials (left) and micro- and mesoporous materials (right).[191]

Furthermore, the gradient of the line can be used to calculate both the external surface area (S_{ext}) and subsequently the micropore surface area (S_μ) using Equations 3.11 and 3.12:

$$S_{ext} = gradient \times C_\rho$$

Equation 3.11

$$S_\mu = S_{BET} - S_{ext}$$

Equation 3.12

Where S_{BET} is the surface area calculated from the BET measurement.

3.4 Solution Analysis Techniques

Quantitative and qualitative analysis of solutions and solvents in contact with porous materials such as RF gels can provide valuable details, used in this work as a means to understanding the kinetics of solvent exchange during xerogel synthesis in addition to determining the adsorption capacity of gels for pollution control. Two methods are employed in this work: Infra-Red (IR) Spectroscopy and UV-Vis Spectroscopy, both of which involve the absorption of radiated energies within the electromagnetic spectrum, and are discussed in detail in the subsequent sections.

3.4.1 The Electromagnetic Spectrum

The electromagnetic spectrum (Figure 3.10) refers to the range of identified radiated energies, spanning wavelengths of 10^{-12} cm within gamma rays, to $5x10^{2}$ cm within radiofrequencies. The infrared (IR) range of the electromagnetic spectrum is found between the visible light spectrum and the microwave spectrum, spanning energy wavelengths of 780 nm – 1, mm, whilst ultraviolet (UV) light is positioned between X-rays and visible light, spanning wavelengths of 10 – 400 nm.

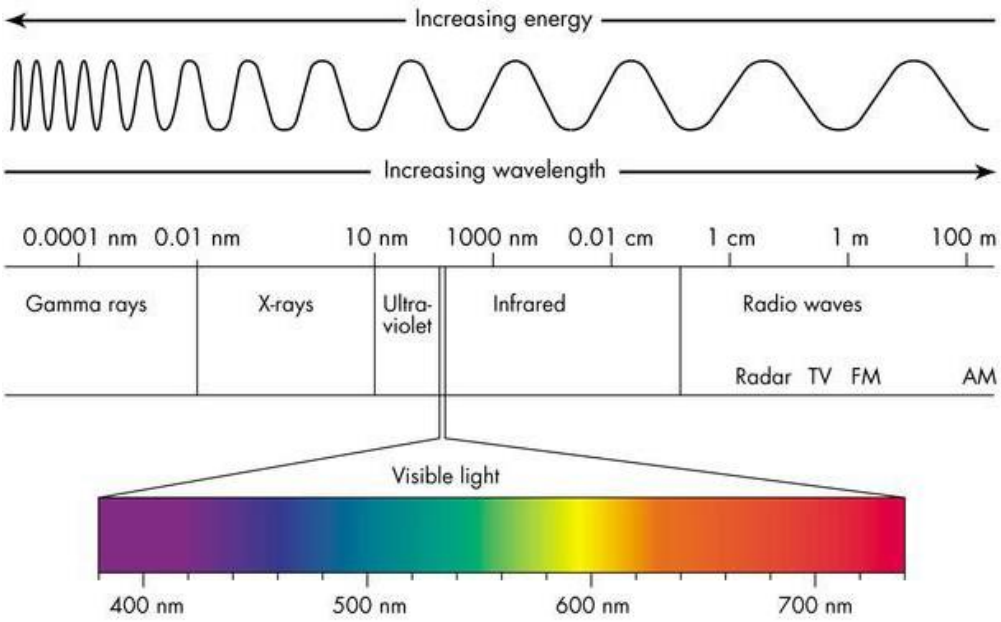

Figure 3.10: The electromagnetic spectrum. [192]

The relationship between parameters of these radiated energies can be useful for analysis, with each of these possessing their own frequency (v), wavelength (λ), wavenumber ($\bar{v}$, determined from $^{1}/_{\lambda}$), and energy (E). The frequency of the radiated energy is defined as the number of wave cycles which pass through a point in one second and is measured in Hz, a unit which is equivalent to cycles per second, whilst the wavelength is the length of one wave cycle. The relationship between frequency and wavelength is as follows:

$$v = \frac{c}{\lambda}$$

Equation 3.13

Where c is the speed of light. The corresponding energy (E), meanwhile, can be determined via the following relationship:

$$E = hv$$

Equation 3.14

Where h is Planck's constant. Using Equations 3.13 and 3.14, we observe the relationship between energy and wavelength, each one varying inversely with the other, with high energy gamma rays possessing the lowest wavelengths within the spectrum.

The way in which physical matter interacts with these radiated energies can elucidate valuable information about the material, such as its elemental composition or concentration. Upon exposure to electromagnetic radiation, processes such as reflection, scattering, and absorbance may take place, with different types of electromagnetic radiation stimulating different responses from materials, given that their wavelengths and corresponding energies will vary greatly.[193] The absorbance of IR radiation provides sufficient energy to excite molecules to higher rotational and vibrational energy states, however, are unable to provide the energy necessary to facilitate transitions to higher electronic states. The energy associated with UV-Vis radiation, on the other hand, is 10-100 times greater than that of IR radiation and is therefore capable of energising molecules to excited electronic levels, marking the main difference between IR and UV-Vis spectroscopy as an analysis technique.

The ratio of the transmitted radiation intensity to the incident radiation intensity (I/I_0) is known as the transmittance (T), sometimes expressed as a percentage. This is related to absorbance (A) in the following way:

$$A = \log\left(\frac{I_0}{I}\right) = -\log(T)$$

Equation 3.15

Given that energy will be absorbed across a range of wavelengths when a material is analysed, the output of these analysis techniques is an absorption spectrum. This can be displayed as transmittance or absorbance as a function of wavenumber for IR spectroscopy, while UV-Vis spectroscopy presents results typically as absorbance as a function of wavelength.[194]

3.4.2 Infra-Red (IR) Spectroscopy

As discussed, the principle behind infrared spectroscopy is based upon the absorption of energy into molecules at specific frequencies depending on their structural characteristics. The frequency of the radiation absorbed is equivalent to that of the vibrational frequency of specific bonds and groups within the molecule, allowing identification of such bonds and groups when infrared radiation energy is absorbed. Vibrational energies within molecules can be as a result of bond stretching, bond bending, or rotational movements, typically associated with changing electric dipole moments.[195] When a molecule absorbs IR radiation, it does so across a range of wavelengths and with varying intensities, producing an absorption spectrum with numerous peaks specific to the individual bonds and groups present. These spectra are complex in appearance, however, compilations of IR spectra are available for all common molecules, with the associated bond or group of each peak identified, allowing analysis of the sample molecule to be carried out. Figure 3.11 shows the IR spectrum observed for the analysis of water, displaying the two main peaks – one within the range of 1,550 – 1,650cm^{-1} as a result of O-H-O scissor bending, and one within the range of 3,000 – 3,500 cm^{-1} as a result of O-H bond stretching.[196]

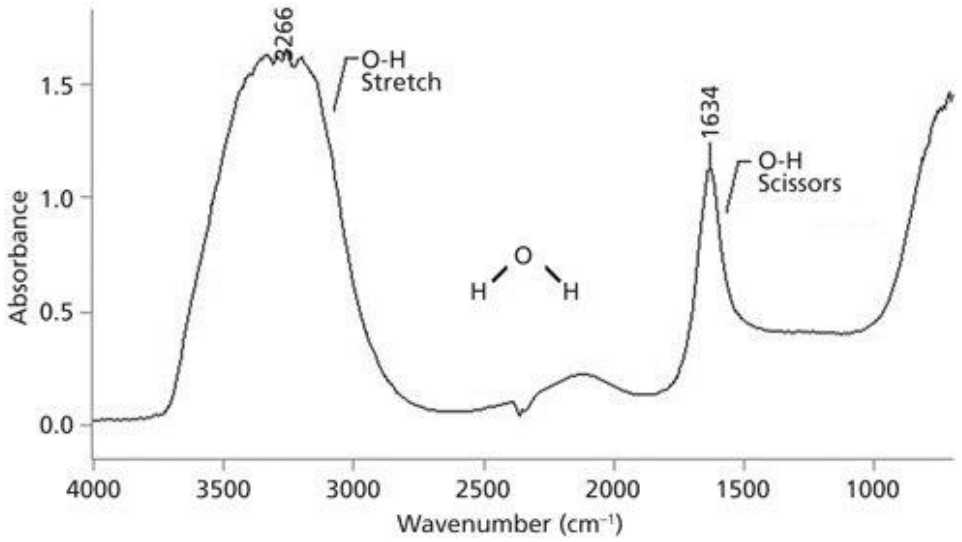

Figure 3.11: IR spectrum for water. [196]

3.4.3 UV-Vis Spectroscopy

UV-Vis spectroscopy explores wavelengths from both UV and visible wavelengths, hence the name, and operates under a similar mechanism to that of IR spectroscopy in that the analysis depends on the absorbance of light by atomic excitations. In UV-Vis measurements, however, atoms and molecules undergo electronic transitions as a result of exposure to light of lower wavelengths, the energies of which are sufficient to excite electrons to a higher energy orbital when absorbed.[193] Similar to IR spectra, the resulting UV-Vis spectra is comprised of the wavelengths at which energy has been absorbed, and the degree of absorbance that has taken place, with each peak corresponding to a specific bond within the molecules analysed. These peaks act as markers, allowing substances to be identified more easily and their concentrations determined through calibration curves.

UV-Vis analysis uses the Beer-Lambert Law to allow concentrations of a substance to be determined from UV-Vis measurements, stating that concentration is directly proportional to absorbance. The intensity of monochromatic radiation – light of a single wavelength – that is passed through a homogenous solution is related to both the path thickness and the concentration of the solution being analysed. We can therefore extend Equation 3.15 discussed in Section 3.4.1 to relate concentration (c) to absorbance (A):

$$A = \log\left(\frac{I_0}{I}\right) = \varepsilon c L$$

Equation 3.16

Where ε is the extinction coefficient – a measure of the probability of electronic transition – and L is the path length through the sample, both of which remain constant for samples containing the same substance in the same vessel. When analysing samples quantitatively, the straight-line plot of peak absorbance at a given wavelength vs corresponding sample concentration can be used to determine the concentration of another solution.[197] An example of such a straight-line plot is shown in Figure 3.12 for the UV-Vis analysis of Rose Bengal

solutions of varying concentrations. This demonstrates the way in which UV-Vis measurements can be used to determine the concentration of various substances, applied in this work to assess the performance of RF gels in removing the endocrine disrupter 3,4-DCA from aqueous solutions.

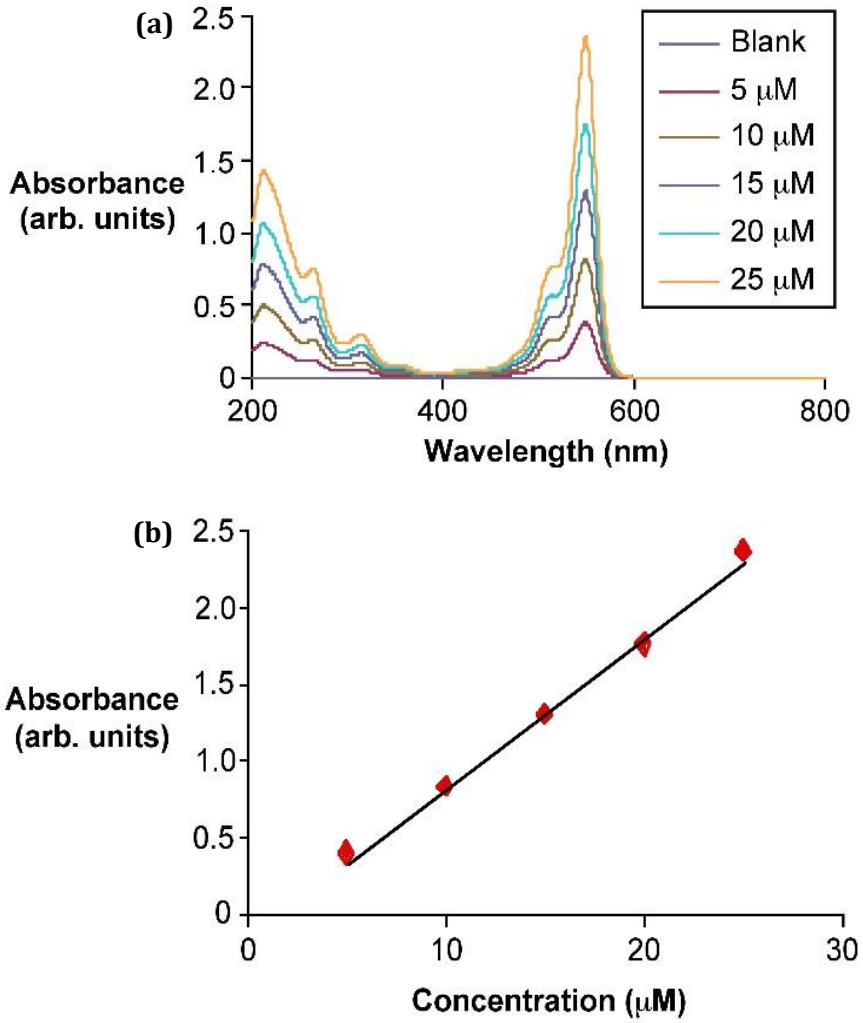

Figure 3.12(a) shows the UV-Vis absorption spectra for Rose Bengal solutions – a commonly used stain – with varying concentrations, while Figure 3.12(b) shows the corresponding plot of peak absorbance with concentration, displaying the resulting linear relationship.[198]

3.5 Summary

The theories behind the experimental analysis techniques used in this work were discussed within this chapter, providing a foundational understanding upon which subsequent chapters can build. This included adsorption analysis techniques, which provide insight into the textural properties of porous materials such as RF gels, in addition to two solution analysis techniques – IR Spectroscopy and UV-Vis Spectroscopy – which are employed to analyse the composition of solvent mixtures and assess the concentration of 3,4-DCA solutions, respectively, within Chapters 5 and 8.

Chapter 4: Computational Techniques and Theory

This chapter introduces the computational techniques used in this work, describing the theories behind them and their applicability to RF gel materials, furthering the discussion included within Chapter 1 detailing previous computational research into porous materials. This includes an introduction to kinetic Monte Carlo theory, which is used to model the formation and growth of RF gels in this work, in addition to fractal analysis techniques such as the determination of fractal dimensions and Hurst exponents. Furthermore, some background into the computational adsorption analysis employed through this work is also provided. Detailed explanations of the algorithms used for modelling both RF gel formation as well as the subsequent adsorption analysis are included in their relevant results chapters – Chapters 6 and 7.

4.1 Formation of Porous Materials

Attempts to understand, estimate, and model processes that appear to be stochastic in nature have taken a variety of approaches over the years. With respect to atomic-level research, the molecular dynamics (MD) technique has emerged as a powerful tool to predict the trajectory and behaviour of individual atoms and molecules using interatomic energy calculations. This has proven invaluable in modelling many atomistic processes, however, its limitations lie both within the small time scales possible and the small length scales readily accessible using this method. The finite element method (FEM), on the other hand, which is commonly used to solve large-scale engineering problems, has the opposite limitation: the extent of its coarse-grain approach renders it incompatible for applications where small-scale interactions are vital to the collective phenomenon observed.[199] The work presented here models the formation of porous materials using the kinetic Monte Carlo (kMC) method – a technique capable of bridging the gap between the micro-effects simulated through MD and the macro-effects simulated through FEM, allowing processes to be modelled beyond the scales accessible for MD, whilst still taking some fine-grain interactions into account.

4.2 Monte Carlo Theory

The Monte Carlo method, which was first proposed by Stan Ulam in 1946[200], encompasses an array of problem-solving algorithms all based upon the use of random numbers – the name making reference to the random nature of gambling within the many casinos of Monte Carlo, Monaco. The flexibility of the Monte Carlo approach is demonstrated in the wide range of processes it has been used to model, from estimating stock market fluctuations[201], to simulating kinetics on catalytic surfaces[202], to the modelling of galaxy formations and distributions.[203]

The kMC approach is a variant of this method that allows the evolution of dynamic processes to be simulated over time, with the kMC method itself being divided into two main sub-categories: rejection kMC and rejection-free kMC. In rejection kMC, a transition step is selected from a uniform distribution, with the step either accepted or rejected based upon

probabilities, dependent on factors such as system energy minimisation. The primary drawback of this method, however, relates to its computational expense, with the repeated generation of random numbers until a step is accepted requiring additional computational work.[204] In rejection-free kMC, on the other hand, a transition step is selected through random number generation, and the selected step is executed without being subject to any further criteria. The likelihood that a given step will be selected, however, is dependent on its pre-determined rate constant, described in more detail below.[205]

The step selection process for rejection-free kMC is shown schematically in Figure 4.1. First, consider that we have N possible pathways that could be taken in a given step, with each pathway possessing a value equal to its rate constant, R_i. The sum of these rate constants, R_N, can therefore be calculated, the value of which can vary throughout the simulation as the system evolves. A random number ($rand_1$) between 0 and 1 is then generated and is multiplied by R_N, the resulting value being used to select the chosen pathway, as illustrated in Figure 4.1. Using this method, the probability that a given pathway will be selected proportional to its pre-determined rate constant.[206,207]

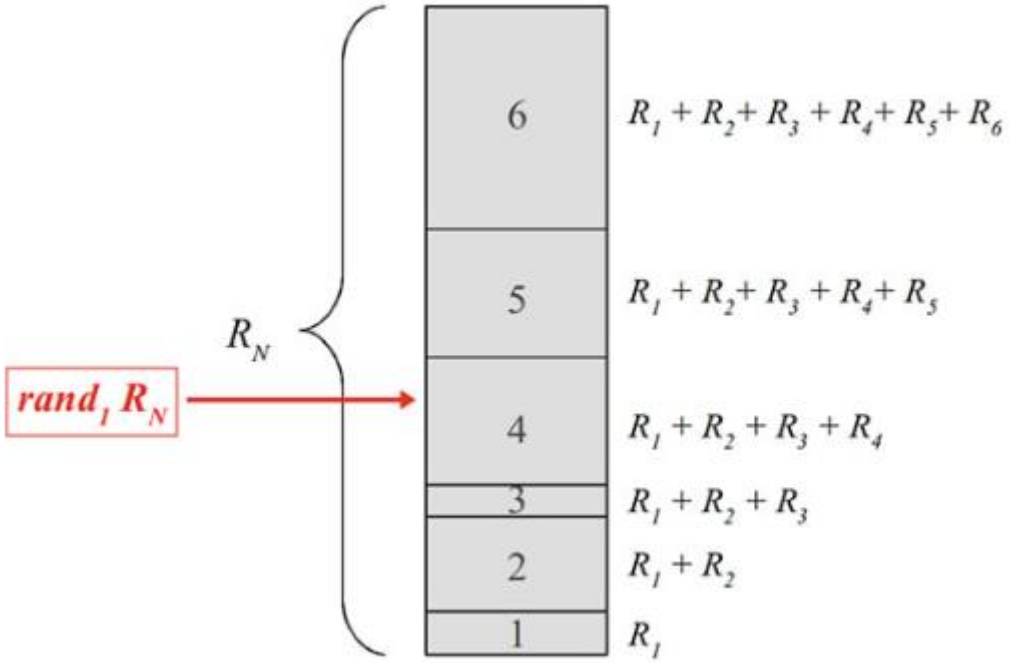

Figure 4.1: Illustration of the kinetic Monte Carlo method using rate constants.[207]

The rejection-free kMC approach is the selected method for the cluster formation and growth model developed in this work. Here, it is used to determine the diffusion steps of monomers and clusters within the 3D lattice, with the rate constant associated with each diffusion step – and therefore the probability that it will be selected – varying inversely with the size of the diffusing species.

4.3 Fractal Analysis

The fractal analysis of RF gel structures produced from the kMC cluster formation and growth model is an important focus of this work, and a variety of analysis methods can be employed to achieve this. Here, we explore the use of fractal dimensions of the structures themselves, in

addition to the Hurst exponent value for a particle diffusing through its porous cavity, the calculation of both allowing the fractal properties of each structure to be assessed.

4.3.1 Fractal Structures

Fractals have been defined as "infinitely complex patterns that are self-similar across different scales" and are formed through the consistent repetition of simple patterns. Fractals are observed frequently in nature, such as in the branches of trees, snowflakes, blood circulatory systems, and coastline geometries.[208,209] Figure 4.2 displays the gradual formation of the well-renowned fractal Koch curve, beginning at the simple initial linear pattern at n=1 which is then continuously repeated as n increases to 2, 3, and 4, with the pattern remaining self-similar as n approaches infinity.

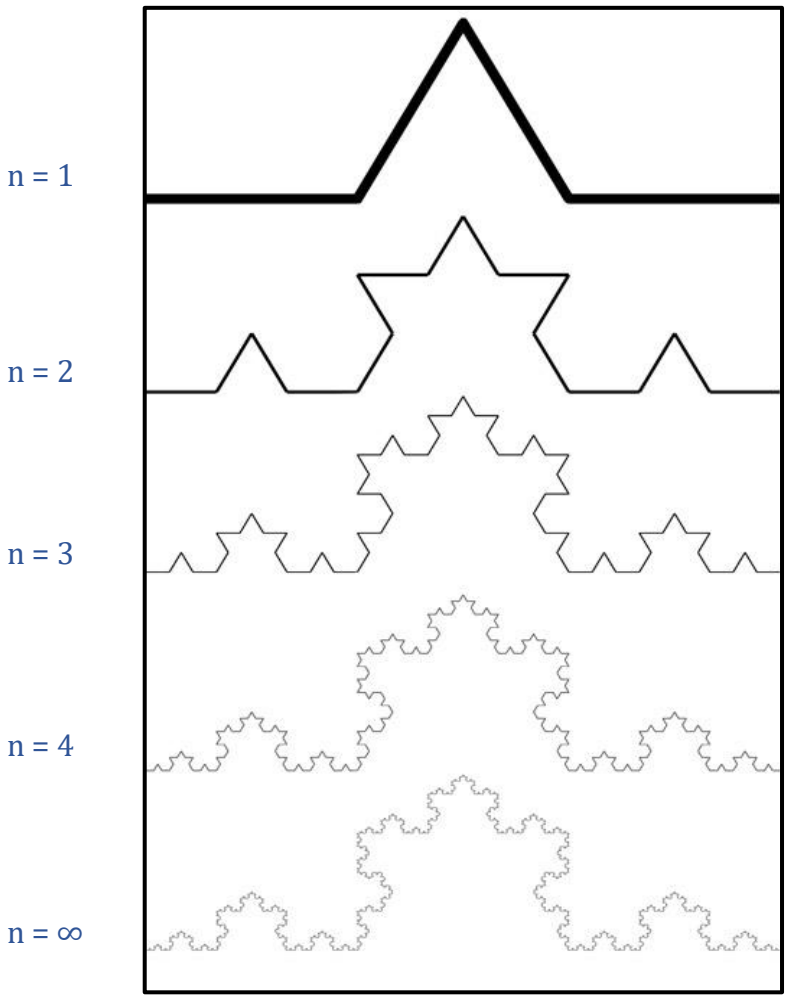

Figure 4.2: The development of the fractal Koch curve.[210]

There are four main properties of fractal materials: infinite intricacy, zoom symmetry, complexity from simplicity, and fractal dimensions.[211] Possessing a fractal dimension means that a material is neither one nor two nor three-dimensional, but rather somewhere in between these, and its fractal dimension value quantifies how the detail of its pattern changes with scale. Two fractal structures may have formed through similar simple pattern repetitions, but even small details can significantly impact both their appearance and their fractal dimension

value. This is demonstrated in Figure 4.2, where two Koch curves are compared – one which has been formed using erection angle of 70°(a) and the other 30°(b), possessing fractal dimension values of 1.404 and 1.053, respectively, and showing significant visual differences.[212]

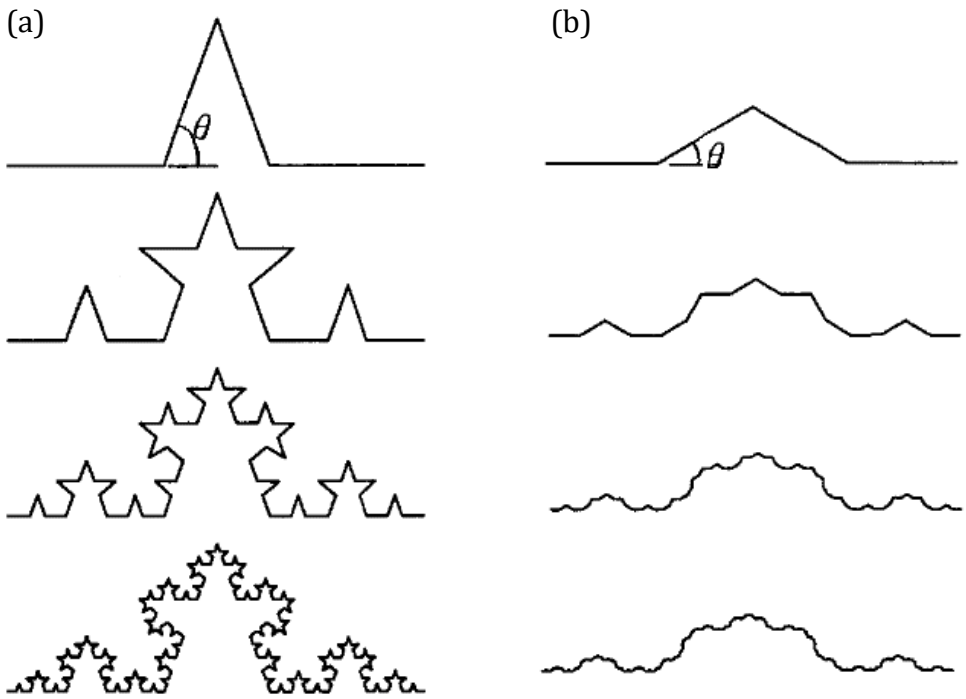

Figure 4.3: The development of Koch curves with different initial erection angles (a) 70° and (b) 30°.[212]

4.3.2 Fractal Dimensions

Fractal properties which can be used to characterise such materials computationally include the box counting dimension (D_b), the information dimension (D_i), and the correlation dimension (D_c). The box counting dimension provides a measure of the system's geometric scaling properties and is regarded as the simplest and most easily understood of the fractal properties.[213] Its calculation is based upon a lattice structure, where the number of boxes containing a part of the structure is counted and scaled logarithmically with box length, as described by Equation 4.1:

$$D_b = \lim_{r \to 0} \frac{\log(N)}{\log(1/r)}$$

Equation 4.1

Where N is the number of boxes occupied by the structure and r is the box length selected. Figure 4.4, below, shows how the box counting dimension analysis can be applied to the fractal Koch curve structures at different box lengths.

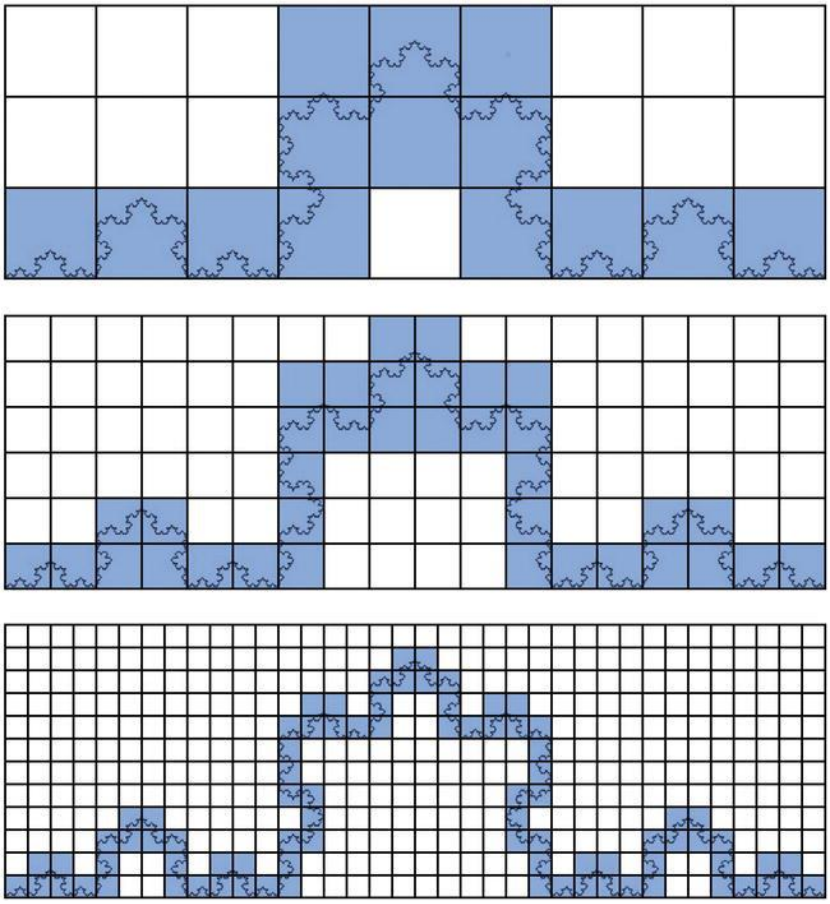

Figure 4.4: Example application of the box counting method for fractal Koch curves.[214]

The information dimension, (D_i), on the other hand, is a more complex property to determine. Similar to the calculation of D_b, it is based upon a lattice structure where the number of boxes containing the structure is determined, however it also analyses the amount of the material which is contained within each box – accounting for the differences in density distribution across the structure. The value of D_i is determined using Equation 4.2, where N and r are, once again, the number of occupied boxes and the box length, respectively, and P_i is the probability of part of the structure occupying box i:

$$D_i = \lim_{r \to 0} \frac{-\sum_{i=1}^{N} P_i \log(P_i)}{\log(1/r)}$$

Equation 4.2

Although estimates of both the box counting dimension and the information dimension are valuable, they are often very computationally expensive to calculate, therefore inhibiting their widespread use.[213] The most common dimension estimate used to characterise a fractal material is the correlation dimension (D_c), which is considerably more computationally efficient to determine, and is based upon the proximity of points within the structure to one another within a spanning radius. Its calculation firstly begins with the determination of the correlation sum (C_r), as determined by Grassberger[215], using Equation 4.3:

$$C_r = \frac{1}{N(N-1)} \sum_{i=1}^{N} \sum_{j=1;j\neq 1}^{N} \theta(r - |X_i - X_j|)$$

Equation 4.3

Where θ is the Heaviside function, r is the radius of the spanning sphere, N is the total number of randomly selected pointed within the structure used for the calculation, and X_i and X_j are the co-ordinates of the two points whose proximity are being analysed within the system. The Heaviside function (θ) is equal to 1 when $r - |X_i - X_j|$ returns a positive value, indicating that the separation of points i and j is less than the spanning radius. Conversely, when $r - |X_i - X_j|$ returns a negative value, indicating that points i and j are outwith the spanning radius, θ is equal to zero. This calculation is carried out across increasing values of spanning radius until the entire structure has been encapsulated and the correlation sum value consequently reaches a plateau.

The value of D_c relates to both the correlation sum and the spanning radius in the following manner:

$$D_c = \lim_{r\to 0} \frac{\log(C_r)}{\log(r)}$$

Equation 4.4

Obtaining the value of the correlation dimension, therefore, can be achieved using a logarithmic plot of the correlation sum vs the spanning radius. Due to the way in which the correlation sum is determined, three regions of the $\log(C_r)$-$\log(r)$ plot are observed: i) the initial scattering of points at low values of r which arise as a result of small scale effects where the error is large, ii) a linear distribution of points as r is increased known as the scaling region, the slope of which is equal to the value of D_c, and iii) a final plateau of points where the entire structure has been encapsulated within the spanning radius, after which point the value of C_r remains the same.[216]

4.3.3 Hurst Exponent

Analysing the fractional Brownian motion trajectory of a particle moving through a porous material is yet another valuable way in which its fractal characteristics can be determined. One such method of quantifying this is through the calculation of the Hurst exponent from the particle trace in the x, y and z directions when the particle takes a 'random walk' – a series of random steps throughout the structure. Three classifications of fractal Brownian motion have been established: 1) Antipersistent motion, where the particle has a tendency to turn back on itself and re-visit previous positions, 2) Neutrally persistent motion, also known as regular Brownian motion, which is observed when the particle is free to move around a lattice with no obstructions, and 3) Persistent motion, where the particle has a tendency to progress its path in a particular direction. The value of the Hurst exponent from the random walk will determine which class of motion is observed, with values less than 0.5 indicating

antipersistence, values of 0.5 exactly indicating regular Brownian, and values greater than 0.5 indicating persistence. Figure 4.5 shows the visual differences in traces for antipersistent motion (H=0.25), regular Brownian motion (H=0.50), and persistent motion (0.75).[217]

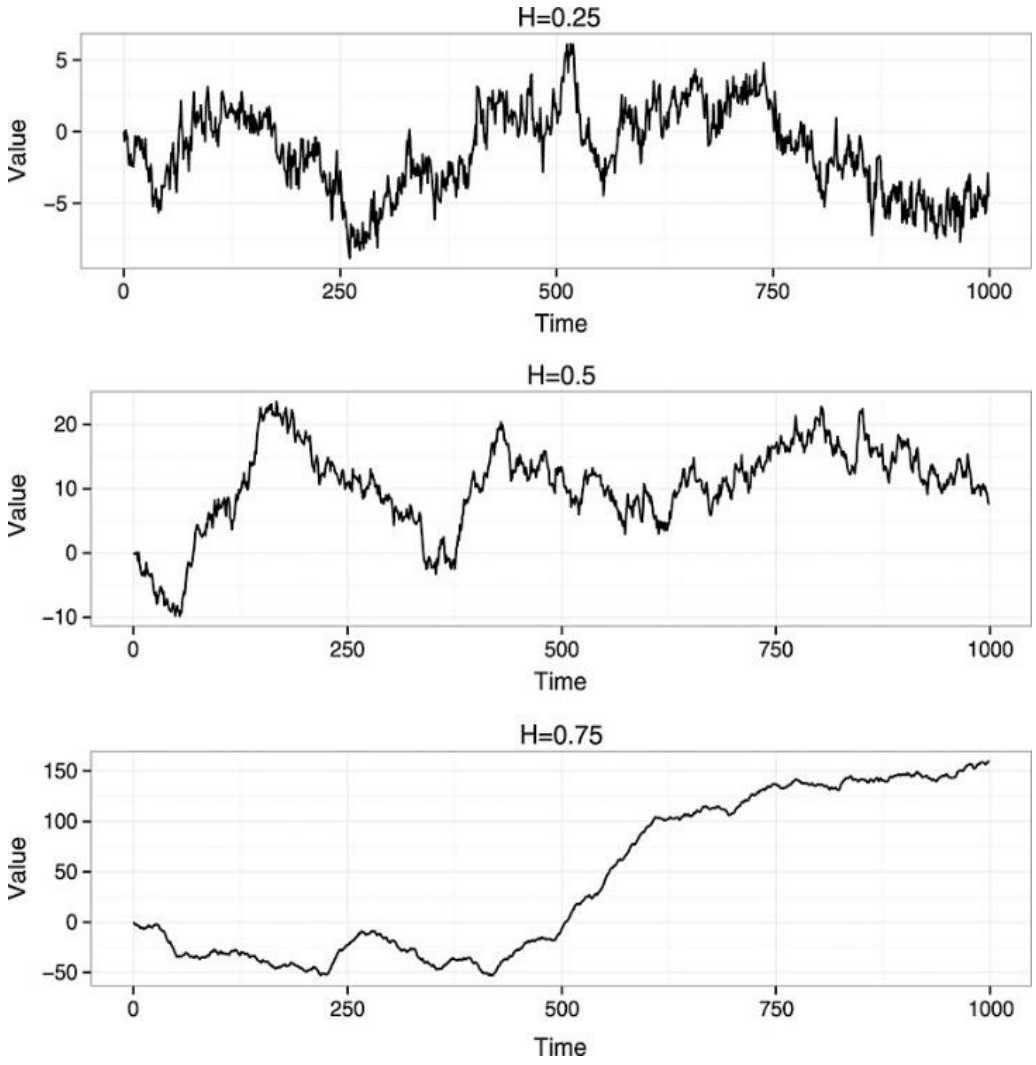

Figure 4.5: Traces for different types of Brownian motion.[217]

The particle displacement from its origin over time is used to calculate the Hurst exponent, where the relationship between the average displacement ($\overline{|\Delta B|}$) across the x, y and z directions and the moving time window size (T_s) is as follows:

$$\overline{|\Delta B|} \propto (T_s)^H$$

Equation 4.5

Where the exponent, H, is the Hurst exponent. In order to determine the Hurst exponent value, therefore, a logarithmic graph of $\overline{|\Delta B|}$ and T_s is plotted, the straight-line gradient of which provides the value of H.[213]

4.4 Gas Adsorption Modelling

As discussed in Chapter 1, the computational modelling of adsorption processes has been explored through both classical density function theory (DFT) techniques in addition to Monte Carlo (MC) and molecular dynamics (MD) simulations, exploring a variety of materials and structures. These approaches are powerful tools for analysing detailed interactions between adsorbents and adsorbates, but are very computationally expensive, limiting their applicability to larger systems. The adsorption analysis simulated here builds upon the work carried out by Monson, which takes a more coarse-grain approach using lattice-based mean field theory (MFT).[165] The qualitative accuracy of this method was confirmed by comparisons of MFT results to those obtained through dynamic MC simulations by Edison and Monson[218], in addition to comparisons to results from MD simulations by Rathi *et al.*[219]

The calculations used for adsorption analysis are described in detail in Chapter 7, where a full explanation of the algorithm used for this work is provided. These calculations are based upon the mean field approximation of the system Helmholtz energy (F), shown in Equation 4.6:

$$F = \left[kT \sum_i (\rho_i \ln \rho_i + (1 - \rho_i) \ln(1 - \rho_i)) \right] - \frac{\epsilon}{2} \sum_i \sum_a \rho_i \rho_{i+a} + \sum_i \rho_i \phi_i$$

Equation 4.6

Where k is the Boltzmann constant, T is the system temperature, ρ_i is the average density of site i within the lattice, ϵ is the nearest neighbour interaction strength, and ϕ_i is the external field at site i. Here, the first expression in Equation 4.6 (within square brackets) is based upon Gibb's expression for entropy, while the second expression is the lattice gas Hamiltonian. The density distribution at equilibrium, where the overall density of the system is fixed, is related to chemical potential (μ) using Equation 4.7:

$$\frac{\partial F}{\partial \rho_i} - \mu = 0$$

Equation 4.7

This relationship can then be used to calculate ρ_i at various μ values and subsequently calculate the average density of the system using an iterative procedure, assuming that μ is equal across the system.

This method can be applied both within individual pores in addition to complex porous structures, as the literature previously discussed exemplifies, and both of these are explored within the work presented here using this approach and related parameters. The resulting isotherms can not only be compared to experimental isotherms obtained from nitrogen adsorption analysis of RF gels, but can also provide insight into pore geometry as well as being used to carry out BJH pore size analysis to quantify the pore widths and distributions.

4.5 Summary

The theories and calculations that form the basis for the computational techniques used in this work were discussed within this chapter, setting the foundation for the subsequent methodologies applied. This included an introduction to kinetic Monte Carlo theory, which is used for the simulation of RF gels, as well as an introduction to the fractal analysis of the resulting materials, the results of both being presented in Chapter 6. The basic theory behind the adsorption analysis of simulated materials was also discussed, with the results from this presented within Chapter 7. As previously mentioned, detailed descriptions of the algorithms used are contained within their respective results chapters.

Chapter 5: Experimental Analysis of RF Gels

This chapter focuses on the experimental analysis of RF gels, investigating various parameters within the synthesis process, and determining the extent of their impact on the final gel properties. The RF gel synthesis methodology is described in detail, including the sol-gel process, the subsequent solvent exchange, and the final drying step. Nitrogen adsorption measurements are used to assess the textural properties of the materials formed under varying synthesis conditions, while Infra-Red (IR) Spectroscopy is used to determine the kinetics of the solvent exchange step carried out for different solvent species. A research article presenting findings from within this chapter has also been published in the journal 'Gels'[220], the full manuscript for which is provided in Appendix D.

5.1 Experimental Methodology

5.1.1 Sol-Gel Synthesis

A series of RF gels were synthesised with varying parameters, each gel formed through an established procedure requiring four reagents: resorcinol, formalin solution, deionised water, and a catalyst. In this work, the catalysts used were sodium carbonate (Na_2CO_3), sodium hydrogen carbonate ($NaHCO_3$), and ammonium hydrogen carbonate (NH_4HCO_3). In the gels investigated here, the volume of liquid added per gel in the initial solution was kept constant at 60 mL, which included the water and methanol content of the formalin solution. The total solids content of the initial mixture was kept constant at 12g, therefore approximately 20% w/v. The mass of resorcinol (R), formaldehyde (F), and catalyst (C) was varied according to the R/C ratio being prepared, all the while maintaining a constant R/F ratio of 0.5 in accordance with the stoichiometry of the resorcinol-formaldehyde reaction. A cylindrical glass jar was used for the RF gel synthesis, measuring 8 cm in diameter and 9 cm in height, which was sealable using a screw-top lid.

To begin, 50 mL of deionised water (Millipore Elix 5 with Progard 2) was pipetted into a sealable cylindrical glass jar, and the required mass of resorcinol (SigmaAldrich, ReagentPlus, 99%) for each corresponding R/C ratio was added, weighed out using a balance with an accuracy to 10^{-5} g. This was stirred using a magnetic stirrer until the resorcinol had completely dissolved, after which point the catalyst (sodium carbonate (SigmaAldrich, anhydrous, ≥99.5%), sodium hydrogen carbonate (SigmaAldrich, anhydrous, ≥99.7%), or ammonium hydrogen carbonate (Fisher Scientific, 99%)), which was weighed into a crucible, was added. After the catalyst had fully dissolved, the required volumes of formaldehyde (as formalin solution, SigmaAldrich, 37wt% formaldehyde in water and methanol) and deionised water – the remaining volume necessary to keep the total liquid in the system, including that from the formalin solution, constant at 60 mL – were added to the mixture using a pipette. Each jar was then sealed with a lid and the mixture stirred for a further 30 min at room temperature. Once this time had elapsed, the stirrer bar was removed and the pH of the mixture was measured, if required, using a Hanna Instruments benchtop pH meter. The sealed jars were then added

to a Memmert ULE-500 oven, which had been preheated to a temperature of 85°C, and left to gel in the oven for 3 days.

In the cases where the specific roles of catalyst anions and cations are investigated, combinations of two catalysts were used, each of which were weighed into separate crucibles and added to the mixture simultaneously, following the synthesis procedure described above. The mass of catalyst required for each combination was calculated based on the percentage of total sodium ions (Na^+) contributed by the two catalysts being compared (in the cases where Na_2CO_3 and $NaHCO_3$ mixtures are used), or the percentage of total hydrogen carbonate ions (HCO_3^-) contributed by the two catalysts being compared (in the cases where $NaHCO_3$ and NH_4HCO_3 mixtures are used). In samples labelled 25Na$_2$-75NaH, this refers to a sample where 25% of the total moles of Na^+ present is contributed by Na_2CO_3, whilst 75% is contributed by $NaHCO_3$. Similarly, in samples labelled 25NaH-75NH$_4$, this refers to a sample where 25% of the total moles of HCO_3^- present is contributed by $NaHCO_3$, whilst 75% is contributed by NH_4HCO_3. All samples within a series such as this maintain a constant concentration of Na^+ or HCO_3^- ions equivalent to that of a standard gel at a given R/C ratio, but with varying contribution percentages from the two catalysts.

In the cases where the impact of varying solvents was investigated, standard Na_2CO_3 gels were prepared as bulk solutions before being divided into standard 60 mL volume gels in each jar. Preparing multiple gels of standard volume, as opposed to one larger gel which could then be divided into smaller samples for solvent exchange, was a step taken to avoid any potential effects on textural properties from the increased gel thickness during gelation.

5.1.2 Solvent Exchange

After the 3 days in the oven had elapsed, the solvent exchange step was carried out, where the water within the gel pores was replaced by a solvent with a lower surface tension. As previously discussed, this is necessary to limit the extent of structural collapse within the gel during the drying stage. Once the jars had been removed from the oven and allowed to cool to room temperature, the gels were cut into pieces of roughly equal size using the edge of a flat spatula. The standard solvent exchange procedure involved adding 100 mL of solvent into the jar with the gel and then shaking it gently – gels with higher R/C ratios (lower catalyst concentrations) are soft and therefore too much force will cause them to disintegrate. Following this, the solvent was drained from the jar and another 80 mL of fresh solvent was added. At this point, they were then sealed with Parafilm and added to a VWR 3500 Analog Orbital Shaker unit, where they were kept at a speed setting of 4. Those gels with higher R/C ratios were often too soft to withstand the shaking motion and were, therefore, kept at the side of the machine during this time. The solvent was drained each day for three days and replenished with 80 mL fresh solvent, with the volume of solvent added totalling 240 mL over the 3-day exchange period.

In the cases where the impact of varying solvents was investigated, gels were divided into halves after gelation and split into two individual jars, with their respective solvent exchange procedure being carried out using half the standard volume of solvent (i.e. 40 mL as opposed to the standard 80 mL). The solvents used for comparison of solvent type were three polar

solvents: acetone (VWR, ACS Reagent, ≥99.5%), methanol (VWR, ≥99.5%), and ethanol (SigmaAldrich, absolute, ≥99.8%), and two non-polar solvents: hexane (SigmaAldrich, anhydrous, 95%) and heptane (SigmaAldrich, anhydrous, 99%).

5.1.3 Vacuum Drying

Following the 3-day solvent exchange period, the gels were drained of all liquid and subsequently dried under vacuum for 2 days using a vacuum oven (Townson and Mercer 1425 Digital Vacuum Oven) with an attached vacuum pump. The plastic lids on the jars were removed and the tops were covered with perforated aluminium foil to allow solvent vapour to escape. The heating element of the vacuum oven was turned off every evening and turned on again every morning, remaining under vacuum overnight, due to safety restrictions within the lab. Insulated canisters containing ice water were positioned between the oven vent tube and the pump, acting as 'solvent traps', capturing and condensing the vapour being released from the gels as they dry. After the 2-day drying period had elapsed, the gels were removed from the oven and placed into labelled sample tubes.

5.1.4 Nitrogen Adsorption Analysis

Adsorption analysis is a commonly employed tool which is valuable for characterising the porous structure present within the RF gels synthesised. This form of analysis provides details of gel properties including surface area, micropore volume, and pore size distribution, all of which can be ascertained from the isotherm data. The Micromeritics ASAP 2420 Surface Area and Porosity Analyser (Figure 5.1) was used to carry out this analysis, employing the two-step process described below.

Figure 5.1: Labelled diagram of the Micromeritics ASAP 2420 Surface Area and Porosity Analyser used for nitrogen adsorption analysis.[221]

Before the adsorption analysis can be carried out, the sample must undergo a degassing process to remove any substances already adsorbed onto the pore walls, such as residual water or solvent molecules remaining on the surface. Firstly, approximately 0.5 g of each gel material was weighed out and added to a glass tube with a bulb base before being attached to a degassing port, where a heating mantle was secured in place around the bulb such that its thermocouple was in direct contact with the glass. The degassing procedure involved gradually elevating the temperature of the sample up to 110°C while under vacuum and maintaining this temperature for 120 min as the sample was evacuated, after which point it was allowed to cool to room temperature and pressure, being backfilled with nitrogen gas.

Following the degassing of the sample, which typically lasted up to 8 h for each sample, the nitrogen adsorption analysis was then carried out. The sample bulb was re-weighed, and the recorded sample mass was adjusted accordingly to account for the mass of contaminants that had been removed. Following this, a filler rod was added to the sample tube to reduce unnecessary unoccupied volume, increasing the accuracy of the measurement. The tube was then fitted with an isothermal jacket to maintain a constant temperature profile throughout the sample during the analysis, before finally being attached to one of the six sample analysis ports (indicated in Figure 5.1). The sample tube was then immersed in liquid nitrogen using an insulated dewar, where a constant temperature of -196°C was maintained, and the nitrogen adsorption analysis proceeded. This process lasted up to 20 - 30 h per sample, collecting 40 data points for adsorption as the relative pressure is incrementally increased from 0.1 - 1, then 30 data points for desorption as the relative pressure is decreased back down from 1 - 0.1. The Micromeritics ASAP 2420 equipment software was then used to analyse the isotherm data using the BET and BJH methods, the theories of which were discussed in Chapter 3, determining valuable characteristics such as the sample's pore size distribution, total pore volume, accessible surface area, and average pore width.

5.1.8 Infra-Red (IR) Spectroscopy

In an effort to gain additional insight into the various factors that affect the performance of solvents in reducing pore shrinkage, the kinetics and exchange rate of acetone, methanol, and ethanol were investigated. This was carried out using IR spectroscopy, with other methods such as UV-Vis deemed unsuitable due to extensive overlapping of absorbance peaks for water and the exchanged solvents. Although IR Spectroscopy is typically used as a qualitative method as opposed to a quantitative method, it is used in this work to determine approximate solvent-water ratios for the purpose of kinetic analysis and is not used to calculate definitive concentrations.

Creating Calibration Curves

In order to analyse water-solvent ratios throughout the solvent exchange process, it was necessary to first produce calibration curves for solutions of known solvent-water ratios. Solvent-water mixtures were prepared according to the following solvent-water percentage volume ratios, measured prior to mixing: 100:0, 80:20, 50:50, 20:80, and 0:100. Note that these solvent-water mixtures are non-ideal mixtures, and therefore the total volume will not be the sum of the volumes added. Still, analysing the approximate rate of exchange is valuable,

allowing the point at which the system reaches equilibrium to be established for each solvent. These ratios were prepared by pipetting the appropriate quantities of both solvent and water into a glass reagent bottle and immediately sealing it with its lid to avoid any evaporation of solvent. Once each of the samples had been prepared, they were transported immediately to the IR Spectroscopy Equipment for analysis. Calibration curves for the following solvents were produced: methanol, ethanol, and acetone. Through comparison of the IR spectra produced from each of the pure solvents in addition to pure water, absorbance peaks that are characteristic only to one species, with little or no overlap with the peaks from the other species in the mixture, were selected as composition indicators. The absorbance value at each of these peaks were recorded for each solvent-water mixture ratio and plotted graphically to produce curves of expected absorbance corresponding to the percentage solvent present.

IR Spectroscopy Analysis

Before beginning IR Spectroscopy on a sample, it is necessary to first carry out an air IR analysis which is used as a reference for further experiments by the software. An ABB MB3000 FT-IR Spectrometer (Figure 5.2) was used for analysis of these solutions with the liquid analysis attachment fitted, and analysis on the empty cell with the cover applied was initially run to obtain the air reference sample. Following this, analysis of the solvent-water mixtures proceeded, beginning with the highest percentage solvent and moving sequentially down to the lowest percentage. The sample was inserted into the cell using a pipette, coating the length of the cell, and the cell cover then applied on top. The analysis was then run through the software, ensuring a signal of approximately 80% was achieved by altering the detector gain for maximum accuracy, and the resulting absorbance data recorded. These steps were carried out with immediacy, once again to avoid any evaporation of solvent, and were cleaned using acetone between samples and dried with a paper towel, operating under the assumption that no residual acetone would remain on the surface. For each of the samples, the measurement was repeated three times, allowing an average of the three to be taken and ensure consistency between measurements.

Figure 5.2: Laboratory FT-IR Spectrometer Equipment [222]

Solvent Exchange Sampling

In order to monitor the kinetics of the solvent exchange process, a procedure was established whereby a solvent (either ethanol, methanol, or acetone) was added to 6 identical gels simultaneously, and the composition of the solvent mixture was analysed at 6 different times. The gels were synthesised as a bulk solution before being divided into three standard gels, as per the procedure in Section 5.1.1. The 3 gels were subsequently divided into a total of 6 halves and separated into individual jars, following which, the gels were cut into pieces of approximately equal size and the relevant solvent added. Each jar was sealed with its lid and wrapped with parafilm before being placed on the shaker unit to begin the solvent exchange process. The jars were labelled according to the time interval at which their solvent composition was to be analysed, for example, the solvent composition of Jar 1 was analysed after 2 h, Jar 2 after 4 h, Jar 3 after 6 h, etc. Due to laboratory access restrictions, samples could not be taken after 5pm each day, therefore samples were analysed at the following time intervals: 2 h, 4 h, 6 h, 24 h, 26 h, and 28 h.

Determining Solvent Composition

The composition of the solvent at each time interval during the solvent exchange process was determined using the calibration curves produced from the prepared solvent mixtures of known ratios. The characteristic absorption peaks selected to form the calibration curves were identified in the IR spectra of the sample measurements and their absorbance recorded. These absorbance values were then plotted on the calibration curves for each peak and the corresponding percentage solvent determined, indicating the extent of solvent exchange that had been achieved within that time interval.

5.2 Results and Discussion

5.2.1 Varying Catalyst Concentration

The effect of varying the molar ratio of resorcinol to catalyst, referred to as R/C ratio, has been studied previously and is pivotal in determining the final textural properties of the RF gel. 'Standard' RF gels were prepared using Na_2CO_3 as the catalyst, with the R/C ratios studied being 100, 200, 300, 400, 500, and 600. Samples of each gel were analysed using nitrogen adsorption, the resulting isotherms from which are displayed in Figure 5.3. The isotherms shown vary significantly with changes in R/C ratio, with differing gradients of uptake observed with increasing relative pressure, as well as differing x-axis positioning of the hysteresis loops, both of which provide important insights into material properties. As can be seen from the plots, an increase in R/C ratio corresponds to a reduced uptake at lower pressures, suggesting that fewer micropores are present, given that micropores are known to fill at lower relative pressures. Instead, the increased mass adsorbed at higher pressures for lower R/C ratio materials points towards the increased presence of macropores within these materials. Furthermore, as the R/C ratio is increased, the hysteresis loop positioning shifts to higher relative pressure values, once again pointing towards the presence of larger pores,

which fill and empty at higher relative pressures. Using the data from the isotherm, the pore size distribution can be calculated using the BJH method, allowing the gels' porous structure to be characterised more precisely. Figure 5.4 displays the pore size distribution for the standard RF gels at R/C ratios of 100 to 600, with the total area below each plot being representative of the total pore volume of that gel, whilst Table 5.1 details the average pore width value of each of the gels studied, in addition to its accessible BET surface area.

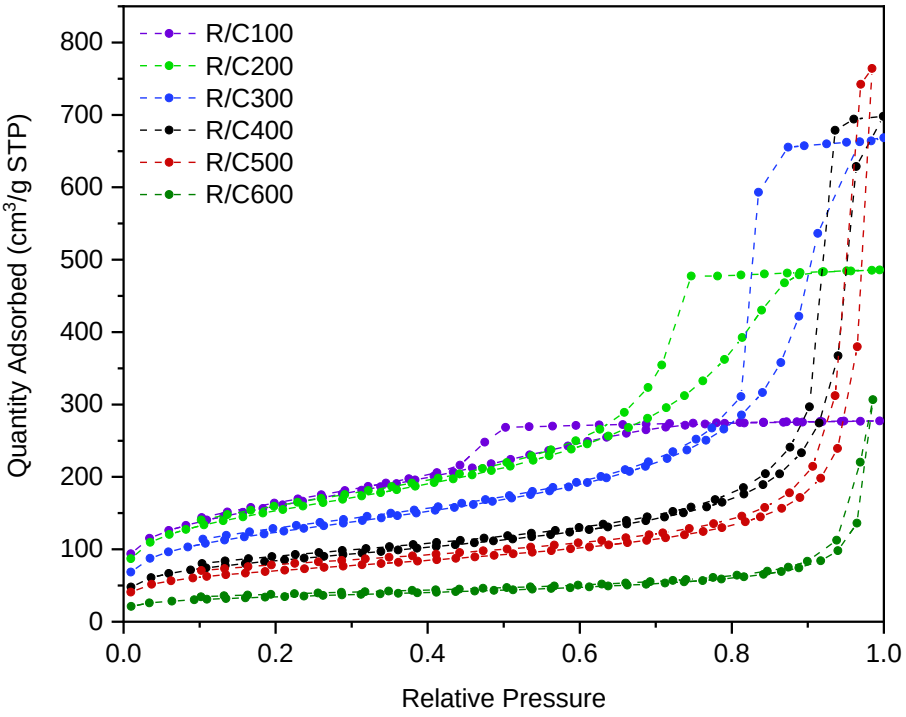

Figure 5.3: Nitrogen adsorption isotherms for sodium carbonate gels at R/C ratios 100-600.

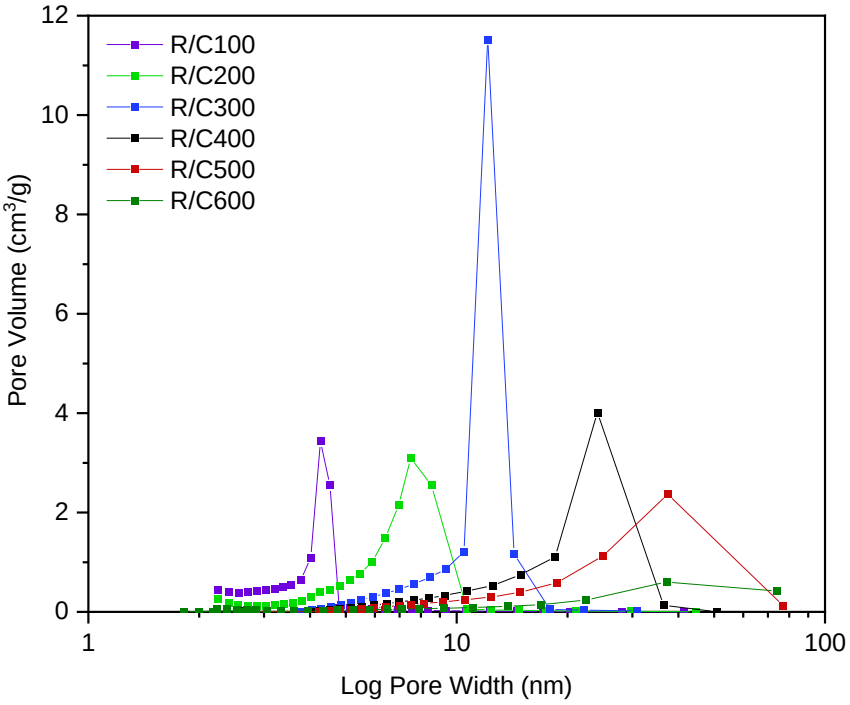

Figure 5.4: Pore size distributions for sodium carbonate gels at R/C ratios 100-600.

Table 5.1: Average pore widths (d_{avg}) and BET surface areas (S_{BET}) for sodium carbonate gels at R/C ratios 100-600. Note that the average pore width values are recorded to an accuracy less than their error, therefore their error values have been omitted.

R/C Ratio	d_{avg}(nm)	S_{BET} (m²/g)
100	4	574
200	7	552
300	11	446
400	19	304
500	26	254
600	28	124

As indicated by the isotherms for the standard gels (Figure 5.3), an increase in R/C ratio is associated with an increase in average pore width. The graph in Figure 5.4 confirms this, displaying the pore size distribution for each sample visibly shifting towards larger pore width values as the R/C ratio increases. The increase in pore size associated with high R/C ratios is thought to be as a result of the reduced number of initial clusters formed, leading to the growth of larger clusters over time, the process of which occurs at a slower rate.[27] These larger clusters subsequently have larger pores between them, impacting the textural properties and overall appearance of the resulting gels. The higher concentration of catalyst present in gels synthesized using lower R/C ratios results in a higher number of initial clusters formed, the total mass therefore being distributed over a greater number of smaller clusters, the process of which takes place more rapidly. Given that the clusters formed are of smaller average size, they subsequently have smaller pores between them, once again impacting the textural properties and overall appearance of the gels formed.[27] The gels formed at low R/C ratios, therefore, possess a higher degree of porosity, with a greater number of pores of smaller widths, and an increased surface area per gram, making them useful for applications such as filters, sorbing media for waste containment, or hydrogen fuel storage.[223]

5.2.2 Varying Catalyst Species

As discussed in detail in Chapter 1, a range of research has been published on the impact of catalyst concentration on the final gel properties, with most referring to the catalyst purely as a means to alter the pH of the initial solution, labelling it simply as a 'pH adjuster'. Whilst the impact of initial solution pH is undeniably fundamental to the final textural properties of the gel, some studies have indicated that the role of the catalyst components extends far beyond this. The main hurdle in fully understanding the role of the catalyst is in attempting to decouple the relationship between the concentration of catalyst components present and the resulting pH of the gel solution, given that one cannot be altered without affecting the other. It is, of course, possible to keep the catalyst concentration constant whilst adjusting the pH through additions of acidic or basic solutions, however this method introduces new additional components into the gel solution, which could ultimately alter the final structure of the gel

formed. With this in mind, this research aims to decouple the relationship between pH and the catalyst concentration, in addition to analysing the role of the specific components of the catalyst used. This is achieved through the preparation and analysis of two sets of gel samples with the following catalyst combinations:

1(i) Na_2CO_3 and $NaHCO_3$ mixtures at constant cation concentrations equivalent to R/C 100
1(ii) Na_2CO_3 and $NaHCO_3$ mixtures at constant cation concentrations equivalent to R/C 300
2(i) $NaHCO_3$ and NH_4HCO_3 mixtures at constant anion concentrations equivalent to R/C 100
2(ii) $NaHCO_3$ and NH_4HCO_3 mixtures at constant anion concentrations equivalent to R/C 300

Using these combinations of catalyst species, the specific roles of the cation and anion can be investigated, with sample sets 1(i) and 1(ii) exploring the effects of varying solution pH with the addition of H^+ ions while the Na^+ concentration remains constant. Sample sets 2(i) and 2(ii), on the other hand, vary the concentration of Na^+ ions while the concentration of HCO_3^- remain constant, providing further insight into the significance of the metal cation's role. The isotherms of these sample sets can be used for valuable comparisons, allowing us to assess the role of the two individual components of the standard sodium carbonate catalyst used – the metal cation (Na^+) and the carbonate anion (CO_3^{2-}) – based on how the gel's structure is impacted by their individual concentrations. The mass of catalyst required for each combination was calculated based on the percentage of total sodium ions (Na^+) contributed by the two catalysts being compared (in the cases where Na_2CO_3 and $NaHCO_3$ mixtures are used), or the percentage of total hydrogen carbonate ions (HCO_3^-) contributed by the two catalysts being compared (in the cases where $NaHCO_3$ and NH_4HCO_3 mixtures are used). In samples labelled 25Na$_2$-75NaH, this refers to a sample where 25% of the total moles of Na^+ present is contributed by Na_2CO_3, whilst 75% is contributed by $NaHCO_3$. Similarly, in samples labelled 25NaH-75NH$_4$, this refers to a sample where 25% of the total moles of HCO_3^- present is contributed by $NaHCO_3$, whilst 75% is contributed by NH_4HCO_3. All samples within a series such as this maintain a constant concentration of Na^+ or HCO_3^- ions equivalent to that of a standard gel at a given R/C ratio, but with varying contribution percentages from the two catalysts.

Catalyst Mixtures – Na_2CO_3/$NaHCO_3$

First, we consider the isotherms of sets 1(i) and (ii), shown in Figure 5.5(a) and (b), where the Na^+ concentration remains constant and equal to that of standard gels prepared at R/C ratios of 100 and 300, respectively. Despite the variations in initial solution pH as the concentration of H^+ ions present increase through the inclusion of $NaHCO_3$, which will be discussed in more detail below, the resulting isotherms remain similar in shape. They each follow the same trend throughout the adsorption process and exhibit similar hysteresis loops, which also occur at very similar relative pressure values. Minute variations in hysteresis loops, such as those observed, are what can be expected between gel samples that are similar in makeup and structure.

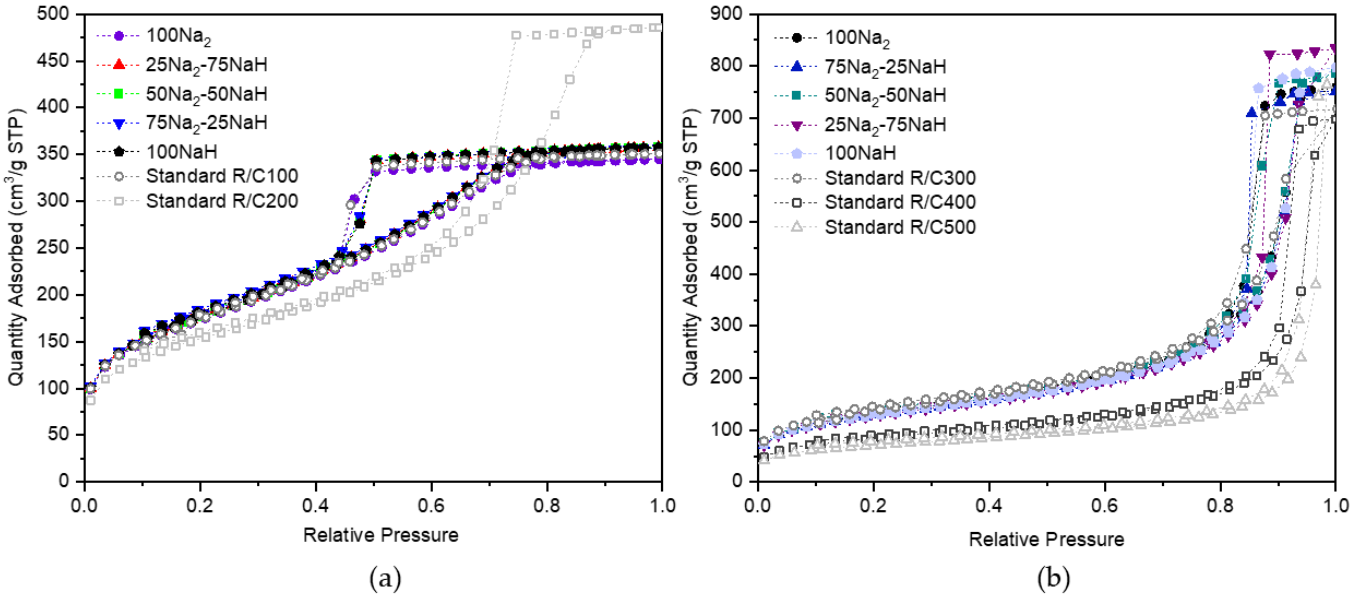

Figure 5.5: (a) Isotherms from sample set 1(i) Na_2-NaH R/C100 Na^+ equivalent, (b) sample set 1(ii) Na_2-NaH R/C300 Na^+ equivalent.

Furthermore, not only are the isotherms within sets 1(i) and 1(ii) indistinguishable from one another within experimental error, but they are also comparable to those obtained for standard gels prepared at the same equivalent R/C ratio in terms of Na^+ concentrations. This suggests that the Na^+ ion is one of the central components in determining the properties of the final material, especially given that the varying concentrations of anions present in the different catalyst mixtures appear to have negligible effects. It is also worth noting that the gels labelled 100NaH, synthesized using 100% $NaHCO_3$ as the catalyst to provide Na^+ concentrations equal to R/C 100 and R/C 300 standard Na_2CO_3 gels, are actually representative of R/C 50 and R/C 150 gels with respect to the molar ratio of resorcinol to $NaHCO_3$ catalyst concentration, given that double the moles of $NaHCO_3$ would be required to meet the required Na^+ moles in comparison to when Na_2CO_3 is used. A comparison between sample set 1(i) and standard R/C 200 gels has been included within Figure 5.5(a), while a comparison between sample set 1(ii) and standard R/C 400 and 500 gels has been included within Figure 5.5(b), both of which will be discussed further when the impact of initial solution pH is investigated.

Catalyst Mixtures – $NaHCO_3$/NH_4HCO_3

Next, we can consider the isotherms for sets 2(i) and (ii) displayed in Figure 5.6(a) and (b), where the anion (HCO_3^- in this case) concentration remains constant and equal to that of standard gels prepared at R/C ratios of 100 and 300, respectively. The isotherms within the R/C100 set (Figure 5.6(a)) show a gradual change as the Na^+ concentration is reduced and replaced by NH_4^+ until 75% of the HCO_3^- ions present are contributed by NH_4HCO_3, at which point the resulting materials prove to be non-porous, failing to adsorb any quantifiable volume of nitrogen. The isotherms shown within Figure 5.6(b) indicate that a porous material was formed only when 100% of the HCO_3^- ions were sourced from $NaHCO_3$ at R/C 300, with any substitution for NH_4HCO_3 producing a non-porous material once again. When the

samples are then compared to those of standard Na_2CO_3 gels prepared at the same equivalent R/C ratio, the isotherms are different again, even varying from those prepared with 100% $NaHCO_3$. This could be explained by the fact that the R/C ratio for this sample set is made equivalent to the anion concentration, therefore resulting in half the Na^+ concentration when $NaHCO_3$ is used in comparison to Na_2CO_3. Importantly, the visual differences displayed here between the isotherms of 100% $NaHCO_3$ R/C 100 gels and standard Na_2CO_3 R/C 100 gels are in strong agreement with those observed in the work carried out by Horikawa *et al*.[29], discussed previously, who used nitrogen adsorption measurements to determine the comparative properties of pyrolyzed RF aerogels catalysed by Na_2CO_3, K_2CO_3, $NaHCO_3$, and $KHCO_3$, each at R/C 50.

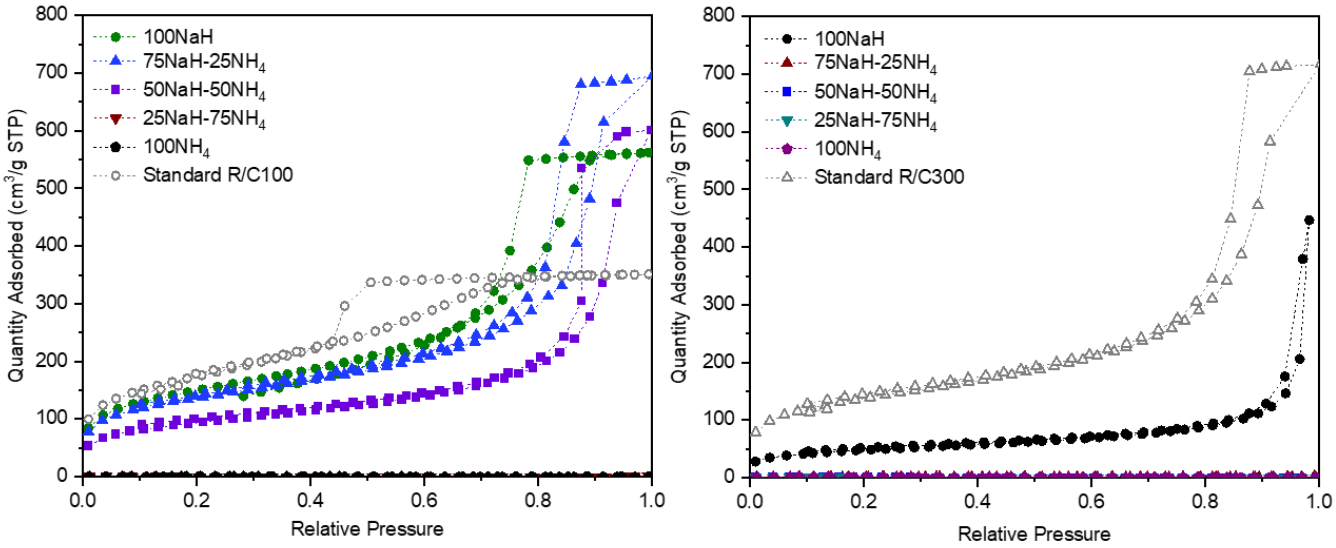

Figure 5.6: Isotherms for (a) sample set 2(i) NaH-NH_4 R/C100 HCO_3^- equivalent, and (b) sample set 2(ii) NaH-NH_4 R/C300 HCO_3^- equivalent.

In this work, the cations used within the catalyst are Na^+ and NH_4^+, where the substitution of one for the other achieved significantly different results. The presence of Na^+ ions appeared to aid the gelation process, leading to the formation of inter-linked porous network structures, while the presence of NH_4^+ failed to promote the gelation process, with its sole use leading to the formation of a non-porous material that had failed to gel completely. Note that the initial solutions for all gels in sample sets 2(i) and 2(ii) fell within the required pH window for the successful formation of porous structures (approximately pH 5.5 to 7.5), the pH values across the samples within these sets ranging between pH 6 and 7. As postulated by Taylor *et al*.[37], the ability of these ions to 'salt-in' or 'salt-out' macromolecules from solution, as with the Hofmeister series, could be an important factor within the results observed. In accordance with the Hofmeister series for cations, shown in Section 1.3.2 in Chapter 1, Na^+ ions have medium kosmotropic effects, therefore promoting the stability of macromolecules, and facilitating the formation of inter-linked porous structures in solution.[43] NH_4^+ ions, on the other hand, have chaotropic effects, therefore contributing to the destabilizing and disordering of macromolecules, and hindering the formation of porous structures in

solution.[44] This could have important implications on the final properties of the structures, with the potential precipitation of solids from solution taking place early in the presence of chaotropic ions (such as NH_4^+), resulting either in the slower growth of the clusters which remain in the solution, or significant precipitation hindering the formation of inter-linked porous structures. These results show promise in elucidating the role of the metal ion, indicating that the concentration of Na^+ present from the catalyst is pivotal in determining the gelation process and subsequent structural properties of the final material.

Structural Impacts of Initial Solution pH

Next, we can use the results obtained from sample sets 1(i) and 1(ii) to investigate the role of the metal cation in comparison to that of the measured initial solution pH, aiming to decouple the overall relationship between catalyst concentration and pH. We can refer back to Figure 5.5, which displays the isotherms from sets 1(i) and 1(ii) alongside isotherms for standard gels across comparable initial solution pH ranges. These can be considered alongside Figure 5.7(a), which shows graphically how the gel's average pore width varies with pH for three sets of samples: sample sets 1(i), 1(ii), and also standard Na_2CO_3 gels at RC ratios 100 – 500, in addition to Table 5.2, which indicates the initial pH of the prepared solutions during gel synthesis for each of the three sets of gels alongside the average pore width determined from nitrogen adsorption analysis of the resulting gels.

Within sample sets 1(i) and 1(ii), a gradient of decreasing initial solution pH is observed, with the concentration of H^+ ions increasing as Na_2CO_3 is substituted for $NaHCO_3$. Using this method to alter the pH introduces no new components into the system, limiting the number of variables being altered at a given time, and therefore allowing a more accurate analysis to be carried out. Figure 5.7(a) shows graphically how the gel's average pore width varies with pH for three sets of samples: sample sets 1(i), 1(ii), and also standard Na_2CO_3 gels at RC ratios 100 – 500, while Table 5.2 indicates the initial pH of the prepared solutions during gel synthesis for each of the three sets of gels alongside the average pore width determined from nitrogen adsorption analysis of the resulting gels.

As the data in Figure 5.7(a) and Table 5.2 shows, the average pore width within the standard Na_2CO_3 gel's structure is significantly impacted by the corresponding R/C ratio used during its synthesis, with average widths ranging from 4 - 26 nm across an R/C ratio range of 100 - 500. Conversely, on inspection of the average pore widths within sample sets 1(i) and 1(ii), very little variation is observed, despite the change in initial solution pH. Furthermore, looking at sample set 1(ii) specifically, the initial solution pH of the gels ranges from 6.44 - 6.72. This range is similar to that observed across standard Na_2CO_3 gels at R/C ratios 300 - 500, which possess initial pH values of 6.48 - 6.78. Despite the similar range of initial pH values observed across the two sets, the final gels formed are markedly different. Samples in set 1(ii), which each possess the same concentration of Na^+ ions, all have average pore widths of around 12 - 14 nm. This is in sharp contrast to that of the standard Na_2CO_3 gels at R/C 300 - 500, which each have different concentrations of Na^+ ions, and whose average pore widths

vary significantly from 11 - 26 nm. The isotherms in Figure 5.5, discussed previously, further highlight the differences in the structures formed, providing a comparison of the adsorption behaviour of the sample within sets 1(i) and 1(ii) with those of standard Na_2CO_3 gels which possess a similar pH range.

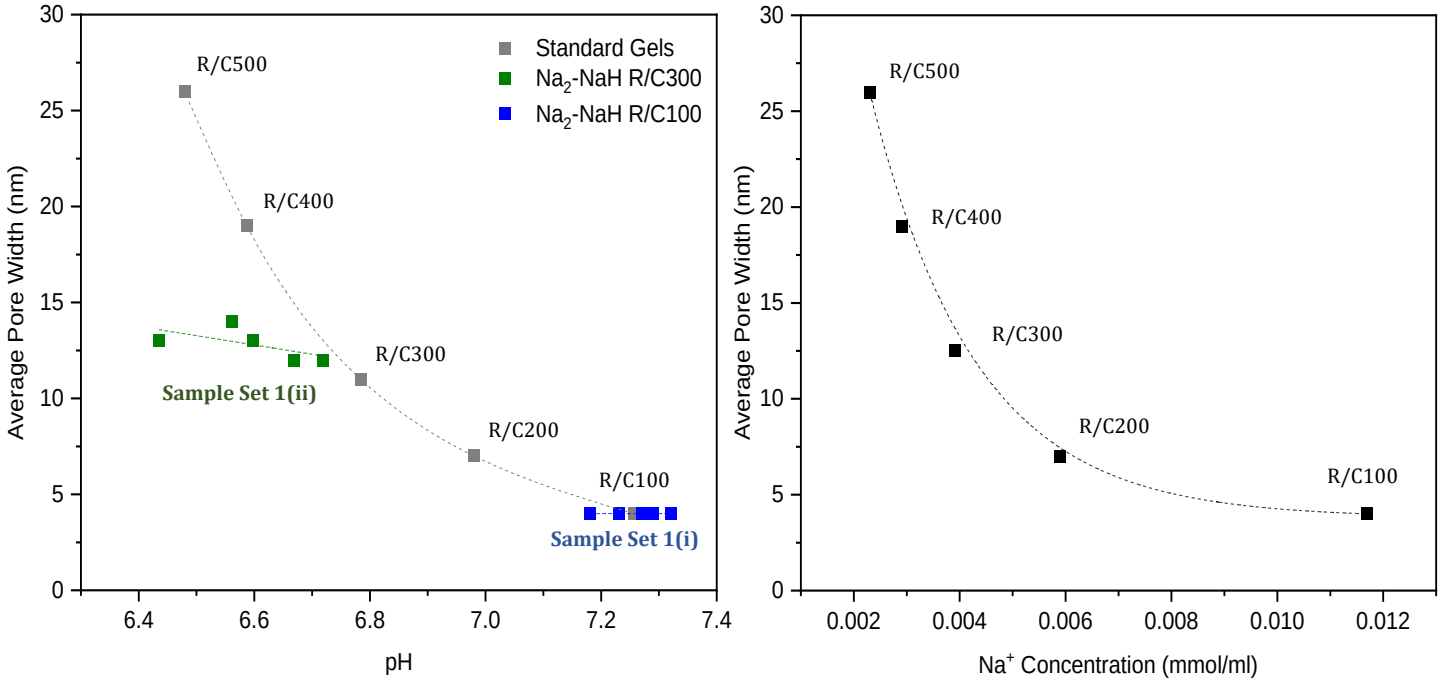

Figure 5.7: (a) Graph of initial solution pH versus average pore width for the three sets of gels. Note that for Sample Sets 1(i) and 1(ii), the points marked on the graph show increasing NaH concentration from right to left. Original R/C 100 – R/C 500 gels are plotted with a dashed line according to exponential decay curve fitting, while a straight line fit is used for Sample Sets 1(i) and 1(ii). (b) Corresponding graph of average pore width with increasing Na^+ concentration, plotted with an exponential decay curve fitting.

Figure 5.7(b) shows directly how the average pore width of each gel varies with its corresponding Na^+ concentration, displaying an exponential decay relationship with increasing Na^+. Note that for the data point at R/C 300, an average value for pore width is taken across the values obtained for Sample Set 1(ii) as well as for the R/C 300 value obtained from the Standard Gels sample set. The results presented in Figures 5.7(a) and (b), in addition to Table 5.2, suggest that the influence of slight pH changes may have been overestimated in previous works, and points towards the pivotal role of the cation in the formation of the gel's porous structure. Although pH undoubtedly plays an important role in the catalysis of the RF reaction, and impacts the textural properties of the final gel when significant pH adjustments are made, this is likely not observed with relatively small changes in pH similar to those in this experiment (<0.4), provided the solution pH falls within the viable range of 5.5 – 7.5 for gels made with a basic catalyst. This could be particularly relevant to the work carried out by Job *et al.*[32], discussed previously within Chapter 1, where RF gels were synthesized at set pH values, achieved through the addition of NaOH solution. In this work, as the pH increased from 5.45 to 7.35, corresponding to the increasing volume of NaOH added, the average pore size consistently decreased from 50 nm to 4 nm. Although the authors concluded that the

change in pH alone was responsible for the significant differences in textural properties achieved, the results presented here suggest that those differences could, in fact, be attributed to the increasing Na^+ concentration as larger volumes of NaOH solution was added.

Table 5.2: Initial pH values of standard gels at varying R/C ratios, in addition to that of samples in sets 1(i) and 1(ii), and their corresponding average pore widths (d_{avg}). The average pore width values are recorded to an accuracy less than their error, therefore their error values have been omitted.

Standard Gels	**pH**	**d_{avg}(nm)**
R/C 100	7.26	4
R/C 200	6.98	7
R/C 300	6.78	11
R/C 400	6.59	19
R/C 500	6.48	26
Sample Set 1(i) R/C 100	**pH**	**d_{avg} (nm)**
100Na_2	7.32	4
75Na_2-25NaH	7.29	4
50Na_2-50NaH	7.27	4
25Na_2-75NaH	7.23	4
100NaH	7.18	4
Sample Set 1(ii) R/C 300	**pH**	**d_{avg} (nm)**
100Na_2	6.72	12
75Na_2-25NaH	6.67	12
50Na_2-50NaH	6.59	13
25Na_2-75NaH	6.56	14
100NaH	6.44	13

5.2.3 Varying Solvent Type

In addition to assessing the impact of parameters within the sol-gel reaction itself, this work also investigates the performance of various solvents used during the solvent exchange step within gel synthesis, analysing their efficacy in preventing structural collapse upon drying. As previously discussed, acetone is the solvent most commonly used for this purpose,

therefore, this work compares the performance of acetone to that of four other solvents of varying surface tensions, analysing the resulting gels from each. Three polar solvents were compared: acetone, methanol, and ethanol, in addition to two non-polar solvents: hexane and heptane. Using a combination of both polar and non-polar solvents, in this case, allows the extent of the hydrophilic or hydrophobic nature of the gel structure to be determined. As described in Chapter 1, as the liquid within the pores is removed throughout the drying process, the capillary forces present cause the pores to become misshapen and drawn inwards, ultimately resulting in structural collapse if the gel is not capable of withstanding such stress. The intensity of the capillary stress (P_r) is impacted by a number of parameters, as described by Equation 5.1:

$$P_r = \frac{2\gamma cos\theta}{r}$$

Equation 5.1

Where γ is the surface tension of the liquid, θ is the wetting angle of the liquid, and r is the pore radius.[54,55] It would, therefore, be expected that a solvent with the lowest surface tension would be most effective in preventing shrinkage from taking place, resulting in gels which better maintain their original structure, therefore enabling a more accurate analysis of their original properties to be carried out. Gel samples at R/C ratios 100, 300, and 600 were prepared, all of which were analysed using acetone, methanol, heptane, and hexane as solvents during the solvent exchange step. Due to the limitations of lab access as a result of COVID-19, the analysis of gels exchanged with ethanol was carried out only for R/C ratios of 100 and 300. Similarly, R/C 100 and R/C 300 gels which underwent no solvent exchange, therefore possessing only water within their pores, were prepared for comparison, labelled 'Water R/C100' and 'Water R/C300'.

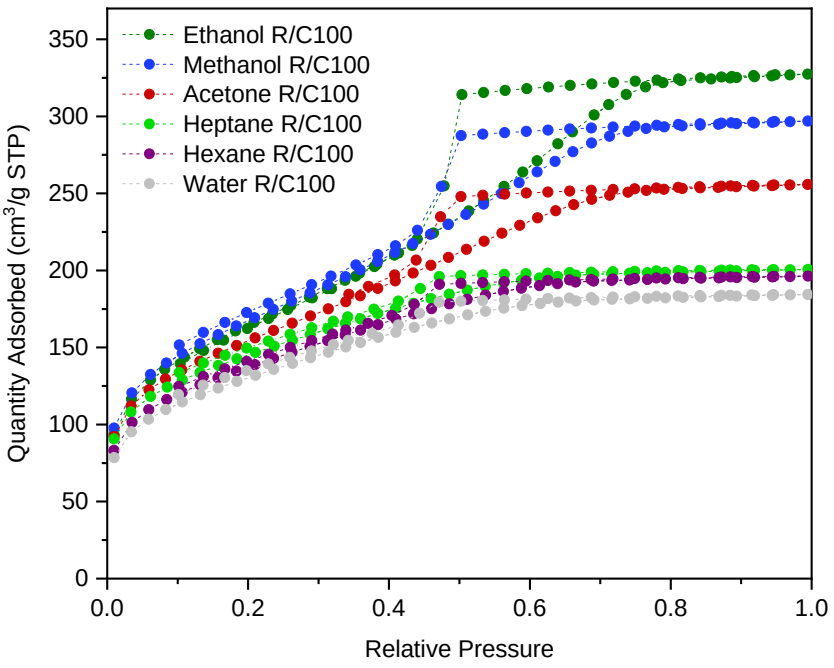

Figure 5.8 Isotherms for R/C 100 sodium carbonate gels synthesised with varying solvents.

Figure 5.8 displays the resulting isotherms from nitrogen adsorption analysis of samples at R/C 100, where the most prominent difference in pore shrinkage was observed. Table 5.3,

meanwhile, displays the comparative average pore width for R/C 100 gels and the total pore volume for all three R/C ratios studied, alongside the corresponding solvent surface tension values for reference. All surface tension values cited are taken at 25°C, a temperature comparable to that of ambient laboratory conditions. Furthermore, Figures 5.9 (a) and (b) display the isotherms from R/C 300 and R/C 600 gels, respectively.

Table 5.3: The total pore volumes (V_T) for each of the R/C 100, 300, and 600 gels, alongside the corresponding solvent surface tension values (γ) at 25°C. The average pore width (d_{avg}) for R/C 100 gels have also been included. Note that the total pore volume and average pore width values are recorded to an accuracy less than their error, therefore their error values have been omitted.

Solvent Used	**γ (mN/m)**	**d_{avg} R/C 100 (nm)**	**V_T (cm³/g)**		
			R/C 100	**R/C 300**	**R/C 600**
Ethanol [61]	21.79	4	0.506	1.254	-
Methanol [224]	22.48	4	0.459	1.089	0.695
Acetone [61]	23.46	4	0.396	1.036	0.515
Heptane [225]	19.49	3	0.310	0.835	0.677
Hexane [226]	17.90	3	0.304	0.842	0.536
Water [61]	71.99	3	0.285	0.822	-

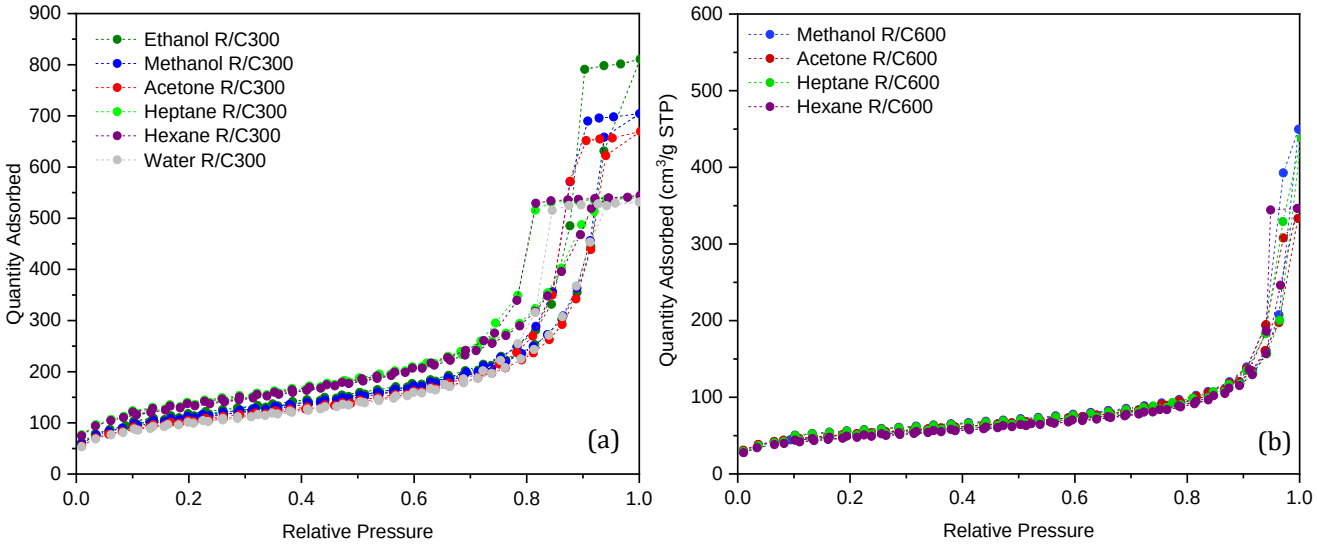

Figure 5.9: Isotherms for sodium carbonate gels with varying solvents (a) 300 and (b) 600.

Analysing the results from R/C 100 and 300 gels, where the most variation in total pore volume (Table 5.3) and quantity adsorbed (Figure 5.8 and 5.9(a) for R/C 100 and 300, respectively) are observed, the comparative performance of solvents in reducing pore shrinkage is as follows: ethanol > methanol > acetone > heptane ≈ hexane > water. Despite heptane and hexane possessing the two lowest surface tension values of the solvents, their performance in

reducing structural collapse was poor. As previously discussed, as non-polar solvents, both hexane and heptane are hydrophobic and, therefore, immiscible with the water present within the gel pores due to their inability to compete with the strong attractive forces between the polar water molecules. Of course, if the gel-water interactions are sufficiently strong to prevent any hexane or heptane molecules from accessing the gel surface, the solvent exchange cannot take place. If, however, there is sufficient attractive forces between the non-polar solvents and the solid structure of the gel, some heptane or hexane may be able to access the pore walls and replace some of the water present. Interestingly, previous research has documented the use of heptane and hexane as solvents for gels whose surface chemistry had been modified to include water-repelling chemical groups, enhancing the solvent exchange process.[55] The poor performance of the non-polar solvents in the results presented here, however, indicates that only minimal amounts of water were exchanged in this case, pointing towards the RF gel's hydrophilic nature, and the resulting samples consequently show only minimal improvements in reduced structural collapse in comparison to that which underwent no solvent exchange step whatsoever.

The polar solvents used (acetone, methanol, and ethanol) are completely miscible with water, and can, therefore, efficiently access the water-filled pores in order to complete the solvent exchange step. A comparison of these three solvents confirms the following trend: as the surface tension of the solvent decreases, its efficacy in reducing structural collapse increases. The total pore volume of R/C 100 gels exchanged with ethanol was 0.506 cm^3/g, while that of those with no solvent exchange was just 0.285 cm^3/g, corresponding to a pore shrinkage of approximately 45%. This is mirrored in the R/C 300 gels, where the same performance trend is observed across the polar solvents studied, this time a pore shrinkage of approximately 35% calculated from the comparative pore volumes of ethanol-exchanged gels and those with no solvent exchange. The effect of surface tension on porous material properties after drying has been studied in detail for concrete mixtures, where the structural integrity is crucial, with the results agreeing with those presented here. The addition of shrinkage-reducing admixtures (SRAs) is common practice in this application to minimise structural collapse during drying, with studies confirming the direct relationship between the reduced surface tension of the liquid phase as a result of SRAs and the subsequent reduction in shrinkage cracking of the dried concrete.[64,65] Furthermore, the results also correlate with those found by Deshpande *et al*.[227] for silica-based xerogels, who investigated the efficacy of a range of solutions with varying surface tensions. Here, a linear trend was observed for the final pore volume of the xerogels, with values of both increasing as the surface tension of the solvent used decreased. A study by Kraiwattanawong *et al*.[61], however, had conflicting findings in their analysis of RF gel final textural properties after employing different drying methods and different solvents for solvent exchange. Although t-Butanol, possessing the lowest surface tension, performed best in reducing pore shrinkage of the solvents studied, the performance of ethanol was the poorest by far, despite possessing the second lowest surface tension. The researchers conclude that the slightly higher polarity index of ethanol – a difference of just 0.1 between ethanol and acetone – contributed to its poorer performance, resulting in gels with surface areas of just 130 m^2/g in comparison to 590 m^2/g for gels exchanged with acetone under the same synthesis conditions. Other analogous results obtained in this study for ethanol exchanged RF gels included the reduced surface area of materials dried under vacuum in comparison to ambient conditions, in contrast to that which would be expected, and also opposite to the trend observed for ambient and vacuum drying of each of the other solvents

studied. The explanation for this is unclear, but could point towards potential synthesis issues producing unreliable results in this case.

Upon inspection of the isotherms for each set of samples, it is evident that the variations in total quantity adsorbed are most prominent for gels at R/C 100 (Figure 5.8), with variations decreasing as R/C ratio increases to 300 (Figure 5.9(a)), and finally to 600 (Figure 5.9(b)). This is likely as a result of the higher average pore width observed at higher R/C ratios, which leads to a gel that is less susceptible to pore shrinkage in comparison to those comprised of narrower pores such as R/C 100 gels. This can be related to Equation 5.1 discussed previously, which describes the factors contributing to the capillary stress exerted on pore walls, the value of which varies inversely with pore width. That is, as pore width increases, the capillary stress exerted on the walls decreases, therefore reducing the gel's susceptibility to structural collapse. Optimising the solvent exchange step for maximum efficacy is, therefore, particularly pertinent to gels synthesised at lower R/C ratios, where significant structural collapse can be observed.

It is worth noting that despite the reduced total pore volume associated with the use of solvents with lower surface tensions for R/C 100 gels, the average pore widths remained similar (shown in Table 5.3), as did the positioning of the hysteresis loop on the x-axis within the isotherms (Figure 5.8). Upon inspection of the R/C 100 isotherm plots, variations in quantity of nitrogen adsorbed are evident between relative pressures of 0 - 0.4 – the pressures between which micropores are known to fill and empty. These results suggest that the pore shrinkage which takes place during drying is particularly pertinent within the microporous range, once again in agreement with the relationship defined by Equation 5.1, where the strength of the capillary stress exerted on the pore walls varies inversely with pore width. Furthermore, the fact that the average pore widths remained similar across the samples, despite the variations in total pore volume, could be attributed in part to the limitations of the BJH pore width analysis. This method accounts for pores within the meso- and macro- range only, therefore the shrinkage or closure of micropores would not affect the final average pore width value. Interestingly, even the shrinkage that does take place within the macroporous range for R/C 100 gels – indicated by the variations in quantity adsorbed at relative pressures between 0.4 – 1 shown in the different isotherms within Figure 5.8 – still appears to have minimal impact on the average pore width, suggesting that the shrinkage in this region is negligible in comparison to the volume of pores that remain intact.

5.2.4 Solvent Exchange Kinetics

In an effort to gain additional insight into the various factors that affect the performance of solvents in reducing pore shrinkage, the kinetics and exchange rate of acetone, methanol, and ethanol were investigated using IR spectroscopy. As mentioned previously, although IR Spectroscopy is typically used as a qualitative method as opposed to a quantitative method, it is used in this work to determine approximate solvent-water ratios for the purpose of kinetic analysis and is not used to calculate definitive concentrations. Once again, these solvent-water mixtures are also non-ideal, introducing further approximations into the measurement. Still, determining the point at which equilibrium is reached for each solvent in this way is valuable,

ensuring the 24-h exchange period used in this work is sufficient, and exploring the potential that lengthy equilibrium times may correlate with poorer solvent performance.

IR Calibration Curves

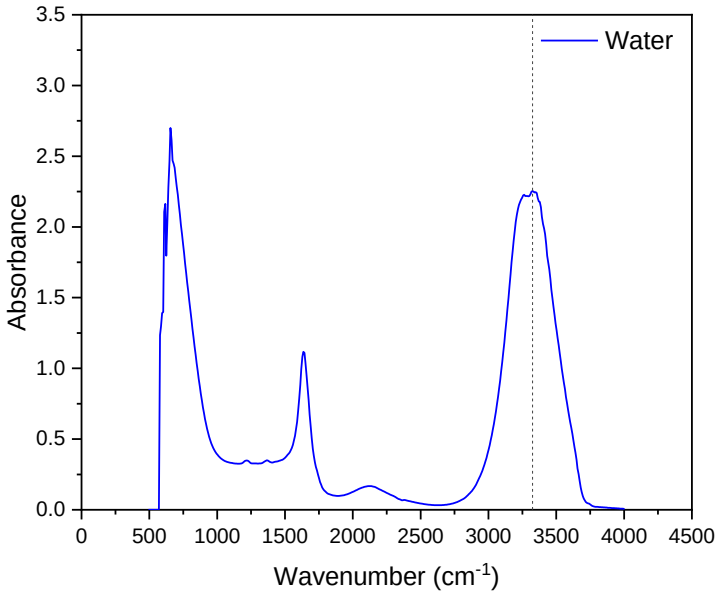

Figure 5.10: IR spectrum for pure deionised water sample.

Figure 5.10 shows the IR spectrum for pure water, with its three main peaks identified at 750 cm^{-1}, 1640 cm^{-1}, and 3325 cm^{-1}. Comparing this spectrum with those obtained for the analysis of the other solvents allows a relevant peak to be selected for each solvent-water mixture, indicating the approximate ratio of water to solvent within each sample. As the solvents are diluted and the percentage of water within each mixture increases, the resulting IR spectrum will show the formation of the water peaks identified while the absorbance peaks associated with the chosen solvent will decrease in value.

Acetone-Water Mixtures

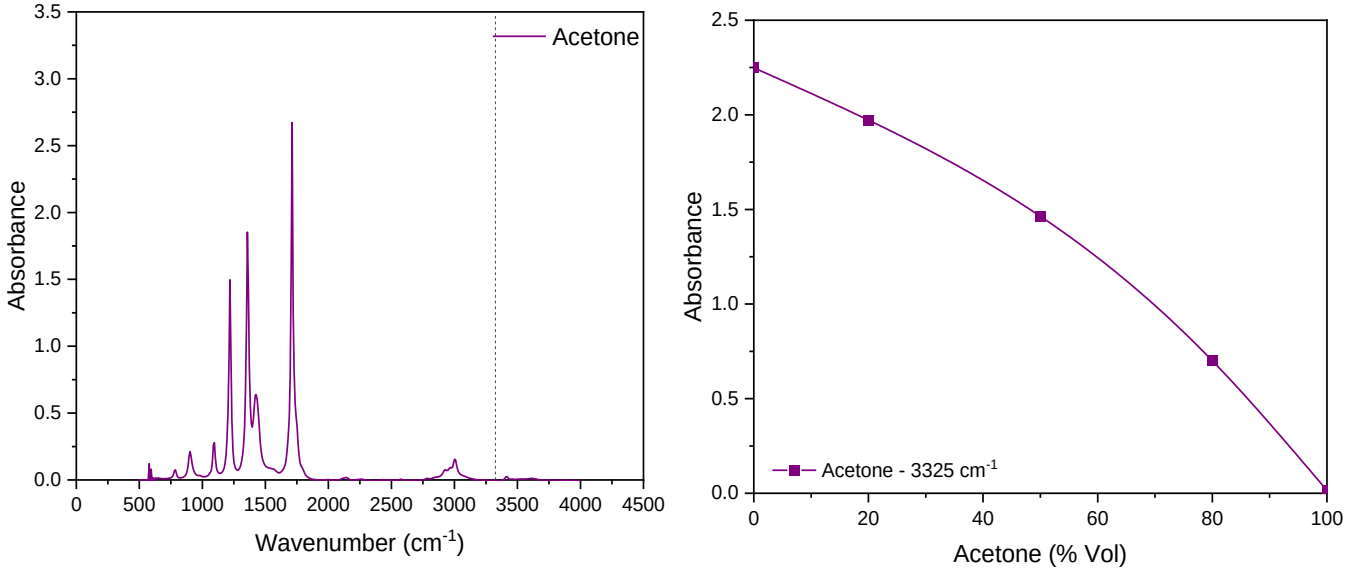

Figure 5.11: IR Spectra for pure acetone with the dashed line indicating the wavenumber used for calibration (a) and the resulting calibration curve for acetone-water mixtures (b).

The first solvent analysed was acetone, which is the original solvent used for solvent exchange when RF gels were first synthesised by Pekala.[14] Figure 5.11(a) shows the IR spectrum for acetone, showing three main peaks around 1200 cm^{-1}, 1350 cm^{-1}, and 1700 cm^{-1}. Given that the IR spectrum for pure water shows absorbance within this range, using these peaks to determine solvent-water ratios could provide results with a low degree of accuracy. Instead, the absorbance peak associated with an increased concentration of water, positioned at 3325 cm^{-1}, was used to create the calibration curve plotted in Figure 5.11(b). Here, acetone-water mixtures were analysed at volume percentage ratios 100:0, 80:20, 50:50, 20:80, and 0:100. It is worth noting that the calibration plot does not follow a linear trend, especially as higher acetone percentages are approached, suggesting that the accuracy within this range is lower.

Methanol-Water Mixtures

In a similar manner, the most suitable peak from the methanol IR spectra (Figure 5.12(a)) was determined as that at 1026 cm^{-1}, with the corresponding calibration curve for plotted in Figure 5.12(b) for methanol-water percentage ratios 100:0, 80:20, 50:50, 20:80, and 0:100. Once again, the calibration plot does not follow a linear trend, especially as higher methanol percentages are approached, suggesting that the accuracy within this range is lower.

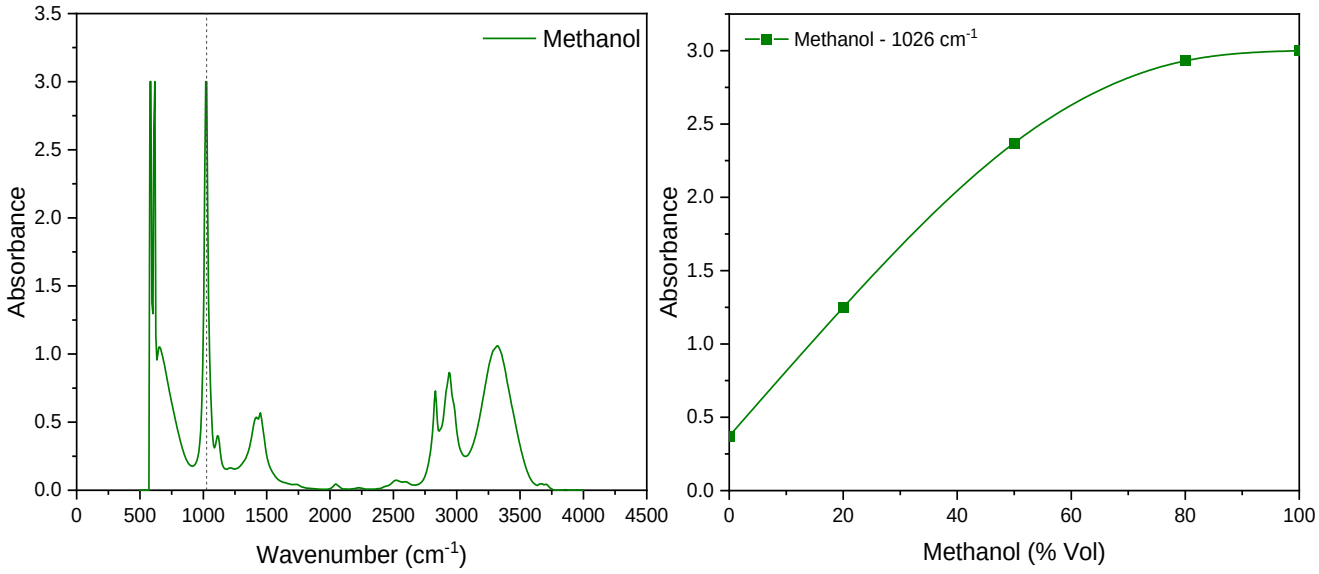

Figure 5.12: IR Spectra for pure methanol with the dashed line indicating the wavenumber used for calibration (a) and the resulting calibration curve for methanol-water mixtures (b).

Ethanol-Water Mixtures

The final solvent to be analysed was ethanol, with its peak at 1040 cm^{-1} selected as the most suitable peak for analysis, shown in Figure 5.13(a). Once again, ethanol-water mixtures were analysed at volume percentage ratios 100:0, 80:20, 50:50, 20:80, and 0:100. As with the acetone and methanol analysis, the calibration plot (Figure 5.13(b)) does not follow a linear trend, especially as higher ethanol percentages are approached, suggesting that the accuracy within this range is lower.

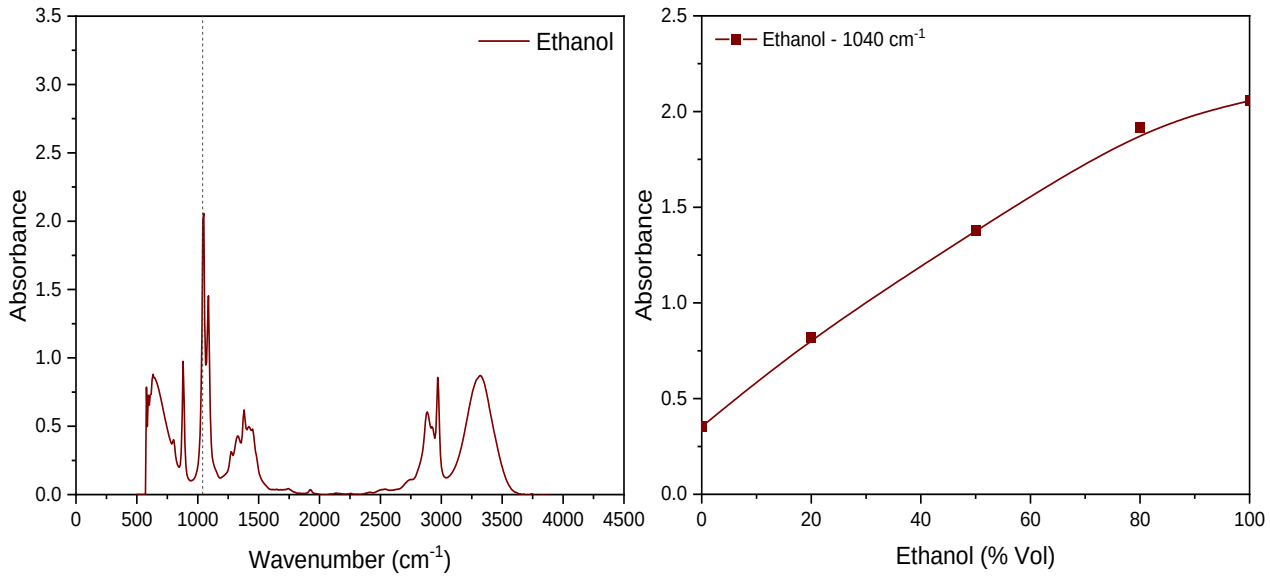

Figure 5.13: IR Spectra for pure ethanol with the dashed line indicating the wavenumber used for calibration (a) and the resulting calibration curve for ethanol-water mixtures (b).

Analysing Solvent Exchange Rates

The rate of exchange for each of the solvents was determined at the following time intervals: 2 h, 4 h, 6 h, 24 h, 26 h, and 28 h, after 40 mL of pure solvent was added to the R/C 300 hydrogel sample. The solvent percentages remaining in the solution at each interval were determined by comparing their IR spectrum peak absorbance values to those in the calibration curves plotted in the previous section, the results of which are shown are graphically in Figure 5.14.

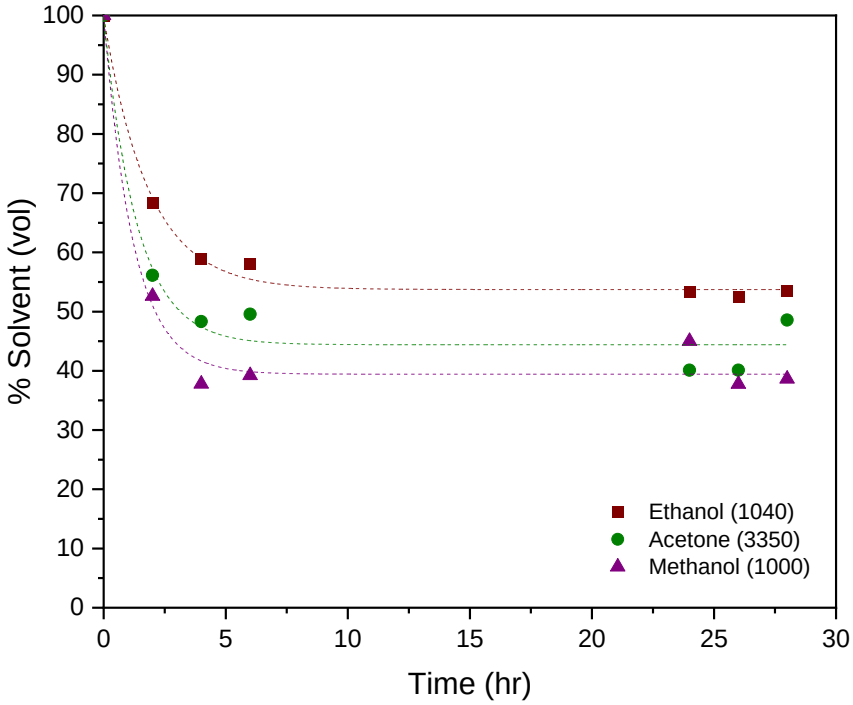

Figure 5.14: Solvent exchange kinetics for ethanol, acetone, and methanol in their removal of water from gel pores, with the dashed lines indicating the exponential decay curve fit for each set of data.

The kinetics of the exchange take place rapidly for each solvent, the first 2 h seeing a substantial decrease in the percentage of solvent present within the solution as it is exchanged by water from the hydrogels. This value continues to decrease and soon reaches a plateau as the system equilibrates, taking place after around 6 h for each solvent studied. Each of the three solvents displayed exchange kinetics which followed an exponential decay trend, shown by the dashed lines in Figure 5.14, with the R^2 value for the exponential decay curve fittings ranging from 0.971 to 0.995. In line with these fittings, the plateau reached for the final remaining solvent percentages at equilibrium are approximately 55%, 45%, and 40% for ethanol, acetone, and methanol, respectively. Note that the variations in percentages here may be attributed to the non-ideal mixing of each of the solvents with water, and are not expected to be indicative of the solvents' comparative ability to exchange water from within the pores.

This analysis confirms that a 24-h period for each solvent exchange step used for xerogel synthesis within other sections of this work is sufficient for equilibrium to be established, after which point the mixture is replaced with fresh, pure solvent and left for another 24 h before being repeated once more. In addition to this, the results presented here also demonstrate that the solvent exchange process could be optimised further by reducing wash times from 24 h to just 6 h, given that this is sufficient for equilibrium to be reached within these systems. This could significantly reduce the total solvent exchange period, which has previously taken 3 days to carry out, but could potentially achieve the same results after just 18 h – a significant reduction within a lengthy synthesis process.

Although previous research has not focused on the comparative kinetics and extent of solvent exchange for water within the RF gel pores, studies have explored the effectiveness of different solvent exchange procedures in their ability to remove the water present. Work by Prostredny *et al.*[69] compared the shrinkage of materials washed with fresh acetone daily for 3 days, in contrast with those subject to a single washing of the same total volume and left to equilibrate for 3 days. The results showed increased effectiveness in reducing structural collapse for gels that underwent fresh washings each day, possessing larger total pore volumes after drying, attributed to the increased driving force associated with the daily renewal of concentration gradient. This allowed a greater total volume of water to be removed across the 3-day exchange, highlighting the insufficiency of a single wash, particularly given that the results shown in the work presented here indicate that, after reaching equilibrium, a significant percentage of solvent still remains in the solution. The insufficiency of a single wash using this simple solvent exchange procedure was further highlighted by the work of Jabeen and Mardan [60], who used azeotropic distillation with n-butanol and amyl acetate to remove the water from RF hydrogel pores, resulting in a significant increase in pore volume of the gels after drying in comparison to those produced from a single acetone wash. Once again, this demonstrates that a single wash with solvent under a simple exchange procedure is not capable of complete water removal from within the pores.

Although the exact volume of water available to be exchanged within the RF gel pores is difficult to quantify, an estimation of its value can be determined from a mass comparison before and after drying. This was carried out for an R/C 300 hydrogel, the results of which are shown in Table 5.4, indicating that approximately 50 g, or 50 mL of water, is removed upon drying. Note that this is for a full-sized gel, in contrast the half-sized gel used in the solvent

comparisons. This means that approximately 25 mL of water is available for exchange within these samples, with equilibrium reached quickly when 40 mL of solvent is added.

Table 5.4: Mass of standard Na_2CO_3 RF gels (including the glass jar used for synthesis) before and after vacuum drying.

Hydrogel Mass (g)	Xerogel Mass (g)	Mass Lost (g)
362.3 ± 0.01	312.7 ± 0.01	49.6 ± 0.01

Overall, the results presented here suggest that the kinetics of the exchange and the point at which equilibrium is reached has no impact on the solvent's effectiveness in reducing structural collapse, given that they are approximately equal for the three solvents studied. Instead, their comparative surface tension values remain as the most likely determining factor in their ability to prevent pore shrinkage upon drying, with ethanol emerging as the most effective – as demonstrated in Section 5.2.3 – possessing the lowest surface tension value of the solvents studied.

5.3 Summary

The results of the experiments carried out have provided valuable details of the various factors which affect the formation and subsequent structure of the RF xerogels, both during the sol-gel reaction and within the post-gelation processing. The experiments carried out on the impact of R/C ratio confirm that the catalyst concentration is crucial in determining the structural properties of the final gel. For gels prepared with higher R/C ratios, corresponding to lower catalyst concentrations, the resulting gels possess pores of larger width and lower total surface area. This is in contrast to those prepared with lower R/C ratios, therefore higher catalyst concentrations, which possess pores of smaller width and higher total surface area – two properties that are central to the performance of the material in a given application.

The role of the individual components within the RF reaction catalyst was investigated, the results of which pointed towards the pivotal role of the metal cation. Gels prepared at a constant hydrogen carbonate (HCO_3^-) concentration with varying sodium ion (Na^+) concentrations were shown to vary significantly, some failing to form a porous gel whatsoever. Conversely, gels prepared with a constant sodium ion concentration with varying carbonate concentrations all possessed almost identical textural properties, despite their differences in initial solution pH. These results confirm the significance of the metal cation in the gel synthesis, and allow its role to be decoupled from the role of pH, which is generally thought to be the most crucial factor in the gelation mechanism. As discussed, the ability of ions to 'salt-in' or 'salt-out' macromolecules in solution is considered for the formation of RF gels, pointing towards the potential for a Hofmeister-like series. In line with this theory, Na^+ ions are proposed to have stabilising (kosmotropic) effects on clusters within solution, facilitating the formation of inter-linked porous structures during gel synthesis.

Ammonium ions (NH_4^+), on the other hand, are proposed to have destabilising (chaotropic) effects, therefore hindering the formation of inter-linked porous structures.

The impact of the solvent type used during solvent exchange within gel synthesis was also investigated, the results of which confirmed the hydrophilic nature of the gel structure, where the gel-water interactions within the pores were sufficiently strong to prevent access for the non-polar solvents. In cases where non-polar solvents were used, the solvents were immiscible with the water present within the gel pores and, therefore, only negligible amounts of solvent could be exchanged. This is in contrast to that of the polar solvents, which were successful in reducing gel structural collapse, with their efficacy correlating with their surface tension values. Gels prepared using ethanol as the solvent - possessing the lowest surface tension of those studied - resulted in the largest total pore volume, and therefore the highest uptake of nitrogen during adsorption analysis. Inspection of the adsorption isotherms also indicated that pore shrinkage was predominantly taking place within the micropore range, in agreement with the theory that the force exerted on pore walls increases with decreasing pore width, making micropores particularly susceptible to shrinkage and collapse.

Lastly, the kinetics of the solvent exchange were investigated, which confirmed that the 24-h exchange period used for solvent exchange during xerogel synthesis is sufficient for each of the solvents studied to reach equilibrium. Equilibrium was reached after ~6 h for each solvent, suggesting that the total solvent exchange period, previously comprising of three 24 h washes, could be reduced significantly and still produce comparable results. Furthermore, the equilibrium times were approximately equal for the three solvents studied, indicating that the exchange kinetics play no role in the effectiveness of the solvent in reducing structural collapse, with the surface tension of each solvent most likely the main determining factor in its efficacy.

Chapter 6: Modelling RF Gel Formation

The formation mechanism of RF gels was investigated experimentally in Chapter 5, providing insight into the impact of different synthesis parameters on final material properties. Capturing this computationally would be particularly advantageous for efficient material design, allowing a variety of structures to be simulated without the need for the time-consuming analogous synthesis processes, and the exploration of a wide range of possible structural properties beyond those materials typically synthesised in the lab. The experimental work carried out to date, both in the literature and within this research, as presented in Chapter 5, has informed the computational model for RF gel formation developed in this work, and provides comparative data for model validation. This model builds upon an initial two-dimensional (2D) code developed by Prostredny *et al.*[228] within the same research group, this work transforming the code into a three-dimensional (3D) simulation, allowing more detailed analysis to be carried out, and providing results which more accurately reflect those obtained from experimental analysis. A research article presenting the findings within this chapter has been published in the journal 'Gels' [229], the full manuscript for which can be found in Appendix D.

6.1 Methodology

6.1.1 Modelling the Formation of Porous Materials

The computational model presented here simulates the formation and growth of RF gels using a lattice-based kinetic Monte Carlo algorithm. A cubic lattice of size 100 x 100 x 100 sites is used, totalling 1,000,000 sites, which is initially populated at random with monomers, according to the desired percentage solids content – an important parameter in the synthesis of RF gels in laboratory experiments. In this research, solids contents of 10 - 60% were simulated, with values above this range producing very densely packed structures. As previously discussed, the laboratory synthesis of RF gels includes a reaction between resorcinol and formaldehyde molecules with the addition of a basic catalyst, the presence of which leads to the formation of negatively charged resorcinol ions. These anionic molecules subsequently act as cluster seeds around which monomers can attach, leading to the formation of primary, approximately spherical, clusters. The spherical cluster structure of the final materials has been visualised by scanning electron microscopy (SEM) and transmission electron microscopy (TEM) [230-232], both of which were also carried out for materials synthesized through this work, the resulting images from which can be found as preliminary results in Appendix B.

The way in which these spherical clusters form has been shown to vary with synthesis conditions, with research by Taylor *et al.*[27] establishing the relationship between catalyst percentage and the number of nuclei sites around which clusters can form. At lower catalyst

concentrations, fewer nuclei sites are observed, and resulting structures are comprised of spherical clusters which are larger in size. Conversely, at higher catalyst concentrations, a greater number of nuclei sites are observed, and resulting structures are comprised of spherical clusters which are smaller in size. This process is modelled in the simulation by 'activating', at random, a percentage of the monomers on the lattice, with each activated monomer acting as a primary cluster seed for the simulation, and where the varying percentage of activated monomers mimics varying catalyst concentration. In this research, activated monomer percentages of 0.5 - 4% are simulated, a range based on the proposed percentage of resorcinol molecules that are deprotonated by a basic catalyst during the RF reaction.[30]

In the simulations developed here, the random diffusion of species around the lattice allows for primary clusters of varying size to form, before their eventual aggregation into monolithic, porous structures. This is in contrast to previous studies, which have focused on the cluster aggregation process for similar porous materials, many beginning the simulation at a point where primary cluster formation had already taken place [154,155], or assuming primary clusters that have formed are of equal size before aggregation occurs.[156,157] This model, therefore, advances towards a more accurate reflection of real systems, where primary cluster size is likely to exhibit some degree of variation.

6.1.2 Simulation Algorithm Overview

The computational work carried out within this section was developed using the GNU Fortran compiler and GNU parallel tool.[233] As explained above, the 3D lattice is initially populated with monomers according to the desired solids content (S_c), and a percentage of these monomers are 'activated' as cluster seeds mimicking catalyst concentration (C_c). The simulation begins with the random diffusion (nearest-neighbour hopping) of monomers on the lattice, with periodic boundary conditions, during which free monomers attach to activated monomers when they come into contact, forming larger primary clusters of monomers. These monomers attach in an approximately spherical sequence, producing primary clusters that also diffuse on the lattice. Two diffusing clusters irreversibly attach when they meet, retaining the primary clusters intact, and the probability of cluster diffusion is inversely proportional to the cluster size. The simulation proceeds until there are no free monomers present and the entire lattice comprises of one monolithic, inter-connected aggregate structure. Each simulation was repeated with 10 different random number seeds, resulting in 10 different structures at each value of S_c and C_c. An average was then calculated for each of the properties analysed across the 10 structures at each S_c and C_c, as well as the corresponding standard deviation of the values calculated. Figure 6.1, overleaf, displays a flowchart which gives an overview of the algorithm used, whilst subsequent sections discuss the individual steps in more detail, with reference to some of the main arrays and subroutines used. The full annotated code used for the simulation, in addition to the analysis codes, can be found in Appendix C.

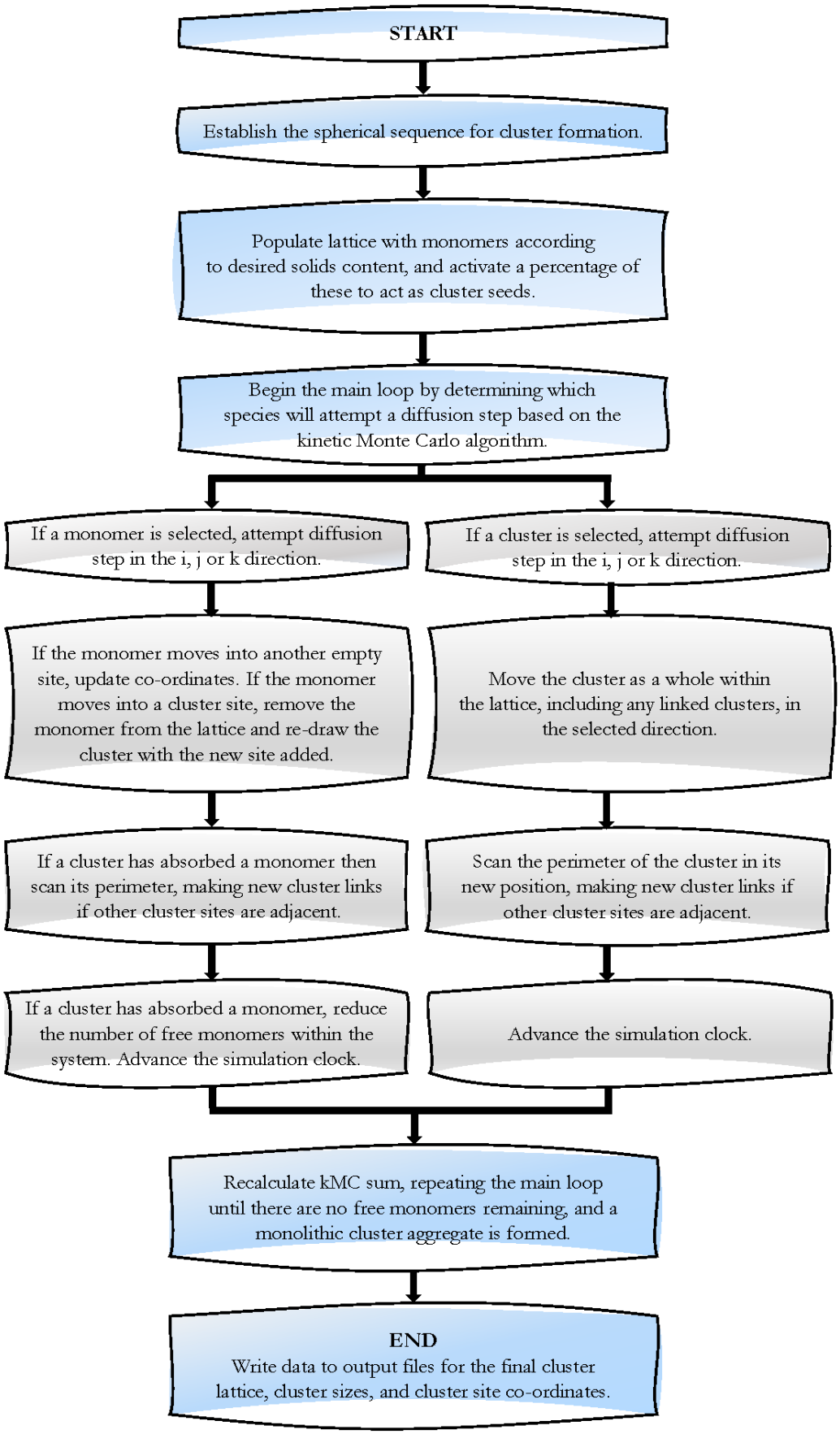

Figure 6.1: Flowchart providing an overview of the kinetic Monte Carlo simulation used within this study.

Lattice Initialisation

The algorithm begins with the declaration of all variables used within the main body of the code along with their variable classification, such as integer, real, or logical. Values of the controlling input parameters are set, that is, the run number (r), the solids content (s), and the percentage of activated monomers (p). The run number is an integer that varies between 1 and 10, given that 10 runs are carried out for each set of synthesis conditions. This determines the seed for the random number generator used for the simulation, producing 10 slightly different structures for each run, allowing for more accurate statistical analysis. Variables s and p are also integers, both of which are used to determine the values of the real type variables for solids percentage and activated monomer percentage (solid and percentage, respectively). The value of solid is determined as solid = s /10, with s values of 1 to 6 explored throughout this work, corresponding to solid percentages of 10 to 60%. This value is subsequently used to determine the total number of monomers populating the 3D lattice, calculated as Nmax = solid x $Nlat^3$. The value for percentage is determined as percentage = p/100 for activated monomer percentages of 1 to 4%, or percentage = p/1000 for activated monomer percentages less than 1% explored through this work. This value is then used in tandem with the Nmax value calculated to determine the number of activated monomers present: Nact = percentage x Nmax. Finally, the number of free monomers (Nmon) can be determined as Nmon = Nmax−Nact.

Before the main diffusion loop begins, the list subroutine is used initially to create the sequence of positions used for the spherical formation of clusters, which is described in more detail in subsequent sections. Following this, random co-ordinates are generated to position the activated monomers in the system within the main 3D lattice Cluster(Nlat,Nlat,Nlat); these are the monomers that become the centre around which clusters form. Free monomers are also placed at random onto the Cluster lattice, as well as on the individual monomer lattice Monomer(Nlat,Nlat,Nlat). These two arrays indicate the locations of occupied lattice sites, with the Cluster array showing sites occupied by clusters as their assigned cluster number and empty sites as 0, whilst the Monomer array shows all occupied sites simply as 1 and empty sites as 0. Additional arrays are created to store the *i*, *j*, and *k* co-ordinates for the monomer sites within each cluster, as well as those of the free monomers on the lattice.

Lattice Diffusion

Diffusion of free monomers, clusters, and cluster aggregates around the lattice is carried out using kinetic Monte Carlo theory, where a species is chosen at random to diffuse, with its size inversely proportional to its diffusion probability. The array MCSum(Nmax) is used to store the kinetic Monte Carlo sum of each species within the system, with its assigned value a measure of the diffusion probability. When the simulation begins, no clusters have been formed, so each monomer has an equal diffusive probability. As the simulation progresses forming both clusters and cluster aggregates which are larger in size, the probability of their diffusion, and therefore the kinetic Monte Carlo sum, decreases. An example of this is shown in Figure 6.2, where we consider a system with 10 monomers, 3 of which are activated as cluster seeds

(shown as green spheres). The diffusion probabilities of each individual monomer are equal (each possessing a probability of 1) at the beginning of the simulation, making the total kMC sum equal to 10, as shown in Figure 6.2(a). As the simulation proceeds and free monomers attach to activated monomers to form clusters, their diffusion probability scales inversely with the change in their size.[154] Figure 6.2(b) shows the first attachment of one free monomer to an activated monomer, doubling the size of the species, and subsequently halving its diffusion probability from 1 to ½, resulting in a total kMC sum of 8½. Figure 6.2(c) shows the attachment process taking place once more between another free monomer and an activated monomer, forming another cluster, bringing the total kMC sum to 7. In Figure 6.2(d), another free monomer attaches to the previous cluster, increasing its size to 3 and therefore reducing its diffusion probability to ⅓ and the total kMC sum value to 5 $^{5}/_{6}$.

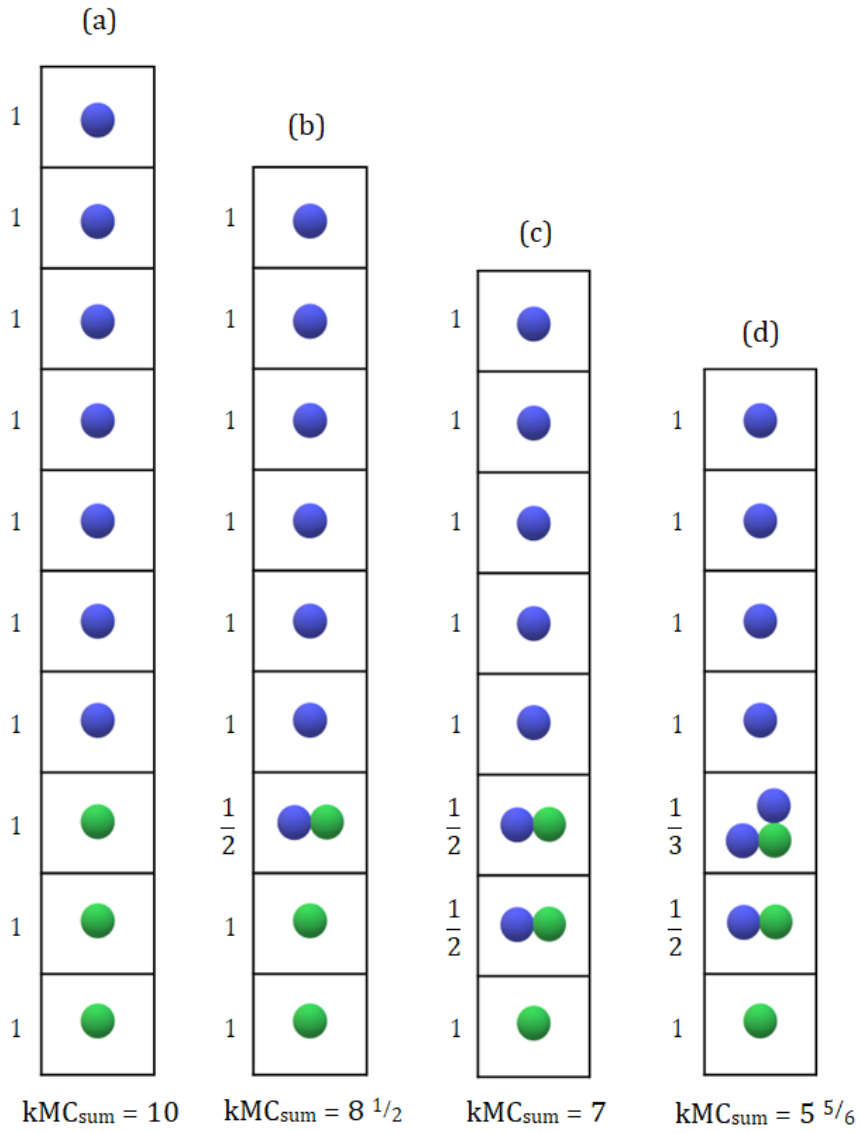

Figure 6.2: Example calculation of the system kinetic Monte Carlo sum (kMCsum), as monomers begin to attach to activated monomers to form clusters throughout the simulation from (a) to (d). Blue spheres represent free monomers while green spheres represent activated monomers.

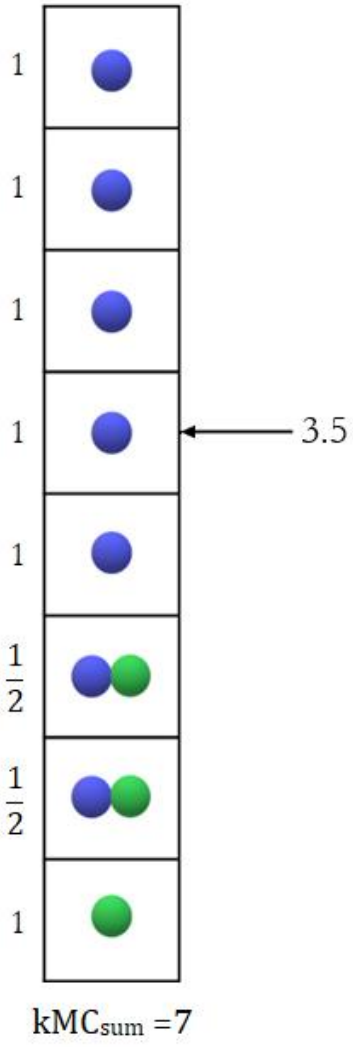

Figure 6.3: Example of the selection of species to attempt diffusion step using a random

To determine which species attempts a diffusion step at each stage, a random number is generated between 0 and the total kMC sum at that step, which will correspond to a monomer or cluster within the system. To exemplify this, we can consider the transition between Figure 6.2(c) and Figure 6.2(d). In this case, a random number between 0 and 7 (the total kMC sum from Figure 6.2(c)) is generated, outputting a value of 3.5 in this example. As shown in Figure 6.3, this value corresponds to a free monomer, with the cumulative sum calculated from the bottom up. Here, the `diffusemonomer` subroutine would then be used, leading to the selected monomer making a random diffusion step within the lattice – a move which would be rejected if the new lattice site was already occupied by another free monomer.

In the case where the random number corresponds to a cluster, the `diffusecluster` subroutine is used, and every monomer within the cluster is moved by one lattice site in the selected direction, applying periodic boundary conditions. Similarly, if the chosen cluster is part of a larger cluster aggregate, then the clusters move as one, with every monomer within the cluster aggregate moved by one lattice site in the selected direction.

Cluster Formation & Aggregation

As the different species diffuse around the lattice throughout the simulation, they will attach irreversibly when they come into contact with one another. When a monomer makes a diffusion step, if the new lattice site is occupied by a cluster, then that monomer will be consumed into the cluster, as previously discussed. This is carried out using the `attach` subroutine, which identifies the cluster number and increases its size by 1 site. The monomer does not necessarily attach at the site it first came into contact with the cluster – instead, the new cluster site is determined according to its approximately spherical growth using the sequence established by the `list` subroutine mentioned previously.

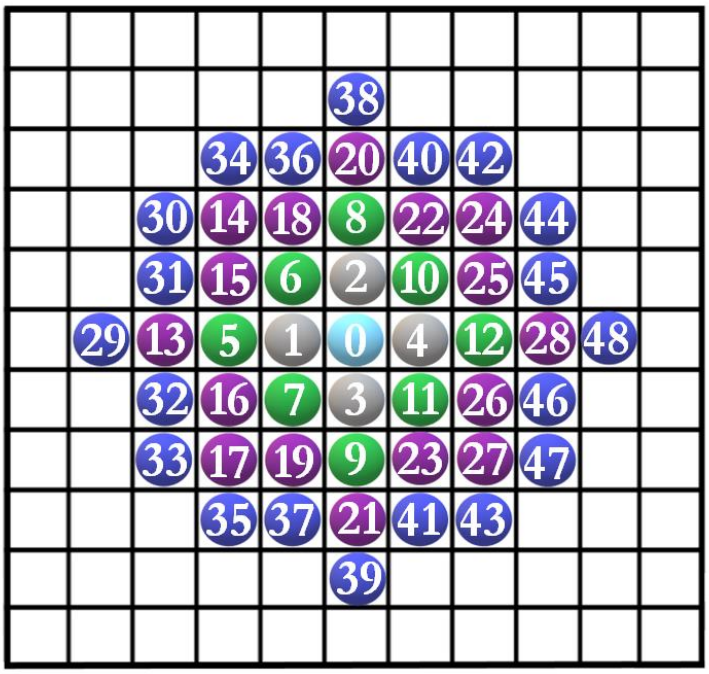

Figure 6.4: 2D illustration of the cluster growth sequence used for creating spherical species, where monomers are added in chronological order and each colour shows an additional layer of growth.

The mechanism by which the clusters grow is more easily visualised in 2D, as shown in Figure 6.4 displaying growth in the *i* and *j* directions, with a similar mechanism applied for 3D growth, this time including the addition of monomer sites in the *k* direction. The `list` subroutine creates the sequence of sites to be occupied, relative to the cluster centre, at the beginning of the simulation, and this sequence is followed as monomers continue to attach throughout the simulation. Once this has taken place, as well as when a cluster has taken a diffusion step, the perimeter of the cluster is scanned to determine if it is adjacent to another cluster. If any of the cluster's perimeter sites are found to be adjacent to another cluster, the `linkclusters` subroutine is used to attach the two clusters and form cluster aggregates. In this case, these individual clusters continue to consume monomers and grow individually following the same approximately spherical sequence of growth, with the next available site used for the addition of monomers, given that only one monomer can occupy a lattice site, as shown in Figure 6.5.

The `FinalSize(Nact)` array, as the name suggests, lists the changing size of each cluster as the simulation proceeds. As previously discussed, this value increases when a monomer is consumed by the cluster, however, when two clusters attach to form a larger cluster aggregate, the total aggregate size is recorded only by one cluster ID within the array, and the other is set to a value of -1 to set it apart from the rest. Consider two clusters, Cluster 1 and Cluster 2, whose sizes are 4 sites and 6 sites, respectively, where their sizes are recorded as `FinalSize(1) = 4` and `FinalSize(2) = 6`. When these two clusters encounter one another and attach, the `FinalSize(Nact)` array is updated to `FinalSize(1) = 10` and `FinalSize(2) = -1`.

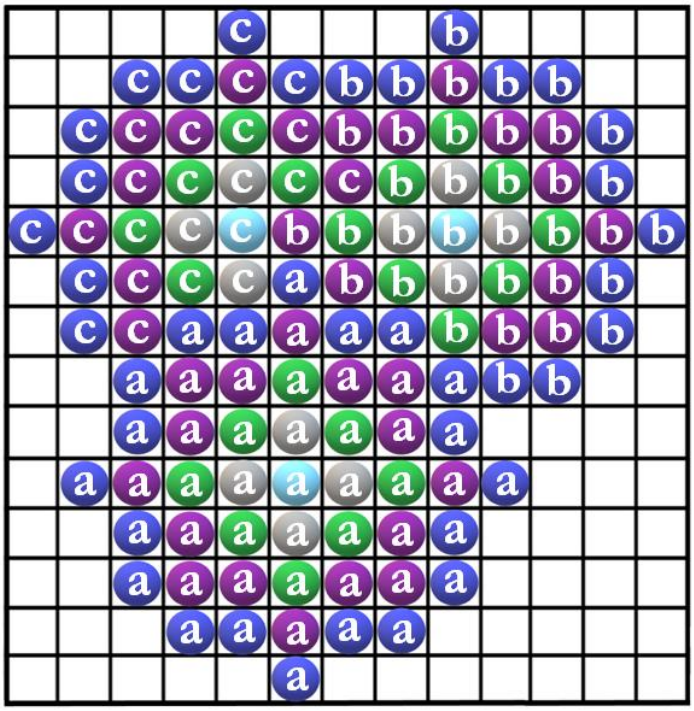

Figure 6.5: 2D illustration showing a cluster aggregate containing three clusters (a, b, and c), each of which continue to grow individually within the structure.

Simulation Time Increments

With each diffusion step of a species, the clock is advanced by a time increment (Δt), which is calculated based upon the probability distribution for an event taking place at time t.[234] Using the total kMC sum for the system at that point (kMC_{sum}, in number per unit time) and a random number (R), Δt is determined using Equation 6.1:

$$\Delta t = -\frac{\ln(R)}{\mathrm{kMC}_{sum}}$$

Equation 6.1

Given that the total kMC_{sum} for the system is reduced as clusters grow and free monomers on the lattice are consumed, the value of Δt will increase as the simulation proceeds. This captures the slowing of the diffusion process as the species within the system increase in size, reflecting the inverse proportionality of species size to diffusion probability. Time is advanced and the kMC_{sum} recalculated for every diffusion step until there are no free monomers remaining on the lattice, with the final resulting structure being a monolithic inter-connected cluster aggregate.

Simulation Outputs

When the simulation has come to an end, the `plotcluster` subroutine is used to write data into the output files created. The first file written is the `Cluster_0.s_0.0p_r.dat` file (where `s` is solids content, `p` is activated monomer percentage, and `r` is run number) which contains the final 3D lattice, written as 2D arrays in chronological order from `k = 1` to `Nlat`. The final size of each primary cluster within the structure is written into a `Size_0.s_0.0p_r.dat` file, while the *i*, *j*, and *k* co-ordinates for the centres of each cluster are written into the relevant i/j/k position file (e.g. `iPos_0.s_0.0p_r.dat`), and these outputs are used for subsequent analysis and visualisation of the resulting structures.

6.1.3 Fractal Analysis of Simulated Structures

Correlation Dimension

As previously discussed, computationally determining the fractal properties of RF gel materials is of interest, especially in light of the conflicting conclusions that have been reached in various experimental studies. The fractal characterisation method used here involves the calculation of the structure's correlation dimension (D_c), which is based upon the proximity of points within the structure to one another within a spanning radius. Its calculation firstly begins with the determination of the correlation sum (C_r), as established by Grassberger [215] using Equation 6.2:

$$C_r = \frac{1}{N(N-1)} \sum_{i=1}^{N} \sum_{j=1;j\neq 1}^{N} \theta\left(r - \left|X_i - X_j\right|\right)$$

Equation 6.2

Here, θ is the Heaviside function, r is the spanning radius, N is the total number of randomly selected reference points within the structure, and X_i and X_j are the coordinates of the two points whose proximity are being analysed within the system. The Heaviside function (θ) is equal to 1 when the separation of points within the system is less than the spanning radius, or equal to 0 when the separation of points is greater than the spanning radius. This calculation is carried out across increasing values of spanning radius until the entire structure has been encapsulated and C_r consequently reaches a plateau. The correlation sum relates to the spanning radius in the following manner:

$$C_r \propto r^{D_c}$$

Equation 6.3

where the exponent D_c is the correlation dimension. Obtaining the value of D_c, therefore, involves a logarithmic plot of the correlation sum vs. the spanning radius. In this work, the correlation dimension for the simulated material is calculated from N=100,000 different reference positions within the structure. Each position is selected at random, and the spanning radius between two reference positions is calculated for each periodic image, with the lowest

value used to determine the correlation sum using Equation 6.2. A logarithmic plot of C_r vs. r is produced in accordance with Equation 6.3, where the central area of the graph is a straight-line plot with no size limitations affecting the results. The value of D_c is subsequently determined from the gradient of this linear section of the plot, minimizing the potential for size effects to impact the conclusions drawn around fractal properties.

Hurst Exponent

Analysing the fractional Brownian motion trajectory of a particle moving through a porous material is another valuable way in which its fractal characteristics can be determined. This is quantified using the original rescaled range method to calculate the Hurst exponent from the particle trace in the x, y and z directions when the particle takes a "random walk"—a series of random steps throughout the structure. The particle displacement from its origin over time is used to calculate the Hurst exponent, where the relationship between the average displacement ($\overline{|\Delta B|}$) across the x, y and z directions and the time window T_s is as follows:

$$\overline{|\Delta B|} \propto (T_s)^H$$

Equation 6.3

Here, the exponent H is the Hurst exponent, evaluated as the gradient of the logarithmic graph of $\overline{|\Delta B|}$ vs T_s. [213] In order to determine H, a random walker is allowed to diffuse through the accessible pore sites within the lattice and its path analysed in the x, y and z directions. The random walker takes 100,000 random steps in total from 100 different starting positions on the percolated structure and the average displacement ($\overline{|\Delta B|}$) for each time window size (T_s) is calculated from the 100 traces. Note that the value of H calculated here is, therefore, that of the percolated porous network contained within the structure and not of the solid structure itself.

6.2 Results & Discussion

6.2.1 Structure Visualisation

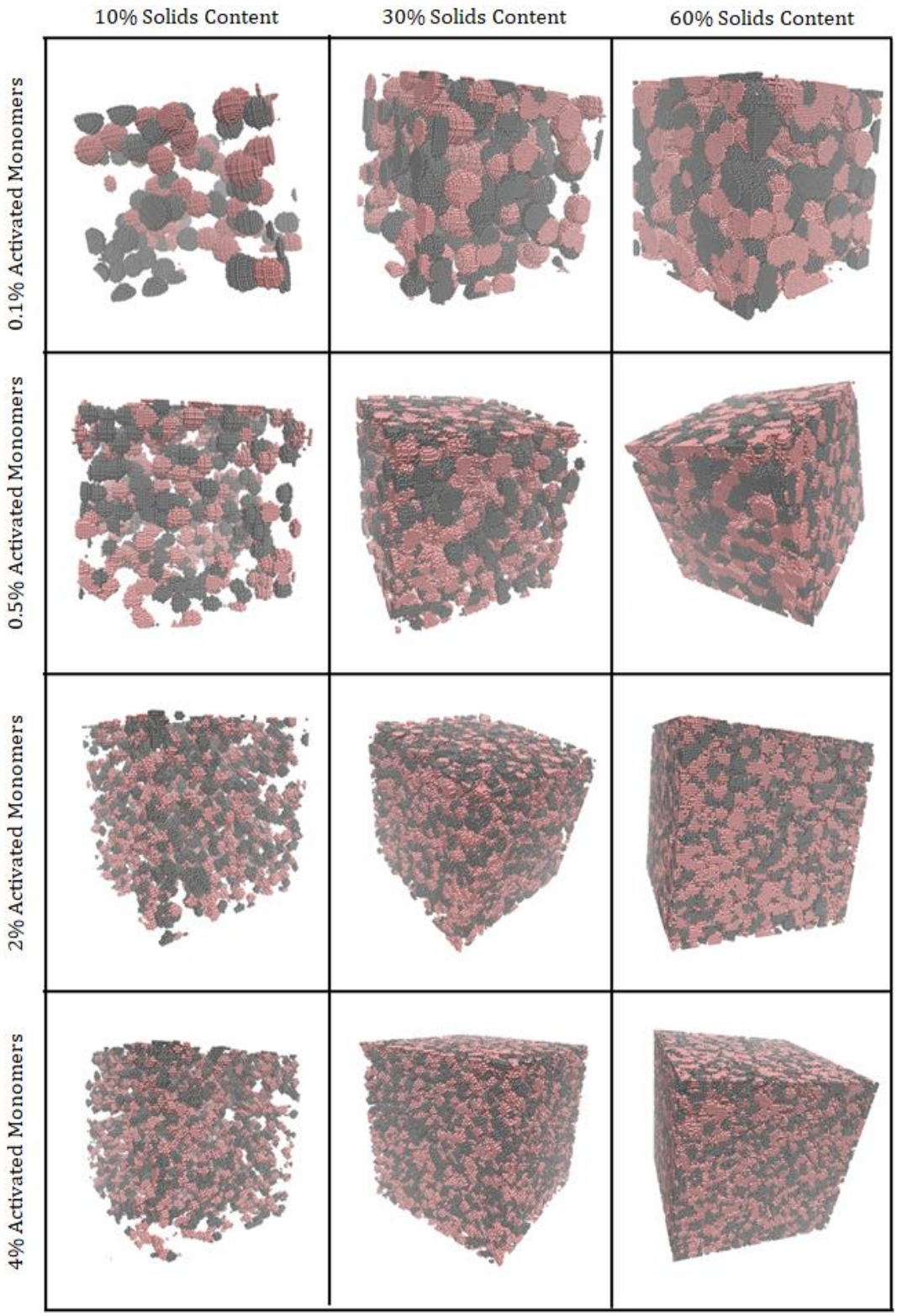

Figure 6.6: Simulated RF gel materials visualised in 3D, where each sphere represents an individual monomer, with different colours of clusters used for visual purposes only. Structures are visualised with increasing solids content (S_c), left to right, and increasing percentage of activated monomers (C_c), top to bottom. Note that structures are connected through periodic boundaries.

Visualisation of the 3D structures is important not only for a comparison between the different simulated materials, but also for visual comparison with materials synthesised experimentally. This was carried out in various ways, initially as 2D slices through the centre of lattice using MATLAB, where the array was plotted with each monomer site within the monolithic cluster aggregate being represented by a circular marker. This approach, while useful for other visualisation means, including in the adsorption analysis carried out in the following chapter (Chapter 7), lacked in visual effectiveness for the 3D structures. Instead, the cluster structures were visualised using Visual Molecular Dynamics (VMD), a software usually used for molecular systems, visualising each atom as a sphere and placing it according to its corresponding co-ordinates. In the first VMD visualisation approach, shown in Figure 6.6, the `Cluster` lattice data was used to create a list of co-ordinates for every monomer site within the monolithic structure and these were written into a VMD-readable input file. Figure 6.6 shows the visualised final structures using this approach for materials simulated with S_c values of 10, 30, and 60% each at C_c values of 0.1, 0.5, 2, and 4%, where each monomer is represented by individual spheres of equal size. Here, different colours (grey and pink) of monomers are used for visual purposes only, allowing the reader to differentiate between different clusters within the monolithic structure. This approach captures the approximately spherical manner in which the clusters grow, as the exact positioning of each individual monomer can be observed.

Despite this, the dense packing of the individual monomers makes grasping the overall cluster structure more difficult using this visualisation technique, particularly for higher solids and activated monomer percentages. For this reason, another visualisation technique using VMD was employed, this time each primary cluster being represented by a sphere as opposed to each individual monomer. Using this method, the number of monomers within each primary cluster was taken to be an equivalent spherical volume, and the equivalent radius was subsequently determined. The co-ordinates of the primary cluster centres are then used to plot spheres of varying size according to their calculated equivalent radius, as shown in Figure 6.7, overleaf, which displays the final structures using this approach. Results for 0.1% C_c structures were also omitted, producing materials that were sparsely distributed at low S_c values. Figure 6.7, therefore, displays materials simulated at C_c values of 0.5, 1, 2, and 4% each at S_c values of 10, 30, and 60%. Once again, the different colours (grey and blue, in this case) of spheres shown are for visual purposes only, allowing the reader to more easily differentiate between different clusters.

Observing the structures within both Figure 6.6 and Figure 6.7, the visual differences between the simulated materials at various S_c values are evident. Higher S_c results in materials that, as expected, are more densely packed, with the primary clusters occupying more space within the lattice. When the average primary cluster sizes within the structures are compared, materials with the same C_c possess the same average volume and radius regardless of S_c. A structure simulated at a higher S_c will, however, have a greater number of primary clusters within its lattice in comparison to one at lower S_c at the same C_c value. This means that, although an increase in S_c results in an increase in monomers within the lattice, these monomers are distributed across a greater number of primary clusters, therefore, resulting in the average primary cluster size remaining constant across the different S_c values.

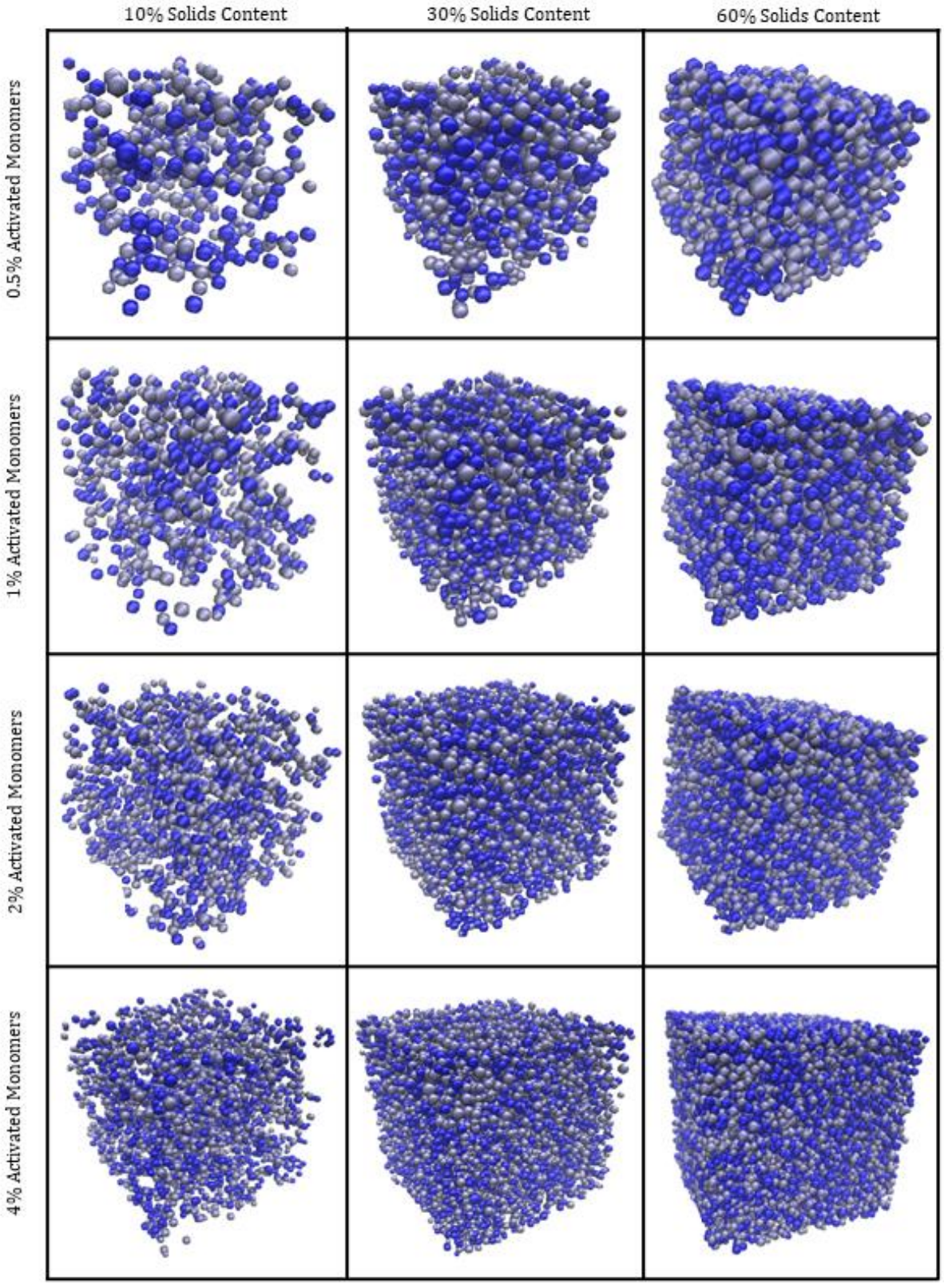

Figure 6.7: Simulated RF gel materials visualised in 3D from their calculated equivalent radius, where each sphere represents an individual cluster, note that the different colours of clusters present are for visual purposes only. Structures are visualised with increasing solids content (S_c), left to right, and increasing percentage of activated monomers (C_c), top to bottom. Note that structures are connected through periodic boundaries.

On the other hand, C_c has a significant impact on the average primary cluster size within the structure. Figure 6.8 displays histograms for the primary cluster volume distribution for various C_c values at 60% S_c. As C_c increases from 0.5% to 4%, the average primary cluster volume decreases from 200 to 25 lattice sites. This is consistent with observations from experimental analysis of RF gels; materials synthesised with low catalyst concentrations comprise of fewer primary clusters that are larger in size, whilst those synthesised with high catalyst concentrations comprise of a greater number of primary clusters that are smaller in size.[17]

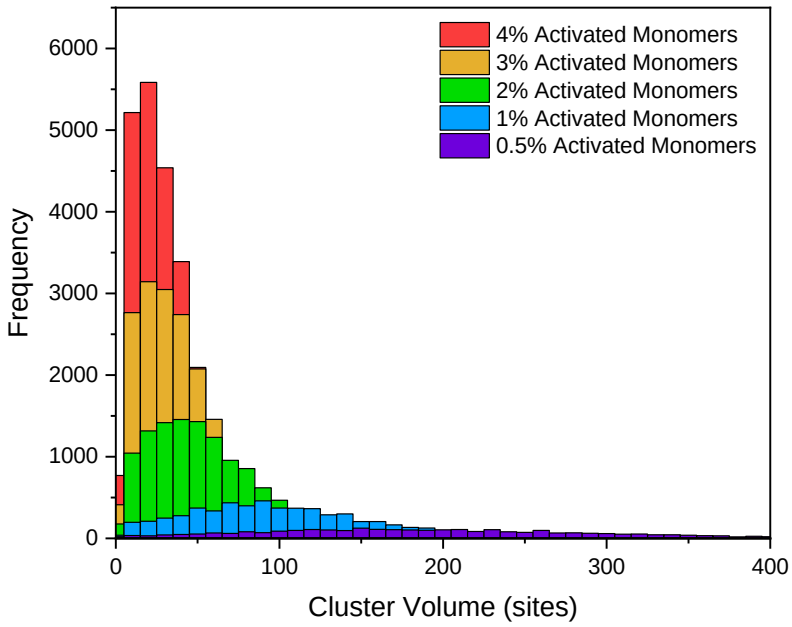

Figure 6.8: Cluster volume distributions for simulated materials at 60% solids content (S_c) and varying activated monomer percentages.

6.2.2 Textural Analysis

Accessible Porosity

The various textural properties of these structures, at varying S_c and C_c, are analysed and compared, including accessibility of pore sites for particles of both 1 and 3 lattice sites in width (hereafter referred to as size 1 and size 3, depicted in Figure 6.9(a) and (b), respectively). The percentage of accessible pore sites for a particle of size 1 is calculated by determining the percolated network of accessible sites within the structure, then expressing the total number of accessible sites within this network as a percentage of the total number of unoccupied sites within the lattice. To analyse the accessibility for a particle of size 3, an exclusion zone of 1 site thickness is added to the simulated structures.

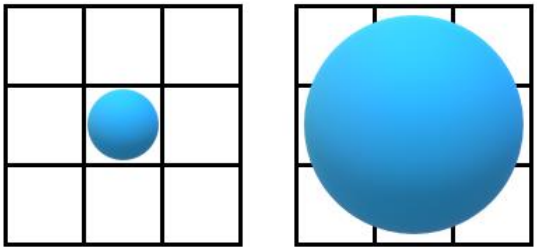

(a) (b)

Figure 6.9: Diffusing particle of (a) one site in width and (b) three sites in width.

The accessibility of pore sites within a porous material is a fundamental consideration when it comes to their application potential, and is, therefore, an important property to analyse within simulated structures. We consider how the accessibility is affected by the size of the guest species, to understand how this might affect potential applications of the porous gel as a host for different molecules. As expected, the percentage of sites that are inaccessible increases with increasing S_c, as the lattices are more densely packed with material and, therefore, more likely to result in closed off porosity. This is true for the accessibility of particles both of 1 and 3 sites in width (corresponding to molecular size of approximately 1 and 3 nm), as shown in Figure 6.10(a) and (b), respectively. Furthermore, the percentage of inaccessible sites also increases with increasing C_c, which is a result of the increased number of clusters present. Structures formed at higher C_c possess a greater number of initial cluster seeds than those at lower values, leading to the formation of numerous smaller clusters, which pack together densely, increasing the likelihood of closed off porosity.

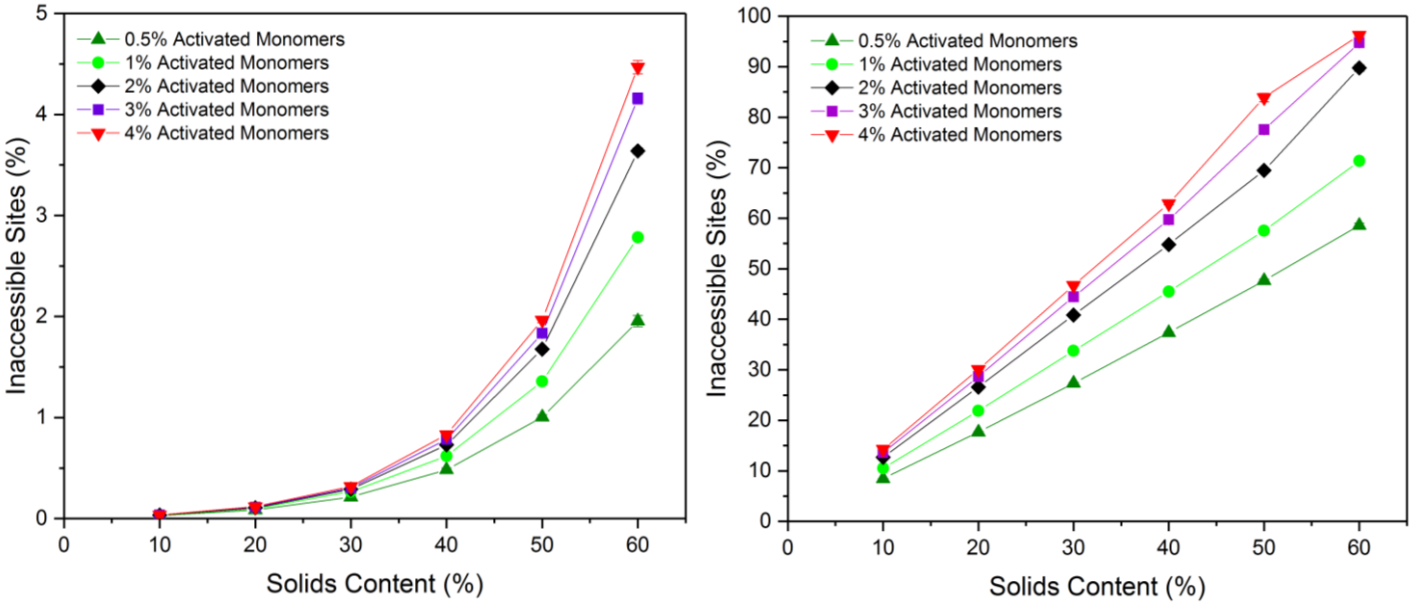

(a) (b)

Figure 6.10: Percentage of inaccessible sites within the lattice with varying solids content (S_c) and activated monomer (C_c) values with respect to a diffusing particle of (a) Size 1 and (b) Size 3. Standard deviation error bars are included for each data point, although these may not be visible due to their size relative to the data point marker.

The percentage of sites inaccessible to a particle of size 1 remains consistently low, ranging from 0.028(2)% at 10% S_c and 0.5% C_c to 4.47(7)% at 60% S_c and 4% C_c. These values are considerably lower than those obtained for the 2D version of the code, which reached up to 25% inaccessible sites for structures formed with 50% S_c and 3% C_c.[228] Simulating the porous structure in three dimensions opens new accessible pathways for connectivity, which would otherwise be limited by the two-dimensional structure, explaining the significant decrease in the percentage of inaccessible sites within the lattice, and providing a more accurate representation of the porous materials synthesised in reality.

When the particle width is increased from 1 site to 3 sites, the percentage of inaccessible sites increases significantly across all S_c and C_c values, and the values obtained span a much wider range. In this case, values range from 8.45(3)% at 10% S_c and 0.5% C_c to 96.24(8)% at 60% S_c and 4% C_c. These results have significant implications for porous materials in their potential use for applications involving larger particles such as biomolecules, where optimisation of S_c and C_c values according to particle size would be imperative, ensuring that the synthesis parameters used produce structures with sufficiently accessible porous networks.

Accessible Surface Area

Figures 6.11(a) and (b) show the accessible surface area per unit mass for particles of size 1 and 3, respectively. For both particle sizes, the accessible surface area per mass gradually decreased as S_c increased across each of the C_c values studied. The increased number of primary clusters present for higher S_c (at a given C_c) results in structures that are more densely packed, as previously discussed. This increases the likelihood that a single primary cluster will be in contact with multiple primary clusters around it, therefore reducing the accessible surface area available for particles moving through the porous structure. Furthermore, as expected, the accessible surface area is consistently higher for a particle of size 1 than for size 3, as the smaller particle can more easily access the narrower pores within the structure.

The effect of variations in C_c can also be compared, the results of which indicate that, for a particle of size 1, an increase in C_c value leads to increased accessible surface area across the S_c values studied. As previously discussed, higher C_c values lead to a greater number of primary clusters present, across which the structure's mass is distributed. Consequently, for lower C_c materials, the larger primary clusters mean that much of the structure's mass is contained within the interior of each cluster, reducing the accessible area available at the surface. Conversely, for higher C_c materials with a greater number of primary clusters present, each of which are smaller in size, the accessible area available at the surface is increased. Similar trends for accessible surface area were also observed for the 2D version of this simulation for a particle of size 1, although the work presented here explores a wider range of S_c and C_c values, as well as including the new analysis for a particle of size 3. Importantly, these results are also consistent with those observed experimentally, where an increase in

catalyst concentration is shown to increase the BET surface area values obtained from nitrogen adsorption measurements of RF gels.[66-68]

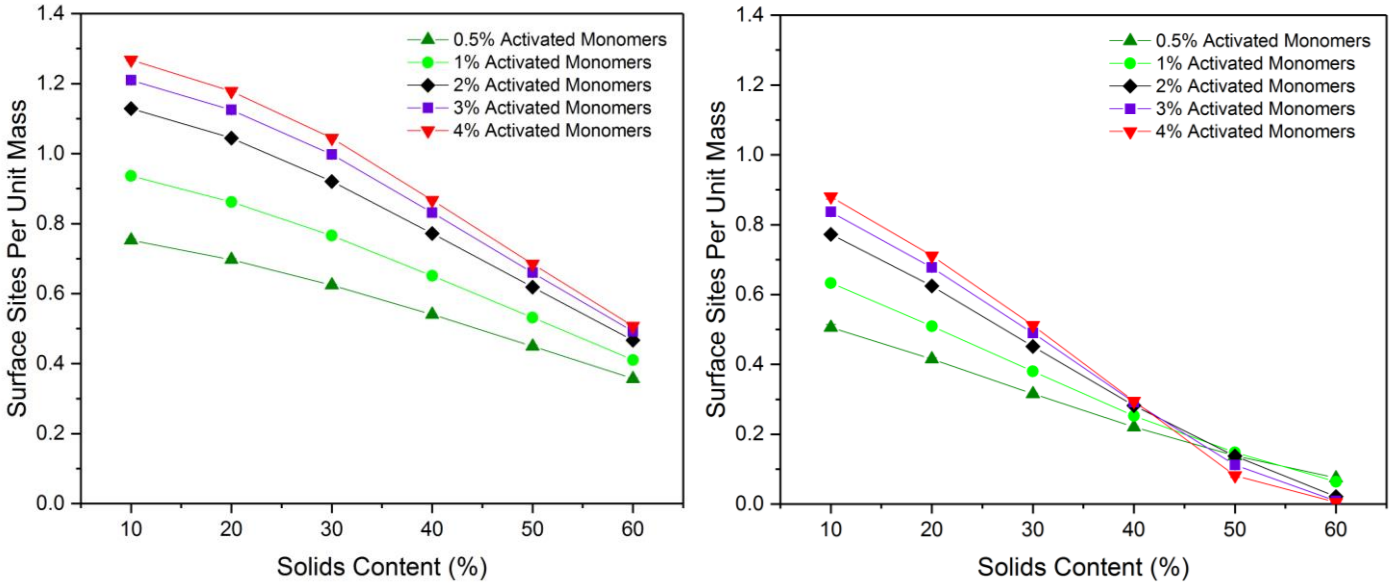

Figure 6.11: Accessible surface sites scaled with total mass with varying solids content (S_c) and activated monomer (C_c) values with respect to a diffusing particle of (a) Size 1 and (b) Size 3. Standard deviation error bars are included for each data point, although these may not be visible due to their size relative to the data point marker.

When the particle width is increased to 3 sites, the same initial trend is observed where an increase in C_c leads to higher values of accessible surface area, however, an eventual crossover point is reached at an S_c value of around 45%. For S_c values above this point, increasing C_c has the inverse effect, where the accessible surface area is hindered by higher C_c values. This likely arises due to the high percentage of inaccessible sites for particles of size 3, which is exacerbated by the increased interconnectivity arising at higher C_c values. An upper limit is therefore reached, where the increased interconnectivity associated with the greater number of primary clusters present is no longer of benefit to the available surface area of the system. Instead, it gives rise to higher rates of closed off porosity and therefore reduces the accessibility of surface sites – an important consideration for the tailoring of these materials to various applications.

6.2.3 Fractal Analysis

Correlation Dimension

For uniformly distributed, densely packed structures in three dimensions, the resulting correlation dimension (D_c) value is equal to 3, whilst fractal structures conversely possess D_c values of less than 3. As previously discussed, questions around the fractal nature of RF gels have been raised over the years with a consensus yet to be reached, therefore calculating D_c for the simulated structures could be pivotal in addressing some of the unanswered questions.

Figure 6.12 shows calculated D_c values for the simulated structures at various S_c and C_c, with additional data provided between 10 and 20% S_c where the most significant changes in D_c are observed. For each C_c, a gradual increase in correlation dimension is observed as S_c increases from 10 to 20%, shortly thereafter plateauing around a value of 3, the value at which a structure is considered to possess no fractal properties. At the lowest S_c of 10%, the structure possesses D_c values of 2.71(1) and 2.76(1) for C_c values of 0.5% and 1%, respectively, indicating that the structures do exhibit some fractal properties under these conditions. For higher C_c structures at 10% S_c, the D_c value approaches 2.9, close to the non-fractal limit of 3. These results indicate that fractal properties can be observed within these materials under specific synthesis conditions – reliant not only on sufficiently low S_c, as previously postulated, but also on sufficiently low C_c values. Under standard gel synthesis conditions within experiments, S_c values of 20% and above are commonly used, perhaps explaining why numerous studies have observed no fractal properties within the structures.

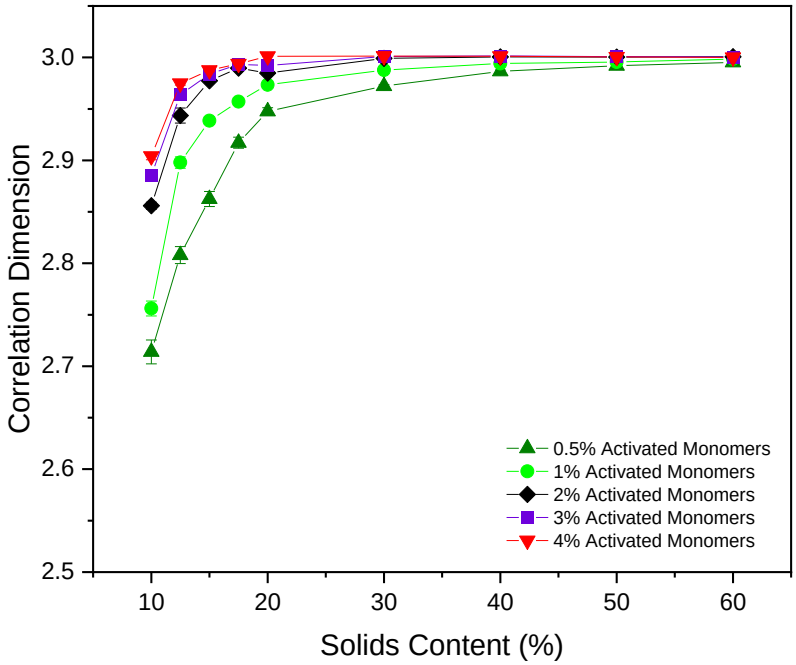

Figure 6.12: Correlation dimension values calculated for simulated materials at varying solids content (S_c)and activated monomer (C_c) values. Standard deviation error bars are included for each data point, although these may not be visible due to their size relative to the data point marker.

These results differ from those obtained from the 2D simulation, in which case the value of a uniformly distributed, densely packed structure yields $D_c = 2$, with fractal structures having $1 < D_c < 2$. For the 2D model, D_c values obtained ranged from as low as ~1.55, and gradually increased with increasing S_c and C_c. The value of D_c slowly reached a plateau at ~2 between 40-50% S_c, in contrast to the faster convergence of values within the 3D analysis. As previously discussed, 2D systems will have more restricted percolation pathways than in 3D structures, consequently influencing their fractal properties, explaining the disparity in calculated values across the two models. The work from the 2D model consequently concluded that the

materials did, in fact, possess fractal properties, even those which had been synthesised at higher S_c and C_c. In light of the results presented here, this conclusion should now be revised.

Correlation Dimension Calculation – Post-Data Analysis Review

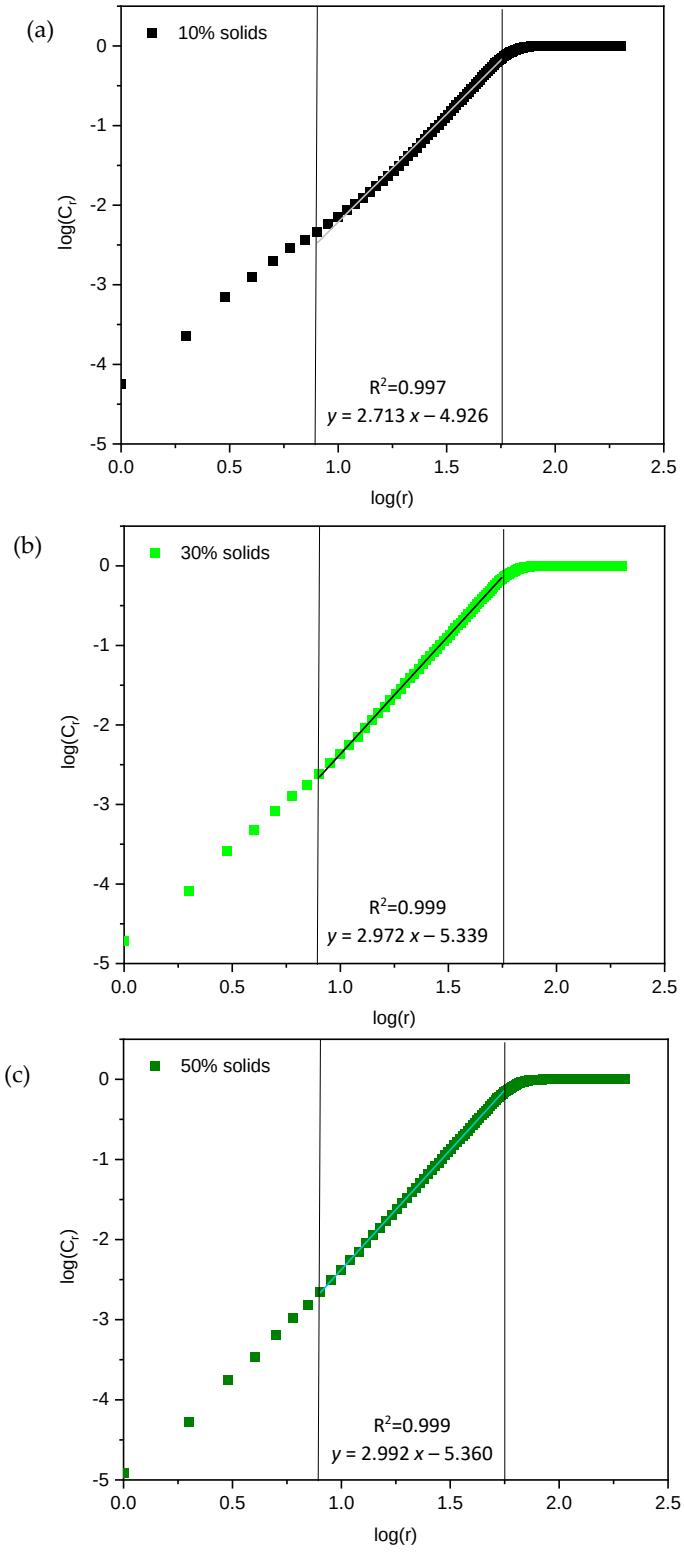

Figure 6.13: Log-log scale plot of the correlation sum (C_r) versus the spanning radius (r) at 0.5% activated monomers and (a) 10% solids, (b) 30% solids, and (c) 50% solids.

As previously described, the value of D_c is determined from the gradient of the straight-line section within the log-log plot of the correlation sum (C_r) versus the spanning radius (r). Examples of this are shown in Figure 6.13 (a)-(c) for simulated structures at solids contents (S_c) of 10%, 30%, and 50%, with 0.5% activated monomers (C_c). The initial scattering of data points arises due to the discrete nature of the lattice, whilst the plateau observed above log(r) values of around 2 is due to large scale effects of the periodic boundary conditions. The straight-line section between these two limits is known as the scaling region, and this is the section used to calculate D_c for the various simulated structures in this work. Note that in each of the example plots in Figure 6.13, the straight-line fit was taken across log(r) values of approximately 0.9 to 1.75, showing a slightly lower R^2 value (0.997) obtained at 10% S_c. Upon inspection post-data analysis, a small number of data points within the initial scattering are included in the straight-line fitting, leading to a small error. The 10% S_c and 0.5% C_c example is, however, the dataset most likely to be affected by this uncertainty, given that it contains the fewest clusters of all the simulated structures. The uncertainty for other structures will, therefore, be lesser, but should be taken into consideration for any potential future research involving the correlation dimension and its calculation.

Hurst Exponent

As previously discussed, the Hurst exponent (H) is determined from the gradient of the straight line section within the log-log plot of the average displacement (ΔB_{avg}) versus the time window (T_s). An example of this is shown in Figure 6.14 for a particle of size 3 diffusing around simulated structures with varying S_c values at 0.5% C_c.

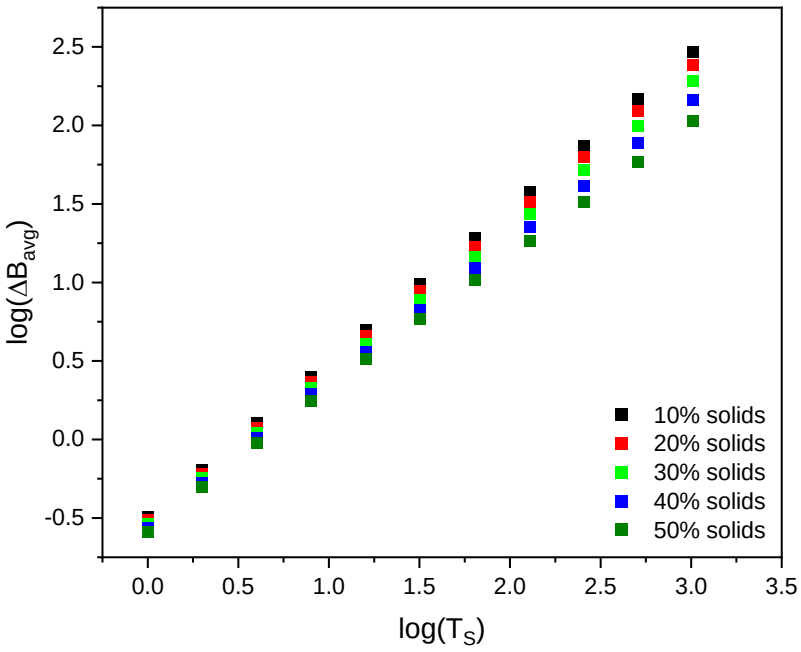

Figure 6.14: Log-log scale plot of the average displacement (ΔB_{avg}) versus the time window (T_s) at 0.5% activated monomers, with varying solids content percentages.

These graphs are plotted and their gradients calculated for each simulated structure, with the resulting H values calculated shown in Figures 6.15(a) and (b) for simulated structures with

various S_c and C_c values, with diffusing particles of size 1 and 3, respectively. In both cases, the H value decreases with increasing S_c, as the path of the random walker becomes more obstructed due to the increased number of occupied sites densely packed within the lattice, directly affecting the particle's motion through the porous network. The value of H also decreases as the value of C_c increases, this time as a result of the increasingly complex, interconnected structures formed from the greater number of primary clusters present. These complex structures create additional obstructions within the path of the random walker, hindering its ability to diffuse freely throughout the lattice and, therefore, decreasing the value of H.

The H values obtained for a random walker of size 1 range from 0.4945(2) at 10% S_c and 0.5% C_c to 0.4338(2) at 60% S_c and 4% C_c. As these values are all below 0.5, they indicate that the random walker motion is antipersistent in nature, as previously discussed. For materials simulated at low S_c and C_c, this value falls only slightly below 0.5 due to the largely open, sparsely-populated structure within the lattice. These H values differ slightly from those cited for the 2D model, where the lowest value obtained reaches below ~0.36 for 50% S_c and 3% C_c. Similar to the comparative analysis of inaccessible sites between the 2D and 3D models, this disparity in H values arises as a result of the new pathway for accessibility opened by the 3D simulation. Once again, opening the structure to the third dimension allows the random walker to diffuse around the lattice more freely, and more accurately reflects how a particle might diffuse through a porous material in reality.

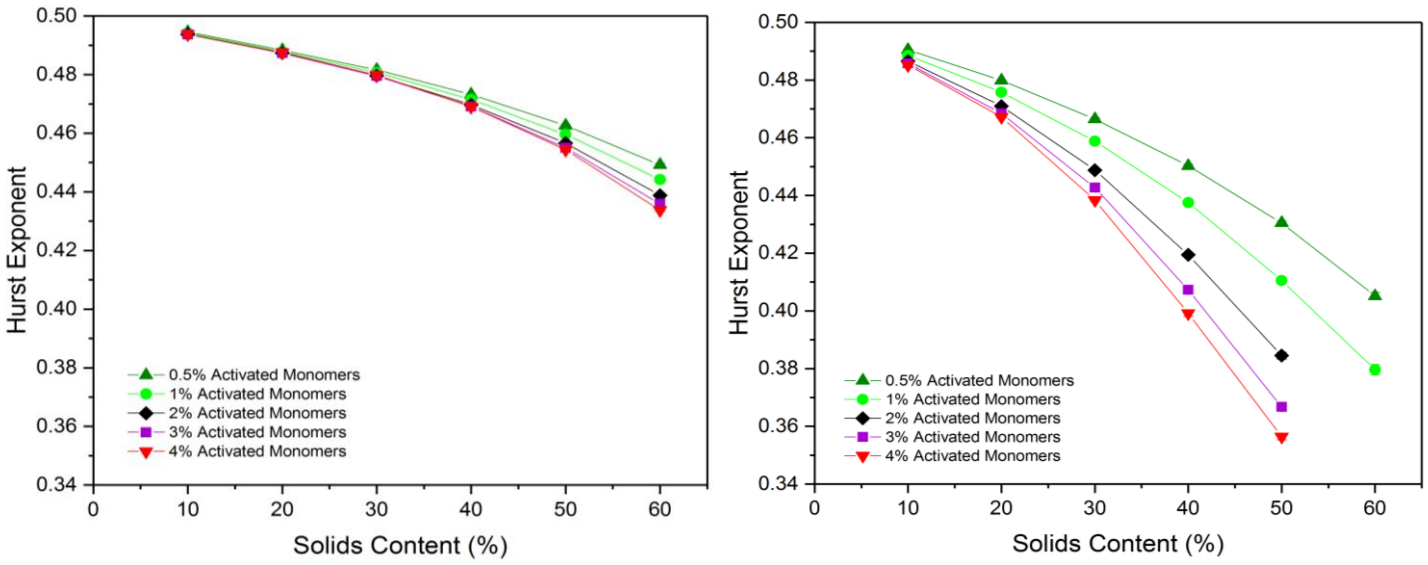

Figure 6.15: Hurst exponent values calculated for varying solids content (S_c) and activated monomer (C_c) values with respect to a diffusing particle of (a) Size 1 and (b) Size 3. Standard deviation error bars are included for each data point, although these may not be visible due to their size relative to the data point marker. Note that a sufficiently percolated structure could not be identified for structures above 1% C_c at 60% S_c for a particle of three sites in size, hence the missing values.

When the random walker size is increased from 1 to 3, the H value obtained decreases far more rapidly as its ability to move around the lattice is restricted by its width. In this case, H values range from 0.4904(2) at 10% S_c and 0.5% C_c to 0.356(1) at 50% S_c and 4% C_c. As with the analysis of the inaccessible sites for a particle of 3 sites in size, assessing the motion of such a particle through a porous material in this manner provides valuable insight for their use in applications involving diffusion of larger particles. Note that a sufficiently percolated pore structure could not be identified for materials formed using 60% S_c at C_c values above 1% for a particle of size 3, meaning that the porosity was too closed off for the particle to freely diffuse through the structure.

Diffusing Particle Pathway

The calculation of H also enables a 3D visual trace of how a particle might move through the porous structure, as shown in Figures 6.16(a), (b), and (c), for S_c values of 10, 30, and 60%, respectively. All visualised traces are for particles of size 3 and at 1% C_c. Note that the axes of each trace differ dependent on the extent to which the particle was able to diffuse through the lattice across periodic boundaries - a box of 100 x 100 x 100 sites in size has been included to allow a comparison of scale.

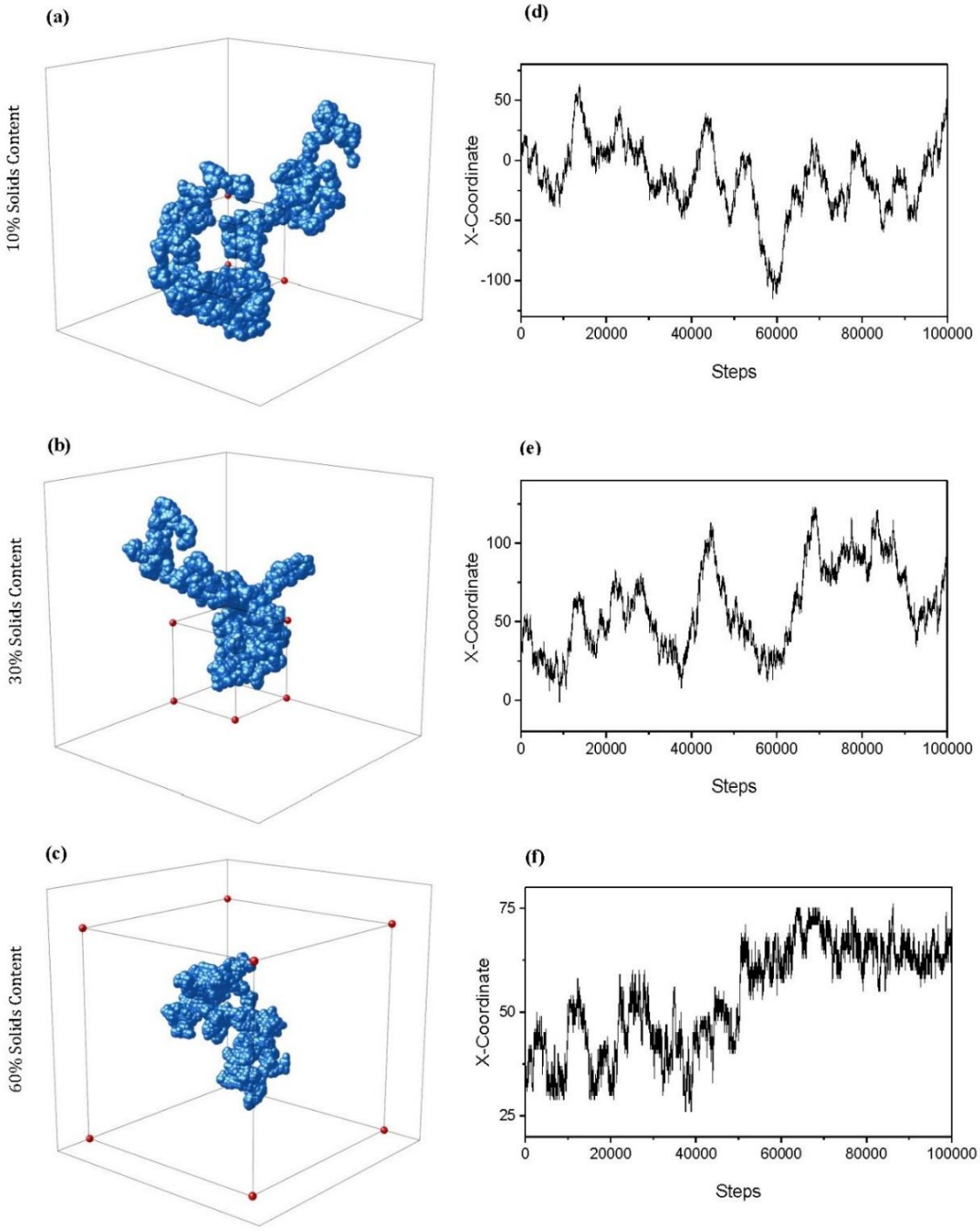

Figure 6.16: Example 3D traces for particles of three sites in size diffusing through simulated structures with 1% activated monomers (C_c) and solids content (S_c) values of (a) 10%, (b) 30%, and (c) 60%. Note that the axes of each trace differ dependent on the extent to which the particle was able to diffuse through the lattice across periodic boundaries—a box of size 100×100×100 sites is included within each trace to allow a comparison of scale. Corresponding x-coordinate traces for each structure at S_c values of (d) 10%, (e) 30%, and (f) 60%.

As S_c increases, the path of the random walker becomes more obstructed, increasing the likelihood that it will turn back on itself as it diffuses around the lattice. This is reflected in the 3D traces visualised, where the particle is unable to explore the lattice to the same extent in the 60% S_c structure in comparison to the 10 or 30% S_c structures within the same number of steps. The periodic boundaries in place allowed the particle to continue to explore the lattice outwith the 100 x 100 x 100 original size, demonstrated particularly within the 10% S_c trace (Figure 6.16(a)) in addition to that of 30% (Figure 6.16(b)). This is in contrast to the 60% S_c diffusing particle (Figure 6.16(c)), whose path was far more limited in terms of the extent to which is was able to explore the densely packed lattice. Figures 16(d), (e), and (f) display the traces of the x coordinate of the particle as it diffuses through the respective lattices, further highlighting the changing diffusive behaviour as the porous networks become more complex and constricted with increased S_c. These traces provide further insight into the internal percolated structure of the simulated material, and demonstrate the antipersistent nature of the particle's motion as it diffuses.

6.3 Summary

The formation mechanism of porous materials, such as resorcinol–formaldehyde (RF) gels, is captured in this work through the development of a 3D cluster growth and aggregation model. The model explores the effect of activated monomer percentage—a parameter that mimics catalyst concentration—and solids content, and allows comparisons to be drawn between the simulated materials and those synthesised in the lab. The resulting simulated material is a monolithic structure of interconnected primary, approximately spherical, clusters, consistent with structures observed experimentally.

Structural analysis of the simulated material was carried out across each solids content and activated monomer percentage studied, including pore accessibility and available surface area. Materials simulated with higher solids contents exhibited a higher percentage of inaccessible pore sites and reduced accessible surface area, both of which are as a result of the densely packed structures. Materials simulated with higher activated monomer percentages, on the other hand, were composed of a greater number of primary clusters that were smaller in size, leading to structures that exhibited an increase in accessible surface area for the diffusion of a particle of size 1. For a particle of size 3, this increase in accessible surface area was observed until an upper limit was reached at a solids content of ~45%, after which the increased interconnectivity was no longer of benefit to the available surface area of the system. Instead, it gave rise to higher proportions of closed-off porosity, consequently reducing the accessibility of surface sites within the structure.

An important aspect of this research was to further explore the fractal properties of RF gels under varying synthesis conditions, and so the correlation dimensions of the simulated structures were calculated. The results obtained indicate that fractal properties can be observed within RF gel materials under specific synthesis conditions—reliant not only on sufficiently low solids content, as previously postulated, but also on sufficiently low catalyst concentrations. Under standard gel synthesis conditions within experiments, solids contents of 20% and above are commonly used, perhaps explaining why numerous studies have

previously observed no fractal properties within the structures. This analysis sheds some light on the ongoing debate over the fractal properties of RF gels, and could explain the conflicting conclusions drawn from different experimental studies.

Hurst exponents for particles diffusing through the material's porous network were also calculated, the results of which point towards the antipersistent motion of the particle. The degree of antipersistence was exacerbated by increasing solids and catalyst concentration, as well as the increase in width from a diffusing particle of size 1 to size 3. Analysing the way in which a particle of varying size diffuses through these porous materials is an important consideration for their application potential and subsequent optimisation, particularly for applications involving larger particles. Furthermore, while the correlation dimension of the material (as measured through SAXS, for example) might not reveal fractal properties, the application of the material as an absorbent still requires consideration of the fractal nature of material diffusion through the porous structure.

This 3D simulation is a continuation of work from a 2D model, which operates under the same principles, with the progression to three dimensions providing a more accurate representation of the materials synthesised in reality. As discussed, the range of values used for activated monomer percentages is based around the percentage of resorcinol molecules expected to be deprotonated in the presence of a basic catalyst, and, although the model successfully captures the trends in material properties as catalyst concentration is altered, an exact comparative experimental resorcinol/catalyst (R/C) ratio has not yet been established.

Chapter 7: Modelling Gas Adsorption

The lattice-based Monte Carlo simulation presented in Chapter 6 has been used to model the formation of RF gels across varying catalyst concentrations and solids contents – two fundamental parameters that have proven to control gel properties in experimental work. The development of a 3D model such as this is a pivotal step toward computational optimisation of porous materials for use in various applications. Building on this, the ability to simulate the anticipated adsorption isotherms of the model structures, and how they vary across a range of synthesis parameters, would be another crucial step forward. Adsorption analysis is one of the most widely employed fundamental techniques used to characterise materials experimentally, so developing a model capable of simulating this computationally would be valuable, giving confidence in the modelling capability that can guide the tailored production of materials optimised for their specific application.

The work presented in this chapter models adsorption analysis both within individual pores and within the simulated porous structures presented in Chapter 6. For the analysis of individual pores, the adsorption behaviour within open transport pores, closed base pores, and bottle neck pores is carried out. The adsorption analysis can be adapted for different systems through varying temperature as well as altering the adsorbate-adsorbent/adsorbate-adsorbate interaction ratio, the impacts of which are also investigated through this work. For the analysis of simulated structures, various catalyst concentrations and solids contents are explored, providing invaluable isotherm and pore size distribution data which can be directly compared to experimental analysis of RF gels which have been synthesised in the lab. A research article presenting findings from within this chapter has also been published in The Journal of Physical Chemistry B[235], the full manuscript for which is provided in Appendix D.

7.1 Methodology

7.1.1 Algorithm Calculations

Adsorption analysis has been carried out in other works through methods such as Monte Carlo and molecular dynamics simulations, even leading to the formation of widely accessible adsorption software. Although these models provide useful insights into specific interactions taking place during adsorption, the industrial application of these models is limited by their significant computational expense and inability to analyse numerous structures simultaneously. The adsorption model presented here, therefore, takes a more coarse-grain approach, allowing various structures to be analysed in a time-efficient manner that would be relevant to industrial applications. This is based upon work by Monson[165], simulating the adsorption process using mean field theory for a lattice gas system, and calculating the changing density across a model system as its chemical potential is altered.

System Grand Potential Calculations

The system analysed in this work is representative of one that is in contact with a heat bath and a particle reservoir, where the temperature, volume, and chemical potential of the system remain constant at each sorption step, whilst the energy of the system and the number of particles present varies. The parameter used for the energy of this system is one which is often used in statistical mechanics – the system grand potential, Ω. The grand potential is defined by the following equation:

$$\Omega = \bar{E} - TS - \mu\bar{N}$$

Equation 7.1

Where $\bar{E}$ is the average particle energy, T is the system temperature, S is the system entropy, μ is the system chemical potential, and $\bar{N}$ is the average number particles present within the system.[236] In order to calculate Ω in real terms for the systems analysed here, both the lattice gas Hamiltonian (H) and the mean field approximation of the Helmholtz energy (F) will be used. First, H is calculated from:

$$H = -\frac{\epsilon}{2}\sum_i\sum_a n_i n_{i+a} + \sum_i n_i\phi_i$$

Equation 7.2

where ϵ is the interaction strength between the nearest neighbour sites within the lattice, n_i is the occupancy of site i (1 for an occupied site, 0 for an unoccupied site), and a denotes each of the nearest neighbour sites with respect to site i.[165] The first part of the expression within Equation 7.2 is effectively a latent heat term, which accounts for the potential energy of nearest neighbour sites, calculating the interaction between these sites and site i. The second expression, meanwhile, accounts for the energy from an external field, where ϕ_i is the external field at site i. The Hamiltonian expression for H in Equation 7.2 can then be used within the Helmholtz energy mean field approximation, where the Helmholtz energy (F) is given by:

$$F = \bar{E} - TS = TS + H$$

Equation 7.3

Following this, the average density of site i (ρ_i), which will have real value between 0 and 1, can be substituted in place of the occupation number (n_i) within Equation 7.2, giving a new expression for H in terms of density. Then, the Gibb's expression for entropy (S) can be incorporated into Equation 7.3, leading to the expanded expression for the calculation of F, where k is the Boltzmann constant:

$$F = \left[kT\sum_i(\rho_i\ln\rho_i + (1-\rho_i)\ln(1-\rho_i))\right] - \frac{\epsilon}{2}\sum_i\sum_a \rho_i\rho_{i+a} + \sum_i \rho_i\phi_i$$

Equation 7.4

The first expression within square brackets accounts for the entropy of lattice sites, whilst the second expression is the lattice gas Hamiltonian equation, as previously discussed. Using Equations 7.2 – 7.4, the expression for Ω therefore becomes:

$$\Omega = F - \mu\bar{N}$$

Equation 7.5

$$\Omega = \left[kT\sum_i(\rho_i \ln \rho_i + (1-\rho_i)\ln(1-\rho_i))\right] - \frac{\epsilon}{2}\sum_i\sum_a \rho_i\rho_{i+a} + \sum_i \rho_i\phi_i - \mu\bar{N}$$

Equation 7.6

Furthermore, these expressions can be used to describe the density distribution at equilibrium, at which point the overall density of the system is constrained to a fixed value, and the system grand potential reaches a minimum. This density distribution is determined from:

$$\frac{\partial F}{\partial \rho_i} - \mu = 0$$

Equation 7.7

$$\therefore kT\ \ln\left[\frac{\rho_i}{1-\rho_i}\right] - \epsilon\sum_a \rho_{i+a} + \phi_i - \mu = 0$$

Equation 7.8

Equation 7.8 can then be rearranged to provide an expression for ρ_i at equilibrium:

$$\rho_i = \frac{1}{1 + \exp\left[\frac{\phi_i - \mu - \epsilon\sum_a \rho_{i+a}}{kT}\right]}$$

Equation 7.9

Note that the value of kT relates to the critical temperature of the system (T^*), which is equal to 1 for a lattice gas whose nearest neighbours are in mean field approximation, determined as:

$$T^* = \frac{kT}{\epsilon} = 1 \quad \text{and} \quad \epsilon = 1 \ \therefore\ kT = 1$$

Equation 7.10

Bulk Gas Systems in Contact With a Solid Surface

In relation to adsorption analysis within pores, we can consider the grand potential of a bulk gas system in contact with a solid surface, where external field contributions can be quantified using the ratio of interaction strength between the solid surface and the fluid (ϵ_{sf}) and the interaction strength between the fluid-fluid nearest neighbour sites (ϵ), denoted by y:

$$y = \frac{\epsilon_{sf}}{\epsilon}$$

Equation 7.11

In the work carried out by Monson, a value of $y = 3$ is used, establishing the external field contribution from solid surface sites as:

$$\phi = -y = -3$$

Equation 7.12

In a model system such as this one, the relationship between Ω and μ will vary as the value of μ increases, corresponding to the change of state at sites adjacent to the solid surface from bulk gas to adsorbed liquid. Initially, as μ begins to increase, the bulk gas at these sites will interact with the solid surface, leading to their eventual condensation and, therefore, to the formation of a liquid layer. This can be effectively treated as a 2D liquid, with 4 nearest neighbour sites contributing to fluid-fluid interactions, given that the sites below are occupied by the solid surface and the sites above occupied by bulk gas. In this case, for the 2D liquid layer sites adjacent to the solid surface, where $\bar{N} = \rho_i = 1$ and $\phi_i = -3$, Equation 7.6 reduces to the straight-line equation:

$$\Omega = -5 - \mu$$

Equation 7.13

As the value of μ increases beyond this to a critical point, the bulk gas sites eventually condense, leading to the multilayer formation of liquid at the solid surface. Thus, the adsorbed liquid sites adjacent to the solid surface can now be treated as part of a 3D liquid, now with 5 nearest neighbour sites contributing to fluid-fluid interactions. Similar to Equation 7.13, the expression for Ω reduces to:

$$\Omega = -5.5 - \mu$$

Equation 7.14

The behaviour of the bulk gas with increasing μ is, therefore, reflective of the behaviour observed experimentally in real systems for increasing pressure. As a direct comparison to relative pressure (p/p_0) used in experiments, an expression for model system relative activity (λ/λ_0) can be established, which for this system can be described by:

$$\frac{\lambda}{\lambda_0} = exp\left(\frac{\mu - \phi}{kT}\right)$$

Equation 7.15

7.1.2 Adsorption Analysis Process

The equations discussed within Section 7.1.1 form the basis for the calculations carried out within the adsorption analysis algorithm, which uses the density at each lattice site, in addition to the average system density, to capture adsorption processes taking place within model systems as the chemical potential is varied. The code for this algorithm was obtained from Prof Monson for 2D analysis of infinite slit pores and was subsequently transformed into a 3D analysis code through this work, which can be found in Appendix C.

A flow chart summarising the algorithm used is displayed in Figure 7.1, overleaf. To begin, all relevant parameters are read from an input file, including variables such as lattice dimensions, system temperature, and interaction ratio, in addition to simulation conditions such as maximum iterations, and maximum density difference. The structure undergoing adsorption analysis was then established using the `ieta` lattice, with geometries manually coded in the case of individual pore analysis, or structures read in from external files for the analysis of porous structures generated from the kinetic Monte Carlo algorithm presented in Chapter 6. The `ieta` lattice takes a binary approach, using a value of either 0 or 1 for each site, distinguishing between those occupied by the structure and those comprising empty pore sites, respectively. The `ieta` lattice was subsequently used to calculate the external field acting upon each bulk gas site (phi_i) using Equation 7.20, taking into consideration each of the 6 nearest neighbour sites surrounding it, the resulting values from which were stored in the `phi` lattice.

$$\mathrm{phi}_i = -\sum_a \left((1 - \mathrm{ieta}_a)y\right)$$

Equation 7.20

For a bulk gas site whose nearest neighbour sites (a) are also entirely comprising bulk gas, the resulting phi_i will always be 0. For a system whose interaction parameter ratio (y), as described in Equation 7.16, is set to a value of 3, a bulk gas site with one nearest neighbour site occupied by the solid structure will result in $\mathrm{phi}_i = -3$, while two nearest neighbour sites will result in $\mathrm{phi}_i = -6$, and so on.

The `rhoold` lattice was used to store the density values of each site before an iteration of the sorption loop, which was initially populated with a starting value for bulk gas sites, read in from the input file discussed previously. The density of each site at the end of an iteration of the sorption loop was subsequently stored in the `rhonew` lattice. Each sorption loop initially calculated the sum of the current densities of the 6 neighbouring sites for each accessible pore site, storing the resulting value in the `snn` lattice (for sum of nearest neighbours).

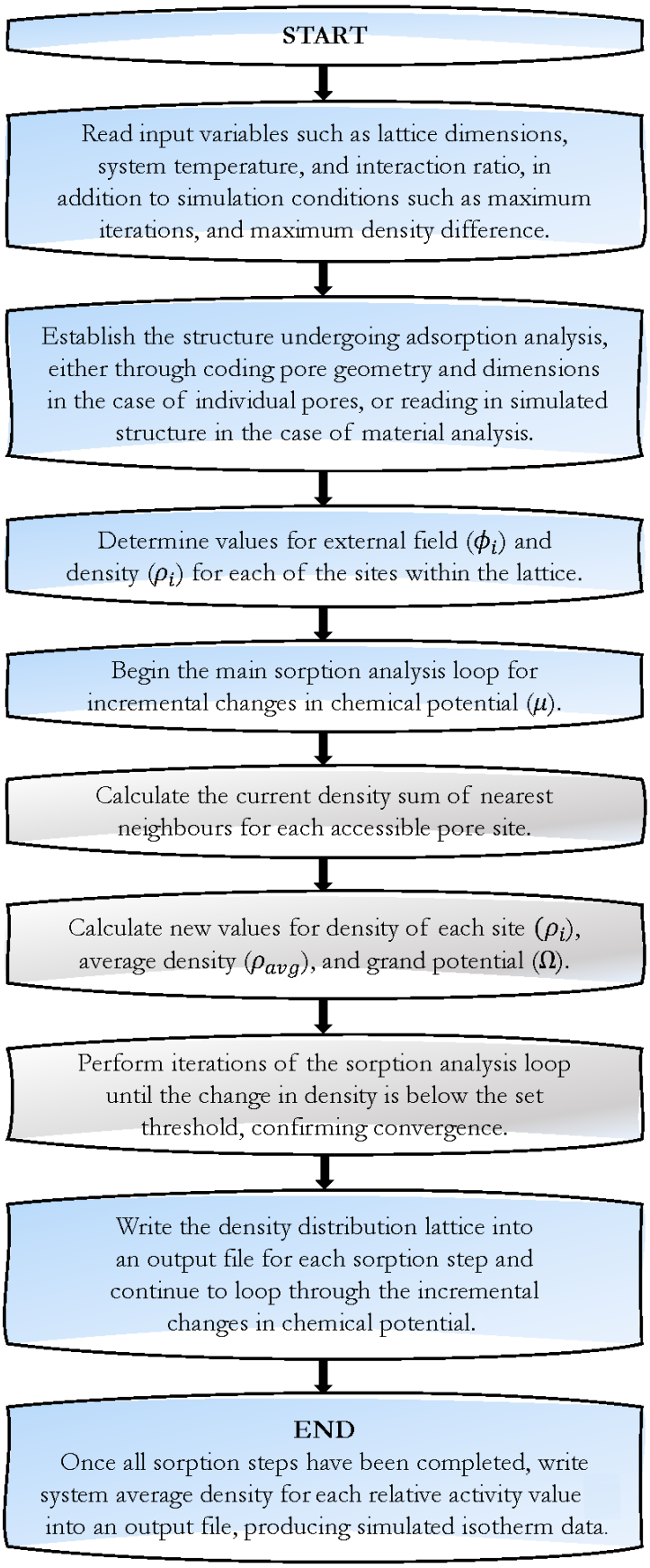

Figure 7.1: Flow chart summarising computational adsorption analysis algorithm.

Based upon the equilibrium density distribution expression shown in Equation 7.8 in addition to the density expression shown in Equation 7.9, values of snn_i and phi_i calculated for the site were used to determine the new density of each site with the incremental change in chemical potential (μ):

$$\mathrm{rhonew}_i = \frac{1}{1 + \exp\left(-x_i\right)}$$

Equation 7.21

$$\text{where} \quad x_i = \frac{\mathrm{snn}_i - \mathrm{phi}_i + \mu}{T^*}$$

Equation 7.22

Following this, the average density of the system was calculated using accessible pore site densities (rhonew_i) and the total number of accessible pore sites (N), the resulting value from which was stored in the `rhoav` lattice.

Finally, the system grand potential (Ω) was determined using Equation 7.23:

$$\Omega = \frac{\frac{1}{2}\sum_i(\mathrm{rhonew}_i\ \mathrm{snn_i}) - \sum_i T^* \ln(1 + \exp\left(x_i\right))}{N}$$

Equation 7.23

To determine whether or not the iteration had converged to achieve a near-equilibrium state, the average density of the system before and after the sorption loop were compared. If the difference in value was below that of the set threshold, the system was assumed to have reached a near-equilibrium state and the sorption step completed; otherwise the sorption loop is re-run. This was carried out for incremental changes in chemical potential, increasing its value such that the system relative activity (λ/λ_0) (as shown in Equation 7.20) increased from 0 to 1 across 2,000 steps and then subsequently decreased from 1 to 0 across 2,000 steps, reflecting the change in relative pressure (p/p_0) used within experimental adsorption analysis, therefore producing a simulated isotherm for the changes in average density with varying λ/λ_0.

Adsorption Analysis in Individual Pores

The calculations discussed above were used to simulate adsorption within individual 3D pores of varying widths and lengths, for open transport pores, bottle neck pores, and closed base pores. The dimensions of the pores were manually coded within the Fortran adsorption analysis algorithm to the desired geometries and sizes. Carrying out adsorption analysis within individual pores allows a comparison to be made between the simulated isotherms and those expected for the various pore sizes and geometries, therefore validating the accuracy of the model, and providing a baseline for the isotherms generated from the adsorption analysis carried out within the porous structures generated from the kinetic Monte Carlo model presented in Chapter 6.

Adsorption Analysis in Simulated Structures

To simulate the adsorption process within the simulated porous materials, the adsorption model was adapted to accommodate the 1,000,000 site lattice structure, and the final material from the cluster-cluster aggregation model was exported into the necessary format for the analysis to be carried out. The adsorption analysis was carried out for the 10 simulated materials which were produced at each solids content and activated monomer percentage, and an average taken across the 10 isotherms.

7.1.3 Adsorption Process Visualisation

Given that the adsorption simulation calculates the density of each lattice site for each sorption step, the adsorption and desorption processes can be visualised as density colourmaps across the lattice at a given point on the isotherm. In this work, this is visualised as a vertical 2D slice through the centre of the lattice – for both individual pores in addition to the simulated structures – and plotted as a colourmap using MATLAB. Wall sites are visualised as a solid red for individual pores and solid white for simulated structures, while the accessible pore sites are visualised using a colour scale that is based upon their density value, which will increase as the bulk gas begins to condense and fill the porous structure. These density profiles provide insight into the visual differences between the adsorption and desorption processes and allow comparisons to be drawn between what is observed visually and what is observed within the isotherm plot.

7.1.4 BJH Pore Size Analysis

The pore size distribution of the simulated structure can be analysed using the desorption branch of the isotherm data, in the same manner as in experimental analysis. The method employed here is based on the Barrett-Joyner-Halenda (BJH) theory[171], which is used frequently within experimental analysis, once again allowing more direct comparisons to be drawn between computational and experimental results. The BJH method is used to determine the pore size distribution and pore volumes within the meso and macroporous range, assuming pores of cylindrical shape are present, with the principle of this method relying on the calculation of the Kelvin core radius of the pore at set pressure intervals using the desorption isotherm data.

As discussed in Chapter 3, the BJH pore size analysis calculations are based around two fundamental equations, the first of which is the Kelvin core radius equation for desorption, which can be applied here to describe the relationship between pore core radius (R_c) and system relative activity (λ/λ_0), as shown in Equation 7.24:

$$Rc_j = \frac{-A}{\ln(\lambda/\lambda_0)_j}$$

Equation 7.24

Where λ/λ_{0_j} is the relative activity at point j, Rc_j is the corresponding Kelvin core radius at point j, and A is the adsorbate property factor. The value of A is calculated to be 0.953 for nitrogen gas, determined from:

$$A = \frac{2\gamma V_m}{RT}$$

Equation 7.25

When BJH analysis is carried out experimentally, an empirical formula is used to determine the thickness of the layer which remains adsorbed onto the pore walls after the core of the pore empties, the coefficients of the equation applying to interactions between specific adsorbents and adsorbates. The total pore radius can, therefore, be determined as the sum of the Kelvin core radius and the thickness of the adsorbed layer at each pressure interval, with pores of new core diameters emptying as desorption proceeds, and the thickness of the layer adsorbed onto the pore walls decreasing as further desorption takes place. A comparison of the total volume desorbed at each point on the isotherm to the corresponding adsorbed layer thickness indicates whether or not new pores are emptying as desorption takes place. In this computational work, however, the intervals within the 2,000 desorption points on the isotherm are assumed to be small enough that the incremental desorption from the adsorbed layer will be negligible in comparison to the volume desorbing when a pore core empties.

The relationship between Rc_j and λ/λ_{0_j} (shown in Equation 7.24) was, therefore, used to determine the size of the new pores that have been emptied, and the volume attributed to the emptying of these pores was then used to plot pore size distributions for the structure being analysed. In order to account for the layer remaining adsorbed onto pore walls after the core has been emptied, the calculated Rc_j is increased by a value of 1, estimating that a monolayer 1 site in thickness remains adsorbed. This analysis was carried out for the 10 isotherms produced through adsorption analysis for each solids content and activated monomer percentage, and an average was taken across the 10 resulting pore size distributions.

7.2 Results and Discussion

7.2.1 Varying System Parameters

As previously discussed, there are two main parameters in the adsorption algorithm that can be altered to reflect the system being studied more accurately – the system temperature (T^*) and the interaction parameter (y), with the latter determined as the ratio of solid-fluid to fluid-fluid interaction strength. In the work published by Monson a value of 1 is used for T^*, which is the critical temperature for condensation, while a value of 3 was used for y, such that the solid-fluid interactions were 3 times that of the fluid-fluid interactions. To ensure that both these values were applicable for the systems typically analysed in the work presented here, the impacts of variations in T^* and y were investigated and the resulting isotherms were assessed. This was carried out for model bottle neck pores that were 40 sites in length and 8 sites in width.

Varying System Temperature

Figure 7.2 displays the resulting isotherms from the analysis of bottle neck pores with T^* values ranging from 0.8 – 1.2. As can be observed, substantial uptake and subsequent monolayer formation takes place at much lower relative activities for adsorption analysis simulated at lower T^* values. Furthermore, a shift in both the size and x-axis positioning of the hysteresis loop is observed with varying T^*, where lower T^* values produce larger hysteresis loops at lower relative activities, while higher T^* values produce smaller hysteresis loops at higher relative activities. This reflects the effect of temperature on adsorption observed in real systems [237], where higher temperatures correspond to less favourable adsorption conditions, particularly where weaker attractive forces are present and, therefore, more interaction time is required between the adsorbent and the adsorbate for physisorption to take place. Similar to the findings of the work carried out by Monson, the size and shape of the hysteresis loop observed for $T^* = 1$ in this analysis, in addition to the gradual initial adsorption uptake displayed at lower relative activities, are similar to those that would be expected for nitrogen adsorption analysis in an open pore such as this one, therefore, this is the value of T^* selected for subsequent adsorption analysis in this work.

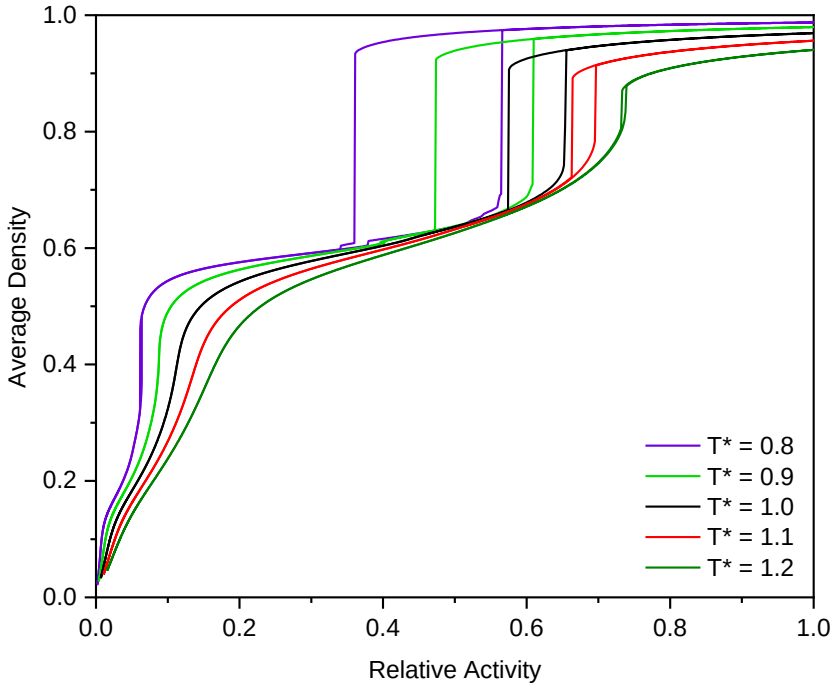

Figure 7.2: Isotherms from adsorption analysis of bottle neck pores at varying system temperature (T^*) values.

Varying Interaction Parameter Ratio

Figure 7.3 displays the resulting isotherms from the analysis of bottle neck pores with y values ranging from 2 – 6. Here, we observe that the main change in hysteresis positioning takes place in the shift from $y = 2$ to $y = 3$, with values above this resulting in hysteresis loops that are almost identical in size, shape, and x-axis position. The most significant variation observed between these isotherms is throughout the adsorption uptake at lower relative activity values,

where an increase in y corresponds to an increase in the initial adsorption, which reaches a plateau – corresponding to monolayer formation – at lower relative activity values. Given that y is measure of the fluid-solid interaction strength in comparison to that of the fluid-fluid interactions, higher values of y correspond to highly favourable adsorption conditions at the adsorbent surface, leading to increased adsorption uptake on the pore walls until monolayer coverage has been achieved. Beyond this point, multilayer adsorption takes place as a result of fluid-fluid interactions, therefore the strength of the solid-fluid interactions is no longer a significant factor in the adsorption mechanism. For this reason, once monolayer formation has taken place, isotherms for y values above 3 begin to converge, resulting in almost identical hysteresis loops. Visual analysis of the resulting isotherm for $y = 3$ confirms its suitability for use as a comparison to nitrogen adsorption measurements carried out experimentally, with the gradual uptake at lower relative activities and the subsequent hysteresis size and geometry similar to those that would be expected for analysis of a pore such as this one. Once again, in line with the work of Monson, this is the value selected for the computational adsorption analysis in this work.

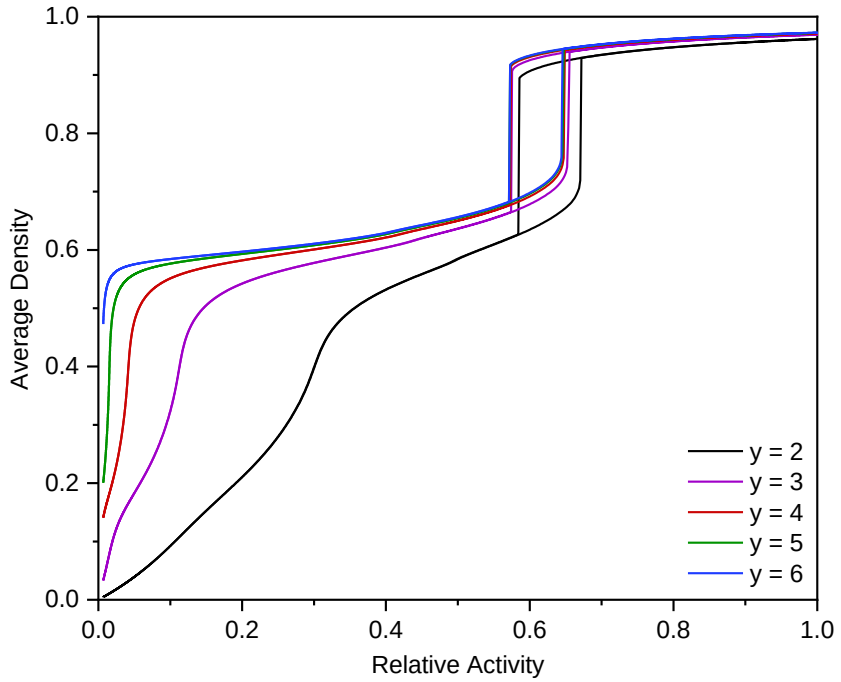

Figure 7.3: Isotherms from adsorption analysis of bottle neck pores with varying interaction parameter (y) values.

7.2.3 Open Transport Pores

Using the system parameters established in the previous section, the lattice-based adsorption analysis was carried out on model pores of varying lengths, widths, and geometries, initially focusing on a simple, four-walled, rectilinear pore which was open to a bulk gas phase at both ends. The lattice is of total length X, containing the pore of length L, and widths Y and Z, each of which are measured in number of lattice sites. We can divide these into horizontal and vertical 'slices', as shown in Figure 7.4, allowing the adsorption at each point to be visualised.

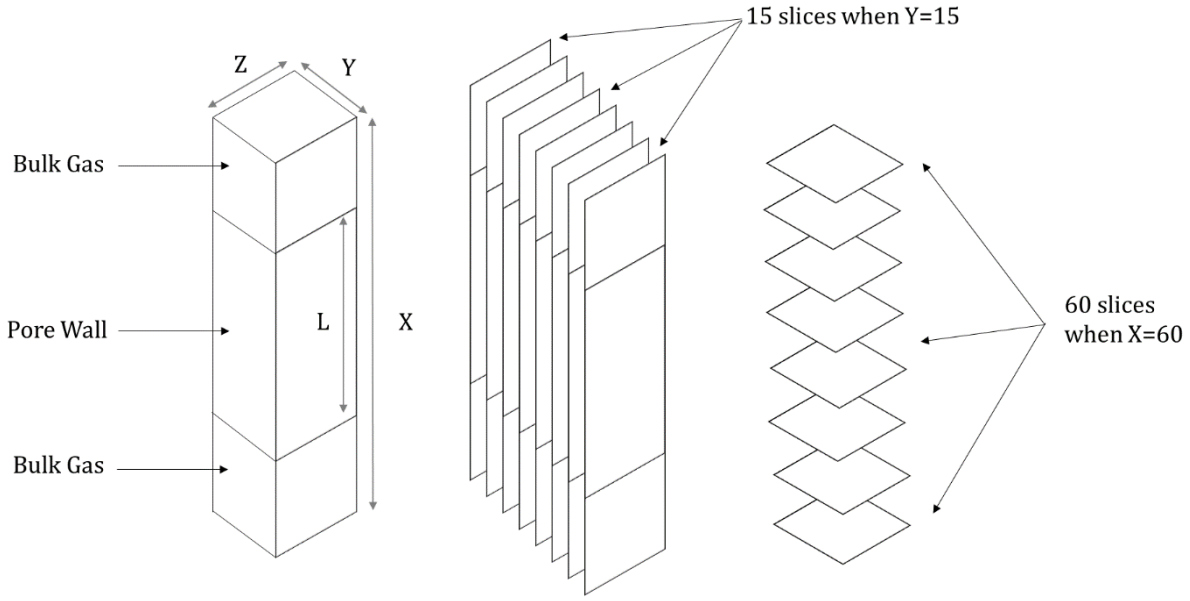

Figure 7.4: Labelled diagram of model open pore used for adsorption analysis.

For all geometries analysed in this model, Y and Z are kept equal to one another, referred to collectively as 'pore width'. As previously discussed, the output data from the code includes a 4000-point isotherm, where average density (ρ_{avg}) corresponds to the amount adsorbed, whilst relative activity (λ/λ_0) is comparable to relative pressure, as used in experimental isotherms. The graphs in Figure 7.5 display the resulting isotherms for adsorption analysis of open pores with varying lengths (Figure 7.5(a)) and varying widths (Figure 7.5(b)). Pores with varying widths were studied using a constant length L=40, whilst pores with varying lengths were studied using a constant width Y, Z=8.

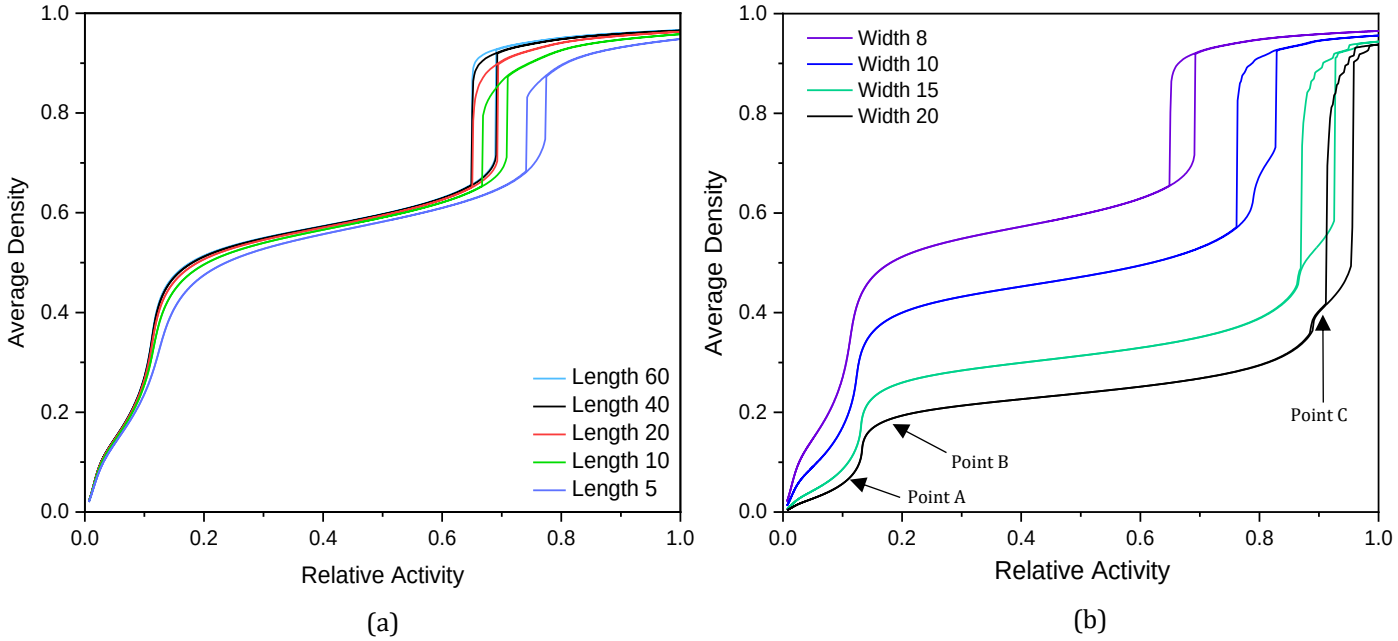

(a) (b)

Figure 7.5: Resulting isotherms from adsorption analysis of open pores with varying lengths (a) and varying widths (b).

The isotherms in Figure 7.5(a) show significant similarities, indicating that the impact of pore length on adsorption behaviour is minimal, with even large variations from L=10 to L=60 following very similar trends as relative activity increases from 0 to 1. Within this range, we see incremental increases in the hysteresis loop size as the length increases, although its position on the x-axis remains unchanged. This is because the constant pore width determines the hysteresis x-axis positioning, whilst the total volume of the pore determines the hysteresis size. Given that increasing pore length corresponds to increasing pore volume, we observe larger hysteresis loops for longer pores as the core of the pore fills and empties. The isotherm for L=5 shows the most variation in terms of hysteresis positioning, attributable to the fact that the length of the pore is less than its width, and therefore cannot technically be classified as a pore according to IUPAC definitions. Although its adsorption behaviour is likely to differ from that of a pore whose length is greater than its width, the adsorption analysis provides an insightful comparison.

In contrast to that of pore length, the impact of pore width is substantial on the adsorption behaviour and, therefore, the resulting isotherm produced, as displayed by the simulated isotherms in Figure 7.5(b). As the pore width is increased, the adsorption uptake is more gradual with increasing relative activities, given that its value is relative to the total volume of the pore, which increases with increasing pore width. In addition to this, the hysteresis loop observed shifts to higher values of relative activity for larger pores, in agreement with previous experimental works that have confirmed the impact of pore width on hysteresis positioning, where larger pores fill at higher relative pressures. Importantly, the shape of the isotherm also agrees with that expected of a pore open at both ends, found in previous studies, where a relatively narrow hysteresis with two largely parallel lines is observed.[238]

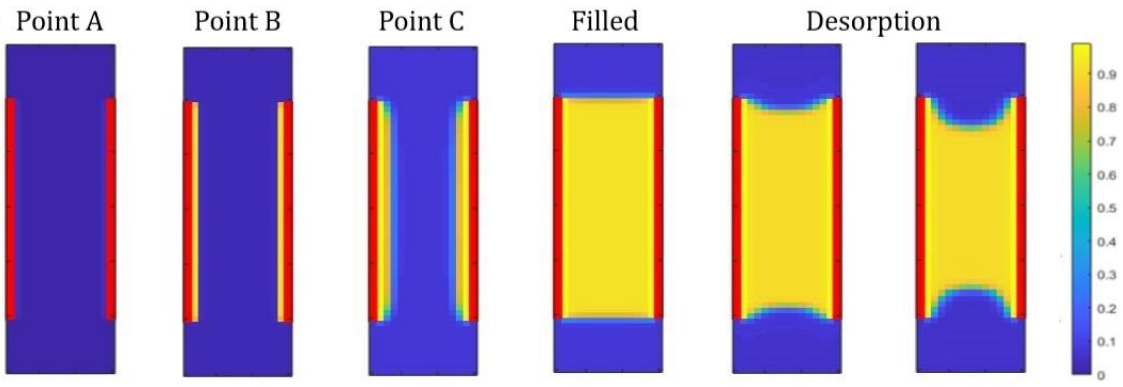

Figure 7.6: Vertical density profiles of the centre of the pore at various stages in the adsorption and desorption process for open transport pores. Red sites show pore wall sites, blue sites empty sites within the pore, and yellow sites where adsorption has taken place, in accordance with the density colour scale shown.

Further analysis of the isotherms allows two or three distinct sections to be identified, depending on the width of the pore. First, there is an initial uptake at Point A on the isotherm, which then begins to plateau at Point B. For larger pore widths, Point C can be observed – a second point at which the uptake begins to plateau once again – before pore filling takes place. In order to further investigate the adsorption process taking place at each of these points, in addition to other significant points within the isotherm, the pore density distribution data can

be used to produce density colour maps. These show, pictorially, where adsorption has taken place within the pore at each of the stages selected, further elucidating the mechanism by which adsorption and desorption occurs. Figure 7.6 shows colour map density profiles of the pore at the different adsorption points indicated for a pore 15 sites in width, displaying a two-dimensional slice down the centre of the pore, where the sites with red markers correspond to pore wall sites, and the colour of the density profile transforms from blue to yellow as adsorption occurs.

Upon inspection of the density profile at Point B within Figure 7.6, it is clear that the related plateau observed on the isotherm at this point corresponds to the formation of a monolayer across each of the four pore walls, after which point further adsorption takes place gradually. In pores of sufficient width, we observe the feature at Point C, which corresponds to the formation of a second layer of adsorbed gas on top of the original monolayer, as depicted on the corresponding density profile, just before the pore fills. The remaining density profiles display the pore as desorption takes place – beginning from the filled state at a relative activity of 1 then showing the initial desorption as relative activity decreases, and finally the pore just before emptying at the desorption branch of the hysteresis. The density profiles show that, whilst the pore fills through the gradual adsorption along the length of the pore walls, it conversely empties through the gradual removal of layers from the meniscus, revealing the difference in the mechanism by which adsorption and desorption takes place. Furthermore, despite showing adsorption taking place on the isotherm at Point A, the corresponding density profile for the 2D central slice of the pore at this stage appears to show no adsorption taking place. Given that the model is in 3D, horizontal density profiles of the cross-section along the length of the pore can be produced, as shown in Figure 7.7(a), allowing areas of the pore not detected by the central vertical profile to be analysed. Here, the cross-section of the pore at point A on the isotherm is illustrated, where we can see adsorption taking place at the corner sites along the length of the pore where two walls meet, which explains this initial adsorption failing to appear on the central vertical density profile. Furthermore, we can also use the cross-sectional density distribution data to create a detailed profile of the meniscus at different points within the isotherm, with Figure 7.7(b) illustrating the layers of the meniscus within the pore just before it empties.

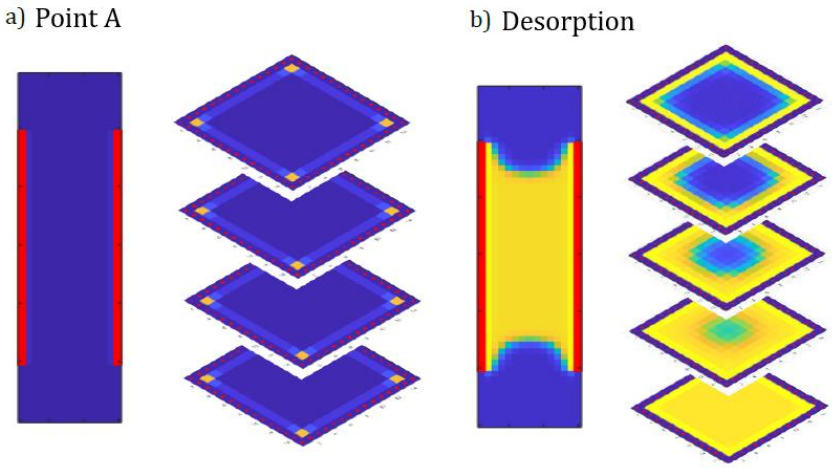

Figure 7.7: (a) Central vertical profile of the open pore at Point A with corresponding cross-sectional profiles and (b) Central vertical profile during desorption with corresponding cross-sectional profile of the upper meniscus.

7.2.4 Bottle Neck Pores

In order to further investigate the impact of pore geometry on adsorption behaviour, the analysis of model bottle neck pores was carried out, once again exploring varying pore widths and the resulting isotherms produced. All pores possessed a length of 40 sites, with a bottle neck entrance width approximately one-third of the total pore width, rounded to the nearest integer. Figure 7.8 shows the resulting isotherms from the adsorption analysis, whilst Figure 7.9 displays the corresponding density profiles of the 2D vertical slice through the centre of the pore, visualising the process. Once again, Points A, B, and C on the isotherm can be identified in the wider pores, with the adsorption at point A this time including adsorption onto the corners of the pore walls below the bottle neck entrance. Similar to the adsorption process taking place in open transport pores, monolayer formation is observed along the walls of the pore at lower relative activities, proceeded by multilayer formation, and saturation of the bottle neck entrance area before the pore itself fills completely. Desorption, once again, takes place through the removal of layers from the meniscus at the bottle neck entrance before the pore itself empties completely when a sufficiently low relative activity is reached. The difference in mechanisms for adsorption and desorption is more prominent for bottle neck pores, given that pore filling takes place much more gradually through the narrow entrance, in contrast to the more immediate emptying of the pore when a sufficiently low relative activity is reached. This is in agreement with the IUPAC hysteresis classifications where the H2 hysteresis loops, which are associated with materials comprised of bottle neck pores, indicate the gradual filling of pores during adsorption, and the sudden emptying of pores during desorption.[174]

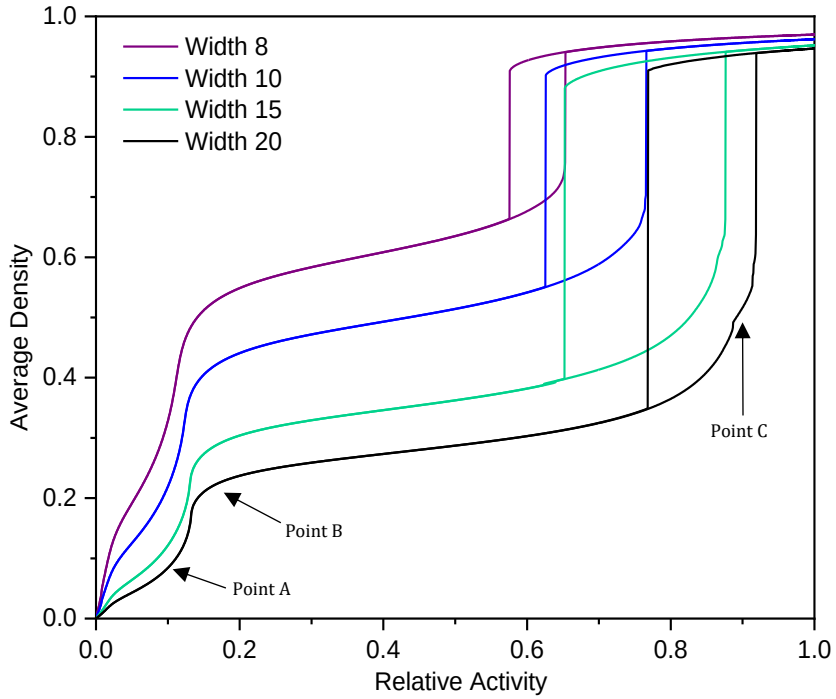

Figure 7.8: Resulting isotherms from adsorption analysis of bottle neck pores with varying widths.

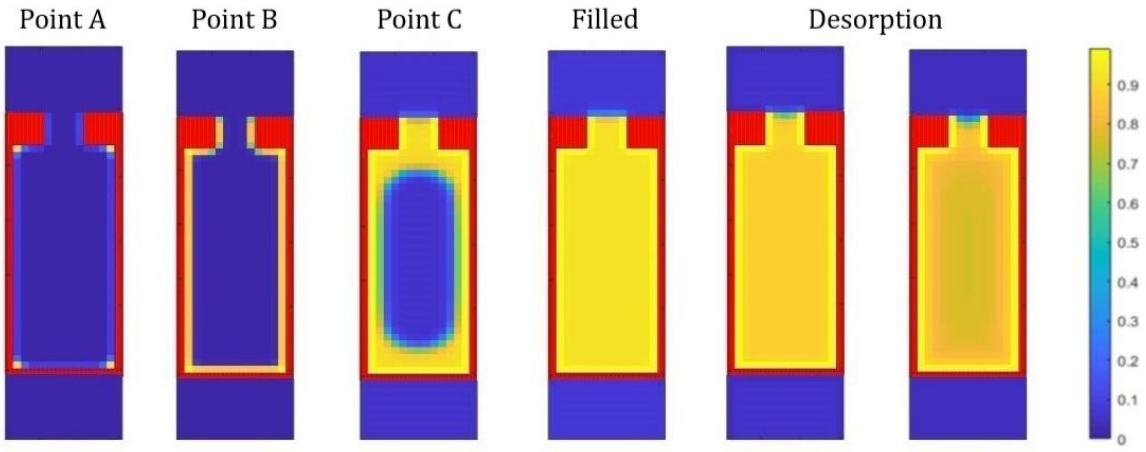

Figure 7.9: Vertical density profiles of the centre of the pore at various stages in the adsorption and desorption process for bottle neck pores. Red sites show pore wall sites, blue sites empty sites within the pore, and yellow sites where adsorption has taken place, in accordance with the density colour scale shown.

7.2.5 Closed-Base Pores

The final pore geometry that was investigated using computational adsorption analysis was a rectilinear pore similar to the open pore presented in Section 7.2.3, this time with a closed base and just one end remaining open to the bulk gas. Figure 7.10 shows the resulting isotherms from the adsorption analysis, whilst Figure 7.11 displays the corresponding density profiles of the 2D vertical slice through the centre of the pore, visualising the process. Once again, Points A, B, and C on the isotherm can be identified in the wider pores, with the adsorption at Point A this time including adsorption onto the base corners of the pore. Similar to open and bottle neck pores, monolayer formation is observed along pore walls at Point B, in addition to multilayer formation at Point C for pores of larger width. The main difference observed in the isotherms for closed base pores in comparison to those of open pores is in the width of the hysteresis loop – whilst the pores desorb at comparable relative activities to their open-end counterparts of the same width, they appear to fill at a lower relative activity, consequently leading to a narrower hysteresis. This can be attributed to the meniscus formation that takes place at lower relative activities for closed base pores, as can be observed at Point C in Figure 7.11, soon after which the core of the pore itself fills. Given that the point at which the pore empties during desorption is consistent for both closed base pores and open pores of the same width, it is the desorption data that should provide the most accurate pore size analysis results, as is typically used for methods such as BJH pore size analysis.

Modelling adsorption within individual pores in this way is valuable, not only in confirming the theories behind the analysis of our laboratory experimental work but also in providing additional insight into specific mechanisms, such as the pore filling taking place along the walls and emptying via the meniscus. Furthermore, given that the results presented for individual pores from this model are in agreement with those cited in the literature, the utility of the adsorption calculations is verified before being applied to the 3D complex structures generated from the kinetic Monte Carlo cluster aggregation simulation.

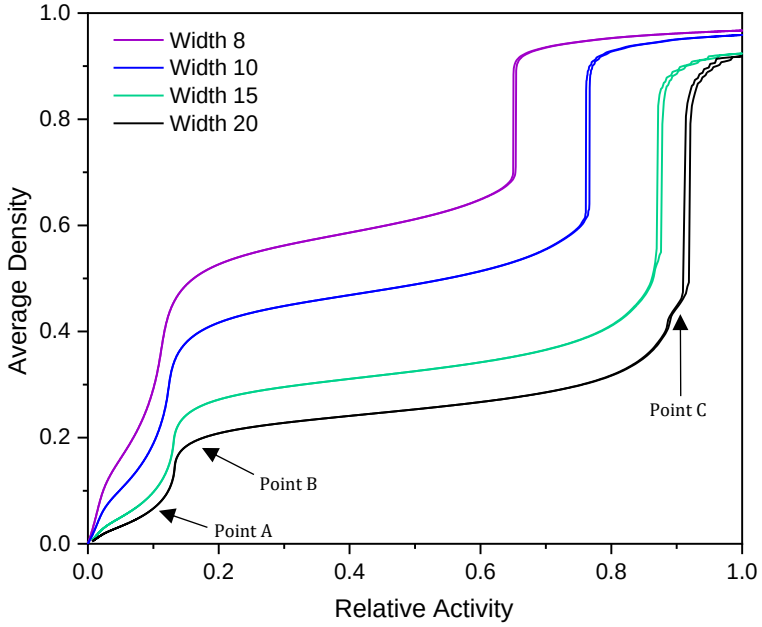

Figure 7.10: Resulting isotherms from adsorption analysis of closed base pores with varying widths.

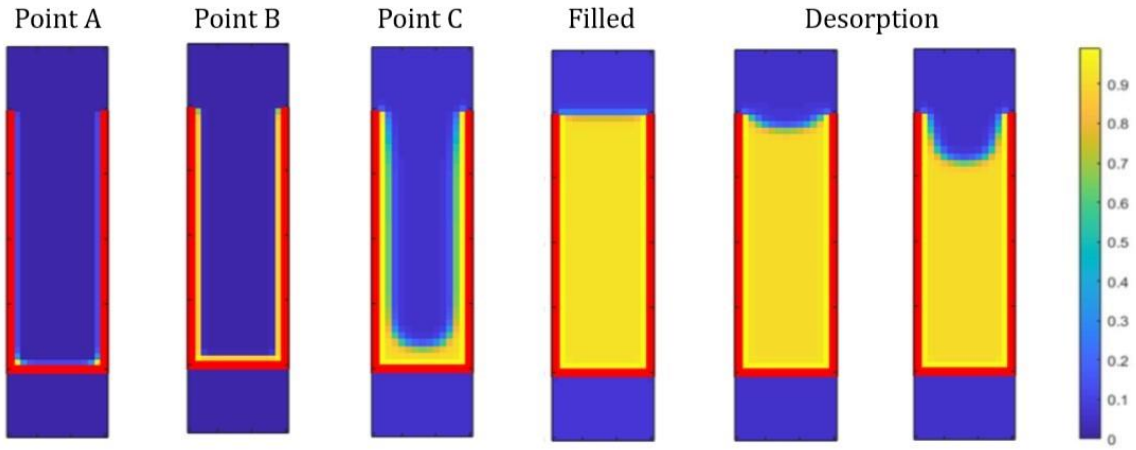

Figure 7.11: Vertical density profiles of the centre of the pore at various stages in the adsorption and desorption process for closed base pores. Red sites show pore wall sites, blue sites empty sites within the pore, and yellow sites where adsorption has taken place, in accordance with the density colour scale shown.

7.2.6 Adsorption in Porous Structures

Varying Solids Content

Adsorption analysis was carried out on the porous structures produced from the kinetic Monte Carlo cluster aggregation model presented in Chapter 6, allowing each of their adsorption behaviours to be investigated and subsequently compared to that of RF xerogels analysed experimentally. Figure 7.12(a) displays the resulting isotherms from a structure

simulated at 1% activated monomers (C_c) and varying solids contents (S_c). We can observe the changes in hysteresis loop shape across the varying S_c percentages, with structures at lower S_c producing isotherms with narrow, elongated hysteresis loops, with largely parallel adsorption and desorption branches. As was confirmed by the analysis carried out in Section 7.2.3, hysteresis loops of this type indicate the presence of open transport pores within the structure. This is in contrast with those observed at higher S_c, whose isotherms possess wider, shorter hysteresis loops, with a gradual increase observed at the adsorption branch alongside a steeper decrease on the desorption branch. As demonstrated by the results presented in Section 7.2.4, hysteresis loops of this kind point towards the presence of bottle neck pores within the structure. The changes in the x-axis position of the hysteresis loop can also be observed, shifting from high to low relative activity values as the solids content is increased from 10% to 50%, indicating that higher solids contents result in structures with narrower pores, as demonstrated within the results already presented in previous sections on varying pore widths.

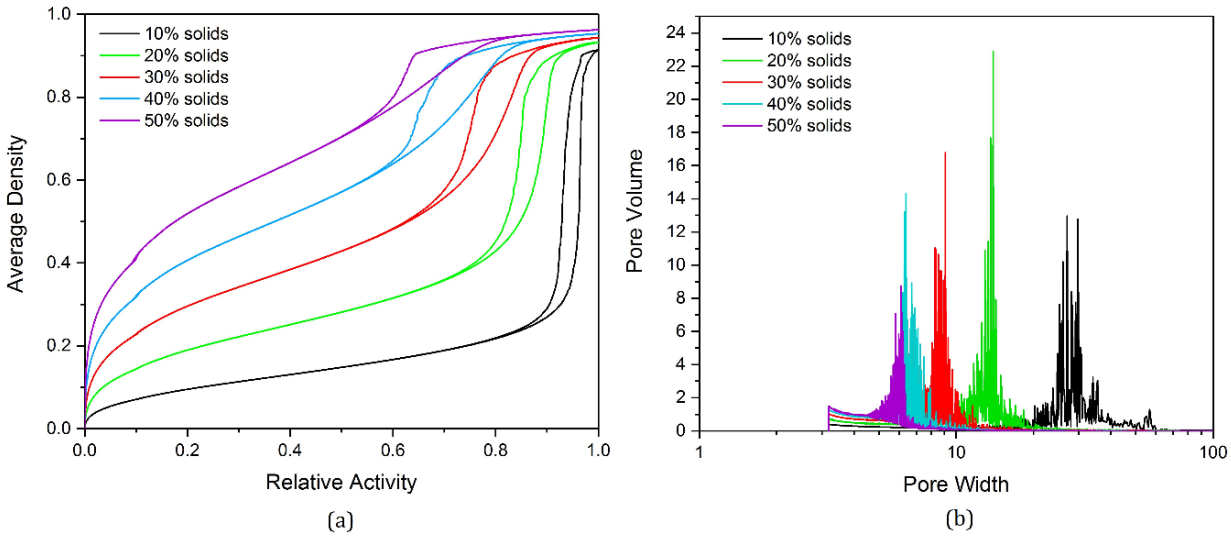

Figure 7.12: (a) Simulated isotherms for the adsorption analysis of model porous structures at 1% activated monomers (C_c) and varying solids contents (S_c). (b) Corresponding pore size distributions.

Furthermore, Figure 7.12(b) shows the pore size distribution results from the subsequent BJH pore size analysis of structures at varying solids contents of 10–50%, where the calculated pore size is measured in lattice sites. These distributions agree with the visual analysis of the simulated adsorption isotherms—quantifying the shift in pore size as solids content is altered, where pores become narrower as the structures become more densely packed with a higher percentage of solids occupying lattice sites. This impact on pore size is also in agreement with the trends observed through experimental analysis of RF gels with varying solids contents from previous studies.[66,69,239] The distribution of pore width also narrows with increasing solids content, where structures at lower solids percentages possess a wider range of pore sizes in comparison to those at higher solids percentages. Note that an increase in volume is observed toward the lowest pore widths (between width values of approximately 3–5 sites) for each distribution in Figure 7.12(b)—this can be attributed to the final layers of adsorbed gas remaining on pore walls, which are the last to desorb from the structure, and the total volume of which will increase for structures of higher solids contents as a result of the increased surface area available.

Varying Catalyst Concentration

The adsorption process was also simulated across structures with varying C_c values, the isotherms for which are shown in Figure 7.13(a) at 30% S_c, with the results indicating similar trends to those observed for varying S_c. Once again, the position of the hysteresis loop on the x-axis shifts toward lower relative activity, pointing toward the presence of pores that are narrower in width. Furthermore, the changing appearance of the hysteresis loop from narrow and elongated in shape to wider and shorter points toward the changing geometry of the pores themselves, with lower C_c structures comprising of open transport pores and higher C_c structures comprising of bottle neck pores.

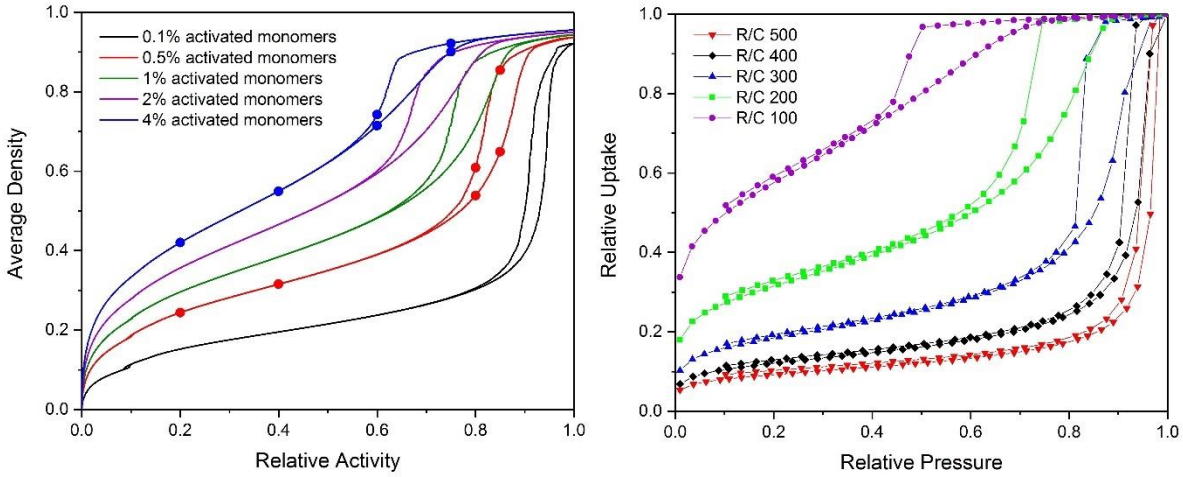

(a) (b)

Figure 7.13: (a) Simulated isotherms for the adsorption analysis of model porous structures at 30% solids content (S_c) and varying catalyst concentrations (C_c). (b) Experimental isotherms for the adsorption analysis of RF xerogels synthesized in the lab at varying catalyst concentrations (R/C ratios), where low R/C ratios correspond to higher catalyst concentrations. Note that the circular points indicated on simulated isotherms in Figure 7.13(a) correspond to those visualized in Figure 7.15.

Importantly, these simulated adsorption isotherms can also be directly compared to those obtained experimentally through nitrogen adsorption experiments for RF gels synthesized in the lab, shown in Figure 7.13(b), for RF gels at varying catalyst concentrations, where high resorcinol/catalyst (R/C) ratios correspond to low catalyst concentrations, and low R/C ratios correspond to high catalyst concentrations. Experimental isotherms have been plotted based on their relative uptake, allowing them to be compared directly to those from the adsorption analysis of model structures. Note that the simulated isotherms are shown for structures at 30% solids content, while the experimental isotherms are shown for RF gels synthesized at 20% solids content. This comparison is made because the laboratory-synthesized gels are subject to shrinkage during drying, making their final solids content more comparable to the higher simulation values. Simulating shrinkage of the simulated materials produced from the kinetic Monte Carlo model and comparing these to the dried RF gels synthesized in the lab, although not performed within this project, is a future focus of this work. The visual similarities between the experimental and simulated isotherms across varying catalyst concentrations are significant, including the same trends observed in the shape and position of the hysteresis loop. These trends are reflected once again in the pore size distribution results

from the BJH analysis, both simulated (Figure 7.14(a)) and experimental (Figure 7.14(b)), displaying the shift from wider pores at lower catalyst concentrations to narrower pores at higher catalyst concentrations. These comparative results are valuable not only for the validation of the kinetic Monte Carlo cluster aggregation model for the formation of RF gels but also in showing promise in the potential for computational tailoring of these materials to optimise their performance in various applications.

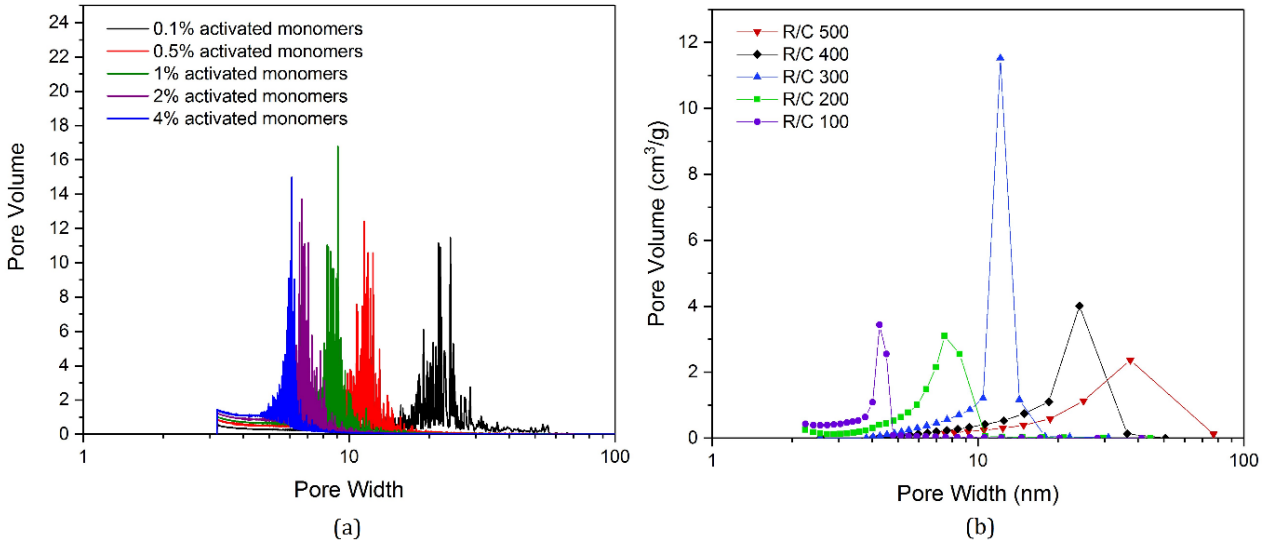

Figure 7.14: (a) Pore size distributions of model porous structures at varying catalyst concentration (C_c). (b) Pore size distributions for RF xerogels synthesized in the lab at varying catalyst concentrations (R/C ratios), where low R/C ratios correspond to higher catalyst concentrations.

7.2.7 Sorption Process Visualised

In addition to the isotherm data produced from the simulated adsorption analysis of the 3D porous structures, density profiles across each were generated throughout the adsorption and desorption process. This is a useful way to visualise processes that cannot be observed by eye in experimental analysis. Figures 7.15(a) and 7.15(b), overleaf, show the visualised adsorption and desorption processes within structures produced at 0.5% and 4% C_c, respectively, both at 30% S_c. The density profiles across the structures are shown at the same relative activity values on the adsorption and desorption branches of the isotherm, corresponding to the markers located on the plots within Figure 7.13(a) and showing the visual differences between each. This provides a visual comparison between the mechanism by which pores fill during adsorption and empty during desorption. The differences are particularly evident in the 0.5% C_c structures, as shown by Figure 7.15(a), where at a relative activity value of 0.85, the desorption branch shows a completely saturated structure while the adsorption branch shows many pores still yet to be filled. This highlights the differing mechanisms by which complex structures adsorb and desorb gases, which could have significant implications when it comes to their widespread use within applications.

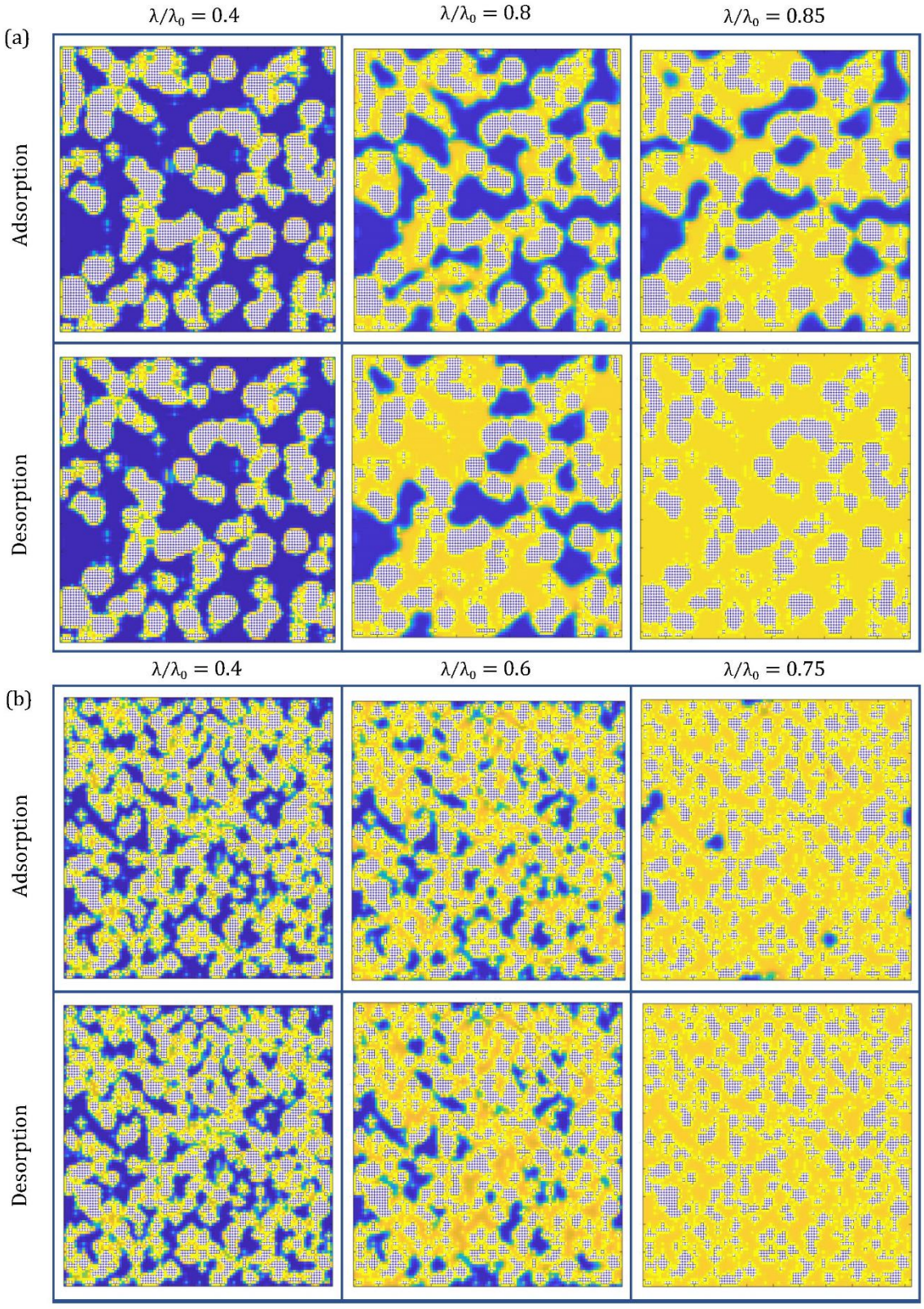

Figure 7.15: Density profiles through the centre of the model porous structure at various relative activity (λ/λ_0) values throughout the adsorption and desorption processes for (a) 30% solids content (S_c) and 0.5% activated monomers (C_c), and (b) 30% S_c and 4% C_c. White sites show the material structure, blue sites empty sites within the pores, and yellow sites where adsorption has taken place.

7.3 Summary

To conclude, the adsorption model presented here successfully captures the adsorption and desorption processes that take place both within individual pores and within complex porous structures, offering a computationally efficient method of simulating and analysing materials such as RF gels, in contrast with the computationally expensive models which have been employed in previous studies. The impacts of two system parameters within the adsorption analysis – temperature and interaction strength – were assessed, and the most appropriate values determined for subsequent work.

The impacts of varying the width and geometry of individual pores were explored through analysis of the isotherm data produced, the results of which are in agreement with those found in literature from both experimental and computational methods. The effect of varying solids content and catalyst concentration on the adsorption and desorption behaviour of the porous structures was also assessed, as demonstrated by the changes in isotherm shape in addition to the visual differences observed from structure density profiles at varying relative activities. The changes observed within the isotherm plots provided insight into the size and geometry of the pores present within the materials, with structures produced with lower solids contents and catalyst concentrations comprising of open transport pores that are larger in width, whilst those at higher solids contents and catalyst concentrations comprised of bottle neck pores that were narrower in width. The adsorption and desorption processes were visualised using density colour maps, providing a visual comparison between the mechanism by which porous structures fill and empty – an imperative consideration when assessing the structural characteristics required for specific applications.

The results of this study also further validate the kinetic Monte Carlo cluster aggregation model, presented in Chapter 6, in capturing the formation of porous materials such as RF gels, as the simulated adsorption analysis results show significant similarities to those obtained experimentally for RF gels synthesised in the lab. The trends observed in the shape of the isotherm and position of the hysteresis loops are consistent between the two, as are the trends observed from the two BJH pore size distributions.

Overall, the results presented here show significant promise in advancing towards the computational tailoring of materials such as these in a manner that is realistically applicable to widespread industry use. A model that can predict and control a material's properties in this way would be invaluable to realising its full application potential, allowing determination of the synthesis parameters required to produce materials with the desired characteristics in a time-efficient and computationally inexpensive manner.

Chapter 8: Water Treatment Application Testing

The previous three chapters, Chapters 5 – 7, have explored the formation mechanism and subsequent properties of RF gels using both experimental and computational methods. This work has demonstrated the tuneability of these materials using two primary synthesis parameters – solids content and catalyst concentration – resulting in the formation of materials possessing various textural and fractal properties, and consequently exhibiting different adsorption behaviours. This chapter explores the practical applications of these materials, testing their efficacy in the removal of an endocrine disrupting chemical (EDC), 3,4-dichloroaniline (3,4-DCA), from aqueous solutions through UV-Vis experiments, and using both the experimental and computational data obtained in the previous chapters to predict and understand the factors impacting their performance. This demonstrates how these materials can be optimised using either an experimental or computational approach for a specific application, with the benefits of efficient computational optimisation over time-consuming experimental tailoring being previously discussed.

A common approach to water purification involves the adsorption of identified pollutants, typically using a porous material possessing a high surface area and an internal structure with channels large enough to facilitate the diffusion of specific pollutant molecules. The attractive and tuneable properties of RF gels, as discussed in previous chapters, make them well-suited to water purification applications, with this work focusing on a particular endocrine disrupting chemical – 3,4-DCA. This chemical acts as an intermediate in the synthesis of fabric pigmentation and pharmaceuticals, as well as extending to use in the production of herbicides such as propanil, diuron, and linuron, which are applied in the farming of numerous crops for human consumption.[119] Environmental contamination with 3,4-DCA arises from the degradation of pesticides into soil and field waters, as well as from industrial wastewater deposits, while human exposure to this chemical is also expected to arise as result of the consumption of food from treated crops.[120,121] Research has documented the chronic and toxic effects of 3,4-DCA in fish [122-125], with suggestions that similarly concerning effects could be relevant to human biology, but the complex nature of human endocrinology means that the full extent of these risks, and the concentrations at which many EDCs become problematic, is still not fully understood.[118] Although the direct impacts of EDCs on humans have been difficult to ascertain, particularly given that significant effects may not become evident until years after exposure, the endocrine disrupting effects of certain medications in humans have already been documented, pointing towards the detrimental effects possible for EDCs within the environment.[116]

As a relatively small, simple molecule, one would predict that the removal of 3,4-DCA from aqueous systems would be maximised by its adsorption onto a porous material with a high surface area, without the need for a large channels within the porous network. With respect to RF gels, the highest accessible surface areas are observed for materials at higher catalyst concentrations (and therefore low R/C ratios in laboratory synthesis), as well as solids contents

that are high enough to facilitate larger surface availability but low enough that their structures do not become so densely packed that their porosity becomes predominantly inaccessible. In order to explore this experimentally, the performance of two laboratory synthesised RF gels – an R/C 100 and an R/C 300 gel, both of which were synthesised at 20% solids content – were compared in their ability to remove 3,4-DCA from water. Once the most suitable gel was identified, its adsorption behaviour and capacity was analysed and its performance compared to other porous materials investigated within the literature. Although 3,4-DCA concentrations of up to ~20 mg/L are typically observed in water systems within the environment, concentrations of up to 400 mg/L were investigated here, allowing the full adsorption capabilities and behaviours of RF gels to be explored. Furthermore, if the gels are capable of adsorbing significant amounts of 3,4-DCA at these concentrations, their use could extend to direct wastewater treatment, removing high concentrations of pollutants before they enter the environment.

8.1 Methodology

8.1.1 3,4-DCA Solution Preparation

To prepare 3,4-DCA solutions at varying concentrations, a 500 mL stock solution of 400 mg/L was initially made and was then diluted to the required concentration of the various solutions to be analysed. To begin, 0.2 g of solid 3,4-DCA (98%, Sigma Aldrich) was weighed into a crucible using a balance with an accuracy to 10^{-4} g, while 500 mL of deionised water (Millipore Pro Guard) was measured using a 500 mL (±1 mL) measuring cylinder, both of which were placed into a 1 L beaker for mixing. A magnetic stirrer bar was added and the beaker was placed on a heated stirring plate to help the 3,4-DCA dissolve into solution. The solution was stirred continuously until the 3,4-DCA had fully dissolved into the water, which took approximately 20 minutes, after which point the solution was transferred into a 500 mL Pyrex storage bottle.

All 3,4-DCA samples used for RF gel adsorption analysis were diluted from the 400 mg/L stock solution, with concentrations of 25, 75, 125, 150, 175, 200, 300, and 350 mg/L solutions prepared through dilution. Samples of 80 mL in volume were prepared using a 10 mL (± 0.01 mL) pipette to measure the volume of 3,4-DCA solution and deionised water required for each concentration. These were prepared on the same day they were used for experimental analysis, being measured directly into glass jars sealed with a screw-top lid.

For the preparation of solutions of known concentrations used to produce a calibration plot, dilution of the 400 mg/L stock solution was once again carried out using a 10 mL (± 0.01 mL) pipette, this time to a volume of 50 mL, and the resulting solutions were kept in 50 mL Pyrex storage bottles.

8.1.2 Adsorption Analysis Sample Preparation

In order to analyse the adsorption behaviour of RF gel materials, pieces of gel of approximately equal size were immersed into 3,4-DCA solutions of varying concentrations, with the final solution concentration being measured following a specified period of contact time. To begin, samples of RF hydrogel – the material formed as a result of the gelation process described in Chapter 5 without undergoing any drying – were cut into small, uniform pieces, 0.5g of which were weighed out and added to each jar of 3,4-DCA solution. The jars were sealed and placed onto a Memmert shaker unit for the required period of time, depending on the type of analysis being carried out.

8.1.3 Analysis of Concentration using UV-Vis

Before carrying out UV-Vis analysis on the samples used for adsorption, a calibration plot was created using 3,4-DCA solutions of known concentration. Each sample was analysed using a Cary 5000 UV-Vis Spectrophotometer (Figure 8.1), filling a quartz cuvette with approximately 4.5 mL of solution and placing it into the equipment. The subsequent analysis between wavelengths of 200 – 800 nm provided an absorption spectrum identifying absorption peaks at wavelengths of 254 nm and 296 nm, in agreement with peaks observed in other works.[240,241] Given that the 254 nm peaks were outwith equipment range at higher concentrations, the 296 nm peak was selected and its corresponding absorbance was plotted for each concentration analysed. The relationship between concentration and absorbance at this wavelength was confirmed to be linear, and the resulting equation of the line was used to calculate all sample concentrations. The linearity of this relationship was confirmed at the beginning of each UV-Vis analysis using three concentrations, allowing the precision of the instrument and measurements to be assessed.

Figure 8.1: Cary 5000 UV-Vis Spectrophotometer.[242]

In the cases where the adsorption kinetics of 3,4-DCA onto the RF gel sample were being assessed, the UV-Vis analysis process was carried out at various time intervals for the same sample jar, subject to lab opening hours and restrictions, each being analysed for up to approximately 336 h (2 weeks). For the collection of isotherm data, carrying out adsorption analysis for varying initial concentrations of 3,4-DCA solution (ranging between 25 to 400 mg/L), one final concentration measurement was taken for each solution after 2 weeks equilibration time.

When each sample was analysed, the jars were firstly removed from the shaker unit and approximately 4.5 mL of each solution was removed using a pipette. This was transferred to a quartz cuvette and placed into the UV-Vis Spectrophotometer as before, with the absorption spectrum once again being obtained from analysis between 200 – 800 nm. The resulting absorbance at 296 nm was then compared to the calibration plot, the straight-line equation from which was used to calculate the concentration of the sample solution. After the sample was analysed, it was placed back into the sample jar, with any volume losses assumed to be negligible, maintaining approximately 80 mL of solution in each jar throughout the analysis.

8.1.4 Isotherm Analysis

After visual inspection of the isotherm plots, three appropriate adsorption models were used for analysis of the data collected: Langmuir, Freundlich, and Harkins-Jura. Each of these involve a straight-line plot of equilibrium concentration against equilibrium mass uptake according to their individual equations, which are detailed below. From these plots, the accuracy of the model for the isotherm data obtained can be ascertained from the R^2 value calculated for the resulting straight-line trend, and the related parameters and constants can then be determined.

Langmuir Analysis

As discussed in Chapter 1, the Langmuir model is one of the most common adsorption models applied for the interpretation of data obtained from a range of adsorption systems, although its assumptions are simplistic. The plateau observed in mass uptake for Langmuir isotherms, as depicted in Figure 8.2(a), marks the point at which monolayer formation takes place, with no further adsorption accounted for, and no adsorbate-adsorbate interactions assumed to take place at the surface. The following equation presents the Langmuir model for equilibrium concentration isotherms:

$$\frac{C_e}{q_e} = \frac{1}{q_{max} K_L} + \frac{C_e}{q_{max}}$$

Equation 8.1

Where q_e is the mass adsorbed at equilibrium, C_e is the solution equilibrium concentration, q_{max} is the maximum mass adsorbed for the system, and K_L is the Langmuir constant associated with adsorption affinity. Using the isotherm data obtained, a straight-line plot of C_e/q_e vs C_e can then be used to determine the accuracy of the model, in addition to values of q_{max} and K_L.

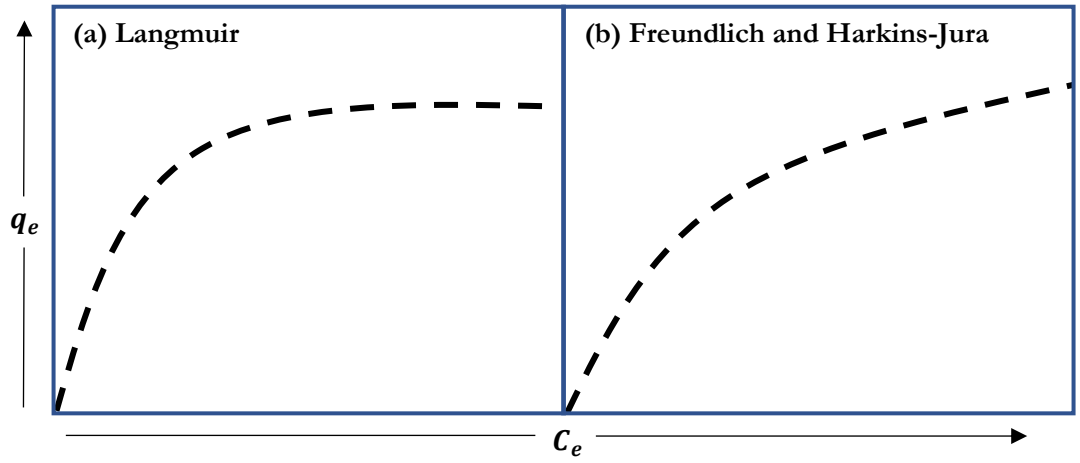

Figure 8.2: Depictions of typical adsorption isotherms for (a) the Langmuir model and (b) the Freundlich and Harkins-Jura models.

Freundlich Analysis

The Freundlich model, as depicted in Figure 8.2(b), accounts for more complex adsorption behaviour than that of Langmuir. This includes the formation of multilayers, the heterogeneity of surface energy, and the potential for adsorbate-adsorbate interactions. The Freundlich model is described by the following equation:

$$\log q_e = \log K_F + \frac{1}{n} \log C_e$$

Equation 8.2

Where K_F is the Freundlich constant, associated with adsorption capacity, and $1/n$ relating to adsorption driving force. Using the isotherm data obtained, a straight-line plot of $\log q_e$ vs $\log C_e$ can then be used to determine the accuracy of the model, in addition to values of n and K_F, with n values above 2 indicating favourable adsorption, values between 1-2 suggesting moderate adsorption capabilities, and values below 1 suggesting poor adsorption capabilities.[243,244]

Harkins-Jura Analysis

The final model applied was Harkins-Jura, also depicted in Figure 8.2(b), the isotherm profile for which is similar in appearance to that of the Freundlich model, and whose principles account for multilayer formation and heterogenous pore distributions. The Harkins-Jura model is described by the following equation:

$$\frac{1}{q_e^2} = \left(\frac{B}{A}\right) - \left(\frac{1}{A}\right) \log C_e$$

Equation 8.3

Where A and B are the Harkins-Jura constants, the values of which are dependent on the accessible surface area of the adsorbent, with higher values of A and B corresponding to larger surface areas.[245,246] In a similar manner as before, using the isotherm data obtained, a straight-line plot of $^1/_{q_e^2}$ vs $\log C_e$ can then be used to determine the accuracy of the model, in addition to values of A and B.

8.2 Results & Discussion

8.2.1 3,4-DCA UV-Vis Calibration Plot

Figure 8.3 displays the UV-Vis spectra for 3,4-DCA solutions at three different concentrations – 10, 50 and 150 mg/L. The peak at 296 nm was selected for use in the calibration plot as well as for the subsequent analysis of all 3,4-DCA samples throughout this work.

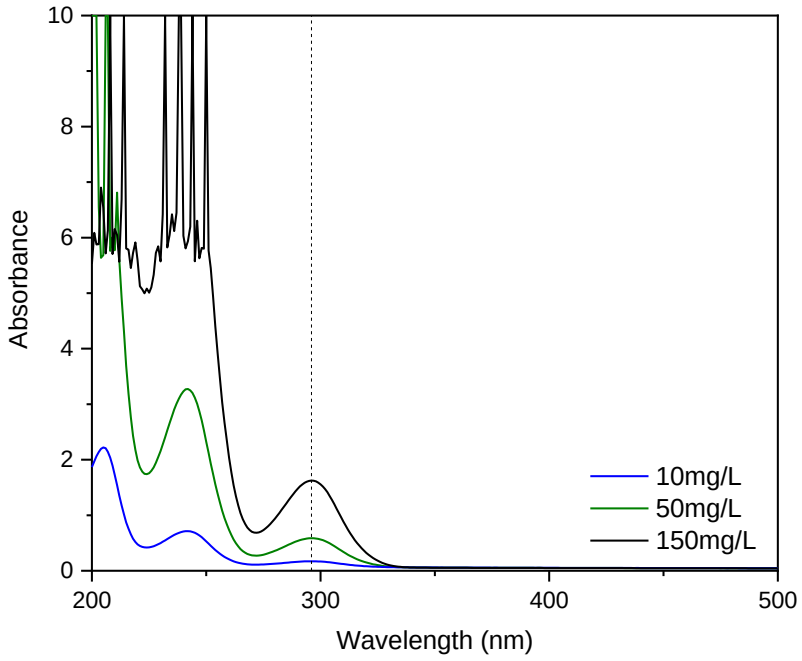

Figure 8.3: 3,4-DCA UV-Vis spectra at varying solution concentrations, with the dashed line marking the point at which the 296 nm peak is observed.

The absorption peak value at 296 nm was plotted for solution concentrations of 5 mg/L to 400 mg/L, resulting in the straight-line graph shown in Figure 8.4, with the straight-line fitting achieving an R^2 value of 0.9998. The high R^2 value achieved, in addition to the reproducibility of the results – with stock solution measurements taken at the beginning of each UV-Vis analysis session to ensure consistency – confirmed the reliability of this method as an effective means to determine accurate 3,4-DCA solution concentrations.

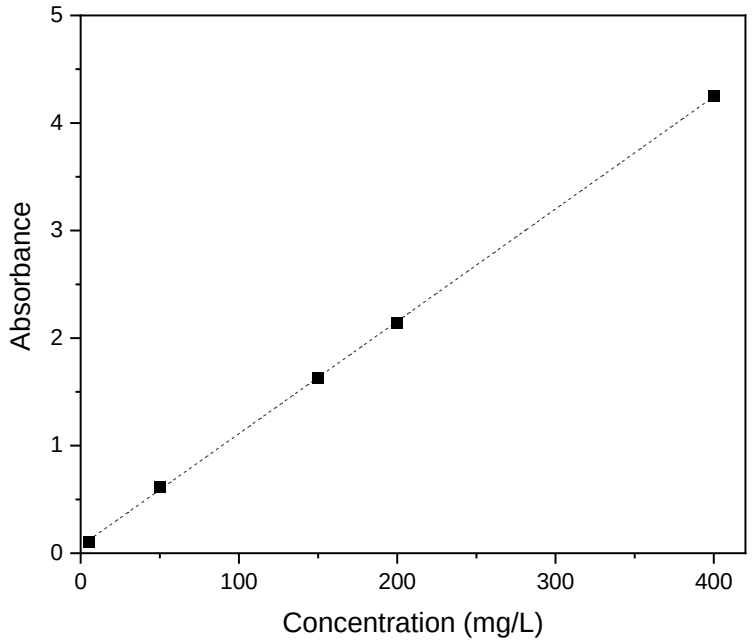

Figure 8.4: Calibration plot for 3,4-DCA solutions, determined using UV-Vis absorbance at 296 nm.

8.2.2 3,4-DCA Adsorption Kinetics

The adsorption kinetics for the removal of 3,4-DCA from a 150 mg/L solution using two RF hydrogel materials were investigated – using one gel synthesised with a high Na_2CO_3 catalyst concentration (R/C 100) and one with a slightly lower Na_2CO_3 catalyst concentration (R/C 300). The textural properties of these materials, taken from data presented in Chapter 5, are compared in Table 8.1, where the increase in catalyst concentration (lower R/C ratio) corresponds to a narrower average pore size in addition to an increased BET surface area – both of which are anticipated to be instrumental in the performance of the materials in this application. Note that this data is for xerogels, which are subject to some structural collapse during the drying process, and whose properties will therefore differ slightly to those of the wet hydrogels used for 3,4-DCA adsorption. Access to supercritical drying equipment to produce comparative aerogels with minimal shrinkage was not possible, however, the trends observed are assumed to be scalable, and therefore still provide a useful metric for comparative gel properties.

Table 8.1: Average pore width (d_{avg}) and BET surface area (S_{BET}) values for RF gels synthesised at R/C 100 and R/C 300.

	R/C 100	**R/C 300**
$\boldsymbol{d_{avg}}$ **(nm)**	4	11
$\boldsymbol{S_{BET}}$ **(m²/g)**	574 ± 2	446 ± 2

To demonstrate the way in which the computational model developed through this work could be used in a similar way to predict and understand the adsorption performance of RF gels, the textural properties of two comparable gels are shown in Table 8.2 – one simulated with a high catalyst concentration (4% C_c) and one with a lower catalyst concentration (1% C_c). Once again, the increased catalyst concentration corresponds to a narrower average pore size alongside an increased accessible surface area, both of which were obtained from the analysis carried out in Chapters 6 and 7.

Table 8.2: Average pore width and accessible surface area data for RF gels simulated at 4% C_c and 1% C_c, both at 30% S_c.

	4% C_c	**1% C_c**
Average Pore Width (sites)	6	9
Accessible Surface Area (sites/unit mass)	1.044(5)	0.765(8)

The kinetics for adsorption of 3,4-DCA onto R/C 100 and R/C 300 hydrogel materials are shown graphically in Figure 8.5, with the analysis carried out with an initial 3,4-DCA solution concentration of 150 mg/L. As can be observed from the plot, the final 3,4-DCA uptake after approximately two weeks was highest for R/C 100, reaching a value of 20.03 mg/g in comparison to the 17.55 mg/g observed for R/C 300. The same trend was observed for the kinetics of the adsorption process with an initial 3,4-DCA concentration of 200 mg/L, as shown in Figure 8.6. Here, the final uptakes after approximately two weeks were 23.96 mg/g and 20.35 mg/g for R/C 100 and R/C 300, respectively.

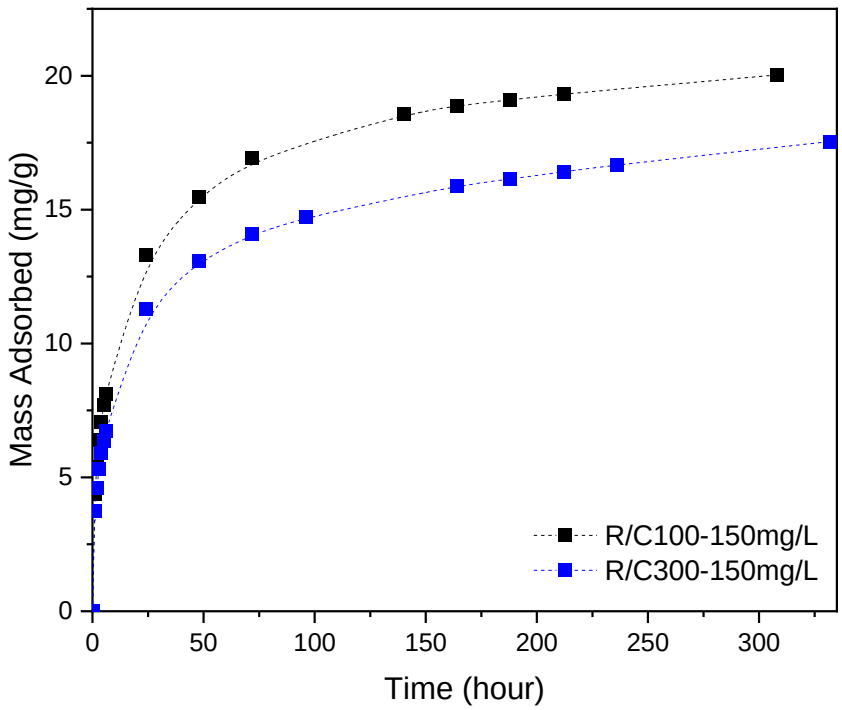

Figure 8.5: Adsorption kinetics for the removal of 3,4-DCA from 150 mg/L solutions using R/C 100 and R/C 300 RF hydrogels.

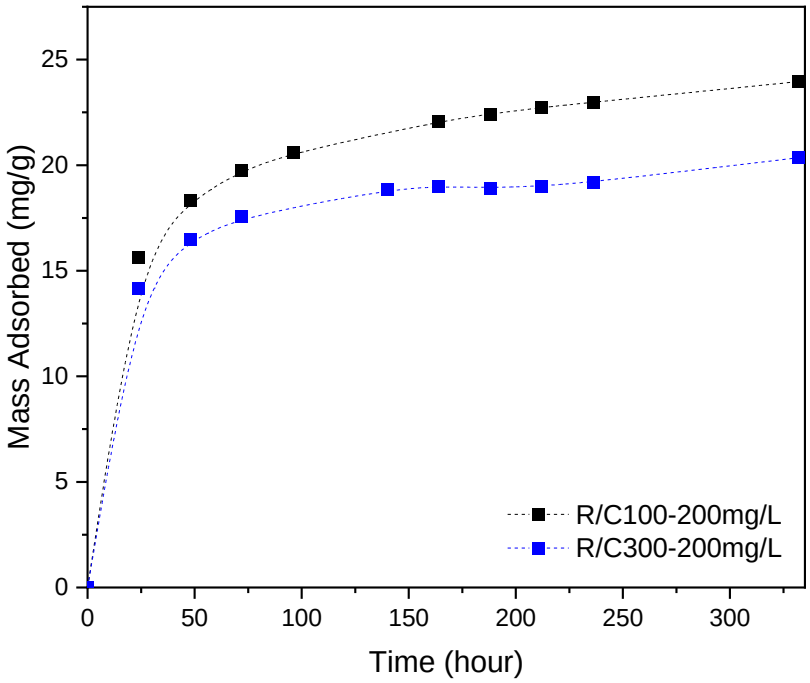

Figure 8.6: Adsorption kinetics for the removal of 3,4-DCA from 200 mg/L solutions using R/C 100 and R/C 300 RF hydrogels.

The two-week period (approximately 336 h) required for the system to reach equilibrium is extensive, which could be associated with the high degree of complexity within the porous structure and subsequent tortuosity of the diffusion pathway, potentially presenting problems for use in this application. Previous studies investigating the use of RF gels as pollutant adsorbents have reported equilibration times ranging between 8 to 120 h[129-131], demonstrating the significant variation in adsorption kinetics depending on the specific system. Furthermore, these studies have all focused on the use of carbonised RF gels in contrast to the RF hydrogels used in this work, which could contribute to the additional equilibration time required here. Still, despite the extensive equilibration time required for 3,4-DCA adsorption onto RF gels, the adsorption capacity of these materials is large, as will be explored further, and they could be useful as adsorbents even without equilibrium being reached for the system.

As previously discussed, the relatively small size (35 $Å^2$)[247] of the 3,4-DCA molecules suggest that a porous network with wide channels would not be necessary to facilitate adsorption. Without the limitations of larger molecular size, therefore, a material whose accessible surface area is maximised would be expected to perform most effectively for the removal of 3,4-DCA. This is exemplified in this performance comparison for the R/C 100 and R/C 300 gels, where the increased adsorption efficiency demonstrated by R/C 100 gels can be attributed to its larger accessible surface area (shown previously in Table 8.1), with the narrower porous network still sufficiently large to facilitate the diffusion of 3,4-DCA molecules. To demonstrate this further, the ratio of R/C 100 and R/C 300 surface areas can be

compared to the ratios of final 3,4-DCA uptakes for R/C 100 and R/C 300 for both 150 mg/L and 200 mg/L solutions. The R/C 100: R/C 300 surface area ratio was calculated to be approximately 1.3, while those of the R/C 100: R/C 300 3,4-DCA uptakes were approximately 1.2 for both initial solution concentrations. Although a direct correlation between R/C ratio and simulated C_c has not yet been established, the computational analysis of simulated materials can be used in a similar manner to understand the performance of the RF gels. Once again, the larger accessible surface area determined for simulated materials at 4% C_c (shown previously in Table 8.2) would enhance its adsorption capacity, while its average pore width value indicates porous channels wide enough to accommodate the diffusion of small molecules such as 3,4-DCA.

Furthermore, the adsorption trends of the four plots shown across Figures 8.5 and 8.6 are visibly alike, each achieving between 80-86% of the total uptake within the first 72 hours before eventually approaching a plateau as the system progresses towards equilibrium. Given the approximate plateaus reached, the two-week adsorption period was determined to be sufficient for subsequent isotherm analysis for the adsorption of 3,4-DCA onto RF gels. Furthermore, given that R/C 100 gels performed best in this application, owed to their high surface areas and accessible porous structure, these gels were selected to be the focus of the subsequent analysis.

8.2.3 3,4-DCA Adsorption Isotherms – Type I

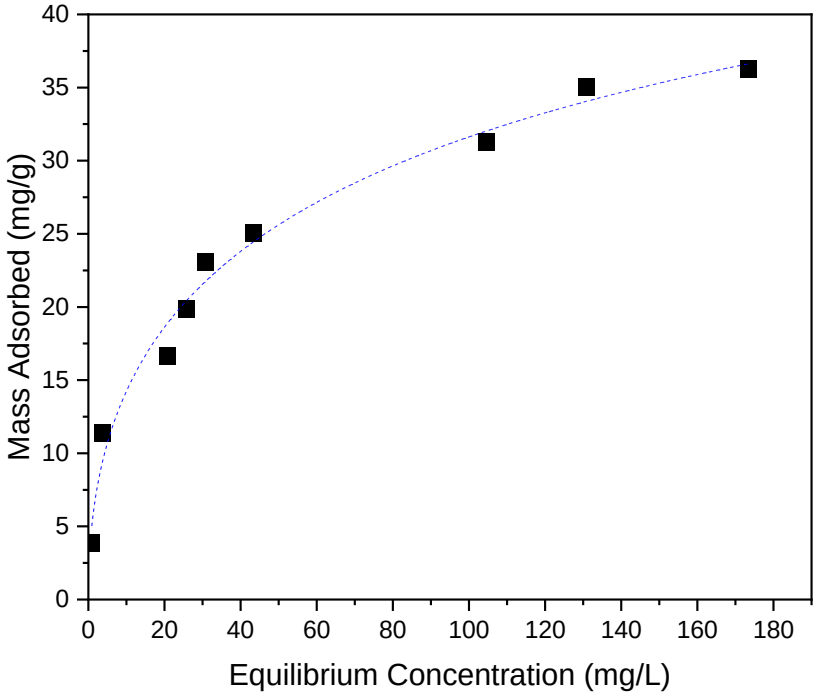

Figure 8.7: Adsorption isotherm for the removal of 3,4-DCA from solutions with initial concentrations of 10-150mg/L using R/C 100 RF hydrogels.

In order to further analyse the adsorption capabilities of RF gels for the removal of 3,4-DCA, particularly in comparison to other materials whose efficacies have also been studied, the

mass adsorbed onto R/C 100 gels – those which were found to perform best in Section 8.2.2 – for solutions of varying 3,4-DCA concentrations (ranging between 25 to 400 mg/L) was investigated. The resulting plot is shown in Figure 8.7, taken as a Type I isotherm and assessed using three adsorption models: Langmuir, Freundlich, and Harkins-Jura.

Table 8.3: Calculated adsorption values using the Langmuir isotherm model.

	R/C 100
K_L **(L/g)**	0.044
q_{max} **(mg/g)**	40.3
R^2	0.988

The Langmuir model, as previously discussed, is based on the assumption that monolayer formation alone takes place. The straight-line plot of $1/q_e$ vs $1/C_e$ is used to calculate K_L and q_{max} – the Langmuir constant and maximum mass adsorbed onto the surface as a monolayer, respectively. The accuracy of this model in relation to the isotherm data presented in Figure 8.7 was strong, returning an R^2 value of 0.988, with values of K_L and q_{max} determined to be 0.044 L/g and 40.3 mg/g, respectively, as shown in Table 8.3.

To assess how RF gels compare to other materials in their 3,4-DCA adsorption capabilities, the q_{max} value obtained can be compared to that of other materials studied in the literature. The performance of clay materials in the removal of 3,4-DCA has been investigated, specifically halloysite [248], kaolinite, and montmorillonite [249], obtaining q_{max} values of 0.078, 0.311, and 0.077 mg/g, respectively. The q_{max} value for activated carbon materials, on the other hand, were substantially larger, with a value of 583 mg/g reported for one, attributed to its exceptionally large surface area of 1028 m^2/g.[247] RF gels, therefore, prove themselves as more effective adsorbents for 3,4-DCA adsorption than clay materials, but less effective than activated carbon materials.

Analysing the data further for RF gel adsorption of 3,4-DCA, the corresponding area per adsorbed molecule within the monolayer can be calculated based on the surface area available within the R/C 100 gel. This was determined to be approximately 380 $Å^2$ per molecule, which is significantly larger than the molecular area of 3,4-DCA at just 35 $Å^2$ [247], suggesting that only a small proportion of the surface area available in the material is being utilised for adsorption. This is in contrast to the area per adsorbed 3,4-DCA molecule for the activated carbon material previously discussed, which was calculated to be ~47 $Å^2$, suggesting that, in this case, the adsorbed 3,4-DCA molecules were able to utilise the surface area available to achieve relatively close-packed monolayer formation. Comparing the two adsorbed molecule areas (380 $Å^2$ and 47 $Å^2$, for RF R/C 100 gel and activated carbon, respectively), therefore, demonstrates the significantly higher number of 3,4-DCA molecules per unit area that are able to adsorb onto the activated carbon surface than onto the R/C 100 RF gel surface. This disparity in adsorbed molecule area could be explained by the increased affinity the 3,4-DCA molecules may have for the activated carbon surface, particularly as a result of benzene ring-benzene ring interactions between the adsorbent and adsorbate. The RF gel surface will possess fewer

sites with comparable benzene ring-benzene ring interactions and, therefore, fewer specific locations for 3,4-DCA molecules to adsorb. This could also explain the lengthy equilibration times required for the 3,4-DCA adsorption onto RF gels, shown in Section 8.2.2, where 3,4-DCA molecules may diffuse around the complex porous structure for extended periods of time until adsorption sites are found.

Table 8.4: Calculated adsorption values using the Freundlich isotherm model.

	R/C 100
$\boldsymbol{K_F}$ **(L/g)**	7.26
$\boldsymbol{n}$	3.2
$\mathbf{R^2}$	0.976

To explore the accuracy of other models, the Freundlich model was selected for data analysis, which involves the calculation of K_F and n using a straight-line plot of $\log q_e$ vs $\log C_e$. This model provided a slight reduction in accuracy, with the R^2 value from the straight-line plot decreasing to 0.976, as shown in Table 8.4. Furthermore, a value of 3.2 determined for the Freundlich parameter n, through this analysis, is indicative of good adsorption affinity between the adsorbent and the adsorbate, where n values above 2 indicate favourable adsorption, values between 1-2 suggest moderate adsorption capabilities, and values below 1 suggest poor adsorption capabilities.[243,244] For comparison, Freundlich analysis was also carried out for the adsorption of 3,4-DCA in the halloysite study previously discussed, determining the value of n to be 1.99.

Table 8.5: Calculated adsorption values using the Harkins-Jura isotherm model.

	R/C 100
$\boldsymbol{A}$	250
$\boldsymbol{B}$	2.3
$\mathbf{R^2}$	0.883

As a final comparative model, the Harkins-Jura model, was applied to the isotherm data, involving the calculation of two Harkin-Jura constants - A and B - from a straight line plot of $1/{q_e}^2$ vs $1/C_e$. The accuracy of this model was slightly lower once again, returning an R^2 value of 0.883, and Harkin-Jura constants A and B values of 250 and 2.3, respectively, as shown in Table 8.5. This model accounts for a heterogenous pore distribution, which is less relevant for low R/C ratio gels, such as the R/C 100 material studied here, possessing a narrow distribution of pore widths, perhaps explaining the reduced accuracy of the model.

Overall, each of the three models applied produce results with some degree of accuracy, and provide valuable comparisons to other materials whose performance in removing 3,4-DCA have been studied. The Langmuir model emerged as the most accurate across the three models, achieving an R^2 value of 0.988. This could suggest that the adsorption of 3,4-DCA onto

R/C 100 gels takes place through monolayer coverage alone, with the plateau approach within the isotherm at higher equilibrium concentrations pointing towards the gradual formation of the monolayer.

8.2.4 3,4-DCA Adsorption Isotherm – Type VI

Analysis in Section 8.2.3 approached the isotherm data as a Type I isotherm, however, this section explores the isotherm data as a Type VI isotherm, where stepwise adsorption is proposed to take place. Note that this is purely exploratory given the trends noticed in the isotherm data, and the observations could simply be as a result of experimental uncertainty, such as errors associated with 3,4-DCA solution synthesis and dilution, in addition to the singularity of the measurements taken. Under the Type VI adsorption mechanism, multilayer formation takes place through the addition of full individual layers, as shown in Figure 8.8, with the molecule spacing dependent on adsorbate-adsorbate interactions in addition to adsorbate-adsorbent interactions. The isotherm data is also shown once again in Figure 8.9, this time with trendlines showing a proposed three step adsorption mechanism.

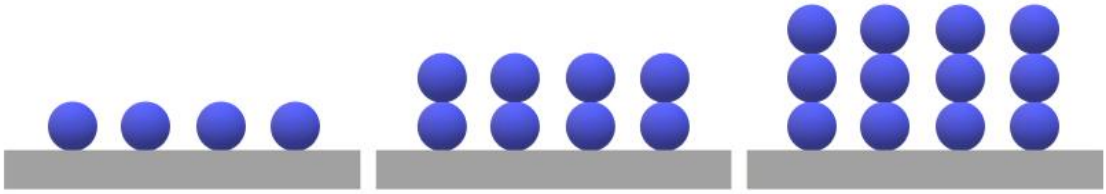

Figure 8.8: Illustration of stepwise adsorption, with the gradual formation of three individual layers taking place from left to right.

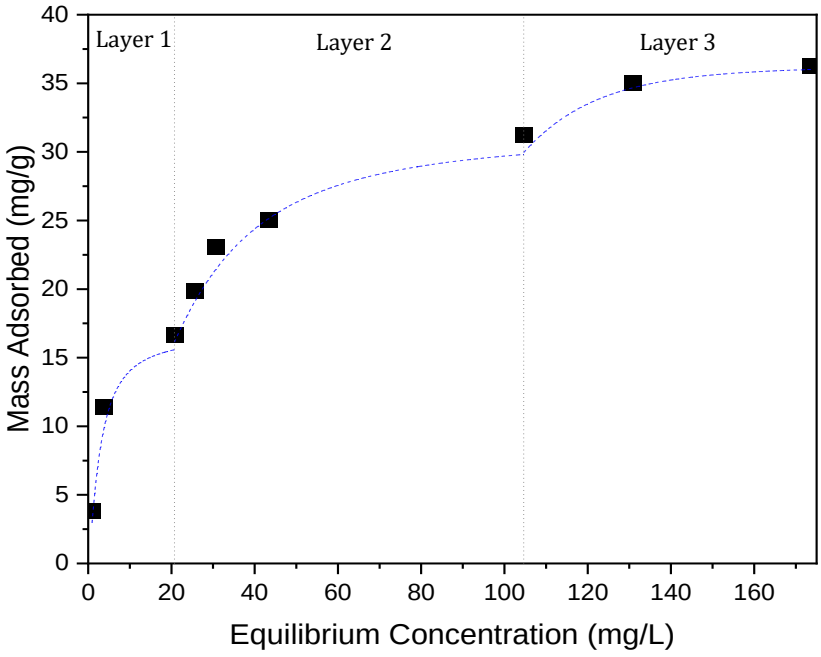

Figure 8.9: Adsorption isotherm for the removal of 3,4-DCA using R/C 100 RF gels, with trendlines showing the proposed stepwise adsorption process.

The data points within each of the three steps were used to assess the mass of the layers formed, with the Langmuir model used for each step and its accuracy once again investigated, the resulting data shown in Table 8.6. The R^2 values obtained indicate good accuracy of the Langmuir model for the individual layers, returning values of 0.998, 0.995, and 0.984 for Layers 1, 2, and 3, respectively. The q_{max} value for Layer 1, corresponding to the mass of the monolayer formed on the surface of the gel, is calculated as 19.3 mg/g. Following the addition of Layer 2, the calculated q_{max} value corresponds to an individual layer mass, once again, of 19.3 mg/g, indicating that the porous network within R/C 100 gels is capable of adsorbing two full layers of 3,4-DCA onto the available surface. The q_{max} value calculated following the addition of Layer 3, on the other hand, corresponds to an individual layer mass of approximately 8.3 mg/g. The inability for a full third layer to form could, in this case, be attributed to a lack of available volume within the pores, where most pores possess a volume large enough to accommodate two full layers only, and subsequent multilayer adsorption takes place only in pores that are larger in size.

Table 8.6: Langmuir analysis of individual layers corresponding to Figure 8.8.

	Layer 1	**Layer 2**	**Layer 3**
$\boldsymbol{K_L}$ (L/g)	0.311	0.042	0.020
$\boldsymbol{q_{max}}$ [layer] (mg/g)	19.3	19.3	8.3
R^2	0.998	0.995	0.984

Finally, based on the surface area available within the R/C 100 RF gel, the corresponding area per 3,4-DCA molecule within Layer 1 is approximately 799 $Å^2$, more than double that previously calculated for the Type I isotherm approach. If stepwise adsorption is taking place, therefore, the number of specific adsorption sites within RF gels for 3,4-DCA molecules may be even lower than previously expected. Once these sites have been utilised, adsorption may continue only through the addition of 3,4-DCA molecules onto ones that have already been adsorbed at the RF gel surface, forming two full layers throughout the material, and a third layer in sufficiently large pores.

Although analysing the isotherm data as a Type I isotherm provided a useful comparison to other materials whose total adsorption capacities had also been assessed using similar models, approaching the isotherm data as a Type VI isotherm provides an alternative analysis of the adsorption process taking place. Regardless of the isotherm analysis approach, the total adsorption capacity for 3,4-DCA within R/C 100 gels remains high in comparison to the clay materials discussed, but lower than that of activated carbon materials. If stepwise adsorption is taking place here, however, then only a very small fraction of available surface area within the RF gel is being utilised, with only a select few sites favourable for 3,4-DCA adsorption. This highlights that, despite the high surface areas possessed by these materials, adsorbate-adsorbent interactions can significantly affect their adsorption capacities. This could be especially important in other RF gel adsorption applications where multilayer formation may not be possible, due to poor adsorbate-adsorbate affinity or due to large molecular size, therefore overall adsorption uptake could remain low.

Once again, analysing the data as a Type VI isotherm is purely exploratory, and the trends observed are likely as a result of experimental uncertainty. Repetition of measurements would be required to confirm any observed trends, however, given the computational results presented in previous chapters which assess the porosity of RF gels, the occurrence of Type VI isotherm multilayer formation is unlikely. In particular, the data presented on the limited diffusion possible for particles 3 sites in width suggest that finding the available space required to facilitate the adsorption of multiple layers within these structures would be unlikely.

8.3 Summary

This chapter has explored the efficacy of RF gels in a practical water treatment application, using these materials as adsorbents for the removal of endocrine disrupter 3,4-dichloroaniline (3,4-DCA). The formation of these materials has been investigated experimentally and computationally in the previous chapters, providing valuable data that allows the factors affecting their adsorption behaviour to be both predicted and explained, based on material properties. Two RF gel materials were compared for this application – an R/C 100 gel and an R/C 300 gel – with UV-Vis analysis used to assess the mass of 3,4-DCA adsorbed by the gels over a two-week period. The comparative uptakes for R/C 100 and R/C 300 gels for both 150 mg/L and 200 mg/L 3,4-DCA solutions demonstrate the differing adsorption capabilities of the two materials. The R/C 100 gels achieved the highest total uptake across the two-week period, with the enhanced performance explained using insights from the experimental and computational analysis carried out in previous chapters. The relatively small size and simplicity of the 3,4-DCA molecules mean that the narrower pores within R/C 100 materials are still sufficiently wide to facilitate adsorption, whilst their adsorption capacity is maximised by their increased accessible surface area.

Using both experimental and computational data to predict and understand RF gel adsorption behaviour in the removal of 3,4-DCA from aqueous systems demonstrates the manner in which material tailoring can take place, with the favourable textural properties observed within RF gels with high catalyst concentrations (low R/C ratios) and mid-range solids contents. The advantages of computational tailoring are significant, where properties can be optimised in a more efficient manner in comparison to time-consuming experimental processes. The results discussed here, therefore, show promise for the use of computational models, such as those presented in previous chapters, in the optimisation of RF gel materials for various applications. Of course, a more precise relationship between computational and experimental synthesis parameters is still to be fully established, but the results presented thus far show promise for the model's ongoing development for future use.

Finally, analysis of the isotherm data for 3,4-DCA adsorption onto R/C 100 gels for initial solution concentrations up to 400 mg/L indicated that, of the three models applied, the Langmuir model most accurately described the adsorption process taking place, approaching the isotherm as Type I. A q_{max} value of 40.3 mg/g was calculated for these materials – a value that could subsequently be used to compare their performance in this application to other porous materials. The potential for stepwise adsorption was also explored, approaching the isotherm as Type VI, with the initial monolayer mass determined to be 19.3 mg/g. Using both isotherm analysis approaches, the calculated area per adsorbed molecule was significantly larger than the area of the 3,4-DCA molecule itself, suggesting that only a small percentage of the RF gel available surface area is composed of specific sites for 3,4-DCA adsorption.

Overall, the efficacy of RF gels in the removal of 3,4-DCA from water proved to be superior to that of clay materials, however, less effective in comparison to activated carbon materials possessing exceptionally large surface areas and high adsorbate-adsorbent affinities. The significant effect of adsorbate-adsorbent interactions on the RF gel's adsorption capacities was highlighted through this work, and is an important consideration for any future adsorption applications explored for these materials.

Chapter 9: Conclusions

The work presented within this thesis includes a variety of research approaches, the over-arching aims of which are to provide further insight into formation mechanism of Resorcinol-Formaldehyde (RF) gels, as well as to progress towards the computational tailoring of these materials for use in different valuable applications. As materials possessing attractive and tuneable properties such as low densities and high surface areas, their application potential could be both widespread and lucrative, particularly for uses that offer solutions to the many environmental concerns facing the modern world. In this work, experimental investigations were carried out that explore the way in which RF gels form, and a 3D model was developed to simulate this formation process, with the final simulated materials computationally analysed and compared to those synthesised in the lab. Finally, the performance of two RF gels were tested experimentally in a water treatment application, with the preceding experimental and computational results used to predict the efficacy of each material based on their synthesis parameters and subsequent textural properties.

Within the synthesis of RF gels, a variety of 'catalyst' materials can be used to promote the reaction. In this work, the crucial role of sodium carbonate as a catalyst was confirmed through the experimental analysis of gels synthesised with varying R/C ratios, where low R/C ratios correspond to higher catalyst concentrations, and vice versa. Lower R/C ratios led to the formation of gels with higher surface areas and narrower pores, whereas gels synthesised at higher R/C ratios possessed lower surface areas and wider pores, the former comprising of bottle neck pores and the latter comprising of open pores. Furthermore, the role of the metal cation within the catalyst was also investigated, with experimental analysis aiming to decouple the complex relationship between initial solution pH and the type and concentration of catalyst used. Through the synthesis of gels with mixtures of sodium carbonate and sodium bicarbonate as catalysts, all with equal Na^+ ion concentrations, the significance of the metal cation was confirmed. Despite possessing variations in initial solution pH – the parameter widely considered to be the primary determining factor in final gel properties – these materials synthesised at constant Na^+ concentrations exhibited almost identical properties. In addition to this, gels were synthesised with mixtures of sodium bicarbonate and ammonium bicarbonate as catalysts, each with constant HCO_3^- concentrations and with varying Na^+ concentrations. In these gels, results varied significantly, with poorer structural properties observed for materials of lower Na^+ concentrations, eventually reaching concentrations so low that gelation of a porous structure did not take place. Although these results prove the important role the metal cation plays in the formation of RF gels, the exact mechanism by which this takes place is still to be elucidated, with previous suggestions including the formation of an intermediate chelated molecule involving resorcinol, formaldehyde, and the metal cation, as well as the potential for 'salting in' or 'salting out' of macromolecules by different ions in solution, similar to the effects established by the Hofmeister series.

The performance of different solvents used during the solvent exchange step of gel synthesis was also investigated, the role of which is to prevent shrinkage and preserve the structural integrity of the gel during drying. The efficacy of three polar solvents were compared: acetone, methanol, and ethanol, with their ability to reduce pore shrinkage measured against gels

produced with no solvent exchange whatsoever, their pores filled only with water. Firstly, it was observed that pore shrinkage was especially apparent in RF gels synthesised at lower R/C ratios where the most significant differences in total pore volume were achieved for the solvents studied. Furthermore, of the solvents investigated, ethanol performed best, producing gels with the highest total pore volume, followed by methanol, and finally acetone. Their performance correlated with their surface tension values, with ethanol possessing the lowest surface tension of the solvents, and all three possessing a value significantly lower than that of water. Despite the variations in total pore volumes for the gels synthesised with different solvents, the average pore width of each gel remained approximately equal. Visual analysis of the isotherms produced from nitrogen adsorption experiments for each gel provided insight into this, showing that although the shape and x-axis position of the hysteresis loop remained constant across each, the initial adsorption uptake into the micropores of the materials varied significantly, shifting the resulting y-axis position of each hysteresis loop. Given that BJH pore size analysis applies only to mesopores and macropores, the change in microporosity would, therefore, have no impact on the average pore width calculated. This reveals that the shrinkage and structural collapse upon drying is taking place largely within micropores, which also explains why the narrower pores within lower R/C ratio gels are more susceptible to collapse than the wider pores possessed by those synthesised at higher R/C ratios. This could have important implications for applications where increased microporosity is desirable, allowing the solvent exchange step to be optimised to preserve the material structure as far as possible.

A 3D lattice-based kinetic Monte Carlo model simulating the formation, growth, and subsequent aggregation of the approximately spherical clusters that comprise the RF gel structure was also developed through this work, its algorithm being based upon the basic formation mechanism established for RF gels in previous works. Different solids contents (S_c) were represented by varying percentages of monomers occupying lattice sites, while different catalyst concentrations (C_c) were represented by varying percentages of activated monomers acting as cluster seeds, allowing the resulting structures from each to be compared to RF gels synthesised in the lab. Materials synthesised at higher S_c were found to possess both reduced accessible porosity and reduced surface area, comprising of a greater number of clusters than those of lower S_c values, the totality of which led to a densely packed structure with inaccessible pores. Materials synthesised at varying C_c, on the other hand, were found to possess a greater number of clusters that were smaller in size, leading to the formation of a complex inter-connected structure. This prove to be beneficial for the accessible surface area available to a particle 1 site in size, however, an upper limit was observed for that of a particle 3 sites in size, where for structures generated at S_c values above ~45%, increasing C_c values showed the opposite trend. The increased interconnectivity associated with increasing C_c at this point gave rise to higher levels of closed-off porosity, consequently reducing the surface area accessible to a particle of 3 sites in size.

Calculating the correlation dimension for simulated structures allowed their fractal properties to be assessed, the potential for which within RF gels has been subject to debate in the literature. The results obtained in this work indicated that fractal properties could be achieved for structures simulated at sufficiently low S_c and C_c percentages, explaining the conflicting conclusions drawn from previous studies wherein researchers have predominantly synthesised gels with solids contents of 20% or more. As the S_c percentage was increased for

the simulated structures, the correlation dimension quickly reached a plateau around a value of 3, indicating that the structures exhibited no fractal properties under those synthesis conditions. The Hurst exponent for particles of both 1 and 3 sites in size diffusing through the porous network of the simulated structure was also determined, showing antipersistent motion in each of the results obtained. The degree of antipersistence was exacerbated by increasing S_c and C_c, as well as by increasing the diffusing particle size from 1 site to 3 sites, demonstrated not only by the Hurst exponent value, but also by the resulting visual particle trace as it moved through the porous network.

Computational adsorption analysis was also carried out for the simulated materials, producing isotherms that could be directly compared to those obtained for RF gels experimentally, in addition to producing density profiles allowing the adsorption process itself to be visualised. The resulting isotherm data was also used to carry out BJH pore size analysis, the combined data from which allowed trends to be determined for the average pore geometries and pore widths observed within materials synthesised at varying S_c and C_c percentages. Structures produced at both lower S_c and C_c values were composed of open pores which were larger in width, while those simulated with higher S_c and C_c values were composed of bottle neck pores which were narrower in width. Importantly, the isotherms produced from the analysis of simulated structures at different C_c values show significant similarities to those produced from the experimental analysis of RF gels at varying R/C ratios, with similar trends observed in both the shape and positioning of their hysteresis loop as the catalyst concentration was varied. Similarities were observed once again across the different pore size distributions for both simulated and laboratory synthesised materials, with these comparative results providing validation for the cluster aggregation model, in addition to demonstrating the potential for models such as this one to accurately predict, control, and analyse structural properties of porous materials.

Finally, the performance of two RF gels synthesised at different R/C ratios were assessed in their ability to remove 3,4-dichloroaniline (3,4-DCA), a known endocrine disrupting pollutant, from solutions of varying concentrations. As predicted both by the experimental and computational results obtained through this work, the properties exhibited by materials synthesised at higher catalyst concentrations (lower R/C ratios) proved beneficial for an application such as this one. The increased interconnectivity observed within materials synthesised at higher catalyst concentrations at this solids percentage corresponded to an increase in total accessible surface area, therefore possessing a greater adsorption capacity, as well as corresponding to a decrease in average pore width. For a relatively small molecule such as 3,4-DCA, this reduced pore width was still sufficiently large to enable diffusion through the porous network, allowing molecules to access the available surface area for adsorption. The adsorption capacity of 3,4-DCA within the R/C 100 RF gel was large, however, not to the extent of other materials such as activated carbons, the results suggesting that fewer favourable adsorption sites could be found for 3,4-DCA molecules on the RF gel surface. Furthermore, the time required for the system to reach equilibrium was substantial for the solution concentrations studied, which may make RF gels impractical for this application. Overall, this analysis demonstrated the way in which the properties of these materials, as determined by experimental or computational means, can be used to predict and explain their application performance. The advantages of using a computational model, such as the one presented in preceding chapters, for the optimisation of these materials are significant, as

discussed previously. The results present here, therefore, show promise for the model's ongoing development for future use in material tailoring.

To conclude, this work has explored the formation mechanism of RF gels, focusing on the tailorability of these materials for use in various applications, progressing towards computational means of optimisation. Given their attractive and tuneable properties, their application potential is significant, including for uses such as water treatment, insulation, gas adsorption, and catalysis support. Understanding the way in which various synthesis parameters affect final material characteristics is imperative, allowing the full range of possible properties to be accessed where desired. The development of a 3D model, such as the one presented here, that can simulate the formation and analysis of RF gels in a time-efficient manner is pivotal to their widespread use, as well as demonstrating how this could be achieved for other porous materials whose textural properties are similarly tuneable.

Chapter 10: Future Work

The findings from this work open numerous pathways for future research and development, both experimental and computational in nature. Although all of these could not be explored within this project, they could be valuable research routes to pursue in order to continue the progress made.

Understanding the specific roles of individual catalyst components in the RF gel reaction was an important aspect of this work, and merits further investigation. The first of the theories suggested in the literature for the way in which the metal cation contributes to gel formation involves its participation in forming an intermediate chelated molecule during the RF addition reaction. Investigating this theory using molecular dynamics software could be of significant value, modelling the interaction between the resorcinol and formaldehyde molecules in solution in the presence of the relevant cations and anions. The addition reaction process could also be modelled using software, such as ReaxFF[250], to help establish any potential mechanism through which the individual ions within the catalyst participate in the RF reaction. The second of the proposed theories around the role of catalyst components included the 'salting in' and 'salting out' of macromolecules in solution by different ions, similar to the effects established by the Hofmeister series. Experimental analysis of gels synthesised using catalysts with a wide variety of both cations and anions within the Hofmeister series would, therefore, provide the data required to observe any trends present in the structural properties of the resulting gels.

In this work, the development of a 3D model that simulates the formation of RF gels was an important progression from the initial 2D version, now producing materials that more accurately reflect those synthesised in the lab, and allowing the computational analysis results to be compared to those obtained experimentally. Despite this, establishing a correlation between the activated monomer percentage in the model and the R/C ratio used in laboratory synthesis is complex, primarily because of the structural collapse that takes place during vacuum drying of the experimental gels. Two routes could be explored to remedy this, one experimental and one computational, both of which could provide valuable results. Experimentally, RF aerogels could be synthesised, where the hydrogels are dried supercritically, therefore preserving their original structure and producing materials that can be directly compared to those of the model. Alternatively, or perhaps alongside this, the process of pore shrinkage during vacuum drying could be modelled computationally for materials already simulated, the resulting gels comparable to the xerogels synthesised in the lab. As an additional comparison between simulated materials and laboratory synthesised materials, experimental SEM and TEM analysis of gels under various synthesis conditions could also be carried out, allowing the visual differences of each to be compared as well as the approximate average cluster size. Preliminary SEM and TEM results in this work (shown in Appendix B) were obtained for two RF xerogel samples during a short collaboration with Svenska Aerogel AB in Sweden, however, due to time constraints and equipment availability, a full analysis could not be carried out.

Future work may also focus on further development of the 3D model itself, including the incorporation of additional complexities into the algorithm, such as the rotational movement of clusters as they diffuse around the lattice and attach to form aggregates. This is, of course, more reflective of the motion of clusters in real systems, and investigating the impact of this on the final material formed could be of interest. Furthermore, the algorithm currently simulates diffusion limited cluster aggregation, where the monomers and clusters always attach when they come into contact. Incorporating an attachment probability into this interaction could produce materials with varying structures, and may reflect the impact of temperature within real systems.

Finally, further exploring the application potential of RF gels in the removal of various emerging pollutants from water could be of interest, using both experimental and computational results to predict the synthesis parameters necessary to produce materials with the desired characteristics. Investigating the material's efficacy with a wide range of pollutants of varying size and surface chemistry would demonstrate their versality, as well as help determine the RF gel uses potentially worth pursuing at an industrial level.

References

1. Ebelmen, M. *Annales de Chimie et de Physique* **1846**, *16*, 129.
2. Pierre, A.C.; Pajonk, G.M. Chemistry of Aerogels and Their Applications. *Chem. Rev.* **2002**, *102*, 4243-4266, doi:10.1021/cr0101306.
3. Brinker, C.J.; Scherer, G.W. CHAPTER 1 - Introduction. In *Sol-Gel Science*, Brinker, C.J., Scherer, G.W., Eds. Academic Press: San Diego, 1990; https://doi.org/10.1016/B978-0-08-057103-4.50006-4pp. xvi-18.
4. Pagliaro, M. *Silica-based materials for advanced chemical applications*; Royal Society of Chemistry: 2009.
5. Kara, D.; Fisher, A. Modified Silica Gels and Their Use for the Preconcentration of Trace Elements. *Separation & Purification Reviews* **2012**, *41*, 267-317, doi:10.1080/15422119.2011.608765.
6. Kistler, S.S. Coherent Expanded-Aerogels. *The Journal of Physical Chemistry* **1932**, *36*, 52-64, doi:10.1021/j150331a003.
7. Teichner, S.J., and Nicolaon, G.A. Method of Preparing Inorganic Aerogels. Patent Number: US3672833A, 1971.
8. Fricke, J.; Tillotson, T. Aerogels: production, characterization, and applications. *Thin Solid Films* **1997**, *297*, 212-223, doi:https://doi.org/10.1016/S0040-6090(96)09441-2.
9. Schmidt, M.; Schwertfeger, F. Applications for silica aerogel products. *J. Non-Cryst. Solids* **1998**, *225*, 364-368, doi:https://doi.org/10.1016/S0022-3093(98)00054-4.
10. NASA. Aerogels: Thinner, Lighter, Stronger. Availabe online: https://www.nasa.gov/topics/technology/features/aerogels.html (accessed on 20/07/2021).
11. Gurav, J.L.; Jung, I.-K.; Park, H.-H.; Kang, E.S.; Nadargi, D.Y. Silica Aerogel: Synthesis and Applications. *Journal of Nanomaterials* **2010**, *2010*, 409310, doi:10.1155/2010/409310.
12. Venkateswara Rao, A.; Hegde, N.D.; Hirashima, H. Absorption and desorption of organic liquids in elastic superhydrophobic silica aerogels. *J. Colloid Interface Sci.* **2007**, *305*, 124-132, doi:10.1016/j.jcis.2006.09.025.
13. Wang, J.; Petit, D.; Ren, S. Transparent thermal insulation silica aerogels. *Nanoscale Advances* **2020**, *2*, 5504-5515.
14. Pekala, R.W. Organic aerogels from the polycondensation of resorcinol with formaldehyde. *J. Mater. Sci.* **1989**, *24*, 3221-3227, doi:10.1007/BF01139044.
15. Raff, R.A.V.; Silverman, B.H. Kinetics of the Uncatalyzed Reactions between Resorcinol and Formaldehyde. *Industrial & Engineering Chemistry* **1951**, *43*, 1423-1427, doi:10.1021/ie50498a044.
16. Prostredny, M. Prediction and control of organic xerogel microstructure: experiments and modelling. PhD Thesis, University of Strathclyde, 2019.
17. Al-Muhtaseb, S.A.; Ritter, J.A. Preparation and Properties of Resorcinol–Formaldehyde Organic and Carbon Gels. *Adv. Mater.* **2003**, *15*, 101-114, doi:10.1002/adma.200390020.
18. Gaca, K.Z.; Parkinson, J.A.; Sefcik, J. Molecular Speciation and Mesoscale Clustering in Formaldehyde–Methanol–Water Solutions in the Presence of Sodium Carbonate. *The Journal of Physical Chemistry B* **2013**, *117*, 10548-10555, doi:10.1021/jp405731g.
19. Gaca, K.Z.; Parkinson, J.A.; Sefcik, J. Kinetics of early stages of resorcinol-formaldehyde polymerization investigated by solution-phase nuclear magnetic resonance spectroscopy. *Polymer* **2017**, *110*, 62-

73, doi:https://doi.org/10.1016/j.polymer.2016.12.069.
20. Pizzi, A., and Mittal, K.L. *Handbook of Adhesive Technology: Second Edition, Revised and Expanded*; Marcel Dekker, Inc.: 2003.
21. Rojas-Cervantes, M.L. Some strategies to lower the production cost of carbon gels. *J. Mater. Sci.* **2015**, *50*, 1017-1040, doi:10.1007/s10853-014-8617-1.
22. Bouchoux, G.; Defaye, D.; McMahon, T.; Likholyot, A.; Mó, O.; Yáñez, M. Structural and energetic aspects of the protonation of phenol, catechol, resorcinol, and hydroquinone. *Chemistry–A European Journal* **2002**, *8*, 2900-2909.
23. Brandt, R.; Petricevic, R.; Pröbstle, H.; Fricke, J. Acetic Acid Catalyzed Carbon Aerogels. *J. Porous Mater.* **2003**, *10*, 171-178, doi:10.1023/A:1027486401135.
24. Berthon, S.; Barbieri, O.; Ehrburger-Dolle, F.; Geissler, E.; Achard, P.; Bley, F.; Hecht, A.-M.; Livet, F.; Pajonk, G.M.; Pinto, N., et al. DLS and SAXS investigations of organic gels and aerogels. *J. Non-Cryst. Solids* **2001**, *285*, 154-161, doi:https://doi.org/10.1016/S0022-3093(01)00447-1.
25. Job, N.; Panariello, F.; Marien, J.; Crine, M.; Pirard, J.-P.; Léonard, A. Synthesis optimization of organic xerogels produced from convective air-drying of resorcinol–formaldehyde gels. *J. Non-Cryst. Solids* **2006**, *352*, 24-34, doi:https://doi.org/10.1016/j.jnoncrysol.2005.11.024.
26. Durairaj, R.B. *Resorcinol: Chemistry, Technology and Applications*; Springer-Verlag Berlin Heidelberg: 2005; 10.1007/3-540-28090-1.
27. Taylor, S.J.; Haw, M.D.; Sefcik, J.; Fletcher, A.J. Gelation Mechanism of Resorcinol-Formaldehyde Gels Investigated by Dynamic Light Scattering. *Langmuir* **2014**, *30*, 10231-10240, doi:10.1021/la502394u.
28. Wen, Z.B.; Qu, Q.T.; Gao, Q.; Zheng, X.W.; Hu, Z.H.; Wu, Y.P.; Liu, Y.F.; Wang, X.J. An activated carbon with high capacitance from carbonization of a resorcinol–formaldehyde resin. *Electrochem. Commun.* **2009**, *11*, 715-718, doi:https://doi.org/10.1016/j.elecom.2009.01.015.
29. Horikawa, T.; Hayashi, J.i.; Muroyama, K. Controllability of pore characteristics of resorcinol–formaldehyde carbon aerogel. *Carbon* **2004**, *42*, 1625-1633, doi:https://doi.org/10.1016/j.carbon.2004.02.016.
30. Lin, C.; Ritter, J.A. Effect of synthesis pH on the structure of carbon xerogels. *Carbon* **1997**, *35*, 1271-1278, doi:https://doi.org/10.1016/S0008-6223(97)00069-9.
31. Mulik, S.; Sotiriou-Leventis, C.; Leventis, N. Time-Efficient Acid-Catalyzed Synthesis of Resorcinol−Formaldehyde Aerogels. *Chem. Mater.* **2007**, *19*, 6138-6144, doi:10.1021/cm071572m.
32. Job, N.; Pirard, R.; Marien, J.; Pirard, J.-P. Porous carbon xerogels with texture tailored by pH control during sol–gel process. *Carbon* **2004**, *42*, 619-628, doi:https://doi.org/10.1016/j.carbon.2003.12.072.
33. ElKhatat, A.M.; Al-Muhtaseb, S.A. Advances in Tailoring Resorcinol-Formaldehyde Organic and Carbon Gels. *Adv. Mater.* **2011**, *23*, 2887-2903, doi:10.1002/adma.201100283.
34. Sharma, C.S.; Kulkarni, M.M.; Sharma, A.; Madou, M. Synthesis of carbon xerogel particles and fractal-like structures. *Chem. Eng. Sci.* **2009**, *64*, 1536-1543, doi:https://doi.org/10.1016/j.ces.2008.12.013.
35. Calvo, E.G.; Menéndez, J.A.; Arenillas, A. Influence of alkaline compounds on the porosity of resorcinol-

formaldehyde xerogels. *J. Non-Cryst. Solids* **2016**, *452*, 286-290, doi:https://doi.org/10.1016/j.jnoncrysol.2016.09.009.

36. Job, N.; Gommes, C.J.; Pirard, R.; Pirard, J.-P. Effect of the counter-ion of the basification agent on the pore texture of organic and carbon xerogels. *J. Non-Cryst. Solids* **2008**, *354*, 4698-4701, doi:https://doi.org/10.1016/j.jnoncrysol.2008.06.102.
37. Taylor, S.J.; Haw, M.D.; Sefcik, J.; Fletcher, A.J. Effects of Secondary Metal Carbonate Addition on the Porous Character of Resorcinol–Formaldehyde Xerogels. *Langmuir* **2015**, *31*, 13571-13580, doi:10.1021/acs.langmuir.5b02483.
38. Grenier-Loustalot, M.-F.; Larroque, S.; Grande, D.; Grenier, P.; Bedel, D. Phenolic resins: 2. Influence of catalyst type on reaction mechanisms and kinetics. *Polymer* **1996**, *37*, 1363-1369, doi:https://doi.org/10.1016/0032-3861(96)81133-5.
39. Hofmeister, F. Zur Lehre von der Wirkung der Salze. *Archiv für experimentelle Pathologie und Pharmakologie* **1888**, *24*, 247-260, doi:10.1007/BF01918191.
40. Zhang, Y.; Furyk, S.; Bergbreiter, D.E.; Cremer, P.S. Specific Ion Effects on the Water Solubility of Macromolecules: PNIPAM and the Hofmeister Series. *J. Am. Chem. Soc.* **2005**, *127*, 14505-14510, doi:10.1021/ja0546424.
41. Bruce, E.E.; Okur, H.I.; Stegmaier, S.; Drexler, C.I.; Rogers, B.A.; van der Vegt, N.F.A.; Roke, S.; Cremer, P.S. Molecular Mechanism for the Interactions of Hofmeister Cations with Macromolecules in Aqueous Solution. *J. Am. Chem. Soc.* **2020**, *142*, 19094-19100, doi:10.1021/jacs.0c07214.
42. Zhang, Y.; Cremer, P.S. Interactions between macromolecules and ions: the Hofmeister series. *Curr. Opin. Chem. Biol.* **2006**, *10*, 658-663, doi:https://doi.org/10.1016/j.cbpa.2006.09.020.
43. Moelbert, S.; Normand, B.; De Los Rios, P. Kosmotropes and chaotropes: modelling preferential exclusion, binding and aggregate stability. *Biophys. Chem.* **2004**, *112*, 45-57, doi:https://doi.org/10.1016/j.bpc.2004.06.012.
44. Timson, D.J. The roles and applications of chaotropes and kosmotropes in industrial fermentation processes. *World J. Microbiol. Biotechnol.* **2020**, *36*, 89, doi:10.1007/s11274-020-02865-8.
45. Mazzini, V.; Craig, V.S.J. What is the fundamental ion-specific series for anions and cations? Ion specificity in standard partial molar volumes of electrolytes and electrostriction in water and non-aqueous solvents. *Chemical Science* **2017**, *8*, 7052-7065, doi:10.1039/C7SC02691A.
46. Schwierz, N.; Horinek, D.; Sivan, U.; Netz, R.R. Reversed Hofmeister series—The rule rather than the exception. *Current Opinion in Colloid & Interface Science* **2016**, *23*, 10-18, doi:https://doi.org/10.1016/j.cocis.2016.04.003.
47. Schwierz, N.; Horinek, D.; Netz, R.R. Anionic and cationic Hofmeister effects on hydrophobic and hydrophilic surfaces. *Langmuir* **2013**, *29*, 2602-2614, doi:10.1021/la303924e.
48. Schwierz, N.; Horinek, D.; Netz, R.R. Reversed anionic Hofmeister series: the interplay of surface charge and surface polarity. *Langmuir* **2010**, *26*, 7370-7379, doi:10.1021/la904397v.
49. Alonso-Buenaposada, I.D.; Rey-Raap, N.; Calvo, E.G.; Menéndez, J.A.; Arenillas, A. Acid-based resorcinol-formaldehyde xerogels synthesized by microwave heating. *J. Sol-Gel Sci. Technol.* **2017**, *84*, 60-69, doi:10.1007/s10971-017-4475-z.
50. Rey-Raap, N.; Arenillas, A.; Menéndez, J.A. Carbon Gels and Their

Applications: A Review of Patents. In *Submicron Porous Materials*, Bettotti, P., Ed. Springer International Publishing: Cham, 2017; 10.1007/978-3-319-53035-2_2pp. 25-52.
51. Zhang, X.; Chang, D.; Liu, J.; Luo, Y. Conducting polymer aerogels from supercritical CO2 drying PEDOT-PSS hydrogels. *J. Mater. Chem.* **2010**, *20*, 5080-5085, doi:10.1039/C0JM00050G.
52. Parashar, M.; Shukla, V.K.; Singh, R. Metal oxides nanoparticles via sol–gel method: a review on synthesis, characterization and applications. *Journal of Materials Science: Materials in Electronics* **2020**, *31*, 3729-3749, doi:10.1007/s10854-020-02994-8.
53. Mathieu, B.; Blacher, S.; Pirard, R.; Pirard, J.P.; Sahouli, B.; Brouers, F. Freeze-dried resorcinol-formaldehyde gels. *J. Non-Cryst. Solids* **1997**, *212*, 250-261, doi:https://doi.org/10.1016/S0022-3093(97)00025-2.
54. Jena, A.; Gupta, K. Advances in Pore Structure Evaluation by Porometry. *Chemical Engineering & Technology* **2010**, *33*, 1241-1250, doi:https://doi.org/10.1002/ceat.201000119.
55. Feng, J.; Su, B.-L.; Xia, H.; Zhao, S.; Gao, C.; Wang, L.; Ogbeide, O.; Feng, J.; Hasan, T. Printed aerogels: Chemistry, processing, and applications. *Chem. Soc. Rev.* **2021**.
56. Scherer, G.W. Theory of Drying. *J. Am. Ceram. Soc.* **1990**, *73*, 3-14, doi:https://doi.org/10.1111/j.1151-2916.1990.tb05082.x.
57. Eberhardt, A.B.; Flatt, R.J. 13 - Working mechanisms of shrinkage-reducing admixtures. In *Science and Technology of Concrete Admixtures*, Aïtcin, P.-C., Flatt, R.J., Eds. Woodhead Publishing: 2016; https://doi.org/10.1016/B978-0-08-100693-1.00013-8pp. 305-320.
58. Laskowski, J.; Milow, B.; Ratke, L. Subcritically dried resorcinol–formaldehyde aerogels from a base–acid catalyzed synthesis route. *Microporous Mesoporous Mater.* **2014**, *197*, 308-315, doi:https://doi.org/10.1016/j.micromeso.2014.06.031.
59. Pekala, R.W. Low Density, Resorcinol-Formaldehyde Aerogels. 1989.
60. Jabeen, N.; Mardan, A.L.I. Effect of water removal on the textural properties of resorcinol/formaldehyde gels by azeotropic distillation. *J. Mater. Sci.* **1998**, *33*, 5451-5453, doi:10.1023/A:1004418921571.
61. Kraiwattanawong, K.; Tamon, H.; Praserthdam, P. Influence of solvent species used in solvent exchange for preparation of mesoporous carbon xerogels from resorcinol and formaldehyde via subcritical drying. *Microporous Mesoporous Mater.* **2011**, *138*, 8-16, doi:https://doi.org/10.1016/j.micromeso.2010.10.001.
62. Folliard, K.J.; Berke, N.S. Properties of high-performance concrete containing shrinkage-reducing admixture. *Cem. Concr. Res.* **1997**, *27*, 1357-1364, doi:https://doi.org/10.1016/S0008-8846(97)00135-X.
63. Collepardi, M.; Borsoi, A.; Collepardi, S.; Ogoumah Olagot, J.J.; Troli, R. Effects of shrinkage reducing admixture in shrinkage compensating concrete under non-wet curing conditions. *Cem. Concr. Compos.* **2005**, *27*, 704-708, doi:https://doi.org/10.1016/j.cemconcomp.2004.09.020.
64. Bentz, D.P. Influence of Shrinkage-Reducing Admixtures on Early-Age Properties of Cement Pastes. *Journal of Advanced Concrete Technology* **2006**, *4*, 423-429, doi:10.3151/jact.4.423.
65. Mora-Ruacho, J.; Gettu, R.; Aguado, A. Influence of shrinkage-reducing admixtures on the reduction of plastic shrinkage cracking in concrete. *Cem.*

Concr. Res. **2009**, *39*, 141-146, doi:https://doi.org/10.1016/j.cemconres.2008.11.011.

66. Job, N.; Théry, A.; Pirard, R.; Marien, J.; Kocon, L.; Rouzaud, J.-N.; Béguin, F.; Pirard, J.-P. Carbon aerogels, cryogels and xerogels: Influence of the drying method on the textural properties of porous carbon materials. *Carbon* **2005**, *43*, 2481-2494, doi:https://doi.org/10.1016/j.carbon.2005.04.031.
67. Petričević, R.; Reichenauer, G.; Bock, V.; Emmerling, A.; Fricke, J. Structure of carbon aerogels near the gelation limit of the resorcinol–formaldehyde precursor. *J. Non-Cryst. Solids* **1998**, *225*, 41-45.
68. Petričević, R.; Glora, M.; Fricke, J. Planar fibre reinforced carbon aerogels for application in PEM fuel cells. *Carbon* **2001**, *39*, 857-867, doi:https://doi.org/10.1016/S0008-6223(00)00190-1.
69. Prostredný, M.; Abduljalil, M.G.M.; Mulheran, P.A.; Fletcher, A.J. Process Variable Optimization in the Manufacture of Resorcinol¯Formaldehyde Gel Materials. *Gels* **2018**, *4*, 36, doi:10.3390/gels4020036.
70. Pekala, R.W.; Schaefer, D.W. Structure of organic aerogels. 1. Morphology and scaling. *Macromolecules* **1993**, *26*, 5487-5493, doi:10.1021/ma00072a029.
71. Tamon, H.; Ishizaka, H. SAXS Study on Gelation Process in Preparation of Resorcinol–Formaldehyde Aerogel. *J. Colloid Interface Sci.* **1998**, *206*, 577-582, doi:https://doi.org/10.1006/jcis.1998.5770.
72. Alshrah, M.; Mark, L.H.; Zhao, C.; Naguib, H.E.; Park, C.B. Nanostructure to thermal property relationship of resorcinol formaldehyde aerogels using the fractal technique. *Nanoscale* **2018**, *10*, 10564-10575.
73. Xu, X.; Li, J.; Li, Y.; Ni, B.; Liu, X.; Pan, L. Chapter 4 - Selection of Carbon Electrode Materials. In *Interface Science and Technology*, Ahualli, S., Delgado, Á.V., Eds. Elsevier: 2018; Vol. 24, pp. 65-83.
74. Tamon, H.; Ishizaka, H.; Mikami, M.; Okazaki, M. Porous structure of organic and carbon aerogels synthesized by sol-gel polycondensation of resorcinol with formaldehyde. *Carbon* **1997**, *35*, 791-796, doi:https://doi.org/10.1016/S0008-6223(97)00024-9.
75. Abolghasemi Mahani, A.; Motahari, S.; Nayyeri, V. Synthesis, characterization and dielectric properties of one-step pyrolyzed / activated resorcinol-formaldehyde based carbon aerogels for electromagnetic interference shielding applications. *Mater. Chem. Phys.* **2018**, *213*, 492-501, doi:https://doi.org/10.1016/j.matchemphys.2018.04.047.
76. muRata. muRata Innovator in Electronics, EDLC. Availabe online: http://www.murata.com/products/edlc/tech_guide/priciple_feature/images/ind_img02.gif (accessed on 22/07/2021).
77. Lin, C.; Ritter, J.A.; Popov, B.N. Development of Carbon-Metal Oxide Supercapacitors from Sol-Gel Derived Carbon-Ruthenium Xerogels. *J. Electrochem. Soc.* **1999**, *146*, 3155-3160, doi:10.1149/1.1392448.
78. Zanto, E.J.; Al-Muhtaseb, S.A.; Ritter, J.A. Sol−Gel-Derived Carbon Aerogels and Xerogels: Design of Experiments Approach to Materials Synthesis. *Industrial & Engineering Chemistry Research* **2002**, *41*, 3151-3162, doi:10.1021/ie020048g.
79. Kim, S.J.; Hwang, S.W.; Hyun, S.H. Preparation of carbon aerogel electrodes for supercapacitor and their electrochemical characteristics. *J. Mater. Sci.* **2005**, *40*, 725-731, doi:10.1007/s10853-005-6313-x.

80. Mezzavilla, S.; Zanella, C.; Aravind, P.R.; Della Volpe, C.; Sorarù, G.D. Carbon xerogels as electrodes for supercapacitors. The influence of the catalyst concentration on the microstructure and on the electrochemical properties. *J. Mater. Sci.* **2012**, *47*, 7175-7180, doi:10.1007/s10853-012-6662-1.
81. Li, J.; Wang, X.; Huang, Q.; Gamboa, S.; Sebastian, P.J. Studies on preparation and performances of carbon aerogel electrodes for the application of supercapacitor. *J. Power Sources* **2006**, *158*, 784-788, doi:https://doi.org/10.1016/j.jpowsour.2005.09.045.
82. Malkova, A.N.; Sipyagina, N.A.; Gozhikova, I.O.; Dobrovolsky, Y.A.; Konev, D.V.; Baranchikov, A.E.; Ivanova, O.S.; Ukshe, A.E.; Lermontov, S.A. Electrochemical Properties of Carbon Aerogel Electrodes: Dependence on Synthesis Temperature. *Molecules* **2019**, *24*, 3847, doi:10.3390/molecules24213847.
83. Xu, P.; Drewes, J.E.; Heil, D.; Wang, G. Treatment of brackish produced water using carbon aerogel-based capacitive deionization technology. *Water Res.* **2008**, *42*, 2605-2617, doi:10.1016/j.watres.2008.01.011.
84. Jung, H.-H.; Hwang, S.-W.; Hyun, S.-H.; Lee, K.-H.; Kim, G.-T. Capacitive deionization characteristics of nanostructured carbon aerogel electrodes synthesized via ambient drying. *Desalination* **2007**, *216*, 377-385, doi:https://doi.org/10.1016/j.desal.2006.11.023.
85. Porada, S.; Weinstein, L.; Dash, R.; van der Wal, A.; Bryjak, M.; Gogotsi, Y.; Biesheuvel, P.M. Water Desalination Using Capacitive Deionization with Microporous Carbon Electrodes. *ACS Applied Materials & Interfaces* **2012**, *4*, 1194-1199, doi:10.1021/am201683j.
86. Rodrigues, E.G.; Pereira, M.F.R.; Órfão, J.J.M. Glycerol oxidation with gold supported on carbon xerogels: Tuning selectivities by varying mesopore sizes. *Applied Catalysis B: Environmental* **2012**, *115-116*, 1-6, doi:https://doi.org/10.1016/j.apcatb.2011.12.008.
87. Smirnova, A.; Dong, X.; Hara, H.; Vasiliev, A.; Sammes, N. Novel carbon aerogel-supported catalysts for PEM fuel cell application. *Int. J. Hydrogen Energy* **2005**, *30*, 149-158, doi:https://doi.org/10.1016/j.ijhydene.2004.04.014.
88. Jin, H.; Zhang, H.; Ma, Y.; Xu, T.; Zhong, H.; Wang, M. Stable support based on highly graphitic carbon xerogel for proton exchange membrane fuel cells. *J. Power Sources* **2010**, *195*, 6323-6328, doi:https://doi.org/10.1016/j.jpowsour.2010.04.050.
89. Lu, X.; Arduini-Schuster, M.; Kuhn, J.; Nilsson, O.; Fricke, J.; Pekala, R. Thermal conductivity of monolithic organic aerogels. *Science* **1992**, *255*, 971-972.
90. Feng, J.; Zhang, C.; Feng, J. Carbon fiber reinforced carbon aerogel composites for thermal insulation prepared by soft reinforcement. *Mater. Lett.* **2012**, *67*, 266-268, doi:https://doi.org/10.1016/j.matlet.2011.09.076.
91. Ye, C.; An, Z.; Zhang, R. Super-elastic carbon-bonded carbon fibre composites impregnated with carbon aerogel for high-temperature thermal insulation. *Advances in Applied Ceramics* **2019**, *118*, 292-299, doi:10.1080/17436753.2019.1572341.
92. Rey-Raap, N.; Calvo, E.; Menéndez, J.; Arenillas, A. Exploring the potential of resorcinol-formaldehyde xerogels as thermal insulators. *Microporous Mesoporous Mater.* **2017**, *244*, 50-54.
93. Czakkel, O.; Nagy, B.; Dobos, G.; Fouquet, P.; Bahn, E.; László, K. Static and dynamic studies of hydrogen adsorption on nanoporous carbon

gels. *Int. J. Hydrogen Energy* **2019**, *44*, 18169-18178, doi:https://doi.org/10.1016/j.ijhydene.2019.05.131.
94. Tian, H.Y.; Buckley, C.E.; Paskevicius, M.; Sheppard, D.A. Acetic acid catalysed carbon xerogels derived from resorcinol-furfural for hydrogen storage. *Int. J. Hydrogen Energy* **2011**, *36*, 671-679, doi:https://doi.org/10.1016/j.ijhydene.2010.10.054.
95. Tian, H.Y.; Buckley, C.E.; Wang, S.B.; Zhou, M.F. Enhanced hydrogen storage capacity in carbon aerogels treated with KOH. *Carbon* **2009**, *47*, 2128-2130, doi:https://doi.org/10.1016/j.carbon.2009.03.063.
96. Kang, K.Y.; Lee, B.I.; Lee, J.S. Hydrogen adsorption on nitrogen-doped carbon xerogels. *Carbon* **2009**, *47*, 1171-1180, doi:https://doi.org/10.1016/j.carbon.2009.01.001.
97. Zubizarreta, L.; Menéndez, J.A.; Job, N.; Marco-Lozar, J.P.; Pirard, J.P.; Pis, J.J.; Linares-Solano, A.; Cazorla-Amorós, D.; Arenillas, A. Ni-doped carbon xerogels for H2 storage. *Carbon* **2010**, *48*, 2722-2733, doi:https://doi.org/10.1016/j.carbon.2010.03.068.
98. Bastos-Neto, M.; Patzschke, C.; Lange, M.; Möllmer, J.; Möller, A.; Fichtner, S.; Schrage, C.; Lässig, D.; Lincke, J.; Staudt, R. Assessment of hydrogen storage by physisorption in porous materials. *Energy & Environmental Science* **2012**, *5*, 8294-8303.
99. Yapo, J.A.; Ello, A.; Serge, e.; Trokourey, A. N-doped carbon aerogels for carbon dioxide (CO2) capture. *African Journal of Pure and Applied Chemistry* **2013**, *7*, 61-66.
100. Robertson, C.; Mokaya, R. Microporous activated carbon aerogels via a simple subcritical drying route for CO2 capture and hydrogen storage. *Microporous Mesoporous Mater.* **2013**, *179*, 151-156, doi:https://doi.org/10.1016/j.micromeso.2013.05.025.
101. Wang, S.; Xu, Y.; Yan, M.; Zhang, L.; Liu, Z. The effect of surfactants on carbon xerogel structure and CO2 capture. *J. Non-Cryst. Solids* **2018**, *499*, 101-106, doi:https://doi.org/10.1016/j.jnoncrysol.2018.07.023.
102. Water Quality and Wastewater. Availabe online: https://www.unwater.org/water-facts/quality-and-wastewater/ (accessed on 02/08/2021).
103. Boretti, A.; Rosa, L. Reassessing the projections of the World Water Development Report. *npj Clean Water* **2019**, *2*, 15, doi:10.1038/s41545-019-0039-9.
104. Inyinbor Adejumoke, A.; Adebesin Babatunde, O.; Oluyori Abimbola, P.; Adelani Akande Tabitha, A.; Dada Adewumi, O.; Oreofe Toyin, A. Water pollution: effects, prevention, and climatic impact. *Water Challenges of an Urbanizing World* **2018**, *33*, 33-47.
105. Kumar, V.; Sharma, A.; Kumar, R.; Bhardwaj, R.; Kumar Thukral, A.; Rodrigo-Comino, J. Assessment of heavy-metal pollution in three different Indian water bodies by combination of multivariate analysis and water pollution indices. *Human and Ecological Risk Assessment: An International Journal* **2020**, *26*, 1-16, doi:10.1080/10807039.2018.1497946.
106. Rochman, C.M. Strategies for reducing ocean plastic debris should be diverse and guided by science. *Environmental Research Letters* **2016**, *11*, 041001.
107. Diamanti-Kandarakis, E.; Bourguignon, J.-P.; Giudice, L.C.; Hauser, R.; Prins, G.S.; Soto, A.M.; Zoeller, R.T.; Gore, A.C. Endocrine-disrupting chemicals: an Endocrine Society scientific statement. *Endocr Rev* **2009**, *30*, 293-342, doi:10.1210/er.2009-0002.
108. Rotchell, J.; Ostrander, G. Molecular Markers of Endocrine Disruption in Aquatic Organisms. *Journal of*

Toxicology and Environmental Health, Part B **2003**, *6*, 453-496, doi:10.1080/10937400306476.
109. Bigsby, R.; Chapin, R.E.; Daston, G.P.; Davis, B.J.; Gorski, J.; Gray, L.E.; Howdeshell, K.L.; Zoeller, R.T.; vom Saal, F.S. Evaluating the effects of endocrine disruptors on endocrine function during development. *Environ. Health Perspect.* **1999**, *107*, 613-618, doi:10.1289/ehp.99107s4613.
110. Jobling, S.; Nolan, M.; Tyler, C.R.; Brighty, G.; Sumpter, J.P. Widespread Sexual Disruption in Wild Fish. *Environmental Science & Technology* **1998**, *32*, 2498-2506, doi:10.1021/es9710870.
111. Jobling, S.; Williams, R.; Johnson, A.; Taylor, A.; Gross-Sorokin, M.; Nolan, M.; Tyler, C.R.; van Aerle, R.; Santos, E.; Brighty, G. Predicted exposures to steroid estrogens in U.K. rivers correlate with widespread sexual disruption in wild fish populations. *Environ. Health Perspect.* **2006**, *114 Suppl 1*, 32-39, doi:10.1289/ehp.8050.
112. Matthiessen, P.; Wheeler, J.R.; Weltje, L. A review of the evidence for endocrine disrupting effects of current-use chemicals on wildlife populations. *Crit. Rev. Toxicol.* **2018**, *48*, 195-216, doi:10.1080/10408444.2017.1397099.
113. Hontela, A. Interrenal dysfunction in fish from contaminated sites: In vivo and in vitro assessment. *Environ. Toxicol. Chem.* **1998**, *17*, 44-48, doi:https://doi.org/10.1002/etc.5620170107.
114. Crofton, K.M. Thyroid disrupting chemicals: mechanisms and mixtures. *International journal of andrology* **2008**, *31*, 209-223.
115. Ghassabian, A.; Trasande, L. Disruption in Thyroid Signaling Pathway: A Mechanism for the Effect of Endocrine-Disrupting Chemicals on Child Neurodevelopment. *Front Endocrinol (Lausanne)* **2018**, *9*, 204-204, doi:10.3389/fendo.2018.00204.
116. Kabir, E.R.; Rahman, M.S.; Rahman, I. A review on endocrine disruptors and their possible impacts on human health. *Environ. Toxicol. Pharmacol.* **2015**, *40*, 241-258, doi:https://doi.org/10.1016/j.etap.2015.06.009.
117. Yilmaz, B.; Terekeci, H.; Sandal, S.; Kelestimur, F. Endocrine disrupting chemicals: exposure, effects on human health, mechanism of action, models for testing and strategies for prevention. *Reviews in Endocrine and Metabolic Disorders* **2020**, *21*, 127-147, doi:10.1007/s11154-019-09521-z.
118. Ribeiro, E.; Ladeira, C.; Viegas, S. EDCs mixtures: a stealthy hazard for human health? *Toxics* **2017**, *5*, 5.
119. Bhuiyan, M.N.H.; Kang, H.; Choi, J.; Lim, S.; Kho, Y.; Choi, K. Effects of 3,4-dichloroaniline (3,4-DCA) and 4,4'-methylenedianiline (4,4'-MDA) on sex hormone regulation and reproduction of adult zebrafish (Danio rerio). *Chemosphere* **2021**, *269*, 128768, doi:https://doi.org/10.1016/j.chemosphere.2020.128768.
120. *Proposed EQS for Water Framework Directive Annex VIII substances: 3,4-dichloroaniline*.
121. *3,4-DICHLOROANILINE (3,4-DCA) - Summary Risk Assessment Report*; 1018-5593; European Commission - Institute for Health and Consumer Protection: 2006.
122. Jak, R.G.; Maas, J.L.; Scholten, M.C.T. Ecotoxicity of 3,4-dichloroaniline in enclosed freshwater plankton communities at different nutrient levels. *Ecotoxicology* **1998**, *7*, 49-60, doi:10.1023/A:1008859718361.
123. van der Hoeven, N. Effect of 3,4-dichloroaniline and metavanadate on Daphnia populations. *Ecotoxicol. Environ. Saf.* **1990**, *20*, 53-70, doi:10.1016/0147-6513(90)90046-8.
124. Zhu, B.; Liu, T.; Hu, X.; Wang, G. Developmental toxicity of 3,4-dichloroaniline on rare minnow (Gobiocypris rarus) embryos and

larvae. *Chemosphere* **2013**, *90*, 1132-1139, doi:https://doi.org/10.1016/j.chemosphere.2012.09.021.

125. Call, D.J.; Poirier, S.H.; Knuth, M.L.; Harting, S.L.; Lindberg, C.A. Toxicity of 3,4-dichloroaniline to fathead minnows, Pimephales promelas, in acute and early life-stage exposures. *Bulletin of environmental contamination and toxicology* **1987**, *38*, 352-358, doi:10.1007/bf01606686.
126. Zhang, B.; Lin, S. Effects of 3,4-Dichloroaniline on Testicle Enzymes as Biological Markers in Rats. *Biomedical and Environmental Sciences* **2009**, *22*, 40-43, doi:https://doi.org/10.1016/S0895-3988(09)60020-9.
127. Yang, B.; Yu, C.; Yu, Q.; Zhang, X.; Li, Z.; Lei, L. N-doped carbon xerogels as adsorbents for the removal of heavy metal ions from aqueous solution. *RSC Adv.* **2015**, *5*, 7182-7191.
128. Veselá, P.; Slovák, V. N-doped carbon xerogels prepared by ammonia assisted pyrolysis: Surface characterisation, thermal properties and adsorption ability for heavy metal ions. *J. Anal. Appl. Pyrolysis* **2014**, *109*, 266-271, doi:https://doi.org/10.1016/j.jaap.2014.06.002.
129. Álvarez, S.; Ribeiro, R.S.; Gomes, H.T.; Sotelo, J.L.; García, J. Synthesis of carbon xerogels and their application in adsorption studies of caffeine and diclofenac as emerging contaminants. *Chem. Eng. Res. Des.* **2015**, *95*, 229-238, doi:https://doi.org/10.1016/j.cherd.2014.11.001.
130. Páez, C.A.; Contreras, M.S.; Léonard, A.; Blacher, S.; Olivera-Fuentes, C.G.; Pirard, J.-P.; Job, N. Effect of CO2 activation of carbon xerogels on the adsorption of methylene blue. *Adsorption* **2012**, *18*, 199-211, doi:10.1007/s10450-012-9394-2.
131. Lee, L.; Zaini, M.A.A. Equilibrium and kinetic adsorption studies of reactive orange onto resorcinol-formaldehyde carbon gel. *Chemical Engineering Transactions* **2017**, *56*, 811-816.
132. Wu, X.; Wu, D.; Fu, R.; Zeng, W. Preparation of carbon aerogels with different pore structures and their fixed bed adsorption properties for dye removal. *Dyes and Pigments* **2012**, *95*, 689-694, doi:https://doi.org/10.1016/j.dyepig.2012.07.001.
133. Catlow, C.R.A.; Van Speybroeck, V.; van Santen, R. *Modelling and Simulation in the Science of Micro-and Meso-porous Materials*; Elsevier: 2017.
134. Parker, S.; Catlow, C.; Cormack, A. Prediction of mineral structure by energy minimisation techniques. *J. Chem. Soc., Chem. Commun.* **1983**, 936-938.
135. Woodley, S.; Battle, P.; Gale, J.; Catlow, C.A. The prediction of inorganic crystal structures using a genetic algorithm and energy minimisation. *PCCP* **1999**, *1*, 2535-2542.
136. Potluri, P.; Sagar, T. Compaction modelling of textile preforms for composite structures. *Compos. Struct.* **2008**, *86*, 177-185.
137. Fan, H.B.; Yuen, M.M.F. Material properties of the cross-linked epoxy resin compound predicted by molecular dynamics simulation. *Polymer* **2007**, *48*, 2174-2178, doi:https://doi.org/10.1016/j.polymer.2007.02.007.
138. Schwieters, C.D.; Clore, G.M. Internal Coordinates for Molecular Dynamics and Minimization in Structure Determination and Refinement. *Journal of Magnetic Resonance* **2001**, *152*, 288-302, doi:https://doi.org/10.1006/jmre.2001.2413.
139. Massobrio, C.; Du, J.; Bernasconi, M.; Salmon, P.S. Molecular dynamics simulations of disordered materials.

Cham: Springer International Publishing **2015**.

140. Ivasishin, O.M.; Shevchenko, S.V.; Vasiliev, N.L.; Semiatin, S.L. A 3-D Monte-Carlo (Potts) model for recrystallization and grain growth in polycrystalline materials. *Materials Science and Engineering: A* **2006**, *433*, 216-232, doi:https://doi.org/10.1016/j.msea.2006.06.115.
141. Saito, Y. The Monte Carlo simulation of microstructural evolution in metals. *Materials Science and Engineering: A* **1997**, *223*, 114-124, doi:https://doi.org/10.1016/S0921-5093(97)80019-6.
142. M. Dieb, T.; Ju, S.; Yoshizoe, K.; Hou, Z.; Shiomi, J.; Tsuda, K. MDTS: automatic complex materials design using Monte Carlo tree search. *Science and Technology of Advanced Materials* **2017**, *18*, 498-503, doi:10.1080/14686996.2017.1344083.
143. Hammes-Schiffer, S.; Andersen, H.C. The advantages of the general Hartree–Fock method for future computer simulation of materials. *J. Chem. Phys.* **1993**, *99*, 1901-1913.
144. Adachi, H.; Mukoyama, T.; Kawai, J. *Hartree-Fock-Slater method for materials science: the DV-X Alpha method for design and characterization of materials*; Springer Science & Business Media: 2006; Vol. 84.
145. Ohno, K.; Esfarjani, K.; Kawazoe, Y. *Computational materials science: from ab initio to Monte Carlo methods*; Springer: 2018.
146. Poblet, J.M.; López, X.; Bo, C. Ab initio and DFT modelling of complex materials: towards the understanding of electronic and magnetic properties of polyoxometalates. *Chem. Soc. Rev.* **2003**, *32*, 297-308.
147. Liu, X.-Y.; Andersson, D.; Uberuaga, B. First-principles DFT modeling of nuclear fuel materials. *J. Mater. Sci.* **2012**, *47*, 7367-7384.
148. Ogata, S.; Lidorikis, E.; Shimojo, F.; Nakano, A.; Vashishta, P.; Kalia, R.K. Hybrid finite-element/molecular-dynamics/electronic-density-functional approach to materials simulations on parallel computers. *Comput. Phys. Commun.* **2001**, *138*, 143-154, doi:https://doi.org/10.1016/S0010-4655(01)00203-X.
149. Orrite, S.D.; Stoll, S.; Schurtenberger, P. Off-lattice Monte Carlo simulations of irreversible and reversible aggregation processes. *Soft Matter* **2005**, *1*, 364-371.
150. Lattuada, M.; Wu, H.; Morbidelli, M. A simple model for the structure of fractal aggregates. *J. Colloid Interface Sci.* **2003**, *268*, 106-120.
151. Rottereau, M.; Gimel, J.C.; Nicolai, T.; Durand, D. Monte Carlo simulation of particle aggregation and gelation: I. Growth, structure and size distribution of the clusters. *The European Physical Journal E* **2004**, *15*, 133-140, doi:10.1140/epje/i2004-10044-x.
152. Jungblut, S.; Joswig, J.-O.; Eychmüller, A. Diffusion-limited cluster aggregation: Impact of rotational diffusion. *The Journal of Physical Chemistry C* **2018**, *123*, 950-954.
153. Jungblut, S.; Joswig, J.-O.; Eychmüller, A. Diffusion-and reaction-limited cluster aggregation revisited. *PCCP* **2019**, *21*, 5723-5729.
154. Meakin, P. Formation of fractal clusters and networks by irreversible diffusion-limited aggregation. *Phys. Rev. Lett.* **1983**, *51*, 1119.
155. Kolb, M.; Botet, R.; Jullien, R. Scaling of kinetically growing clusters. *Phys. Rev. Lett.* **1983**, *51*, 1123.
156. Gavalda, S.; Kaneko, K.; Thomson, K.T.; Gubbins, K.E. Molecular modeling of carbon aerogels. *Colloids and surfaces A: Physicochemical and engineering aspects* **2001**, *187*, 531-538.
157. Gavalda, S.; Gubbins, K.; Hanzawa, Y.; Kaneko, K.; Thomson, K. Nitrogen

adsorption in carbon aerogels: A molecular simulation study. *Langmuir* **2002**, *18*, 2141-2151.
158. Ravikovitch, P.I.; Domhnaill, S.C.O.; Neimark, A.V.; Schueth, F.; Unger, K.K. Capillary Hysteresis in Nanopores: Theoretical and Experimental Studies of Nitrogen Adsorption on MCM-41. *Langmuir* **1995**, *11*, 4765-4772, doi:10.1021/la00012a030.
159. Gor, G.Y.; Thommes, M.; Cychosz, K.A.; Neimark, A.V. Quenched solid density functional theory method for characterization of mesoporous carbons by nitrogen adsorption. *Carbon* **2012**, *50*, 1583-1590, doi:https://doi.org/10.1016/j.carbon.2011.11.037.
160. Fan, C.; Do, D.D.; Nicholson, D.; Jagiello, J.; Kenvin, J.; Puzan, M. Monte Carlo simulation and experimental studies on the low temperature characterization of nitrogen adsorption on graphite. *Carbon* **2013**, *52*, 158-170, doi:https://doi.org/10.1016/j.carbon.2012.09.017.
161. Coasne, B.; Galarneau, A.; Di Renzo, F.; Pellenq, R. Molecular simulation of nitrogen adsorption in nanoporous silica. *Langmuir* **2010**, *26*, 10872-10881.
162. Düren, T.; Bae, Y.-S.; Snurr, R. Using molecular simulation to characterise metal-organic frameworks for adsorption applications. *Chem. Soc. Rev.* **2009**, *38*, 1237-1247, doi:10.1039/b803498m.
163. Dubbeldam, D.; Calero, S.; Ellis, D.E.; Snurr, R.Q. RASPA: molecular simulation software for adsorption and diffusion in flexible nanoporous materials. *Mol. Simul.* **2016**, *42*, 81-101, doi:10.1080/08927022.2015.1010082.
164. Monson, P.A. Recent progress in molecular modeling of adsorption and hysteresis in mesoporous materials. *Adsorption* **2005**, *11*, 29-35.
165. Monson, P.A. Mean field kinetic theory for a lattice gas model of fluids confined in porous materials. *J. Chem. Phys.* **2008**, *128*, 084701, doi:10.1063/1.2837287.
166. Schneider, D.; Valiullin, R.; Monson, P.A. Modeling the Influence of Side Stream and Ink Bottle Structures on Adsorption/Desorption Dynamics of Fluids in Long Pores. *Langmuir* **2015**, *31*, 188-198, doi:10.1021/la503482j.
167. Casselman, J.A.; Desouza, A.; Monson, P.A. Modelling the dynamics of condensation and evaporation of fluids in three-dimensional slit pores. *Mol. Phys.* **2015**, *113*, 1250-1260, doi:10.1080/00268976.2015.1009954.
168. Sarkisov, L.; Monson, P.A. Lattice model of adsorption in disordered porous materials: Mean-field density functional theory and Monte Carlo simulations. *Phys. Rev. E* **2001**, *65*, 011202, doi:10.1103/PhysRevE.65.011202.
169. Langmuir, I. The Constitution and Fundamental Properties of Solids and Liquids. Part I. Solids. *J. Am. Chem. Soc.* **1916**, *38*, 2221-2295, doi:10.1021/ja02268a002.
170. Brunauer, S.; Emmett, P.H.; Teller, E. Adsorption of gases in multimolecular layers. *J. Am. Chem. Soc.* **1938**, *60*, 309-319.
171. Barrett, E.P.; Joyner, L.G.; Halenda, P.P. The Determination of Pore Volume and Area Distributions in Porous Substances. I. Computations from Nitrogen Isotherms. *J. Am. Chem. Soc.* **1951**, *73*, 373-380, doi:10.1021/ja01145a126.
172. Kolasinski, K.W. Chapter 3: Chemisorption, Physisorption and Dynamics. In *Surf. Sci.*, John Wiley & Sons: 2012; https://doi.org/10.1002/9781119941798.ch3pp. 115-183.
173. Patel, H.A.; Byun, J.; Yavuz, C.T. Carbon Dioxide Capture Adsorbents: Chemistry and Methods. *ChemSusChem* **2017**, *10*, 1303-1317, doi:https://doi.org/10.1002/cssc.201601545.

174. Thommes, M.; Kaneko, K.; Neimark, A.V.; Olivier, J.P.; Rodriguez-Reinoso, F.; Rouquerol, J.; Sing, K.S.W. Physisorption of gases, with special reference to the evaluation of surface area and pore size distribution (IUPAC Technical Report). *Pure Appl. Chem.* **2015**, *87*, 1051-1069, doi:doi:10.1515/pac-2014-1117.
175. Chang, Q. Chapter 10 - Surface of Solids. In *Colloid and Interface Chemistry for Water Quality Control*, Chang, Q., Ed. Academic Press: 2016; https://doi.org/10.1016/B978-0-12-809315-3.00010-4pp. 175-225.
176. ParticleTestingAuthority. Gas Adsorption Technique. Availabe online: https://www.particletesting.com/pore-analysis/ (accessed on 22/07/2021).
177. Rouquerol, J.; Avnir, D.; Fairbridge, C.W.; Everett, D.H.; Haynes, J.M.; Pernicone, N.; Ramsay, J.D.F.; Sing, K.S.W.; Unger, K.K. Recommendations for the characterization of porous solids (Technical Report). *Pure Appl. Chem.* **1994**, *66*, 1739-1758, doi:doi:10.1351/pac199466081739.
178. Tang, X.; Ripepi, N.; Gilliland, E. Isothermal adsorption kinetics properties of carbon dioxide in crushed coal. *Greenhouse Gases: Science and Technology* **2016**, *6*, 260-274.
179. Yurdakal, S.; Garlisi, C.; Özcan, L.; Bellardita, M.; Palmisano, G. Chapter 4 - (Photo)catalyst Characterization Techniques: Adsorption Isotherms and BET, SEM, FTIR, UV–Vis, Photoluminescence, and Electrochemical Characterizations. In *Heterogeneous Photocatalysis*, Marcì, G., Palmisano, L., Eds. Elsevier: 2019; https://doi.org/10.1016/B978-0-444-64015-4.00004-3pp. 87-152.
180. Cychosz, K.A.; Thommes, M. Progress in the Physisorption Characterization of Nanoporous Gas Storage Materials. *Engineering* **2018**, *4*, 559-566, doi:https://doi.org/10.1016/j.eng.2018.06.001.
181. Sing, K.S.W. Reporting physisorption data for gas/solid systems with special reference to the determination of surface area and porosity (Recommendations 1984). *Pure Appl. Chem.* **1985**, *57*, 603-619, doi:https://doi.org/10.1351/pac198557040603.
182. Alothman, Z. A Review: Fundamental Aspects of Silicate Mesoporous Materials. *Materials* **2012**, *5*, 2874-2902, doi:10.3390/ma5122874.
183. Butt, H., Graf, K., and Kappl, M. Chapter 9: Adsorption. In *Physics and Chemistry of Interfaces*, Wiley-VCH Verlag GmbH & Co. KGaA: 2003; https://doi.org/10.1002/3527602313.ch9pp. 177-205.
184. Li, T.; Jiang, Z.; Chenlu, X.; Liu, B.; Liu, G.; Wang, P.; Li, X.; Chen, W.; Ning, C.; Wang, Z. Effect of pore structure on shale oil accumulation in the lower third member of the Shahejie formation, Zhanhua Sag, eastern China: Evidence from gas adsorption and nuclear magnetic resonance. *Marine and Petroleum Geology* **2017**, *88*, doi:10.1016/j.marpetgeo.2017.09.030.
185. Naito, M.; Yokoyama, T.; Hosokawa, K.; Nogi, K. Chapter 5 - Characterization Methods for Nanostructure of Materials. In *Nanoparticle Technology Handbook (Third Edition)*, Elsevier: 2018; https://doi.org/10.1016/B978-0-444-64110-6.00005-6pp. 255-300.
186. Unuabonah, E.I.; Omorogie, M.O.; Oladoja, N.A. 5 - Modeling in Adsorption: Fundamentals and Applications. In *Composite Nanoadsorbents*, Kyzas, G.Z., Mitropoulos, A.C., Eds. Elsevier: 2019; https://doi.org/10.1016/B978-0-12-814132-8.00005-8pp. 85-118.
187. Rouquerol, J.; Llewellyn, P.; Rouquerol, F. Is the bet equation applicable to microporous adsorbents? In *Stud. Surf. Sci. Catal.*, Llewellyn, P.L., Rodriquez-Reinoso, F.,

Rouqerol, J., Seaton, N., Eds. Elsevier: 2007; Vol. 160, pp. 49-56.
188. Sing, K.S.W.; Rouquerol, F.; Rouquerol, J.; Llewellyn, P. 8 - Assessment of Mesoporosity. In *Adsorption by Powders and Porous Solids (Second Edition)*, Rouquerol, F., Rouquerol, J., Sing, K.S.W., Llewellyn, P., Maurin, G., Eds. Academic Press: Oxford, 2014; https://doi.org/10.1016/B978-0-08-097035-6.00008-5pp. 269-302.
189. ASTM D6556-17: Standard Test Method for Carbon Black — Total and External

Surface Area by Nitrogen Adsorption. ASTM-International: Pennsylvania, USA, 2017; 10.1520/D6556-17.
190. Lippens, B.C.; de Boer, J.H. Studies on pore systems in catalysts: V. The t method. *J. Catal.* **1965**, *4*, 319-323, doi:https://doi.org/10.1016/0021-9517(65)90307-6.
191. Storck, S.; Bretinger, H.; Maier, W.F. Characterization of micro- and mesoporous solids by physisorption methods and pore-size analysis. *Applied Catalysis A: General* **1998**, *174*, 137-146, doi:https://doi.org/10.1016/S0926-860X(98)00164-1.
192. CyberPhysics.co.uk. The Electromagnetic Spectrum. Availabe online: https://www.cyberphysics.co.uk/topics/light/emspect.htm (accessed on 22/07/2021).
193. Owen, T. *Fundamentals of Modern UV-visible Spectroscopy: A Primer*; Hewlett-Packard: 1996.
194. Wiester, J.B. Investigating the Similarities and Differences among UV/Vis, Infrared, Fluorescence, and Raman Spectroscopies through Discussion of Light–Matter Interactions. In *Raman Spectroscopy in the Undergraduate Curriculum*, American Chemical Society: 2018; Vol. 1305, pp. 13-33.
195. Larkin, P.J. Chapter 2 - Basic Principles. In *Infrared and Raman Spectroscopy (Second Edition)*, Larkin, P.J., Ed. Elsevier: 2018; https://doi.org/10.1016/B978-0-12-804162-8.00002-1pp. 7-28.
196. SpectroscopyOnline. Alcohols - The Rest of the Story. Availabe online: https://www.spectroscopyonline.com/view/alcohols-rest-story-alf3 (accessed on 22/07/2021).
197. Wang, H.; Chu, P.K. Chapter 4 - Surface Characterization of Biomaterials. In *Characterization of Biomaterials*, Bandyopadhyay, A., Bose, S., Eds. Academic Press: Oxford, 2013; https://doi.org/10.1016/B978-0-12-415800-9.00004-8pp. 105-174.
198. Raja, P.M.V.; Barron, A.R. UV-Visible Spectroscopy. 2021.
199. Battaile, C.C. The Kinetic Monte Carlo method: Foundation, implementation, and application. *Computer Methods in Applied Mechanics and Engineering* **2008**, *197*, 3386-3398, doi:https://doi.org/10.1016/j.cma.2008.03.010.
200. Neumann, J.a.R., R.D. *Statistical Methods in Neutron Diffusion - LAMS-551*; Los Alamos Scientific Laboratory: 1947.
201. Egenter, E.; Lux, T.; Stauffer, D. Finite-size effects in Monte Carlo simulations of two stock market models. *Physica A: Statistical Mechanics and its Applications* **1999**, *268*, 250-256, doi:https://doi.org/10.1016/S0378-4371(99)00059-X.
202. Stamatakis, M.; Vlachos, D.G. Unraveling the Complexity of Catalytic Reactions via Kinetic Monte Carlo Simulation: Current Status and Frontiers. *ACS Catalysis* **2012**, *2*, 2648-2663, doi:10.1021/cs3005709.
203. Baratta, P.; Bel, J.; Plaszczynski, S.; Ealet, A. High-precision Monte Carlo modelling of galaxy distribution. *A&A* **2020**, *633*, A26.
204. Serebrinsky, S.A. Physical time scale in kinetic Monte Carlo simulations of continuous-time Markov chains. *Phys.*

Rev. E **2011**, *83*, 037701, doi:10.1103/PhysRevE.83.037701.
205. Schulze, T.P. Efficient kinetic monte carlo simulation. *Journal of Computational Physics* **2008**, *227*, 2455-2462.
206. Voter, A.F. Introduction to the Kinetic Monte Carlo Method. In *Radiation Effects in Solids*, Sickafus, K.E., Kotomin, E.A., Uberuaga, B.P., Eds. Springer Netherlands: Dordrecht, 2007; pp. 1-23.
207. Balbuena, J.; Caturla, M.J.; Martinez, E. Kinetic Monte Carlo Algorithms for Nuclear Materials Applications. *Handbook of Materials Modeling: Applications: Current and Emerging Materials* **2018**, 1-22.
208. Mandelbrot, B.B.; Frame, M. Fractals. *Encyclopedia of physical science and technology* **1987**, *5*, 579-593.
209. Voss, R.F. Fractals in nature: from characterization to simulation. In *The science of fractal images*, Springer: 1988; pp. 21-70.
210. Ungar, Š. The Koch Curve: A Geometric Proof. *The American Mathematical Monthly* **2007**, *114*, 61-66, doi:10.1080/00029890.2007.11920392.
211. Conversation, T. Explainer: What Are Fractals? Availabe online: https://theconversation.com/explainer-what-are-fractals-10865 (accessed on 22/07/2021).
212. Vinoy, K.; Jose, K.; Varadan, V. Multi-band characteristics and fractal dimension of dipole antennas with Koch curve geometry. In Proceedings of IEEE Antennas and Propagation Society International Symposium (IEEE Cat. No. 02CH37313); pp. 106-109.
213. Addison, P.S. *Fractals and chaos: an illustrated course*; CRC Press: 1997.
214. Pilgrim, I.a.T., R.P. Fractal Analysis of Time-Series Data Sets: Methods and Challenges. In *Fractal Analysis*, IntechOpen: 2018; 10.5772/intechopen.81958.
215. Grassberger, P.; Procaccia, I. Characterization of Strange Attractors. *Phys. Rev. Lett.* **1983**, *50*, 346-349, doi:10.1103/PhysRevLett.50.346.
216. Nerenberg, M.; Essex, C. Correlation dimension and systematic geometric effects. *Physical Review A* **1990**, *42*, 7065.
217. Stirrup, O.T.; Babiker, A.G.; Carpenter, J.R.; Copas, A.J. Fractional Brownian motion and multivariate-t models for longitudinal biomedical data, with application to CD4 counts in HIV-positive patients. *Statistics in medicine* **2016**, *35*, 1514-1532, doi:10.1002/sim.6788.
218. Edison, J.R.; Monson, P.A. Dynamics of capillary condensation in lattice gas models of confined fluids: a comparison of dynamic mean field theory with dynamic Monte Carlo simulations. *J. Chem. Phys.* **2013**, *138*, 234709, doi:10.1063/1.4811111.
219. Rathi, A.; Kikkinides, E.S.; Ford, D.M.; Monson, P.A. A comparison of dynamic mean field theory and grand canonical molecular dynamics for the dynamics of pore filling and capillary condensation of fluids in mesopores. *J. Chem. Phys.* **2018**, *149*, 014703, doi:10.1063/1.5026414.
220. Martin, E.; Prostredny, M.; Fletcher, A. Investigating the Role of the Catalyst within Resorcinol–Formaldehyde Gel Synthesis. *Gels* **2021**, *7*, 142.
221. Micromeritics. ASAP 2420 Accelerated Surface Area and Porosimetry System Brochure. Availabe online: https://www.micromeritics.com/Repository/Files/ASAP_2420_Brochure_1.pdf (accessed on 22/07/2021).
222. ABB. Versatile FT-IR Laboratory Spectrometer

MB3000. Availabe online: https://new.abb.com/products/measurement-products/analytical/ft-ir-and-ft-nir-analyzers/laboratory-spectrometers/mb3000 (accessed on 22/07/2021).

223. Hrubesh, L.W. Aerogel applications. *J. Non-Cryst. Solids* **1998**, *225*, 335-342.
224. DDBST. Surface Tension of Methanol. Availabe online: http://www.ddbst.com/en/EED/PCP/SFT_C110.php (accessed on 22/07/2021).
225. Rolo, L.I.; Caço, A.I.; Queimada, A.J.; Marrucho, I.M.; Coutinho, J.A.P. Surface Tension of Heptane, Decane, Hexadecane, Eicosane, and Some of Their Binary Mixtures. *J. Chem. Eng. Data* **2002**, *47*, 1442-1445, doi:10.1021/je025536+.
226. DDBST. Surface Tension of Hexane. Availabe online: http://www.ddbst.com/en/EED/PCP/SFT_C89.php (accessed on 23/07/2021).
227. Deshpande, R.; Hua, D.-W.; Smith, D.M.; Brinker, C.J. Pore structure evolution in silica gel during aging/drying. III. Effects of surface tension. *J. Non-Cryst. Solids* **1992**, *144*, 32-44, doi:https://doi.org/10.1016/S0022-3093(05)80380-1.
228. Prostredny, M.; Fletcher, A.; Mulheran, P. Modelling the formation of porous organic gels – how structural properties depend on growth conditions. *RSC Adv.* **2019**, *9*, 20065-20074, doi:10.1039/C9RA01979K.
229. Martin, E.; Prostredny, M.; Fletcher, A.; Mulheran, P. Modelling Organic Gel Growth in Three Dimensions: Textural and Fractal Properties of Resorcinol-Formaldehyde Gels. *Gels* **2020**, *6*, doi:10.3390/gels6030023.
230. Ruben, G.C.; Pekala, R.W. High Resolution Tem of Organic Aerogels and Inorganic Aerogels. *MRS Proceedings* **2011**, *180*, 785, doi:10.1557/PROC-180-785.
231. Haghgoo, M.; Yousefi, A.A.; Zohuriaan Mehr, M.J. Nano porous structure of resorcinol–formaldehyde xerogels and aerogels: effect of sodium dodecylbenzene sulfonate. *Iranian Polymer Journal* **2012**, *21*, 211-219, doi:10.1007/s13726-012-0023-4.
232. Yamamoto, T.; Nishimura, T.; Suzuki, T.; Tamon, H. Control of mesoporosity of carbon gels prepared by sol–gel polycondensation and freeze drying. *J. Non-Cryst. Solids* **2001**, *288*, 46-55, doi:https://doi.org/10.1016/S0022-3093(01)00619-6.
233. Tange, O. Gnu parallel-the command-line power tool. *The USENIX Magazine* **2011**.
234. Andersen, M.; Panosetti, C.; Reuter, K. A Practical Guide to Surface Kinetic Monte Carlo Simulations. *Frontiers in Chemistry* **2019**, *7*, doi:10.3389/fchem.2019.00202.
235. Martin, E.; Prostredny, M.; Fletcher, A.; Mulheran, P. Advancing Computational Analysis of Porous Materials—Modeling Three-Dimensional Gas Adsorption in Organic Gels. *The Journal of Physical Chemistry B* **2021**, *125*, 1960-1969.
236. Mandl, F. *Statistical Physics*; Wiley: Chichester, 1994; Vol. 2nd Edition.
237. Striolo, A.; Gubbins, K.E.; Gruszkiewicz, M.S.; Cole, D.R.; Simonson, J.M.; Chialvo, A.A.; Cummings, P.T.; Burchell, T.D.; More, K.L. Effect of Temperature on the Adsorption of Water in Porous Carbons. *Langmuir* **2005**, *21*, 9457-9467, doi:10.1021/la051120t.
238. Wang, Z.; Jiang, X.; Pan, M.; Shi, Y. Nano-Scale Pore Structure and Its Multi-Fractal Characteristics of Tight Sandstone by N2 Adsorption/Desorption Analyses: A Case Study of Shihezi Formation from the Sulige Gas Filed, Ordos Basin, China. *Minerals* **2020**, *10*, doi:10.3390/min10040377.
239. Rey-Raap, N.; Angel Menéndez, J.; Arenillas, A. RF xerogels with tailored porosity over the entire nanoscale. *Microporous Mesoporous Mater.* **2014**, *195*, 266-275, doi:https://doi.org/10.1016/j.micromeso.2014.04.048.

240. Du, X.; Zhan, P.; Gan, N.; Cao, Y.; Li, T.; Sang, W.; Wang, L. Highly Selective Molecular Recognition and Ultrasensitive Detection of 3,4-dichloroaniline Based on Molecularly Imprinted Sol-Gel Film Combined with Multi-Walled Carbon Nanotubes. *J. Electrochem. Soc.* **2013**, *160*, H742-H748, doi:10.1149/2.082310jes.
241. Thomas, O.; Brogat, M. Chapter 12 - UV Spectra Library. In *UV-Visible Spectrophotometry of Water and Wastewater (Second Edition)*, Thomas, O., Burgess, C., Eds. Elsevier: 2017; https://doi.org/10.1016/B978-0-444-63897-7.00012-3pp. 379-517.
242. Cary 5000 UV-Vis Spectrophotometer. Availabe online: https://www.agilent.com/en/product/molecular-spectroscopy/uv-vis-uv-vis-nir-spectroscopy/uv-vis-uv-vis-nir-systems/cary-5000-uv-vis-nir (accessed on 11/08/2021).
243. McKay, G.; Blair, H.S.; Gardner, J.R. Adsorption of dyes on chitin. I. Equilibrium studies. *J. Appl. Polym. Sci.* **1982**, *27*, 3043-3057, doi:https://doi.org/10.1002/app.1982.070270827.
244. Chen, H.; Zhao, J.; Wu, J.; Dai, G. Isotherm, thermodynamic, kinetics and adsorption mechanism studies of methyl orange by surfactant modified silkworm exuviae. *J. Hazard. Mater.* **2011**, *192*, 246-254, doi:https://doi.org/10.1016/j.jhazmat.2011.05.014.
245. Iyer, K.; Kunju, A. Extension of Harkins—Jura adsorption isotherm to solute adsorption. *Colloids and surfaces* **1992**, *63*, 235-240.
246. Tomohiko, S. On the Harkins—Jura's Adsorption Isotherm and Its Constants. *Bull. Chem. Soc. Jpn.* **1953**, *26*, 213-218, doi:10.1246/bcsj.26.213.
247. Bakhaeva, L.P.; Vasilyeva, G.; Surovtseva, E.; Mukhin, V. Microbial Degradation of 3,4-Dichloroaniline Sorbed by Activated Carbon. *Microbiology* **2004**, *70*, 277-284.
248. Szczepanik, B.; Słomkiewicz, P.; Garnuszek, M.; Czech, K. Adsorption of chloroanilines from aqueous solutions on the modified halloysite. *Applied Clay Science* **2014**, *101*, 260-264, doi:https://doi.org/10.1016/j.clay.2014.08.013.
249. Polati, S.; Gosetti, F.; Gianotti, V.; Gennaro, M.C. Sorption and Desorption Behavior of Chloroanilines and Chlorophenols on Montmorillonite and Kaolinite. *Journal of Environmental Science and Health, Part B* **2006**, *41*, 765-779, doi:10.1080/03601230600805774.
250. van Duin, A.C.T.; Dasgupta, S.; Lorant, F.; Goddard, W.A. ReaxFF: A Reactive Force Field for Hydrocarbons. *The Journal of Physical Chemistry A* **2001**, *105*, 9396-9409, doi:10.1021/jp004368u.

Appendices

Appendix A – RF Sol-Gel Initial Solution Compositions

Table A.1: Initial Solution Composition for Na_2CO_3 Gels

R/C Ratio	Resorcinol (g)	Formaldehyde (g)	Na_2CO_3 (g)
100	7.7170	4.2087	0.07428
200	7.7409	4.3318	0.03726
300	7.7490	4.2262	0.02486
400	7.7530	4.2284	0.01866
500	7.7554	4.2297	0.01493
600	7.7570	4.2306	0.01244

Table A.2: Initial Solution Composition for Na_2CO_3/$NaHCO_3$ Mixture Gels – R/C100 Equivalent

Na_2:NaH Na^+ Source Ratio	Resorcinol (g)	Formaldehyde (g)	Na_2CO_3 (g)	$NaHCO_3$ (g)
100:0	7.7170	4.2087	0.07428	-
75:25	7.7030	4.2049	0.05566	0.02941
50:50	7.6961	4.2011	0.03707	0.05877
25:75	7.6961	4.1973	0.01852	0.08807
0:100	7.6891	4.1935	-	0.11733

Table A.3: Initial Solution Composition for Na_2CO_3/$NaHCO_3$ Mixture Gels – R/C300 Equivalent

Na_2:NaH Na^+ Source Ratio	Resorcinol (g)	Formaldehyde (g)	Na_2CO_3 (g)	$NaHCO_3$ (g)
100:0	7.7490	4.2262	0.02486	-
75:25	7.7466	4.2249	0.01864	0.00985
50:50	7.7443	4.2236	0.01242	0.01969
25:75	7.7419	4.2223	0.00621	0.02953
0:100	7.7396	4.2211	-	0.03937

Table A.4: Initial Solution Composition for $NaHCO_3$/NH_4CO_3 Mixture Gels – R/C100 Equivalent

NaH:$NH_4HCO_3^-$ Source Ratio	Resorcinol (g)	Formaldehyde (g)	$NaHCO_3$ (g)	NH_4HCO_3 (g)
100:0	7.7269	4.2141	0.05895	-
75:25	7.7275	4.2144	0.04422	0.01387
50:50	7.7280	4.2148	0.02948	0.02774
25:75	7.7286	4.2151	0.01474	0.04162
0:100	7.7291	4.2154	-	0.05549

Table A.5: Initial Solution Composition for $NaHCO_3/NH_4CO_3$ Mixture Gels – R/C300 Equivalent

$NaH:NH_4$ HCO_3^- Source Ratio	**Resorcinol (g)**	**Formaldehyde (g)**	**$NaHCO_3$ (g)**	**NH_4HCO_3 (g)**
100:0	7.7523	4.2280	0.01972	-
75:25	7.7525	4.2281	0.01479	0.00464
50:50	7.7527	4.2282	0.00986	0.00928
25:75	7.7529	4.2283	0.00493	0.01392
0:100	7.7530	4.2284	-	0.01855

Appendix B – Preliminary Results

SEM and TEM RF Gel Analysis

SEM and TEM analysis was carried out on RF gel samples at Angstrom Laboratory, Uppsala University, Sweden, in collaboration with Farnaz Ghajeri from Svenska Aerogel AB. The images obtained varied in quality, and due to time constraints of the working trip, further analysis could not be carried out. Future analysis using both methods could provide valuable insight into the structure and appearance of the RF gels, including a comparison of cluster size and structural complexity with varying catalyst concentration.

B.1 SEM Analysis

Carl Zeiss Merlin Field Emission Scanning Electron Microscope (FE-SEM) equipment was used to carry out the SEM analysis, located within the Angstrom Laboratory at Uppsala University. To prepare samples for SEM analysis, chunks of RF xerogel were ground down into finer pieces using a mortar and pestle. Following this, circular carbon tape was placed onto a metal sample holder (Figure B.1.1) and the ground RF gel pieces were gently poured on top, sticking to the surface of the carbon tape, after which point a strip of aluminium tape was added across the sample holder to minimise charging during analysis.

Figure B.1.1: Labelled image of the sample holder and sample wheel used for SEM analysis.

Each sample holder was positioned on the sample wheel, which was then placed into the sample port of the Merlin FE-SEM for analysis. The magnification and position was altered until a clear image of the sample was obtained, the results of which are shown in Figure B.1.2 for R/C 600 gels, which was the gel that produced the highest quality images.

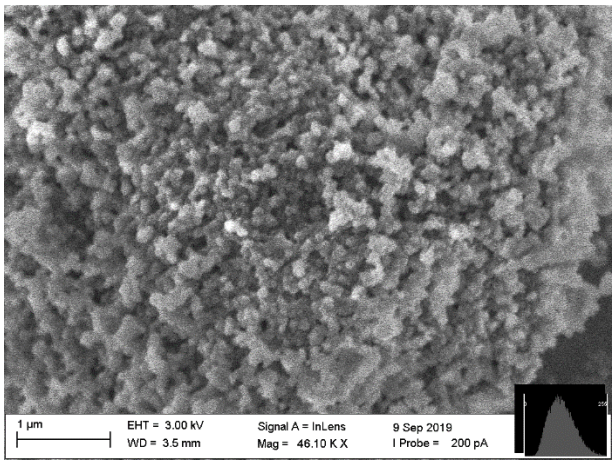

Figure B.1.2(a): SEM image of R/C 600 RF xerogel at 46.10 K X magnification

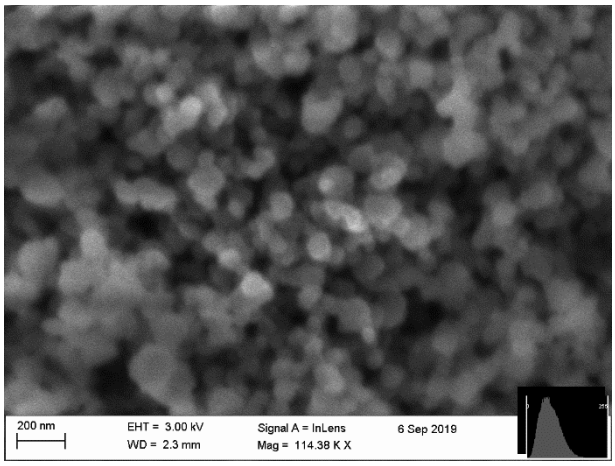

Figure B.1.2(b): SEM image of R/C 600 RF xerogel at 114.38 K X magnification

B.2 TEM Analysis

Thermo Fisher Scientific Titan Themis 200, once again located within the Angstrom Laboratory at Uppsala University, was used to carry out the TEM analysis of RF gels in this work. To begin, the RF gel was ground into a fine powder using a mortar and pestle and added to 5 mL of ethanol which had been pipetted into a plastic screw top sample tube. The tube was shaken to help disperse the powder before being placed into an ultrasonic bath for 10 minutes to further enhance dispersion. Following this, one drop of the sample was deposited on a 3 mm diameter TEM sample grid and left to dry overnight at room temperature. The next day, the grid was placed onto a sample holder chamber that was

inserted directly into the Titan Themis 200 for analysis. The magnification and grid position was altered until a clear image of the sample was achieved, the results of which are shown in Figures B.2.1 and B.2.2 for samples synthesised at R/C 600 and R/C 300, respectively.

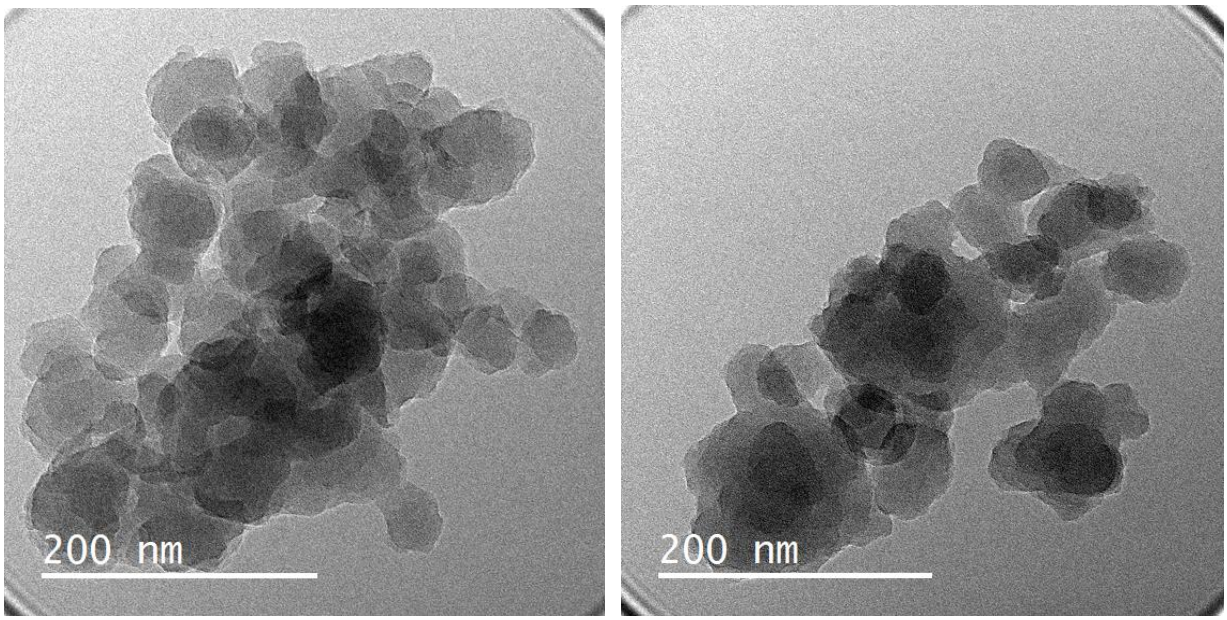

Figure B.2.2: TEM image of R/C 600 RF xerogel (a) first sample and (b) second sample

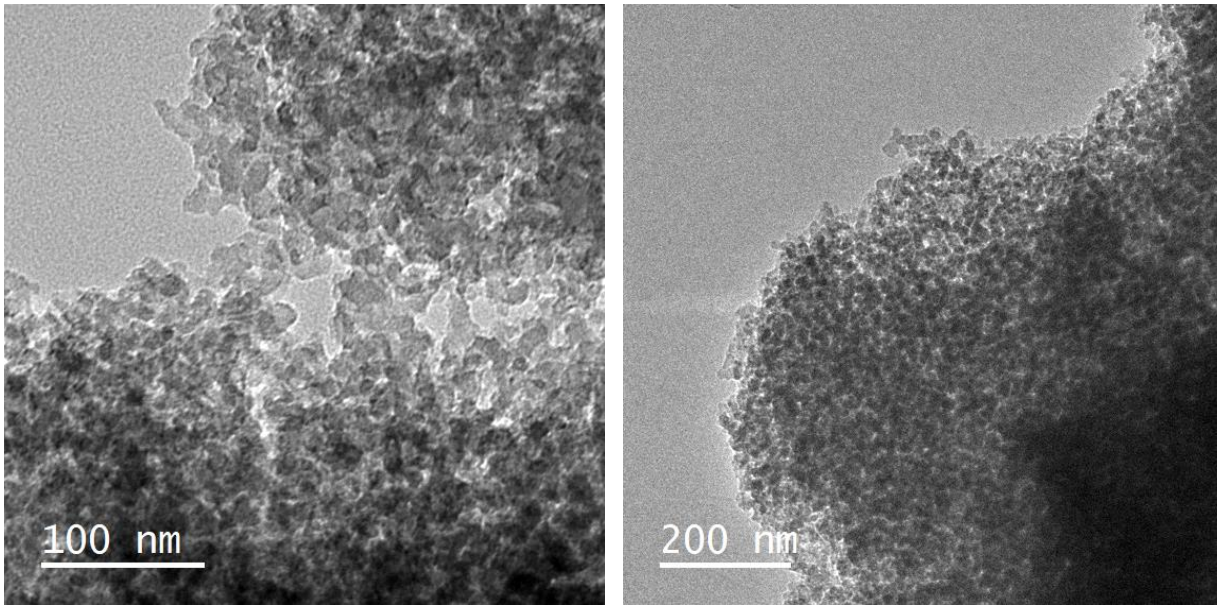

Figure B.2.2: TEM image of R/C 300 RF xerogel (a) first sample and (b) second sample

B.3 Summary

In the preliminary results obtained from both SEM and TEM analysis, the spherical clusters that comprise the interconnected structure of the gels can be observed, which is the basis of

the simulated structures produced from the 3D Cluster Formation model developed through this work. From the TEM results shown in Figures B.2.1 and B.2.2, the difference in cluster size between R/C 600 and R/C 300 gels can be observed, agreeing with results both from literature and from the simulated structures presented within this work, confirming that lower R/C ratios (and therefore higher catalyst concentrations) produce gels comprising of smaller primary clusters. As discussed in earlier chapters, this is attributed to the increased number of "cluster seeds" present as a result of the increased deprotonation of resorcinol molecules during the RF addition reaction when a higher concentration of catalyst is added. This is valuable for the validation of the model, however, a more thorough analysis of the full range of R/C ratios would be required for a more comprehensive comparison to simulated structures, including an approximate measurement of cluster size for each using imaging analysis software if sufficiently clear images are obtained.

Appendix C – Computational Codes

C.1 3D Cluster Formation and Growth

```
PROGRAM ClusterFormation
    IMPLICIT NONE

    !program version that places activated and normal monomers on lattice, then lets both monomers and clusters diffuse using
    !kinetic Monte Carlo (KMC) algorithm, probability of diffusion is reversly proportional to entity size, cluster links are stored in SuperCluster lattice,
    !size of individual clusters is stored in ClusterSize and size of aggregates in FinalSize
    INTEGER, PARAMETER :: Nlat=100, dp=selected_real_kind(15, 307)
    !Nlat=size of lattice, dp=for real number precision (up to 15 significant digits and 10^(+-307))
    INTEGER ::  Nmax, Nact, Nmon
    !Nmax=number of all particles (monomers+clusters); Nact=number of activated monomers (activated monomers according to a percentage estimated from literature)
    REAL :: solid, percentage, Iav
    !solid=solid content (in experiments we use a solid content of 20% so then solid = 0.2); percentage=percentage of activated monomers, Iav=average cluster size
    INTEGER, ALLOCATABLE :: iCluster(:,:), jCluster(:,:), kCluster(:,:), iMonomer(:), jMonomer(:), kMonomer(:)
    !iCluster, jCluster=positions of points occupied by clusters, (Cluster ID, position); iMonomer, jMonomer=position of monomer;
    !Monomer=monomer distribution lattice; Cluster=cluster distribution lattice

    INTEGER, ALLOCATABLE :: ClusterSize(:), ClusterCounter(:), FinalSize(:), SuperCluster(:,:), Monomer(:,:,:), Cluster(:,:,:)
    !ClusterSize=stores size of each cluster; ClusterCounter=stores position counter for drawing clusters; FinalSize=stores size of aggregates
    !SuperCluster=stores cluster links, where if (1,2)=1 1 and 2 are linked, otherwise = 0
    REAL(KIND=dp), ALLOCATABLE :: MCSum(:)
    !array of sums for KMC
    INTEGER :: MonDiff, FreeMon, i,j, k, ios, ClusterSum, MonomerSum, SizeSum, s, p, r, No, current, UnoccSite
    !MonDiff=monomer to diffuse; FreeMon=number of free monomers; i,j,k=lattice coordinates; ios=for opening files; ClusterSum=sum of positions occupied by clusters on lattice
    !MonomerSum=sum of monomers on the lattice in the beginning of a run; SizeSum=sum of cluster sizes; s,p,r=solid, percentage, run
    INTEGER :: rnd(1:8), WorkMon, WorkCluster, MonAbs, iList(Nlat*Nlat*Nlat), jList(Nlat*Nlat*Nlat)
    INTEGER :: kList(Nlat*Nlat*Nlat), move, ID, Clusters
    !rnd=for random numbers; WorkMon - a placeholder for the monomer you're currently working with,WorkCluster=monomer/cluster currently working with;
    !MonAbs=monomers being absorbed by growing cluster(for attach subroutine)
    !iList, jList=i and j coordinates for list subroutine and cluster drawing, move=for diffusion, ID=Cluster ID, Clusters=number of remaining clusters
    INTEGER, DIMENSION(24) :: seed
    !seed=for random number generator
    REAL(KIND=dp) :: ireal, jreal, kreal, MCmove, time, time_monomer, time_final
    !ireal, jreal,kreal=for random number generator, MCmove=used for KMC, time=measures time for KMC Kinetic Monte Carlo
    CHARACTER(LEN=26) :: ClusterFile, SizeFile, iFile, jFile, kfile, TimeFile, FinalFile, SummaryFile
    !file names of the cluster distribution file and files storing additional information(cluster size, i and j coordinates of clusters)
    LOGICAL :: coalesce, last     !used to recalculate MCSum only when it changes due to a coalescent event


    WRITE(25,*) '-------- Program started --------'
    !inform user the program has started

    CALL list(Nlat, iList, jList, kList)
        !create list of positions for drawing clusters

    r = replacerun
    seed = r*100                                !seed for random number generator
    s = replacesolid                            !run over solid content 0.1-0.9
    solid = 1.0*s/1000                  !changed for lower increment
```

```
62        p = replacepercentage                    !run over 1-3% activated monomers
63        percentage = (1.0*p)/1000
64
65        Nmax = NINT(solid*Nlat*Nlat*Nlat) !NINT is rounding to the nearest integer. Nmax is the maximum number of
66    monomers (the solid content * the number of lattice points).
67        Nact = NINT(percentage*Nmax) !Nact is the activated monomers (the percentage activated * the maximum number)
68        !calculate current values of number of particles and activated monomers
69        FreeMon = Nmax-Nact !Free Monomers are the maximum number of monomers  - the activated monomers
70        Nmon = FreeMon !Using Nmon in place of FreeMon
71
72        ios = 0
73
74        ALLOCATE( iCluster(Nact,Nlat*Nlat*2), jCluster(Nact,Nlat*Nlat*2), kCluster(Nact,Nlat*Nlat*2),
75    iMonomer(FreeMon), &
76              jMonomer(FreeMon), kMonomer(Freemon), Monomer(Nlat,Nlat,Nlat), Cluster(Nlat,Nlat,Nlat),
77    ClusterSize(Nact), &
78             ClusterCounter(Nact), SuperCluster(Nact,Nact), FinalSize(Nact), MCSum(Nmax), STAT=ios )
79
80        IF (ios/=0) THEN
81            WRITE(25,*) 'Error allocating arrays'
82            STOP
83        END IF
84
85
86        WRITE(ClusterFile,'(A8,F5.3,A1,F5.3,A1,I1,A4)') 'Cluster_', solid, '_', percentage, '_', r, '.dat'
87        WRITE(25,*) ClusterFile
88        WRITE(SizeFile,'(A5,F5.3,A1,F5.3,A1,I1,A4)') 'Size_', solid, '_', percentage, '_', r, '.dat'
89        WRITE(iFile,'(A5,F5.3,A1,F5.3,A1,I1,A4)') 'iPos_', solid, '_', percentage, '_', r, '.dat'
90        WRITE(jFile,'(A5,F5.3,A1,F5.3,A1,I1,A4)') 'jPos_', solid, '_', percentage, '_', r, '.dat'
91        WRITE(kFile,'(A5,F5.3,A1,F5.3,A1,I1,A4)') 'kPos_', solid, '_', percentage, '_', r, '.dat'
92        WRITE(TimeFile,'(A5,F5.3,A1,F5.3,A1,I1,A4)') 'Time_', solid, '_', percentage, '_', r, '.dat'
93        WRITE(FinalFile,'(A6,F5.3,A1,F5.3,A1,I1,A4)') 'Final_', solid, '_', percentage, '_', r, '.dat'
94        WRITE(SummaryFile,'(A4,F5.3,A1,F5.3,A1,I1,A4)') 'DEL_', solid, '_', percentage, '_', r, '.dat'
95        !create file names
96
97        ios = 0
98        OPEN(8, FILE=ClusterFile, STATUS='REPLACE', IOSTAT=ios)
99        IF (ios/=0) THEN
100           WRITE(25,*) 'Error opening file Cluster.dat', ios
101           STOP
102       END IF
103
104       ios = 0
105       OPEN(11, FILE=SizeFile, STATUS='REPLACE', IOSTAT=ios)
106       IF (ios/=0) THEN
107           WRITE(25,*) 'Error opening file Size.dat', ios
108           STOP
109       END IF
110       !open a file for writing cluster size distribution
111
112       ios = 0
113       OPEN(12, FILE=iFile, STATUS='REPLACE', IOSTAT=ios)
114       IF (ios/=0) THEN
115           WRITE(25,*) 'Error opening file iPos.dat', ios
116           STOP
117       END IF
118       !open a file for writing i coordinates of clusters
119
120       ios = 0
121       OPEN(13, FILE=jFile, STATUS='REPLACE', IOSTAT=ios)
122       IF (ios/=0) THEN
123           WRITE(25,*) 'Error opening file jPos.dat', ios
124           STOP
125       END IF
126       !open a file for writing j coordinates of clusters
127
128       OPEN(16, FILE=kFile, STATUS='REPLACE', IOSTAT=ios)
129       IF (ios/=0) THEN
130           WRITE(25,*) 'Error opening file kPos.dat', ios
```

```
131         STOP
132     END IF
133     !open a file for writing k coordinates of clusters
134
135     ios = 0
136     OPEN(14, FILE=TimeFile, STATUS='REPLACE', IOSTAT=ios)
137     IF (ios/=0) THEN
138         WRITE(25,*) 'Error opening file Super.dat', ios
139         STOP
140     END IF
141     !open a file for writing supercluster lattice that stores cluster links
142
143      !set monomer and activated monomer density to 0 for whole lattice, ie. reset the lattice
144     Monomer = 0
145     Cluster = 0
146     ClusterCounter = 1
147     current = 0
148     SuperCluster = 0        !reset SuperCluster lattice and link clusters with themselves
149     DO i=1,Nact
150         SuperCluster(i,i) = 1
151     END DO
152     FinalSize = 1           !set size for all clusters to 1
153     iCluster = 0
154     jCluster = 0            !reset cluster coordinates
155     kCluster = 0
156     MCSum(1) = 1            !Have MCSum value start at 1 for the first point (1)
157     DO i=2,Nmax             !calculate MCSum at the beginning for KMC
158         MCSum(i) = MCSum(i-1) + 1
159     END DO
160     time = 0                !reset time to 0
161     WRITE(14,'(5A20)') 'Time elapsed', 'Remaining monomers', 'Number of clusters', 'No', 'current'
162
163
164     CALL RANDOM_SEED(PUT=seed)
165
166     !place activated monomers on lattice
167     WorkMon = Nact !WorkMon is set equal to the number of activated monomers
168     DO WHILE (WorkMon > 0) !Do this loop for as long as the number of activated monomers is greater than zero
169         CALL RANDOM_NUMBER(ireal)
170         CALL RANDOM_NUMBER(jreal)
171         CALL RANDOM_NUMBER(kreal)
172         iCluster(WorkMon,1) = INT(Nlat*ireal)+1
173         jCluster(WorkMon,1) = INT(Nlat*jreal)+1
174         kCluster(WorkMon,1) = INT(Nlat*kreal)+1
175         !get a random position on lattice by generating a random number for ireal etc, then multiplying it by
176 the number of lattice points +1
177         !and converting it to integer type. This has the dimensions of the WorkMon value (ie the number of
178 activated monomers) and point 1.
179
180         IF (Cluster(iCluster(WorkMon,1),jCluster(WorkMon,1), kCluster(WorkMon,1))==0) THEN
181             Cluster(iCluster(WorkMon,1),jCluster(WorkMon,1), kCluster(WorkMon,1)) = WorkMon !put cluster number
182 on lattice to distinguish clusters
183             ClusterSize(WorkMon) = 1   !make the cluster size 1 as a start
184
185             OPEN(25,FILE='Centre.dat')
186             WRITE (25,*) Nact, WorkMon, INT(Nlat*ireal)+1, INT(Nlat*jreal)+1, INT(Nlat*kreal)+1
187
188
189             WorkMon = WorkMon - 1
190             !if the position is empty (IE IF i,j,k is 0), place the monomer and move the counter to next monomer
191 (ie WorkMon-1)
192         END IF
193     END DO
194     CLOSE(25)
195
196     !place monomers on lattice
197     WorkMon = FreeMon
198     DO WHILE (WorkMon > 0) !Do this loop for as long as the number of activated monomers is greater than zero
199         CALL RANDOM_NUMBER(ireal)
```

```
200           CALL RANDOM_NUMBER(jreal)
201           CALL RANDOM_NUMBER(kreal)
202           iMonomer(WorkMon) = INT(Nlat*ireal)+1
203           jMonomer(WorkMon) = INT(Nlat*jreal)+1
204           kMonomer(WorkMon) = INT(Nlat*kreal)+1
205            !get a random position on lattice, same as above
206
207           IF ((Cluster(iMonomer(WorkMon),jMonomer(WorkMon),kMonomer(WorkMon))==0) .AND. &
208               (Monomer(iMonomer(WorkMon),jMonomer(WorkMon),kMonomer(WorkMon))==0)) THEN
209              Monomer(iMonomer(WorkMon),jMonomer(WorkMon),kMonomer(WorkMon)) = &
210                  Monomer(iMonomer(WorkMon),jMonomer(WorkMon),kMonomer(WorkMon)) + 1
211              WorkMon = WorkMon - 1
212            !if the position is not occupied (either by activated or normal monomer), place the monomer and move
213    the counter, similar to above
214           END IF
215       END DO
216
217       coalesce = .TRUE.       !set to true, so that first time cluster sum is calculated
218       No = 1
219       current = Nact
220       last = .TRUE.
221
222       !loop until there is only one cluster left
223       mainloop:    DO
224           !check if there's only one cluster left, if yes, exit the main loop and finalise the run
225           IF (coalesce) THEN
226              Clusters = 0
227              endloop: DO i=1,Nact
228                 IF (FinalSize(i)>0) THEN
229                     Clusters = Clusters + 1 !Increase the number of cluster by 1 if the finalsize(i)>0
230                 END IF
231              END DO endloop
232              WRITE(25,*) Clusters
233              IF ((Clusters==20) .AND. (last)) THEN
234                 current = 20
235                 last = .FALSE.
236              END IF
237              IF ((Clusters==current) .AND. (Clusters>20)) THEN
238                 WRITE(14,'(F20.2,4I20)') time, FreeMon, Clusters, No, current
239                 current = current - Nact/100
240                 No = No + 1
241              ELSEIF ((Clusters==current) .AND. (Clusters .LE. 20)) THEN
242                 WRITE(14,'(F20.2,4I20)') time, FreeMon, Clusters, No, current
243                 current = current - 1
244                 No = No + 1
245              END IF
246           END IF
247
248           IF ((Clusters==1) .AND. (FreeMon<1)) EXIT mainloop
249           coalesce = .FALSE.
250
251           !get a random number within MCSum
252           CALL RANDOM_NUMBER(ireal)
253           MCmove = ireal * MCSum(Nmax)
254
255           MCfind: DO i=1,Nmax
256              IF (MCSum(i)>MCmove) EXIT MCfind
257           END DO MCfind
258
259
260           IF (i .LE. Nact) THEN   !move a cluster
261              WorkCluster = i
262              CALL diffuse_cluster(Cluster, Nlat, Nact, WorkCluster, iCluster, jCluster, kCluster, SuperCluster,
263    ClusterSize)
264
265              DO j=1,Nact
266                 IF (SuperCluster(WorkCluster,j)==1) THEN
267                     CALL HK_scan(j, Nact, Nlat, Cluster, ClusterSize, iList, jList, kList, &
268                         iCluster, jCluster, kCluster, SuperCluster, coalesce)
```

```
                END IF
            END DO
        ELSE                    !move a monomer
            WorkMon = i - Nact
            CALL diffuse_monomer(Monomer, Nlat, Nmon, iMonomer, jMonomer, kMonomer, WorkMon)
            !diffuse the monomer one step on lattice using diffuse subroutine
            IF (Cluster(iMonomer(WorkMon),jMonomer(WorkMon), kMonomer(WorkMon))/=0) THEN
                !if there is a cluster at the position, call attach subroutine and make the monomer stick to the
cluster

                CALL attach(iMonomer(WorkMon), jMonomer(WorkMon), kMonomer(WorkMon), Nlat, Nact, &
                    iCluster, jCluster, kCluster, Cluster, &
                    ClusterSize, ClusterCounter, iList, jList, kList, FinalSize)
                Monomer(iMonomer(WorkMon),jMonomer(WorkMon),kMonomer(WorkMon)) = 0
                !remove the absorbed monomer from the lattice

ios = 0
DO i=1,Nlat
        DO j=1,Nlat
            DO k=1,Nlat
            IF (Cluster(i,j,k)/=0)    ios = ios + 1
            END DO
        END DO
END DO
WRITE(25,*) ios, FreeMon


                coalesce = .TRUE.

                !check if the grown cluster touched another cluster
                WorkCluster = Cluster(iMonomer(WorkMon),jMonomer(WorkMon),kMonomer(WorkMon))
                CALL HK_scan(WorkCluster, Nact, Nlat, Cluster, ClusterSize, iList, jList, kList, &
                    iCluster, jCluster, kCluster, SuperCluster, coalesce)

                iMonomer(WorkMon) = 0
                jMonomer(WorkMon) = 0
                kMonomer(WorkMon) = 0
                FreeMon = FreeMon - 1
            END IF
        END IF

        !advance the clock
        CALL RANDOM_NUMBER(ireal)
        time = time - (LOG(ireal)/MCSum(Nmax))
        IF (FreeMon==0) THEN
            time_monomer = time
            FreeMon = -1
        END IF

        IF (coalesce) THEN
            DO i=1,Nmax
                IF (i==1) THEN  !set the probability for first cluster depending on its size
                    IF (FinalSize(1)>0) THEN
                        MCSum(i) = 1/(REAL(FinalSize(i)))
                    ELSE    !if the value is negative, set the probability to move to 0, so cluster is counted
only once
                        MCSum(i) = 0
                    END IF
                ELSEIF ((i .LE. Nact) .AND. (i>1)) THEN !set probabilities for the rest of clusters
                    IF (FinalSize(i)>0) THEN
                        MCSum(i) = MCSum(i-1) + 1/(REAL(FinalSize(i)))
                    ELSE
                        MCSum(i) = MCSum(i-1)
                    END IF
                ELSE                                    !set probabilities for monomers
                    IF (iMonomer(i-Nact)/=0) THEN
                        MCSum(i) = MCSum(i-1) + 1
                    ELSE
                        MCSum(i) = MCSum(i-1)
```

```
                    END IF
                END IF
            END DO
        END IF

    END DO mainloop

    CALL plotcluster(Cluster,Nlat, FreeMon)
        !write out cluster distribution lattice to a file

    time_final = time
DO i=1,Nact
    WRITE(11,'(X,1000I6)') (ClusterSize(i))
    WRITE(12,*) ((iCluster(i,j)), j=1,Nlat*Nlat*2)
    WRITE(13,*) ((jCluster(i,j)), j=1,Nlat*Nlat*2)
    WRITE(16,*) ((kCluster(i,j)), j=1,Nlat*Nlat*2)

 END DO

    Iav = 0
    DO i=1,Nact
        IF (FinalSize(i)>0) THEN
            Iav = Iav + REAL(FinalSize(i))**2
        END IF
    END DO

    Iav = Iav/(1.0*solid*1000*1000)
    Iav = Iav - REAL(MAXVAL(FinalSize))**2/(1.0*solid*1000*1000)

    CLOSE(8)
    DO i=11,16
        CLOSE(i)
    END DO

    ios = 0
    DEALLOCATE( iCluster, jCluster, kCluster, iMonomer, jMonomer, kMonomer, Monomer, Cluster, ClusterSize, &
        ClusterCounter, SuperCluster, FinalSize, MCSum, STAT=ios )
    IF (ios/=0) THEN
        WRITE(25,*) 'Error deallocating arrays'
        STOP
    END IF


    WRITE(25,*) '-------- Program finished --------'

CONTAINS
    SUBROUTINE diffuse_monomer(Monomer, Nlat, Nmon, iMonomer, jMonomer, kMonomer, MonDiff)
        !subroutine to make monomers diffuse on a lattice by one random step
        IMPLICIT NONE
        INTEGER, INTENT(IN) :: Nlat, Nmon, MonDiff
        !Nlat=size of lattice;Nmax=max No of monomers; MonDiff=monomer to diffuse
        INTEGER, INTENT(INOUT) :: iMonomer(Nmon), jMonomer(Nmon), kMonomer(Nmon), Monomer(Nlat,Nlat,Nlat)
        !iMonomer,jMonomer=position of monomer; Monomer=monomer distribution lattice
        INTEGER :: i, j, k, move



        i = iMonomer(MonDiff)
        j = jMonomer(MonDiff)
        k = kMonomer(MonDiff)
        !get the position of monomer to diffuse into dummy variables

        !make a random step up/down/left/right/back/forward
        move=INT(6*RAND())+1
        SELECT CASE (move)
            CASE (1)
                i = i + 1
            CASE (2)
                i = i - 1
```

```
            CASE (3)
                j = j + 1
            CASE (4)
                j = j - 1
            CASE (5)
                k = k + 1
            CASE (6)
                k = k - 1
        END SELECT

        !periodic boundary
        IF (i > Nlat)  i = i - Nlat
        IF (i < 1)     i = i + Nlat
        IF (j > Nlat)  j = j - Nlat
        IF (j < 1)     j = j + Nlat
        IF (k > Nlat)  k = k - Nlat
        IF (k < 1)     k = k + Nlat

        !check if the new position is empty
        IF (Monomer(i,j,k)==0) THEN  !if there is no monomer at new site, make the diffusion step
            Monomer(iMonomer(MonDiff),jMonomer(MonDiff),kMonomer(MonDiff)) = &
                Monomer(iMonomer(MonDiff),jMonomer(MonDiff),kMonomer(MonDiff)) - 1
            !remove the monomer from the original position
            Monomer(i,j,k) = Monomer(i,j,k) + 1
            !place it in the new position

            iMonomer(MonDiff) = i
            jMonomer(MonDiff) = j
            kMonomer(MonDiff) = k
           !set new position for the monomer

        END IF

    END SUBROUTINE diffuse_monomer

    SUBROUTINE diffuse_cluster(Cluster, Nlat, Nact, ClusterDiff, iCluster, jCluster, kCluster, SuperCluster,
ClusterSize)
        !subroutine to make clusters diffuse on a lattice by one step
        IMPLICIT NONE
        INTEGER, INTENT(IN) :: Nlat, Nact, ClusterDiff
        !Nlat=size of lattice,Nmax=max No of monomers, ClusterDiff=cluster to diffuse
        INTEGER, INTENT(IN) :: SuperCluster(Nact,Nact), ClusterSize(Nact)
        INTEGER, INTENT(INOUT) :: Cluster(Nlat,Nlat,Nlat), iCluster(Nact,Nlat*Nlat*2),
jCluster(Nact,Nlat*Nlat*2), &
         kCluster(Nact,Nlat*Nlat*2)
        !iCluster,jCluster,kCluster=positions of cluster sites, Cluster=cluster distribution lattice
        INTEGER :: i, j, k, move
        INTEGER :: ios, ClusterNo
        !dummy variables

        !remove cluster(s) from lattice
        DO i=1,Nact
            IF (SuperCluster(ClusterDiff,i)==1) THEN
                DO j=1,ClusterSize(i)
                    Cluster(iCluster(i,j),jCluster(i,j),kCluster(i,j)) = 0
                END DO
            END IF
        END DO

        move=INT(6*RAND())+1
        SELECT CASE (move)
            CASE (1)
                outer1: DO i=1,Nact                              !loop through all clusters
                    IF (SuperCluster(ClusterDiff,i)==1) THEN
                        inner1: DO j=1,Nlat*Nlat*2                    !loop through all positions occupied by
current cluster
                            IF (iCluster(i,j)==0) EXIT inner1   !loop until all the positions have been changed
                            iCluster(i,j) = iCluster(i,j) + 1
                            IF (iCluster(i,j) > Nlat)  iCluster(i,j) = iCluster(i,j) - Nlat
```

```
                        Cluster(iCluster(i,j),jCluster(i,j),kCluster(i,j)) = i  !put cluster back on lattice
                    END DO inner1
                END IF
            END DO outer1
        CASE (2)
            outer2: DO i=1,Nact                             !loop through all clusters
                IF (SuperCluster(ClusterDiff,i)==1) THEN    !for clusters connected to diffusing cluster
                    inner2: DO j=1,Nlat*Nlat*2      !loop through all positions occupied by current cluster
                        IF (iCluster(i,j)==0) EXIT inner2   !loop until all the positions have been changed
                        iCluster(i,j) = iCluster(i,j) - 1
                        IF (iCluster(i,j) < 1)      iCluster(i,j) = iCluster(i,j) + Nlat
                        Cluster(iCluster(i,j),jCluster(i,j),kCluster(i,j)) = i
                    END DO inner2
                END IF
            END DO outer2
        CASE (3)
            outer3: DO i=1,Nact                             !loop through all clusters
                IF (SuperCluster(ClusterDiff,i)==1) THEN    !for clusters connected to diffusing cluster
                    inner3: DO j=1,Nlat*Nlat*2      !loop through all positions occupied by current cluster
                        IF (jCluster(i,j)==0) EXIT inner3   !loop until all the positions have been changed
                        jCluster(i,j) = jCluster(i,j) + 1
                        IF (jCluster(i,j) > Nlat)   jCluster(i,j) = jCluster(i,j) - Nlat
                        Cluster(iCluster(i,j),jCluster(i,j),kCluster(i,j)) = i
                    END DO inner3
                END IF
            END DO outer3
        CASE (4)
            outer4: DO i=1,Nact                             !loop through all clusters
                IF (SuperCluster(ClusterDiff,i)==1) THEN    !for clusters connected to diffusing cluster
                    inner4: DO j=1,Nlat*Nlat*2      !loop through all positions occupied by current cluster
                        IF (jCluster(i,j)==0) EXIT inner4   !loop until all the positions have been changed
                        jCluster(i,j) = jCluster(i,j) - 1
                        IF (jCluster(i,j) < 1)      jCluster(i,j) = jCluster(i,j) + Nlat
                        Cluster(iCluster(i,j),jCluster(i,j),kCluster(i,j)) = i
                    END DO inner4
                END IF
            END DO outer4
        CASE (5)
            outer5: DO i=1,Nact                             !loop through all clusters
                IF (SuperCluster(ClusterDiff,i)==1) THEN    !for clusters connected to diffusing cluster
                    inner5: DO j=1,Nlat*Nlat*2      !loop through all positions occupied by current cluster
                        IF (kCluster(i,j)==0) EXIT inner5   !loop until all the positions have been changed
                        kCluster(i,j) = kCluster(i,j) + 1
                        IF (kCluster(i,j) > Nlat)   kCluster(i,j) = kCluster(i,j) - Nlat
                        Cluster(iCluster(i,j),jCluster(i,j),kCluster(i,j)) = i
                    END DO inner5
                END IF
            END DO outer5
        CASE (6)
            outer6: DO i=1,Nact
                IF (SuperCluster(ClusterDiff,i)==1) THEN    !for clusters connected to diffusing cluster
                    inner6: DO j=1,Nlat*Nlat*2      !loop through all positions occupied by current cluster
                        IF (kCluster(i,j)==0) EXIT inner6   !loop until all the positions have been changed
                        kCluster(i,j) = kCluster(i,j) - 1
                        IF (kCluster(i,j) < 1)      kCluster(i,j) = kCluster(i,j) + Nlat
                        Cluster(iCluster(i,j),jCluster(i,j),kCluster(i,j)) = i
                    END DO inner6
                END IF
            END DO outer6
    END SELECT

END SUBROUTINE diffuse_cluster


    SUBROUTINE attach(i, j, k, Nlat, Nact, iCluster, jCluster, kCluster, Cluster, ClusterSize, ClusterCounter,
iList, jList, &
        kList, FinalSize)
        !subroutine to attach a monomer to a cluster and draw the cluster on Cluster lattice
        IMPLICIT NONE
```

```
545         INTEGER, INTENT(IN) :: i, j, k, Nlat, Nact
546         !i,j=coordinates, Nlat=size of lattice, Nact=number of clusters
547         INTEGER, INTENT(IN) :: iList(Nlat*Nlat*Nlat), jList(Nlat*Nlat*Nlat), kList(Nlat*Nlat*Nlat)
548         !iList,jList=i,j coordinates for drawing clusters
549         INTEGER, INTENT(INOUT) :: iCluster(Nact,Nlat*Nlat*2), jCluster(Nact,Nlat*Nlat*2),
550   kCluster(Nact,Nlat*Nlat*2), &
551         FinalSize(Nact)
552         !iCluster,jCluster=positions of cluster sites, FinalSize=stores size of aggregates
553         INTEGER, INTENT(INOUT) :: Cluster(Nlat,Nlat,Nlat), ClusterSize(Nact), ClusterCounter(Nact)
554         !Cluster=distribution of clusters on lattice, ClusterSize=size of each cluster(No of monomers)
555         !ClusterCounter=counter for drawing clusters
556         INTEGER :: ClusterNo, iC, jC, kC, iPos, jPos, kPos, ID
557         !ClusterNo=dummy variable for cluster number, iC,jC=cluster centre position, iPos,jPos=dummy variables
558   for moving through cluster positions,
559         !ID=Cluster ID for FinalSize
560
561
562         ClusterNo = Cluster(i,j,k)     !get cluster number at the location
563         ClusterSize(ClusterNo) = ClusterSize(ClusterNo) + 1 !increase cluster size
564
565         IF (ClusterSize(ClusterNo)>Nlat*Nlat*2) THEN
566             WRITE(25,*) 'Cluster size is larger than i/j/kCluster array! Need to increase array size!'
567             STOP
568         END IF
569
570         IF (FinalSize(ClusterNo)>0) THEN
571             FinalSize(ClusterNo) = FinalSize(ClusterNo) + 1
572         ELSE
573             ID = -(FinalSize(ClusterNo))
574             FinalSize(ID) = FinalSize(ID) + 1
575         END IF
576
577         iC = iCluster(ClusterNo,1)
578         jC = jCluster(ClusterNo,1)
579         kC = kCluster(ClusterNo,1)
580
581         check:DO
582             iPos = iC + iList(ClusterCounter(ClusterNo))
583             jPos = jC + jList(ClusterCounter(ClusterNo))
584             kPos = kC + kList(ClusterCounter(ClusterNo))
585             IF (iPos > Nlat)  iPos = iPos - Nlat
586             IF (iPos < 1)     iPos = iPos + Nlat      !periodic boundary
587             IF (jPos > Nlat)  jPos = jPos - Nlat
588             IF (jPos < 1)     jPos = jPos + Nlat      !periodic boundary
589             IF (kPos > Nlat)  kPos = kPos - Nlat
590             IF (kPos < 1)     kPos = kPos + Nlat      !periodic boundary
591
592             IF (Cluster(iPos,jPos,kPos)==0) THEN
593                 Cluster(iPos,jPos,kPos) = ClusterNo
594                 iCluster(ClusterNo,ClusterSize(ClusterNo)) = iPos
595                 jCluster(ClusterNo,ClusterSize(ClusterNo)) = jPos
596                 kCluster(ClusterNo,ClusterSize(ClusterNo)) = kPos
597                 ClusterCounter(ClusterNo) = ClusterCounter(ClusterNo) + 1
598                 EXIT check
599             ELSE
600                 ClusterCounter(ClusterNo) = ClusterCounter(ClusterNo) + 1
601   !increase cluster counter and loop back
602             END IF
603         END DO check
604
605     END SUBROUTINE attach
606
607     SUBROUTINE HK_scan(WorkCluster, Nact, Nlat, Cluster, ClusterSize, iList, jList, kList, &
608         iCluster, jCluster, kCluster, SuperCluster, coalesce)
609
610   !subroutine to scan perimeter of a cluster to see if it's touching another cluster, if it does, it links them
611   !using link_clusters subroutine
612         IMPLICIT NONE
613         INTEGER, INTENT(IN) :: Nact, Nlat
```

```
614         !Nlat=size of lattice, Nact=number of clusters
615         INTEGER, INTENT(IN) :: Cluster(Nlat,Nlat,Nlat), ClusterSize(Nact), iCluster(Nact,Nlat*Nlat*2), &
616             jCluster(Nact,Nlat*Nlat*2), kCluster(Nact,Nlat*Nlat*2)
617         !Cluster=distribution of clusters on lattice, ClusterCounter=counter for drawing clusters
618         !iCluster,jCluster=positions of cluster sites
619         INTEGER, INTENT(IN) :: iList(Nlat*Nlat*Nlat), jList(Nlat*Nlat*Nlat), kList(Nlat*Nlat*Nlat), WorkCluster
620         !iList,jList=i,j coordinates for drawing clusters, WorkCluster=current cluster
621         INTEGER, INTENT(INOUT):: SuperCluster(Nact,Nact)
622         !SuperCluster=stores cluster links
623         LOGICAL, INTENT(OUT) :: coalesce
624         INTEGER :: i, j, k, iPos, jPos, kPos, CheckCluster
625         INTEGER :: neighbourUp, neighbourDown, neighbourLeft, neighbourRight, &
626            neighbourBack, neighbourForward
627         INTEGER :: left, right, up, down, back, forward
628         LOGICAL :: perimeter, touch, linked
629
630
631         !loop backwards through the list of positions
632         inner: DO i=ClusterSize(WorkCluster),1,-1
633             !set default logical values of perimeter and touch in the beginning of loop
634             perimeter = .TRUE.
635             touch = .FALSE.
636             neighbourUp = 0
637             neighbourDown = 0
638             neighbourLeft = 0
639             neighbourRight = 0
640             neighbourBack = 0
641             neighbourForward = 0
642
643             !get the current position from list
644             iPos = iCluster(WorkCluster,i)
645             jPos = jCluster(WorkCluster,i)
646             kPos = kCluster(WorkCluster,i)
647             IF (iPos > Nlat)   iPos = iPos - Nlat
648             IF (iPos < 1)      iPos = iPos + Nlat        !periodic boundary
649             IF (jPos > Nlat)   jPos = jPos - Nlat
650             IF (jPos < 1)      jPos = jPos + Nlat        !periodic boundary
651             IF (kPos > Nlat)   kPos = kPos - Nlat
652             IF (kPos < 1)      kPos = kPos + Nlat        !periodic boundary
653             !check if the current position contains the cluster, if not move on
654             IF (Cluster(iPos,jPos,kPos)/=WorkCluster) THEN
655                 CYCLE inner
656             END IF
657
658             left = iPos - 1
659             IF (left > Nlat)     left = left - Nlat
660             IF (left < 1)        left = left + Nlat      !periodic boundary
661             right = iPos + 1
662             IF (right > Nlat)    right = right - Nlat
663             IF (right < 1)       right = right + Nlat    !periodic boundary
664             down = jPos - 1
665             IF (down > Nlat)     down = down - Nlat
666             IF (down < 1)        down = down + Nlat      !periodic boundary
667             up = jPos + 1
668             IF (up > Nlat)       up = up - Nlat
669             IF (up < 1)          up = up + Nlat          !periodic boundary
670             back = kPos - 1
671             IF (back > Nlat)     back = back - Nlat
672             IF (back < 1)        back = back + Nlat      !periodic boundary
673             forward = kPos + 1
674             IF (forward > Nlat)       forward = forward - Nlat
675             IF (forward < 1)          forward = forward + Nlat     !periodic boundary
676
677             !if the position is on perimeter, check if there is a neighbour touching
678             IF (perimeter) THEN
679                 IF ((Cluster(right,jPos,kPos)/=WorkCluster) .AND. (Cluster(right,jPos,kPos)/=0)) THEN
680                     touch = .TRUE.
681                     neighbourRight = Cluster(right,jPos,kPos)
682                 END IF
```

```
683                 IF ((Cluster(left, jPos, kPos)/=WorkCluster) .AND. (Cluster(left, jPos, kPos)/=0)) THEN
684                     touch = .TRUE.
685                     neighbourLeft = Cluster(left, jPos, kPos)
686                 END IF
687                 IF ((Cluster(iPos, up, kPos)/=WorkCluster) .AND. (Cluster(iPos, up, kPos)/=0)) THEN
688                     touch = .TRUE.
689                     neighbourDown = Cluster(iPos, up, kPos)
690                 END IF
691                 IF ((Cluster(iPos, down, kPos)/=WorkCluster) .AND. (Cluster(iPos, down, kPos)/=0)) THEN
692                     touch = .TRUE.
693                     neighbourUp = Cluster(iPos, down, kPos)
694                 END IF
695                 IF ((Cluster(iPos, jPos, back)/=WorkCluster) .AND. (Cluster(iPos, jPos, back)/=0)) THEN
696                     touch = .TRUE.
697                     neighbourBack = Cluster(iPos, jPos, back)
698                 END IF
699                 IF ((Cluster(iPos, jPos, forward)/=WorkCluster) .AND. (Cluster(iPos, jPos, forward)/=0)) THEN
700                     touch = .TRUE.
701                     neighbourForward = Cluster(iPos, jPos, forward)
702                 END IF
703                 !if there's a neighbour touching, link the clusters
704                 IF (touch) THEN
705                     coalesce = .TRUE.
706                     IF (neighbourUp/=0) THEN     !if there's a neighbour above, link it
707                         CALL link_clusters(neighbourUp, Nact, SuperCluster, WorkCluster, FinalSize)
708                     END IF
709                     IF (neighbourDown/=0) THEN     !if there's a neighbour below, link it
710                         CALL link_clusters(neighbourDown, Nact, SuperCluster, WorkCluster, FinalSize)
711                     END IF
712                     IF (neighbourLeft/=0) THEN     !if there's a neighbour to left, link it
713                         CALL link_clusters(neighbourLeft, Nact,  SuperCluster, WorkCluster, FinalSize)
714                     END IF
715                     IF (neighbourRight/=0) THEN     !if there's a neighbour to right, link it
716                         CALL link_clusters(neighbourRight, Nact, SuperCluster, WorkCluster, FinalSize)
717                     END IF
718                     IF (neighbourForward/=0) THEN     !if there's a neighbour forward, link it
719                         CALL link_clusters(neighbourForward, Nact,  SuperCluster, WorkCluster, FinalSize)
720                     END IF
721                     IF (neighbourBack/=0) THEN     !if there's a neighbour back, link it
722                         CALL link_clusters(neighbourBack, Nact, SuperCluster, WorkCluster, FinalSize)
723                     END IF
724                 END IF
725             ELSE
726                 EXIT inner
727             END IF
728         END DO inner
729
730     END SUBROUTINE HK_scan
731
732     SUBROUTINE link_clusters(neighbour, Nact, SuperCluster, WorkCluster, FinalSize)
733         !subroutine for linking two touching clusters/aggregates
734         IMPLICIT NONE
735         INTEGER, INTENT(IN) :: Nact, WorkCluster, neighbour
736         !Nact=number of clusters, WorkCluster,neighbour=cluster IDs to be linked
737         INTEGER, INTENT(INOUT) :: SuperCluster(Nact,Nact), FinalSize(Nact)
738         !SuperCluster=stores cluster links, FinalSize=stores size of aggregates
739         INTEGER :: i, ID1, ID2
740         !dummy variables i for loops and ID1,ID2 for cluster ID for FinalSize
741         INTEGER :: CopyRow(Nact)
742         !CopyRow=row from SuperCluster array that is combination of links of both WorkCluster and neighbour and
743 is copied to all linked clusters
744
745         IF (SuperCluster(WorkCluster,neighbour)==1) RETURN
746         CopyRow = SuperCluster(WorkCluster,:) + SuperCluster(neighbour,:)
747         WHERE (CopyRow > 1) CopyRow = 1
748
749         !get IDs of both clusters
750         IF (FinalSize(WorkCluster)>0) THEN
751             ID1 = WorkCluster
```

```
752             ELSE
753                 ID1 = -(FinalSize(WorkCluster))
754             END IF
755             IF (FinalSize(neighbour)>0) THEN
756                 ID2 = neighbour
757             ELSE
758                 ID2 = -(FinalSize(neighbour))
759             END IF
760
761             !compare the ID labels, use the lower one (this makes the last cluster have ID=1)
762             IF (ID1<ID2) THEN
763                 WHERE (FinalSize==(-ID2)) FinalSize = -ID1
764     !Clusters that were pointing to cluster 2 then points to cluster 1
765                 FinalSize(ID1) = FinalSize(ID1) + FinalSize(ID2) !Sum of the two clusters
766                 FinalSize(ID2) = -ID1 !Make this cluster point to cluster 1
767             ELSE
768                 WHERE (FinalSize==(-ID1)) FinalSize = -ID2
769                 FinalSize(ID2) = FinalSize(ID2) + FinalSize(ID1)
770                 FinalSize(ID1) = -ID2
771             END IF
772
773             !link the two clusters and their linked clusters
774             DO i = 1,Nact
775                 IF (CopyRow(i)/=0) THEN
776                     SuperCluster(i,:) = CopyRow
777                 END IF
778             END DO
779
780         END SUBROUTINE link_clusters
781
782         SUBROUTINE list(Nlat, iList, jList, kList)
783             !subroutine for making a list of positions for drawing clusters on lattice
784             IMPLICIT NONE
785             INTEGER, INTENT(IN) :: Nlat
786             !Nlat=size of lattice
787             INTEGER, INTENT(INOUT) :: iList(Nlat*Nlat*Nlat), jList(Nlat*Nlat*Nlat), kList(Nlat*Nlat*Nlat)
788             !iList,jList=i,j coordinates for drawing clusters
789             INTEGER :: radius, size, Lattice(Nlat,Nlat,Nlat), No
790                     !dummy variables for the subroutine
791
792             !reset everything
793             Lattice = 0
794             Lattice(Nlat/2,Nlat/2,Nlat/2) = 1 !Start in the  middle and span until radius is half of your lattice
795             No = 1
796             size = 1
797             iList = 0
798             jList = 0
799             kList = 0
800             radius = 1
801
802             !draw until the cluster diameter is equal to lattice size
803             DO WHILE (radius<Nlat/2)
804                 !drawing subroutine
805                 CALL draw_list(Nlat, radius, Lattice)
806
807                 !scan subroutine - will add to the list
808                 CALL scan_list(Nlat, radius, Lattice, No, iList, jList, kList)
809
810                 !increase radius and repeat
811                 radius = radius + 1
812             END DO
813
814         END SUBROUTINE list
815
816         SUBROUTINE draw_list(Nlat, radius, Lattice)
817             !subroutine for list subroutine used for list of sites for drawing clusters on lattice
818             IMPLICIT NONE
819             INTEGER, INTENT(IN) :: Nlat, radius
820             !Nlat=size of lattice, radius=radius of a cluster
```

```
821         INTEGER, INTENT(INOUT) :: Lattice(Nlat,Nlat,Nlat)
822         !Lattice=similar to Cluster, stores cluster imprint for list subroutine
823         INTEGER :: iC, jC, kC, m, mi, n, nj, o, ok, jradius, kradius
824
825
826         !put cluster centre in the middle of lattice
827         iC = Nlat/2
828         jC = Nlat/2
829         kC = Nlat/2
830
831         DO m = (iC-radius),(iC+radius),1       !loop through i direction
832             mi = m      !dummy variable, so value of m doesn't change, since it's a counter
833             IF (mi > Nlat)  mi = mi - Nlat
834             IF (mi < 1)     mi = mi + Nlat      !periodic boundary
835             jradius = INT(SQRT(1.0*(radius)**(2)-1.0*(m-iC)**(2)))      !calculate radius in j direction
836             DO n = (jC-jradius),(jC+jradius),1         !loop through j direction
837                 !increase the number on lattice, so that the new edge is equal to 1
838                 kradius = INT(SQRT(1.0*(jradius)**(2)-1.0*(n-jC)**(2)))
839                 DO o = (kC-kradius),(kC+kradius),1         !loop through k direction
840                     nj = n
841                     ok = o  !dummy variable, so value of m doesn't change, since it's a counter
842                     IF (nj > Nlat)  nj = nj - Nlat
843                     IF (nj < 1)     nj = nj + Nlat
844                     IF (ok > Nlat)  ok = ok - Nlat
845                     IF (ok < 1)     ok = ok + Nlat      !periodic boundary
846                     Lattice(mi,nj,ok) = Lattice(mi,nj,ok) + 1
847                 !increase the number on lattice, so that the new edge is equal to 1
848         !Looping through i positions, then j positions with kradius being calculated with respect to j positions
849                 END DO
850             END DO
851         END DO
852
853     END SUBROUTINE draw_list
854
855     SUBROUTINE scan_list(Nlat, radius, Lattice, No, iList, jList, kList)
856         !subroutine for list subroutine used to add the new layer of sites to the lists
857         IMPLICIT NONE
858         INTEGER, INTENT(IN) :: Nlat, radius
859         !Nlat=size of lattice, radius=radius of a cluster
860         INTEGER, INTENT(INOUT) :: Lattice(Nlat,Nlat,Nlat), No, iList(Nlat*Nlat*Nlat), jList(Nlat*Nlat*Nlat),
861 kList(Nlat*Nlat*Nlat)
862         !Lattice=similar to Cluster, stores cluster imprint for list subroutine, No=number of site
863         !iList,jList=relative position of a site number No from cluster centre
864         INTEGER :: iC, jC, kC, m, mi, n, nj, o, ok, jradius, kradius
865
866
867         iC = Nlat/2
868         jC = Nlat/2
869         kC = Nlat/2
870
871         DO m = (iC-radius),(iC+radius),1       !loop through i direction
872             mi = m      !dummy variable, so value of m doesn't change, since it's a counter
873             IF (mi > Nlat)  mi = mi - Nlat
874             IF (mi < 1)     mi = mi + Nlat      !periodic boundary
875             jradius = INT(SQRT(1.0*(radius)**(2)-1.0*(m-iC)**(2)))      !calculate radius in j direction
876             DO n = (jC-jradius),(jC+jradius),1         !loop through j direction
877                 nj = n  !dummy variable, so value of m doesn't change, since it's a counter
878                 IF (nj > Nlat)  nj = nj - Nlat
879                 IF (nj < 1)     nj = nj + Nlat      !periodic boundary
880                 kradius = INT(SQRT(1.0*(jradius)**(2)-1.0*(n-jC)**(2)))
881                 DO o = (kC-kradius),(kC+kradius),1         !loop through j direction
882                     ok = o  !dummy variable, so value of m doesn't change, since it's a counter
883                     IF (ok > Nlat)  ok = ok - Nlat
884                     IF (ok < 1)     ok = ok + Nlat      !periodic boundary
885                     IF (Lattice(mi,nj,ok)==1) THEN
886                         No = No + 1
887                         iList(No) = mi - iC !Position is relative to the centre, increasing No
888                         jList(No) = nj - jC
889                         kList(No) = ok - kC
```

```
                    END IF
                END DO
            END DO
        END DO

    END SUBROUTINE scan_list

    SUBROUTINE plotmonomer(Monomer, Nlat, FreeMon)
        !subroutine to write monomer distribution on lattice to a file
        IMPLICIT NONE
        INTEGER :: i,j, k
        INTEGER, INTENT(IN) :: Nlat                 !size of lattice
        INTEGER, INTENT(IN) :: Monomer(Nlat,Nlat,Nlat)    !monomer density
        INTEGER, INTENT(IN) :: FreeMon                !free monomers in the system

        DO i=1,Nlat,1
            WRITE(7,'(X,1000I3)') k,  (Monomer(i,j,k),  j=1,Nlat,1)
        END DO
        WRITE(7,*)

    END SUBROUTINE plotmonomer

    SUBROUTINE plotcluster(Cluster, Nlat, FreeMon)
        !subroutine to write activated monomer distribution on lattice to a file
        IMPLICIT NONE
        INTEGER :: i,j, k
        INTEGER, INTENT(IN) :: Nlat                 !size of lattice
        INTEGER, INTENT(IN) :: Cluster(Nlat,Nlat,Nlat)    !activated monomer density
        INTEGER, INTENT(IN) :: FreeMon                !free monomers in the system
        CHARACTER(LEN=20) :: fmt

        DO i=1,Nlat,1
            DO k=1,Nlat,1
                WRITE(8,'(X,1000(I6,X))') k,  (Cluster(i,j,k),  j=1,Nlat,1)
            END DO
        END DO
        WRITE(8,*)


    END SUBROUTINE plotcluster

END PROGRAM ClusterFormation
```

C.2 Accessible Porosity Code

```
PROGRAM AccPerc
    USE percolation3D
    IMPLICIT NONE
    INTEGER :: nsite, nporesites, mx, mz, my, l, ios, ncp, nc, i, j, k, ifile, iads, ides, maxit, icp, iter, r,
s, p
    REAL :: solid, percentage
    INTEGER :: seed, Nmon, Nact, FreeMon, Nmax
    INTEGER, PARAMETER :: Nlat=100
    ! number of sites (mx*mz*my), (read from a file)
    INTEGER, ALLOCATABLE :: lattice(:,:,:), Cluster(:,:,:), accessible(:,:,:)
    !pore lattice and arrays storing values of density
    INTEGER, ALLOCATABLE :: ieta(:,:,:)
    !ieta - interaction strength (distinguishes walls and bulk points), phi - external field
    REAL :: y, tstar, cp0, m
    REAL(KIND=8) :: pi, snnl, sumf, sumgp, sumh0, sumrho, sumrho1, sumsq, xi, error, dcp, rhog, gp, rhoav,
rhoav1, cp
    REAL(KIND=8) :: x, x0, dx
    REAL(KIND=8), ALLOCATABLE :: phi(:,:,:), rhoold(:,:,:), rhonew(:,:,:)
    CHARACTER(LEN=30) :: fname1, fname2, fmt, ClusterFile, Xfile, Yfile, Tfile

    INTEGER :: is, jj

    r = replacerun
    seed = r*100                              !seed for random number generator

    s = replacesolid                        !run over solid contents
    solid = 1.0*s/1000  !changed for lower increment

    p = replacepercentage                   !run over activated monomers %
    percentage = (1.0*p)/1000

    Nmax = NINT(solid*Nlat*Nlat*Nlat) !Nmax is the maximum number of monomers (the solid content * the number of
lattice points).
    Nact = NINT(percentage*Nmax) !Nact is the activated monomers (the percentage activated * the maximum number)
    !calculate current values of number of particles and activated monomers
    FreeMon = Nmax-Nact !Free Monomers are the maximum number of monomers  - the activated monomers
    Nmon = FreeMon !Using Nmon in place of FreeMon

        !create file names
    IF (r.LT.10) THEN
        WRITE(ClusterFile,'(A8,F5.3,A1,F5.3,A1,I1,A4)') 'Cluster_', solid, '_', percentage, '_', r, '.dat'
    ELSE IF ((r.GE.10).AND.(r.LT.100)) THEN
        WRITE(ClusterFile,'(A8,F5.3,A1,F5.3,A1,I2,A4)') 'Cluster_', solid, '_', percentage, '_', r, '.dat'
    END IF

    ios = 0
    OPEN(10,FILE=ClusterFile,STATUS='OLD', IOSTAT=ios)
    IF (ios/=0) THEN
        WRITE(*,*) 'Error opening file Cluster.dat', ios
        STOP
    END IF

    ios = 0
    ALLOCATE( lattice(Nlat,Nlat,Nlat), rhoold(Nlat,Nlat,Nlat), rhonew(Nlat,Nlat,Nlat), ieta(Nlat,Nlat,Nlat),
phi(Nlat,Nlat,Nlat))
    ALLOCATE(Cluster(Nlat,Nlat,Nlat), accessible(Nlat,Nlat,Nlat), STAT=ios)
    IF (ios/=0) THEN
        WRITE(*,*) 'Error allocating arrays'
        STOP
    END IF

    ifile = 0
    !ifile is a counter for determining the filenames on the density profile output files

    nc = 4          !nc is the coordination number (6 for simple cubic lattice)
    pi = 3.141592654
```

```
67
68          DO i=1,Nlat,1
69              DO j=1,Nlat,1
70                  READ(10,'(X,1000(I6,X))') k,  (Cluster(i,j,k), k=1,Nlat,1)
71                !read in Cluster file
72              END DO
73          END DO
74          !initialize lattice coordinates and determine list of nearest neighbor sites for each site on the lattice
75
76          CALL accessible_sites(accessible,Cluster,Nlat, solid, percentage, r)
77
78      END PROGRAM AccPer
```

C.3 Percolation Module

```
MODULE percolation3D
    IMPLICIT NONE
    LOGICAL :: percolated

CONTAINS

    SUBROUTINE accessible_sites(accessible,Cluster,Nlat,solid, percentage, r)
        !this version marks pore sites accessible from the outside
        IMPLICIT NONE
        INTEGER, INTENT(IN) :: Nlat, Cluster(Nlat,Nlat,Nlat)
        INTEGER, INTENT(OUT) :: accessible(Nlat,Nlat,Nlat)
        LOGICAL :: percolated
        INTEGER :: iC, jC, kC, ios, ClusterBorder(Nlat+2,Nlat+2,Nlat+2), i, j, k, lattice(Nlat+2,Nlat+2,Nlat+2)
        INTEGER :: AccSite, UnoccSite, r
        INTEGER, ALLOCATABLE :: SuperLattice(:,:,:)
        REAL :: ireal, solid, percentage, PercentAcc
        CHARACTER(LEN=31) :: SiteCount, AccessFile

          IF (r.LT.10) THEN
        WRITE(SiteCount,'(A10,F5.3,A1,F5.3,A1,I1,A4)') 'SiteCount_', solid, '_', percentage, '_', r, '.dat'
        WRITE(AccessFile,'(A7,F5.3,A1,F5.3,A1,I1,A4)') 'Access_', solid, '_', percentage, '_', r, '.dat'
    ELSE IF ((r.GE.10).AND.(r.LT.100)) THEN
       WRITE(SiteCount,'(A10,F5.3,A1,F5.3,A1,I2,A4)') 'SiteCount_', solid, '_', percentage, '_', r, '.dat'
       WRITE(AccessFile,'(A7,F5.3,A1,F5.3,A1,I2,A4)') 'Access_', solid, '_', percentage, '_', r, '.dat'
       END IF

     ios = 0
    OPEN(8,FILE=AccessFile,STATUS='REPLACE', IOSTAT=ios)
    IF (ios/=0) THEN
        WRITE(*,*) 'Error opening file Accessible.dat', ios
        STOP
    END IF

         ios = 0
    OPEN(9,FILE=SiteCount,STATUS='REPLACE', IOSTAT=ios)
    IF (ios/=0) THEN
        WRITE(*,*) 'Error opening file SiteCount.dat', ios
        STOP
    END IF

        ClusterBorder = 0
        DO i=1,Nlat
            DO j=1,Nlat
                DO k=1,Nlat
                    ClusterBorder(i+1, j+1, k+1) = Cluster(i, j, k)
                END DO
            END DO
        END DO

        UnoccSite=0
        DO i=1,Nlat
            DO j=1,Nlat
                DO k=1,Nlat
                    IF (Cluster(i, j, k)==0) THEN
                        UnoccSite=UnoccSite+1
                    END IF
                END DO
            END DO
        END DO

        WRITE(9,*) 'UnoccSite', UnoccSite

        iC = 1
        jC = 1
        kC=1
        accessible = 0
```

```
67          lattice = 0
68          CALL eff_diff(iC, jC, kC, Nlat+2, lattice, ClusterBorder)
69          lattice(iC, jC, kC) = 1
70          DO i=1,Nlat
71              DO j=1,Nlat
72                  DO k=1,Nlat
73                      accessible(i, j, k) = lattice(i+1, j+1, k+1)
74                  END DO
75              END DO
76          END DO
77          WHERE(accessible>0) accessible = 1
78
79
80          AccSite=0
81          DO i=1,Nlat
82              DO j=1,Nlat
83                  DO k=1,Nlat
84                      IF (accessible(i, j, k)==1) THEN
85                          AccSite=AccSite+1
86                      END IF
87                  END DO
88              END DO
89          END DO
90
91           !WRITE(*,*) 'AccSite', AccSite
92
93      ios=0
94      k=1
95          DO i=1,Nlat
96              DO j=1,Nlat
97                  WRITE(8,'(X,1000(I6,X))', iostat=ios) j, (accessible(i, j, k), k=1,Nlat)
98                  IF (ios/=0) WRITE(*,*) ios
99              END DO
100         END DO
101
102         PercentAcc = (AccSite/UnoccSite)*100
103
104         WRITE(9,*) PercentAcc, 'PercentAccessibleSites', AccSite, 'AccessibleSites', UnoccSite, 'Unoccupied
105 Sites'
106
107        CLOSE(8)
108        CLOSE(9)
109
110     END SUBROUTINE accessible_sites
111
112     SUBROUTINE temp_next(Nlat, iNext, jNext, kNext, iTemp, jTemp, kTemp)
113         !subroutine to copy Temp arrays into Next arrays and put 0 to Temp
114         IMPLICIT NONE
115         INTEGER, INTENT(IN) :: Nlat
116         INTEGER, INTENT(INOUT) :: iNext(Nlat*Nlat*Nlat), jNext(Nlat*Nlat*Nlat), kNext(Nlat*Nlat*Nlat)
117         INTEGER, INTENT(INOUT) :: iTemp(Nlat*Nlat*Nlat), jTemp(Nlat*Nlat*Nlat), kTemp(Nlat*Nlat*Nlat)
118         iNext = iTemp
119         jNext = jTemp
120         kNext = kTemp
121         iTemp = 0
122         jTemp = 0
123         kTemp = 0
124     END SUBROUTINE temp_next
125
126     SUBROUTINE eff_diff(iC, jC, kC, Nlat, Lattice, Cluster)
127         !subroutine for calculating diffusion on lattice
128         IMPLICIT NONE
129         INTEGER, INTENT(IN) :: Nlat, iC, jC, kC
130         !Nlat=size of lattice, iC,jC=initial coordinates
131         INTEGER, INTENT(IN) :: Cluster(Nlat,Nlat,Nlat)   !cluster distribution
132         INTEGER, INTENT(OUT) :: Lattice(Nlat,Nlat,Nlat)  !lattice with number of diffusion steps
133         INTEGER :: steps, No, i, j, k, counterNext, counterTemp, u, d, l, r
134         INTEGER :: iNext(Nlat*Nlat*Nlat), jNext(Nlat*Nlat*Nlat), kNext(Nlat*Nlat*Nlat), &
135             iTemp(Nlat*Nlat*Nlat), jTemp(Nlat*Nlat*Nlat), kTemp(Nlat*Nlat*Nlat)
```

```
136
137
138           !reset everything
139           Lattice = 0
140           Lattice(iC, jC,kC) = -1
141           No = 1
142           steps = 1
143           counterNext = 1
144           counterTemp = 1
145           iNext = 0
146           jNext = 0
147           kNext = 0
148           iTemp = 0
149           jTemp = 0
150           kTemp = 0
151           !         percolated = .FALSE.
152
153           !check if the chosen site is not occupied by a cluster
154           IF (Cluster(iC, jC,kC)/=0) THEN
155               WRITE(*,*) 'First position occupied by a cluster!'
156               STOP
157           END IF
158
159           !check initial first 4 neighbouring sites
160           CALL scan_neighbours(iC, jC, kC, steps, Nlat, Cluster, counterTemp, iTemp, jTemp, kTemp, Lattice)
161           CALL temp_next(Nlat, iNext, jNext, kNext, iTemp, jTemp, kTemp)
162           steps = steps + 1
163
164           !continue through the lattice until all available sites have been covered
165           DO
166
167               !
168               CALL advance(steps, Nlat, Cluster, counterNext, iNext, jNext, kNext, iTemp, jTemp, kTemp, Lattice)
169
170                           !if there are no more positions in Next arrays, all the lattice has been covered
171               IF (iTemp(1)==0) EXIT
172               !copy data from temporary arrays to next arrays
173               CALL temp_next(Nlat, iNext, jNext, kNext, iTemp, jTemp, kTemp)
174
175               steps = steps + 1
176
177           END DO
178
179       END SUBROUTINE eff_diff
180
181       SUBROUTINE scan_neighbours(iC, jC, kC, steps, Nlat, Cluster, counterTemp, iTemp, jTemp, kTemp, Lattice)
182           !subroutine to scan 4 neighbour sites (up, down, left, right) if it is accesible
183           IMPLICIT NONE
184           INTEGER, INTENT(IN) :: Nlat, Cluster(Nlat,Nlat,Nlat), iC, jC, kC, steps
185           INTEGER, INTENT(INOUT) :: counterTemp, iTemp(Nlat*Nlat*Nlat), jTemp(Nlat*Nlat*Nlat),
186   kTemp(Nlat*Nlat*Nlat)
187           INTEGER, INTENT(INOUT) :: Lattice(Nlat,Nlat,Nlat)
188           INTEGER :: i, j, k
189           INTEGER :: u, d, l, r
190
191           i=iC    !look at first neighbour site
192           j=jC-1
193           CALL periodic_boundary(j,Nlat)
194           !if the site is not occupied by a cluster and hasn't been looked at
195           IF ((Cluster(i, j,k)==0) .AND. (Lattice(i, j,k)==0)) THEN
196               Lattice(i, j,k)=steps              !put number of steps to reach the site
197               iTemp(counterTemp) = i
198               jTemp(counterTemp) = j          !put current site to temp array so its neighbours are checked in
199   next iteration
200               kTemp(counterTemp) = k
201               counterTemp = counterTemp + 1   !increase the counter for temp arrays
202           END IF
203
204           j=jC+1  !look at second neighbour site
```

```
205             CALL periodic_boundary(j,Nlat)
206             IF ((Cluster(i,j,k)==0) .AND. (Lattice(i,j,k)==0)) THEN
207                 Lattice(i,j,k)=steps
208                 iTemp(counterTemp) = i
209                 jTemp(counterTemp) = j
210                 kTemp(counterTemp) = k
211                 counterTemp = counterTemp + 1
212             END IF
213
214             i=iC-1  !look at third neighbour site
215             j=jC
216             CALL periodic_boundary(i,Nlat)
217             IF ((Cluster(i,j,k)==0) .AND. (Lattice(i,j,k)==0)) THEN
218                 Lattice(i,j,k)=steps
219                 iTemp(counterTemp) = i
220                 jTemp(counterTemp) = j
221                 kTemp(counterTemp) = k
222                 counterTemp = counterTemp + 1
223             END IF
224
225             i=iC+1  !look at fourth neighbour site
226             CALL periodic_boundary(i,Nlat)
227             IF ((Cluster(i,j,k)==0) .AND. (Lattice(i,j,k)==0)) THEN
228                 Lattice(i,j,k)=steps
229                 iTemp(counterTemp) = i
230                 jTemp(counterTemp) = j
231                 kTemp(counterTemp) = k
232                 counterTemp = counterTemp + 1
233             END IF
234
235             i=iC
236             k=kC-1
237             CALL periodic_boundary(k,Nlat)
238             IF ((Cluster(i,j,k)==0) .AND. (Lattice(i,j,k)==0)) THEN
239                 Lattice(i,j,k)=steps
240                 iTemp(counterTemp) = i
241                 jTemp(counterTemp) = j
242                 kTemp(counterTemp) = k
243                 counterTemp = counterTemp + 1
244             END IF
245
246             k=kC+1
247             CALL periodic_boundary(k,Nlat)
248             IF ((Cluster(i,j,k)==0) .AND. (Lattice(i,j,k)==0)) THEN
249                 Lattice(i,j,k)=steps
250                 iTemp(counterTemp) = i
251                 jTemp(counterTemp) = j
252                 kTemp(counterTemp) = k
253                 counterTemp = counterTemp + 1
254             END IF
255
256         END SUBROUTINE scan_neighbours
257
258         SUBROUTINE periodic_boundary(i,Nlat)
259             !subroutine for including periodic boundaries when a move is occuring
260             IMPLICIT NONE
261             INTEGER, INTENT(IN) :: Nlat
262             INTEGER, INTENT(INOUT) :: i
263             IF (i > Nlat)  i = i - Nlat
264             IF (i < 1)     i = i + Nlat      !periodic boundary
265         END SUBROUTINE periodic_boundary
266
267         SUBROUTINE advance(steps, Nlat, Cluster, counterNext, iNext, jNext, kNext, iTemp, jTemp, kTemp, Lattice)
268             IMPLICIT NONE
269             INTEGER, INTENT(IN) :: Nlat, Cluster(Nlat,Nlat,Nlat), steps
270             INTEGER, INTENT(INOUT) :: iNext(Nlat*Nlat*Nlat), jNext(Nlat*Nlat*Nlat), kNext(Nlat*Nlat*Nlat)
271             INTEGER, INTENT(INOUT) :: Lattice(Nlat,Nlat,Nlat), iTemp(Nlat*Nlat*Nlat), jTemp(Nlat*Nlat*Nlat),
272     kTemp(Nlat*Nlat*Nlat)
273             INTEGER :: counterNext, counterTemp
```

```
274
275         !initialise counters for next and temp arrays
276         counterNext = 1
277         counterTemp = 1
278
279         DO  !loop until all the sites have been covered
280             IF (iNext(counterNext)==0) EXIT
281
282             !check neighbouring sites
283             CALL scan_neighbours(iNext(counterNext), jNext(counterNext), kNext(counterNext), steps, &
284                 Nlat, Cluster, counterTemp, iTemp, jTemp, kTemp, Lattice)
285
286             counterNext = counterNext + 1       !increase counter for next arrays
287         END DO
288
289     END SUBROUTINE advance
290
291 END MODULE percolation3D
```

C.4 Accessible Surface Area Analysis

```
PROGRAM AccessSurfArea
    IMPLICIT NONE

    INTEGER :: ios, i, j, k, SurfArea, r, s, p, seed
    REAL :: SurfSitesPerMass, solid, percentage
    INTEGER, PARAMETER :: Nlat=100
    INTEGER, ALLOCATABLE :: lattice(:,:,:), Cluster(:,:,:), Accessible(:,:,:)
    LOGICAL :: SurfSite
    CHARACTER (LEN=31) :: AccessFile, SurfAreaAcc


     r = replacerun
    seed = r*100                              !seed for random number generator

    s = replacesolid                        !run over solid contents
    solid = 1.0*s/1000    !changed for lower increment

    p = replacepercentage                   !run over activated monomers %
    percentage = (1.0*p)/1000

    ALLOCATE(Accessible(Nlat,Nlat,Nlat))

    IF (r.LT.10) THEN
        WRITE(AccessFile,'(A7,F5.3,A1,F5.3,A1,I1,A4)') 'Access_', solid, '_', percentage, '_', r, '.dat'
        WRITE(SurfAreaAcc,'(A12,F5.3,A1,F5.3,A1,I1,A4)') 'NewSAreaAcc_', solid, '_', percentage, '_', r, '.dat'
    ELSE IF ((r.GE.10).AND.(r.LT.100)) THEN
        WRITE(AccessFile,'(A7,F5.3,A1,F5.3,A1,I2,A4)') 'Access_', solid, '_', percentage, '_', r, '.dat'
        WRITE(SurfAreaAcc,'(A12,F5.3,A1,F5.3,A1,I2,A4)') 'NewSAreaAcc_', solid, '_', percentage, '_', r, '.dat'
        END IF

     ios = 0
    OPEN(10,FILE=AccessFile,STATUS='OLD', IOSTAT=ios)
    IF (ios/=0) THEN
        WRITE(*,*) 'Error opening file Accessible.dat', ios
        STOP
    END IF

         ios = 0
    OPEN(11,FILE=SurfAreaAcc,STATUS='REPLACE', IOSTAT=ios)
    IF (ios/=0) THEN
        WRITE(*,*) 'Error opening file SurfAreaAcc.dat', ios
        STOP
    END IF

    DO i=1,100
        DO j=1,100
            READ(10,'(X,1000(I6,X))') k, (Accessible(i,j,k), k=1,100,1)
          !read in AccessCluster file
        END DO
    END DO

       SurfArea = 0

        DO i=1,Nlat
        DO j=1,Nlat
        DO k=1,Nlat
        SurfSite=.FALSE.
            IF (Accessible(i,j,k).EQ.1) THEN
            IF ((i.LT.Nlat).AND.(Accessible(i+1,j,k).EQ.0)) SurfSite=.TRUE.
            IF ((j.LT.Nlat).AND.(Accessible(i,j+1,k).EQ.0)) SurfSite=.TRUE.
            IF ((k.LT.Nlat).AND.(Accessible(i,j,k+1).EQ.0)) SurfSite=.TRUE.
            IF ((i.GT.1).AND.(Accessible(i-1,j,k).EQ.0)) SurfSite=.TRUE.
            IF ((j.GT.1).AND.(Accessible(i,j-1,k).EQ.0)) SurfSite=.TRUE.
            IF ((k.GT.1).AND.(Accessible(i,j,k-1).EQ.0)) SurfSite=.TRUE.
            IF (SurfSite) THEN
            SurfArea = SurfArea + 1
```

```
67              END IF
68              END IF
69          END DO
70      END DO
71      END DO
72
73      !Calculate Surface Area per uni mass
74      SurfSitesPerMass = SurfArea/(s*100000)
75
76              WRITE(11,*) SurfSitesPerMass, 'SurfSitesPerMass', SurfArea, 'SurfaceArea', s, 'solids'
77
78      END PROGRAM AccessSurfArea
```

C.5 Correlation Dimension Calculation

```
PROGRAM fractal
    IMPLICIT NONE
    INTEGER, PARAMETER :: Nlat=100, dp=selected_real_kind(15, 307)
    !Nlat=size of lattice(check write to file in plot subroutine when changing size!), dp=for real number
precision (up to 15 significant digits and 10^(+-307))
    INTEGER ::  Nmax, Nact, Nmon
    !Nmax=number of all particles (monomers+clusters); Nact=number of activated monomers
    REAL :: solid, percentage, d
    !solid=solid content; percentage=percentage of activated monomers from all monomers, Iav=average cluster
size
    REAL(KIND=dp) :: C(200)     !increased precision of correlation dimension calculation
    INTEGER, ALLOCATABLE :: iCluster(:), jCluster(:), kCluster(:), Cluster(:,:,:), iCen(:,:), jCen(:,:),
kCen(:,:)
    !iCluster,jCluster=positions of points occupied by clusters, (Cluster ID, position); Cluster=cluster
distribution lattice
    INTEGER :: FreeMon, i,j,k, e, ios, s, p, r, iC, jC, kC, radius, distance, q
    !MonDiff=monomer to diffuse; FreeMon=number of free monomers; i,j=lattice coordinates; k=dummy integer;
ios=for opening files; ClusterSum=sum of positions occupied by clusters on lattice
    !MonomerSum=sum of monomers on the lattice in the beginning of a run; SizeSum=sum of cluster sizes;
s,p,r=solid, percentage, run values to be replaced
    !No, current=dummy variables
    CHARACTER(LEN=26) :: ClusterFile, iFile, jFile, kFile, CFile
      !file names of the cluster distribution file and files storing additional information(cluster size, i and
j coordinates of clusters)
    INTEGER, DIMENSION(24) :: seed


    r = replacerun
    seed = r*100                            !seed for random number generator

    s = replacesolid                    !run over solid contents
    solid = 1.0*s/1000    !changed for lower increment

    p = replacepercentage               !run over activated monomers %
    percentage = (1.0*p)/1000

    CALL RANDOM_SEED(PUT=seed)

    Nmax = NINT(solid*Nlat*Nlat*Nlat)
    Nact=100000
    FreeMon = Nmax-Nact
    Nmon = FreeMon

    IF (r.LT.10) THEN
        WRITE(ClusterFile,'(A8,F5.3,A1,F5.3,A1,I1,A4)') 'Cluster_', solid, '_', percentage, '_', r, '.dat'
        WRITE(CFile,'(A6,F5.3,A1,F5.3,A1,I1,A4)') 'CFile_', solid, '_', percentage, '_', r, '.dat'
    ELSE IF ((r.GE.10).AND.(r.LT.100)) THEN
        WRITE(ClusterFile,'(A8,F5.3,A1,F5.3,A1,I2,A4)') 'Cluster_', solid, '_', percentage, '_', r, '.dat'
        WRITE(CFile,'(A6,F5.3,A1,F5.3,A1,I2,A4)') 'CFile_', solid, '_', percentage, '_', r, '.dat'
    END IF


    ios = 0
    ALLOCATE( iCluster(Nact), jCluster(Nact), kCluster(Nact), Cluster(Nlat,Nlat,Nlat), STAT=ios, &
        iCen(Nact,Nlat), jCen(Nact,Nlat), kCen(Nact,Nlat))
    IF (ios/=0) THEN
        WRITE(*,*) 'Error allocating arrays'
        STOP
    END IF

    ios = 0
    OPEN(10,FILE=ClusterFile,STATUS='OLD', IOSTAT=ios)
    IF (ios/=0) THEN
        WRITE(*,*) 'Error opening file Cluster.dat', ios
        STOP
    END IF

```

```
68          ios = 0
69          OPEN(14, FILE=CFile, STATUS='REPLACE', ACTION='WRITE', IOSTAT=ios)
70          IF (ios/=0) THEN
71              WRITE(*,*) 'Error opening file CFile.dat', ios
72              STOP
73          END IF
74
75          C = 0
76
77          DO i=1,100
78              DO j=1,100
79                  READ(10,'(X,1000(I6,X))') k,  (Cluster(i,j,k), k=1,100,1)
80                !read in Cluster file
81              END DO
82          END DO
83
84
85          ! 100,000 random points to be generated.  If the point selected is occupied (ie equals 1)
86          !then the point is used for the calculation.
87          DO q=1,100000
88              posloop: DO
89                  iCluster(q)=INT(100*RAND())+1
90                  jCluster(q)=INT(100*RAND())+1
91                  kCluster(q)=INT(100*RAND())+1
92
93                  IF (Cluster(iCluster(q),jCluster(q),kCluster(q))==0) THEN
94                      CYCLE posloop
95                  ELSE
96                      EXIT posloop
97                  END IF
98
99              END DO posloop
100         END DO
101
102         iloop: DO i=1,Nact
103             jloop: DO j=1,Nact
104                 IF (i==j) CYCLE jloop
105                 CALL dist(i,  j,  d,  Nlat,  Nact,  iCluster,  jCluster,  kCluster)
106                 distance = CEILING(d)
107                 cloop: DO e=distance,200
108                     C(e) = C(e) + 1.0/Nact
109                 END DO cloop
110             END DO jloop
111         END DO iloop
112         C = C/(1.0*(Nact-1))
113
114         DO i=1,200
115             WRITE(14,'(X,I6,X,F15.12,X,F15.12,X,F15.12)') i,  C(i),  LOG10(1.0*i),  LOG10(1.0*C(i))
116         END DO
117
118         DO i=12,14
119             CLOSE(i)
120         END DO
121
122         ios = 0
123         DEALLOCATE( iCluster,  jCluster,  kCluster,  Cluster,  STAT=ios )
124         IF (ios/=0) THEN
125             WRITE(*,*) 'Error deallocating arrays'
126             STOP
127         END IF
128
129     !dynamic arrays to free up allocated memory
130
131     CONTAINS
132
133         SUBROUTINE dist(Cluster1,  Cluster2,  distance,  Nlat,  Nact,  iCluster,  jCluster,  kCluster)
134             IMPLICIT NONE
135             INTEGER,  INTENT(IN) :: Cluster1,  Cluster2,  Nact,  Nlat
136             INTEGER,  INTENT(IN) :: iCluster(Nact),  jCluster(Nact),  kCluster(Nact)
```

```
137         REAL, INTENT(OUT) :: distance
138         INTEGER :: i1, j1, k1, i2, j2, k2
139         REAL :: d(27)
140
141         i1 = iCluster(Cluster1)
142         j1 = jCluster(Cluster1)
143         k1=kCluster(Cluster1)
144         i2 = iCluster(Cluster2)
145         j2 = jCluster(Cluster2)
146         k2=kCluster(Cluster2)
147
148
149         d(1) = SQRT(1.0*((i2+Nlat)-i1)**2 + 1.0*((j2+Nlat)-j1)**2 + 1.0*((k2+Nlat)-k1)**2)
150         d(2) = SQRT(1.0*((i2-Nlat)-i1)**2 + 1.0*((j2-Nlat)-j1)**2 + 1.0*((k2-Nlat)-k1)**2)
151         d(3) = SQRT(1.0*(i2-i1)**2 + 1.0*(j2-j1)**2 + 1.0*((k2-k1)**2))
152
153         d(4) = SQRT(1.0*((i2+Nlat)-i1)**2 + 1.0*((j2-Nlat)-j1)**2 + 1.0*((k2-Nlat)-k1)**2)
154         d(5) = SQRT(1.0*((i2+Nlat)-i1)**2 + 1.0*((j2-Nlat)-j1)**2 + 1.0*((k2-k1)**2))
155         d(6) = SQRT(1.0*((i2+Nlat)-i1)**2 + 1.0*(j2-j1)**2 + 1.0*((k2-k1)**2))
156         d(7) = SQRT(1.0*((i2+Nlat)-i1)**2 + 1.0*(j2-j1)**2 + 1.0*((k2-Nlat)-k1)**2)
157         d(8) = SQRT(1.0*((i2+Nlat)-i1)**2 + 1.0*((j2+Nlat)-j1)**2 + 1.0*((k2-k1)**2))
158         d(9) = SQRT(1.0*((i2+Nlat)-i1)**2 + 1.0*((j2+Nlat)-j1)**2 + 1.0*((k2-Nlat)-k1)**2)
159         d(10) = SQRT(1.0*((i2+Nlat)-i1)**2 + 1.0*(j2-j1)**2 + 1.0*((k2+Nlat)-k1)**2)
160         d(11) = SQRT(1.0*((i2+Nlat)-i1)**2 + 1.0*((j2-Nlat)-j1)**2 + 1.0*((k2+Nlat)-k1)**2)
161
162         d(12) = SQRT(1.0*((i2-Nlat)-i1)**2 + 1.0*((j2-Nlat)-j1)**2 + 1.0*((k2-Nlat)-k1)**2)
163         d(13) = SQRT(1.0*((i2-Nlat)-i1)**2 + 1.0*((j2-Nlat)-j1)**2 + 1.0*((k2-k1)**2))
164         d(14) = SQRT(1.0*((i2-Nlat)-i1)**2 + 1.0*(j2-j1)**2 + 1.0*((k2-k1)**2))
165         d(15) = SQRT(1.0*((i2-Nlat)-i1)**2 + 1.0*(j2-j1)**2 + 1.0*((k2-Nlat)-k1)**2)
166         d(16) = SQRT(1.0*((i2-Nlat)-i1)**2 + 1.0*((j2+Nlat)-j1)**2 + 1.0*((k2-k1)**2))
167         d(17) = SQRT(1.0*((i2-Nlat)-i1)**2 + 1.0*((j2+Nlat)-j1)**2 + 1.0*((k2-Nlat)-k1)**2)
168         d(18) = SQRT(1.0*((i2-Nlat)-i1)**2 + 1.0*(j2-j1)**2 + 1.0*((k2+Nlat)-k1)**2)
169         d(19) = SQRT(1.0*((i2-Nlat)-i1)**2 + 1.0*((j2-Nlat)-j1)**2 + 1.0*((k2+Nlat)-k1)**2)
170
171         d(20) = SQRT(1.0*(i2-i1)**2 + 1.0*((j2-Nlat)-j1)**2 + 1.0*((k2-Nlat)-k1)**2)
172         d(21) = SQRT(1.0*(i2-i1)**2 + 1.0*((j2-Nlat)-j1)**2 + 1.0*((k2-k1)**2))
173         d(22) = SQRT(1.0*(i2-i1)**2 + 1.0*(j2-j1)**2 + 1.0*((k2-k1)**2))
174         d(23) = SQRT(1.0*(i2-i1)**2 + 1.0*(j2-j1)**2 + 1.0*((k2-Nlat)-k1)**2)
175         d(24) = SQRT(1.0*(i2-i1)**2 + 1.0*((j2+Nlat)-j1)**2 + 1.0*((k2-k1)**2))
176         d(25) = SQRT(1.0*(i2-i1)**2 + 1.0*((j2+Nlat)-j1)**2 + 1.0*((k2-Nlat)-k1)**2)
177         d(26) = SQRT(1.0*(i2-i1)**2 + 1.0*(j2-j1)**2 + 1.0*((k2+Nlat)-k1)**2)
178         d(27) = SQRT(1.0*(i2-i1)**2 + 1.0*((j2-Nlat)-j1)**2 + 1.0*((k2+Nlat)-k1)**2)
179
180
181         distance = MINVAL(d)
182
183     END SUBROUTINE dist
184
185     SUBROUTINE scan_radius(CheckCluster, radius, Nlat, Nact, iCluster, jCluster, kCluster, Lattice, C)
186         !subroutine for list subroutine used to add the new layer of sites to the lists
187         IMPLICIT NONE
188         INTEGER, INTENT(IN) :: Nlat, radius, CheckCluster, Nact
189         !Nlat=size of lattice, radius=radius of a cluster
190         INTEGER, INTENT(IN) :: iCluster(Nact,Nlat), jCluster(Nact,Nlat), kCluster(Nact,Nlat)
191         INTEGER, INTENT(INOUT) :: Lattice(Nlat,Nlat,Nlat)
192         REAL, INTENT(INOUT) :: C(Nlat)
193         !Lattice=similar to Cluster, stores cluster imprint for list subroutine
194         INTEGER :: m, mi, n, nj, o, ok,  jradius, kradius, iC, jC, kC, Cluster2, List(Nact), counter, theta
195         REAL :: d
196
197         counter = 1
198         List = 0
199         iC = iCluster(CheckCluster,1)
200         jC = jCluster(CheckCluster,1)
201         kC = kCluster(CheckCluster,1)
202
203         mloop: DO m = (iC-radius),(iC+radius),1       !loop through i direction
204             mi = m      !dummy variable, so value of m doesn't change, since it's a counter
205             IF (mi > Nlat)  mi = mi - Nlat
```

```
206             IF (mi < 1)      mi = mi + Nlat       !periodic boundary
207             jradius = INT(SQRT(1.0*(radius)**(2)-1.0*(m-iC)**(2)))       !calculate radius in j direction
208             nloop: DO n = (jC-jradius),(jC+jradius),1         !loop through j direction
209                 nj = n  !dummy variable
210                 IF (nj > Nlat)  nj = nj - Nlat
211                 IF (nj < 1)      nj = nj + Nlat       !periodic boundary
212                 kradius = INT(SQRT(1.0*(jradius)**(2)-1.0*(n-jC)**(2)))
213                 oloop: DO o = (kC-kradius),(kC+kradius),1         !loop through j direction
214                     ok = o  !dummy variable, so value of m doesn't change, since it's a counter
215                     IF (ok > Nlat)  ok = ok - Nlat
216                     IF (ok < 1)      ok = ok + Nlat       !periodic boundary
217                     IF ((Lattice(mi,nj,ok)/=0) .AND. (Lattice(mi,nj,ok)/=CheckCluster)) THEN
218                         Cluster2 = Lattice(mi,nj,ok)
219                         IF (ANY( List==Cluster2 )) CYCLE nloop
220                         CALL dist(CheckCluster, Cluster2, d, Nlat, Nact, iCluster, jCluster, kCluster)
221                         IF ((radius - d) .GE. 0) THEN
222                             theta = 1
223                         ELSE
224                             theta = 0
225                         END IF
226                         C(radius) = C(radius) + theta
227                     END IF
228                 END DO oloop
229             END DO nloop
230         END DO mloop
231
232     END SUBROUTINE scan_radius
233
234 END PROGRAM fractal
```

C.6 Hurst Exponent Calculation

```
PROGRAM RF_brownian_110517
    IMPLICIT NONE
    INTEGER, PARAMETER :: Nlat=100, dp=selected_real_kind(15, 307)
    !Nlat=size of lattice(check write to file in plot subroutine when changing size!), dp=for real number
precision (up to 15 significant digits and 10^(+-307))
    INTEGER :: Nmax, Nact, Nmon, Nsteps, Npositions, position, TimeWindows, pos_counter
    !Nmax=number of all particles (monomers+clusters); Nact=number of activated monomers
    REAL :: solid, percentage, d, ireal
    !solid=solid content; percentage=percentage of activated monomers from all monomers, Iav=average cluster
size
    !    REAL(KIND=dp), ALLOCATABLE :: T(:)    !increased precision of correlation dimension calculation
    INTEGER, ALLOCATABLE :: X(:), Y(:), Z(:), Bx(:), By(:), Bz(:), SuperLattice(:,:,:), dT(:) !F(Nlat,Nlat),
E(Nlat,Nlat),
    !iCluster,jCluster=positions of points occupied by clusters, (Cluster ID, position); Cluster=cluster
distribution lattice
    INTEGER :: FreeMon, i,j,k, o, ios, s, p, r, iC, jC, kC, radius, Cluster(Nlat,Nlat,Nlat),
Walk(Nlat,Nlat,Nlat), q
    !MonDiff=monomer to diffuse; FreeMon=number of free monomers; i,j=lattice coordinates; k=dummy integer;
ios=for opening files; ClusterSum=sum of positions occupied by clusters on lattice
    !MonomerSum=sum of monomers on the lattice in the beginning of a run; SizeSum=sum of cluster sizes;
s,p,r=solid, percentage, run values to be replaced
    !No, cur14rent=dummy variables
    CHARACTER(LEN=26) :: ClusterFile, Xfile, Yfile, Tfile, CoOrds
    !file names of the cluster distribution file and files storing additional information(cluster size, i and j
coordinates of clusters)
    INTEGER, DIMENSION(12) :: seed
    REAL(KIND=dp) :: average, stdev
    REAL(KIND=dp), ALLOCATABLE :: Xaverage(:), Yaverage(:), Zaverage(:), Xstdev(:), Ystdev(:), Zstdev(:),
XYZAvLog(:)
    REAL(KIND=dp), ALLOCATABLE :: LogXAv(:), LogYAv(:), LogZAv(:)
    LOGICAL :: percolated

     r = replacerun
    !seed = r*100                              !seed for random number generator

    s = replacesolid                    !run over solid contents
    solid = 1.0*s/1000                      !changed for lower increment

    p = replacepercentage                 !run over activated monomers %
    percentage = (1.0*p)/100

    Nmax = NINT(solid*Nlat*Nlat)
    Nact = NINT(percentage*Nmax)
    !calculate current values of number of particles and activated monomers
    FreeMon = Nmax-Nact
    Nmon = FreeMon
    Nsteps = 1000*Nlat
    Npositions = 100
    TimeWindows = 11
    pos_counter = 1
    seed = 500
    CALL RANDOM_SEED(PUT=seed)

    ios = 0
    ALLOCATE( X(Nsteps), Y(Nsteps), Z(Nsteps), Bx(Nsteps), By(Nsteps), Bz(Nsteps), dT(TimeWindows),
Xaverage(TimeWindows), &
        Yaverage(TimeWindows), Zaverage(TimeWindows), Xstdev(TimeWindows), Ystdev(TimeWindows),
Zstdev(TimeWindows), &
         XYZAvLog(TimeWindows), LogXAv(TimeWindows), LogYAv(TimeWindows), LogZAv(TimeWindows),  STAT=ios )
    IF (ios/=0) THEN
        WRITE(*,*) 'Error allocating arrays'
        STOP
    END IF
     !allocate dynamic arrays

    !time windows for calculating Hurst exponent
```

```
67          dT(1) = 1
68          DO i=2,TimeWindows
69              dT(i) = 2*dT(i-1)
70          END DO
71
72              !create file names
73          IF (r.LT.10) THEN
74              WRITE(ClusterFile,'(A8,F5.3,A1,F5.3,A1,I1,A4)') 'Cluster_', solid, '_', percentage, '_', r, '.dat'
75              WRITE(Xfile,'(A6,F5.3,A1,F5.3,A1,I1,A4)') 'Hurst_', solid, '_', percentage, '_', r, '.dat'
76              WRITE(Tfile,'(A5,F5.3,A1,F5.3,A1,I1,A4)') 'Time_', solid, '_', percentage, '_', r, '.dat'
77              WRITE(CoOrds,'(A5,F5.3,A1,F5.3,A1,I1,A4)') 'CoOr_', solid, '_', percentage, '_', r, '.dat'
78          ELSE IF ((r.GE.10).AND.(r.LT.100)) THEN
79              WRITE(ClusterFile,'(A8,F5.3,A1,F5.3,A1,I2,A4)') 'Cluster_', solid, '_', percentage, '_', r, '.dat'
80              WRITE(Xfile,'(A6,F5.3,A1,F5.3,A1,I2,A4)') 'Hurst_', solid, '_', percentage, '_', r, '.dat'
81              WRITE(Tfile,'(A5,F5.3,A1,F5.3,A1,I2,A4)') 'Time_', solid, '_', percentage, '_', r, '.dat'
82              WRITE(CoOrds,'(A5,F5.3,A1,F5.3,A1,I2,A4)') 'CoOr_', solid, '_', percentage, '_', r, '.dat'
83          END IF
84
85          ios = 0
86          OPEN(12, FILE=ClusterFile, STATUS='OLD', ACTION='READ', IOSTAT=ios)
87          IF (ios/=0) THEN
88              WRITE(*,*) 'Error opening file Cluster.dat', ios
89              STOP
90          END IF
91          !open a file with cluster structure
92
93          ios = 0
94          OPEN(13, FILE=Xfile, STATUS='REPLACE', ACTION='WRITE', IOSTAT=ios)
95          IF (ios/=0) THEN
96              WRITE(*,*) 'Error opening file X.dat', ios
97              STOP
98          END IF
99          !open a file for writing i coordinates of clusters
100
101             ios = 0
102         OPEN(14, FILE=CoOrds, STATUS='REPLACE', ACTION='WRITE', IOSTAT=ios)
103         IF (ios/=0) THEN
104             WRITE(*,*) 'Error opening file CoOrds.dat', ios
105             STOP
106         END IF
107         !open a file for random walker path coords
108
109
110         DO i=1,Nlat,1
111             DO k=1,Nlat,1
112                 READ(12,'(X,1000(I6,X))') j, (Cluster(i,j,k), j=1,Nlat,1)
113             END DO
114         END DO
115         CLOSE(12)
116
117         Xaverage = 0
118         Yaverage = 0
119         Zaverage = 0
120         Xstdev = 0
121         Ystdev = 0
122         Zstdev = 0
123         DO position = 1,Npositions
124             WRITE(25,*) position, ' of ', Npositions
125
126             pos_counter = 1
127             pos_loop: DO
128                 CALL RANDOM_NUMBER(ireal)
129                 iC = INT(Nlat*ireal)+1
130                 CALL RANDOM_NUMBER(ireal)
131                 jC = INT(Nlat*ireal)+1
132                 CALL RANDOM_NUMBER(ireal)
133                 kC = INT(Nlat*ireal)+1
134
135                 !Generate random co-ordinates, check if site is occupied
```

```
136
137             IF (Cluster(iC,jC,kC)==0) THEN
138
139             !If site is empty then call copy superlattice and percolate subroutines
140
141                 ios = 0
142                 ALLOCATE( SuperLattice(3*Nlat,3*Nlat, 3*Nlat), STAT=ios )
143                 IF (ios/=0) THEN
144                     WRITE(*,*) 'Error allocating SuperLattice array'
145                     STOP
146                 END IF
147
148                 CALL copy_SuperLattice(iC, jC, kC, Nlat, Cluster, SuperLattice)
149                 CALL percolate(iC, jC, kC, Nlat, SuperLattice, percolated)
150
151                 ios = 0
152                 DEALLOCATE( SuperLattice, STAT=ios )
153                 IF (ios/=0) THEN
154                     WRITE(*,*) 'Error deallocating SuperLattice array'
155                     STOP
156                 END IF
157                 !dynamic arrays to free up allocated memory
158
159                 IF (percolated) THEN
160                     EXIT pos_loop
161                 ELSE
162                     IF (pos_counter.GT.NINT(0.01*Nlat*Nlat*Nlat)) THEN
163                         WRITE(*,*) '****could not find percolated structure****'
164                         STOP
165                     ELSE
166                         pos_counter = pos_counter + 1
167                         CYCLE pos_loop
168                     END IF
169                 END IF
170
171             END IF
172         END DO pos_loop
173
174         !reset everything in the beginning
175         X = 0
176         Y = 0
177         Z = 0
178         Walk = 0
179
180         !initial position
181         X(1) = iC
182         Y(1) = jC
183         Z(1)=kC
184
185         !loop through all diffusion steps
186         DO o=2,Nsteps
187             CALL diffuse(Cluster,o,Nlat,X,Y,Z,Walk)
188         END DO
189
190         DO o=1,TimeWindows
191             Bx = 0
192             By = 0
193             Bz = 0
194             DO i=(dT(o)+1),Nsteps
195                 Bx(i) = (X(i) - X(i-dT(o)))**2
196                 By(i) = (Y(i) - Y(i-dT(o)))**2
197                 Bz(i) = (Z(i) - Z(i-dT(o)))**2
198             END DO
199
200             CALL stat(Bx(dT(o)+1:),average,stdev)
201
202             Xaverage(o) = Xaverage(o) + average
203             Xstdev(o) = Xstdev(o) + stdev
204             CALL stat(By(dT(o)+1:),average,stdev)
```

```
205
206                 Yaverage(o) = Yaverage(o) + average
207                 Ystdev(o) = Ystdev(o) + stdev
208                 CALL stat(Bz(dT(o)+1:),average,stdev)
209
210                 Zaverage(o) = Zaverage(o) + average
211                 Zstdev(o) = Zstdev(o) + stdev
212             END DO
213
214         END DO
215
216         Xaverage = Xaverage/Npositions
217         Yaverage = Yaverage/Npositions
218         Zaverage = Zaverage/Npositions
219         Xstdev = Xstdev/Npositions
220         Ystdev = Ystdev/Npositions
221         Zstdev = Zstdev/Npositions
222
223          DO o=1,TimeWindows
224         LogXAv(o) = LOG10(Xaverage(o))
225         LogYAv(o) = LOG10(Yaverage(o))
226         LogZAv(o) = LOG10(Zaverage(o))
227         XYZAvLog(o) = (LogXAv(o)+LogYAv(o)+LogZAv(o))/3
228         END DO
229
230
231         WRITE(13,'(12A15)') 't', 'Xaverage', 'Yaverage', 'Zaverage', 'Xstdev', 'Ystdev', 'Zstdev', 'log(t)',
232     'log(|X|^2)', &
233             'log(|Y|^2)', 'log(|Z|^2)', 'AvgLog|XYZ|^2'
234         DO o=1,TimeWindows
235             WRITE(13,'(I15,11F15.3)') dT(o), Xaverage(o), Yaverage(o), Zaverage(o), Xstdev(o), Ystdev(o), Zstdev(o),
236     &
237                 LOG10(1.0*dT(o)), LOG10(Xaverage(o)), LOG10(Yaverage(o)), LOG10(Zaverage(o)), XYZAvLog(o)
238         END DO
239
240             !Write random walker path coords
241             DO i=1,100*Nlat
242             WRITE(14,'(X,I3,X,I3,X,I3)') X(i), Y(i), Z(i)
243             END DO
244
245
246         ios = 0
247         DEALLOCATE( X, Y, Z, Bx, By, Bz, dT, Xaverage, Yaverage, Zaverage, Xstdev, Ystdev, Zstdev, STAT=ios )
248         IF (ios/=0) THEN
249             WRITE(*,*) 'Error deallocating arrays'
250             STOP
251         END IF
252
253         DO i=13,14
254             CLOSE(i)
255         END DO
256
257
258     CONTAINS
259
260         SUBROUTINE diffuse(Cluster,No,Nlat,X,Y,Z,Walk)
261             !subroutine to make monomers diffuse on a lattice by one random step
262             IMPLICIT NONE
263             INTEGER, INTENT(IN) :: Nlat, No
264             !Nlat=size of lattice;No=no of steps, used as a counter
265             INTEGER, INTENT(IN) :: Cluster(Nlat,Nlat,Nlat)
266             !Cluster=cluster distribution lattice
267             INTEGER, INTENT(INOUT) :: X(:), Y(:), Z(:)     !arrays to store i and j coordinates
268             INTEGER, INTENT(INOUT) :: Walk(:,:,:)
269             INTEGER :: i, j, k, move
270
271             i = X(No-1)
272             j = Y(No-1)
273             k = Z(No-1)
```

```
274         !get the previous position for diffusion into dummy variables
275
276         !periodic boundary
277         CALL periodic_boundary(i,Nlat)
278         CALL periodic_boundary(j,Nlat)
279         CALL periodic_boundary(k,Nlat)
280
281         !make a random step up/down/left/right (same sequence of random moves!)
282         move=INT(6*RAND())+1
283         SELECT CASE (move)
284             CASE (1)
285                 i = i + 1
286             CASE (2)
287                 i = i - 1
288             CASE (3)
289                 j = j + 1
290             CASE (4)
291                 j = j - 1
292             CASE (5)
293                 k = k + 1
294             CASE (6)
295                 k = k - 1
296         END SELECT
297
298         !periodic boundary
299         CALL periodic_boundary(i,Nlat)
300         CALL periodic_boundary(j,Nlat)
301         CALL periodic_boundary(k,Nlat)
302
303
304         !check if the new position is empty
305         IF (Cluster(i,j,k)==0) THEN   !if there is no cluster at new site, make the diffusion step
306             IF (Walk(i,j,k)==0) Walk(i,j,k) = 100
307             SELECT CASE (move)
308                 CASE (1)
309                     X(No) = X(No-1) + 1
310                     Y(No) = Y(No-1)
311                     Z(No) = Z(No-1)
312                 CASE (2)
313                     X(No) = X(No-1) - 1
314                     Y(No) = Y(No-1)
315                     Z(No) = Z(No-1)
316                 CASE (3)
317                     Y(No) = Y(No-1) + 1
318                     X(No) = X(No-1)
319                     Z(No) = Z(No-1)
320                 CASE (4)
321                     Y(No) = Y(No-1) - 1
322                     X(No) = X(No-1)
323                     Z(No) = Z(No-1)
324                 CASE (5)
325                     Z(No) = Z(No-1) + 1
326                     X(No) = X(No-1)
327                     Y(No) = Y(No-1)
328                 CASE (6)
329                     Z(No) = Z(No-1) - 1
330                     X(No) = X(No-1)
331                     Y(No) = Y(No-1)
332             END SELECT
333         ELSE                        !if there's a cluster at new site, stay in the same position
334             X(No) = X(No-1)
335             Y(No) = Y(No-1)
336             Z(No) = Z(No-1)
337         END IF
338
339     END SUBROUTINE diffuse
340
341     SUBROUTINE periodic_boundary(i,Nlat)
342         !subroutine for putting in periodic boundaries when a move is occuring
```

```
343         IMPLICIT NONE
344         INTEGER, INTENT(IN) :: Nlat
345         INTEGER, INTENT(INOUT) :: i
346         DO
347             IF (i > Nlat)  i = i - Nlat
348             IF (i < 1)     i = i + Nlat      !periodic boundary
349             IF ((i .GE. 1) .AND. (i .LE. Nlat)) EXIT
350         END DO
351     END SUBROUTINE periodic_boundary
352
353     SUBROUTINE stat(data,ave,sdev)
354         !subroutine to calculate average and standard deviation for set of data (taken from Numerical Recipes in
355 Fortran 90)
356         IMPLICIT NONE
357         REAL(KIND=dp), INTENT(OUT) :: ave, sdev
358         INTEGER, INTENT(IN) :: data(:)
359         INTEGER :: n
360         REAL :: ep, var
361         REAL, DIMENSION(SIZE(data)) :: p,s
362
363         n = size(data)
364         ave = SUM(REAL(data))/n
365         s = data - ave
366         ep = SUM(s)
367         p = s*s
368         var = SUM(p)
369         p = p*s
370         p = p*s
371         var = (var-ep**2/n)/(n-1)
372         sdev = SQRT(var)
373
374     END SUBROUTINE stat
375
376     SUBROUTINE percolate(iC, jC, kC, Nlat, SuperLattice, percolated)
377         !subroutine for calculating diffusion on lattice
378         IMPLICIT NONE
379         INTEGER, INTENT(IN) :: Nlat, iC, jC, kC
380         !Nlat=size of lattice, iC,jC=initial coordinates
381         INTEGER, INTENT(INOUT) :: SuperLattice(:,:,:)   !cluster distribution
382         !        INTEGER, INTENT(OUT) :: Lattice(Nlat,Nlat)  !lattice with number of diffusion steps
383         INTEGER :: steps, No, i, j, k, counterNext, counterTemp, u, d, l, r
384         INTEGER :: iNext(Nlat*Nlat*Nlat), jNext(Nlat*Nlat*Nlat), kNext(Nlat*Nlat*Nlat)
385         INTEGER ::  iTemp(Nlat*Nlat*Nlat), jTemp(Nlat*Nlat*Nlat), kTemp(Nlat*Nlat*Nlat)
386         LOGICAL, INTENT(OUT) :: percolated
387
388         i = iC + Nlat
389         j = jC + Nlat
390         k = kC + Nlat
391         No = 1
392         steps = 1
393         counterNext = 1
394         counterTemp = 1
395         iNext = 0
396         jNext = 0
397         kNext = 0
398         iTemp = 0
399         jTemp = 0
400         kTemp = 0
401         percolated = .FALSE.
402
403         !check initial first 4 neighbouring sites
404         CALL scan_neighbours_percolate(i, j, k, steps, counterTemp, iTemp, jTemp, kTemp, percolated,
405 SuperLattice)
406         CALL temp_next(iNext, jNext, kNext, iTemp, jTemp, kTemp)
407         steps = steps + 1
408
409         !continue through the lattice until all available sites have been covered
410         DO
411
```

```
412             !
413             CALL advance_percolate(steps, Nlat, Cluster, counterNext, iNext, jNext, kNext, iTemp, jTemp, &
414                 kTemp, SuperLattice, percolated)
415
416             IF (percolated) EXIT
417             IF (iTemp(1)==0) EXIT
418             !copy data from temporary arrays to next arrays
419             CALL temp_next(iNext, jNext, kNext, iTemp, jTemp, kTemp)
420             steps = steps + 1
421
422
423         END DO
424
425     END SUBROUTINE percolate
426
427    SUBROUTINE scan_neighbours_percolate(iC, jC, kC,  steps, counterTemp, iTemp, jTemp, kTemp, percolated,
428 SuperLattice)
429         !subroutine to scan 4 neighbour sites (up, down, left, right) if it is accesible
430         IMPLICIT NONE
431         INTEGER, INTENT(IN) :: iC, jC, kC, steps
432         INTEGER, INTENT(INOUT) :: counterTemp, iTemp(Nlat*Nlat*Nlat), jTemp(Nlat*Nlat*Nlat)
433         INTEGER, INTENT(INOUT) :: kTemp(Nlat*Nlat*Nlat), SuperLattice(:,:,:)
434         LOGICAL, INTENT(INOUT) :: percolated
435         INTEGER :: i, j, k
436         !        INTEGER :: u, d, l, r, k
437
438         i=iC    !look at first neighbour site
439         j=jC-1
440         k=kC
441         IF (j .GE. 1) THEN
442             !if the site is not occupied by a cluster and hasn't been looked at
443             IF (SuperLattice(i,j,k)==0) THEN
444                 SuperLattice(i,j,k)=steps              !put number of steps to reach the site
445                 iTemp(counterTemp) = i
446                 jTemp(counterTemp) = j          !put current site to temp array so its neighbours are checked in
447 next iteration
448                 kTemp(counterTemp) = k
449                 counterTemp = counterTemp + 1   !increase the counter for temp arrays
450             ELSEIF (SuperLattice(i,j,k).LT.0) THEN
451                 percolated = .TRUE.
452                 RETURN
453             END IF
454         END IF
455
456         j=jC+1  !look at second neighbour site
457         IF (j .LE. 3*Nlat) THEN
458             IF (SuperLattice(i,j,k)==0) THEN
459                 SuperLattice(i,j,k)=steps
460                 iTemp(counterTemp) = i
461                 jTemp(counterTemp) = j
462                 kTemp(counterTemp) = k
463                 counterTemp = counterTemp + 1
464             ELSEIF (SuperLattice(i,j,k).LT.0) THEN
465                 percolated = .TRUE.
466                 RETURN
467             END IF
468         END IF
469
470         i=iC-1  !look at third neighbour site
471         j=jC
472         IF (i .GE. 1) THEN
473             IF (SuperLattice(i,j,k)==0) THEN
474                 SuperLattice(i,j,k)=steps
475                 iTemp(counterTemp) = i
476                 jTemp(counterTemp) = j
477                 kTemp(counterTemp) = k
478                 counterTemp = counterTemp + 1
479             ELSEIF (SuperLattice(i,j,k).LT.0) THEN
480                 percolated = .TRUE.
```

```
                RETURN
            END IF
        END IF

        i=iC+1  !look at fourth neighbour site
        IF (i .LE. 3*Nlat) THEN
            IF (SuperLattice(i,j,k)==0) THEN
                SuperLattice(i,j,k)=steps
                iTemp(counterTemp) = i
                jTemp(counterTemp) = j
                kTemp(counterTemp) = k
                counterTemp = counterTemp + 1
            ELSEIF (SuperLattice(i,j,k).LT.0) THEN
                percolated = .TRUE.
                RETURN
            END IF
        END IF

        i=iC
        k=kC-1
        IF (k .GE. 1) THEN
            IF (SuperLattice(i,j,k)==0) THEN
                SuperLattice(i,j,k)=steps
                iTemp(counterTemp) = i
                jTemp(counterTemp) = j
                kTemp(counterTemp) = k
                counterTemp = counterTemp + 1
            ELSEIF (SuperLattice(i,j,k).LT.0) THEN
                percolated = .TRUE.
                RETURN
            END IF
        END IF

        k=kC+1
        IF (k .LE. 3*Nlat) THEN
            IF (SuperLattice(i,j,k)==0) THEN
                SuperLattice(i,j,k)=steps
                iTemp(counterTemp) = i
                jTemp(counterTemp) = j
                kTemp(counterTemp) = k
                counterTemp = counterTemp + 1
            ELSEIF (SuperLattice(i,j,k).LT.0) THEN
                percolated = .TRUE.
                RETURN
            END IF
        END IF

    END SUBROUTINE scan_neighbours_percolate

    SUBROUTINE advance_percolate(steps, Nlat, Cluster, counterNext, iNext, jNext, kNext,  iTemp, jTemp, &
        kTemp, SuperLattice, percolated)
        IMPLICIT NONE
        INTEGER, INTENT(IN) :: Nlat, Cluster(Nlat,Nlat,Nlat), steps
        INTEGER, INTENT(INOUT) :: iNext(Nlat*Nlat*Nlat), jNext(Nlat*Nlat*Nlat), kNext(Nlat*Nlat*Nlat)
        INTEGER, INTENT(INOUT) :: SuperLattice(:,:,:), iTemp(Nlat*Nlat*Nlat), jTemp(Nlat*Nlat*Nlat),
kTemp(Nlat*Nlat*Nlat)
        LOGICAL, INTENT(INOUT) :: percolated
        INTEGER :: counterNext, counterTemp

        !initialise counters for next and temp arrays
        counterNext = 1
        counterTemp = 1

        DO  !loop until all the sites have been covered
            IF (iNext(counterNext)==0) EXIT
            IF (percolated) EXIT

            !check neighbouring sites
```

```
                CALL scan_neighbours_percolate(iNext(counterNext), jNext(counterNext),kNext(counterNext),
steps, counterTemp, &
               iTemp, jTemp, kTemp, percolated, SuperLattice)

           counterNext = counterNext + 1       !increase counter for next arrays
        END DO

    END SUBROUTINE advance_percolate

     SUBROUTINE temp_next(iNext, jNext, kNext, iTemp, jTemp, kTemp)
        !subroutine to copy Temp arrays into Next arrays and put 0 to Temp
        IMPLICIT NONE
        INTEGER, INTENT(INOUT) :: iNext(Nlat*Nlat*Nlat), jNext(Nlat*Nlat*Nlat), kNext(Nlat*Nlat*Nlat)
        INTEGER, INTENT(INOUT) :: iTemp(Nlat*Nlat*Nlat), jTemp(Nlat*Nlat*Nlat), kTemp(Nlat*Nlat*Nlat)
        INTEGER :: r, p, q

        iNext = iTemp
        jNext = jTemp
        kNext = kTemp
        iTemp = 0
        jTemp = 0
        kTemp = 0
    END SUBROUTINE temp_next

 SUBROUTINE copy_SuperLattice(i, j, k, Nlat, Cluster, SuperLattice)
        IMPLICIT NONE
        INTEGER, INTENT(IN) :: Nlat, Cluster(Nlat,Nlat,Nlat), i, j, k
        INTEGER, INTENT(OUT):: SuperLattice(:,:,:)

        SuperLattice = 0
        !create 27 copies of cluster lattice
        SuperLattice(1:Nlat,          1:Nlat, 1:Nlat)          = Cluster(1:Nlat,1:Nlat, 1:Nlat)

        SuperLattice(Nlat+1:2*Nlat,   1:Nlat, 1:Nlat)          = Cluster(1:Nlat,1:Nlat, 1:Nlat)
        SuperLattice(2*Nlat+1:3*Nlat, 1:Nlat, 1:Nlat)          = Cluster(1:Nlat,1:Nlat, 1:Nlat)
        SuperLattice(1:Nlat,          Nlat+1:2*Nlat, 1:Nlat)   = Cluster(1:Nlat,1:Nlat, 1:Nlat)
        SuperLattice(Nlat+1:2*Nlat,   Nlat+1:2*Nlat, 1:Nlat)   = Cluster(1:Nlat,1:Nlat, 1:Nlat)
        SuperLattice(2*Nlat+1:3*Nlat, Nlat+1:2*Nlat, 1:Nlat)   = Cluster(1:Nlat,1:Nlat, 1:Nlat)
        SuperLattice(1:Nlat,          2*Nlat+1:3*Nlat, 1:Nlat) = Cluster(1:Nlat,1:Nlat, 1:Nlat)
        SuperLattice(Nlat+1:2*Nlat,   2*Nlat+1:3*Nlat, 1:Nlat) = Cluster(1:Nlat,1:Nlat, 1:Nlat)
        SuperLattice(2*Nlat+1:3*Nlat, 2*Nlat+1:3*Nlat, 1:Nlat) = Cluster(1:Nlat,1:Nlat, 1:Nlat)



        SuperLattice(1:Nlat,          1:Nlat, Nlat+1:2*Nlat)          = Cluster(1:Nlat,1:Nlat, 1:Nlat)
        SuperLattice(Nlat+1:2*Nlat,   1:Nlat, Nlat+1:2*Nlat)          = Cluster(1:Nlat,1:Nlat, 1:Nlat)
        SuperLattice(2*Nlat+1:3*Nlat, 1:Nlat, Nlat+1:2*Nlat)          = Cluster(1:Nlat,1:Nlat, 1:Nlat)
        SuperLattice(1:Nlat,          Nlat+1:2*Nlat, Nlat+1:2*Nlat)   = Cluster(1:Nlat,1:Nlat, 1:Nlat)
        SuperLattice(Nlat+1:2*Nlat,   Nlat+1:2*Nlat, Nlat+1:2*Nlat)   = Cluster(1:Nlat,1:Nlat, 1:Nlat)
        SuperLattice(2*Nlat+1:3*Nlat, Nlat+1:2*Nlat, Nlat+1:2*Nlat)   = Cluster(1:Nlat,1:Nlat, 1:Nlat)
        SuperLattice(1:Nlat,          2*Nlat+1:3*Nlat, Nlat+1:2*Nlat) = Cluster(1:Nlat,1:Nlat, 1:Nlat)
        SuperLattice(Nlat+1:2*Nlat,   2*Nlat+1:3*Nlat, Nlat+1:2*Nlat) = Cluster(1:Nlat,1:Nlat, 1:Nlat)
        SuperLattice(2*Nlat+1:3*Nlat, 2*Nlat+1:3*Nlat, Nlat+1:2*Nlat) = Cluster(1:Nlat,1:Nlat, 1:Nlat)



        SuperLattice(1:Nlat,          1:Nlat, 2*Nlat+1:3*Nlat)          = Cluster(1:Nlat,1:Nlat, 1:Nlat)
        SuperLattice(Nlat+1:2*Nlat,   1:Nlat, 2*Nlat+1:3*Nlat)          = Cluster(1:Nlat,1:Nlat, 1:Nlat)
        SuperLattice(2*Nlat+1:3*Nlat, 1:Nlat, 2*Nlat+1:3*Nlat)          = Cluster(1:Nlat,1:Nlat, 1:Nlat)
        SuperLattice(1:Nlat,          Nlat+1:2*Nlat, 2*Nlat+1:3*Nlat)   = Cluster(1:Nlat,1:Nlat, 1:Nlat)
        SuperLattice(Nlat+1:2*Nlat,   Nlat+1:2*Nlat, 2*Nlat+1:3*Nlat)   = Cluster(1:Nlat,1:Nlat, 1:Nlat)
        SuperLattice(2*Nlat+1:3*Nlat, Nlat+1:2*Nlat, 2*Nlat+1:3*Nlat)   = Cluster(1:Nlat,1:Nlat, 1:Nlat)
        SuperLattice(1:Nlat,          2*Nlat+1:3*Nlat, 2*Nlat+1:3*Nlat) = Cluster(1:Nlat,1:Nlat, 1:Nlat)
        SuperLattice(Nlat+1:2*Nlat,   2*Nlat+1:3*Nlat, 2*Nlat+1:3*Nlat) = Cluster(1:Nlat,1:Nlat, 1:Nlat)
        SuperLattice(2*Nlat+1:3*Nlat, 2*Nlat+1:3*Nlat, 2*Nlat+1:3*Nlat) = Cluster(1:Nlat,1:Nlat, 1:Nlat)


        !put in 8 copies of the initial point to the 8 surrounding lattices
        SuperLattice(i,j,k) = -1
```

```
618             SuperLattice(i+Nlat, j,k) = -1
619             SuperLattice(i+2*Nlat, j,k) = -1
620             SuperLattice(i, j+Nlat,k) = -1
621             SuperLattice(i, j+2*Nlat,k) = -1
622             SuperLattice(i+Nlat, j+2*Nlat,k) = -1
623             SuperLattice(i+2*Nlat, j+2*Nlat,k) = -1
624             SuperLattice(i+Nlat, j+Nlat,k) = -1
625             SuperLattice(i+2*Nlat, j+Nlat,k) = -1
626
627             SuperLattice(i, j,k+Nlat) = -1
628             SuperLattice(i+Nlat, j,k+Nlat) = -1
629             SuperLattice(i+2*Nlat, j,k+Nlat) = -1
630             SuperLattice(i, j+Nlat,k+Nlat) = -1
631             SuperLattice(i, j+2*Nlat,k+Nlat) = -1
632             SuperLattice(i+Nlat, j+2*Nlat,k+Nlat) = -1
633             SuperLattice(i+2*Nlat, j+2*Nlat,k+Nlat) = -1
634             SuperLattice(i+2*Nlat, j+Nlat,k+Nlat) = -1
635
636             SuperLattice(i, j,k+2*Nlat) = -1
637             SuperLattice(i+Nlat, j,k+2*Nlat) = -1
638             SuperLattice(i+2*Nlat, j,k+2*Nlat) = -1
639             SuperLattice(i, j+Nlat,k+2*Nlat) = -1
640             SuperLattice(i, j+2*Nlat,k+2*Nlat) = -1
641             SuperLattice(i+Nlat, j+2*Nlat,k+2*Nlat) = -1
642             SuperLattice(i+2*Nlat, j+2*Nlat,k+2*Nlat) = -1
643             SuperLattice(i+Nlat, j+Nlat,k+2*Nlat) = -1
644             SuperLattice(i+2*Nlat, j+Nlat,k+2*Nlat) = -1
645
646
647             SuperLattice(i+Nlat, j+Nlat,k+Nlat) = 0      !this is the central initial point where we will start
648
649
650         END SUBROUTINE copy_SuperLattice
651
652     END PROGRAM RF_brownian_110517
```

C.7 Adsorption Analysis

```
PROGRAM mft_slit
    IMPLICIT NONE
    ! Program based on a code by Peter A. Monson. Original intro:
    ! Solution of the mean field equations for a 3D lattice gas model in finite length slit pore with nearest
    ! neighbor interactions.
    ! Peter A. Monson (February 2007)

    INTEGER :: nsite, nporesites, mx, mz, my, l, ios, ncp, nc, i, j, k, ifile, iads, ides, maxit, icp, iter
    ! number of sites (mx*mz*my), (read from a file)
    INTEGER, ALLOCATABLE :: lattice(:,:,:), accessible(:,:,:)
    !pore lattice and arrays storing values of density
    INTEGER, ALLOCATABLE :: ieta(:,:,:)
    !ieta - interaction strength (distinguishes walls and bulk points), phi - external field
    REAL :: y, tstar, cp0, m
    REAL(KIND=8) :: pi, snnl, sumf, sumgp, sumh0, sumrho, sumrho1, sumsq, xi, error, dcp, rhog, gp, rhoav,
rhoav1, cp
    REAL(KIND=8) :: x, x0, dx
    REAL(KIND=8), ALLOCATABLE :: phi(:,:,:), rhoold(:,:,:), rhonew(:,:,:)
    CHARACTER(LEN=12) :: fname1, fname2, fmt
    CHARACTER(LEN=31) :: IsoFile, AccessFile
    INTEGER :: r, s, p, seed
    REAL :: solid, percentage

    INTEGER :: is, jj

    r = replacerun
    seed = r*100                                !seed for random number generator

    s = replacesolid                        !run over solid contents
    solid = 1.0*s/10   !changed for lower increment

    p = replacepercentage                   !run over activated monomers %
    percentage = (1.0*p)/1000

    IF (r.LT.10) THEN
        WRITE(AccessFile,'(A7,F5.3,A1,F5.3,A1,I1,A4)') 'Access_', solid, '_', percentage, '_', r, '.dat'
        WRITE(IsoFile,'(A10,F5.3,A1,F5.3,A1,I1,A4)') 'IsothermNP', solid, '_', percentage, '_', r, '.dat'
    ELSE IF ((r.GE.10).AND.(r.LT.100)) THEN
        WRITE(AccessFile,'(A7,F5.3,A1,F5.3,A1,I2,A4)') 'Access_', solid, '_', percentage, '_', r, '.dat'
        WRITE(IsoFile,'(A10,F5.3,A1,F5.3,A1,I2,A4)') 'IsothermNP', solid, '_', percentage, '_', r, '.dat'
    END IF

    ios = 0
    OPEN(10,FILE=AccessFile,STATUS='OLD', IOSTAT=ios)
    IF (ios/=0) THEN
        WRITE(*,*) 'Error opening file access.dat', ios, solid, percentage
        STOP
    END IF


    OPEN(2,FILE=IsoFile, STATUS='REPLACE', IOSTAT=ios)
    IF (ios/=0) THEN
        WRITE(*,*) 'Error opening file output1.dat', ios
        STOP
    END IF
    !open a output file to store tstar,cp,exp((cp+3.0d0)/tstar),rhoav1,gp


    y=3.0
    mx=102
    my=102
    mz=102
    l=102
    tstar=1.0
    ncp=2001
    x0=0.0
```

```
      dx=0.0005
      ides=2
      rhog=0.00001
      maxit=100000
      error=1.0e-8

      !     !y - ratio of solid-fluid to fluid-fluid interactions
      !     !dimension of lattice is mx x my x mz
      !     !l - length of the pore
      !     !tstar - kT/eff; ncp,cp0,dcp,ides - parameters for fixing bulk chemical potential
      !     !maxit - maximum number of iterations
      !     !error - convergence criterion is that mean square change in local density between iterations is less
than error


      ios = 0
      ALLOCATE( lattice(mx,mz,my), rhoold(mx,mz,my), rhonew(mx,mz,my), ieta(mx,mz,my), phi(mx,mz,my), &
                                  accessible(100,100,100), STAT=ios )
      IF (ios/=0) THEN
          WRITE(*,*) 'Error allocating arrays'
          STOP
      END IF

      ifile = 0
      !ifile is a counter for determining the filenames on the density profile output files

      nc = 4          !nc is the coordination number (6 for simple cubic lattice)
      pi = 3.141592654

      DO i=1,100,1
          DO j=1,100,1
              READ(10,'(X,1000(I6,X))') k,  (accessible(i,j,k), k=1,100,1)
            !read in Cluster file
          END DO
      END DO

      lattice = 1
      DO i=1,100
          DO j=1,100
              DO k=1,100
                  lattice(i+1,j+1,k+1) = accessible(i,j,k)
              END DO
          END DO
      END DO


      ieta = 1
      nsite=0
      DO k=1,  mz
          DO i=1,mx
              DO j=1,my
                  IF (lattice(i,j,k).EQ.0) THEN
                      ieta(i,j,k) = 0
                  END IF
              END DO
          END DO
      END DO


      DO i=1,mx
          DO j=1,mz
              DO k=1,my
                  IF (ieta(i,j,k)/=0) nsite = nsite+1
              END DO
          END DO
      END DO

         !Initialize density distribution and external field
      phi = REAL(0)
```

```
136         rhoold = rhog
137         DO i=1,mx
138             DO j=1,mz
139                 DO k=1,my
140                     IF(ieta(i,j,k).EQ.0) THEN
141                         IF (ieta(i+1,j,k).EQ.1)  phi(i+1,j,k) = phi(i+1,j,k) - (1.0-REAL(ieta(i,j,k)))*y
142                         IF (ieta(i-1,j,k).EQ.1)  phi(i-1,j,k) = phi(i-1,j,k) - (1.0-REAL(ieta(i,j,k)))*y
143                         IF (ieta(i,j+1,k).EQ.1)  phi(i,j+1,k) = phi(i,j+1,k) - (1.0-REAL(ieta(i,j,k)))*y
144                         IF (ieta(i,j-1,k).EQ.1)  phi(i,j-1,k) = phi(i,j-1,k) - (1.0-REAL(ieta(i,j,k)))*y
145                         IF (ieta(i,j,k+1).EQ.1)  phi(i,j,k+1) = phi(i,j,k+1) - (1.0-REAL(ieta(i,j,k)))*y
146                         IF (ieta(i,j,k-1).EQ.1)  phi(i,j,k-1) = phi(i,j,k-1) - (1.0-REAL(ieta(i,j,k)))*y
147                     END IF
148                 END DO
149             END DO
150         END DO
151
152         DO iads=1,ides
153             !loop is for adsorption and desorption isotherms
154             DO icp = 1,ncp
155                 x = x0 + (icp - 1)*dx
156                 cp = Tstar*LOG(x)-3
157                 !Start the iteration loop
158                 iter = 0
159                 iterloop: DO
160                     iter = iter + 1
161
162                     IF(iter.GT.maxit) THEN
163                         WRITE(*,*) 'Maximum number of iterations exceeded!'
164                         WRITE(*,'(A,I2,A,F10.7)') 'iads = ', iads, '  chemical potential = ', cp
165                         STOP !100
166                     END IF
167                     !At each iteration check for convergence (based on mean square
168                     !changes in local density), compute grand free energy and average density.
169
170                     sumsq = 0.0
171                     sumrho = 0.0
172                     sumrho1 = 0.0
173                     sumh0 = 0.0
174                     sumgp = 0.0
175                     sumf = 0.0
176
177                     DO i=1,mx
178                         DO j=1,mz
179                             DO k=1,my
180                                 IF(ieta(i,j,k).EQ.1) THEN
181                                     !Compute nearest neighbor sum for rhoj
182                                     snn1=REAL(0)
183
184                                     IF (ieta(i+1,j,k).EQ.1) snn1 = snn1 + rhoold(i+1,j,k)
185                                     IF (ieta(i-1,j,k).EQ.1) snn1 = snn1 + rhoold(i-1,j,k)
186                                     IF (ieta(i,j-1,k).EQ.1) snn1 = snn1 + rhoold(i,j-1,k)
187                                     IF (ieta(i,j+1,k).EQ.1) snn1 = snn1 + rhoold(i,j+1,k)
188                                     IF (ieta(i,j,k-1).EQ.1) snn1=snn1 + rhoold(i,j,k-1)
189                                     IF (ieta(i,j,k+1).EQ.1) snn1=snn1 + rhoold(i,j,k+1)
190
191
192                                     xi = (snn1-phi(i,j,k)+cp)/tstar
193                                     rhonew(i,j,k) = 1.0/(1.0+EXP(-xi))
194                                     !eq 5 in the paper
195                                     sumsq = sumsq + (rhonew(i,j,k) - rhoold(i,j,k))**2
196                                     sumrho = sumrho + rhonew(i,j,k)
197                                     sumgp = sumgp - ieta(i,j,k)*tstar*LOG(1.0+EXP(xi)
198                                     sumh0 = sumh0 + rhonew(i,j,k)*snn1
199
200                                 ENDIF
201                             END DO
202                         END DO
203                     END DO
204
```

```
205                 DO i = 1,mx
206                     DO j = 1,mz
207                         DO k=1,my
208                             IF(ieta(i,j,k).EQ.1) THEN
209                                 rhoold(i,j,k) = rhonew(i,j,k)
210                             !copy over the new value of density
211                             END IF
212                         END DO
213                     END DO
214                 END DO
215 
216                 sumsq = sumsq/nsite
217                 !rhoav = sumrho/nporesites
218                 rhoav = sumrho/nsite
219                 !rhoav1 = sumrho1/(mz-2)*(my-2)
220 
221                 !sumgp = sumgp/nporesites
222                 !sumh0 = sumh0/2.0/nporesites
223                 sumgp = sumgp/nsite
224                 sumh0 = sumh0/2.0/nsite
225                 gp = sumgp + sumh0
226                 IF (sumsq.LT.error) EXIT iterloop
227             END DO iterloop
228 
229             WRITE(2,'(2(F7.3,X),4(ES20.12,X))') tstar,cp,exp((cp+3.0d0)/tstar),rhoav1,gp, rhoav
230 
231             ifile = ifile + 1
232 
233         END DO
234         !switch to desorption
235         x0 = x-dx
236         dx = -dx
237         ncp = ncp-1
238 
239     END DO
240 
241     WRITE(10,*) "quit"
242     CLOSE(2)
243 
244 
245 CONTAINS
246     SUBROUTINE namef(i,fname1,fname2)
247 
248         INTEGER, INTENT(IN) :: i
249         CHARACTER(LEN=12), INTENT(OUT) :: fname1,fname2
250 
251         IF(i.LT.10) THEN
252             WRITE(fname1,'(A7,I1,A4)') 'rho_000', i, '.dat'
253             WRITE(fname2,'(A7,I1,A4)') 'rho_000', i, '.gif'
254         ELSE IF(i.LT.100) THEN
255             WRITE(fname1,'(A6,I2,A4)') 'rho_00', i, '.dat'
256             WRITE(fname2,'(A6,I2,A4)') 'rho_00', i, '.gif'
257         ELSE IF(i.LT.1000) THEN
258             WRITE(fname1,'(A5,I3,A4)') 'rho_0', i, '.dat'
259             WRITE(fname2,'(A5,I3,A4)') 'rho_0', i, '.gif'
260         ELSE
261             WRITE(fname1,'(A4,I4,A4)') 'rho_', i, '.dat'
262             WRITE(fname2,'(A4,I4,A4)') 'rho_', i, '.gif'
263         ENDIF
264 
265         RETURN
266     END SUBROUTINE namef
267 
268 END PROGRAM mft_slit
```

C.8 BJH Pore Size Analysis

```
1   PROGRAM BJHAnalysis
2       IMPLICIT NONE
3
4       REAL, PARAMETER :: y=5, R=8.3144, pi=3.14159
5       INTEGER, PARAMETER :: N=4000
6       REAL, DIMENSION(N) :: P, V, Rc, Tw, VL, Vd, Pk, VLk, Rck, Vck, Vdk, Davgk, Pavgk, Twavgk, dTdk !Sets as
7   arrays with 30 data points for 30 desorp points
8       REAL, DIMENSION(N) :: dTw, CSAa, CSAc, LP, Davg, Vc, Pavg, dTd, Twavg, Davgk2, Rc2, Dp, VP, PSD !Sets as
9   arrays with 29 data points
10      REAL :: D, A, SAw, cp, sum1, sum2, tstar,gp, rhoav1, sum4, BinVol(100)
11      INTEGER :: i, j, k, ios, count, x, Npoints, s, perc, start, end, Bin(100)
12      INTEGER :: run, sol, per, seed
13      REAL :: solid, percentage
14      CHARACTER(LEN=30) :: fname1, fname2, IsoFile, BJHFile, BinFile
15      LOGICAL :: desorp
16
17      !P is the relative pressure p/po, Rc is the core radius
18      !Tw is the wall layer thickness, V is the volume of gas adsorbed, Rp is the average pore radius
19      D = 0.0015468 !Density conversion factor, from software
20      A = 0.953 !Adsorption property factor, from software
21
22      run = replacerun
23      seed = run*100                          !seed for random number generator
24
25      sol = replacesolid                      !run over solid contents
26      solid = 1.0*sol/10    !changed for lower increment
27
28      per = replacepercentage                 !run over activated monomers %
29      percentage = (1.0*per)/100
30
31      IF (r.LT.10) THEN
32          WRITE(BJHFile,'(A4,F5.3,A1,F5.3,A1,I1,A4)') 'BJH_', solid, '_', percentage, '_', run, '.dat'
33          WRITE(BinFile,'(A7,F5.3,A1,F5.3,A1,I1,A4)') 'BJHBin_', solid, '_', percentage, '_', run, '.dat'
34          WRITE(IsoFile,'(A10,F5.3,A1,F5.3,A1,I1,A4)') 'IsothermNP', solid, '_', percentage, '_', run, '.dat'
35      ELSE IF ((r.GE.10).AND.(r.LT.100)) THEN
36          WRITE(BJHFile,'(A4,F5.3,A1,F5.3,A1,I2,A4)') 'BJH_', solid, '_', percentage, '_', run, '.dat'
37          WRITE(BinFile,'(A7,F5.3,A1,F5.3,A1,I2,A4)') 'BJHBin_', solid, '_', percentage, '_', run, '.dat'
38          WRITE(IsoFile,'(A10,F5.3,A1,F5.3,A1,I2,A4)') 'IsothermNP', solid, '_', percentage, '_', run, '.dat'
39      END IF
40
41
42      OPEN(3,FILE=IsoFile,STATUS='OLD')
43      READ(3,*)
44      desorp = .FALSE.
45      DO i=1,3999
46          READ(3,'(2(F7.3,X),4(ES20.12,X))') tstar,cp,P(i), rhoav1, gp, V(i)
47          IF (desorp) WRITE(*,*) P(i), V(i)
48          IF (P(i)==1.0) start = i+1 !desorp = .TRUE.
49          IF (P(i)==0.2) end = i !desorp = .FALSE.
50          IF (ios<0) EXIT
51      END DO
52      CLOSE(3)
53
54      Rc = (-A)/(LOG(P))+1
55
56      DO i=start,end-1
57          Davgk(i)=(2.0*(Rc(i)+Rc(i+1))*Rc(i)*Rc(i+1))/(Rc(i)**2+Rc(i+1)**2)
58      END DO
59      DO i=start,end-1
60          VP(i) = (V(i)-V(i+1))/LOG10(Davgk(i)/Davgk(i+1))
61      END DO
```

```
62
63          OPEN(15,FILE=BJHFile,STATUS='REPLACE',IOSTAT=ios)
64          IF (ios/=0) THEN
65              WRITE(*,*) 'Error opening file BJH_data.dat', ios
66              STOP
67          END IF
68          WRITE(15,'(2A20)') 'Pore width (nm)', 'dV/dlog(D)'
69          DO i=start,end-1
70              WRITE(15,'(F20.5,ES20.5)') Davgk(i), VP(i)
71          END DO
72          CLOSE(15)
73
74          Bin(1)=0
75          DO i=2,40
76              Bin(i) = Bin(i-1)+2
77          END DO
78
79
80          BinVol = 0
81          DO i=1,N
82              DO j=1,40
83                  IF ((Davgk(i).LE.80).AND.(Davgk(i).GE.2)) THEN
84                      x = NINT(Davgk(i)) !/BinSize(j))
85                      IF ((Davgk(i).LE.Bin(j+1)).AND.(Davgk(i).GE.Bin(j))) THEN
86                          BinVol(j) = BinVol(j) + VP(i)
87                      END IF
88                  END IF
89              END DO
90          END DO
91
92          WRITE(*,*) fname2
93          OPEN(12,FILE=BinFile,STATUS='REPLACE',IOSTAT=ios)
94          IF (ios/=0) THEN
95              WRITE(*,*) 'Error opening file BJH_data.dat', ios
96              STOP
97          END IF
98
99          WRITE(12,'(A10,A20)') 'Bin size', 'Cumulative volume'
100         DO i=1,40
101             WRITE(12,'(I10,F20.10)') Bin(i), BinVol(i)
102         END DO
103
104         CLOSE(12)
105
106 END PROGRAM BJHAnalysis
107
```

Appendix D – Publications

D.1 Modelling Organic Gel Growth in Three Dimensions – Textural and Fractal Properties of Resorcinol-Formaldehyde Gels (Published)

gels

MDPI

Article

Modelling Organic Gel Growth in Three Dimensions: Textural and Fractal Properties of Resorcinol–Formaldehyde Gels

Elisha Martin, Martin Prostredny, Ashleigh Fletcher and Paul Mulheran *

Department of Chemical and Process Engineering, University of Strathclyde, Glasgow G1 1XJ, UK; elisha.martin@strath.ac.uk (E.M.); martin.prostredny@strath.ac.uk (M.P.); ashleigh.fletcher@strath.ac.uk (A.F.)
* Correspondence: paul.mulheran@strath.ac.uk; Tel.: +44-(0)141-548-2385

Received: 8 July 2020; Accepted: 3 August 2020; Published: 5 August 2020

Abstract: Tailoring the properties of porous organic materials, such as resorcinol–formaldehyde gels, for use in various applications has been a central focus for many studies in recent years. In order to achieve effective optimisation for each application, this work aims to assess the impact of the various synthesis parameters on the final textural properties of the gel. Here, the formation of porous organic gels is modelled using a three-dimensional lattice-based Monte Carlo simulation. We model growth from monomer species into the interconnected primary clusters of a gel, and account for varying catalyst concentration and solids content, two parameters proven to control gel properties in experimental work. In addition to analysing the textural properties of the simulated materials, we also explore their fractal properties through correlation dimension and Hurst exponent calculations. The correlation dimension shows that while fractal properties are not typically observed in scattering experiments, they are possible to achieve with sufficiently low solids content and catalyst concentration. Furthermore, fractal properties are also apparent from the analysis of the diffusion path of guest species through the gel's porous network. This model, therefore, provides insight into how porous organic gels can be manufactured with their textural and fractal properties computationally tailored according to the intended application.

Keywords: gel modelling; RF gels; nanomaterials; cluster aggregation; gel formation; fractal analysis; aerogels; xerogels

1. Introduction

The application potential for porous organic materials has been investigated extensively over the years, with a particular focus on those which possess attractive properties, such as low densities and high surface areas. Materials such as these have proven to be effective in a wide range of applications, many of which are imperative in reducing or eradicating detrimental environmental impacts of industry, heightening their pertinence to recent research. To date, applications for porous organic materials have included gas adsorption and storage [1,2], water treatment [3,4], and thermal insulation [5,6], as well as use in their carbonised forms for applications involving electrical conductivity [4,7].

This work focuses on one such class of organic porous materials—resorcinol–formaldehyde (RF) gels—which are formed via a sol–gel process and subsequently dried, producing the lightweight, nanoporous structure of the final gel. Despite extensive research into these porous materials in recent years, their formation mechanism is not yet fully understood, and their application potential is yet to be fully elucidated. Understanding the mechanism by which these materials form is crucial in determining how various synthesis parameters affect the final structural properties of the gel, and modelling this computationally could permit future optimisation of materials according to their relevant application.

The synthesis of these gels involves a base-catalysed addition reaction between resorcinol and formaldehyde molecules, resulting in the formation of hydroxymethyl derivative monomers. A condensation reaction proceeds as these monomers become interconnected via methylene and methyl-ether bridges, with the resulting compounds forming primary spherical clusters. The condensation reaction continues, with the eventual aggregation of these primary clusters leading to the cross-linked network structure of the final gel [8].

The proposed mechanism by which this growth process is initiated begins with the abstraction of a proton from resorcinol in the presence of the basic catalyst, resulting in increased reactivity of the anionic resorcinol molecule [9]. This subsequently acts as a cluster seed around which other monomers can attach, forming the primary spherical particles. The resulting structure can be observed experimentally using Scanning Electron Microscopy (see Figure 1), as has been reported in previous studies on RF gels [10,11].

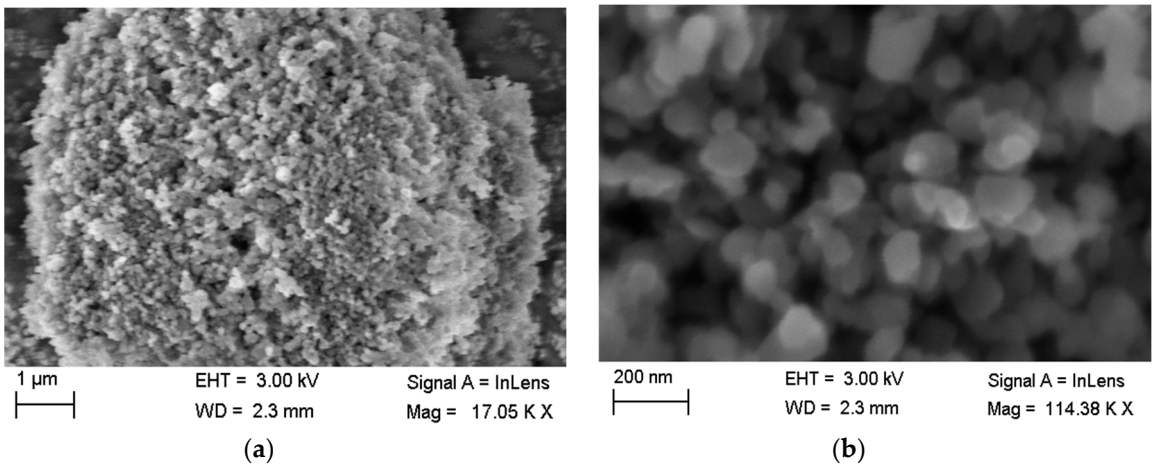

Figure 1. SEM images of resorcinol–formaldehyde (RF) xerogels synthesised at 20% solids content and a resorcinol/catalyst ratio of 600 at (**a**) 17.05 K X magnification and (**b**) 114.38 K X magnification. This SEM analysis was performed in collaboration with Farnaz Ghajeri at Angstrom Laboratory, Uppsala University.

This growth pathway forms the basis for the computational work presented here, a three-dimensional (3D) simulation that models the formation and growth of porous materials, such as RF gels, using a kinetic Monte Carlo methodology. This software has been developed in-house and builds upon a previous 2D simulation from within our group [12].

Substantial computational research into basic cluster–cluster aggregation systems has been carried out over the years, which have simulated the formation of complex structures from both diffusion-limited and reaction-limited cluster aggregation [13–15]. Recent studies have furthered this work, with a focus on the fractal properties of systems modelled with repulsive and attractive forces in place, and the rotational diffusion of aggregating clusters implemented [16,17]. The model presented here uses a novel approach to cluster–cluster aggregation to simulate the formation of porous materials, originating from the initial monomer species. The subsequent growth of primary clusters around cluster seeds, therefore, allows for primary clusters of varying sizes to form, before their final aggregation into monolithic, porous structures. This is in contrast to previous studies, which have focused on the cluster aggregation process for similar porous materials, many beginning the simulation at a point where primary cluster formation had already taken place [18,19], or assuming primary clusters which have formed are of equal size before aggregation occurs [20,21]. These models, therefore, are not reflective of a real system, where such properties are likely to exhibit some degree of variation. Although the model presented in this work does not account for additional forces or

rotational effects exhibited by real systems, basic diffusional moves sufficiently capture the stochastic nature of the growth given that the aggregation process is modelled within a crowded environment.

Various analytical techniques have been applied to gain a deeper insight into the internal structural properties of porous materials, using both experimental and computational methods. Experimentally, adsorption analysis in particular has been used to provide details on the accessible pore volume of RF gel materials, in addition to their accessible surface area, average pore width, and approximate pore geometry [22,23]. In addition to this, assessing whether these materials have fractal properties has also been addressed, since the scaling properties of a porous material need to be properly recognised when designing it for an application.

Over the years, research has been conducted into the fractal properties of RF gels using Small-Angle X-Ray Scattering (SAXS) measurements, the results of which are used to determine surface fractal dimension values, with values below three indicating fractal properties. The studies carried out to date have reached conflicting conclusions, with some categorically concluding that RF gels—unlike their silica gel counterparts—do not possess any fractal properties whatsoever. This includes a study by Pekala (who was the first to synthesise RF gels in 1989 [24]) and Schaefer (1993) [25] who conducted SAXS analysis on base-catalysed RF aerogels. The results obtained show no fractal properties for any of the materials studied, although the authors suggest that fractal behaviour may be possible for samples synthesised with particularly low densities, which is something explored in this work. The results of subsequent studies have pointed towards the possibility of some fractal properties of the gels synthesised under certain conditions, with a general consensus yet to be reached.

Tamon and Ishizaka (1998) [26] assessed the fractal properties of RF gels at different time intervals throughout their gelation process, as well as after a period of ageing. While they find evidence of fractal structures during growth, the final gel structures did not display fractal properties in SAXS measurements. Berthon et al. (2001) [27] also carried out SAXS analysis of RF gels which had been synthesised at solids percentages of 5% and 20% using both acidic and basic reaction conditions, as well as using both acetone and water as solvents for the sol–gel process. The results of this work indicated that fractal properties could be observed for RF gels synthesised at low solids percentages (5%) under acidic reaction conditions using acetone as a solvent, with a calculated surface fractal dimension value of 2.5. RF gels synthesised at higher solids percentages (20%), however, did not exhibit any fractal properties. More recently, research published by Alshrah et al. (2018) [28] analysed the relationship between fractal and thermal properties within these materials. Gels were synthesised at different catalyst concentrations and solids percentages, both of which remained low across the ranges studied, and surface fractal dimension values were determined following SAXS analysis, with values pointing towards fractal properties.

The dichotomous conclusions reached as a result of the different studies carried out over the years reinforce the unanswered questions around the fractal properties of RF gels. Furthermore, in our group's earlier two-dimensional model, which simulated the formation of RF gels, the resulting structures did exhibit fractal properties, even at the higher solids percentages studied. Of course, two-dimensional systems will have more restricted percolation pathways than the three-dimensional structures observed in reality, consequently influencing their fractal properties. The work presented here, therefore, aims to explore this further, this time using a three-dimensional computational model to determine fractal dimension values of the simulated material at various solids percentages and catalyst concentrations. Reflective of the materials studied experimentally by SAXS analysis in the different studies discussed, one would anticipate that the simulated structures may exhibit some fractal properties at sufficiently low solids percentages, while appearing largely nonfractal at the higher solid percentages, which are more commonly used for material synthesis in experimental analysis.

The various porous structures produced through the 3D simulation developed in this work are analysed in terms of their textural and fractal properties, and compared not only to one another, but also to materials that have been examined experimentally. The transformation of this model from 2D to 3D has been crucial in achieving an accurate comparison to materials synthesised through experimental

work, and is a pivotal step towards achieving computational optimisation of these materials for use in various applications.

2. Results and Discussion

2.1. Visualisation and Cluster Size

Figure 2 displays histograms for the primary cluster volume distributions at various catalyst concentrations, while Figure 3 shows the visualised final structures. As explained in the Methodology section, S_c is the solids content in the simulation and C_c is the catalyst concentration, mirroring experimental conditions. The simulation yields approximately spherical "primary particles" that have also aggregated to form the gel structure. Figure 3 displays structures created with S_c values of 10%, 30%, and 60% each at C_c values of 0.5%, 1%, 2%, and 4% on a $100 \times 100 \times 100$ site lattice. The structures visualised are monolithic, despite some clusters at the edges appearing unattached; these are connected to the structure via periodic boundaries. GIFs of the simulated materials can also be found in the Electronic Supporting Information (available from the University of Strathclyde KnowledgeBase [29]).

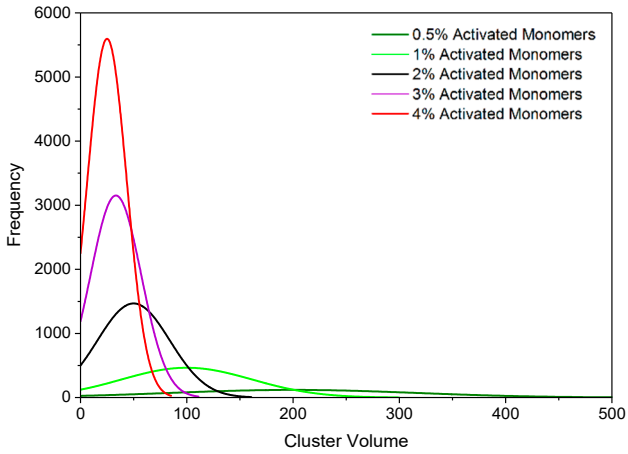

Figure 2. Histogram plots of primary cluster volume distributions at activated monomer (C_c) values of 0.5%–4%. Data are presented for 60% solids content (S_c).

The visual differences between the structures at various S_c values are evident. Higher S_c results in materials that, as expected, are more densely packed, with the primary clusters occupying more space within the lattice. When the average primary cluster sizes within the structures are compared, materials with the same C_c possess the same average volume and radius regardless of S_c. A structure simulated at a higher S_c will, however, have a greater number of primary clusters within its lattice in comparison to one at lower S_c at the same C_c value. This means that, although an increase in S_c results in an increase in monomers within the lattice, these monomers are distributed across a greater number of primary clusters, therefore, resulting in the average primary cluster size remaining constant across the different S_c values.

On the other hand, C_c has a significant impact on the average primary cluster size within the structure, as shown in Figure 2. As C_c increases from 0.5% to 4%, the average primary cluster volume decreases from 200 to 25 lattice sites. This is consistent with observations from experimental analysis of RF gels; materials synthesised with low catalyst concentrations comprise of fewer primary clusters that are larger in size, while those synthesised with high catalyst concentrations comprise of a greater number of primary clusters that are smaller in size [8].

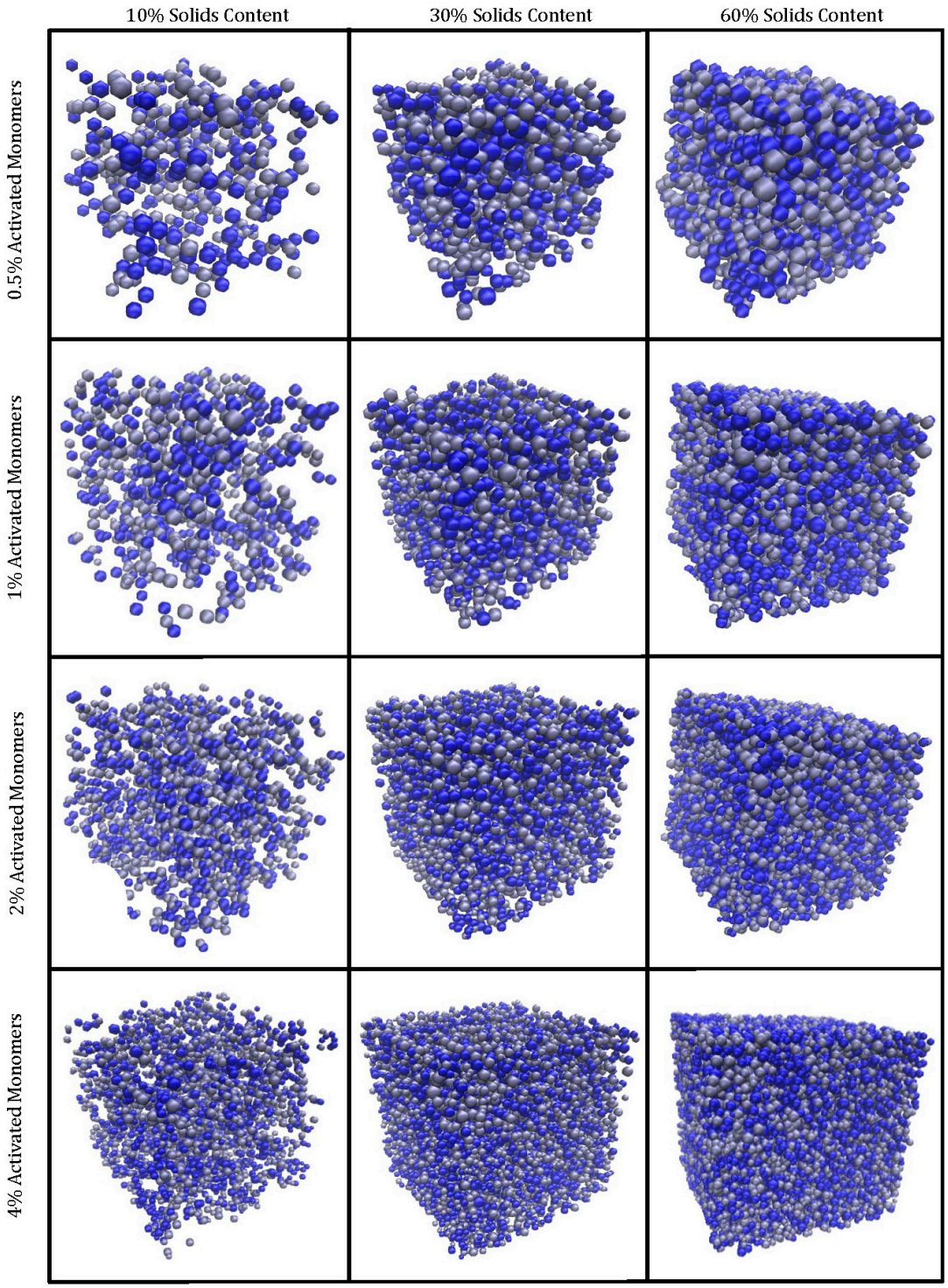

Figure 3. Simulated RF gel materials visualised in 3D, with increasing solids content (S_c), left to right, and an increasing percentage of activated monomers (C_c), top to bottom. Note that each sphere represents an individual cluster, and the different colours of clusters present are for visual purposes only.

2.2. *Accessibility of Sites*

The accessibility of pore sites within a porous material is a fundamental consideration when it comes to their application potential, and is, therefore, an important property to analyse within simulated structures. We consider how the accessibility is affected by the size of the guest species,

to understand how this might affect potential applications of the porous gel as a host for different molecules. As expected, the percentage of sites that are inaccessible increases with increasing S_c, as the lattices are more densely packed with material and, therefore, more likely to result in closed-off porosity. This is true for the accessibility of particles both of one and three sites in size (corresponding to molecular size of approximately 1 and 3 nm), as shown in Figure 4a,b, respectively. Furthermore, the percentage of inaccessible sites also increases with increasing C_c, which is a result of the increased number of clusters present. Structures formed at higher C_c possess a greater number of initial cluster seeds than those at lower values, leading to the formation of numerous smaller clusters, which pack together densely, increasing the likelihood of closed-off porosity.

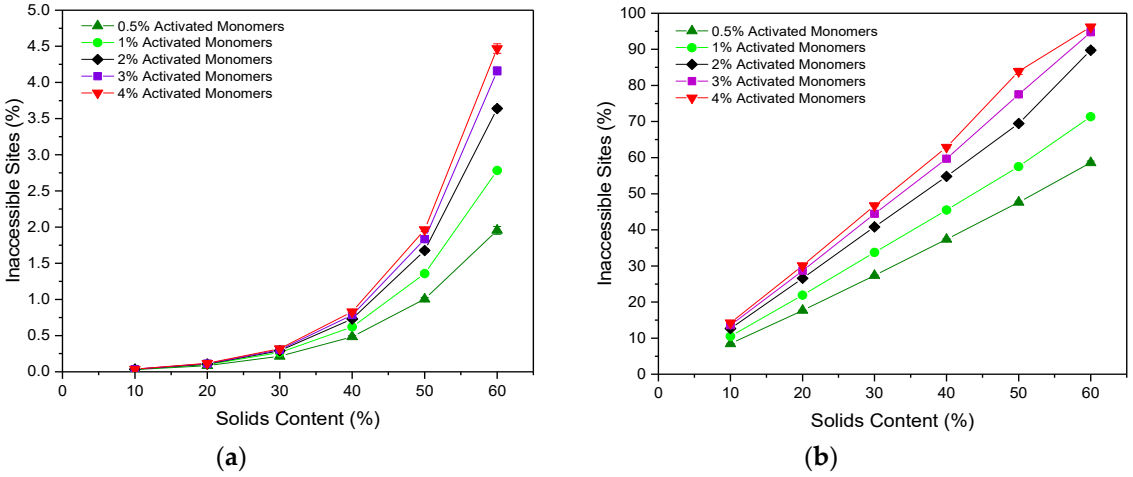

Figure 4. Percentage of inaccessible sites within the lattice with varying solids content (S_c) and activated monomer (C_c) values with respect to a diffusing particle of (**a**) Size 1 and (**b**) Size 3. Standard deviation error bars are present around each data point, although may not be visible due to their size relative to the data point marker.

The percentage of sites inaccessible to a particle of Size 1 remains consistently low, ranging from 0.028(2)% at 10% S_c and 0.5% C_c to 4.47(7)% at 60% S_c and 4% C_c. These values are considerably lower than those obtained for the 2D version of the code, which reached up to 25% inaccessible sites for structures formed with 50% S_c and 3% C_c [12]. Simulating the porous structure in three dimensions opens new accessible pathways for connectivity, which would otherwise be limited by the two-dimensional structure, explaining the significant decrease in the percentage of inaccessible sites within the lattice, and providing a more accurate representation of the porous materials synthesised in reality.

When the particle size is increased from one site to three sites, the percentage of inaccessible sites increases significantly across all S_c and C_c values, and the values obtained span a much wider range. In this case, values range from 8.45(3)% at 10% S_c and 0.5% C_c to 96.24(8)% at 60% S_c and 4% C_c. These results have significant implications for porous materials in their potential use for applications involving larger particles such as biomolecules, where optimisation of S_c and C_c values according to particle size would be imperative, ensuring that the synthesis parameters used produce structures with sufficiently accessible porous networks.

2.3. Surface Area

Figure 5a,b shows the accessible surface area per unit mass for particles of Sizes 1 and 3, respectively. For both particle sizes, the accessible surface area per mass gradually decreased as S_c increased across each of the C_c values studied. The increased number of primary clusters present for higher S_c (at a given C_c) results in structures that are more densely packed, as previously discussed. This increases the likelihood that a single primary cluster will be in contact with multiple primary clusters around

it, therefore reducing the accessible surface area available for particles moving through the porous structure. Furthermore, as expected, the accessible surface area is consistently higher for a particle of Size 1 than for Size 3, as the smaller particle can more easily access the narrower pores within the structure.

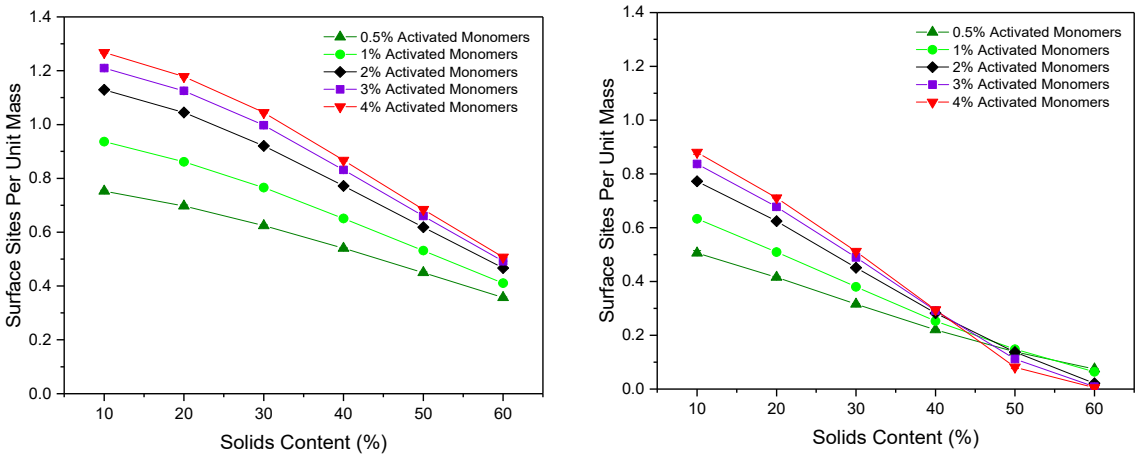

Figure 5. Accessible surface sites scaled with total mass with varying solids content (S_c) and activated monomer (C_c) values with respect to a diffusing particle of (**a**) Size 1 and (**b**) Size 3. Standard deviation error bars are present around each data point, although may not be visible due to their size relative to the data point marker.

The effect of variations in C_c can also be compared, the results of which indicate that, for a particle of one site in size, an increase in C_c value leads to an increased accessible surface area across the S_c values studied. As previously discussed, higher C_c values lead to a greater number of primary clusters present, across which the structure's mass is distributed. Consequently, for lower C_c materials, the larger primary clusters mean that much of the structure's mass is contained within the interior of each cluster, reducing the accessible area available at the surface. Conversely, for higher C_c materials with a greater number of primary clusters present, each of which is smaller in size, the accessible area available at the surface is increased. Similar trends for accessible surface area were also observed for the 2D version of this simulation for a particle of one site in size, although the work presented here explores a wider range of S_c and C_c values, as well as including the new analysis for a particle of three sites in size.

Importantly, these results are also consistent with those observed experimentally, where an increase in catalyst concentration is shown to increase the BET surface area values obtained from nitrogen adsorption measurements of RF gels [25,30].

When the particle size is increased to three sites, the same initial trend is observed where an increase in C_c leads to higher values of accessible surface area, however, an eventual crossover point is reached at an S_c value of around 45%. For S_c values above this point, increasing C_c has the inverse effect, where the accessible surface area is hindered by higher C_c values. This likely arises due to the high percentage of inaccessible sites for particles of Size 3, which is exacerbated by the increased interconnectivity arising at higher C_c values. An upper limit is therefore reached, where the increased interconnectivity associated with the greater number of primary clusters present is no longer of benefit to the available surface area of the system. Instead, it gives rise to higher rates of closed-off porosity and therefore reduces the accessibility of surface sites—an important consideration for the tailoring of these materials to various applications.

2.4. Correlation Dimension

The correlation dimension (D_c) of a structure is a measure of its fractal properties, with uniformly distributed, densely packed structures in three dimensions having $D_c = 3$, and fractal structures conversely having $D_c < 3$. As previously discussed, questions around the fractal nature of RF gels have been raised over the years with a consensus yet to be reached, therefore calculating D_c for the simulated structures could be pivotal in addressing some of the unanswered questions.

Figure 6 shows D_c for the simulated structures at various S_c and C_c, with most data provided between 10% and 20% S_c where the most significant changes in D_c are observed. For each C_c, a gradual increase in correlation dimension is observed as S_c increases from 10% to 20%, shortly thereafter plateauing around a value of 3, the value at which a structure is considered to possess no fractal properties. At the lowest S_c of 10%, the structure possesses D_c values of 2.68(1) and 2.76(1) for C_c values of 0.5% and 1%, respectively, indicating that the structures do exhibit some fractal properties under these conditions. These lower limit values are approaching that which would be expected of dilute cluster aggregation systems, determined to possess D_c values of ~2.5 [31]. For higher C_c structures at 10% S_c, the D_c value approaches 2.9, close to the nonfractal limit of three. These results indicate that fractal properties can be observed within these materials under specific synthesis conditions—reliant not only on sufficiently low S_c, as previously postulated, but also on sufficiently low C_c values. Under standard gel synthesis conditions within experiments, S_c values of 20% and above are commonly used, perhaps explaining why numerous studies have observed no fractal properties within the structures.

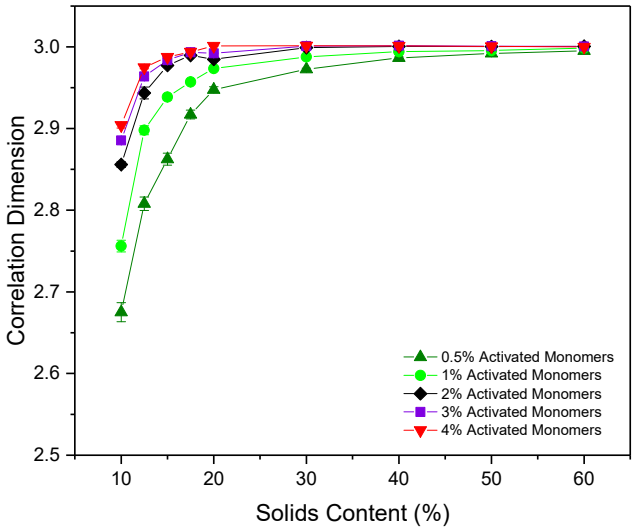

Figure 6. Correlation dimension values calculated for simulated materials at varying solids content (S_c) and activated monomer (C_c) values. Standard deviation error bars are present around each data point, although may not be visible due to their size relative to the data point marker.

These results differ from those obtained from the 2D simulation, where the value of a uniformly distributed, densely packed structure yields $D_c = 2$, with fractal structures having $1 < D_c < 2$. For the 2D model, D_c values obtained ranged from as low as ~1.55, and gradually increased with increasing S_c and C_c. D_c slowly reached a plateau at a value of two between 40% and 50% S_c, in contrast to the faster convergence of values within the 3D analysis. As previously discussed, 2D systems will have more restricted percolation pathways than in 3D structures, consequently influencing their fractal properties, explaining the disparity in calculated values across the two models. The work from the 2D model consequently concluded that the materials did, in fact, possess fractal properties, even those which had been synthesised at higher S_c and C_c. In light of the results presented here, this conclusion should now be revised.

2.5. Hurst Exponent for Diffusion through the Porous Structures

As discussed in the Methodology section, the Hurst exponent (H) of a particle moving through an empty lattice should be 0.5, indicating regular Brownian motion, with values below this pointing towards antipersistent motion. Figure 7a,b displays the H values calculated for simulated structures with various S_c and C_c values, for particles of Sizes 1 and 3, respectively. In both cases, the H value decreases with increasing S_c, as the path of the random walker becomes more obstructed due to the increased number of occupied sites densely packed within the lattice, directly affecting the particle's motion through the porous network.

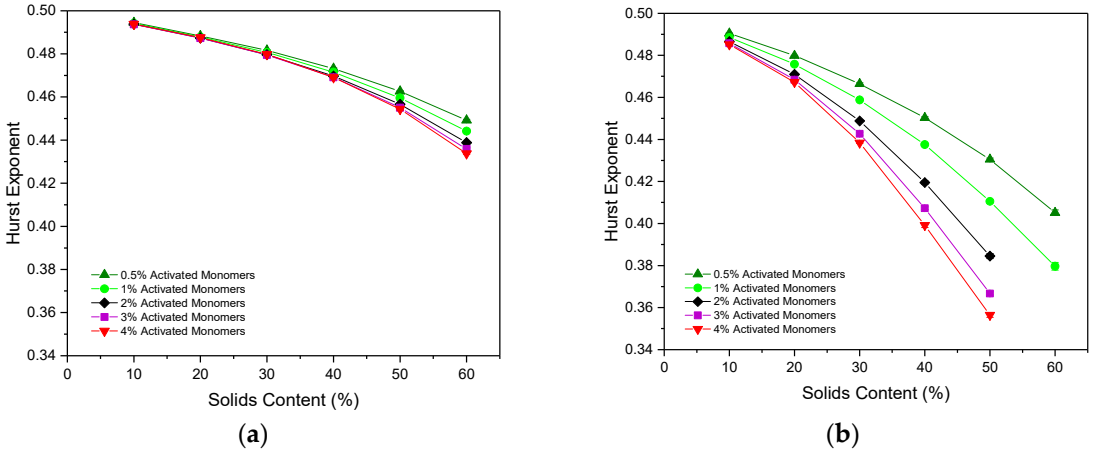

Figure 7. Hurst exponent values calculated for varying solids content (S_c) and activated monomer (C_c) values with respect to a diffusing particle of (**a**) Size 1 and (**b**) Size 3. Standard deviation error bars are present around each data point, although may not be visible due to their size relative to the data point marker. Note that a sufficiently percolated structure could not be identified for structures above 1% C_c at 60% S_c for a particle of three sites in size, hence the missing values.

The value of H also decreases as the value of C_c increases, this time as a result of the increasingly complex, interconnected structures formed from the greater number of primary clusters present. These complex structures create additional obstructions within the path of the random walker, hindering its ability to diffuse freely throughout the lattice and, therefore, decreasing the value of H.

The H values obtained for a random walker of Size 1 range from 0.4945(2) at 10% S_c and 0.5% C_c to 0.4338(2) at 60% S_c and 4% C_c. As these values are all below 0.5, they indicate that the random walker motion is antipersistent in nature, as previously discussed. For materials simulated at low S_c and C_c, this value falls only slightly below 0.5 due to the largely open, sparsely-populated structure within the lattice. These H values differ slightly from those cited for the 2D model, where the lowest value obtained reaches below ~0.36 for 50% S_c and 3% C_c. Similar to the comparative analysis of inaccessible sites between the 2D and 3D models, this disparity in H values arises as a result of the new pathway for accessibility opened by the 3D simulation. Once again, opening the structure to the third dimension allows the random walker to diffuse around the lattice more freely, and more accurately reflects how a particle might diffuse through a porous material in reality.

When the random walker size is increased from one to three, the H value obtained decreases far more rapidly as its ability to move around the lattice is restricted by its width. In this case, H values range from 0.4904(2) at 10% S_c and 0.5% C_c to 0.356(1) at 50% S_c and 4% C_c, close to the limit of 1/3 that is expected at the percolation threshold [12]. As with the analysis of the inaccessible sites for a particle of three sites in size, assessing the motion of such a particle through a porous material in this manner provides valuable insight for their use in applications involving diffusion of larger particles. Note that a sufficiently percolated pore structure could not be identified for materials formed using 60% S_c at C_c

values above 1% for a particle of Size 3, meaning that the porosity was too closed-off for the particle to freely diffuse through the structure.

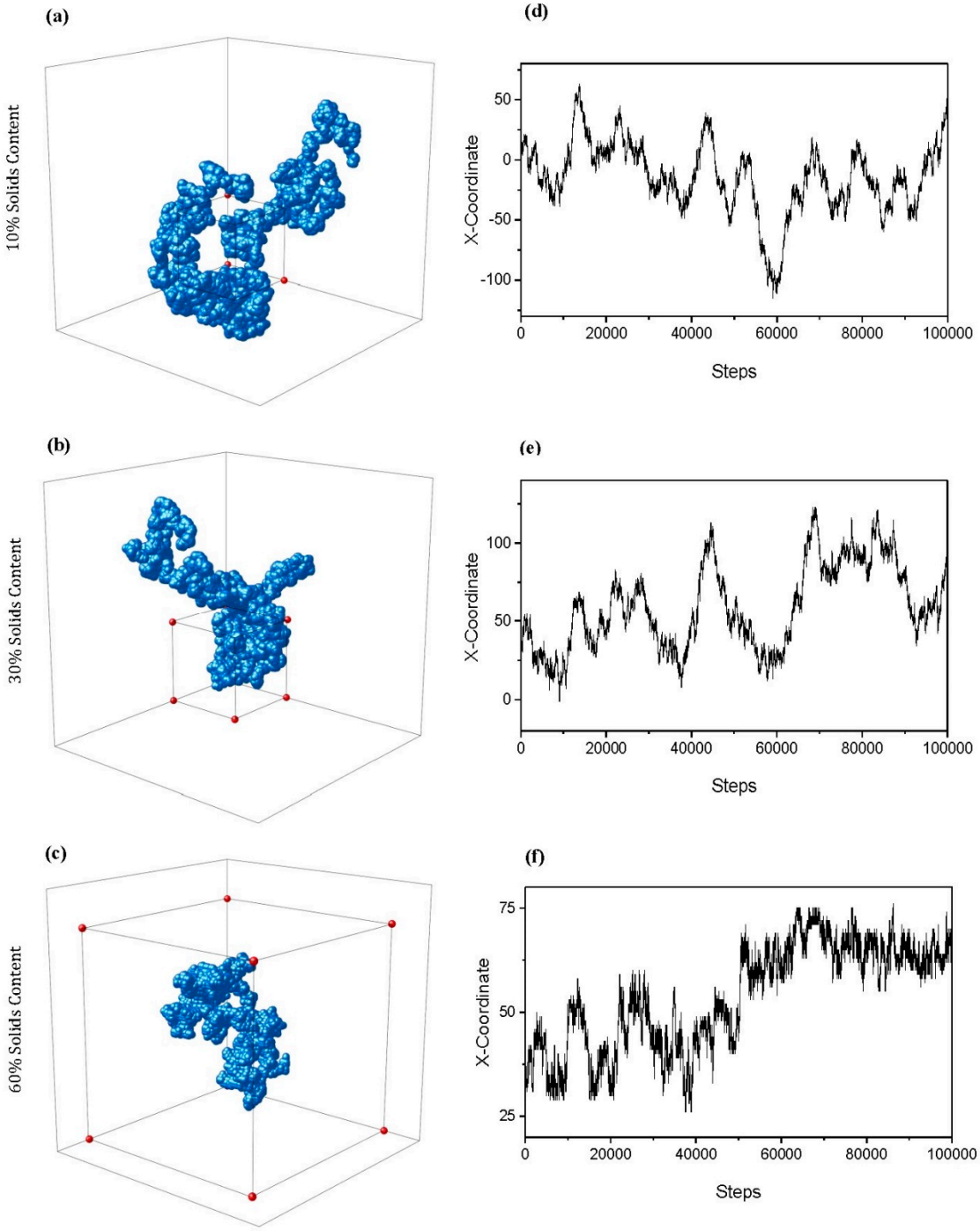

Figure 8. Example 3D traces for particles of three sites in size diffusing through simulated structures with 1% activated monomers (C_c) and solids content (S_c) values of (**a**) 10%, (**b**) 30%, and (**c**) 60%. Note that the axes of each trace differ dependent on the extent to which the particle was able to diffuse through the lattice across periodic boundaries—a box of size 100 × 100 × 100 sites is included within each trace to allow a comparison of scale. Corresponding *x* coordinate traces for each structure at S_c values of (**d**) 10%, (**e**) 30%, and (**f**) 60%.

The calculation of H also enables a 3D visual trace of how a particle might move through the porous structure, as shown in Figure 8a–c, for S_c values of 10, 30, and 60%, respectively. All visualised traces are for particles of Size 3 and $C_c = 1\%$. Note that the axes of each trace differ depending on the extent to which the particle was able to diffuse through the lattice across periodic boundaries—a box of $100 \times 100 \times 100$ sites in size has been included to allow a comparison of scale. As S_c increases, the path of the random walker becomes more obstructed, increasing the likelihood that it will turn back on itself as it diffuses around the lattice. This is reflected in the 3D traces visualised, where the particle is unable to explore the lattice to the same extent in the 60% S_c structure in comparison to the 10 or 30% S_c structures within the same number of steps. The periodic boundaries in place allowed the particle to continue to explore the lattice out with the $100 \times 100 \times 100$ original size, demonstrated particularly within the 10% S_c trace (Figure 8a) in addition to that of 30% (Figure 8b). This is in contrast to the 60% S_c diffusing particle (Figure 8c), whose path was far more limited in terms of the extent to which was able to explore the densely packed lattice. Figure 8d–f displays the traces of the x coordinate of the particle as it diffuses through the respective lattice, further highlighting the changing diffusive behaviour as the porous networks become more complex and constricted with increased S_c. These traces provide further insight into the internal percolated structure of the simulated material, and demonstrate the antipersistent nature of the particle's motion as it diffuses.

3. Conclusions

The formation mechanism of porous materials such as resorcinol–formaldehyde gels is captured in this work through the development of a 3D cluster growth and aggregation model. The model explores the effect of activated monomer percentage—a parameter that mimics catalyst concentration—and solids content, and allows comparisons to be drawn between the simulated materials and those synthesised in the lab. The resulting simulated material is a monolithic structure of interconnected primary (approximately spherical) clusters, consistent with structures observed experimentally.

Structural analysis of the simulated material was carried out across each solids content and activated monomer percentage studied, including pore accessibility and available surface area. Materials simulated with higher solids contents exhibited a higher percentage of inaccessible pore sites and reduced accessible surface area, both of which are as a result of the densely packed structures. Materials simulated with higher activated monomer percentages, on the other hand, were composed of a greater number of primary clusters that were smaller in size, leading to structures that exhibited an increase in accessible surface area for the diffusion of a particle of Size 1. For a particle of Size 3, this increase in accessible surface area was observed until an upper limit at a solids content of ~45%, after which the increased interconnectivity was no longer of benefit to the available surface area of the system. Instead, it gave rise to higher proportions of closed-off porosity, consequently reducing the accessibility of surface sites within the structure.

An important aspect of this research was to further explore the fractal properties of RF gels under varying synthesis conditions, and so the correlation dimensions of the simulated structures were calculated. The results obtained indicate that fractal properties can be observed within RF gel materials under specific synthesis conditions—reliant not only on sufficiently low solids content, as previously postulated, but also on sufficiently low catalyst concentrations. Under standard gel synthesis conditions within experiments, solids contents of 20% and above are commonly used, perhaps explaining why numerous studies have previously observed no fractal properties within the structures. This analysis sheds some light on the ongoing debate over the fractal properties of RF gels, and could explain the conflicting conclusions drawn from different experimental studies.

Hurst exponents for particles diffusing through the material's porous network were also calculated, the results of which point towards the antipersistent motion of the particle. The degree of antipersistence was exacerbated by increasing solids and catalyst concentration, as well as the increase in width from a diffusing particle of one site to three sites in size. Analysing the way in which a particle of varying size diffuses through these porous materials is an important consideration for their application potential

and subsequent optimisation, particularly for applications involving larger particles such as enzymes and antibodies. Furthermore, while the correlation dimension of the material (as measured through SAXS, for example) might not reveal fractal properties, the application of the material as an absorbent still requires consideration of the fractal nature of material diffusion through the porous structure.

This 3D simulation is a continuation of work from a 2D model, which operates under the same principles, with the progression to three dimensions providing a more accurate representation of the materials synthesised in reality. A direct comparison between specific experimental and computational materials is complex, however, due to the intricate nature of the resorcinol–formaldehyde reaction, in addition to the various synthesis conditions that significantly impact gel properties. As discussed, the range of values used for activated monomer percentages is based around the percentage of resorcinol molecules expected to be deprotonated in the presence of a basic catalyst, and, although the model successfully captures the trends in material properties as catalyst concentration is altered, an exact comparative experimental resorcinol/catalyst (R/C) ratio has not yet been established. Future work that uses sorption analysis to compare experimental and computational isotherms, allowing a more direct comparison to be drawn between activated monomer percentages and specific R/C ratios, is planned within our research group. Furthermore, the adaptation of this model to reflect acid-catalysed gels, where the final material comprises branched chains of spherical particles as opposed to aggregated clusters, could be of interest.

4. Materials and Methods

4.1. Simulation Procedure

The 3D model presented here builds on the work published by Prostredny et al. [12]—a 2D simulation which operates under the same principles—where a detailed description of the simulation process can be found. Here, a cubic lattice of Size 100 × 100 × 100 sites, totalling 1,000,000 sites, was initially populated at random with monomers according to the desired percentage solids content (S_c), an important parameter in the synthesis of RF gels in laboratory experiments. In this research, solids contents of 10%–60% were simulated, with values above this range proving to result in densely packed structures with pores that are predominantly inaccessible. This model was developed with GNU Fortran compiler and GNU parallel tool [32].

As previously discussed, the laboratory synthesis of RF gels includes a reaction between resorcinol and formaldehyde molecules with the addition of a basic catalyst, the presence of which leads to the formation of negatively charged resorcinol ions. These anionic molecules subsequently act as cluster seeds around which monomers can attach, leading to the formation of primary (approximately spherical) clusters. This process is modelled in the simulation by "activating" at random a percentage of the monomers on the lattice, with each activated monomer acting as a primary cluster seed for the simulation, and where the varying percentage of activated monomers is comparable to varying catalyst concentration (C_c). In this research, activated monomer percentages of 0.5%–4% are simulated, a range based on the proposed percentage of resorcinol molecules that are deprotonated by a basic catalyst during the RF reaction [33].

The simulation begins with the random diffusion (nearest-neighbour hopping) of monomers on the lattice, with periodic boundary conditions, during which free monomers attach to activated monomers when they come into contact, forming larger primary clusters of monomers. These monomers attach in an approximately spherical sequence, as described in the work by Prostredny et al. [12], producing primary clusters that also diffuse on the lattice following the same basic scaling laws for diffusion. Two diffusing clusters irreversibly attach when they meet, retaining the primary clusters intact. The probability of cluster diffusion is inversely proportional to its mass, which takes into account the aggregation of primary particles to create irregular aggregates for diffusion. We only include simple nearest-neighbour hops in this model, since the growth occurs in a crowded environment so that effects

of rotational diffusion or finite reactivity are expected to be minimal; further work on this aspect could be undertaken if required to explain experimental data.

The simulation proceeds until there are no free monomers present and the entire lattice comprises one monolithic, interconnected aggregate structure. The final structure is a porous network comprising primary clusters aggregated together, similar to that observed for RF gels as evident in Figure 1. Note, however, that the simulation could also be applicable to other porous materials whose formation mechanism operates under similar principles.

Each simulation was repeated with 10 different random number seeds, resulting in 10 different structures at each value of S_c and C_c. An average was then calculated for each of the properties analysed across the 10 structures at each S_c and C_c, as well as the corresponding standard deviation of the values calculated.

4.2. Visualisation

Visualisation of these three-dimensional structures is important not only for a comparison between the different simulated materials, but also for visual comparison with materials synthesised experimentally. The 3D structures from this simulation are visualised using Visual Molecular Dynamics (VMD) software, with each primary cluster represented by a sphere, the coordinates of which are taken from the lattice and inserted into a VMD-readable file format. The average number of monomers within each primary cluster was taken to be an equivalent spherical volume, and the average equivalent radius was subsequently determined and used to visualise the clusters as spheres. In this way, a structure that is easy to visualise, while reflecting the most important characteristics in terms of primary particles and the aggregated gel structure, is generated.

4.3. Textural Analysis

The various textural properties of these structures, at varying S_c and C_c, are analysed and compared, including accessibility of pore sites for particles of both 1 and 3 lattice sites in size (hereafter referred to as Sizes 1 and 3). The length scale of the lattice is comparable to that of the RF dimer at ~1 nm [12], so a particle of Size 3 is comparable to a typical globular protein. The percentage of accessible pore sites for a particle of Size 1 is calculated by determining the percolated network of accessible sites within the structure, then expressing the total number of accessible sites within this network as a percentage of the total number of unoccupied sites within the lattice. To analyse the accessibility for a particle of Size 3, an exclusion zone of 1 site thickness is added to the simulated structures.

The accessible surface area of each structure with respect to its mass was also analysed for particles of Size 1 and 3. For a particle of Size 1, the total number of unoccupied sites adjacent to the surface of the cluster structure is divided by the total number of monomer sites within the structure. A similar procedure is carried out for a particle of Size 3, this time counting only unoccupied sites adjacent to the exclusion zone.

4.4. Fractal Analysis

As previously mentioned, computationally determining the fractal properties of RF gel materials, in particular, is of interest, especially in light of the conflicting conclusions that have been reached in various experimental studies. Suitable characterisation methods include the box counting dimension (D_b), the information dimension (D_i), and the correlation dimension (D_c). Of these, the most common dimension estimate used to characterise a fractal material is the correlation dimension, which is the more computationally efficient to determine of the three, and is based upon the proximity of points within the structure to one another within a spanning radius. Its calculation firstly begins with the determination of the correlation sum (C_r), as established by Grassberger [34] using Equation (1):

$$C_r = \frac{1}{N(N-1)} \sum_{i=1}^{N} \sum_{j=1;j\neq 1}^{N} \theta\left(r - \left|X_i - X_j\right|\right) \quad (1)$$

Here, θ is the Heaviside function, r is the spanning radius, N is the total number of randomly selected reference points within the structure, and X_i and X_j are the coordinates of the two points whose proximity are being analysed within the system. The Heaviside function (θ) is equal to 1 when $\left(r - \left|X_i - X_j\right|\right)$ returns a positive value, indicating that the separation of points i and j is within the spanning radius. Conversely, when $\left(r - \left|X_i - X_j\right|\right)$ returns a negative value, θ is equal to 0. This calculation is carried out across increasing values of spanning radius until the entire structure has been encapsulated and C_r consequently reaches a plateau.

The correlation sum relates to the spanning radius in the following manner:

$$C_r \propto r^{D_c} \quad (2)$$

where the exponent D_c is the correlation dimension. Obtaining the value of D_c, therefore, involves a logarithmic plot of the correlation sum vs. the spanning radius.

In this work, the correlation dimension for the simulated material is calculated from $N = 100{,}000$ different reference positions within the structure. Each position is selected at random, and the spanning radius between two reference positions is calculated for all periodic images, with the lowest value used to determine the correlation sum using Equation (1). A logarithmic plot of C_r vs. r is produced in accordance with Equation (2), where the central area of the graph is a straight-line plot with no size limitations affecting the results, as described in the work by Prostredny et al. [12]. The value of D_c is subsequently determined from the gradient of this linear section of the plot, eliminating the potential for finite size effects to impact the conclusions drawn around fractal properties. Example plots used to determine D_c are shown in Figures S1 and S2 in the Supplementary Materials.

Analysing the fractional Brownian motion trajectory of a particle moving through a porous material is another valuable way in which its fractal characteristics can be determined. This is quantified using the original rescaled range method to calculate the Hurst exponent from the particle trace in the x, y and z directions when the particle takes a "random walk"—a series of random steps throughout the structure. Three classifications of fractal Brownian motion have been established: (1) Antipersistent motion, where the particle has a tendency to turn back on itself and revisit previous positions; (2) Neutrally persistent motion, also known as regular Brownian motion, which is observed when the particle is free to move around a lattice with no obstructions; (3) Persistent motion, where the particle has a tendency to progress its path in a particular direction. The value of the Hurst exponent from the random walk will determine which class of motion is observed, with values below 0.5 indicating antipersistence, values of 0.5 exactly indicating regular Brownian, and values above 0.5 indicating persistence.

The particle displacement from its origin over time is used to calculate the Hurst exponent, where the relationship between the average displacement (ΔB) across the x, y, and z directions and the time window T_s is as follows:

$$\overline{|\Delta B|} \propto (T_s)^H \quad (3)$$

Here, the exponent H is the Hurst exponent, evaluated as the gradient of the logarithmic graph of ΔB vs. T_s [35]. Example plots used to calculate H are shown in Figures S3 and S4.

In order to determine H, a random walker is allowed to diffuse through the accessible pore sites within the lattice and its path analysed in the x, y and z directions. The random walker takes 100,000 random steps in total from 100 different starting positions on the percolated structure (determined as above), and the average displacement (ΔB) for each time window size (T_s) is calculated from the 100 traces. Note that the value of H calculated here is, therefore, that of the percolated porous network contained within the structure and not of the solid structure itself.

Supplementary Materials: Supplementary materials can be found at http://www.mdpi.com/2310-2861/6/3/23/s1.

Author Contributions: Conceptualization, A.F. and P.M.; formal analysis, E.M. and M.P.; funding acquisition, A.F. and P.M.; methodology, E.M. and M.P.; project administration, A.F.; Supervision, A.F. and P.M.; writing—original draft, E.M.; writing—review and editing, E.M., M.P., A.F. and P.M. All authors have read and agreed to the published version of the manuscript.

Funding: This research was funded by the Engineering and Physical Sciences Research Council (EPSRC) through the National Productivity Investment Fund (NPIF). Grant number: EP/R512205/1.

Acknowledgments: Elisha Martin thanks the Chemical and Process Engineering Department at the University of Strathclyde, and the Engineering and Physical Sciences Research Council for funding this work. The authors would also like to acknowledge the SEM analysis carried out at Angstrom Laboratory in Uppsala University, Sweden, in collaboration with Farnaz Ghajeri and Svenska Aerogel AB.

Conflicts of Interest: The authors declare no conflicts of interest.

References

1. Das, S.; Heasman, P.; Ben, T.; Qiu, S. Porous Organic Materials: Strategic Design and Structure–Function Correlation. *Chem. Rev.* **2017**, *117*, 1515–1563. [CrossRef] [PubMed]
2. Xie, L.-H.; Suh, M.P. High CO2-Capture Ability of a Porous Organic Polymer Bifunctionalized with Carboxy and Triazole Groups. *Chem. Eur. J.* **2013**, *19*, 11590–11597. [CrossRef] [PubMed]
3. Yuan, W.; Zhang, X.; Zhao, J.; Li, Q.; Ao, C.; Xia, T.; Zhang, W.; Lu, C. Ultra-lightweight and highly porous carbon aerogels from bamboo pulp fibers as an effective sorbent for water treatment. *Results Phys.* **2017**, *7*, 2919–2924. [CrossRef]
4. Xu, P.; Drewes, J.E.; Heil, D.; Wang, G. Treatment of brackish produced water using carbon aerogel-based capacitive deionization technology. *Water Res.* **2008**, *42*, 2605–2617. [CrossRef] [PubMed]
5. Thapliyal, P.C.; Singh, K. Aerogels as Promising Thermal Insulating Materials: An Overview. *J. Mater.* **2014**, *2014*, 127049. [CrossRef]
6. Feng, J.; Zhang, C.; Feng, J. Carbon fiber reinforced carbon aerogel composites for thermal insulation prepared by soft reinforcement. *Mater. Lett.* **2012**, *67*, 266–268. [CrossRef]
7. Li, J.; Wang, X.; Huang, Q.; Gamboa, S.; Sebastian, P.J. Studies on preparation and performances of carbon aerogel electrodes for the application of supercapacitor. *J. Power Sources* **2006**, *158*, 784–788. [CrossRef]
8. Al-Muhtaseb, S.A.; Ritter, J.A. Preparation and Properties of Resorcinol–Formaldehyde Organic and Carbon Gels. *Adv. Mater.* **2003**, *15*, 101–114. [CrossRef]
9. Taylor, S.J.; Haw, M.D.; Sefcik, J.; Fletcher, A.J. Gelation Mechanism of Resorcinol-Formaldehyde Gels Investigated by Dynamic Light Scattering. *Langmuir* **2014**, *30*, 10231–10240. [CrossRef] [PubMed]
10. Shen, J.; Hou, J.; Guo, Y.; Xue, H.; Wu, G.; Zhou, B. Microstructure Control of RF and Carbon Aerogels Prepared by Sol-Gel Process. *J. Sol-Gel Sci. Technol.* **2005**, *36*, 131–136. [CrossRef]
11. Awadallah-F, A.; Elkhatat, A.; Al-Muhtaseb, S. Impact of synthesis conditions on meso- and macropore structures of resorcinol–formaldehyde xerogels. *J. Mater. Sci.* **2011**, *46*, 7760–7769. [CrossRef]
12. Prostredny, M.; Fletcher, A.; Mulheran, P. Modelling the formation of porous organic gels – how structural properties depend on growth conditions. *RSC Adv.* **2019**, *9*, 20065–20074. [CrossRef]
13. Díez Orrite, S.; Stoll, S.; Schurtenberger, P. Off-lattice Monte Carlo simulations of irreversible and reversible aggregation processes. *Soft Matter* **2005**, *1*, 364–371. [CrossRef] [PubMed]
14. Lattuada, M.; Wu, H.; Morbidelli, M. A simple model for the structure of fractal aggregates. *J. Colloid Interface Sci.* **2003**, *268*, 106–120. [CrossRef]
15. Rottereau, M.; Gimel, J.C.; Nicolai, T.; Durand, D. Monte Carlo simulation of particle aggregation and gelation: I. Growth, structure and size distribution of the clusters. *Eur. Phys. J. E* **2004**, *15*, 133–140. [CrossRef]
16. Jungblut, S.; Joswig, J.-O.; Eychmüller, A. Diffusion-Limited Cluster Aggregation: Impact of Rotational Diffusion. *J. Phys. Chem. C* **2019**, *123*, 950–954. [CrossRef]
17. Jungblut, S.; Joswig, J.-O.; Eychmüller, A. Diffusion- and reaction-limited cluster aggregation revisited. *Phys. Chem. Chem. Phys.* **2019**, *21*, 5723–5729. [CrossRef]
18. Meakin, P. Formation of Fractal Clusters and Networks by Irreversible Diffusion-Limited Aggregation. *Phys. Rev. Lett.* **1983**, *51*, 1119–1122. [CrossRef]
19. Kolb, M.; Botet, R.; Jullien, R. Scaling of Kinetically Growing Clusters. *Phys. Rev. Lett.* **1983**, *51*, 1123–1126. [CrossRef]

20. Gavalda, S.; Kaneko, K.; Thomson, K.T.; Gubbins, K.E. Molecular modeling of carbon aerogels. *Colloids Surf. A* **2001**, *187–188*, 531–538. [CrossRef]
21. Gavalda, S.; Gubbins, K.E.; Hanzawa, Y.; Kaneko, K.; Thomson, K.T. Nitrogen Adsorption in Carbon Aerogels: A Molecular Simulation Study. *Langmuir* **2002**, *18*, 2141–2151. [CrossRef]
22. Tamon, H.; Ishizaka, H. Influence of Gelation Temperature and Catalysts on the Mesoporous Structure of Resorcinol–Formaldehyde Aerogels. *J. Colloid Interface Sci.* **2000**, *223*, 305–307. [CrossRef] [PubMed]
23. Horikawa, T.; Hayashi, J.I.; Muroyama, K. Controllability of pore characteristics of resorcinol–formaldehyde carbon aerogel. *Carbon* **2004**, *42*, 1625–1633. [CrossRef]
24. Pekala, R.W. Organic aerogels from the polycondensation of resorcinol with formaldehyde. *J. Mater. Sci.* **1989**, *24*, 3221–3227. [CrossRef]
25. Pekala, R.W.; Schaefer, D.W. Structure of organic aerogels. 1. Morphology and scaling. *Macromolecules* **1993**, *26*, 5487–5493. [CrossRef]
26. Tamon, H.; Ishizaka, H. SAXS Study on Gelation Process in Preparation of Resorcinol–Formaldehyde Aerogel. *J. Colloid Interface Sci.* **1998**, *206*, 577–582. [CrossRef]
27. Berthon, S.; Barbieri, O.; Ehrburger-Dolle, F.; Geissler, E.; Achard, P.; Bley, F.; Hecht, A.-M.; Livet, F.; Pajonk, G.M.; Pinto, N.; et al. DLS and SAXS investigations of organic gels and aerogels. *J. Non-Cryst. Solids* **2001**, *285*, 154–161. [CrossRef]
28. Alshrah, M.; Mark, L.H.; Zhao, C.; Naguib, H.E.; Park, C.B. Nanostructure to thermal property relationship of resorcinol formaldehyde aerogels using the fractal technique. *Nanoscale* **2018**, *10*, 10564–10575. [CrossRef]
29. Data for: "Modelling Organic Gel Growth in Three-Dimensions: Textural and Fractal Properties of Resorcinol-Formaldehyde Gels". Available online: https://pureportal.strath.ac.uk/en/datasets/data-for-modelling-organic-gel-growth-in-three-dimensions-textura (accessed on 8 July 2020).
30. Prostredný, M.; Abduljalil, M.G.M.; Mulheran, P.A.; Fletcher, A.J. Process Variable Optimization in the Manufacture of Resorcinol-Formaldehyde Gel Materials. *Gels* **2018**, *4*, 36. [CrossRef]
31. Bowler, N.E.; Ball, R.C. Off-lattice noise reduced diffusion-limited aggregation in three dimensions. *Phys. Rev. E* **2005**, *71*, 011403. [CrossRef]
32. Tange, O. GNU Parallel—The Command-Line Power Tool. *USENIX Mag.* **2011**, *36*, 42–47.
33. Lin, C.; Ritter, J.A. Effect of synthesis pH on the structure of carbon xerogels. *Carbon* **1997**, *35*, 1271–1278. [CrossRef]
34. Grassberger, P.; Procaccia, I. Characterization of Strange Attractors. *Phys. Rev. Lett.* **1983**, *50*, 346–349. [CrossRef]
35. Addison, P.S. *Fractals and Chaos: An Illustrated Course*; CRC Press: Boca Raton, FL, USA, 1997.

D.2 Advancing Computational Analysis of Porous Materials – Modeling Three-Dimensional Gas Adsorption in Organic Gels (Published)

THE JOURNAL OF PHYSICAL CHEMISTRY B
A JOURNAL OF THE AMERICAN CHEMICAL SOCIETY

pubs.acs.org/JPCB

Article

Advancing Computational Analysis of Porous Materials—Modeling Three-Dimensional Gas Adsorption in Organic Gels

Elisha Martin, Martin Prostredny, Ashleigh Fletcher, and Paul Mulheran*

Cite This: *J. Phys. Chem. B* 2021, 125, 1960–1969

Read Online

ACCESS | Metrics & More | Article Recommendations | Supporting Information

ABSTRACT: Assessing the efficacy of specific porous materials for use in various applications has been a central focus for many experimental studies over the years, with a view to altering the material properties according to the desired characteristics. The application potential for one such class of nanoporous materials—organic resorcinol-formaldehyde (RF) gels—is of particular interest, due to their attractive and adjustable properties. In this work, we simulate adsorption analysis using lattice-based mean field theory, both in individual pores and within three-dimensional porous materials generated from a kinetic Monte Carlo cluster aggregation model. We investigate the impacts of varying pore size and geometry on the adsorptive behavior, with results agreeing with those previously postulated in the literature. The adsorption analysis is carried out for porous materials simulated with varying catalyst concentrations and solids contents, allowing their structural properties to be assessed from resulting isotherms and the adsorption and desorption processes visualized using density color maps. Isotherm analysis indicated that both low catalyst concentrations and low solids contents resulted in structures with open transport pores that were larger in width, while high catalyst concentrations and solids contents resulted in structures with bottleneck pores that were narrower. We present results from both the simulated isotherms and pore size analysis distributions, in addition to results from RF gels synthesized in the lab and analyzed experimentally, with significant similarities observed between the two. Not only do the results of this comparison validate the kinetic Monte Carlo model's ability to successfully capture the formation of RF gels under varying synthesis parameters, but they also show significant promise for the tailoring of material properties in an efficient and computationally inexpensive manner—something which would be pivotal in realizing their full application potential, and could be applied to other porous materials whose formation mechanism operates under similar principles.

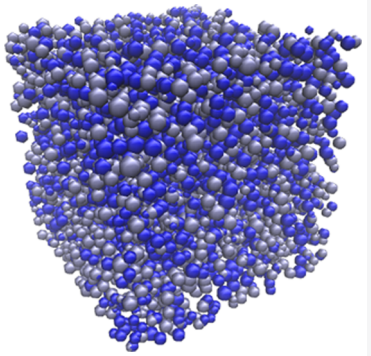

1. INTRODUCTION

The properties of various porous materials have been investigated extensively over the years through experimental work, with a view to understanding the impacts of various synthesis parameters, in addition to optimizing such materials for use in specific applications. To date, applications for porous organic materials have ranged from gas adsorption[1] and water treatment[2,3] to thermal insulation[4] and energy storage.[5] This work focuses on resorcinol-formaldehyde (RF) gels, which are organic materials with high surface areas, low densities, and high porosities and whose exceptional structural properties can be tailored according to application requirements. Further exploring the application potential of these materials is pivotal; however, experimental studies investigating the properties of RF gels and their application performance commonly report a time-consuming synthesis process, with traditional gel formation as first described by Pekala (1989)[6] followed by drying and analysis stages, requiring several days, occasionally weeks, to complete.[7] Although not yet widely adopted, microwave synthesis of RF gels has proven to significantly reduce the time required for synthesis in the lab, although analysis time requirements, of course, remain the same.[8,9] This presents an opportunity, therefore, to explore computational means of investigating the properties of porous materials such as these, allowing their characteristics to be tailored more efficiently according to application requirements.

One of the most fundamental analysis methods for porous materials is nitrogen adsorption measurements, the isotherm data from which provides crucial details on the material's internal structure, including the size, geometry, and total volume of the pores present, as well as the adsorption behavior of the gas on the material's surface, such as observations of monolayer or multilayer formation. Different isotherm and hysteresis types have been categorized by the International Union of Pure and Applied Chemistry (IUPAC) according to their shape, detailing the implications of these in terms of the material's structure.[10]

Computational adsorption analysis as a means to understanding porous structures in greater detail has also been

Received: December 9, 2020
Revised: February 2, 2021
Published: February 16, 2021

studied, providing insight into the adsorption and desorption mechanisms and allowing material properties to be determined. Multiple techniques have been employed to model the adsorption process, including classical density functional theory (DFT) calculations,[11,12] in addition to Monte Carlo and molecular dynamics simulations, which have explored adsorption within materials such as graphite,[13] nanoporous silica,[14] and metal organic frameworks,[15] producing adsorption isotherms for the simulated materials studied. Recent progress in models such as these has even led to the development of widely accessible adsorption software.[16] Although adsorption models such as these provide valuable insights into the detailed interactions between adsorbates and adsorbents, their relevance to industrial applications is limited by their significant computational expense.[17] Furthermore, many of the studies which utilize these methods are able to simulate adsorption within just a few structures, or within specific individual pores, as opposed to performing the analysis over a wide range of varying structures that would be valuable for tailoring materials.

In an effort to advance toward more computationally efficient adsorption analysis, more recent studies have taken a coarse-grain approach using lattice-based mean field theory (MFT), with studies focusing on understanding the adsorption mechanism within individual pores of varying sizes and geometries[18−20] and further work extending to adsorption analysis within complex porous structures.[21,22] This approach has also been applied to silica gels, using it predominantly as a tool to elucidate the mechanisms behind hysteresis formation.[23,24] The work presented here builds upon this approach, applying these lattice-based MFT calculations to three-dimensional simulated porous organic gels to model adsorption analysis within materials produced across a range of synthesis parameters, allowing an extensive range of structures to be explored and analyzed, with a view to enable material tailoring.

We have previously reported our findings from a 3D model developed within our group that simulates the growth of porous organic materials, such as RF gels, from the initial monomer species through to the interconnected final cluster structure.[25,26] This lattice-based Monte Carlo simulation has modeled the formation of RF gels across varying catalyst concentrations and solids contents—two fundamental parameters that have proven to control gel properties in experimental work—and the resulting materials were analyzed for their textural and fractal properties such as average cluster size, accessible surface area, and correlation dimension. The development of a 3D model such as this is a pivotal step toward computational optimization of porous materials for use in various applications, and being able to perform adsorption analysis of materials produced across a range of synthesis parameters would be crucial in advancing toward this reality, especially given that adsorption analysis is one of the most fundamental techniques used to characterize materials in experimental work. The work presented here, therefore, models adsorption analysis of the porous structures which have been created from our lattice-based Monte Carlo simulation, across varying catalyst concentrations and solids contents, the results of which can be directly compared to experimental analysis of RF gels which have been synthesized in the lab.

2. METHODOLOGY

2.1. Porous Structure Simulation Procedure. The structures analyzed in this work are produced from a three-dimensional lattice-based model, which simulates the formation and growth of porous materials through kinetic Monte Carlo cluster−cluster aggregation. A full description of the simulation process, in addition to the textural and fractal properties of the materials produced, can be found in the previously published works.[25,26] The models presented both in our previous works and in this work were developed with the GNU Fortran compiler and GNU parallel tool.[27]

This simulation is performed on a 1 000 000 site lattice, where the desired solids content is achieved by populating a percentage of the lattice sites with monomers. The laboratory synthesis of RF gels includes a reaction between resorcinol and formaldehyde molecules with the addition of a basic catalyst, the presence of which leads to the formation of negatively charged resorcinol ions. These act as cluster seeds with which monomers can react, leading to the formation of monomer clusters. This process is modeled in the simulation by "activating" at random a percentage of the monomers on the lattice, with each activated monomer acting as a cluster seed for the simulation, and where the varying percentage of activated monomers is comparable to varying catalyst concentration (C_C). In this research, activated monomer percentages of 0.1−4% are simulated, a range based on the proposed percentage of resorcinol molecules that are deprotonated by a basic catalyst during the RF reaction.[28] Solids contents (S_C) of 10−50% were used for the work presented here, once again selecting relevant values comparable to materials commonly synthesized experimentally.

Each simulation was repeated with 10 different seeds for the random number generator, resulting in 10 different structures at each S_C and C_C percentage. The final material is a porous network of primary spherical clusters similar to that of RF gels; however, the simulation could also be applicable to other porous materials whose formation mechanism operates under similar principles. Figure 1 shows the final simulated porous material, visualized in 3D, at 30% S_C and 2% C_C.

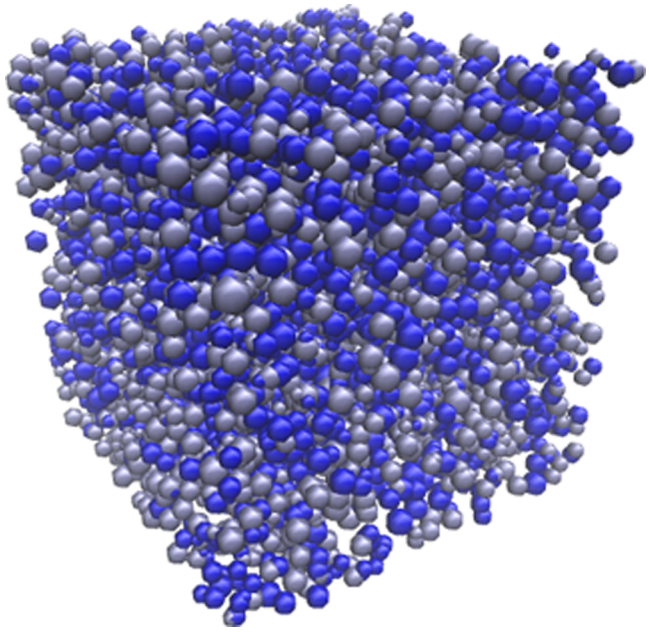

Figure 1. Simulated organic gel visualized in 3D at 30% solids content (S_C) and 2% activated monomers (C_C). Note that each sphere represents an individual cluster, and the different colors of clusters present are for visual purposes only.

https://dx.doi.org/10.1021/acs.jpcb.0c11000
J. Phys. Chem. B 2021, 125, 1960−1969

2.2. Adsorption Analysis Procedure. Given that adsorption analysis is one of the most common methods employed to characterize porous materials experimentally, modeling this process computationally for simulated structures allows helpful comparisons to be drawn between experimental and computational results. The adsorption model used to analyze the cluster structure presented here is based upon work by Monson,[18] which has been implemented in a three-dimensional lattice for this work so that it is applicable to individual pores as well as larger porous structures. This simulates the adsorption process using mean field theory for a lattice gas system, calculating the gas density across the lattice with varying relative activity—a chemical potential parameter relating directly to the relative pressure of the gas. A detailed explanation of the calculations carried out within this model is provided in the original paper by Monson.[18]

These calculations for adsorption analysis are based upon the mean field approximation of the system Helmholtz energy (F), shown in eq 1:

$$F = kT \sum_i [\rho_i \ln \rho_i + (1 - \rho_i) \ln(1 - \rho_i)] - \frac{\in}{2} \sum_i \sum_a \rho_i \rho_{i+a} + \sum_i \rho_i \Phi_i \quad (1)$$

where k is the Boltzmann constant, T is the system temperature, ρ_i is the average density of site i within the lattice, $\in$ is the nearest neighbor interaction strength, and Φ_i is the external field at site i. The density distribution at equilibrium, where the overall density of the system is fixed, is related to chemical potential (μ) using eq 2:

$$\frac{\partial F}{\partial \rho_i} - \mu = 0 \quad (2)$$

This relationship can then be used to calculate ρ_i at various μ values and subsequently calculate the average density of the system using the iterative procedure described in detail by Monson, assuming that μ is equal across the system. The system activity (λ) is then related to μ using eq 3:

$$\lambda = \exp\left(\frac{\mu}{kT}\right) \quad (3)$$

This is calculated for 2000 adsorption points and 2000 desorption points, and the resulting isotherms are plotted with respect to relative activity (λ/λ_0), which is directly comparable to relative pressure (p/p_0) in nitrogen adsorption experiments.[18]

Here, this model is used to simulate adsorption initially within individual 3D pores of varying widths and lengths, for both open transport pores and bottleneck pores which are closed at one end. This allows a comparison to be made between the simulated isotherms and those expected for the various pore sizes and geometries, therefore validating the model and providing a baseline for the isotherms generated from the simulated adsorption process within the porous structures. To simulate the adsorption process within the simulated porous material, the adsorption model was adapted to accommodate the 1 000 000 site lattice structure, and the final material from the cluster−cluster aggregation model was exported into the necessary format for the analysis to be carried out.

The adsorption analysis was carried out for 10 different simulated materials produced at each solids content and activated monomer percentage, and an average was taken across the 10 isotherms.

2.3. Adsorption Process Visualization. Given that the adsorption simulation calculates the density of each lattice site for various chemical potentials, the adsorption and desorption processes can be visualized as density profiles across the lattice at a given point on the isotherm. In this work, this is visualized as a vertical 2D slice through the center of the lattice—for both individual pores in addition to the simulated structures—and plotted as a color map using MATLAB. Here, the wall sites are visualized as a solid red color, while the pore sites are visualized using a color scale that is based upon the density value of each site, with higher density values indicating where adsorption has taken place. These density profiles provide insight into the visual differences between the adsorption and desorption processes and allow comparisons to be drawn between what is observed visually and what is observed within the isotherm.

2.4. Pore Size Analysis. The pore size distribution of the simulated structure can be analyzed using the isotherm data from the adsorption analysis, in the same manner as in experimental analysis. The method employed here is based on the Barrett, Joyner, and Halenda (BJH) theory,[29] which is used frequently within experimental analysis, once again allowing more direct comparisons to be drawn between computational and experimental results. The BJH method is used to determine the pore size distribution and pore volumes within the meso- and macroporous range, assuming pores of cylindrical shape are present, with the principle of this method relying on the calculation of the Kelvin core radius of the pore at set pressure intervals using the desorption isotherm data.

The pore size calculations are predominantly based around the Kelvin core radius equation for desorption (eq 4), which defines the relationship between relative pressure (or, in this case, relative activity) and core radius:

$$\mathrm{Rc}_i = \frac{-A}{\ln(\lambda/\lambda_0)_i} \quad (4)$$

where $(\lambda/\lambda_0)_i$ is the relative activity at point i, Rc_i is the corresponding Kelvin core radius at point i, and A is the adsorbate property factor—a value that accounts for properties such as surface tension and molar volume—and is equal to 0.953 for nitrogen gas.

When BJH analysis is carried out experimentally, an empirical formula is used to determine the thickness of the layer which remains adsorbed onto the pore walls after the core of the pore empties, the coefficients of the equation applying to interactions between specific adsorbents and adsorbates. The total pore radius can, therefore, be determined as the sum of the Kelvin core radius and the thickness of the adsorbed layer at each pressure interval, with pores of new core diameters emptying as desorption proceeds, and the thickness of the layer adsorbed onto the pore walls decreasing as further desorption takes place. A comparison of the total volume desorbed at each point on the isotherm to the corresponding adsorbed layer thickness indicates whether or not new pores are emptying as desorption takes place. In this computational work, however, the intervals within the 2000 desorption points on the isotherm are assumed to be small enough that the incremental desorption from the adsorbed layer will be negligible in comparison to the volume desorbing when a pore core empties.

The relationship between Rc_i and $(\lambda/\lambda_0)_i$ (eq 4) is, therefore, used to determine the diameter of the new pores that have been emptied, and the volume attributed to the emptying of these

https://dx.doi.org/10.1021/acs.jpcb.0c11000
J. Phys. Chem. B 2021, 125, 1960−1969

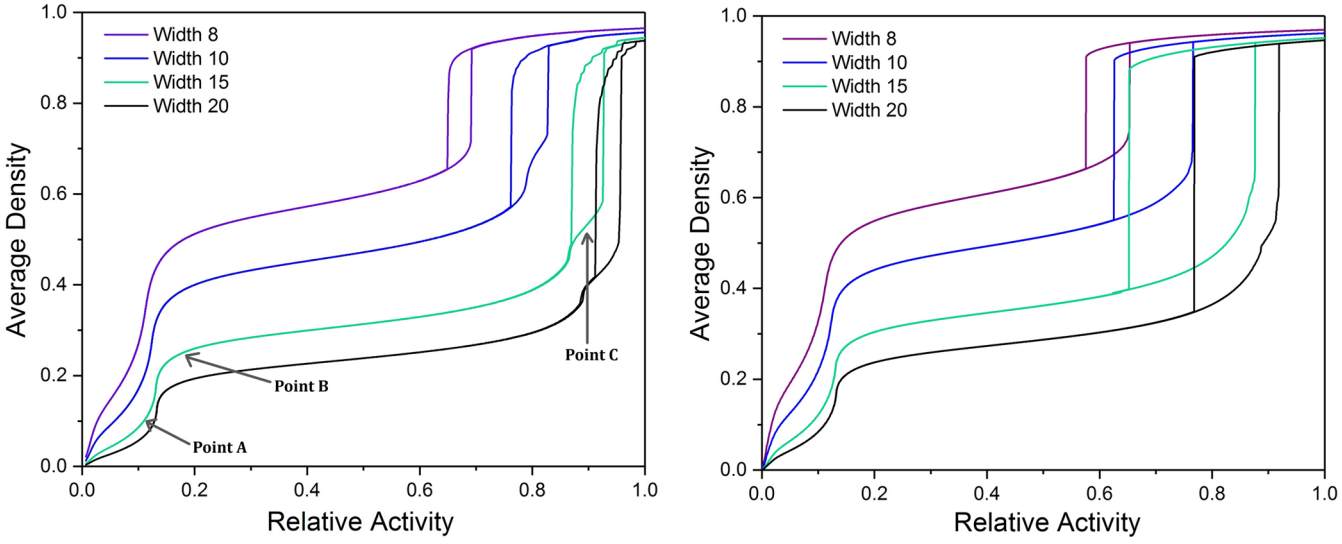

Figure 2. Simulated isotherms for adsorption and desorption within individual pores of varying widths in (a) open transport pores and (b) bottleneck pores.

pores can then be used to plot pore size distributions for the structure being analyzed. In order to account for the layer remaining adsorbed onto pore walls after the core has been emptied, the calculated Rc_i is increased by a value of 1, estimating that a monolayer 1 site in thickness remains adsorbed. This analysis was carried out for the 10 isotherms produced through adsorption analysis for each solids content and activated monomer percentage, and an average was taken across the 10 resulting pore size distributions.

2.5. Gel Synthesis. To allow for accurate comparisons to be drawn between the simulated materials and those synthesized in the lab, the work here presents results from the experimental analysis of RF gels. A standard preparation method is carried out for each gel synthesis, the full details of which can be found within previous work carried out by the group.[30]

The RF gel synthesis involves the use of four reagents:

(1) resorcinol (SigmaAldrich, ReagentPlus, 99%);

(2) formaldehyde (as formalin solution, SigmaAldrich, 37 wt % formaldehyde in water and methanol);

(3) deionized water (produced in-house with Millipore Elix 5, Progard 2); and

(4) catalyst, sodium carbonate (SigmaAldrich, anhydrous, ≥99.5%).

These reagents were combined in separate glass containers according to the desired catalyst concentration, which is generally quantified with respect to the resorcinol/catalyst molar ratio (R/C ratio). All gels were prepared at a solids percentage of 20%, and a resorcinol/formaldehyde molar ratio of 1:2 in accordance with the stoichiometry of the accepted RF reaction.[31] The containers were sealed and placed in a Memmert ULE-500 oven at a temperature of 85 °C for 3 days, where the gelation process took place. Following gelation, a 3 day solvent exchange procedure was performed, where the water within the porous hydrogel was replaced by acetone—a solvent possessing a significantly lower surface tension value—which is a necessary step to reduce the extent of structural collapse during drying. All gels were dried at 85 °C for 2 days using a vacuum oven (Townson and Mercer 1425 digital vacuum oven) with an attached vacuum pump, resulting in the formation of final materials known as xerogels.

2.6. Experimental Nitrogen Adsorption Analysis. As with the synthesis process of the RF gels, the nitrogen adsorption method used here follows a standard procedure which has been documented in detail within previous work carried out by the research group.[30] A dried gel sample of approximately 0.5 g was degassed before undergoing the nitrogen adsorption analysis using a Micromeritics ASAP 2420 surface area and porosity analyzer. The adsorption analysis lasts around 20−30 h per sample, collecting 40 data points for adsorption as the relative pressure is incrementally increased from 0.1 to 1 and then 30 data points for desorption as the relative pressure is decreased from 1 to 0.1. The Micromeritics ASAP 2420 equipment software is utilized to analyze the isotherm data to provide results such as the sample's BJH pore size distribution, total pore volume, accessible surface area, and average pore width.

3. RESULTS AND DISCUSSION

3.1. Computational Adsorption Isotherms. Figure 2a displays the simulated isotherms from adsorption analysis of open rectilinear transport pores with varying pore widths, all of which are measured in terms of lattice sites and possess pore lengths of 40 sites. Figure 2b shows simulated isotherms of bottleneck pores, also possessing a length of 40 sites, with a bottleneck entrance width approximately one-third of the total pore width, rounded to the nearest integer. As discussed, previous experimental and computational works have demonstrated the significant effect pore width has on adsorption behavior and therefore on the shape of the isotherm produced, and this is reflected in the work presented here. Across both sets of isotherms, as the pore width is increased, the adsorption uptake is more gradual, and the hysteresis loop—the point at which the pore fills and empties—shifts to higher values of relative activity on the x-axis. Furthermore, the shape of the isotherms within Figure 2a agrees with that of pores open at both ends found in previous studies, where a relatively narrow hysteresis with two largely parallel lines is observed. The wider,

https://dx.doi.org/10.1021/acs.jpcb.0c11000
J. Phys. Chem. B 2021, 125, 1960−1969

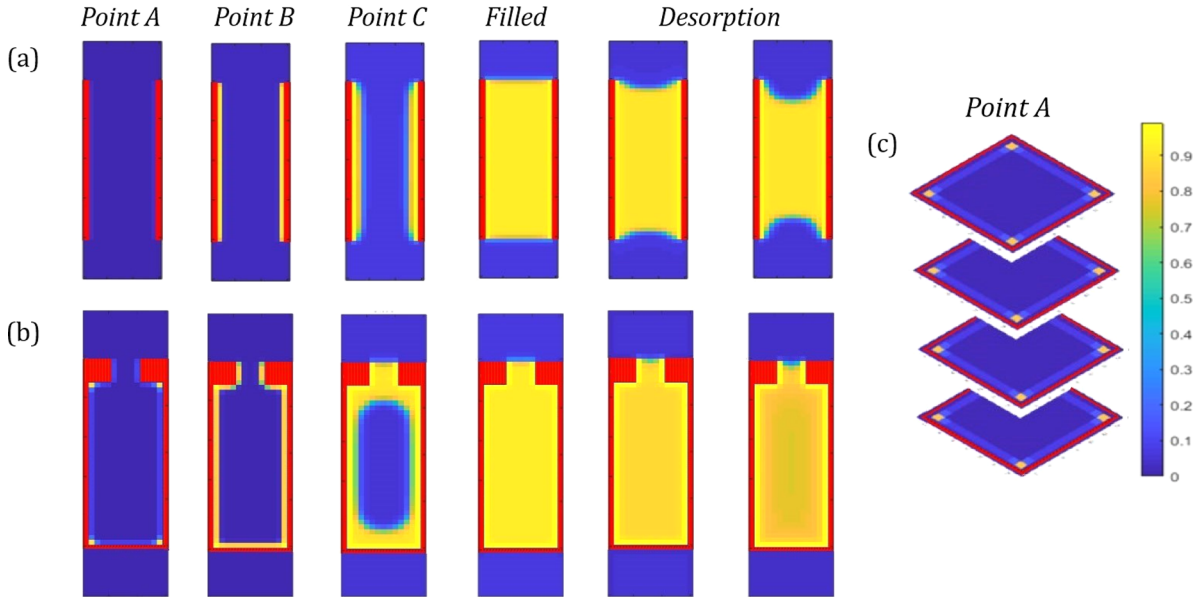

Figure 3. Vertical density profiles of the center of the pore at various stages in the adsorption and desorption process for open transport pores (a) and bottleneck pores (b), in addition to horizontal density profiles for an open pore showing initial adsorption along the corners within the pore (c). Red sites show pore wall sites, blue sites empty sites within the pore, and yellow sites where adsorption has taken place, in accordance with the density color scale shown.

more gradual hysteresis loops observed within Figure 2b, meanwhile, are in agreement with those observed in previous studies for bottleneck pores.

It is possible to identify two or three distinct sections of these isotherms, depending on the width of the pore. First, there is an initial rapid uptake at **Point A** on the isotherm, which then begins to plateau at **Point B**. For larger pore widths, **Point C** can be observed—a second point at which a rapid uptake begins to plateau—before pore filling takes place. Each of these points will be discussed in Section 3.2 where their corresponding density profiles will be analyzed.

3.2. Adsorption Density Profiles. In order to further investigate the adsorption process taking place at each of the points identified, in addition to other significant points within the isotherm, the pore density distribution data can be used to produce density color maps. These show, pictorially, where adsorption has taken place within the pore at each of the stages selected, further elucidating the mechanism by which adsorption and desorption occur. Figure 3a shows color map density profiles of the pore at the different adsorption points indicated for an open transport pore 15 sites in width, displaying a two-dimensional slice down the center of the pore, where the sites with red markers correspond to pore wall sites, and the color of the density profile transforms from blue to yellow as adsorption occurs. Upon inspection of the density profile at **Point B** within Figure 3a, it is clear that the plateau observed on the isotherm here corresponds to the formation of a monolayer across each of the four pore walls, after which point further adsorption takes place gradually. In pores of sufficient width, we observe the feature at **Point C**, which corresponds to the formation of a second layer of adsorbed gas on top of the original monolayer, as depicted on the corresponding density profile, just before the pore fills. The remaining density profiles display the pore as desorption takes place—beginning from the filled state at a relative activity of 1 and then showing the initial desorption as relative activity decreases, and finally the pore just before emptying at the desorption branch of the hysteresis. The density profiles show that, while the pore fills through the gradual adsorption along the length of the pore walls, it conversely empties through the gradual removal of layers from the meniscus, revealing the difference in the mechanism by which adsorption and desorption takes place.

The adsorption and desorption process in bottleneck pores is also shown, once again using the central vertical density profiles, displayed in Figure 3b. Similar to the adsorption process taking place in open transport pores, monolayer formation is observed along the walls of the pore at lower relative activities, proceeded by multilayer formation and saturation of the bottleneck entrance area before the pore itself fills completely. Desorption, once again, takes place through the removal of layers from the meniscus at the bottleneck entrance, before the pore itself empties completely when a sufficiently low relative activity is reached. The difference in mechanisms for adsorption and desorption is more prominent for bottleneck pores as the pore filling takes place much more gradually through the narrow entrance, in contrast to the more immediate emptying of the pore at lower relative activities. This is in agreement with the IUPAC hysteresis classifications where the H2 hysteresis loops, which are associated with materials composed of bottleneck pores, indicate the gradual filling of pores during adsorption and the sudden emptying of pores during desorption.

Despite showing adsorption taking place on the isotherm at **Point A**, the corresponding density profile for the 2D central slice of the open transport pore at this stage appears to show no adsorption taking place. Given that the model is in 3D, horizontal density profiles of the cross-section along the length of the pore can be produced, as shown in Figure 3c, allowing areas of the pore not detected by the central vertical profile to be analyzed. Here, the cross-section of the pore at **Point A** on the isotherm is illustrated, where we can see adsorption taking place at the corner sites along the length of the pore where two walls meet, which explains this initial adsorption failing to appear on the central vertical density profile. This initial adsorption along the pore corners was also observed for bottleneck pores, this

https://dx.doi.org/10.1021/acs.jpcb.0c11000
J. Phys. Chem. B 2021, 125, 1960−1969

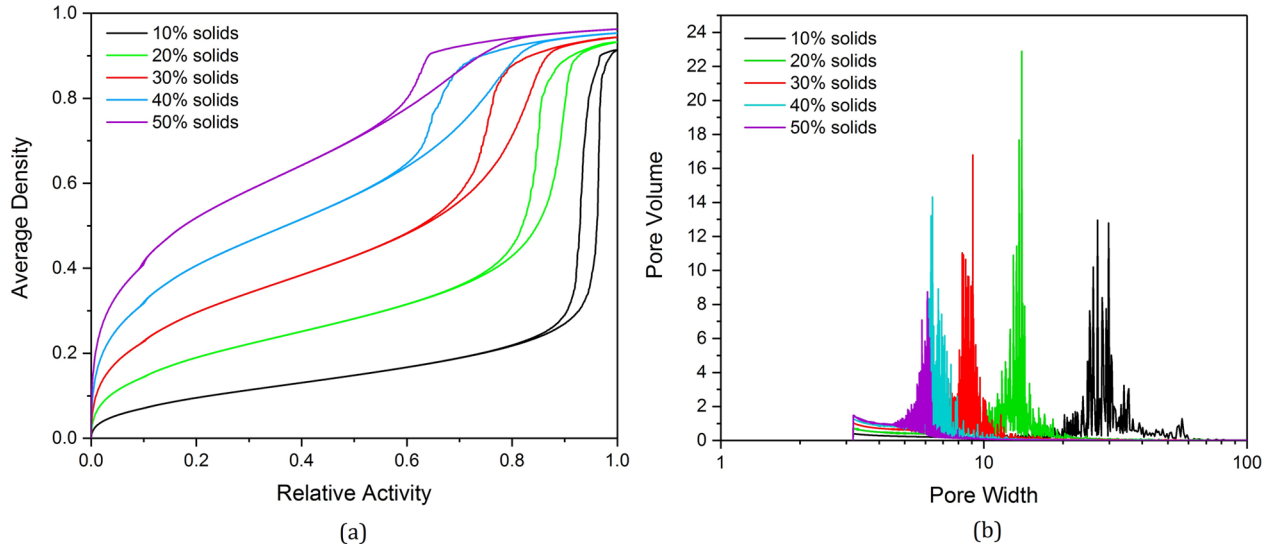

Figure 4. (a) Simulated isotherms for the adsorption analysis of model porous structures at 1% activated monomers (C_C) and varying solids contents (S_C). (b) Corresponding pore size distributions.

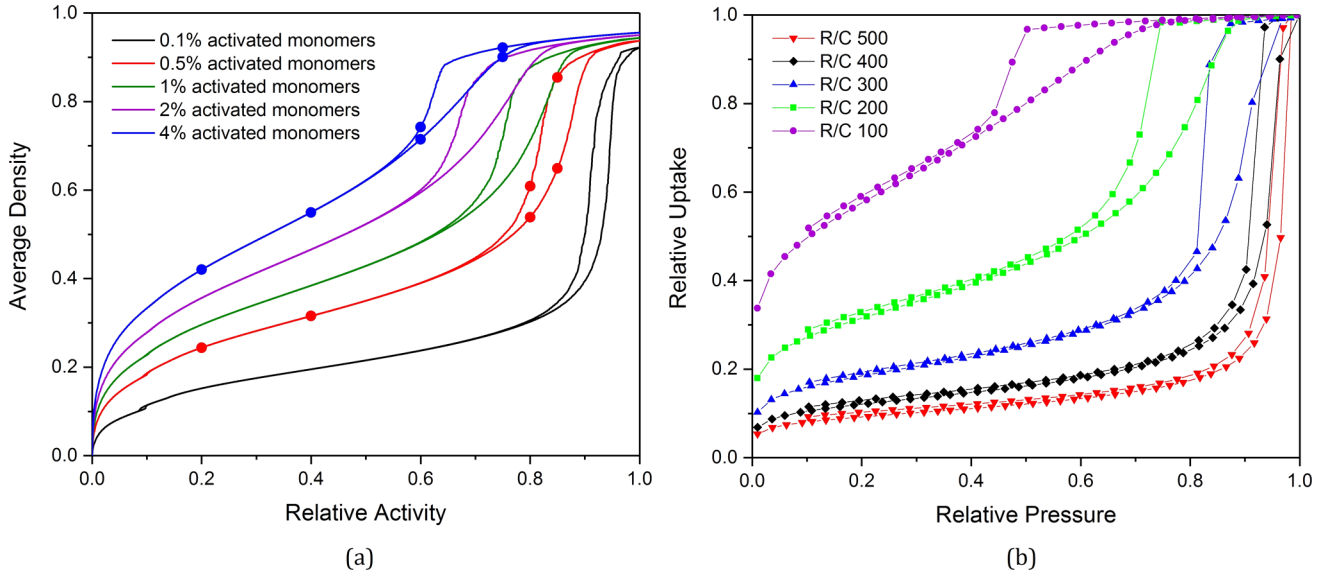

Figure 5. (a) Simulated isotherms for the adsorption analysis of model porous structures at 30% solids content (S_C) and varying catalyst concentrations (C_C). (b) Experimental isotherms for the adsorption analysis of RF xerogels synthesized in the lab at varying catalyst concentrations (R/C ratios), where low R/C ratios correspond to higher catalyst concentrations. Note that the circular points indicated on simulated isotherms in Figure 5a correspond to those visualized in Figure 7.

time including adsorption onto the corners of the pore walls below the bottleneck entrance.

Modeling adsorption within individual pores in this way is valuable, not only in confirming the theories behind the analysis of our laboratory experimental work but also in providing additional insight into specific mechanisms, such as the pore filling taking place along the walls and emptying via the meniscus. Furthermore, given that the results presented for individual pores from this model are in agreement with those cited in the literature, the utility of the adsorption calculations is verified before being applied to the 3D complex structures generated from the kinetic Monte Carlo cluster aggregation simulation.

3.3. Adsorption in Porous Structures. *Varying Solids Content.* Figure 4a shows the resulting isotherms from adsorption analysis of the porous structures produced from the kinetic Monte Carlo cluster aggregation model at 1% activated monomers (C_C) with varying solids contents (S_C). We can observe the changes in hysteresis loop shape across the varying S_C percentages, with structures at lower S_C producing isotherms with narrow, elongated hysteresis loops, indicating the presence of open transport pores. This is in contrast with those at higher S_C, which possess wider, shorter hysteresis loops, indicating the presence of bottleneck pores within the structure. The changes in the *x*-axis position of the hysteresis loop can also be observed, shifting from high to low relative activity values as the solids content is increased from 10% to 50%, indicating that higher solids contents result in structures with narrower pores, as demonstrated within the results already presented in Section 3.1 on varying pore widths. Figure 4b shows the pore size distribution results from the subsequent BJH pore size analysis of structures at varying solids contents of 10−50%, where the

https://dx.doi.org/10.1021/acs.jpcb.0c11000
J. Phys. Chem. B 2021, 125, 1960−1969

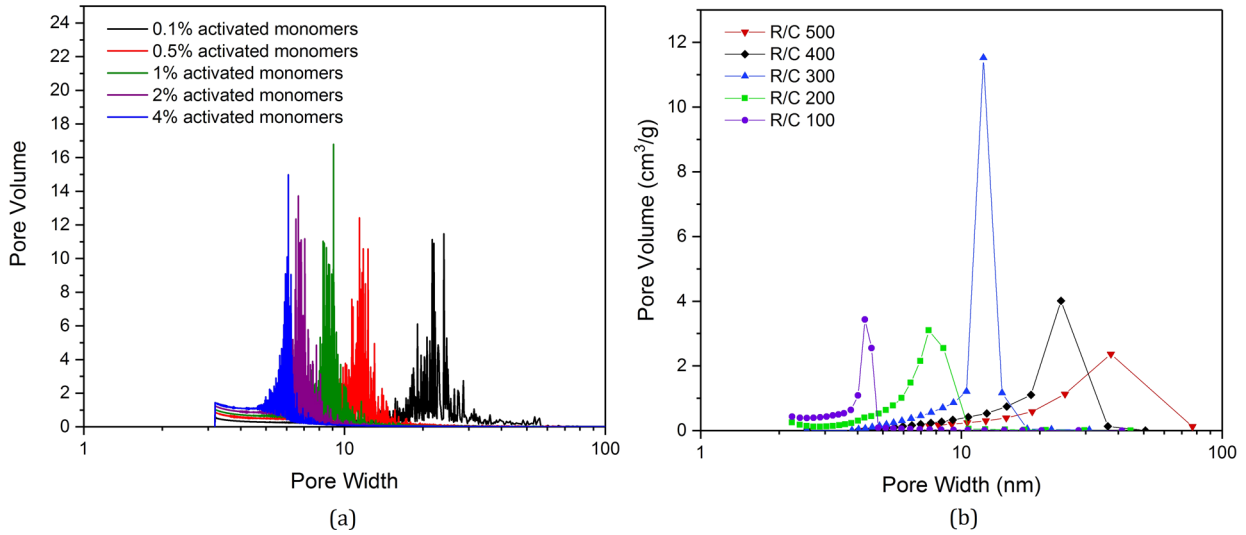

Figure 6. (a) Pore size distributions of model porous structures at varying catalyst concentration (C_C). (b) Pore size distributions for RF xerogels synthesized in the lab at varying catalyst concentrations (R/C ratios), where low R/C ratios correspond to higher catalyst concentrations.

calculated pore size is measured in lattice sites. These distributions agree with the visual analysis of the adsorption isotherms—quantifying the shift in pore size as solids content is altered, where pores become narrower as the structures become more densely packed with higher solids contents. The distribution of pore width also narrows with increasing solids content, where structures at lower solids percentages possess a wider range of pore sizes in comparison to those at higher solids percentages. An increase in volume is observed toward the lowest pore widths (between width values of approximately 3−5 sites) for each distribution in Figure 4b—this can be attributed to the final layers of adsorbed gas remaining on pore walls, which are the last to desorb from the structure, and the total volume of which will increase for structures of higher solids contents as a result of the increased surface area available.

Varying Catalyst Concentration. The adsorption process was also simulated across structures with varying C_C values, the isotherms for which are shown in Figure 5a at 30% S_C, with the results indicating similar trends to those observed for varying S_C. Once again, the position of the hysteresis loop on the x-axis shifts toward lower relative activity, pointing toward the presence of pores that are narrower in width. The changing appearance of the hysteresis loop from narrow and elongated in shape to wider and shorter points toward the changing geometry of the pores themselves, with lower C_C structures comprising open transport pores and higher C_C structures comprising bottleneck pores.

These simulated adsorption isotherms can also be directly compared to those obtained experimentally through nitrogen adsorption experiments for RF gels synthesized in the lab, shown in Figure 5b, for RF gels at varying catalyst concentrations, where high resorcinol/catalyst (R/C) ratios correspond to low catalyst concentrations, and low R/C ratios correspond to high catalyst concentrations. Experimental isotherms have been plotted based on their relative uptake, allowing them to be compared directly to those from the adsorption analysis of model structures. Note that the simulated isotherms are shown for structures at 30% solids content, while the experimental isotherms are shown for RF gels synthesized at 20% solids content. This comparison is made because the laboratory-synthesized gels are subject to shrinkage during drying, making their final solids content more comparable to the higher simulation values. Simulating shrinkage of the simulated materials produced from the kinetic Monte Carlo model and comparing these to the dried RF gels synthesized in the lab, although not performed here, would be useful for future work. The visual similarities between the experimental and simulated isotherms across varying catalyst concentrations are significant, with the same trends observed in the shape and position of the hysteresis loop. These trends are reflected once again in the pore size distribution results from the BJH analysis, both simulated (Figure 6a) and experimental (Figure 6b), displaying the shift from wider pores at lower catalyst concentrations to narrower pores at higher catalyst concentrations. These comparative results are valuable not only for the validation of the kinetic Monte Carlo cluster aggregation model for the formation of RF gels but also in showing promise in the potential for computational tailoring of these materials to optimize their performance in various applications.

3.4. Adsorption Process Visualized. In addition to the isotherm data produced from the simulated adsorption analysis, density profiles across the porous structures were generated at each point throughout the adsorption and desorption process. This is a useful way to visualize processes that cannot be observed by eye in experimental analysis. Figure 7a,b shows the visualized adsorption and desorption processes within structures produced at 0.5% and 4% C_C, respectively, both at 30% S_C. The density profiles across the structures are shown at the same relative activity values on the adsorption and desorption branches of the isotherm, corresponding to the markers located on the plots within Figure 5a and showing the visual differences between each. This provides a visual comparison between the mechanism by which pores fill during adsorption and empty during desorption. The differences are particularly evident in the 0.5% C_C structures, as shown by Figure 7a, where at a relative activity value of 0.85, the desorption branch shows a completely saturated structure while the adsorption branch shows many pores still yet to be filled. This highlights the differing mechanisms by which complex structures adsorb and desorb gases, which could have significant implications when it comes to the use of these materials in various applications. These images have also been compiled in video files, showing the

https://dx.doi.org/10.1021/acs.jpcb.0c11000
J. Phys. Chem. B 2021, 125, 1960−1969

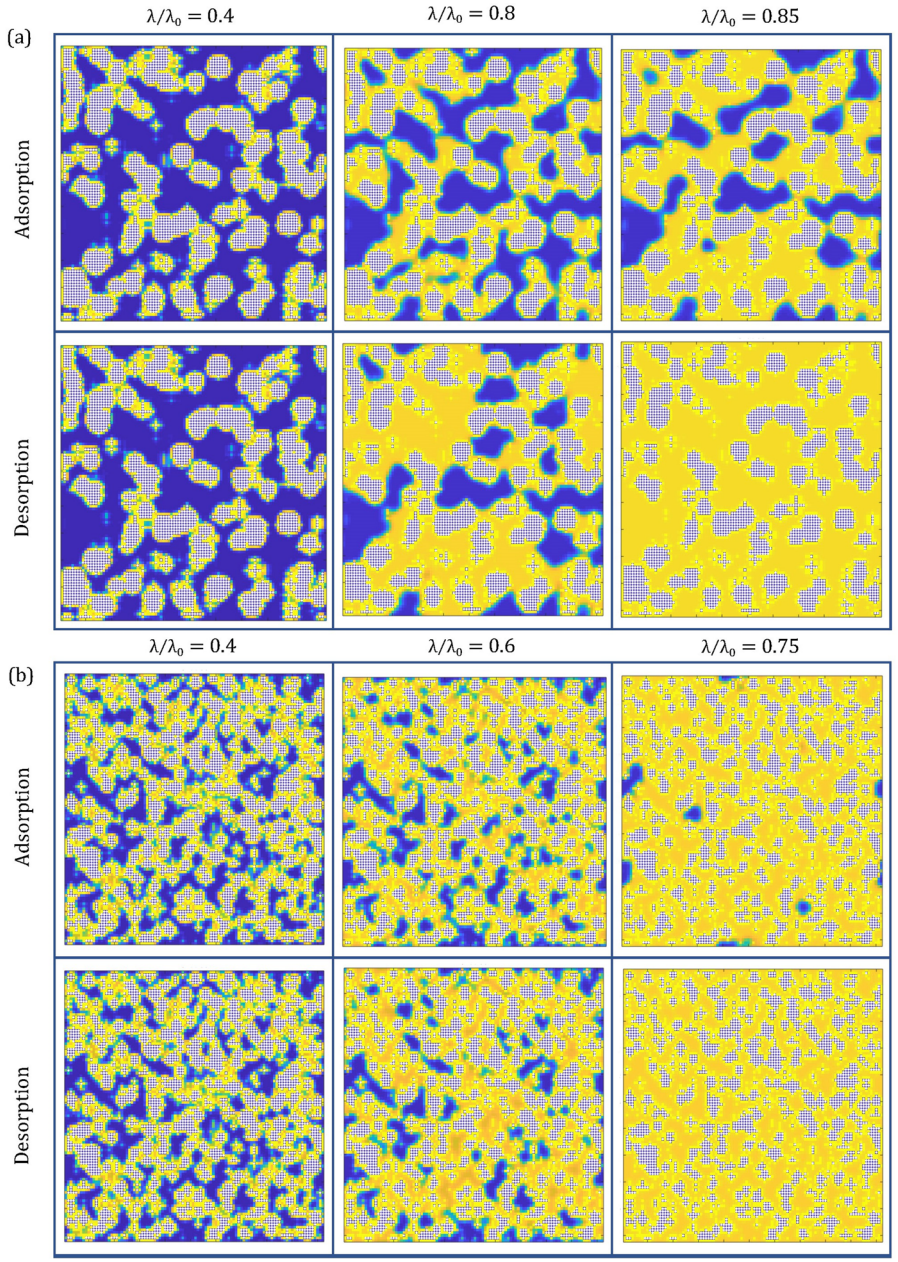

Figure 7. Density profiles through the center of the model porous structure at various relative activity (λ/λ_0) values throughout the adsorption and desorption processes for (a) 30% solids content (S_C) and 0.5% activated monomers (C_C), and (b) 30% S_C and 4% C_C. White sites show the material structure, blue sites empty sites within the pores, and yellow sites where adsorption has taken place.

adsorption and desorption processes at different points within the isotherm, which are available within the Supporting Information.

4. CONCLUSIONS

To conclude, the adsorption model presented here successfully captures the adsorption and desorption processes that take place both within individual pores and within complex porous structures, offering a computationally efficient method of simulating and analyzing materials such as RF gels, in contrast with the computationally expensive models which have been employed in previous studies.

The impacts of varying the width and geometry of individual pores were explored through analysis of the isotherm data produced, the results of which are in agreement with those found in the literature from both experimental and computational methods. The effect of varying solids content and catalyst concentration on the adsorption and desorption behavior of the porous structures was also assessed, as demonstrated by the changes in isotherm shape in addition to the visual differences observed from the density profiles at varying relative activities. The changes observed within the isotherm plots provided insight into the size and geometry of the pores present within the materials, with structures produced with lower solids content and catalyst concentrations comprising open transport pores which are larger in width, while those at higher solids content and catalyst concentrations comprised bottleneck pores which were narrower in width. The adsorption and desorption processes were visualized using density color maps, providing a visual comparison between the mechanism by which porous

https://dx.doi.org/10.1021/acs.jpcb.0c11000
J. Phys. Chem. B 2021, 125, 1960−1969

structures fill and empty—an imperative consideration when assessing the structural characteristics required for specific applications.

The results of this study also further validate the kinetic Monte Carlo cluster aggregation model from our previous works in capturing the formation of porous materials such as RF gels, as the simulated adsorption analysis results show significant similarities to those obtained experimentally for RF gels synthesized in the lab. The trends observed in the shape of the isotherm and position of the hysteresis loops are consistent between the two, as are the trends observed from the two BJH pore size distributions.

Overall, the results presented here show significant promise in advancing toward the computational tailoring of materials such as these in a manner that is realistically applicable to widespread industry use. A model that can predict and control a material's properties in this way would be invaluable to realizing its full application potential, allowing determination of the synthesis parameters required to produce materials with the desired characteristics in a time-efficient and computationally inexpensive manner.

■ ASSOCIATED CONTENT

Supporting Information

The Supporting Information is available free of charge at https://pubs.acs.org/doi/10.1021/acs.jpcb.0c11000.

Video of the adsorption process for structures at 30% S_C and 0.5% C_C (MP4)

Video of the adsorption process for structures at 30% S_C and 4% C_C (MP4)

■ AUTHOR INFORMATION

Corresponding Author

Paul Mulheran − *Department of Chemical & Process Engineering, University of Strathclyde, Glasgow G1 1XL, United Kingdom;* orcid.org/0000-0002-9469-8010; Email: paul.mulheran@strath.ac.uk

Authors

Elisha Martin − *Department of Chemical & Process Engineering, University of Strathclyde, Glasgow G1 1XL, United Kingdom;* orcid.org/0000-0003-4142-2093

Martin Prostredny − *Department of Chemical & Process Engineering, University of Strathclyde, Glasgow G1 1XL, United Kingdom;* orcid.org/0000-0001-5326-2408

Ashleigh Fletcher − *Department of Chemical & Process Engineering, University of Strathclyde, Glasgow G1 1XL, United Kingdom*

Complete contact information is available at: https://pubs.acs.org/10.1021/acs.jpcb.0c11000

Notes

The authors declare no competing financial interest.

■ ACKNOWLEDGMENTS

The authors thank Peter Monson from the Department of Chemical Engineering at the University of Massachusetts, Amherst, whose MFT adsorption model was built upon through this work. The authors also thank the Department of Chemical & Process Engineering at the University of Strathclyde, and the Engineering and Physical Sciences Research Council for funding this work. Grant number: EP/R512205/1.

■ REFERENCES

(1) Guarín-Romero, J. R.; Rodríguez-Estupiñán, P.; Giraldo, L.; Moreno-Piraján, J. C. Study of Adsorption of CO2 and CH4 on Resorcinol−Formaldehyde Aerogels at High Pressures. *J. Chem. Eng. Data* **2019**, *64*, 5263−5274.

(2) Yuan, W.; Zhang, X.; Zhao, J.; Li, Q.; Ao, C.; Xia, T.; Zhang, W.; Lu, C. Ultra-Lightweight and Highly Porous Carbon Aerogels from Bamboo Pulp Fibers as an Effective Sorbent for Water Treatment. *Results Phys.* **2017**, *7*, 2919−2924.

(3) Xu, P.; Drewes, J. E.; Heil, D.; Wang, G. Treatment of Brackish Produced Water Using Carbon Aerogel-Based Capacitive Deionization Technology. *Water Res.* **2008**, *42*, 2605−17.

(4) Feng, J.; Zhang, C.; Feng, J. Carbon Fiber Reinforced Carbon Aerogel Composites for Thermal Insulation Prepared by Soft Reinforcement. *Mater. Lett.* **2012**, *67*, 266−268.

(5) Li, F.; Xie, L.; Sun, G.; Kong, Q.; Su, F.; Cao, Y.; Wei, J.; Ahmad, A.; Guo, X.; Chen, C.-M. Resorcinol-Formaldehyde Based Carbon Aerogel: Preparation, Structure and Applications in Energy Storage Devices. *Microporous Mesoporous Mater.* **2019**, *279*, 293−315.

(6) Pekala, R. W. Organic Aerogels from the Polycondensation of Resorcinol with Formaldehyde. *J. Mater. Sci.* **1989**, *24*, 3221−3227.

(7) ElKhatat, A. M.; Al-Muhtaseb, S. A. Advances in Tailoring Resorcinol-Formaldehyde Organic and Carbon Gels. *Adv. Mater.* **2011**, *23*, 2887−2903.

(8) Calvo, E. G.; Juárez-Pérez, E. J.; Menéndez, J. A.; Arenillas, A. Fast Microwave-Assisted Synthesis of Tailored Mesoporous Carbon Xerogels. *J. Colloid Interface Sci.* **2011**, *357*, 541−547.

(9) Calvo, E. G.; Ferrera Lorenzo, N.; Menéndez, J. A.; Arenillas, A. Microwave Synthesis of Micro-Mesoporous Activated Carbon Xerogels for High Performance Supercapacitors. *Microporous Mesoporous Mater.* **2013**, *168*, 206−212.

(10) Sing, K. S. W. Reporting Physisorption Data for Gas/Solid Systems with Special Reference to the Determination of Surface Area and Porosity (Recommendations 1984). *Pure Appl. Chem.* **1985**, *57*, 603−619.

(11) Ravikovitch, P. I.; Domhnaill, S. C. O.; Neimark, A. V.; Schueth, F.; Unger, K. K. Capillary Hysteresis in Nanopores: Theoretical and Experimental Studies of Nitrogen Adsorption on Mcm-41. *Langmuir* **1995**, *11*, 4765−4772.

(12) Gor, G. Y.; Thommes, M.; Cychosz, K. A.; Neimark, A. V. Quenched Solid Density Functional Theory Method for Characterization of Mesoporous Carbons by Nitrogen Adsorption. *Carbon* **2012**, *50*, 1583−1590.

(13) Fan, C.; Do, D. D.; Nicholson, D.; Jagiello, J.; Kenvin, J.; Puzan, M. Monte Carlo Simulation and Experimental Studies on the Low Temperature Characterization of Nitrogen Adsorption on Graphite. *Carbon* **2013**, *52*, 158−170.

(14) Coasne, B.; Galarneau, A.; Di Renzo, F.; Pellenq, R. J. M. Molecular Simulation of Nitrogen Adsorption in Nanoporous Silica. *Langmuir* **2010**, *26*, 10872−10881.

(15) Düren, T.; Bae, Y.-S.; Snurr, R. Using Molecular Simulation to Characterise Metal-Organic Frameworks for Adsorption Applications. *Chem. Soc. Rev.* **2009**, *38*, 1237−47.

(16) Dubbeldam, D.; Calero, S.; Ellis, D. E.; Snurr, R. Q. Raspa: Molecular Simulation Software for Adsorption and Diffusion in Flexible Nanoporous Materials. *Mol. Simul.* **2016**, *42*, 81−101.

(17) Monson, P. A. Recent Progress in Molecular Modeling of Adsorption and Hysteresis in Mesoporous Materials. *Adsorption* **2005**, *11*, 29−35.

(18) Monson, P. A. Mean Field Kinetic Theory for a Lattice Gas Model of Fluids Confined in Porous Materials. *J. Chem. Phys.* **2008**, *128*, 084701.

(19) Schneider, D.; Valiullin, R.; Monson, P. A. Modeling the Influence of Side Stream and Ink Bottle Structures on Adsorption/Desorption Dynamics of Fluids in Long Pores. *Langmuir* **2015**, *31*, 188−198.

(20) Casselman, J. A.; Desouza, A.; Monson, P. A. Modelling the Dynamics of Condensation and Evaporation of Fluids in Three-Dimensional Slit Pores. *Mol. Phys.* **2015**, *113*, 1250−1260.

(21) Sarkisov, L.; Monson, P. A. Lattice Model of Adsorption in Disordered Porous Materials: Mean-Field Density Functional Theory and Monte Carlo Simulations. *Phys. Rev. E: Stat. Phys., Plasmas, Fluids, Relat. Interdiscip. Top.* **2001**, *65*, 011202.
(22) Svidrytski, A.; Rathi, A.; Hlushkou, D.; Ford, D. M.; Monson, P. A.; Tallarek, U. Morphology of Fluids Confined in Physically Reconstructed Mesoporous Silica: Experiment and Mean Field Density Functional Theory. *Langmuir* **2018**, *34*, 9936−9945.
(23) Detcheverry, F.; Kierlik, E.; Rosinberg, M. L.; Tarjus, G. Local Mean-Field Study of Capillary Condensation in Silica Aerogels. *Phys. Rev. E: Stat. Phys., Plasmas, Fluids, Relat. Interdiscip. Top.* **2003**, *68*, 061504.
(24) Detcheverry, F.; Kierlik, E.; Rosinberg, M. L.; Tarjus, G. Mechanisms for Gas Adsorption and Desorption in Silica Aerogels: The Effect of Temperature. *Langmuir* **2004**, *20*, 8006−8014.
(25) Prostredny, M.; Fletcher, A.; Mulheran, P. Modelling the Formation of Porous Organic Gels − How Structural Properties Depend on Growth Conditions. *RSC Adv.* **2019**, *9*, 20065−20074.
(26) Martin, E.; Prostredny, M.; Fletcher, A.; Mulheran, P. Modelling Organic Gel Growth in Three Dimensions: Textural and Fractal Properties of Resorcinol-Formaldehyde Gels. *Gels* **2020**, *6*, 23.
(27) Tange, O. Gnu Parallel: The Command-Line Power Tool; In *login*; USENIX, 2011; Vol. *36*.
(28) Lin, C.; Ritter, J. A. Effect of Synthesis pH on the Structure of Carbon Xerogels. *Carbon* **1997**, *35*, 1271−1278.
(29) Barrett, E. P.; Joyner, L. G.; Halenda, P. P. The Determination of Pore Volume and Area Distributions in Porous Substances. I. Computations from Nitrogen Isotherms. *J. Am. Chem. Soc.* **1951**, *73*, 373−380.
(30) Taylor, S. J.; Haw, M. D.; Sefcik, J.; Fletcher, A. J. Gelation Mechanism of Resorcinol-Formaldehyde Gels Investigated by Dynamic Light Scattering. *Langmuir* **2014**, *30*, 10231−10240.
(31) Al-Muhtaseb, S. A.; Ritter, J. A. Preparation and Properties of Resorcinol−Formaldehyde Organic and Carbon Gels. *Adv. Mater.* **2003**, *15*, 101−114.

https://dx.doi.org/10.1021/acs.jpcb.0c11000
J. Phys. Chem. B 2021, 125, 1960−1969

D.3 Investigating the Role of the Catalyst Within Resorcinol-Formaldehyde Gel Synthesis (Published)

gels

MDPI

Article

Investigating the Role of the Catalyst within Resorcinol–Formaldehyde Gel Synthesis

Elisha Martin, Martin Prostredny and Ashleigh Fletcher *

Department of Chemical and Process Engineering, University of Strathclyde, Glasgow G1 1XJ, UK; elisha.martin@strath.ac.uk (E.M.); martin.prostredny@strath.ac.uk (M.P.)
* Correspondence: ashleigh.fletcher@strath.ac.uk; Tel.: +44-(0)141-548-2431

Abstract: Resorcinol–formaldehyde (RF) gels are porous materials synthesized via a sol–gel reaction and subsequently dried, producing structures with high surface areas and low densities—properties that are highly attractive for use in various applications. The RF gel reaction takes place in the presence of a catalyst, either acidic or basic in nature, the concentration of which significantly impacts final gel properties. The full extent of the catalyst's role, however, has been subject to debate, with the general consensus within the field being that it is simply a pH-adjuster. The work presented here explores this theory, in addition to other theories postulated in the literature, through the synthesis and analysis of RF gels catalysed by mixtures of relevant compounds with varying concentrations. The relationship between catalyst concentration and initial solution pH is decoupled, and the individual roles of both the cation and the anion within the catalyst are investigated. The results presented here point towards the significance of the metal cation within the RF gel reaction, with similar structural properties observed for gels synthesized at constant Na^+ concentrations, regardless of the initial solution pH. Furthermore, through the use of alternative cations and anions within catalyst compounds, the potential effects of ions on the stabilization of macromolecules in solution are explored, the results of which suggest a 'Hofmeister-like' series could be applicable within the catalysis of RF gel reactions.

Keywords: resorcinol–formaldehyde; xerogels; aerogels; porous; sol–gel; pH

Citation: Martin, E.; Prostredny, M.; Fletcher, A. Investigating the Role of the Catalyst within Resorcinol–Formaldehyde Gel Synthesis. *Gels* **2021**, *7*, 142. https://doi.org/10.3390/gels7030142

Academic Editor: David A. Schiraldi

Received: 20 August 2021
Accepted: 13 September 2021
Published: 15 September 2021

1. Introduction

1.1. Resorcinol–Formaldehyde Gels

Owing to their highly attractive and tuneable properties, resorcinol–formaldehyde (RF) gels have been the focus of numerous studies over the years [1–4]. Their synthesis procedure, as established by Pekala [5], involves a sol–gel reaction, a subsequent solvent exchange step, and, lastly, a drying process to produce the lightweight, porous structure of the final gel. Attempts to optimize this synthesis process have included explorations of gelation temperature [6] and drying methods [7], as well as extending to investigations into material doping [8,9]. Furthermore, the computational modelling of RF gel formation and analysis has also been explored, progressing towards efficient computational tailoring of their properties [10–12].

Although widely accepted within the field, the 'catalyst' used in the RF sol–gel reaction cannot technically be considered a catalyst, given that it is used up and cannot be recovered at the end of the process. Still, the term 'catalyst' remains commonly used in this context and will, therefore, be used in the work discussed here. Either an acidic or basic catalyst can be used within RF gel synthesis, each increasing the rate of reaction through different mechanisms. In the case where the RF reaction takes place in the presence of a basic catalyst, the addition reaction begins with the abstraction of a proton from the resorcinol molecule, forming an anion. This abstraction subsequently leads to increased reactivity of the resorcinol molecules. The addition reaction proceeds, typically with molecules of

formaldehyde positioning themselves at two available carbon atoms on the benzene ring, with the resulting molecules being known as hydroxymethyl derivatives. This addition reaction, under basic catalysis, is fast, producing numerous hydroxymethyl derivatives, which react to form many small clusters. After this point, a condensation reaction proceeds, the hydroxymethyl derivatives releasing H_2O as they form bridged structures, linking with other hydroxymethyl groups or with unreacted resorcinol molecules. The condensation step takes place slowly under basic catalysis; however, this step takes place quickly under acid catalysis, with the acid increasing the rate of reaction through protonation of hydroxymethyl derivatives, producing structurally different materials. The pH of the catalyst used, therefore, is crucial to the properties of the materials formed. However, research conducted over the years has indicated that its role may be far more complex. Elucidating the full extent of this role could provide invaluable insight into the RF gel formation mechanism, as well as opening new avenues for material tailoring to achieve a wide range of structural properties.

1.2. The Role of pH

When Pekala first established the process of synthesizing RF gels, he made use of a basic catalyst, sodium carbonate (Na_2CO_3), which has remained as the most common catalyst used for RF gel formation. As previously mentioned, acid catalysts can also be utilized, in addition to other basic compounds such as potassium hydroxide [13], lithium carbonate [14], and sodium hydrogen carbonate [15], amongst others. The nature of the catalyst, being acidic or basic, in addition to its concentration, will impact the initial pH value of the RF solution, consequently impacting the rate at which the resorcinol–formaldehyde reaction takes place and, therefore, impacting the final structural properties. The role of the catalyst beyond this has been subject to some debate, where many works have concluded that the pH-determining impact of the anion (CO_3^{2-} in the case of sodium carbonate) is the predominant role, if not the sole role. Other works, meanwhile, have explored the impact of the cation (Na^+ in the case of sodium carbonate), concluding that it is also significant in determining final gel properties, and that its role cannot be discounted. Direct comparisons between research presented in the literature is, however, very complex, given that the wide variety of synthesis conditions used within each study leads to the formation of materials with markedly different textural properties, some of which result in the observation of different trends.

In an attempt to understand the role of pH alone, research was carried out by Lin and Ritter [16] which made use of dilute nitric acid to adjust the initial solution pH of sodium carbonate-catalysed RF gels. This work involved the synthesis of R/C50 gels with initial solutions containing 5 w/v% solids, which then underwent acetone solvent exchange before ambient drying, followed by gel pyrolysis. Nitrogen adsorption analysis of the final gels revealed a clear trend—as the initial solution pH incrementally decreased from pH 7 to pH 6, the resulting gel surface area increased significantly. Gels produced from initial solution pH values above 7 were found to yield almost no surface area, whilst those produced from pH values between 5.5 and 6 achieved equally high surface areas. This work highlights the crucial role of pH in the RF gel reaction, where the condensation reaction rate is increased by the presence of additional H^+ ions, resulting in the formation of increasingly cross-linked structures. Despite this, the specific roles of the catalyst components were not explored in this work, and new components were included in the system through the addition of nitric acid. This could have implications on the final gel structure, including through the potential acid–base reaction that may have taken place, with the addition of HNO_3 resulting in decreased concentration of carbonate, given that HNO_3 is a stronger acid and carbonic acid is unstable. In the cases where an acidic catalyst alone is used, studies have found that the initial mixture must possess a pH within the range of 1–4 in order to produce a gel with a viable structure, albeit with visual and textural properties that are distinct from those of base-catalysed reactions [17]. Finally, initial solution pH values below 1 have been shown to result in precipitation, while pH values within the range of

4–5.5 have been found to be insufficient for the successful catalysis of either the addition or the condensation reactions taking place, the resulting product being a non-porous powder rather than an interlinked porous structure [14]. From experiments carried out within our research group, the pH of an initial RF gel solution with no catalyst added whatsoever is 4.1, which, as expected, fails to produce inter-connected porous materials.

The role of pH was explored further by Job et al. [18], who synthesized RF gels using sodium hydroxide solution to achieve set initial solution pH values ranging from 5.45 to 7.35. For gels analysed after vacuum drying, as solution pH increased from 5.45 to 6.5, the total surface area also increased from 330 to 510 m^2/g, with a decrease observed after this point at pH 7.35. Given that the increasing solution pH corresponds to increasing Na^+ concentration from the addition of sodium hydroxide solution, the role of Na^+ could be considered in this work, however, Job et al. conclude that the cation present in the standard Na_2CO_3 catalyst plays no direct role whatsoever and that pH alone is the determining factor in final gel properties. Subsequent studies have affirmed pH-altering as the catalyst's sole purpose, this becoming the general consensus within the field, with suggestions that the same effects from pH alterations could be achieved using any base that does not react with resorcinol or formaldehyde [2,19].

1.3. The Role of Individual Catalyst Components

A small number of studies have attempted to look beyond the pH-adjusting role of the catalyst, and instead focus on the role of its components in greater detail. One such study by Horikawa et al. [15] investigated the impacts of changing both the anion and cation present, comparing the textural properties of pyrolyzed RF aerogels catalysed by Na_2CO_3, K_2CO_3, $NaHCO_3$, and $KHCO_3$ at R/C50. Nitrogen adsorption analysis of the resulting gels produced isotherm profiles for each, the visual inspection of which can provide insight into both the size and type of pores present. The results revealed clear similarities, with Na_2CO_3 and K_2CO_3 gels producing visually comparable isotherms, suggesting that their structural properties were also comparable. The isotherm profiles of $NaHCO_3$ and $KHCO_3$ were also visually similar, indicating that the impact of changing cation from Na^+ to K^+ is negligible. The change in structural properties when the anion was changed from CO_3^{2-} to HCO_3^- were evident, including in the isotherm profile, the total pore volume, and the average pore width observed across the four gel samples, with HCO_3^- gels possessing larger pores with a greater total pore volume in comparison to those of the CO_3^{2-} gels. In this case, an additional complexity is involved, given that changing the anion from CO_3^{2-} to HCO_3^- also halves the concentration of metal cations present, making the specific role of each difficult to ascertain.

A study carried out by Calvo et al. [20] took a different approach to investigating the role of the catalyst in the RF reaction, this time producing microwave-synthesized xerogels catalysed by five different compounds—Na_2CO_3, Li_2CO_3, $NaHCO_3$, $Ca(OH)_2$, and NaOH. In this work, as opposed to synthesizing gels at a set R/C ratio, the catalyst was added until the desired pH was reached, therefore the mass of catalyst added depended on its alkalinity. No definitive trends were observed for variations in the cation used, however, clear porosity differences were evident for anion variations. Gels synthesized using hydroxide catalysts ($Ca(OH)_2$, and NaOH) possessed smaller pores, also with narrower pore size distributions, in comparison with those synthesized by carbonate catalysts. The total mesopore volumes of the gels were also significantly reduced, with hydroxide catalysed gels possessing mesopore volumes approximately one-third of those observed for gels produced from carbonate catalysts. Calvo et al. suggest that this could be attributable to the size of the anions used, with the larger CO_3^- ions causing steric hindrances and leading to the formation of wider pores. The conclusion drawn was that the role of the anion within the catalyst is far more significant than that of the cation; however, the same complexity discussed previously still applies. Although the pH values of the initial solutions are equal for each gel synthesized in this study, the concentration of both cations and anions

vary depending on the catalyst alkalinity, therefore, elucidating their individual roles is more complex.

Further research was carried out by Job et al. [21] where RF xerogels were prepared with six different catalysts—LiOH, NaOH, KOH, $Ca(OH)_2$, $Ba(OH)_2$, and $Sr(OH)_2$—once again with different masses added until the desired pH was reached. Their findings revealed distinct differences in the properties of gels formed by alkali metal hydroxides (LiOH, NaOH, and KOH, each possessing cations of M+ charge) in comparison to those of alkaline earth metal hydroxides ($Ca(OH)_2$, $Ba(OH)_2$, and $Sr(OH)_2$), each possessing cations of M^{2+} charge), with the two groups producing structures with average pore widths in the ranges of 50–80 nm and 70–100 nm, respectively. Taylor et al. [14,22] investigated the specific role of the cation further, this time using RF xerogels synthesized using four alkali metal carbonates—Li_2CO_3, Na_2CO_3, K_2CO_3, and Cs_2CO_3—all prepared at equal R/C ratios, alongside their subsequent work, which included alkaline earth metal carbonates, $CaCO_3$ and $BaCO_3$. Once again, gels synthesized using alkaline earth metal carbonates, possessing M^{2+} cations as opposed to M^+ within alkali metal carbonates, comprised of pores much larger in diameter, alongside an increase in total pore volume, indicating that the role of the cation present could be significant.

Earlier research carried out by Grenier-Loustalot et al. [23] investigated the impact of the valency and ionic radius of the metal cation used within the catalyst for the formation of phenol–formaldehyde (PF) gels. This study found that the use of divalent cations resulted in an increased rate of formaldehyde consumption during the PF reaction in comparison to monovalent species, as did the use of cations with larger ionic radii, allowing the authors to conclude that the nature of the cation plays an important role in the reaction kinetics. The study proposed a mechanism by which this could takes place, where the metal cation participates in establishing an intermediate chelated molecule during the phenol–formaldehyde addition reaction, which could also be applicable for RF reactions.

The studies discussed here, which often produce variable or conflicting results, demonstrate the complexity of the RF gel formation mechanism, and the difficultly with which many research groups have attempted to determine the role of the catalyst within the RF reaction. The work carried out to date has provided valuable insight into the different parameters influencing the RF reaction, however, the roles of the individual catalyst components are still yet to be fully understood, particularly given the difficultly in decoupling their relationship with one another and with the resulting pH.

1.4. Ionic Solution Effects—The Hofmeister Series

Through the work carried out by Taylor et al. [14,22], another theory emerged suggesting that the ions present within the catalyst could contribute to RF gel formation based on their ability to 'salt-in' or 'salt-out' macromolecules from solution. This is comparable to the Hofmeister series, which was established in 1888 by Franz Hofmeister [24], and which arranges ions based on the stability or instability they create for proteins in solution.

Given that the RF gel catalysts studied comprise ionic compounds, in addition to the pivotal role solubility plays in the sol–gel process, these potential effects could be an important consideration. As the mass of macromolecules increases with cluster growth, in addition to their increased cross-linking, the resulting solubility decreases, eventually reaching the point of gelation where a solid interlinked structure is formed. Investigating how different parameters impact the solubility of macromolecules, such as those observed in the RF reaction, has been the focus of various studies over the years [25–27]. Amongst the theories postulated, the kosmotropic and chaotropic effects of ions is of particular interest. Kosmotropes are compounds that promote the stability and rigidity of macromolecules, stabilising their intramolecular interactions, and facilitating the formation of ordered structures [28]. Chaotropes, on the other hand, contribute to the destabilising and disordering of macromolecules, disrupting non-covalent interactions, and hindering the formation of stable structures [29].

As previously mentioned, the Hofmeister series was created with respect to the impact of ions on proteins in solution. For hydrophilic surfaces such as RF gels, the effects of anions have shown to be reversed as a result of the ion–surface interactions taking place, and the anion Hofmeister series is reversed to reflect this [30], as shown in Figure 1a, while the Hofmeister series for cations is shown in Figure 1b. The traditional catalyst of sodium carbonate ($NaCO_3$), therefore, comprises a cation with a medium kosmotropic effect and an anion with a significant kosmotropic effect. Investigating the impact of various cations and anions within the RF reaction catalysis, particularly with respect to their positioning within the Hofmeister series, could provide a deeper understanding of their role.

(a) **Chaotropic** $SCN^- < I^- < ClO_3^- < NO_3^- < Cl^- < F^- < H_2PO_4^- < SO_4^{2-} < CO_3^{2-}$ **Kosmotropic**

(b) **Chaotropic** $N(CH_3)_4^+ < NH_4^+ < Cs^+ < Rb^+ < K^+ < Na^+ < Li^+ < Mg^{2+} < Ca^{2+}$ **Kosmotropic**

Figure 1. (**a**) Reversed Hofmeister series for anions, and (**b**) Hofmeister series for cations [30,31].

2. Results and Discussion

2.1. Varying Catalyst Concentration

The effect of varying the molar ratio of resorcinol to catalyst, referred to as R/C ratio, has been studied previously and is pivotal in determining the final textural properties of the RF gel. 'Standard' RF gels were prepared using Na_2CO_3 as the catalyst, with the R/C ratios studied being 100, 200, 300, 400, 500, and 600. Samples of each gel were analysed using nitrogen adsorption, the resulting isotherms from which are displayed in Figure 2. The isotherms shown vary significantly with changes in R/C ratio, with differing gradients of initial uptake observed, as well as hysteresis loops occurring at varying relative pressure values. As can be seen from the plots, an increase in R/C ratio corresponds to a reduced uptake at lower pressures, suggesting that fewer micropores are present, given that micropores are known to fill at lower relative pressures. Instead, the relative increase in uptake at higher pressures for lower R/C ratio materials points towards the increased presence of mesopores within these materials. Furthermore, as the R/C ratio is increased, a shift in the position of the hysteresis loop is observed, with pores filling and emptying at higher pressures, once again pointing towards the presence of larger pores, which fill at higher relative pressures. Using the data from the isotherm, the pore size distribution can be calculated using the BJH method [32], allowing further characterization of the gels' porous structure through more than simple isotherm interpretation. Figure 3 displays the pore size distribution for the standard RF gels at R/C ratios of 100 to 600, where the y-axis is the pore volume corresponding to each pore width on the x-axis, with the total area below each plot being representative of the total pore volume of the analysed gel. Table 1 details the average pore width value of each of the gels studied, in addition to its BET [33] surface area.

Table 1. The corresponding average pore widths and Brunauer-Emmet-Teller (BET) surface areas. Values are reported to an accuracy less than their error; therefore, their error values have been omitted. Note that S_{BET} is BET surface area, $\overline{\phi}$ is average pore width, and R/C ratio is the molar ratio of resorcinol to catalyst.

R/C Ratio	$\overline{\phi}$ (nm)	S_{BET} (m^2/g)
100	4	574
200	7	552
300	11	446
400	19	304
500	26	254
600	28	124

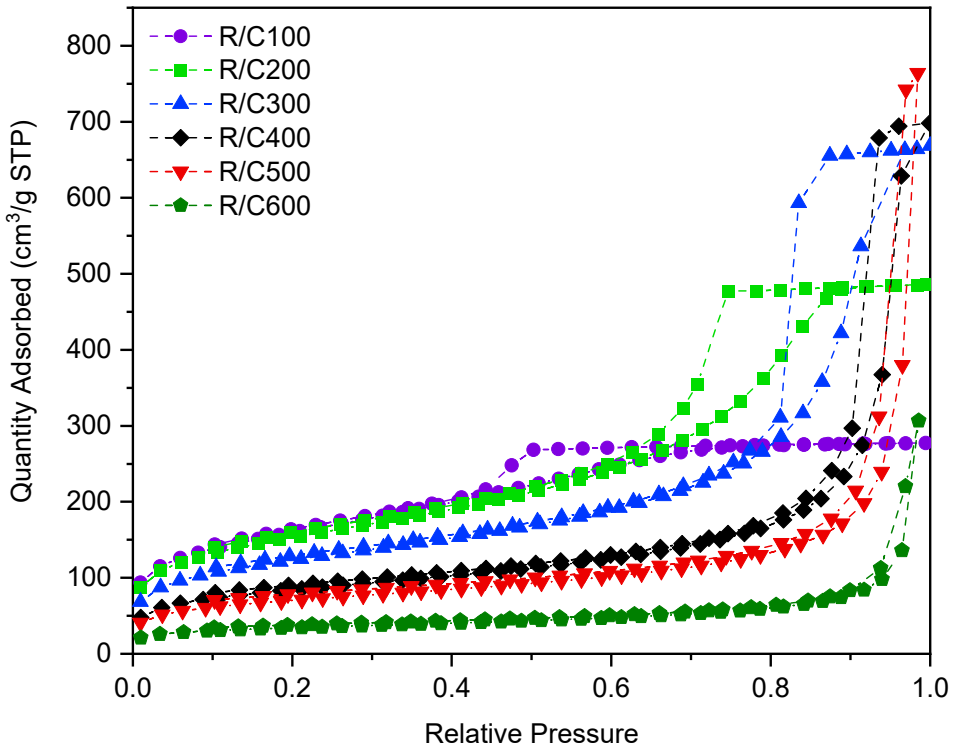

Figure 2. Nitrogen adsorption isotherms for sodium carbonate gels at resorcinol/catalyst molar ratios (R/C ratios) 100–600. STP abbreviates standard temperature and pressure.

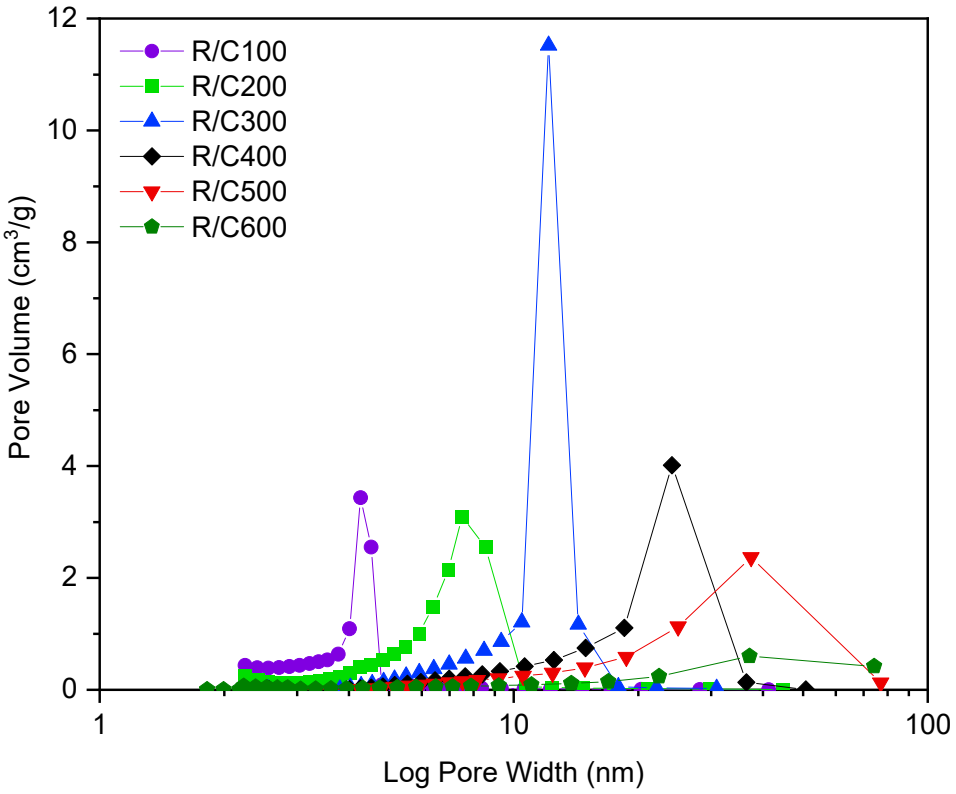

Figure 3. Pore size distributions for sodium carbonate gels at resorcinol/catalyst molar ratios (R/C ratios) 100–600.

As indicated by the isotherms for the standard gels (Figure 2), an increase in R/C ratio is thought to lead to an increase in average pore width. The graph in Figure 3 confirms this, displaying the pore size distribution for each sample visibly shifting towards larger pore width values, as the R/C ratio increases. The increase in pore size associated with high R/C ratios is thought to be as a result of the reduced number of initial clusters formed, leading to the growth of larger clusters over time, the process of which occurs at a slower rate [14]. These larger clusters subsequently have larger pores between them, impacting the textural properties and overall appearance of the resulting gels. The higher concentration of catalyst present in gels synthesized using lower R/C ratios results in a higher number of initial clusters formed, the total mass therefore being distributed over a greater number of smaller clusters, the process of which takes place more rapidly. Given that the clusters formed are of smaller average size, they subsequently have smaller pores between them, once again impacting the textural properties and overall appearance of the gels formed [14]. The gels formed at low R/C ratios, therefore, possess a higher degree of porosity, with a greater number of pores of smaller widths, and an increased surface area per gram, making them useful for applications such as filters, sorbing media for waste containment, or hydrogen fuel storage [34].

2.2. Investigating the Role of the Cation

As has been previously discussed, various research has been published on the impact of catalyst concentration on the final gel properties, with most referring to the catalyst purely as a means to alter the pH of the initial solution, labelling it simply as a 'pH adjuster'. Whilst the impact of initial solution pH is undeniably fundamental to the final textural properties of the gel, as outlined above, some studies have indicated that the role of the catalyst components extends far beyond this. The main hurdle in fully understanding the role of the catalyst is in attempting to decouple the relationship between the concentration of catalyst components present and the resulting pH of the gel solution, given that one cannot be altered without affecting the other. It is, of course, possible to keep the catalyst concentration constant whilst adjusting the pH through additions of acidic or basic solutions, however, this method introduces new additional components into the gel solution, which could ultimately alter the final structure of the gel formed, potentially as a result of 'salting-out' effects previously discussed. With this in mind, the research presented here aims to decouple the relationship between pH and the catalyst concentration, in addition to analysing the role of the specific components of the catalyst used. Firstly, the role of the cation used within the catalyst was assessed through the preparation and analysis of different sets of gel samples with the following catalyst combinations:

1(i) Na_2CO_3/$NaHCO_3$ mixture at constant cation concentrations equivalent to R/C100

1(ii) Na_2CO_3/$NaHCO_3$ mixture at constant cation concentrations equivalent to R/C300

2(i) $NaHCO_3$/NH_4HCO_3 mixture at constant anion concentrations equivalent to R/C100

2(ii) $NaHCO_3$/NH_4HCO_3 mixture at constant anion concentrations equivalent to R/C300

Using these combinations of catalyst species, the specific roles of the cation and anion can be investigated, with sample sets 1(i) and 1(ii) exploring the effects of varying solution pH with the addition of H^+ ions while the Na^+ concentration remains constant. Sample sets 2(i) and 2(ii), on the other hand, vary the concentration of Na^+ ions while the concentration of HCO_3^- remains constant, providing further insight into the significance of the role of the metal cation. The mass of catalyst required for each combination was calculated based on the percentage of total sodium ions (Na^+) contributed by the two catalysts being compared (in the cases where Na_2CO_3 and $NaHCO_3$ mixtures are used), or the percentage of total hydrogen carbonate ions (HCO_3^-) contributed by the two catalysts being compared (in the cases where $NaHCO_3$ and NH_4HCO_3 mixtures are used). In samples labelled 25Na_2:75NaH, this refers to a sample where 25% of the total moles of Na^+ present are contributed by Na_2CO_3, whilst 75% are contributed by $NaHCO_3$. Similarly, in

samples labelled 25NaH:75NH_4, this refers to a sample where 25% of the total moles of HCO_3^- present are contributed by $NaHCO_3$, whilst 75% are contributed by NH_4HCO_3. All samples within a series such as this maintain a constant concentration of Na^+ or HCO_3^- ions equivalent to that of a standard gel at a given R/C ratio, but with varying contribution percentages from the two catalysts.

2.2.1. Catalyst Mixtures—Na_2CO_3/$NaHCO_3$

First, consider the isotherms of sets 1(i) and (ii), shown in Figure 4a,b, where the Na^+ concentration remains constant and equal to that of standard gels prepared at R/C ratios of 100 and 300, respectively. Despite the variations in initial solution pH as the concentration of H^+ ions present increases through the addition of $NaHCO_3$, which will be discussed in more detail below, the resulting isotherms remain similar in shape. They each follow the same trend throughout the adsorption process and exhibit similar hysteresis loops, which also occur at very similar partial pressure values. Minute variations in hysteresis loops, such as those observed, are to be expected between gel samples that are similar in makeup and structure. Furthermore, not only are the isotherms within sets 1(i) and 1(ii) indistinguishable from one another within experimental error, but they are also comparable to those obtained for standard gels prepared at the same equivalent R/C ratio in terms of Na^+ concentrations. This suggests that the Na^+ ion is one of the central components in determining the properties of the final material, especially given that the varying concentrations of anions present in the different catalyst mixtures appear to have negligible effects. It is also worth noting that the gels labelled 100NaH, synthesized using 100% $NaHCO_3$ as the catalyst to provide Na^+ concentrations equal to R/C100 and R/C300 standard Na_2CO_3 gels, are actually representative of R/C50 and R/C150 gels with respect to the ratio of resorcinol to $NaHCO_3$ catalyst concentration.

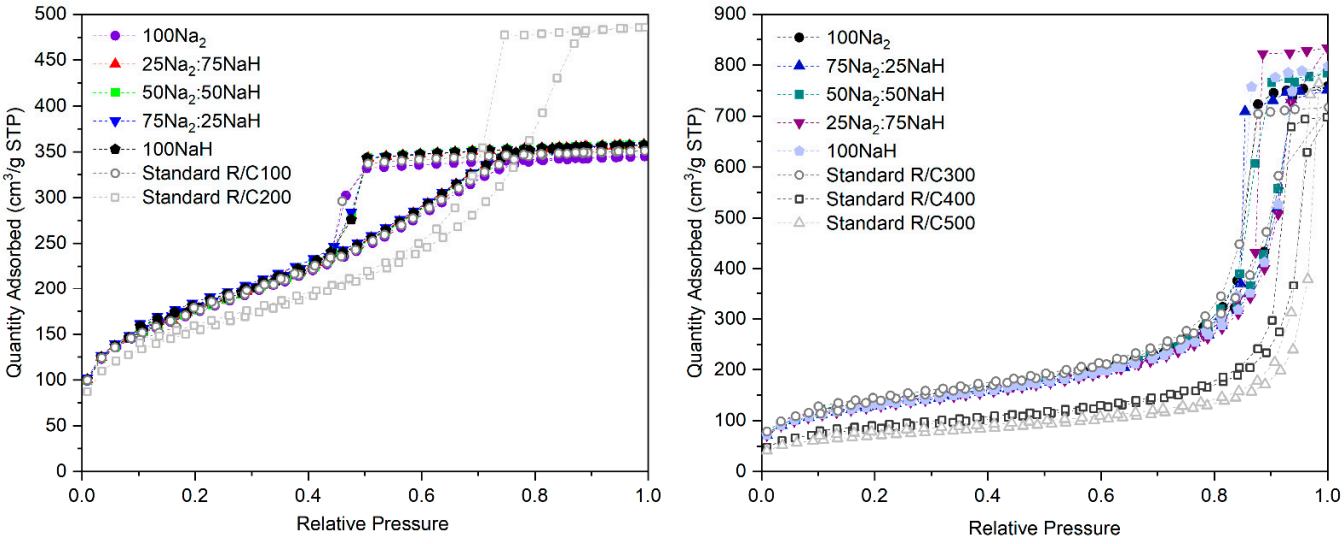

Figure 4. (**a**) Isotherms from sample set 1(i) Na_2/NaH R/C100 Na^+ equivalent, (**b**) sample set 1(ii) Na_2/NaH R/C300 Na^+ equivalent. Note that R/C is the resorcinol/catalyst molar ratio.

2.2.2. Catalyst Mixtures—$NaHCO_3$/NH_4HCO_3

Next, consider the isotherms for sets 2(i) and (ii) displayed in Figure 5a,b, where the HCO_3^- concentration remains constant and equal to that of standard gels prepared at R/C ratios of 100 and 300, respectively. The isotherms within the R/C100 set (Figure 5a) show a gradual change as the Na^+ concentration is reduced and replaced by NH_4^+ until 75% of the HCO_3^- ions present are contributed by NH_4HCO_3, at which point the resulting materials prove to be non-porous. The isotherms shown within Figure 5b indicate that a porous

material was formed only when 100% of the HCO_3^- ions were sourced from $NaHCO_3$ at R/C300, with any substitution for NH_4HCO_3 producing a non-porous material. When the samples are then compared to those of standard gels prepared at the same equivalent R/C ratio, the isotherms are different again, even varying from those prepared with 100% $NaHCO_3$. This could be explained by the fact that the R/C ratio for this sample set is made on the basis of equivalency in anion concentration, therefore resulting in half the Na^+ concentration when $NaHCO_3$ is used in comparison to Na_2CO_3. Note that the initial solutions for all gels in sample sets 2(i) and 2(ii) fell within the required pH window for the successful formation of porous structures previously discussed, with pH values across the samples ranging between 6 and 7. Importantly, the visual differences displayed here between the isotherms of 100% $NaHCO_3$ R/C100 gels and standard Na_2CO_3 R/C100 gels are in strong agreement with those observed in the work carried out by Horikawa et al. [15], discussed previously, who used nitrogen adsorption measurements to determine the comparative properties of pyrolyzed RF aerogels catalysed by Na_2CO_3, K_2CO_3, $NaHCO_3$, and $KHCO_3$, each at R/C50.

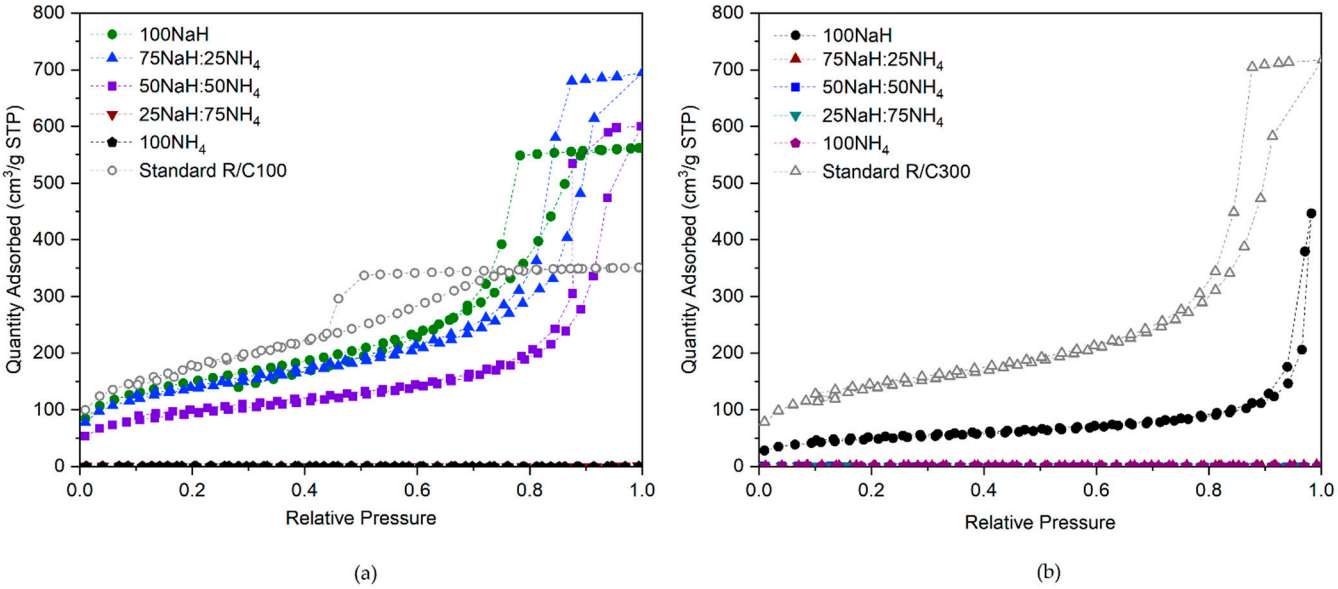

Figure 5. Isotherms for (**a**) sample set 2(i) NaH/NH_4 R/C100 HCO_3^- equivalent, and (**b**) sample set 2(ii) NaH/NH_4 R/C300 HCO_3^- equivalent. Note that R/C is the resorcinol/catalyst molar ratio.

In this work, the cations used within the catalyst are Na^+ and NH_4^+, where the substitution of one for the other achieved significantly different results. The presence of Na^+ ions appeared to aid the gelation process, leading to the formation of inter-linked porous network structures, while the presence of NH_4^+ failed to promote the gelation process, with its sole use leading to the formation of a non-porous material that had failed to gel completely. As postulated by Taylor et al. [22], the ability of these ions to 'salt-in' or 'salt-out' macromolecules from solution, as with the Hofmeister series, could be an important factor within the results observed. In accordance with the reverse Hofmeister series suggested for hydrophilic surfaces, shown in Figure 1a, Na^+ ions have medium kosmotropic effects, therefore promoting the stability of macromolecules in solution, and facilitating the formation of inter-linked porous structures in solution [28]. NH_4^+ ions, on the other hand, have chaotropic effects, therefore contributing to the destabilizing and disordering of macromolecules, and hindering the formation of porous structures in solution [29]. This could have important implications on the final properties of the structures, with the potential precipitation of solids from solution taking place early in the presence of chaotropic ions (such as NH_4^+), resulting either in the slower growth of the clusters which remain in the solution, or significant precipitation hindering the formation of inter-linked porous structures. Furthermore, if the particles within the solution become

too large without interconnections, the system is no longer colloidal, and the large particles will sediment.

These results show promise in elucidating the role of the metal ion, indicating that the concentration of Na^+ present from the catalyst is pivotal in determining the gelation process and subsequent structural properties of the final material.

2.3. Structural Impacts of Initial Solution pH

The results obtained from sample sets 1(i) and 1(ii) can be used to investigate the role of the metal ion in comparison to that of the measured initial solution pH, aiming to decouple the overall relationship between catalyst concentration and pH. Referring back to Figure 4, which displays the isotherms from sets 1(i) and 1(ii) alongside isotherms for standard gels across comparable initial solution pH ranges, these can be considered in addition to the resulting gel textural properties from the analysis shown in Table 2.

Table 2. Initial pH values of standard gels at varying resorcinol/catalyst molar ratios (R/C ratios), in addition to that of samples in sets 1(i) and 1(ii), and their corresponding average pore widths. The average pore width values are recorded to an accuracy less than their error, therefore their error values have been omitted. Note that $\overline{\phi}$ is average pore width.

Standard Gels	**pH**	$\overline{\phi}$ **(nm)**
R/C100	7.26	4
R/C200	6.98	7
R/C300	6.78	11
R/C400	6.59	19
R/C500	6.48	26
Sample Set 1(i) R/C100	**pH**	$\overline{\phi}$ **(nm)**
$100Na_2$	7.32	4
$75Na_2$:25NaH	7.29	4
$50Na_2$:50NaH	7.27	4
$25Na_2$:75NaH	7.23	4
100NaH	7.18	4
Sample Set 1(ii) R/C300	**pH**	$\overline{\phi}$ **(nm)**
$100Na_2$	6.72	12
$75Na_2$:5NaH	6.67	12
$50Na_2$:50NaH	6.59	13
$25Na_2$:75NaH	6.56	14
100NaH	6.44	13

Within sample sets 1(i) and 1(ii), a gradient of decreasing initial solution pH is observed, with the concentration of H^+ ions increasing as Na_2CO_3 is substituted for $NaHCO_3$. Using this method to alter the pH introduces no new components into the system, limiting the number of variables being altered at a given time, and therefore allowing a more accurate analysis to be carried out. Figure 6 shows graphically how the average pore widths of the gels vary with pH for three sets of samples: sample sets 1(i), 1(ii), and also standard Na_2CO_3 gels at RC ratios 100–500, while Table 2 indicates the initial pH of the prepared solutions during gel synthesis for each of the three sets of gels alongside the average pore width determined from nitrogen adsorption analysis of the resulting gels.

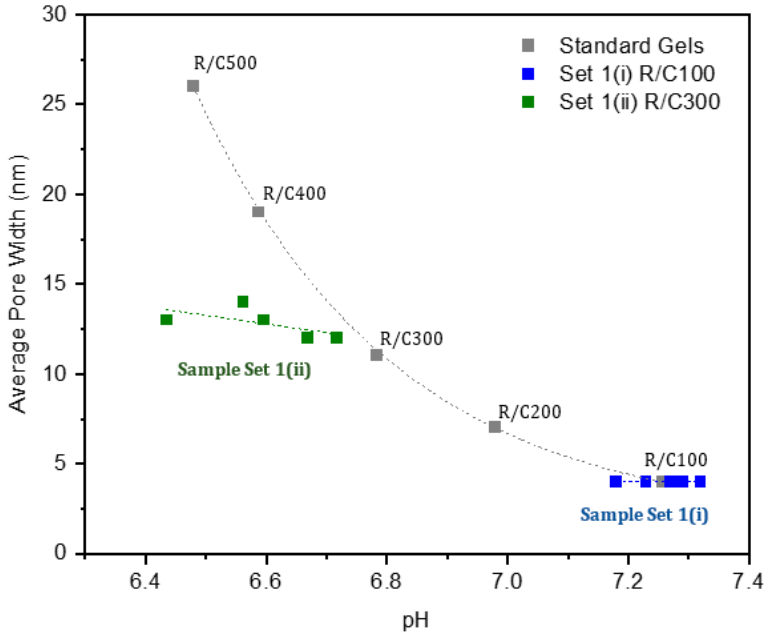

Figure 6. Graph of initial solution pH versus average pore width for the three sets of gels. Note that for sample sets 1(i) and 1(ii), the points marked on the graph show increasing NaH concentration from right to left. Original R/C100–R/C500 gels are plotted with a dashed line according to exponential decay curve fitting, while a straight-line fit is used for sample sets 1(i) and 1(ii). R/C is the resorcinol/catalyst molar ratio.

As the data in Table 2 shows, the average pore width within the standard Na_2CO_3 gel structure is significantly impacted by the corresponding R/C ratio used during its synthesis, with average widths ranging from 4–26 nm across an R/C ratio range of 100–500. Conversely, on inspection of the average pore widths within sample sets 1(i) and 1(ii), very little variation is observed, despite the change in initial solution pH. Furthermore, looking at sample set 1(ii) specifically, the initial solution pH of the gels ranges from 6.44–6.72. This range is similar to that observed across standard Na_2CO_3 gels at R/C ratios 300–500, which possess initial pH values of 6.48–6.78. Despite the similar range of initial pH values observed across the two sets, the final gels formed are markedly different. Samples in set 1(ii), which each possess the same concentration of Na^+ ions, all have average pore widths of around 12–14 nm. This is in sharp contrast to that of the standard Na_2CO_3 gels, which each have different concentrations of Na^+ ions, and whose average pore widths vary significantly from 11–26 nm. The isotherms in Figure 4, discussed previously, further highlight the differences in the structures formed, providing a comparison of the adsorption behaviour of the sample within sets 1(i) and 1(ii) with those of standard Na_2CO_3 gels which possess a similar pH range.

Although pH undoubtedly plays an important role in the catalysis of the RF reaction and impacts the textural properties of the final gel when significant pH adjustments are made, this is likely not observed with relatively small changes in pH such as those in this experiment (<0.4), provided the solution pH falls within the viable range of 5.5–7 for gels made with a basic catalyst. Instead, the variations observed in gel properties within the pH ranges studied suggests that the influence of pH alone may have previously been overestimated, and points towards the pivotal role of the cation in the formation of the porous structure of the gel. This could be particularly relevant to the work carried out by Job et al. [18], discussed previously, where RF gels were synthesized at set pH values, achieved through the addition of NaOH solution. In this work, as the pH increased from 5.45 to 7.35, corresponding to the increasing volume of NaOH added, the average pore size consistently decreased from 50 nm to 4 nm. Although the authors concluded that the change in pH was responsible for the significant differences in textural properties achieved,

the results presented here suggest that those differences could, in fact, be attributed to the increasing Na^+ concentration, as larger volumes of NaOH solution was added.

2.4. Investigating the Role of the Anion

In order to further investigate the role of the anion within the catalyst, two other sodium salts, containing alternative anions that do not hydrolyse, thus should not change the solution pH, were added as catalysts during RF gel synthesis. Sodium chloride (NaCl) and sodium sulphate (Na_2SO_4) were chosen in this work and the combined amounts of both salts were based on molar ratio of sodium ions to resorcinol molecules in the solution, so that the total amount of sodium ions was kept constant and equal to the amount in solution for an RF gel prepared using only sodium carbonate and R/C100. For example, a sample of Na_2CO_3 200 NaCl 100 was made using the amount of Na_2CO_3 as for a standard gel with R/C200 and amount of NaCl to adjust the sodium ion concentration in the reaction solution to match that of a standard gel solution for R/C100, the numbers used in the sample name represent the individual R/C ratios for the salts used. When a gel was made without sodium carbonate, its R/C ratio was labelled as Na_2CO_3 INF.

Nitrogen sorption isotherms and their corresponding pore size distributions for samples prepared in this section are presented in Figures 7–10, along with data for selected samples prepared with only sodium carbonate. It can be seen from Figure 7 that both nitrogen sorption isotherms and pore size distributions for gels made with Na_2CO_3 200 and added NaCl or Na_2SO_4 exhibit similar shapes to that of a standard gel with R/C300, rather than R/C100 or 200. The solutions for samples with varying catalyst compositions had the same sodium ion concentration as a sample with R/C100, so if sodium ion concentration was the main factor influencing the final structure, these should exhibit similar textural properties. However, the solution pH would differ from a standard R/C100 solution, since both chloride and sulphate anions do not hydrolyse in an aqueous solution resulting in a similar pH to that of a R/C200 solution. However, the pH values presented in Table 3 show a slight difference between the solutions with and without the additional salts present. It should be noted that the pH probe used converts a voltage measurement into a pH value, which means the voltage reading could be influenced by the other ions present in the solution. Nevertheless, there is a general trend of decreasing pH with increasing R/C ratio, as a result of decreasing concentration of hydrolysing carbonate ions. Due to the strong electrolyte nature of Na_2CO_3, its dissociation in an aqueous solution should not be affected by the addition of Na^+ ions.

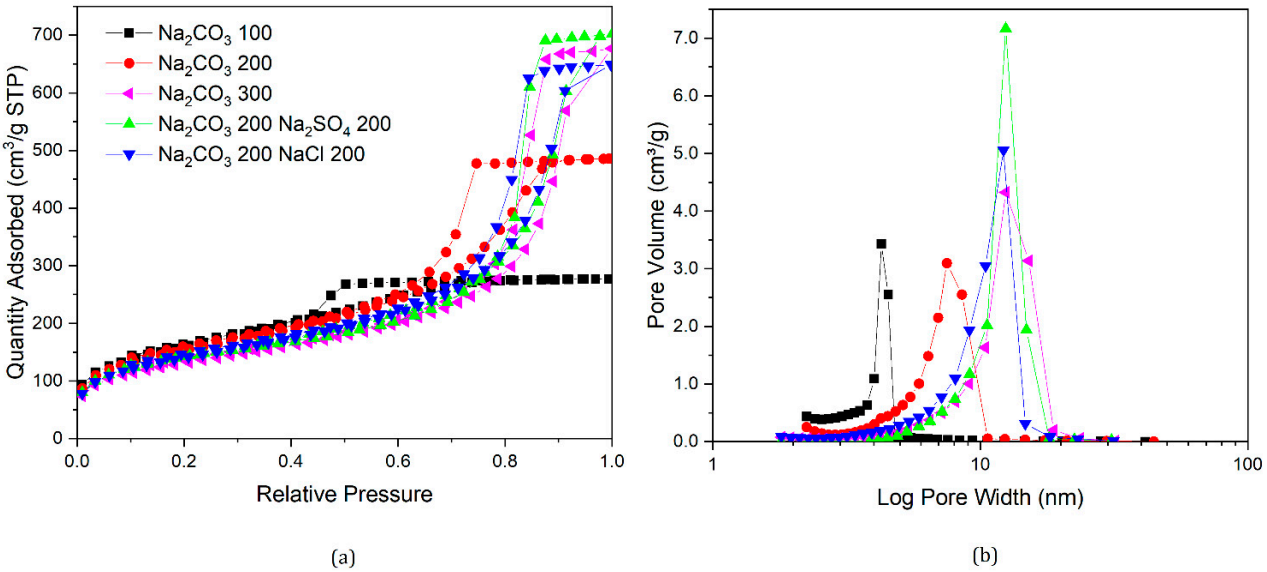

Figure 7. Nitrogen sorption isotherms of gels with varying catalyst compositions (**a**), and corresponding pore size distributions (**b**).

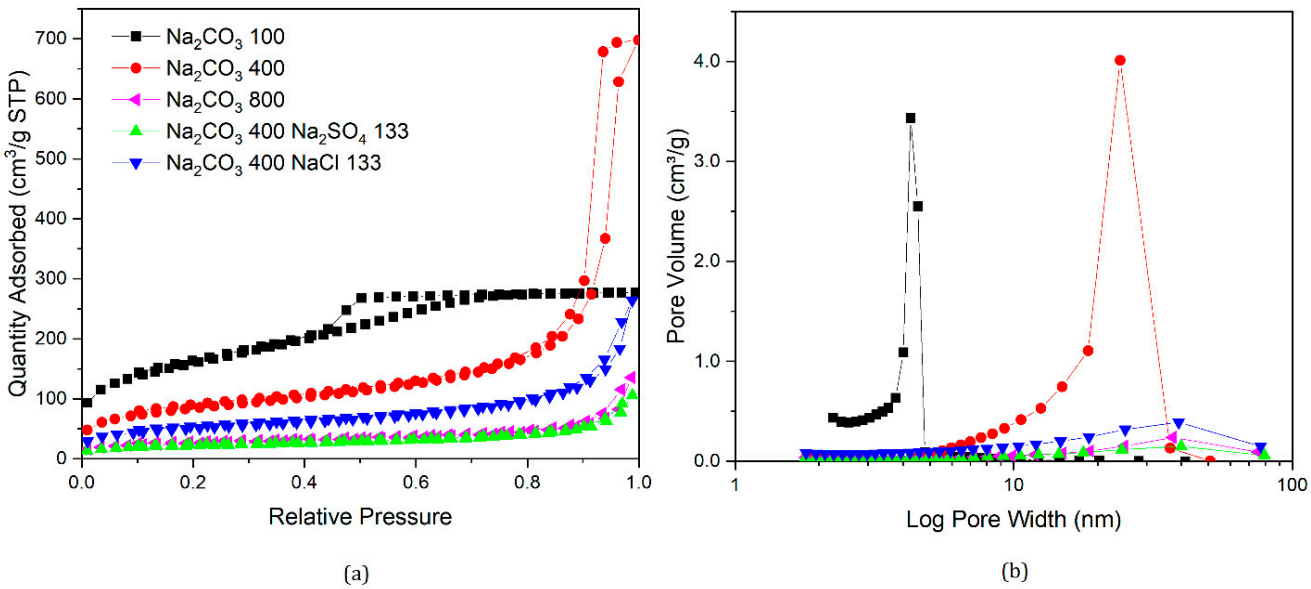

Figure 8. Nitrogen sorption isotherms of gels with modified catalyst composition (**a**) and corresponding pore size distributions (**b**).

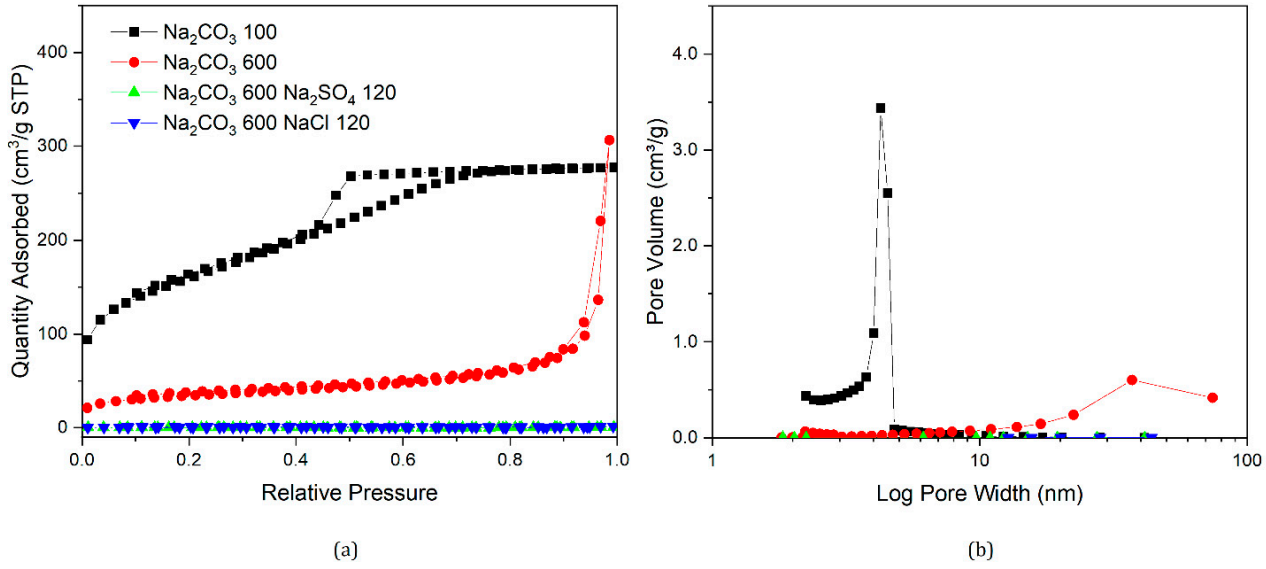

Figure 9. Nitrogen sorption isotherms of gels with modified catalyst composition (**a**) and corresponding pore size distributions (**b**).

Similar trends can be observed in Figures 8 and 9 where the nitrogen sorption data for samples with additional salts are closer to samples prepared with a higher R/C ratio than the ones with the same Na_2CO_3 amount or sodium ion concentration. Samples with Na_2CO_3 400 exhibit similar properties to a standard gel with R/C ratio 800. Interestingly, when either Na_2SO_4 or NaCl are added to a gel with Na_2CO_3 600, a non-porous material is obtained, similar to when no catalyst is used, even though RF gels prepared using only Na_2CO_3 at R/C ratio 600 are still porous materials.

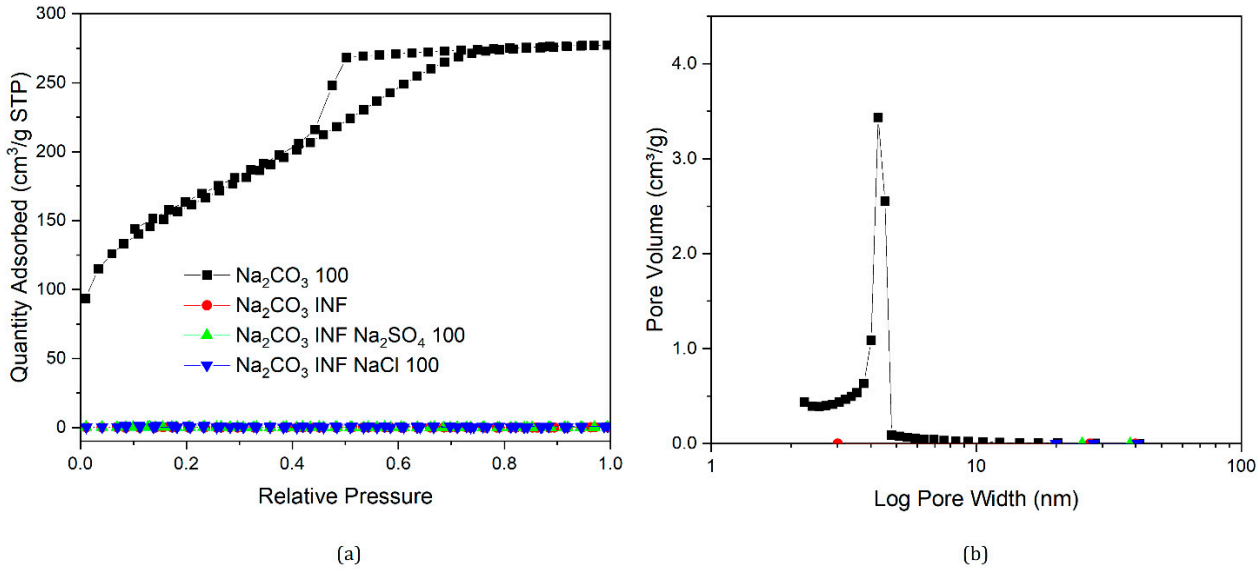

Figure 10. Nitrogen sorption isotherms of gels with modified catalyst composition (**a**) and corresponding pore size distributions (**b**). Note that INF represents infinite resorcinol/catalyst molar ratio (R/C ratio); therefore, zero concentration.

Table 3. pH values of initial solutions and textural properties for gels with different resorcinol/catalyst molar ratios (R/C ratios) of sodium carbonate (Na_2CO_3), sodium sulphate (Na_2SO_4), and sodium chloride (NaCl). Note that S_{BET} is Brunauer-Emmet-Teller (BET) surface area, V_T is total pore volume, V_u is micropore volume, and $\overline{\phi}$ is average pore width.

R/C Ratio			pH	S_{BET} (m^2/g)	V_T (cm^3/g)	V_u (cm^3/g)	$\overline{\phi}$ (nm)
Na_2CO_3	Na_2SO_4	NaCl					
100	-	-	7.26	574	0.43	0.06	4
200	-	-	6.98	552	0.75	0.06	7
400	-	-	6.59	304	1.08	0.04	19
600	-	-	6.27	124	0.30	0.02	28
-	-	-	4.1	-	-	-	-
200	200	-	7.4	490	0.95	0.06	9
200	-	100	7.3	500	0.99	0.06	10
400	133	-	7.0	120	0.30	0.02	16
400	-	67	6.9	130	0.34	0.02	17
600	120	-	6.7	1	-	-	34
600	-	60	6.6	-	-	-	39
-	100	-	3.3	-	-	-	-
-	-	50	3.1	-	-	-	-

According to the work by Taylor et al. [14,22], discussed previously, dynamic light scattering (DLS) experiments showed that RF clusters that are formed in the reaction solution gradually grow and adhere to each other, resulting in the final structures observed in the dried materials. Textural properties of RF xerogels, therefore, depend on the final cluster size and their packing in three dimensions. The anions used in this part of the study are arranged in the reversed Hofmeister series [30], as presented in Section 1.3 for hydrophilic surfaces, in the following order of ability to salt-out macromolecules from solution: $CO_3^{2-} < SO_4^{2-} < Cl^-$. This suggests, that in the solution containing only the

carbonate (CO_3^{2-}) ions, the growing clusters will precipitate from the solution at later stages compared with solutions, where a proportion of the carbonate ions are substituted by anions with higher salting-out ability, such as sulphate (SO_4^{2-}) and chloride (Cl^-) anions.

The gelation mechanism of RF gels has been investigated by dynamic light scattering (DLS) by Taylor et al. [14], providing new insights into the proposed cluster formation and growth process. As clusters grow in the reaction solution, they can potentially grow at slightly different rates, based on the diffusion of reagents towards the reactive centres. When a cluster reaches critical size, leading to local phase separation, the newly created interface will lead to adsorption of species dissolved in the solution, reagents, and on this interface. In a solution containing ions with a higher salting-out ability (SO_4^{2-} and Cl^-), clusters might precipitate at an earlier stage, leading to a faster subsequent growth of these clusters due to the reagent adsorption effects. This could lead to the clusters left in solution growing at a slower pace, with the reactants being depleted by the faster growing precipitated clusters. This might result in an increased final size of clusters in from these solutions, compared to when only CO_3^{2-} is present. Without the SO_4^{2-} and Cl^- ions, a larger number of clusters grow at a similar rate for longer time, with larger clusters present when phase separations occur, leading to more uniform and, on average, smaller particles present in the final material. The larger clusters, arising from an earlier phase separation, would have larger gaps in between them, observed as larger pore sizes from nitrogen sorption measurements. However, it is important to keep in mind that only pores up to the upper limit of mesopores, up to ~50–100 nm [35–37], are observable by this technique, with the macropores not filling, and thus, not contributing towards the average pore size.

A series of RF gels using only sodium chloride as a catalyst were prepared, in order to investigate whether the presence of sodium ions is the major driving force for RF gel formation rather than solution pH. Samples with NaCl R/C 12.5, 200, and 400 (corresponding to sodium ion concentrations for Na_2CO_3 R/C ratios of 25, 400, and 800) were prepared; however, all of the final materials were found to be non-porous. The values of solution pH, after all the reagents had dissolved and a 30-min stirring period, were measured as 3.40, 3.30, and 3.24 for NaCl R/C 12.5, 200, and 400, respectively. This, in addition to the results presented previously, suggests that both the presence of sodium ions and appropriate solution pH value are necessary in order to obtain a viable porous gel structure. It can, therefore, be concluded that both the cation and the anion within the catalyst play a central role, the potential 'salting-in' or 'salting-out' effect of both being pivotal to the structural properties of the final gel formed, in addition to the required solution pH window discussed previously.

An interesting observation can be made by visually comparing dried RF xerogels made with and without the additional salts, photographs of these xerogels are presented in Figure 11. Xerogels prepared with either sodium sulphate or sodium chloride added have a very similar appearance and differ significantly from the standard xerogels prepared with sodium carbonate only. It is also worth mentioning that samples with Na_2CO_3 R/C ratios 400 and 600 made with additional salts did not exhibit the usual level of shrinkage after subcritical drying, as all the other studied materials do, even though they were all cut into similar sized pieces (~1 cm), which can be used as a visual guide in comparing samples, prior to the solvent exchange step. This might be explained by the larger pore sizes present in these samples, eliminating capillary forces during drying while preserving the extent of cross-linking, leading to a lower degree of material shrinkage. If large macropores are present in these samples, as described above, the liquid–vapor interface would not cause a collapse of this large-scale porous structure, leading to only a small shrinkage of these materials even under subcritical conditions. However, it is important to note that for many applications, such as gas storage, this macroporosity is not as useful as the presence of mesopores or micropores.

Figure 11. RF xerogels prepared with varying R/C rations of Na_2CO_3, Na_2SO_4, and NaCl.

3. Conclusions

The role of the individual catalyst components within the RF gelation reaction was investigated, the results of which point towards a pivotal role beyond simply just pH-adjusting—the theory that is generally accepted within the RF gel research field. Gels prepared at a constant hydrogen carbonate concentration with varying sodium ion concentrations were shown to vary significantly, some failing to gel whatsoever. Conversely, gels prepared with a constant sodium ion concentration with varying carbonate concentrations

all possessed similar textural properties, despite their differences in initial solution pH. These results confirm the significance of the metal cation in the gel synthesis and allow its role to be decoupled from the role of pH, which is generally thought to be the most crucial factor in the gelation mechanism.

Furthermore, replacing a proportion of the sodium carbonate catalyst with sodium chloride or sodium sulphate leads to materials with significantly different textural properties. The introduction of chloride or sulphate ions into the reaction solution appeared to have a similar effect to that observed for increasing sodium carbonate R/C ratio (decreasing catalyst concentration), suggesting that the presence of these ions has a comparatively adverse effect on gelation. Given that the addition of sodium chloride and sodium sulphate increased the concentration of sodium ions present, yet still had this adverse effect on gelation, the ability of ions to 'salt-in' or 'salt-out' macromolecules from solution was considered. A Hofmeister-like series for the RF gel reaction could, therefore, be possible. In the case of sodium sulphate and sodium chloride, the cation has strong 'salting-in' capabilities while the anions have weaker 'salting-in' capabilities, or even strong 'salting-out' capabilities in comparison the carbonate anion typically used. This affects the point at which the aggregating clusters precipitate from solution, resulting in gels that possess different structural properties to those catalysed using sodium carbonate alone.

4. Materials and Methods

4.1. RF Gel Synthesis

A series of RF gels were synthesised with varying compositions, each gel formed through an established procedure requiring four reagents: resorcinol (ReagentPlus, 99%, Sigma-Aldrich, Poole, UK), formalin solution (37 wt % formaldehyde in water and methanol, Sigma-Aldrich, Poole, UK), deionised water (produced in-house with Millipore Elix 5, Progard 2), and a catalyst. In this work, the catalysts used were sodium carbonate (Na_2CO_3, anhydrous, ≥99.5%, Sigma-Aldrich, Poole, UK), sodium hydrogen carbonate ($NaHCO_3$, anhydrous, ≥99.5%, Sigma-Aldrich, Poole, UK), ammonium hydrogen carbonate (NH_4HCO_3, 99%, Fisher Scientific, Loughborough, UK), sodium sulphate (Na_2SO_4, anhydrous, ≥99.0%, Sigma-Aldrich, Poole, UK), and sodium chloride (NaCl, Redi-Dri, anhydrous, ≥99%, Sigma-Aldrich, Poole, UK).

In the preparation of the gels investigated here, the volume of liquid added per gel in the initial solution was kept constant at 60 mL, which included the water and methanol content of the formalin solution. The total solids content of the initial mixture was kept constant at 12 g, which included the mass of formaldehyde contained within the formalin solution. The mass of resorcinol (R), formaldehyde (F), and catalyst (C) was varied according to the R/C ratio being prepared, all the while maintaining a constant R/F ratio of 0.5 in accordance with the stoichiometry of the resorcinol–formaldehyde reaction. Data for the mass of individual components of each reagent are included within the Supplementary Materials, in addition to details of how the volume of formalin required for each gel was calculated.

The RF gel synthesis follows a standard procedure, with the reagents initially combined in individual circular glass jars according to the desired catalyst concentration and mixture, forming the initial RF solution. For gels synthesized using a combination of two catalysts, the two compounds were weighed into separate crucibles and added to the mixture simultaneously. The resulting solution pH was measured using a Hanna Instruments benchtop pH meter (Leighton Buzzard, Bedfordshire, UK), after which point the jar was sealed and placed into a Memmert ULE-500 oven (Büchenbach, Germany) at 85 °C and left to gel for a 3-day period.

After the gelation period was complete, the gels underwent a 3-day solvent exchange process, where the water within the pores was exchanged for acetone. Acetone was selected as a solvent for exchange, due to its low surface tension value (23.46 mN/m for acetone in comparison to 71.99 mN/m for water; both values taken at 25 °C [38]),

therefore, minimizing the extent of pore shrinkage upon drying, in addition to its miscibility with water.

Finally, following the completion of the 3-day solvent exchange step, the jars containing RF gel samples were drained, covered with perforated aluminum foil, and placed into a Towson and Mercer 1425 Digital Vacuum Oven (Stretford, UK). After closing the vacuum oven door, the oven heating was turned on and the temperature was set to 110 °C, which corresponds to 85 ± 5 °C inside the oven (monitored using a thermometer placed inside the oven). The vacuum pump (Vacuubrand MZ 2C NT, Wertheim, Germany) attached to the oven was turned on, with two solvent traps with water/ice mixture placed between the oven and the pump, to condense acetone evaporating from the gel samples. The solvent traps were used to preserve the vacuum pump, limiting the amount of solvent vapor that came into contact with the membranes, as well as monitoring sample drying. For safety purposes, the oven and the pump were not left running overnight but were turned on at the beginning of each working day for 8 h. The gels were dried for 2 days, after which they were transferred into labelled sample containers.

4.2. Nitrogen Sorption Measurements

Nitrogen sorption measurements were carried out to determine the structural properties of the final gels, again following a standard procedure. Once the RF gels had been dried, a sample of approximately 0.5 g was weighed into a bulb tube, initially undergoing a degassing process using a Micromeritics ASAP 2420 surface area and porosity analyser (Hexton, UK). Following this, the sample was transferred to an analysis port within the equipment and the nitrogen sorption measurements were carried out. The analysis lasted for approximately 20–30 h per sample, collecting 40 data points for adsorption as the relative pressure was incrementally increased from 0.1 to 1 and then 30 data points for desorption as the relative pressure was decreased from 1 to 0.1. Subsequent analysis of the isotherm data included surface area determination using BET theory [33], and the Rouquerol correction for microporous samples [35]. Where calculations of total pore volume and micropore volume were carried out, the t-plot method [39] was employed, and finally, average pore size determination using the Barrett–Joyner–Halenda (BJH) method [32]. The BJH method was used to determine the pore size distribution within the meso- and macroporous range, assuming pores of cylindrical shape were present, applying data taken from the desorption branch of the isotherm. The principle of the BJH method relies on the calculation of the Kelvin core radius at each relative pressure interval:

$$\ln\left(\frac{p}{p_o}\right) = \frac{2\gamma V_m}{r_c RT} \quad (1)$$

where p/p_o is relative pressure, r_c is pore meniscus radius, γ is the surface tension of the liquid–vapor interface, V_m is the liquid molar volume, R is the universal gas constant and T is temperature. The total pore radius is composed of the meniscus radius (r_c) in addition to the thickness of the remaining layer adsorbed onto the pore walls (t). The BJH method, therefore, includes the calculation of this thickness in order to calculate the total pore width, and for calculations applicable to nitrogen adsorption onto RF gels, an empirical formula known as the carbon black equation [40] was used:

$$t = 2.98 + 6.45\left(\frac{p}{p_o}\right) + 0.88\left(\frac{p}{p_o}\right)^2 \quad (2)$$

Supplementary Materials: Data for the mass of individual components of each reagent used within gel synthesis is available online at https://www.mdpi.com/article/10.3390/gels7030142/s1, Table S1: Initial Solution Composition for Na_2CO_3 Gels, Table S2: Initial Solution Composition for Na2CO3/NaHCO3 Mixture Gels—R/C100 Equivalent, Table S3: Initial Solution Composition for Na2CO3/NaHCO3 Mixture Gels—R/C300 Equivalent, Table S4: Initial Solution Composition for

NaHCO3/NH4CO3 Mixture Gels—R/C100 Equivalent, Table S5: Initial Solution Composition for NaHCO3/NH4CO3 Mixture Gels—R/C300 Equivalent, Table S6: RF gel solution compositions for study of sodium chloride as additional source of sodium ions. Numbers in sample name correspond to R/C ratios of catalyst salts, INF represents infinite R/C ratio (zero concentration), and Table S7: RF gel solution compositions for study of sodium sulphate as additional source of sodium ions. Numbers in sample name correspond to R/C ratios of catalyst salts, INF represents infinite R/C ratio (zero concentration).

Author Contributions: Conceptualization, A.F.; methodology, E.M. and M.P.; formal analysis, E.M. and M.P.; writing—original draft preparation, E.M. and M.P.; writing—review and editing, E.M., M.P., and A.F.; supervision, A.F.; project administration, A.F.; funding acquisition, A.F. All authors have read and agreed to the published version of the manuscript.

Funding: This research was funded by the Engineering and Physical Sciences Research Council (EPSRC) through the National Productivity Investment Fund (NPIF). Grant number: EP/R512205/1.

Data Availability Statement: The data presented in this study are openly available in the University of Strathclyde KnowledgeBase Pure Portal, https://doi.org/10.15129/17dfa992-9818-42d6-8afe-20da1ece457d (accessed on 7 September 2021).

Acknowledgments: The authors would like to thank the Chemical and Process Engineering Department at the University of Strathclyde, and the Engineering and Physical Sciences Research Council for funding this work.

Conflicts of Interest: The authors declare no conflict of interest.

References

1. Al-Muhtaseb, S.A.; Ritter, J.A. Preparation and Properties of Resorcinol–Formaldehyde Organic and Carbon Gels. *Adv. Mater.* **2003**, *15*, 101–114. [CrossRef]
2. ElKhatat, A.M.; Al-Muhtaseb, S.A. Advances in Tailoring Resorcinol-Formaldehyde Organic and Carbon Gels. *Adv. Mater.* **2011**, *23*, 2887–2903. [CrossRef] [PubMed]
3. Alshrah, M.; Mark, L.H.; Zhao, C.; Naguib, H.E.; Park, C.B. Nanostructure to thermal property relationship of resorcinol formaldehyde aerogels using the fractal technique. *Nanoscale* **2018**, *10*, 10564–10575. [CrossRef] [PubMed]
4. Li, F.; Xie, L.; Sun, G.; Kong, Q.; Su, F.; Cao, Y.; Wei, J.; Ahmad, A.; Guo, X.; Chen, C.-M. Resorcinol-formaldehyde based carbon aerogel: Preparation, structure and applications in energy storage devices. *Microporous Mesoporous Mater.* **2019**, *279*, 293–315. [CrossRef]
5. Pekala, R.W. Organic aerogels from the polycondensation of resorcinol with formaldehyde. *J. Mater. Sci.* **1989**, *24*, 3221–3227. [CrossRef]
6. Prostredný, M.; Abduljalil, M.G.M.; Mulheran, P.A.; Fletcher, A.J. Process Variable Optimization in the Manufacture of Resorcinol-Formaldehyde Gel Materials. *Gels* **2018**, *4*, 36. [CrossRef] [PubMed]
7. Job, N.; Théry, A.; Pirard, R.; Marien, J.; Kocon, L.; Rouzaud, J.-N.; Béguin, F.; Pirard, J.-P. Carbon aerogels, cryogels and xerogels: Influence of the drying method on the textural properties of porous carbon materials. *Carbon* **2005**, *43*, 2481–2494. [CrossRef]
8. Yang, B.; Yu, C.; Yu, Q.; Zhang, X.; Li, Z.; Lei, L. N-doped carbon xerogels as adsorbents for the removal of heavy metal ions from aqueous solution. *RSC Adv.* **2015**, *5*, 7182–7191. [CrossRef]
9. Zubizarreta, L.; Menéndez, J.A.; Job, N.; Marco-Lozar, J.P.; Pirard, J.P.; Pis, J.J.; Linares-Solano, A.; Cazorla-Amorós, D.; Arenillas, A. Ni-doped carbon xerogels for H_2 storage. *Carbon* **2010**, *48*, 2722–2733. [CrossRef]
10. Prostredny, M.; Fletcher, A.; Mulheran, P. Modelling the formation of porous organic gels—How structural properties depend on growth conditions. *RSC Adv.* **2019**, *9*, 20065–20074. [CrossRef]
11. Martin, E.; Prostredny, M.; Fletcher, A.; Mulheran, P. Modelling Organic Gel Growth in Three Dimensions: Textural and Fractal Properties of Resorcinol–Formaldehyde Gels. *Gels* **2020**, *6*, 23. [CrossRef] [PubMed]
12. Martin, E.; Prostredny, M.; Fletcher, A.; Mulheran, P. Advancing Computational Analysis of Porous Materials—Modeling Three-Dimensional Gas Adsorption in Organic Gels. *J. Phys. Chem. B* **2021**, *125*, 1960–1969. [CrossRef]
13. Wen, Z.B.; Qu, Q.T.; Gao, Q.; Zheng, X.W.; Hu, Z.H.; Wu, Y.P.; Liu, Y.F.; Wang, X.J. An activated carbon with high capacitance from carbonization of a resorcinol–formaldehyde resin. *Electrochem. Commun.* **2009**, *11*, 715–718. [CrossRef]
14. Taylor, S.J.; Haw, M.D.; Sefcik, J.; Fletcher, A.J. Gelation Mechanism of Resorcinol-Formaldehyde Gels Investigated by Dynamic Light Scattering. *Langmuir* **2014**, *30*, 10231–10240. [CrossRef] [PubMed]
15. Horikawa, T.; Hayashi, J.i.; Muroyama, K. Controllability of pore characteristics of resorcinol–formaldehyde carbon aerogel. *Carbon* **2004**, *42*, 1625–1633. [CrossRef]
16. Lin, C.; Ritter, J.A. Effect of synthesis pH on the structure of carbon xerogels. *Carbon* **1997**, *35*, 1271–1278. [CrossRef]
17. Mulik, S.; Sotiriou-Leventis, C.; Leventis, N. Time-Efficient Acid-Catalyzed Synthesis of Resorcinol−Formaldehyde Aerogels. *Chem. Mater.* **2007**, *19*, 6138–6144. [CrossRef]

18. Job, N.; Pirard, R.; Marien, J.; Pirard, J.-P. Porous carbon xerogels with texture tailored by pH control during sol–gel process. *Carbon* **2004**, *42*, 619–628. [CrossRef]
19. Sharma, C.S.; Kulkarni, M.M.; Sharma, A.; Madou, M. Synthesis of carbon xerogel particles and fractal-like structures. *Chem. Eng. Sci.* **2009**, *64*, 1536–1543. [CrossRef]
20. Calvo, E.G.; Menéndez, J.A.; Arenillas, A. Influence of alkaline compounds on the porosity of resorcinol-formaldehyde xerogels. *J. Non-Cryst. Solids* **2016**, *452*, 286–290. [CrossRef]
21. Job, N.; Gommes, C.J.; Pirard, R.; Pirard, J.-P. Effect of the counter-ion of the basification agent on the pore texture of organic and carbon xerogels. *J. Non-Cryst. Solids* **2008**, *354*, 4698–4701. [CrossRef]
22. Taylor, S.J.; Haw, M.D.; Sefcik, J.; Fletcher, A.J. Effects of Secondary Metal Carbonate Addition on the Porous Character of Resorcinol–Formaldehyde Xerogels. *Langmuir* **2015**, *31*, 13571–13580. [CrossRef]
23. Grenier-Loustalot, M.-F.; Larroque, S.; Grande, D.; Grenier, P.; Bedel, D. Phenolic resins: 2. Influence of catalyst type on reaction mechanisms and kinetics. *Polymer* **1996**, *37*, 1363–1369. [CrossRef]
24. Hofmeister, F. Zur Lehre von der Wirkung der Salze. *Arch. Exp. Pathol. Pharmakol.* **1888**, *24*, 247–260. [CrossRef]
25. Zhang, Y.; Furyk, S.; Bergbreiter, D.E.; Cremer, P.S. Specific Ion Effects on the Water Solubility of Macromolecules: PNIPAM and the Hofmeister Series. *J. Am. Chem. Soc.* **2005**, *127*, 14505–14510. [CrossRef] [PubMed]
26. Bruce, E.E.; Okur, H.I.; Stegmaier, S.; Drexler, C.I.; Rogers, B.A.; van der Vegt, N.F.A.; Roke, S.; Cremer, P.S. Molecular Mechanism for the Interactions of Hofmeister Cations with Macromolecules in Aqueous Solution. *J. Am. Chem. Soc.* **2020**, *142*, 19094–19100. [CrossRef]
27. Zhang, Y.; Cremer, P.S. Interactions between macromolecules and ions: The Hofmeister series. *Curr. Opin. Chem. Biol.* **2006**, *10*, 658–663. [CrossRef]
28. Moelbert, S.; Normand, B.; De Los Rios, P. Kosmotropes and chaotropes: Modelling preferential exclusion, binding and aggregate stability. *Biophys. Chem.* **2004**, *112*, 45–57. [CrossRef]
29. Timson, D.J. The roles and applications of chaotropes and kosmotropes in industrial fermentation processes. *World J. Microbiol. Biotechnol.* **2020**, *36*, 89. [CrossRef]
30. Schwierz, N.; Horinek, D.; Sivan, U.; Netz, R.R. Reversed Hofmeister series—The rule rather than the exception. *Curr. Opin. Colloid Interface Sci.* **2016**, *23*, 10–18. [CrossRef]
31. Mazzini, V.; Craig, V.S.J. What is the fundamental ion-specific series for anions and cations? Ion specificity in standard partial molar volumes of electrolytes and electrostriction in water and non-aqueous solvents. *Chem. Sci.* **2017**, *8*, 7052–7065. [CrossRef]
32. Barrett, E.P.; Joyner, L.G.; Halenda, P.P. The Determination of Pore Volume and Area Distributions in Porous Substances. I. Computations from Nitrogen Isotherms. *J. Am. Chem. Soc.* **1951**, *73*, 373–380. [CrossRef]
33. Brunauer, S.; Emmett, P.H.; Teller, E. Adsorption of gases in multimolecular layers. *J. Am. Chem. Soc.* **1938**, *60*, 309–319. [CrossRef]
34. Hrubesh, L.W. Aerogel applications. *J. Non-Cryst. Solids* **1998**, *225*, 335–342. [CrossRef]
35. Thommes, M.; Kaneko, K.; Neimark, A.V.; Olivier, J.P.; Rodriguez-Reinoso, F.; Rouquerol, J.; Sing, K.S.W. Physisorption of gases, with special reference to the evaluation of surface area and pore size distribution (IUPAC Technical Report). *Pure Appl. Chem.* **2015**, *87*, 1051–1069. [CrossRef]
36. Rouquerol, J.; Avnir, D.; Fairbridge, C.W.; Everett, D.H.; Haynes, J.M.; Pernicone, N.; Ramsay, J.D.F.; Sing, K.S.W.; Unger, K.K. Recommendations for the characterization of porous solids (Technical Report). *Pure Appl. Chem.* **1994**, *66*, 1739–1758. [CrossRef]
37. Langmuir, I. The Adsorption of Gases on Plane Surfaces of Glass, Mica and Platinum. *J. Am. Chem. Soc.* **1918**, *40*, 1361–1403. [CrossRef]
38. Kraiwattanawong, K.; Tamon, H.; Praserthdam, P. Influence of solvent species used in solvent exchange for preparation of mesoporous carbon xerogels from resorcinol and formaldehyde via subcritical drying. *Microporous Mesoporous Mater.* **2011**, *138*, 8–16. [CrossRef]
39. Lowell, S.; Shields, J.E.; Thomas, M.A.; Thommes, M. Micropore analysis. In *Characterization of Porous Solids and Powders: Surface Area, Pore Size and Density*; Springer: Berlin/Heidelberg, Germany, 2004; pp. 129–156.
40. ASTM-International. *ASTM D6556-17: Standard Test Method for Carbon Black—Total and External Surface Area by Nitrogen Adsorption*; ASTM-International: West Conshohocken, PA, USA, 2017. [CrossRef]